

**Analysis of novel drug target enzymes  
in *Mycobacterium tuberculosis***

A thesis submitted to The University of Manchester for the degree  
of Doctor of Philosophy  
In the Faculty of Life Sciences

**2011**

**Duyet V. Le**

## TABLE OF CONTENTS

Table of contents .....	2
List of Figures .....	7
List of Tables .....	13
Abbreviations .....	14
Abstract .....	16
Declaration .....	17
Copyright statement .....	17
Acknowledgements .....	18
<b>1 INTRODUCTION.....</b>	<b>19</b>
1.1 Tuberculosis .....	19
1.2 The global problem of TB and Multi Drug Resistant TB .....	22
1.3 Mycobacterium tuberculosis .....	23
1.4 The genome sequence of Mtb .....	26
1.5 The cytochrome P450 .....	26
1.5.1 History and general background.....	26
1.5.2 Physical properties.....	28
1.5.3 P450 location and function .....	31
1.5.4 The cytochrome P450 catalytic cycle.....	32
1.5.5 Redox partners .....	34
1.5.6 Azole inhibitors .....	38
1.5.7 Mtb P450 structures.....	41
1.5.8 Aims and objectives.....	49
<b>2 MATERIALS AND METHODS .....</b>	<b>51</b>
2.1 Growth media for <i>E. coli</i> .....	51
2.2 Antibiotics .....	52
2.3 Bacterial strains .....	52
2.4 Molecular biology .....	53
2.4.1 PCR amplification of ferredoxin ( <i>Rv1786</i> ) from Mtb .....	53
2.4.2 PCR amplification of ferredoxin reductase ( <i>Rv0688</i> ) from Mtb .....	54
2.4.3 Agarose gel electrophoresis.....	54
2.4.4 Diagnostic restriction enzyme digests .....	55
2.4.5 Extraction and purification of DNA from agarose gels.....	55
2.4.6 'A' tailing of PCR fragments.....	55

2.4.7 Cloning of PCR- and restriction digest-generated fragments into pGEM-T Easy and pET15b plasmid vector.....	56
2.4.8 Transformation of competent cells with plasmid DNA.....	57
2.4.9 Isolation of plasmid DNA.....	58
2.4.10 Automated DNA sequencing.....	58
2.5 Protein expression of histidine-tagged CYP126, CYP141, FdR, Fdx <sub>1,2</sub> , and non-histidine-tagged FLDR, and FLD .....	59
2.6 Cell Lysis .....	61
2.7 Protein Purification .....	61
2.8 Spectrophotometric analysis of purified proteins .....	62
2.9 Carbon monoxide and nitric oxide binding.....	63
2.10 Concentration determination.....	63
2.11 Hemoprotein concentration determination using the pyridine hemochromagen .....	64
2.12 Redox potentiometry.....	64
2.13 pH titration .....	65
2.14 Inhibitor binding .....	65
2.15 Differential Scanning Calorimetry.....	66
2.16 Light scattering .....	67
2.17 Mass spectrometry .....	67
2.18 Steady-state kinetics.....	68
2.19 Circular dichroism.....	68
2.20 Magnetic circular dichroism .....	69
2.21 Electron paramagnetic resonance.....	69
2.22 Stopped-flow kinetic studies.....	69
2.23 Crystallization .....	70
2.24 Reconstitution of a Mtb P450 redox partner electron transport chain .....	71
<b>3 EXPRESSION, PURIFICATION AND CHARACTERIZATION OF CYP126..</b>	<b>72</b>
3.1 Introduction.....	72
3.2 Results.....	76
3.2.1 Expression and purification of CYP126.....	76
3.2.2 Spectrophotometric analysis of CYP126.....	80
3.2.3 Pyridine hemochromagen of CYP126.....	83
3.2.4 Circular Dichroism .....	84
3.2.5 Azole inhibitor binding.....	87
3.2.5.1 Ketoconazole binding.....	87

3.2.5.2 Miconazole binding.....	89
3.2.5.3 Econazole binding.....	90
3.2.5.4 Imidazole binding.....	92
3.2.6 Redox potentiometry.....	93
3.2.7 pH effects on spectral properties of CYP126.....	96
3.2.8 Differential Scanning Calorimetry.....	99
3.2.8.1 CYP126 in the ligand-free state.....	99
3.2.8.2 DSC of CYP126 with ketoconazole bound.....	101
3.2.9 Electron paramagnetic resonance spectroscopy.....	102
3.2.9.1 EPR spectra of ligand-free CYP126.....	104
3.2.9.2 EPR spectrum of clotrimazole-bound CYP126.....	105
3.2.10 Magnetic circular dichroism.....	108
3.2.11 Mass spectrometry.....	111
3.2.12 Light scattering.....	112
3.2.13 Crystallography.....	113
3.2.13.1 Crystallization of free-ligand CYP126.....	114
3.2.13.2 Crystallization of ketoconazole-bound CYP126.....	128
3.2.14 Identification and characterization of inhibitors and substrates binding to CYP126 from a compound library screen.....	132
3.2.14.1 Identification of binding hits.....	133
3.2.14.2 Redox potentiometric analysis for CYP126 bound to a substrate-like compound from the library screen (compound 32027).....	140
3.2.14.3 EPR analysis of type I and type II binding to CYP126.....	142
3.2.14.4 Crystal structure of CYP126 in complex with compound 32027 and compound 35125.....	143
3.3 Discussion.....	145
<b>4 EXPRESSION, PURIFICATION AND CHARACTERIZATION OF CYP141</b>	<b>154</b>
4.1 Introduction.....	154
4.2 Results.....	155
4.2.1 Expression and purification of CYP141.....	155
4.2.2 Spectrophotometric characterization.....	158
4.2.3 Determination of heme absorption coefficient using the pyridine hemochromagen method.....	160
4.2.4 Circular dichroism.....	162
4.2.5 Azole inhibitor binding.....	163

4.2.5.1 Fluconazole binding .....	164
4.2.5.2 Econazole binding .....	166
4.2.5.3 Ketoconazole binding.....	167
4.2.5.4 Miconazole binding.....	169
4.2.5.5 Itraconazole binding .....	171
4.2.5.6 Clotrimazole binding.....	173
4.2.6 Redox potential determination.....	175
4.2.7 pH dependence of heme ligation in CYP141 .....	178
4.2.8 Differential Scanning Calorimetry .....	181
4.2.8.1 DSC analysis of ligand-free CYP141 .....	181
4.2.8.2 DSC analysis of clotrimazole-bound CYP141 .....	182
4.2.9 Electron paramagnetic resonance spectroscopy .....	184
4.2.10 Magnetic circular dichroism of CYP141 .....	187
4.2.11 Mass spectrometry of CYP141 .....	189
4.2.12 Light scattering analysis of CYP141 .....	190
4.2.13 Crystallography of CYP141 .....	192
4.3 Discussion.....	195
<b>5 CLONING, EXPRESSION, PURIFICATION, CHARACTERIZATION, AND FUNCTIONAL ANALYSIS OF P450 REDOX PARTNERS.....</b>	<b>204</b>
5.1 Introduction.....	204
5.2 Results.....	207
5.2.1 Cloning, expression, purification and characterization of Mtb FdR - <i>Rv0688</i> ...	207
5.2.1.1 Cloning, expression and purification of a Mtb ferredoxin reductase .....	207
5.2.1.2 General properties of FdR .....	211
5.2.1.3 Reduction of FdR by NAD(P)H .....	213
5.2.1.4 Kinetic properties of FdR .....	215
5.2.1.5 Stopped-flow (PDA) studies of FdR .....	217
5.2.1.6 Light scattering analysis of FdR.....	219
5.2.1.7 Differential Scanning Calorimetry analysis of FdR .....	220
5.2.1.8 Potentiometric analysis of FdR.....	222
5.2.2 Expression and purification of flavodoxin NADP <sup>+</sup> oxidoreductase (FLDR)....	224
5.2.3 Expression and purification of FprA .....	226
5.2.4 Expression and purification of ferredoxin (Fdx <sub>1</sub> - <i>Rv0763c</i> ) .....	228
5.2.5 Cloning, expression, purification and characterization of Mtb Fdx <sub>2</sub> - <i>Rv1786</i> .	231
5.2.5.1 Cloning, expression, and purification of Fdx <sub>2</sub> .....	231

5.2.5.2 Spectrophotometric analysis of Fdx <sub>2</sub> .....	234
5.2.5.3 Light scattering analysis of Fdx <sub>2</sub> .....	235
5.2.5.4 Circular dichroism analysis of Fdx <sub>2</sub> .....	236
5.2.5.5 Electron paramagnetic resonance analysis of Fdx <sub>2</sub> .....	238
5.2.5.6 Reduction potential determination.....	240
5.2.5.7 Crystallography of Fdx <sub>2</sub> .....	242
5.2.6 Expression and purification of FLD.....	243
5.2.7 Electron transport pathway of CYP126.....	246
5.2.7.1 Spectroscopic interactions of CYP126 with FdR and Fdx proteins.....	246
5.2.7.2 Spectroscopic analysis of the interaction of CYP126 with FLDR, using FLD and Fdx partners.....	248
5.2.7.3 Spectroscopic interactions of CYP126 with FprA and FLD/Fdx.....	252
5.2.8 Electron transport pathway of CYP141.....	256
5.2.8.1 Establishment of FdR and Fdx systems for electron transfer to CYP141.....	256
5.2.8.2 Use of FLDR-FLD/Fdx <sub>1,2</sub> as electron transport chains to CYP141.....	258
5.2.8.3 Use of FprA and FLD/Fdx <sub>1,2</sub> as an electron transfer chain for CYP141..	260
5.2.9 Reconstitution of electron transport pathways for known-substrate P450s.....	265
5.2.9.1 Electron transport pathway for CYP51B1.....	265
5.2.9.2 Electron transport systems for CYP121.....	269
5.2.9.3 Electron transport pathway for CYP125.....	272
5.2.9.4 Electron transport pathway for CYP142.....	276
5.3 Discussion.....	280
<b>6 CONCLUSIONS AND FUTURE WORK.....</b>	<b>287</b>
6.1 Biochemical and biophysical properties of CYP126, CYP141, FdR, and Fdx <sub>2</sub> .....	287
6.2 Crystal structure of CYP126 and crystallization of CYP141 and Fdx <sub>2</sub> .....	289
6.3 Electron transfer chain of Mtb P450s.....	290
6.4 Substrate and inhibitor identification of CYP126.....	290
6.5 Future work.....	291
6.5.1 Identification of products formed by substrate oxidation in CYP126.....	291
6.5.2 Determination of CYP126 structure with compounds 32027 and 35125.....	291
6.5.3 Structural determination of CYP141 by X-ray crystallography.....	292
6.5.4. Addressing the substrate specificity profile of CYP141.....	292
6.5.5 Determination of the crystal structure of Fdx <sub>2</sub> .....	293
6.6 Conclusion.....	293
<b>REFERENCES.....</b>	<b>295</b>

## LIST OF FIGURES

Figure 1.1. Chemical structure of several inhibitors used for TB treatment.....	20
Figure 1.2. The genus <i>Mycobacterium</i> is classified by heat shock protein 65 sequences ...	21
Figure 1.3. Acid-fast stain of <i>Mycobacterium tuberculosis</i> .....	23
Figure 1.4. Schematic of the <i>M. tuberculosis</i> cell envelope .....	24
Figure 1.5. Phylogeny of the bacteria .....	25
Figure 1.6. UV-visible spectra of a typical P450 enzyme.....	27
Figure 1.7. A secondary structure diagram of a P450 protein .....	29
Figure 1.8. A ribbon representation of the tertiary structure of a P450 protein (CYP126) in the closed conformation .....	30
Figure 1.9. The heme active site of substrate-free Mtb CYP126.....	31
Figure 1.10. A scheme for the catalytic cycle of cytochrome P450s.....	32
Figure 1.11. The redox reaction of NAD(P)(H) molecules .....	35
Figure 1.12. Chemical structures and reduction steps of isoalloxazine centres in FAD and FMN flavin cofactors .....	36
Figure 1.13. Iron sulfur clusters .....	37
Figure 1.14. Chemical structures of imidazole derivatives used as antifungals .....	39
Figure 1.15. Chemical structures of triazole derivatives used as antifungals.....	40
Figure 1.16. Molecular structure of CYP51B1 from <i>M. tuberculosis</i> .....	42
Figure 1.17. Mtb CYP121 structure.....	43
Figure 1.18. Crystal structure of CYP130 (PBD code 2UUQ).....	45
Figure 1.19. The dimer interface of CYP130.....	45
Figure 1.20. Overview of cholest-4-en-3-one-bound CYP125 crystal structure .....	46
Figure 1.21. The active site of CYP124 in complex with phytanic acid .....	47
Figure 1.22. Conformational features of ligand-free CYP142.....	48
Figure 2.1. Map of pGEM-T Easy vector .....	56
Figure 2.2. pET15b vector map.....	57
Figure 3.0. A diagram of the predicted purine biosynthesis pathway in <i>E. coli</i> .....	73
Figure 3.1. Organization of CYP126 and its adjacent genes in the chromosome of Mtb H37Rv .....	74
Figure 3.2. SDS gel of CYP126 trial expression in <i>Escherichia coli</i> BL21 (DE3).....	76
Figure 3.3. SDS PAGE gel of CYP126 purification trial .....	78
Figure 3.4. Purification steps of CYP126 .....	79
Figure 3.5. UV-visible absorbance spectrum of pure CYP126.....	80
Figure 3.6. UV-visible spectrum of Mtb CYP126 on reaction with carbon monoxide .....	81
Figure 3.7. UV-visible spectrum of CYP126 bound to NO.....	82
Figure 3.8. Pyridine hemochromagen spectra of CYP126.....	83

Figure 3.9. Far UV CD spectrum for CYP126.....	85
Figure 3.10. Near UV-visible CD spectrum for CYP126.....	86
Figure 3.11. Binding of ketoconazole to CYP126.....	88
Figure 3.12. Titration curve for the binding of ketoconazole to CYP126.....	89
Figure 3.13. Binding of miconazole to CYP126.....	90
Figure 3.14. Titration curve for the binding of miconazole to CYP126.....	90
Figure 3.15. Binding of econazole to CYP126.....	91
Figure 3.16. Titration curve for the binding of econazole to CYP126.....	91
Figure 3.17. Binding of imidazole to CYP126.....	92
Figure 3.18. Titration curve for the binding of imidazole to CYP126.....	92
Figure 3.19. Spectroelectrochemical redox titration of CYP126.....	94
Figure 3.20. Plot of change in Soret absorbance against applied potential for CYP126.....	95
Figure 3.21. pH dependence of the UV-visible spectrum of CYP126 in the ferrous (Fe <sup>II</sup> ) state.....	97
Figure 3.22. Plot of data from pH titration of the CYP126 Fe <sup>II</sup> form.....	98
Figure 3.23. DSC analysis of ligand-free CYP126.....	100
Figure 3.24. DSC analysis of ketoconazole-bound CYP126.....	101
Figure 3.25. Superimposed DSC curves for CYP126 in ligand-free and ketoconazole-bound forms.....	102
Figure 3.26. EPR spectrum obtained for ligand-free CYP126.....	105
Figure 3.27. EPR spectrum obtained for ketoconazole-bound CYP126.....	106
Figure 3.28. Divergent EPR signals observed in overlaid spectra for ligand-free and ketoconazole-bound forms of CYP126.....	107
Figure 3.29. MCD spectra for CYP126.....	109
Figure 3.30. The MCD spectrum for CYP126 in the near IR region.....	110
Figure 3.31. Mass spectrometry of CYP126 using a Waters LCT Mass spectrometer.....	111
Figure 3.32. Superdex – 200 10/300 GL gel filtration chromatography and MALLS analysis of CYP126.....	112
Figure 3.33. Native crystals of CYP126.....	114
Figure 3.34. A representative X-ray diffraction image obtained from CYP126 crystals..	115
Figure 3.35. Overall view of CYP126.....	116
Figure 3.36. A surface representation of CYP126.....	117
Figure 3.37. A detailed view of the dimerization interface of CYP126.....	118
Figure 3.38. Superimposition of the ligand-free (closed) and imidazole-bound (open) CYP126 monomers.....	120
Figure 3.39. Open-open conformational form of CYP126.....	121
Figure 3.40. Closed-closed conformational form of CYP126.....	121

Figure 3.41. Divergent stereo view of an overlay of both open–open and closed–closed forms of CYP126 .....	122
Figure 3.42. Structural alignment of the CYP126 closed form with CYP51B1, CYP121, CYP130, CYP124 and CYP125 crystal structures .....	123
Figure 3.43. Active site pocket of CYP126 (closed form).....	125
Figure 3.44. Detailed view of the active site of the open form of CYP126.....	126
Figure 3.45. An overlay of the active sites of the closed and open CYP126 monomers...	127
Figure 3.46. Native crystals of ketoconazole-bound CYP126.....	128
Figure 3.47. Overall view of CYP126 ketoconazole-bound complex .....	130
Figure 3.48. Superimposition of the ligand-free (closed) and ketoconazole-bound (open) CYP126 monomers .....	131
Figure 3.49. An overlay of the active sites of the ligand-free and ketoconazole-bound CYP126 monomers.....	132
Figure 3.50. The difference spectra produced by subtraction of the ligand-free CYP126 spectrum from successive spectra for both type I and type II bound species	134
Figure 3.51. Type I high throughput screen hits for CYP126.....	135
Figure 3.52. Chemical structures of chloramphenicol and azidamphenicol .....	137
Figure 3.53. CYP126 spectral titration with compound 32027 .....	137
Figure 3.54. Type II high throughput hits for CYP126 .....	138
Figure 3.55. CYP126 spectral titration with compound 35125 .....	139
Figure 3.56. Potentiometric titration for CYP126 bound to substrate-like compound 32027 .....	141
Figure 3.57. EPR spectra of CYP126 in complex with compounds 32027 and 35125 .....	142
Figure 3.58. Co-crystallization of CYP126 with compounds 32027 and 35125 .....	144
Figure 4.1.1. SDS PAGE gel of CYP141 trial expression in <i>Escherichia coli</i> BL21 cells	155
Figure 4.1.2. SDS PAGE gel of CYP141 trial purification in <i>Escherichia coli</i> BL21 cells	156
Figure 4.2. SDS PAGE gel of CYP141 expression and purification by Ni-NTA column chromatography .....	157
Figure 4.3. SDS PAGE gel analysis of CYP141 protein purification steps using a Q-Sepharose column.....	157
Figure 4.4. Electronic absorption spectra for pure CYP141 .....	158
Figure 4.5. UV-visible spectrometry of CO-bound CYP141.....	159
Figure 4.6. UV-visible spectrometry of NO-bound CYP141 .....	160
Figure 4.7. Pyridine hemochromagen spectra of CYP141.....	161
Figure 4.8. Far UV CD spectrum for CYP141.....	162
Figure 4.9. Near UV-visible CD spectrum of CYP141 .....	163
Figure 4.10. Binding of fluconazole to CYP141 .....	164
Figure 4.11. Titration curve for the binding of fluconazole to CYP141.....	165
Figure 4.12. Binding of econazole to CYP141 .....	166

Figure 4.13. Titration curve for the binding of econazole to CYP141 .....	167
Figure 4.14. Binding of ketoconazole to CYP141 .....	168
Figure 4.15. Titration curve for the binding of ketoconazole to CYP141 .....	169
Figure 4.16. Binding of miconazole to CYP141 .....	170
Figure 4.17. Titration curve for the binding of miconazole to CYP141 .....	171
Figure 4.18. Binding of itraconazole to CYP141 .....	172
Figure 4.19. Titration curve for the binding of itraconazole to CYP141 .....	173
Figure 4.20. Binding of clotrimazole to CYP141 .....	174
Figure 4.21. Titration curve for the binding of clotrimazole to CYP141 .....	175
Figure 4.22. UV-vis spectra of CYP141 during redox titration.....	176
Figure 4.23. Plot of absorbance change versus potential ( $E'$ , mV versus NHE) during reductive titration .....	177
Figure 4.24. pH dependence of the optical properties of CYP141 in its reduced form.....	179
Figure 4.25. The influence of pH on the spectrum of the ferric CYP141 enzyme .....	180
Figure 4.26. Determination of the midpoint pH ( $pK_a$ ) for the ferrous heme optical transition in CYP141 .....	181
Figure 4.27. DSC analysis of ligand-free CYP141 .....	182
Figure 4.28. DSC analysis of the clotrimazole-bound form of CYP141 .....	183
Figure 4.29. Superimposed DSC thermograms for ligand-free and clotrimazole-bound CYP141 .....	183
Figure 4.30. EPR spectrum obtained for solution state ligand-free CYP141 .....	185
Figure 4.31. EPR spectrum obtained for solution state clotrimazole-bound CYP141.....	186
Figure 4.32. EPR spectra overlaid for solution state ligand-free CYP141 (red) and for the clotrimazole-bound form (blue).....	187
Figure 4.33. MCD and optical spectra for CYP141 .....	188
Figure 4.34. The MCD spectrum for CYP141 in the near IR region.....	189
Figure 4.35. Mass spectrum of CYP141 using a Waters LCT Mass spectrometer.....	190
Figure 4.36. Superdex–200 10/300 GL gel filtration chromatography and MALLS analysis of CYP141 .....	191
Figure 4.37. Crystals of CYP141 grown in 0.2 M $MgCl_2$ , 0.1 M Tris-HCl, pH 8.5, 15% (w/v) PEG 4000 .....	192
Figure 4.38. Crystals of CYP141 grown in 1 M lithium chloride, 0.1 M Bicine, 10% (w/v) PEG 6000 .....	193
Figure 4.39. A representative X-ray diffraction pattern of CYP141 crystals .....	194
Figure 5.1. PCR amplification of <i>Rv0688</i> .....	207
Figure 5.2. Digestion products of a recombinant pET15b vector containing the <i>Rv0688</i> gene .....	208
Figure 5.3. SDS-PAGE gel of FdR trial expression in <i>Escherichia coli</i> HMS174 (DE3) cells.....	209

Figure 5.4. SDS-PAGE gel of FdR trial purification in HMS174 (DE3).....	210
Figure 5.5. SDS-PAGE gel of large scale purification scheme for FdR.....	210
Figure 5.6. Ultraviolet-visible absorbance spectra of pure FdR .....	211
Figure 5.7. Re-oxidation of FdR under aerobic conditions.....	213
Figure 5.8. UV-visible spectra of Mtb FdR (45 $\mu$ M) during reduction by NAD(P)H.....	214
Figure 5.9. Steady-state kinetics of NADH- and NADPH-dependent ferricyanide reduction in FdR.....	216
Figure 5.10. PDA UV-vis absorption spectra for oxidative, reductive reactions of FdR ..	218
Figure 5.11. Superdex–200 10/300 GL gel filtration chromatography and MALLS analysis of Mtb FdR .....	220
Figure 5.12. DSC analysis of Mtb FdR.....	221
Figure 5.13. UV-visible spectra of Mtb FdR during redox titration .....	223
Figure 5.14. Analysis of potentiometric data for FdR .....	224
Figure 5.15. SDS-PAGE analysis of <i>E. coli</i> flavodoxin NADP <sup>+</sup> oxidoreductase (FLDR) purification steps .....	225
Figure 5.16. UV-vis spectrum of <i>E. coli</i> FLDR.....	226
Figure 5.17. SDS–PAGE analysis of FprA protein purification steps using a Q-Sepharose column.....	227
Figure 5.18. Electronic absorption spectrum of purified FprA and its dithionite-reduced form .....	228
Figure 5.19. Purification of recombinant Fdx <sub>1</sub> (Rv0763c) as analyzed by SDS-PAGE....	229
Figure 5.20. Electronic absorption spectrum of purified Fdx <sub>1</sub> .....	230
Figure 5.21. PCR products of the Mtb <i>Rv1786</i> gene .....	231
Figure 5.22. Digestion products of a recombinant pET15b vector containing the <i>Rv1786</i> gene.....	232
Figure 5.23. SDS-PAGE of Fdx <sub>2</sub> trial expression in <i>Escherichia coli</i> HMS174 cells.....	233
Figure 5.24. SDS-PAGE of the purified Fdx <sub>2</sub> .....	234
Figure 5.25. UV-visible spectra of Mtb-Fdx2 in its oxidized and reduced forms .....	235
Figure 5.26. Oligomerization status of Fdx <sub>2</sub> .....	236
Figure 5.27. CD spectroscopic analysis of Mtb Fdx <sub>2</sub> in the far UV region .....	237
Figure 5.28. CD spectrum of Mtb Fdx <sub>2</sub> in the near UV-visible region.....	238
Figure 5.29. EPR spectroscopic analysis of Mtb Fdx <sub>2</sub> .....	239
Figure 5.30. Potentiometric titration of Mtb Fdx <sub>2</sub> .....	241
Figure 5.31. Plot of proportion of Mtb Fdx <sub>2</sub> reduced versus potential (E', mV) during reductive titration .....	242
Figure 5.32. Native crystals of Mtb Fdx <sub>1</sub> .....	243
Figure 5.33. SDS-PAGE of <i>E. coli</i> flavodoxin purification steps .....	244
Figure 5.34. Spectral properties of FLD in its different redox states.....	245

Figure 5.35. Fe(II)CO complex formation in CYP126 with redox partners FdR and Fdx <sub>1</sub>	247
Figure 5.36. Fe(II)CO complex formation in CYP126 with FdR+Fdx <sub>2</sub>	248
Figure 5.37. Fe(II)CO complex formation in CYP126 with FLDR and FLD	249
Figure 5.38. Fe(II)CO complex formation in CYP126 (4 μM) with FLDR and Fdx <sub>1</sub>	250
Figure 5.39. Fe(II)CO complex formation in CYP126 with FLDR and Fdx <sub>2</sub>	251
Figure 5.40. Fe(II)CO complex formation in CYP126 with FprA and FLD proteins	253
Figure 5.41. Fe(II)CO complex formation in CYP126 with FprA and Fdx <sub>1</sub>	254
Figure 5.42. Fe(II)CO complex formation in CYP126 with FprA and Fdx <sub>2</sub>	255
Figure 5.43. Fe(II)CO complex formation in CYP141 using Fdx <sub>1</sub> and FdR	256
Figure 5.44. Fe(II)CO complex formation in CYP141 using Fdx <sub>2</sub> and FdR	257
Figure 5.45. Fe(II)CO complex formation in CYP141 with FLDR and FLD	258
Figure 5.46. Fe(II)CO complex formation in CYP141 with FLDR and Fdx <sub>1</sub>	259
Figure 5.47. Fe(II)CO complex formation in CYP141 with FLDR and Fdx <sub>2</sub>	260
Figure 5.48. Fe(II)CO complex formation in CYP141 with FprA and FLD	261
Figure 5.49. Fe(II)CO complex formation in CYP141 with FprA and Fdx <sub>1</sub>	262
Figure 5.50. Fe(II)CO complex formation in CYP141 with FprA and Fdx <sub>2</sub>	263
Figure 5.51. Reconstitution of Mtb redox systems and electron transfer to CYP51B1	266
Figure 5.52. The reduction of estriol-bound CYP51B1 using an FdR-Fdx <sub>1</sub> electron transfer system	267
Figure 5.53. The reduction of estriol-bound CYP51B1 using an FdR-Fdx <sub>2</sub> electron transfer system	268
Figure 5.54. A redox system for CYP121 using FdR-Fdx <sub>2</sub>	269
Figure 5.55. Fe(II)CO complex formation in cYY-bound CYP121 using FdR and Fdx <sub>1</sub> redox partner enzymes	270
Figure 5.56. Reduction of CYP121 by the FdR-Fdx <sub>2</sub> system	271
Figure 5.57. Reduction of cYY-bound CYP121 by the FdR-Fdx <sub>2</sub> system	272
Figure 5.58. Reduction of substrate-free CYP125 using the FdR-Fdx <sub>1</sub> electron transfer system	273
Figure 5.59. Reduction of cholesterol-bound CYP125 using the FdR-Fdx <sub>1</sub> electron transfer system	274
Figure 5.60. Reduction of substrate-free CYP125 by the FdR-Fdx <sub>2</sub> system	275
Figure 5.61. Reduction of cholesterol-bound CYP125 by FdR-Fdx <sub>2</sub>	276
Figure 5.62. Anaerobic reduction of substrate-free CYP142 by the FdR-Fdx <sub>1</sub> system in the presence of CO	277
Figure 5.63. Reduction of cholesterol-bound CYP142 by the FdR-Fdx <sub>1</sub> system	278
Figure 5.64. Schemes of electron flow for Mtb P450s' Fe(II)CO complex formation	285

## LIST OF TABLES

Table 3.1. $K_d$ values for the binding of various azole drugs to the seven Mtb P450s characterized to date .....	75
Table 3.2. Summary purification steps for native CYP126 in 1 litre culture .....	79
Table 3.3. Dissociation constants for azole drugs binding to CYP126.....	93
Table 3.4. Summary of the thermodynamic data for CYP126.....	102
Table 3.5. X-ray data collection and refinement statistics for ligand-free CYP126.....	115
Table 3.6. The values of dissociation constants of the three selected library compounds for type I binding to CYP126.....	136
Table 3.7. The values of dissociation constants of the three selected library compounds for type II binding to CYP126.....	140
Table 3.8. Summary of a comparison of the CYP126 dissociation constant values.....	147
Table 4.1. Summary of dissociation constants for azole drugs binding to CYP141.....	175
Table 4.2. Summary of the thermodynamic data for CYP141 from DSC analysis .....	184
Table 4.3. Comparison of the azole dissociation constant values for Mtb P450s.....	197
Table 5.1. Steady-state kinetic parameters for wild-type FdR.....	216
Table 5.2. Calorimetrically derived thermodynamic parameters for unfolding of FdR ....	222
Table 5.3. Summary of the rate constants for CYP141/CYP126 Fe(II)CO complex Formation using different redox partner systems.....	264
Table 5.4. Rate constants for Fe(II)CO complex formation by the reconstituted FdR - Fdx <sub>1</sub> , <sub>2</sub> - P450 (CYP51B1, CYP121, CYP125, CYP142) systems.....	279

## ABBREVIATIONS

Amp	Ampicillin
AIDS	Acquired Immunodeficiency Syndrome
ATP	Adenosine Triphosphate
ACN	Acetonitrile
BCG	Bacillus Calmette-Guerin
BV	Benzyl Viologen
BSA	Bovine Serum Albumin
Bp	Base pair
CO	Carbon Monoxide
CYP	Cytochrome P450
CPR	Cytochrome P450 Reductase
Carb	Carbenicillin
Cm	Chloramphenicol
CTP	Cytosine Triphosphate
CD	Circular Dichroism
DMSO	Dimethyl Sulfoxide
DSC	Differential Scanning Calorimetry
DNA	Deoxyribonucleic Acid
DTT	Dithiothreitol
EDTA	Ethylenediaminetetraacetic Acid
EPR	Electron Paramagnetic Resonance
FAD	Flavin Adenine Dinucleotide
FMN	Flavin Mononucleotide
Fdx	Ferredoxin
Fe-S	Iron Sulfur
FDR	Ferredoxin Reductase
FLDR	Flavodoxin Reductase
FprA	Flavoprotein Reductase A
G + C	Guanine and Cytosine
HIV	Human Immunodeficiency Virus
HS	High spin
HNQ	2-hydroxy-1,4-naphthoquinone
IPTG	Isopropyl- $\beta$ -D-thio-galactoside
JCSG	Joint Centre for Structural Genomics

Kan	Kanamycin
kDa	kilo Dalton
LS	Low Spin
LB	Luria Bertani
Mtb	<i>Mycobacterium tuberculosis</i>
MV	Methyl Viologen
MCD	Magnetic Circular Dichroism
NADP	Nicotinamide Adenine Dinucleotide Phosphate
NADPH	NADP (reduced form)
NO	Nitric Oxide
NMR	Nuclear Magnetic Resonance
NTP	Nucleotide Triphosphate
OD	Optical Density
PCR	Polymerase Chain Reaction
PDA	Photodiode Array
PDB	Protein Data Bank
PMS	Phenazine Methosulfate
PEG	Polyethylene Glycol
Rif	Rifampicin
RNA	Ribonucleic Acid
SOC	Super Optimal Broth
SER	Smooth Endoplasmic Reticulum
SDS-PAGE	Sodium Dodecyl Sulfate Polyacrylamide Gel Electrophoresis
SDS gel	Sodium Dodecyl Sulfate gel
TB	Tuberculosis
Tet	Tetracycline
TAE	Tris Acetate EDTA
TE	Tris-EDTA
TOF	Time Of Flight
TTP	Thymidine Triphosphate
UV	Ultraviolet
YT	Yeast Tryptone
WHO	World Health Organization

## ABSTRACT

CYP126 and CYP141 are novel cytochrome P450 (CYP, P450) proteins from the human pathogen *Mycobacterium tuberculosis* (Mtb). In this thesis, both proteins were successfully expressed and characterized spectroscopically, kinetically, and structurally. UV-visible spectroscopy, magnetic circular dichroism (MCD) and electron paramagnetic resonance (EPR) showed that CYP126 is a normal P450 enzyme with the major oxidized heme (Soret) band at 418 nm, shifting to 450 nm (hence P450) after heme iron reduction and CO binding. In contrast, CYP141 has distinct properties, including a mixture of high-spin and low-spin ferric heme iron states and a Soret band shift to 440 nm on binding CO, instead of the typical P450 shift to 450 nm. Reduction potential analysis showed that CYP126 has a quite negative potential (-332 mV vs. NHE), comparable to certain other substrate-free Mtb and bacterial P450s, whereas CYP141 has an extremely positive potential (-50 mV) that is approximately 300 mV higher than those of other Mtb P450s. Both enzymes bind to a range of imidazole and triazole antifungal drugs, inducing a type II (red) spectral shift of the ferric heme iron. CYP126 and CYP141 were successfully crystallized, as was the Mtb ferredoxin Fdx<sub>2</sub> – the latter expressed and purified as a potential Mtb P450 redox partner. The CYP126 crystal structure was solved, exhibiting a dimer with one monomer in the “open” form (with respect to active site access) and the other in the “closed” form. The structure of the CYP126-ketoconazole complex was also determined by X-ray crystallography, revealing a monomeric P450 in the crystal and with the ketoconazole imidazole nitrogen ligated directly to the heme iron, replacing a water molecule found as the heme iron distal ligand in the resting form of CYP126. To reconstitute an electron transport system supporting CYP141 and CYP126, endogenous (FprA and FdR flavoprotein dehydrogenases, Fdx<sub>1</sub> and Fdx<sub>2</sub> ferredoxins) and exogenous (*E. coli* FLDR flavoprotein dehydrogenase and FLD flavodoxin) redox partner proteins were successfully cloned, expressed and purified, and reconstituted with CYP126, CYP141, and other characterized Mtb P450s. These redox partner proteins successfully mediated electron transport from NAD(P)H to Mtb P450s, with exogenous redox partners typically revealing higher electron transfer rates than Mtb redox partner proteins. Compound screening for CYP126 allowed identification of several inhibitors and potential substrates from a library of 20,000 organic molecules. Approximately 30 compounds were identified based on their inducing good type I or type II binding spectra. CYP126 interactions with one of the top type I hits (compound 32027) and the top type II hit (compound 35125) were analyzed biochemically and biophysically. UV-visible and EPR spectroscopy showed that compound 32027 binding to CYP126 induced accumulation of high-spin ferric heme iron, consistent with type I binding, and elevated the heme iron redox potential from -332 mV to -176 mV, accelerating electron transfer from redox partners to CYP126. The CYP126 complexes with compounds 32027 and 35125 were successfully crystallized, leading to structural analysis.

## **Declaration**

No portion of the work referred to in this thesis has been submitted in support of an application for another degree or qualification of this or any other university or other institute of learning.

## **Copyright Statement**

- i. The author of this thesis (including any appendices and/or schedules to this thesis) own any copyright in it (the “Copyright”) and s/he has given The University of Manchester the right to use such Copyright for any administrative, promotional, educational and/or teaching purposes.
- ii. Copies of this thesis, either in full or in extracts, may be made only in accordance with the regulations of the John Rylands University Library of Manchester. Details of these regulations may be obtained from the Librarian. This page must form part of any such copies made.
- iii. The ownership of any patents, designs, trade marks and any and all other intellectual property rights except for the Copyright (the “Intellectual Property Rights”) and any reproductions of copy right works, for example graphs and tables (“Reproductions”), which may be described in this thesis, may not be owned by the author and may be owned by third parties. Such Intellectual Property Rights and Reproductions cannot and must not be made available for use without the prior written permission of the owner(s) of the relevant Intellectual Property Rights and/or Reproductions.
- iv. Further information on the conditions under which disclosure, publication and exploitation of this thesis, the Copyright and any Intellectual Property Rights and/or Reproductions described in it may take place is available from the Head of (or the Vice-President) and the Dean of the Faculty of Life Sciences, for faculty of Life Sciences’s candidates.

## ACKNOWLEDGMENTS

I would like to thank my supervisor, Prof. Andrew Munro, for giving me an opportunity to study in his laboratory. His knowledge, continued patience, understanding, personal guidance, enthusiasm and encouragement have been of great value for the accomplishment of my PhD project.

My thanks must go to Vietnamese Government and Vietnam Education and Training, who provided almost funding for my PhD. I also greatly appreciated the financial supports from Prof. Andrew Munro and Faculty of Life Sciences - The University of Manchester, for paying the shortfall of the tuition fees.

I would like to send a huge thanks to Dr. Kirsty Mclean for teaching me. I sincerely appreciate her great deal of help, endless patience and advice during my time in the lab.

I wish to express my gratitude to Prof. David Leys and Dr Colin Levy, who taught me crystallography and solved the crystal structure of CYP126, and also to a number of other people including Dr. Stephen Rigby for assistance with EPR, Dr. Thomas Jowitt/Mrs Marjorie Howard for MALLS and DSC, Mr. Reynard Spies for ISI-MS, and Dr. Hazel Girvan for MCD analysis.

My thanks go out to my friends and colleagues in the Munro, Scrutton, and Leys groups for all their help, discussions, and communication.

Finally, I would like to thank my family, my parents, and my wife who give me a great support and understanding for my studies in Manchester.

# 1 INTRODUCTION

## 1.1 Tuberculosis

Mycobacteria appeared on the earth about 150 million years ago and began presenting in the community of Egypt from 2400 B.C (1). The descriptive name of tuberculosis (phthisis) was mentioned in Greek literature in 460 BC, which identified tuberculosis as the most dangerous and widespread disease at that time (2, 3). However, after thousands of years the exact TB infection phenomena were described in the seventeenth century by Sylvius and other physicians (4). In the late nineteenth century, a German physician, Robert Koch, found a staining method to inspect *Mycobacterium tuberculosis* (Mtb) morphology visually, and it was determined as the causative agent of TB, and he was presented the Nobel prize for his findings in 1905 (5). A further important event was provided by the French bacteriologist and veterinarian, Calmette and Guerin, who used specific culture media to produce the bovine tuberculosis bacterium with very low virulence, creating the BCG vaccine, which is a unique vaccine for TB prevention to date (6).

However, this vaccine was not used for TB prevention in the community due to initial opposition and thus did not prevent increases in infection and of cases of TB, the numbers of which peaked in the middle of World War II (7). At that time, a new therapeutic method for treatment of TB was proposed by the use of sulfonamide and penicillin (Figure 1.1), but these drugs were ineffective and unable to prevent Mtb infection (8), leading to a pressure to discover new drugs with better inhibitory efficiency. In 1940, a potent drug against TB, actinomycin (Figure 1.1), was isolated from an actinomycete soil bacterium (9). However, this antibiotic was very toxic, and was not used for human or animal treatments (10). Three years later, an antibiotic was isolated from *Streptomyces griseus*, streptomycin, and had excellent potency against Mtb without side effects (11). In the subsequent years, the discovery of new anti-TB drugs was rapidly successful, but the resistance to these individual compounds began to appear within a short time following any monotherapeutic treatment (12). However, the drug-resistant bacteria could be treated by the use of several drug mixtures. Since then, many effective antibiotics have been isolated, such as *p*-aminosalicylic acid (1949), isoniazid (1952), pyrazinamide (1954), cycloserine (1955), ethambutol (1962) and rifampicin (1962) (Figure 1.1). These have played, and still do play, a central role as therapeutics for infection with TB (13, 14).

The *Mycobacterium tuberculosis* complex, which includes a number of mycobacteria, is the major causative agent of TB in humans and animals (15, 16) (Figure 1.2). The predominant pathogen in humans is *Mycobacterium tuberculosis* (Mtb), the genome of which was

sequenced in 1998 and revealed some unusual features relating to lipid metabolism, including an abundance of cytochrome P450-encoding genes (17). *Mycobacterium bovis* causes TB in bovine species, and it was a common cause of human TB before milk was sterilised by the Pasteur method (18). Another member of the complex is *Mycobacterium africanum*, causing TB in Africa (16). In addition, *Mycobacterium microti* is the pathogen that is responsible for TB in voles, wood mice and shrews (19), and the host infection and transmission mode of *Mycobacterium canetti* are still unknown (20).

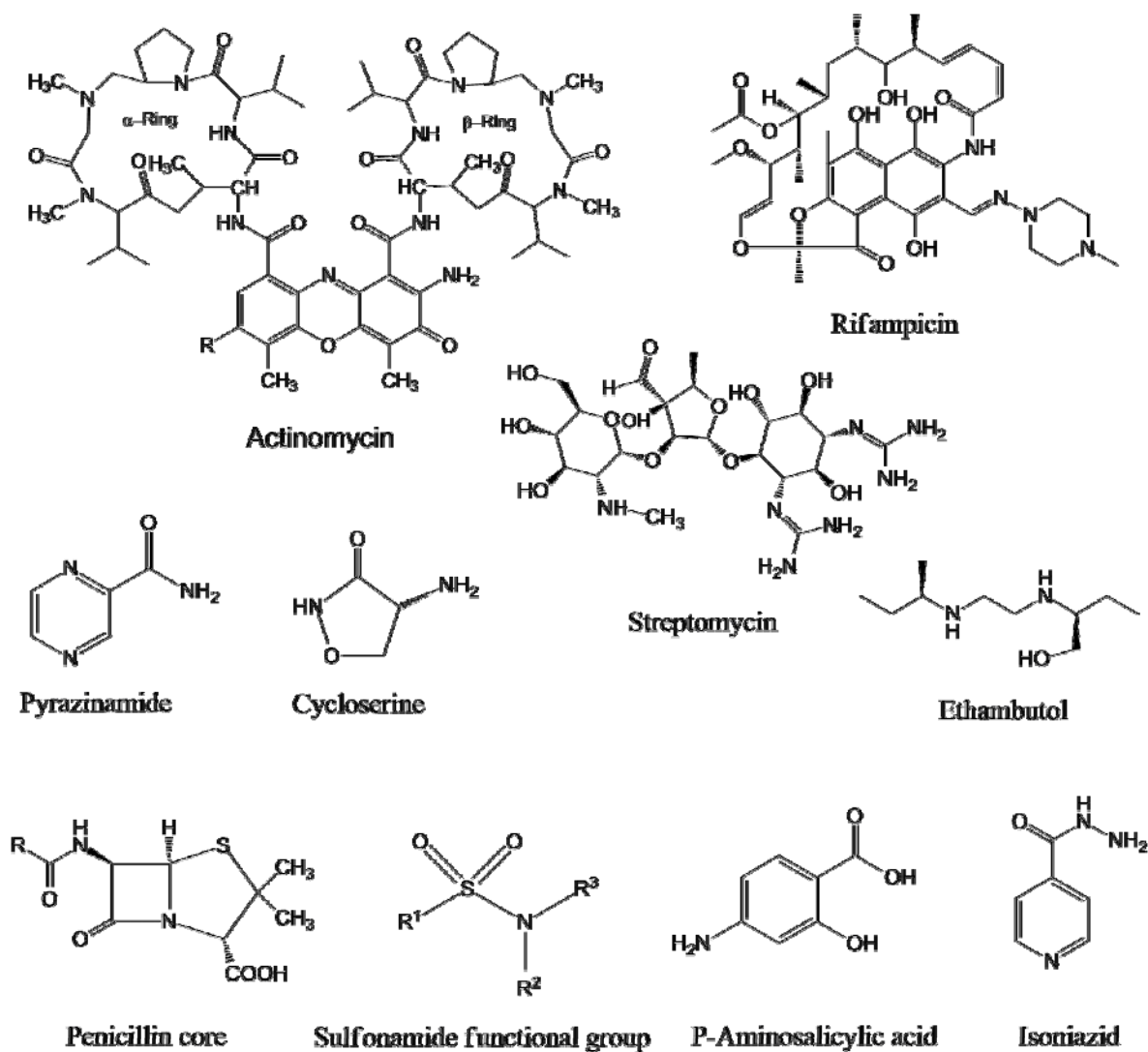


**Figure 1.1. Chemical structures of several inhibitors used for TB treatment**  
Figure redrawn from images shown at <http://en.wikipedia.org>



**Figure 1.2.** The genus *Mycobacterium* is classified by heat shock protein 65 sequences (21). Heat shock proteins 65 are major immunoreactive proteins of mycobacteria. The phylogenetic tree presents different groups of mycobacteria that have similar Hsp65 sequences, as indicated by the various numbers. The red box shows a complex of mycobacteria that cause tuberculosis in humans and animals, including *M. africanum*, *M. bovis*, *M. microti*, *M. tuberculosis* and *M. caprae*.

TB is the second most dangerous infectious disease after human immunodeficiency virus (HIV), with around 30 percent of the world's population estimated to be infected with Mtb

(22). Currently, the BCG (Bacillus Calmette-Guerin) vaccine is the only vaccine available for TB prevention (8). It is a live *M. bovis* strain that was attenuated by sub-culturing in a glycine-bile-potato mixture media in order to obtain less virulent forms (23). Although the BCG vaccine is still used to prevent TB infection, more and more drug-resistant strains are being isolated. This demands fresh investigations into drug discovery and drug design to control TB. The sequencing of the Mtb genome, and continued efforts to understand its biology should contribute to the greater understanding of pathological mechanisms, and provide possible targets for new drugs (24).

## **1.2 The global problem of TB and Multi Drug Resistant TB**

The data from the World Health Organization (WHO) showed that TB was not in decline in many developed countries, but that the number of incidences was actually increasing. This requires scientists to expand research to discover new potent drugs for TB treatment (25). In some regions, notably Africa and Asia, the cases of TB infection have increased tremendously in the past few decades, and it is widely considered that TB is now beyond the control of the relevant health organizations (26). To respond to this alarm, in the early 1990s, the WHO warned of the spread of TB and drug- and multidrug-resistant (MDR) strains of Mtb, and the resultant danger to the health of humanity (27). In spite of efforts in the treatment of TB, numerous new cases with TB infection were detected, and a significant proportion of the world's population (around one third) is known to be infected with Mtb. The therapy for TB takes a long time (on average 6 months of treatment), and involves using a mixture of many types of antibiotics to overcome drug resistance. Thus, the cost of TB treatment has increased several times over recent years. The TB treatment for the majority of patients in underdeveloped countries is therefore often not completed due to the high cost of the drugs (particularly in poor areas) as well as due to patient non-compliance. The disruption in treatment of TB is a major reason leading to drug-resistance (28).

Multidrug resistant tuberculosis (MDR TB) is a survival phenomenon of mycobacteria during exposure to many antibiotics, and this is especially true in relation to Mtb isoniazid and rifampicin resistance (29). In this type of case, it is very difficult to produce effective treatment for patients. To treat MDR TB effectively, the treatment time needs to be extended, and combined with the use of antibiotic mixtures (30). In some areas of the world, the proportion of TB drug resistance in Mtb strains is up to 50% (13).

### 1.3 *Mycobacterium tuberculosis*

**Characteristics:** Mtb is an acid-fast Gram-positive, obligate aerobic, rod-shaped, non-motile bacterium (Figure 1.3) (31). Bacilli are found in different sizes and shapes. The rods are normally 2-5 micrometres in length and 0.2-0.4 micrometres in width (32), (33). Due to their obligate aerobic characteristics, the bacteria are often found surviving in an oxygen rich area like the lungs. Unlike some fast growing organisms, Mtb is rarely pleomorphic, and no filaments or branch chained cell types are isolated. Specifically, under the microscope, the appearance of Mtb does not allow one to distinguish between the pathogenic agent Mtb and other mycobacteria, although some characteristics are given to identify Mtb among other mycobacteria (34).

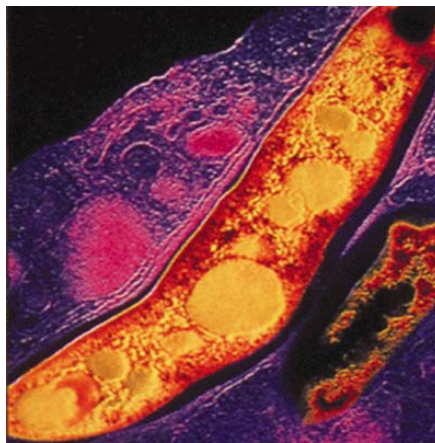


**Figure 1.3. Acid-fast stain of *Mycobacterium tuberculosis***

The purple indicates Mtb's cell wall and the yellow is Mtb's endoplasm. Image taken from <http://www.bact.wisc.edu/> University of Wisconsin-Madison.

It is clearly seen in Figure 1.4 that the Mtb cell envelope contains a thick peptidoglycan layer and no phospholipid outer membrane, which is quite different from the usual Gram-negative and Gram-positive cell wall structures. Because of the unusual cell wall, the bacterium is not stained effectively with typical Gram stain reagents, since layers of lipids surrounding the peptidoglycan in the mycobacterium are quite thick. Commonly, Gram-negative bacteria have approximately 5-20% lipid content by weight. In contrast, *M. tuberculosis* possesses a special cell envelope which contains approximately 60% lipids, showing a very large percentage for this component part of the bacterium. Among these lipids, mycolic acids account for the majority of the content. This special envelope prevents the penetration of many antibiotics and therefore aids Mtb bacterial survival from the host response and drug treatments (35). Thus, the complicated cell wall plays a key role for the viability of Mtb, and therefore proteins that are involved in the biosynthesis of the cell wall may be identified as potential new drug targets.

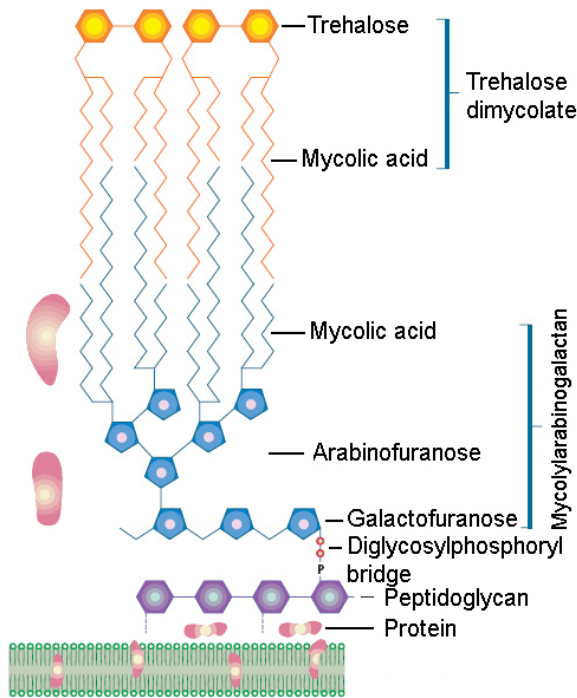


**Figure 1.4. Schematic of the *M. tuberculosis* cell envelope**

The Mtb cell wall structure with key components of the cell membrane and its waxy outer envelope are shown. The thick mycolic acid layer is in red. Different components of the cell wall are labelled and colour/shape coded (36).

### **Classification:**

According to Bergey's Manual of Systematic Bacteriology (*Bergey's Manual of Systematic Bacteriology* 2<sup>nd</sup> edition, volume 1), *Mycobacterium tuberculosis* is classified as follows: Kingdom – bacteria, phylum – actinobacteria, class – actinobacteria, order – actinomycetales, family – mycobacteriaceae, genus – *Mycobacterium*, and species – *tuberculosis*.

*Mycobacterium tuberculosis* belongs to the kingdom Bacteria that possess thick cell walls and do not contain nuclei (37). The phylum Actinobacteria is classified by the dominant characteristics of Gram-positive bacteria with a high guanine–cytosine (G-C) percentage of the DNA (Figure 1.5) (38). While many actinobacteria exhibit metabolic diversity and are non-pathogenic to humans, other actinobacteria are pathogens of plants and animals. Moreover, *M. tuberculosis* is grouped in the order Actinomycetales due to its rigid and rod-shaped characteristics. The sub-order Corynebacterineae possess a typical Gram-positive cell wall (39). The family Mycobacteriaceae is defined by unbranched cells with a form of mycelium (40). The genus *Mycobacterium* belongs to the Mycobacteriaceae family, which show slow-growing and acid-fast staining characteristics (41). The *Mycobacterium* species

*tuberculosis* is distinct from most other *Mycobacterium* species due to its pathogenic characteristics (32).

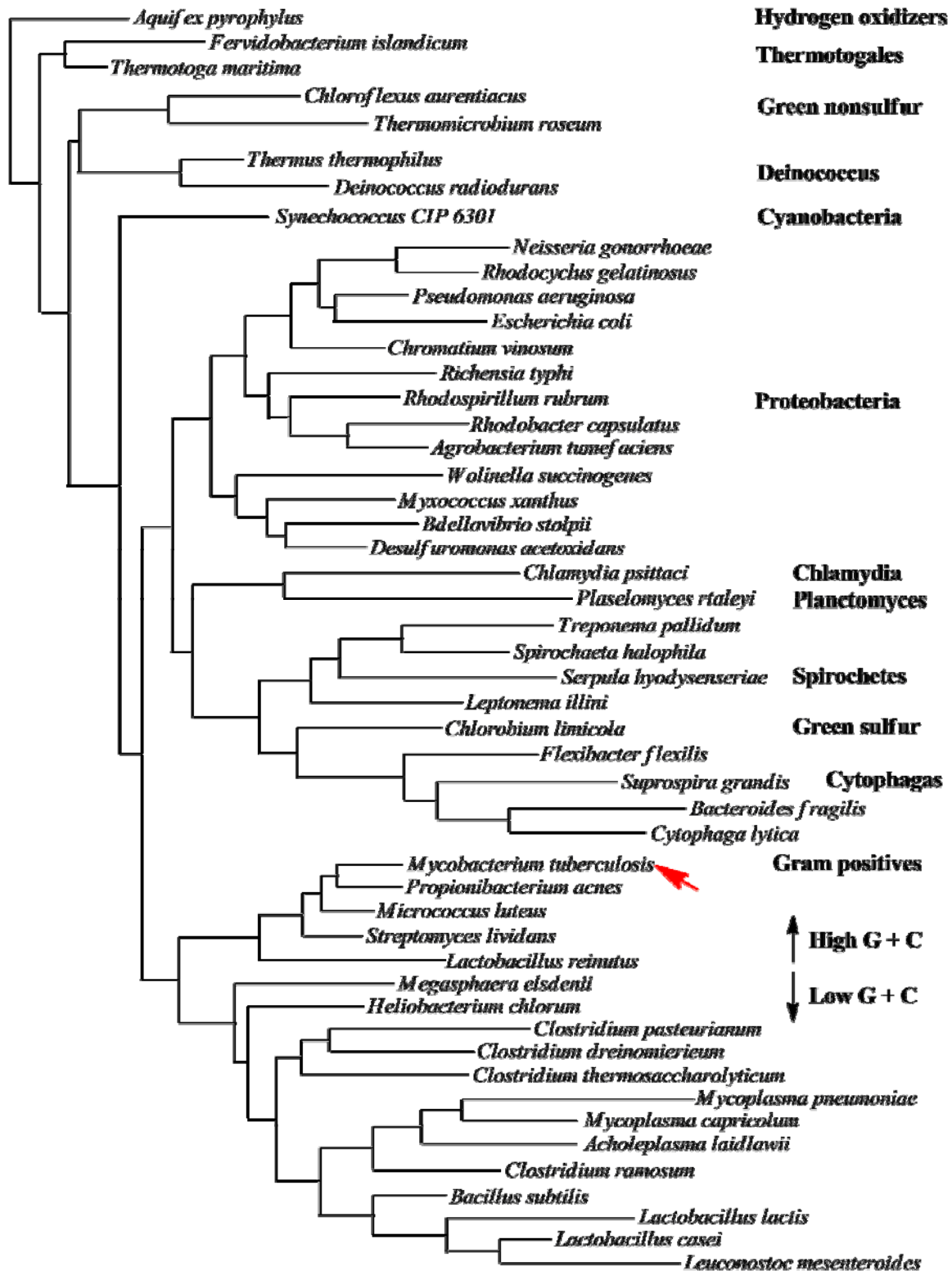


**Figure 1.5. Phylogeny of the bacteria**

Phylogenetic tree showing relationships among the bacterial kingdom. The red arrow indicates the position of *Mycobacterium tuberculosis* within the grouping. Figure redrawn from images shown at:

[http://bioweb.uwlax.edu/bio203/s2007/millard\\_ashl/classification.htm](http://bioweb.uwlax.edu/bio203/s2007/millard_ashl/classification.htm).

## 1.4 The genome sequence of Mtb

The Mtb genome was sequenced in 1998 by Stewart Cole and co-workers in order to elucidate its biology and pathogenic mechanisms, and to gain further information for drug target investigation (42, 43). The *M. tuberculosis* genome is composed of 4,411,522 base pairs, coding for 3,924 predicted proteins (44). Only ~52% of the genes have functions predicted accurately, and ~48% are assigned hypothetical functions (or are of unknown function). The DNA sequence also indicates a high G+C percentage of 65.5% (45). Possessing approximately 4.4 Mb, the genome size of *M. tuberculosis* is smaller than only those of *E. coli* (4.6 Mb) (46) and *Streptomyces coelicolor* (6.6 Mb) (47). According to the Mtb genome sequence, a large number of genes encode proteins that function in the biosynthesis and metabolism of lipids (48). This explains why Mtb produces a large amount of lipophilic molecules, such as mycolic acids, which are major components of the Mtb cell wall structure (49).

Surprisingly, the Mtb genome codes for 20 cytochrome P450 proteins (CYPs or P450s). This is a much higher CYP gene “density” than is found in eukaryotes, and in most other bacteria. Bacterial P450s have diverse functions in biosynthesis and metabolism of important compounds, including polyketides, fatty acids and steroids (50). Interestingly, in comparison with the human genome, which possesses approximately 3000 Mb but encodes only 57 CYPs, Mtb’s genome size is only 4.4 Mb but codes for 20 CYPs. Hence, the density of P450 genes in Mtb is much higher (~240 fold) than in humans, suggesting that P450 enzymes should play essential roles in the growth, viability, virulence, and infectivity of Mtb, and that they could be used as drug targets for controlling TB (51).

## 1.5 The cytochromes P450

### 1.5.1 History and general background

In 1955, Axelrod and co-workers first isolated a protein system located in the liver endoplasmic reticulum that functioned in oxidation of xenobiotic compounds (52). Three years later, in 1958, two scientists, Garfinkel and Klingenberg, did experiments to reveal the protein was able to bind carbon monoxide (CO), forming a complex that absorbs light maximally at 450 nm (53). Further investigations were carried out in 1964 and these demonstrated that the protein contained a *b*-type heme that plays a key role in the reaction with CO. The protein was thus named cytochrome P450 (Figure 1.6) (54). Several pieces of evidence revealed that P450 in its resting state is a low-spin ferric heme with a thiolate

residue serving as the fifth ligand to the heme iron, leading to the formation of distinctive Soret absorptions on binding to e.g. CO, NO, substrates and inhibitors, and due to the Fe-S bond between cysteine thiolate and heme iron (55). The term Soret absorption is normally used to describe the most intense peak of a heme porphyrin. The heme absorbs light in the UV-visible region (400-750 nm), with the Soret maximum usually located around 400 nm. Major heme absorption bands (including the Soret) are thought to arise mainly from  $\pi\text{-}\pi^*$  transitions in the heme porphyrin, and in the cytochromes P450 the cysteine thiolate sulfur electrons are also thought to contribute to the absorption. The unusual position and intensity of the Soret feature for the P450 Fe(II)CO complex may arise as a consequence of mixing of the sulfur  $p \rightarrow \pi_{eg}^*$  transition with the  $\pi \rightarrow \pi_{eg}^*$  heme porphyrin transition (56).

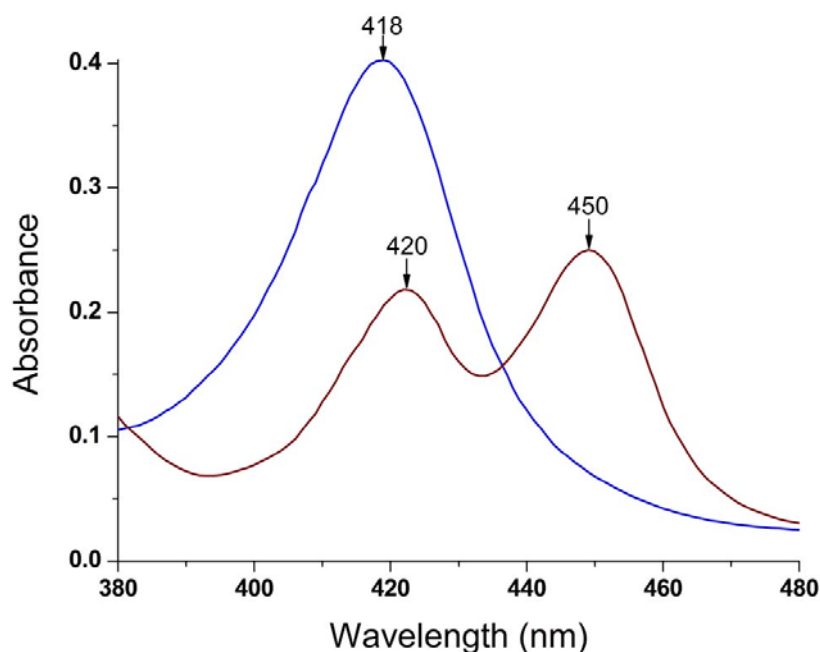


**Figure 1.6. UV-visible spectra of a typical P450 enzyme**

The absorption spectrum of a cytochrome P450 Fe<sup>2+</sup>-CO complex showing the characteristic Soret peak at approximately 450 nm (brown line), created using data for the *Mycobacterium tuberculosis* CYP126 enzyme. A substantial amount of the P420 form (resulting from a thiol-coordinated Fe<sup>2+</sup>-CO complex) is also present at ~420 nm. The blue line shows the spectrum for the oxidized form of the P450 (~4.5  $\mu$ M).

Cytochrome P450 proteins usually contain around five hundred residues in their amino acid sequence and one type-*b* heme serves as the prosthetic group (57). A cysteine residue from the protein links to heme iron via a Fe-S bond that forms the fifth ligand, known as the proximal axial ligand (58). In addition, another four nitrogen atoms act as equatorial ligands to the heme iron. In many heme-containing proteins, a nitrogen atom from a histidine residue acts as a proximal axial ligand to the iron (e.g. hemoglobin). However, on

the binding of CO to the distal side of a ferrous ( $\text{Fe}^{2+}$ ) P450 enzyme (59), a CO-heme complex absorption maximum occurs at around 450 nm (rather than at e.g. ~420 nm for hemoglobin). This absorbance shift is used as a specific feature for the identification of a P450 enzyme and for the measurement of the P450 concentration (60, 61).

To date, there have been around 11,200 P450 (*CYP*) genes identified. These are widely distributed in prokaryotes and eukaryotes, but show wide variations in numbers in different organisms (62). Although the P450 proteins are considered to have originated from prokaryotes, the genome sequence of *Escherichia coli* encodes no P450s. In contrast, 20 P450s were found in *Mycobacterium tuberculosis* (51), 3 P450s in baker's yeast (63), and 83 in the fruit fly *Drosophila melanogaster* (60, 64). Interestingly, higher plants possess a very high number of P450 genes. For example, 286 P450 genes were identified in *Arabidopsis thaliana*, highlighting many essential functions of P450s in plants (60).

### 1.5.2 Physical properties

The number of P450 crystal structures has increased rapidly in the past two decades. Although the identity of amino acid sequence among P450 proteins from different families is generally low (fluctuating between 10-30%), the structural fold of P450s is highly similar, including conserved amino acids in the heme binding motif (containing the iron-ligating cysteine), and retention of important structural elements: e.g. the I helix, F/G helices and BC loop regions involved in substrate interactions and active site access (60, 65-67). Only a few residues are absolutely conserved, but these are ones involved in binding the heme and regulating its properties, explaining why the catalytic cycle is relatively similar in different P450s (68). The active site core normally contains three important components:

- 1) A cysteine residue that serves as the fifth ligand to the heme iron, and which plays a key role in stabilizing thiolate ligation for P450 activity. In detail, the active site core of a P450 is composed of several helices and sheets, including the D, E, I, L, K, J helices and  $\beta_1$ ,  $\beta_2$  sheets (Figure 1.7) (69, 70).
- 2) The Glu-X-X-Arg motif in helix K to help maintain the structure of the active site cavity.

3) Several residues such as Ala, Gly, Asp, Glu, Thr, and Ser in the I helix usually act to form hydrophobic interactions with substrates and to control proton transfer to the oxygen-bound heme iron (67, 71, 72).

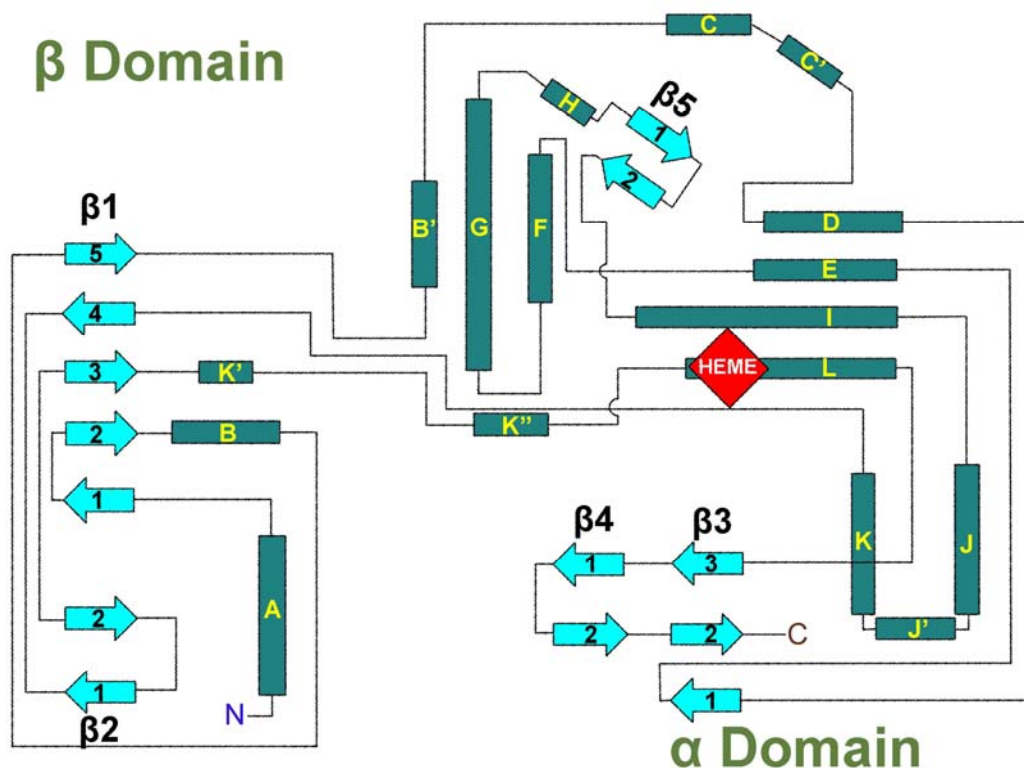


**Figure 1.7. A secondary structure diagram of a P450 protein**

The P450 secondary structure is composed of two distinct  $\alpha$  and  $\beta$  domains. The P450 structure is usually composed of five  $\beta$  sheets and 13  $\alpha$  helices, defining one domain that is predominantly  $\beta$  sheet (the  $\beta$  domain), and the other (larger) domain that is predominantly  $\alpha$  helical (the  $\alpha$  domain). The heme is sandwiched between the two domains (60).

Figure 1.8 represents the crystal structure of a soluble Mtb P450 (the CYP126 P450 protein, as described later in this thesis), showing it in a typical topological form with a closed conformation with respect to active site entry. Heme is shown in red, and the I helix is in green. The  $\alpha$  domain is at the bottom with two bundles of  $\beta$  sheets, which are coloured in yellow. The I helix locates above the heme, close to the substrate-binding site. The Cys<sup>363</sup> residue on the L helix locates below the heme, and serves as the fifth ligand to the heme iron. The B and C helices and the loop connecting these helices are visible above the heme protoporphyrin (in red). The flexibility of the F/G loop in making open/closed motions defines the access of substrates to the active site. The channel for substrate/inhibitor entry is usually located in close contact with the F/G loop, the I helix

and  $\beta$  strands 1-1 and 1-2. The back face of the protein (at the heme site) is involved in redox partner recognition and electron transfer to the active site, and the protons (needed for protonation of iron-oxy intermediates in catalysis) flow into the active site from the distal face, probably via water molecules.

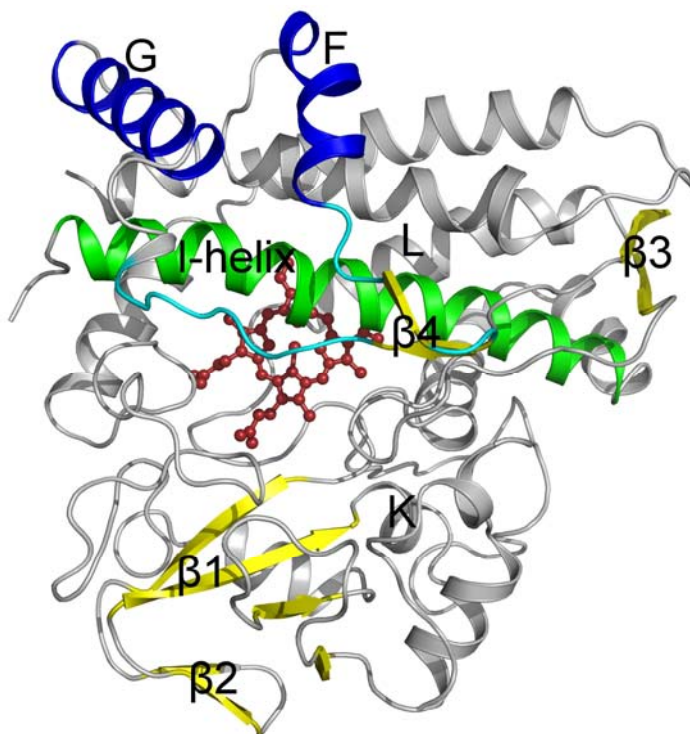


**Figure 1.8. A ribbon representation of the tertiary structure of a P450 protein (CYP126) in the closed conformation.** Helices and sheets are labelled as in the secondary structural elements diagram (Figure 1.7). The heme is in red, the F and G helices and the F/G loop are highlighted in blue and cyan, respectively. Four bundles of  $\beta$ -sheet are shown in yellow. The FG helices slide over the surface of the I helix (green), which provides an open/closed motion of the access channel leading to the active site.

The ferric heme iron has five 3d electronic orbitals and exists in two states (see more detailed discussion in section 3.2.9), the low spin state ( $S = 1/2$  – one unpaired electron) and the high spin state ( $S = 5/2$  – five unpaired electrons) (73). In the resting state (LS), the ferric heme has its Soret band at  $\sim 418$  nm, with (typically) a water molecule as the distal ligand. Binding of various (e.g. nitrogenous) ligands in place of the water is inhibitory and leads to a further red shift in the Soret band, while maintaining and stabilizing the LS state of the heme iron (six-coordinated  $\text{Fe}^{3+}$ ) (74). The high-spin state (HS) is normally associated with the binding of substrate, and occurs when the water molecule is expelled from heme iron, leaving a five-coordinated  $\text{Fe}^{3+}$  heme iron (75) (Figure 1.9).

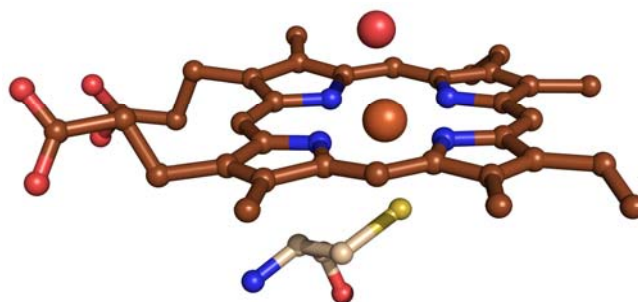


**Figure 1.9. The heme active site of substrate-free Mtb CYP126**

An oxygen from a water molecule ligates to heme iron as the sixth axial ligand (shown in red), nitrogen is in light blue, sulfur is in yellow and iron is in firebrick. Carbon atoms are shown in ruby as bonds only and hydrogens have been omitted from this figure for clarity.

In terms of ligand binding, there are in general two major kinds of P450 binding, type I and type II, and these are distinguished by the shift of the Soret absorption (76). Type I is recognised by a blue shift of Soret absorption from  $\sim 418$  nm to  $\sim 390$  nm, causing a change of heme spin state from LS to HS, and the binding of substrate generally corresponds to this shift. Type II spectral changes are characterised by a red shift of Soret absorption to longer wavelength ( $\sim 425$  to  $435$  nm), correlating with an increase of heme iron LS character. The binding of inhibitors to P450 heme iron typically corresponds to a type II spectral change, in which cases the inhibitor replaces the axial water ligand, and binds directly to the iron (77).

### 1.5.3 P450 localization and function

In recent years, a large numbers of cytochromes P450 from bacteria, fungi, plant, insects and animals have been characterized and reported (52). Most eukaryotic cytochrome P450s are found in association with the smooth endoplasmic reticulum (microsomal P450s) and with the mitochondrial inner membrane, and are involved in e.g. the biosynthesis of several hormones and steroids, as well as in drug detoxification (78). Contrary to eukaryotic P450s, P450s from bacteria are normally soluble proteins and function in e.g. detoxification of xenobiotic compounds, metabolism of carbon sources, and antibiotic biosynthesis (79). Cytochrome P450-containing monooxygenase systems can be classified into at least four major classes depending on the types of electron transport pathway: In the class I systems, electrons are delivered from NAD(P)H to P450 via FAD-containing reductase and iron sulfur proteins. In class II systems, the FAD/FMN-containing P450 reductase (CPR) acts as electron carrier to deliver electrons from NAD(P)H to P450. Class III P450 can catalyse substrate conversion without additional electron donor proteins. Finally, electrons are delivered directly from NAD(P)H to class IV P450s (60, 80).

The similarity of amino acid sequences between P450 enzymes is usually relatively low (< 20%). However, for classification, P450 proteins that share at least 40% identity at the amino acid level belong to the same family. In the case of the subfamily classification, these P450s must share >55% identity. There are currently 1015 CYP families with more than 11200 named cytochrome P450 sequences identified to date, of which 18 families and 44 subfamilies are from humans (62, 63, 81).

### 1.5.4 The cytochrome P450 catalytic cycle

The monooxygenation reaction of P450 can be summarized as follows:



A scheme for the catalytic cycle of cytochrome P450 is presented with eight steps in the reaction cycle, as shown in Figure 1.10 (71).

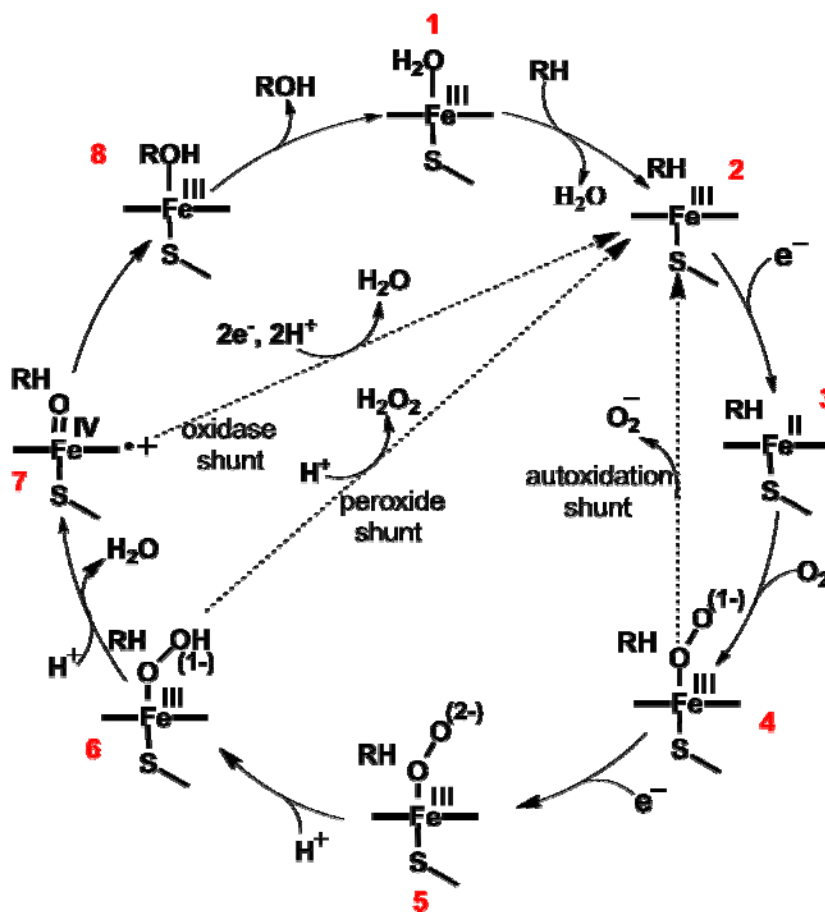


**Figure 1.10. A scheme for the catalytic cycle of cytochrome P450s**

The fate of the individual oxygen atoms from dioxygen (one into water, the other into oxidized product) is indicated. The binding of carbon monoxide (CO) to species III (ferrous heme iron) can also occur. This is competitive with dioxygen to form a stable and characteristic P450 product. The non-productive collapse of various oxy intermediates gives rise to formation of superoxide (complex 4), peroxide (complex 6) and water (complex 7), respectively.

1. **Substrate binding:** The binding of substrate (RH) to the native enzyme (complex 1) is the starting step of the P450 catalytic cycle, forming a HS, five-coordinated ferric form (complex 2). Substrate binding typically leads to displacement of a water molecule as the sixth ligand to the heme iron and causes a change of the spin-state of the heme iron from the low-spin to the high-spin form. The spin state change is accompanied by a change of the heme iron redox potential, allowing electron transfer from NAD(P)H to the heme iron via redox partner proteins. The binding of substrate generally increases the redox potential, as has been demonstrated in several bacterial P450s. For instance, the Mtb sterol demethylase CYP51B1, shows an increase in redox potential of 150 mV (-375 mV to -225 mV) upon binding of estriol (82). A similar result was also obtained for the *Bacillus megaterium* fatty acid hydroxylase P450 BM3 in the arachidonate-bound form (-427 mV to -289 mV) (83).

2. **The first reduction:** The shift of spin state from a low-spin to high-spin form results in an increase in the redox potential of the heme iron that facilitates electron transfer. One electron derived from NAD(P)H is delivered via redox partner(s) and reduces the heme iron, converting the pentacoordinate high-spin ferric form into a pentacoordinate ferrous form (complex 3). For bacterial P450 systems, electrons are delivered by two different proteins, these typically being a ferredoxin NADP<sup>+</sup>-reductase (FNR)-like protein and a ferredoxin. FNR-like proteins can accept two electrons from NAD(P)H and donate these one at a time to a ferredoxin, which then transfers these electrons one by one to P450 for reduction and catalysis. Electron transfer between redox partners and P450 has been extensively studied for the CYP105D5 system from *Streptomyces coelicolor* A3, demonstrating hydroxylation of fatty acids (oleic acid and lauric acid) when the P450 was reconstituted by ferredoxin reductase (FDR) and ferredoxin (Fdx) proteins (84).

3. **Oxygen binding:** In the next step, the pentacoordinate ferrous form (complex 3) is attractive for the binding of dioxygen (O<sub>2</sub>) covalently to the distal axial coordination position of the heme iron, in order to form a semi-stable low-spin, hexacoordinate ferrous-O<sub>2</sub> (or ferric superoxy) form (complex 4). The cysteinate ligand (fifth ligand) is a strong electron donor, and therefore the dioxygen is activated for the second reductive reaction.

4. **Second reduction:** After the binding and activation of the oxygen molecule, the dioxygen adduct (complex 4) is further reduced by another single electron delivered from

the redox partner, forming a negatively charge peroxy group on the heme iron, and more specifically a  $\text{Fe}^{3+}\text{-O-O}^{(2-)}$  species (ferric peroxy) (complex 5). This is a short lived intermediate state in the catalytic cycle of the P450s.

**5. The first protonation:** The ferric peroxy adduct is rapidly protonated by local transfer from active site water and/or from surrounding amino acid side chains to give the ferric hydroperoxy form, known as compound 0 (complex 6). A strongly conserved threonine (or serine) residue is implicated in the oxygen binding/protonation process (85).

**6. The second protonation:** A further protonation of the bound dioxygen molecule (as described above) then leads to heterolytic O-O bond cleavage releasing water, and generating the oxo-ferryl porphyrin radical intermediate, compound I, which is equivalent to the high-valent iron oxo form found in peroxidase enzymes (complex 7).

**7. Product formation:** Oxygen atom transfer from complex 6 to the substrate yields oxidized product (complex 8), presumably by an oxygen rebound mechanism (86). Depending on the enzyme and the substrate involved, P450s can catalyze a wide of variety of reactions. Most P450s are known to be involved in lipid hydroxylation, such as the fatty acid hydroxylase P450 BM3 (CYP102A1) from *Bacillus megaterium*.

**8. Product release:** The P450 reaction cycle is completed when the oxidized product is released to regenerate complex 1, after which a water molecule rebinds the ferric heme iron.

### 1.5.5 Redox partners

Cytochrome P450s usually require redox partners for their function, since electron transfer to P450s is a critical part of the P450 catalytic cycle. To accomplish their monooxygenation activity, P450s receive two electrons from [NAD(P)H] via redox partner proteins. Bacterial and mitochondrial P450s are often reduced by a soluble iron-sulfur protein, but the microsomal P450 proteins require electrons to be delivered via FAD/FMN cofactors bound in the protein CPR (cytochrome P450 reductase) (87, 88). In these electron transport chains, electrons are almost invariably delivered from pyridine nucleotide coenzymes [NAD(P)H] to the P450 via redox partners (89, 90).

## Pyridine nucleotide coenzymes:

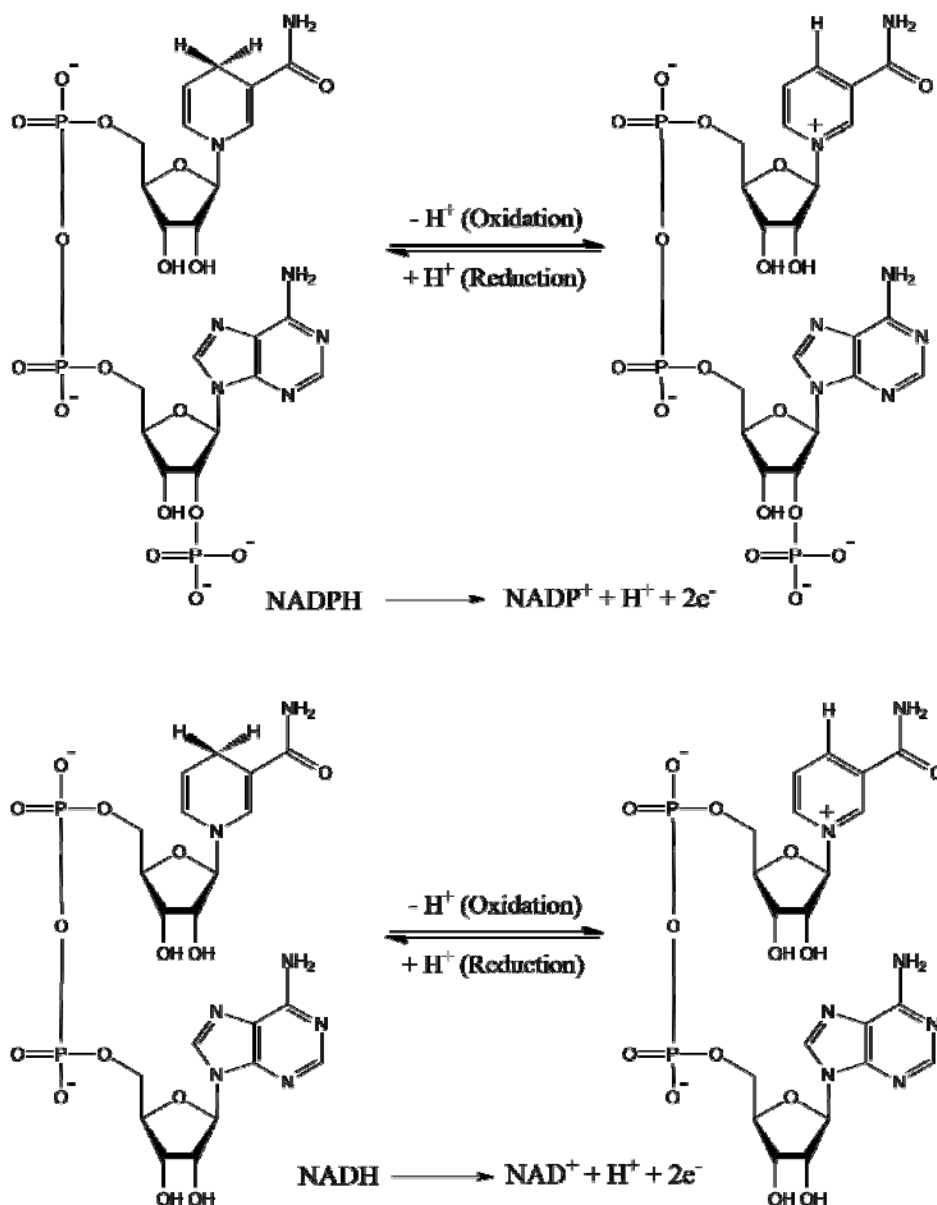


**Figure 1.11. The redox reaction of NAD(P)H molecules**

The nicotinamide coenzymes NAD<sup>+</sup> (nicotinamide adenine dinucleotide) and NADP<sup>+</sup> (nicotinamide adenine dinucleotide phosphate) are important electron sources for almost all P450s activity. Generally, NAD<sup>+</sup> or NADP<sup>+</sup> are able to receive two electrons and a proton as a hydride ion to become NADH or NADPH, respectively (Figure 1.11). In P450 reduction, hydride ions are most often transferred to a flavin (FAD) cofactor bound in a redox partner protein, facilitating an overall 2-electron reduction of the flavin from its quinone form to the hydroquinone state. These electrons can then be shuttled to the P450, most commonly through another redox partner containing an iron sulfur or (occasionally) flavin centre (91).

## Flavin containing redox components:

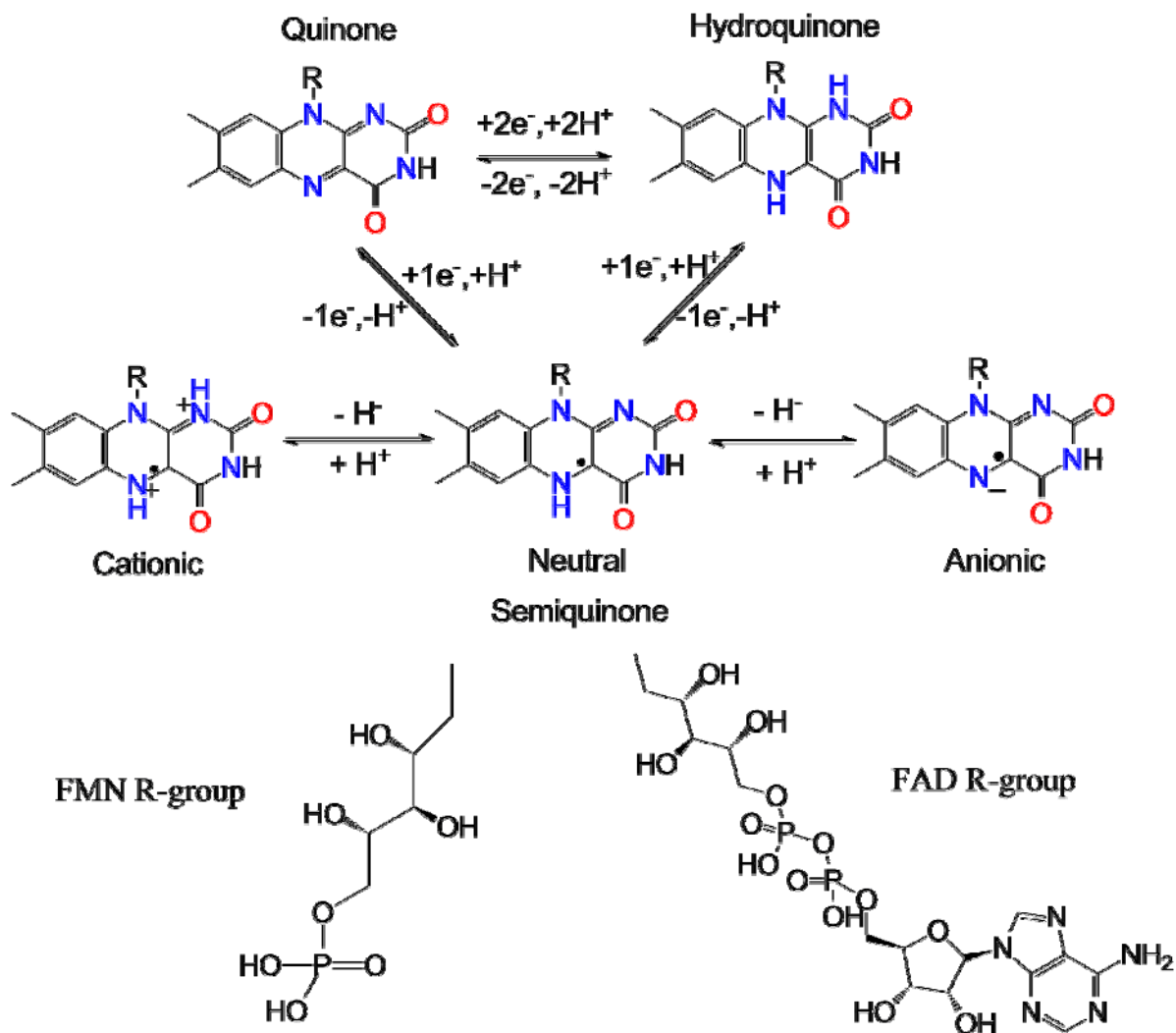


**Figure 1.12. Chemical structures and redox steps of isoalloxazine centres in FAD and FMN flavin cofactors.** Both FAD and FMN have the isoalloxazine ring as their redox active centre. This is a three ring structure that can accept two electrons and two protons from NAD(P)H to become a hydroquinone (FADH<sub>2</sub>) form, or one electron and one proton to become a blue (neutral) semiquinone form (FADH). This may be deprotonated to form a red (anionic) semiquinone, or protonated to form a cationic semiquinone. The structures of these three different kinds of semiquinones are detailed in the figure. The reduction steps of flavin cofactors are shown based on reference (92).

Flavin adenine dinucleotide (FAD) and flavin mononucleotide (FMN) are cofactors produced from riboflavin, which act as prosthetic groups in certain oxidoreductases (and particularly in CPR, where both FAD and FMN are bound) during the P450 catalytic cycle. FMN and FAD are redox active cofactors that can take part in both one and two electron transfers (Figure 1.12). FAD is produced by the adenylation of FMN, and this form of

flavin is also involved in various important reactions in metabolism, as well as being a cofactor in CPR and in ferredoxin reductases that support P450 function. The diflavin enzyme CPR requires FAD as an electron acceptor from NADPH, and FMN as the flavin which accepts electrons from FAD and shuttles them to the P450 heme iron. Aside from their redox activity in supporting P450 reduction, flavins as prosthetic groups are also important in a number of different roles e.g. electron transport leading to oxidative phosphorylation in the mitochondrion (93, 94).

**Iron-sulfur redox components:**

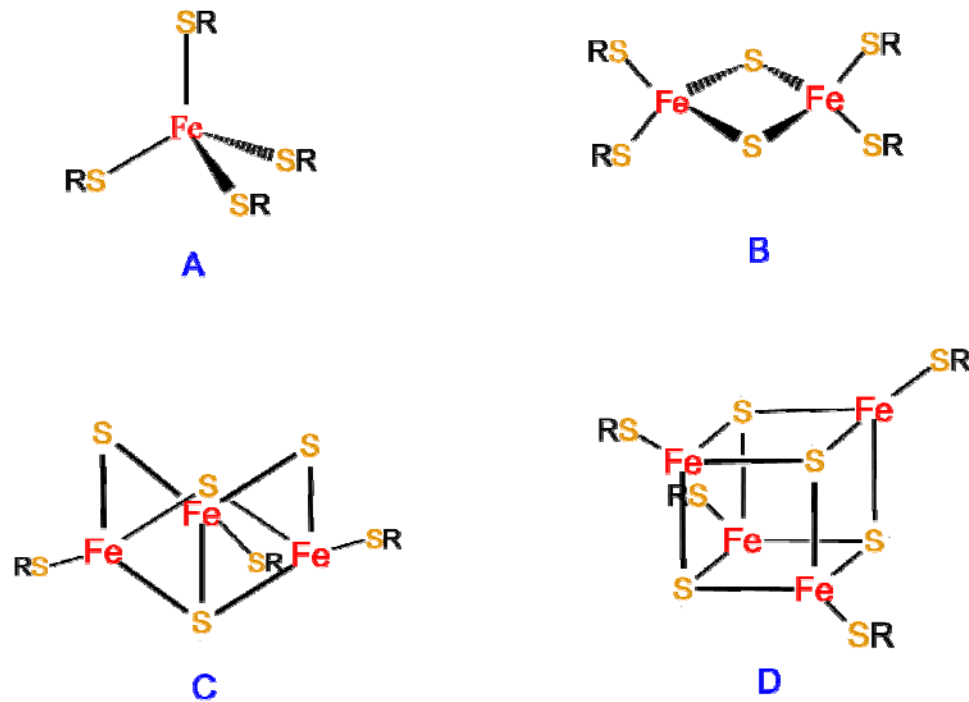


**Figure 1.13. Iron sulfur clusters**

A: Rubredoxin form with one iron in centre coordinated by cysteine residues from the protein polypeptide backbone (SR). B: [2Fe-2S] cluster. C: [3Fe-4S] cluster. D: [4Fe-4S] cluster. In B, C and D, iron is also ligated by inorganic sulfide (S) (95).

Iron-sulfur (Fe-S) centres (usually as 2Fe2S, 3Fe4S or 4Fe4S) are cofactors found in several small soluble proteins (ferredoxins) which are abundant in bacteria and many other organisms (96). They function in several reactions, including redox and hydration/dehydration reactions. The structure of the simplest type of Fe-S is composed of an iron atom connected to four cysteine residues via sulfur atoms, and this is referred to as a rubredoxin (97). However, rubredoxins are generally not known to support electron transfer to P450s. The other types of Fe-S clusters mentioned (2Fe2S, 3Fe4S or 4Fe4S), however, are all known to support various P450 systems (Figure 1.13). These iron-sulfur clusters all

contain iron atoms coordinated to polypeptide (usually cysteine) residues and also linked by inorganic sulfide. In P450 systems, iron-sulfur clusters in ferredoxins are single electron carriers that mediate successive electron transfers between flavin-binding reductases and the P450 proteins. Examples are putidaredoxin (98), a 2Fe-2S ferredoxin that carries electrons to the *Pseudomonas putida* camphor hydroxylase P450cam, and the mitochondrial 2Fe-2S adrenodoxin that supports function of P450s involved in steroid metabolism (99, 100).

### 1.5.6 Azole inhibitors

P450s are found in almost all organisms, from bacteria through to fungi, plants and mammals (63, 65, 81). In each organism, most P450s have specific functions in order to contribute to catalytic pathways required for the survival of that organism. In humans, hepatic P450s function in the metabolism of drugs, therefore they inadvertently inhibit treatments given to patients. In that way, the biological activity of the drugs is changed and subsequently may lead to potentially harmful drug-drug interactions, as well as to further modification and excretion of the drugs (101-104). The genome of Mtb reveals P450 genes coding for 20 CYPs, for some of which the catalytic function has been determined. Many are likely to be involved in lipid transformations and synthesis – since Mtb has numerous important oxygenated lipid compounds in its thick membrane envelope that contributes to the survival of Mtb during infection. For example, mycolic acids (long, hydrophobic, cyclopropane ring-containing lipids) are very important components that form a lipid layer around the Mtb cell. Hence, it could be useful to inhibit the biological activity of various P450s in order to prevent e.g. the passive function of those CYPs in human that influence drug metabolism, as well as to terminate the biosynthesis processes of CYP enzymes that could lead to inhibition of growth of the bacterial pathogen Mtb.

P450 activity is disrupted by several inhibitor classes, including azole antifungal drugs. The mechanism of inhibition has been elucidated, involving the binding of the azole group to the heme iron (shorter distance 2.108-2.156 Å) (77), replacing the water in the sixth ligand position (longer distance 2.8-3.0 Å) (77, 105). This action usually inhibits electron transfer to the heme iron, and thereby blocks dioxygen binding to the heme iron, meaning that the P450 cannot insert oxygen atom into the substrate. The azole antifungal class is divided into two groups, imidazoles and triazoles. Each group has different structures but share a similar mode of action.

**Imidazoles:** Including ketoconazole, clotrimazole, econazole, and miconazole.

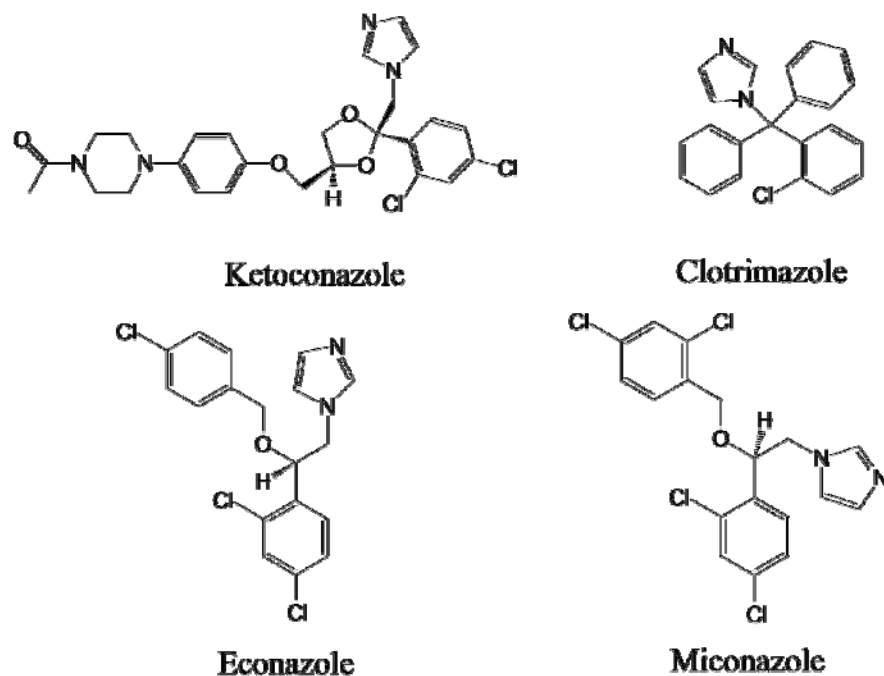


**Figure 1.14. Chemical structures of imidazole derivatives used as antifungals**

Figure redrawn from images shown at: <http://en.wikipedia.org/wiki>

The imidazole derivatives were first discovered in the late 1960s and introduced into commercial/clinical use in the early 1970s (106, 107). The azole structure consists of two nitrogen atoms, located at 1 and 3 positions of a five-membered ring (Figure 1.14). These bind directly to heme iron of the P450 and inhibit the catalytic function (108-110). The mechanism of action of such imidazoles often results in attacks to the structure and function of the target cell, such as in the cellular membranes (111-113). Specifically, imidazoles are able to block the biosynthesis of ergosterol, the main sterol in the membrane of the fungal cell (114-116). These agents also prevent the biosynthesis of triglycerides and phospholipids, and perturb oxidative and peroxidative enzyme activities (117, 118). In Mtb, some imidazole derivatives (such as econazole, miconazole, clotrimazole and ketoconazole) were found to be potent inhibitors (tight binding) of the activity of Mtb P450s such as (i) CYP51B1 - an enzyme that functions as a lanosterol-14 $\alpha$ -demethylase (119), (ii) CYP121 - which catalyzes formation of an intracellular C-C bond between two tyrosyl carbon atoms in the unusual cyclic dipeptide cyclo-L-Tyr-L-Tyr (cYY) (120), and (iii) CYP125 and CYP142 - two enzymes involved in cholesterol hydroxylation for energy derivation and/or host cell modulation (121-124).

**Triazoles:** Including fluconazole, voriconazole, ravuconazole, and itraconazole.

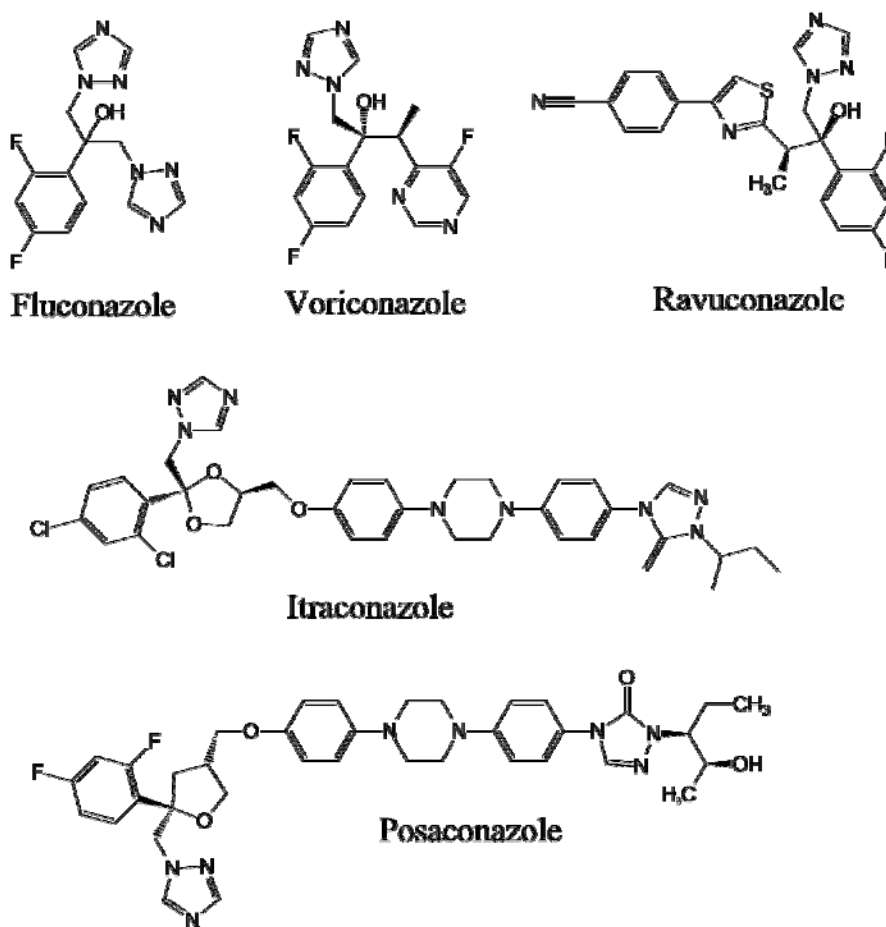


**Figure 1.15. Chemical structures of triazole derivatives used as antifungals**

Figure redrawn from images shown at: <http://en.wikipedia.org/wiki>

Triazole is the newer generation azole class, which was first introduced in the early 1990s. In contrast to the imidazole group, the triazole structure contains three nitrogen atoms in the five-membered ring (125-128) (Figure 1.15). Compared to the imidazole derivatives, triazoles are more powerful, and have better target specificity, higher potency and a more widely expanded activity spectrum. Fluconazole and itraconazole are the first generation of the triazole class, and the second generation includes voriconazole, posaconazole, and ravuconazole (129-131). The predominant activity of the first generation is the inhibition of cytochrome P450 activity involved in biosynthesis of ergosterol from lanosterol, causing the accumulation of 14 $\alpha$ -methylsterol in fungi, and therefore altering fungal cell membrane structure and function, and finally inhibiting the cell growth and replication of the target organism (132-134). Fluconazole and itraconazole also have other activities in killing dermatophytes such as *Candida* spp., *Cryptococcus neoformans*, and *Aspergillus* spp. The structures of ravuconazole and voriconazole are related to fluconazole, whereas

posaconazole is very similar to the itraconazole structure. The second generation triazoles have potential for significant drug-drug interactions through handling by the host P450 enzyme systems.

### 1.5.7 Mtb P450 structures

The location of 20 P450 enzymes in *M. tuberculosis* suggests important roles for them in Mtb physiology and, hence, their potential use as therapeutic targets. To date, only seven of the Mtb P450s (CYP51B1, CYP121, CYP130, CYP125, CYP124, CYP142, and CYP144) have been studied in detail as individually expressed recombinant proteins. These P450s have all been shown to bind tightly to econazole (the azole drug with the highest known antimycobacterial activity and which has been extensively studied and reported active against latent/persistent Mtb (119, 121, 124, 135-139)) as well as to other azoles and triazole drugs. The crystal structures of six of these enzymes have been solved by x-ray crystallography, including complexes showing the interaction of these enzymes with azole inhibitors.

**CYP51 (Cytochrome P450 14 $\alpha$ -sterol demethylases)**: The 2.1 Å crystal structure was reported for the Mtb CYP51B1, which was the first Mtb P450 structure solved by Podust *et al.*, and was a potential drug target (yeast and fungal CYP51 isoforms are targets for azole drugs). CYP51B1 exhibits the typical P450 fold, excepting two distinct features (Figure 1.16). These are a bent I helix (where the I helix is a long helix spanning the entire protein and running across the face of the heme and comprising several substrate-contacting residues), and the fact that the BC loop makes an “open gate”, leading to creation of a second channel for substrate entry. This channel is not open at the surface in the substrate analogue (estriol)-bound and fluconazole-bound forms (119). The existence of two channels, with one open at the surface (as, indeed, is observed in the ligand-free structure of CYP51B1), suggests that the opening and closure of these channels relates to the regulation of substrate/inhibitor entrance/exit in CYP51B1. The distinct crystal structures of Mtb CYP51B1 provide fundamental information for the design of effective drugs as well as analysis of catalytic activity of P450 enzymes (140).

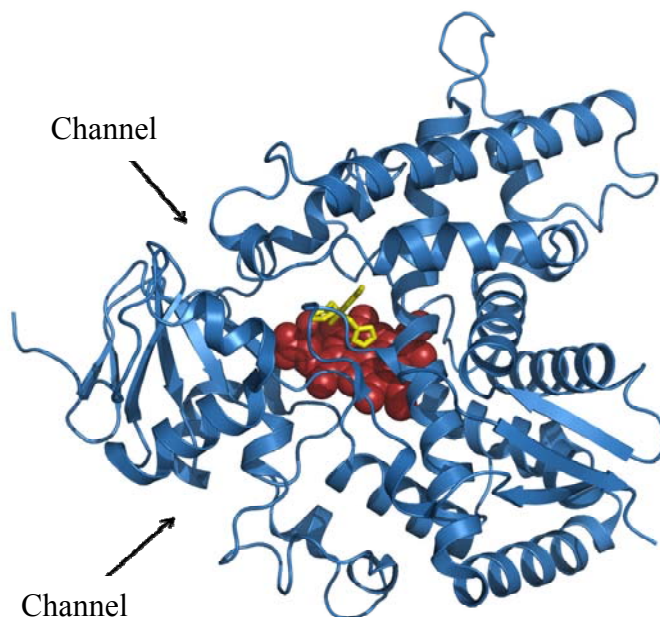


**Figure 1.16. Molecular structure of CYP51B1 from *M. tuberculosis***

The two putative entry/exit ports for substrate/product are identified, as are the various important secondary structural elements (helices and sheets) in the P450 (PDB code 1EA1). Figure was created using Pymol (141).

As with the other members of the CYP51 family, CYP51B1 from Mtb also catalyses the oxidation of the 14 $\alpha$ -methyl group of lanosterol to form 14-hydroxymethyl, 14-carbonaldehyde, and 14-formyl derivatives. The best substrate is the plant sterol obtusifoliol (142, 143). However, there is no known sterol biosynthetic pathway in Mtb, and as yet there is no clear reason for the sterol demethylase activity. Thus, it remains unclear as to what the function of the Mtb CYP51B1 might be in bacterial metabolism or (possibly) host sterol modification (144-146).

Due to its potential involvement in lipid metabolism, CYP51B1 was investigated as a drug target for antifungal azoles. Several inhibitors such as econazole ( $K_d = 0.77 \mu\text{M}$ ), fluconazole ( $K_d = 19.0 \mu\text{M}$ ), miconazole ( $K_d = 0.59 \mu\text{M}$ ), and clotrimazole ( $K_d < 0.1 \mu\text{M}$ ) were shown to bind to the protein (119, 140), suggesting the enzyme would be able to become an effective target drug for the treatment of Mtb. In addition, the crystal structures of CYP51B1 in complex with twoazole inhibitors (fluconazole and 4-phenylimidazole) were determined, demonstrating that both imidazole and triazole rings are coordinated to the heme iron, overlapping the substrate binding site and preventing the binding of dioxygen to the heme (105, 147-152). In recent studies, two endogenous redox partner proteins, a ferredoxin reductase (FprA, the product of the *Rv0688* gene) and a ferredoxin (Fdx1, the product of *CYP51B1*'s adjacent *Rv1763c* gene), were shown to deliver electrons from NAD(P)H to CYP51B1 to facilitate sterol demethylation (153). The adjacent

ferredoxin is an obvious redox partner system for CYP51B1, but other ferredoxin reductases may also be involved. Other studies have shown that heterologous redox proteins (e.g. *E. coli* flavodoxin reductase/flavodoxin) can also interact productively with CYP51B1.

**CYP121**: The Mtb CYP121 (*Rv2276*) crystal structure was solved at resolution of 1.06 Å. The structure shows that CYP121 has a large  $\alpha$ -helical content, as is the case in all P450s structurally analyzed thus far (Figure 1.17). The heme iron is located in the centre between alpha and beta domains. It is clearly seen that the FG loop creates an entrance for substrate/inhibitor access. Further structural analysis revealed that the heme iron is located under the I helix, which contains several hydrophobic residues known to be responsible for substrate/inhibitor interactions as well as proton transfer. The active site is rigid when compared to the remainder of the structure, suggesting that large conformational readjustments may not occur on substrate binding (82, 139, 149).

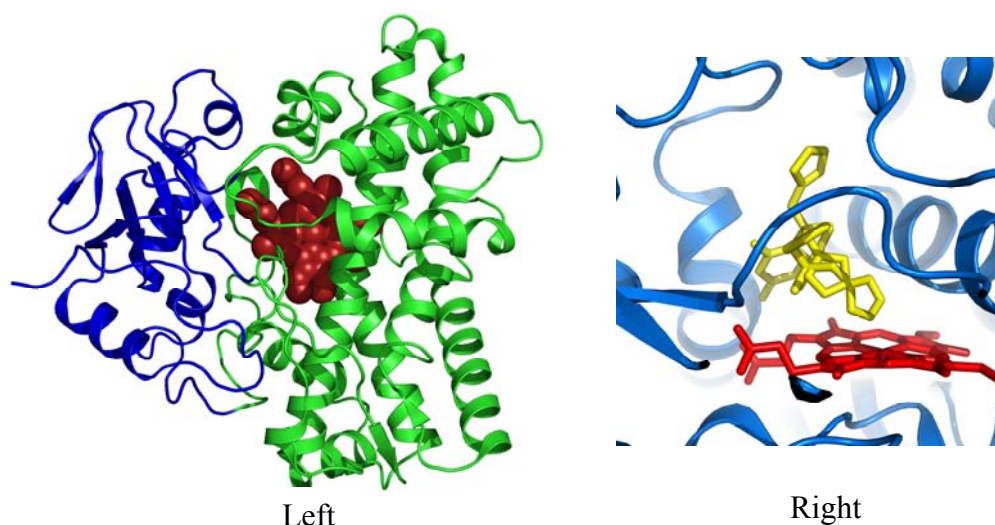


**Figure 1.17. Mtb CYP121 structure**

Left hand side: Atomic structure of Mtb CYP121 obtained at a resolution of 1.06 Å, showing the  $\alpha$ -helix rich domain in green and the smaller  $\beta$ -sheet rich domain in blue. Heme is in red at the centre of the structure (PDB code 1N40). Right hand side: active site of CYP121 in complex with fluconazole (yellow). Figures were created using Pymol (141).

The crystal structure of the fluconazole-bound CYP121 exhibits a distinct ligation mode, in which fluconazole binds to the heme iron in two different ways. One mode exhibits direct ligation of the triazole ring nitrogen with the heme iron, which is similar to other P450 azole complexes such as CYP51B1-econazole and CYP130-econazole (119, 137). However, the direct ligation of fluconazole is not perpendicular with the heme iron as seen in other P450-azole complexes, instead leaning at 25° to the axis. The second fluconazole-

CYP121 conformation reveals an indirect ligation with the CYP121 heme iron, in which the triazole ring of fluconazole binds to the sixth ligand water molecule, indicating that the water is not replaced during the ligation of fluconazole, as would be seen in other P450-azole complexes. The existence of two novel interaction modes of the azole drug with the heme iron of CYP121 contributes to our understanding of varied interactions between P450s and their inhibitors.

The function of CYP121 was shown to be in formation of a C-C bond between 2 tyrosyl carbon atoms of cyclo-L-Tyr-L-Tyr (cYY), a cyclic dipeptide whose formation is catalysed by the cyclodipeptide synthase product of the adjacent gene (*Rv2275*). The function of this molecule remains uncertain. By using exogenous redox partner proteins (ferredoxin reductase and ferredoxin from spinach) electron transfer to the P450 for catalysis was demonstrated (120). In addition, gene knock-out experiments indicated that the *CYP121* is an essential gene for *M. tuberculosis* viability, and therefore that the enzyme is a potential drug target for treating *M. tuberculosis* infection (154).

**CYP130:** The *CYP130* gene is missing from both *M. bovis* and *M. bovis* BCG strains, suggesting that it may relate to the infectivity of Mtb. Both ligand-free and econazole-bound forms of CYP130 crystal structures were determined (137, 155). The CYP130 structure is overall similar to the other P450 enzymes. However, in the presence of inhibitor, it exhibits a dimeric form, whereas the ligand-free CYP130 is a monomer with an open conformation (Figure 1.18), possessing an extended conformation of the BC-loop unmasking a route for substrate access. The BC-loop region is composed of two short helices,  $\alpha B'$  and  $\alpha B''$ . A hydrogen-bonding network of water molecules links the distal water ligand on the heme iron to the I helix, and likely provides a route for proton relay to the heme iron (70, 80).

In the presence of the azole drug econazole, CYP130 is in a dimeric form in the crystal structure. There is a rearrangement of the BC region, in which the secondary structure was lost and relocated in a new position to interact with the econazole molecule (Figure 1.19). In addition, the FG helices are also changed by gaining one turn for the F helix and losing one turn for the G helix, resulting in a drift of the FG loop. Therefore, the FG loop of CYP130 is much shorter than in other P450s. However, it is clear that the FG loop still plays the role of a barrier for the substrate/inhibitor access channel. As yet, there is no

further information on CYP130's natural substrate(s), redox partners or catalytic reaction(s).

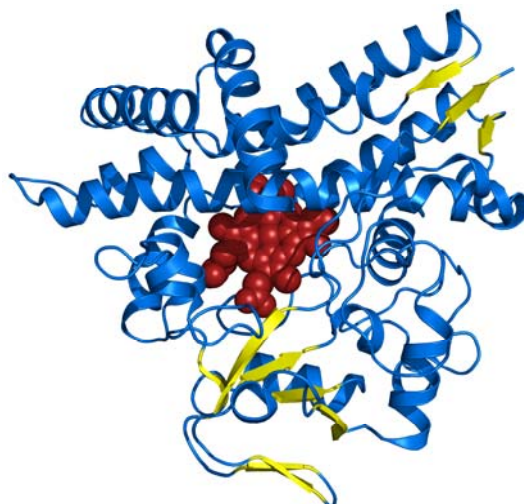


**Figure 1.18. Crystal structure of CYP130 (PDB code 2UUQ)**

Ligand-free CYP130 is shown in a ribbon representation with the alpha helices coloured in blue and the beta sheets coloured in yellow. Heme is in firebrick spacefill. Figure was created using Pymol (141).

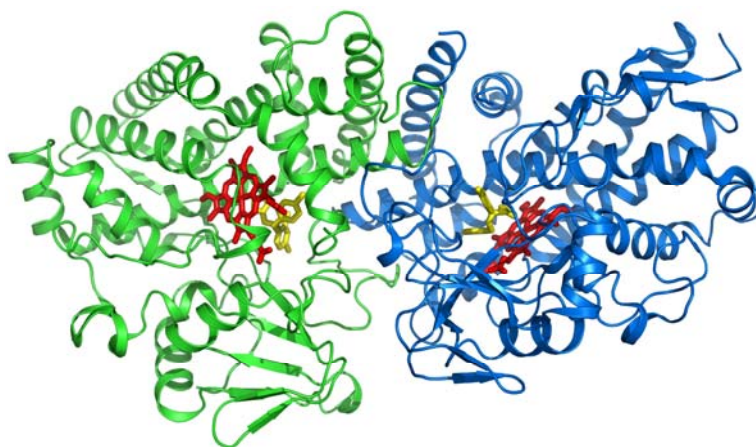


**Figure 1.19. The dimer interface of CYP130**

The CYP130 dimeric form is seen for the econazole-bound form of the enzyme (PDB code 2UVN). Hemes are presented in red and econazole molecules are in yellow. Figures were created using Pymol (141).

**CYP125:** Recently, the crystal structure of Mtb CYP125 was reported at a resolution of 1.4 Å. For the ligand-free form, CYP125 appears as a monomer and has a similar conformational fold to other typical P450 enzymes, with the heme sandwiched between  $\alpha$  helix and  $\beta$  sheet components (Figure 1.20). The FG loop is created by the extension of G and F helices and is visible as a gate for enabling substrate/inhibitor entrance above the heme cofactor. According to McLean *et al.* (121), another crystal structure was obtained at 1.7 Å resolution, and the P450 also appears here as a monomer in the asymmetric unit.

Comparing the structural fold revealed no significant changes between the two forms of CYP125.

The *CYP125* gene was reported to be essential for Mtb infection in mice, and likely participates in hydroxylation of host cholesterol as a carbon source in order to support energy for the growth and viability of *M. tuberculosis* (121). An electron transport chain supporting CYP125 function was also established by using two exogenous redox proteins (*E. coli* flavodoxin reductase and *E. coli* flavodoxin). Reconstitution of CYP125 activity with these proteins indicated that CYP125 catalyzed oxidation of cholesterol C27 into 27-hydroxycholesterol (121). Like other Mtb CYPs, CYP125 is able to bind several azole antifungal drugs such as econazole, fluconazole, ketoconazole, itraconazole, miconazole and clotrimazole with  $K_d$  values of 1.17, 43.2, 27.1, 30.2, 4.6, and 5.3  $\mu\text{M}$ , respectively (121, 122). The crystal structures of the CYP125-econazole and cholest-3-en-4-one complexes (Figure 1.20) were solved to resolutions of 2.2 and 1.58 Å, respectively, showing the econazole molecule bound within the active site cavity and with direct ligation to the heme iron, similar to that previously observed in other P450-azole complexes such as those for CYP130, CYP51B1 and for one of the forms of CYP121 (119, 137, 139).

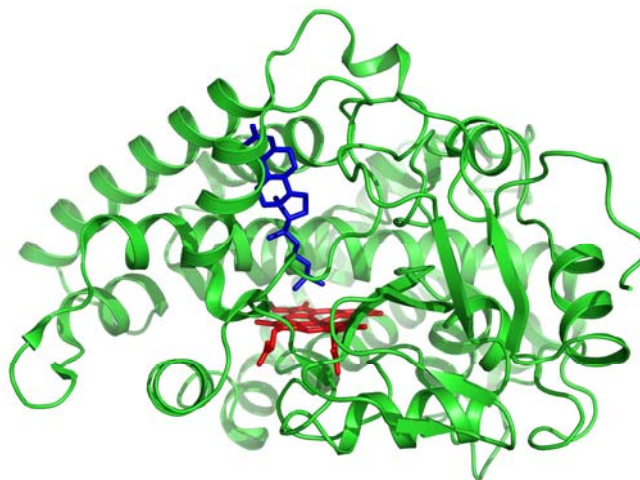


**Figure 1.20. Overview of cholest-4-en-3-one-bound CYP125 crystal structure (PDB code 2X5W).** The overall topology of CYP125 is shown with heme coloured in red,  $\alpha$  helices and  $\beta$  sheets coloured in green, the I helix shown crossing over the heme cofactor, and the cholest-3-en-4-one molecule in blue. Figure was created using Pymol (141).

**CYP124:** CYP124 is present in many bacteria including mycobacterial species, actinomycetes, and proteobacteria (136), suggesting that it plays important roles in these bacteria. The crystal structure of Mtb CYP124 was defined in 2009 by Johnston and co-workers (136). The structure of the ligand-free form was obtained at a resolution of 1.5 Å, revealing structural features similar and comparable with other Mtb P450 proteins. In

detail, the active site of CYP124 is created by several features such as the heme, I, F, G, C, and L helices, and the proximal Cys<sup>379</sup> thiolate, which anchors the heme iron and serves as the proximal axial ligand (Figure 1.21). Similar to other P450s, the FG loop is formed by the extension of two F and G helices and acts as the channel “door” for allowing substrate/inhibitor in or out of the active site. However, the FG loop in CYP124 is shorter than in other Mtb P450s for which structures are known. In addition, the  $\beta$ 1 bundle (composed of four antiparallel strands) is involved in forming a half of the active site cavity (136).

The catalytic activity of CYP124 is related to catalysis of  $\omega$ -hydroxylation of methyl-branched lipids (136), an important building material of the thick lipid membrane of Mtb. Due to the absence of a sterol biosynthesis pathway, *M. tuberculosis* is not able to synthesize sterols *de novo*, therefore it may not be surprising that the Mtb genome encodes many other enzymes participating in lipid metabolism, which are necessary for building and retaining the dense cell membrane. The reconstitution of spinach ferredoxin-NADP<sup>+</sup> reductase and spinach ferredoxin was successful in supporting electron transfer for the catalytic cycle of CYP124. In addition, the crystal structure of the CYP124-phytanic bound complex showed a reorganization of secondary structural elements (especially in the F, G, B, C, and D helices) compared to the ligand-free structure. The terminal methyl group of phytanic acid is bound very close to the high-spin heme iron, facilitating the  $\omega$ -hydroxylase activity (Figure 1.21). The structure of the CYP124-phytanic acid complex provides important insights into how CYP124 accommodates a substrate and catalyses its  $\omega$ -hydroxylation (136).

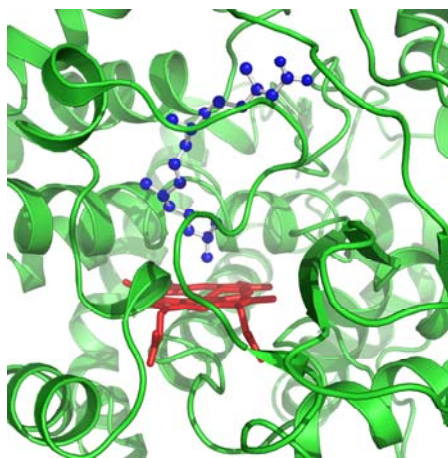


**Figure 1.21. The active site of CYP124 in complex with phytanic acid (PDB code 2WM4).** Heme is in red and phytanic acid is in blue ball-and-stick presentation. Figure was created using Pymol (141).

***CYP142***: A novel cholesterol oxidase CYP142 was recently characterized by Driscoll *et al.* The crystal structure studies on Mtb CYP142 have shown its overall fold is similar to the crystal structures of CYP124 and CYP125, where the latter also has the same function in cholesterol hydroxylation as does CYP142 (124). The ligand-free CYP142 structure was solved at a resolution of 1.65 Å using CYP124 as a search model. The structural conformation reveals that the active site of CYP142 is composed of common features such as the F, G, B, C, and I helices, and that these are highly similar to those in previously reported Mtb P450 structure. However, the FG loop conformation, FG helices orientation, and BC loop of CYP142 were slightly different from other P450s. In addition, compared to the structures of CYP124/CYP125, the enzyme does not possess a loop that connects the  $\beta$ 1 and  $\beta$ 2 strands. The active site of CYP142 is identical to CYP125 in terms of topology, with the substrate/inhibitor channel formed by FG and BC loops, and by the I helix, and the active site channel lined by predominantly hydrophobic residues. A cholesterol docking model was also obtained for CYP142 using molecular modelling, showing that the cholesterol alkyl chain points to the heme iron. Furthermore, the dynamic docking data indicated that the cholesterol molecule was deeply buried in the active site and that it interacted with several hydrophobic residues such as Leu<sup>226</sup>, Ile<sup>76</sup>, Met<sup>280</sup>, Val<sup>227</sup> and Phe<sup>380</sup>.

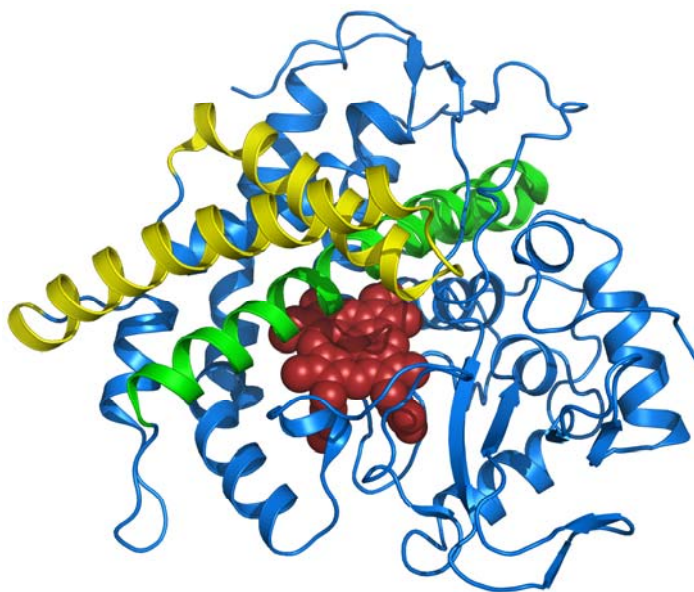


**Figure 1.22. Conformational features of ligand-free CYP142 (PDB code 2XKR)**

Heme is coloured in red, I helix is in green, and FG helices are in yellow. Figure was created using Pymol (141).

Like CYP125, CYP142 also participates in cholesterol hydroxylation. Cholesterol metabolism is crucial for the survival and infection of Mtb in the host. The electron transport pathway of the enzyme was also assembled by reconstitution of exogenous redox

partner proteins (spinach ferredoxin reductase and ferredoxin), demonstrating electron support for processive oxidations at the terminal position on the cholesterol methyl branched side chain in order to produce 5-cholestenoic acid, a likely product required for cholesterol catabolism. However, CYP142 reconstitution with *E. coli* flavodoxin reductase and flavodoxin was also successful, leading to a single oxidation event and formation of 27-hydroxycholesterol, indicating that, by using different redox systems, the protein may be able to generate different products. The 27-hydroxycholesterol product may be used to control cholesterol transport in macrophages in which the Mtb bacterium is engulfed (156-158).

In summary, the crystal structures of six Mtb P450 enzymes that have been determined to date reveal a conserved fold of structure, including heme position, the active site cavity, I helix and other components. The crystal structures of ligand-free and inhibitor/substrate-bound forms of these proteins enables comparisons between the structural folds of the Mtb P450 enzymes and analysis of structural adaptations for ligand binding. Among these P450s, five of the proteins (CYP51B1, CYP121, CYP125, CYP124, and CYP142) have had substrates identified, and have variously been shown to be involved in lipid metabolism and secondary metabolism of the host cell. Twenty P450 enzymes were found in Mtb and many of these are potential drug targets in order to discover new and more effective treatments for the tuberculosis infection. Therefore, the understanding in more detail of all 20 Mtb P450 enzyme structures, substrate specificity and P450 biophysical and biochemical properties will provide important clues about their functions *in vivo*, and thereafter provide immensely useful tools as scaffolds for design of specific inhibitors.

### **1.5.8 Aims and objectives**

As mentioned previously, the Mtb genome reveals a large number of P450 genes, indicating important functions for the growth and viability of this mycobacterium. To elucidate more detail about the function of these P450 enzymes, this thesis describes the characterization of two novel cytochrome P450 enzymes, CYP126 and CYP141, from Mtb, and also analysis of a number of redox partner proteins in order to build a model of these P450's reactions, as well as to determine substrate specificity and to identify and analyse inhibitor interactions.

**Specific objectives include:**

- 1- Biochemical, biophysical and crystal structure determination of two novel Mtb P450s (CYP126 and CYP141) including analysis of interactions with six different Mtb and heterologous redox partner proteins (FdR, FprA, *E. coli* FLDR, *E. coli* FLD, Fdx<sub>1</sub> and Fdx<sub>2</sub>).
- 2- Reconstitution of electron transport pathways for two novel P450 proteins and for four other well-known Mtb CYPs (CYP51B1, CYP121, CYP125 and CYP142) for which substrates have been identified.
- 3- Screening a compound library to identify scaffolds for inhibitors and substrates for CYP126, including analysis of ligand binding and substrate oxidation.

## 2 MATERIALS AND METHODS

This chapter contains specific methodologies used in experiments presented in this thesis. These experiments include the cloning, expression and purification of target cytochrome P450 and redox partner enzymes, along with spectroscopic, kinetic and structural techniques used to examine the target proteins, their three dimensional structures, binding of inhibitor-like and substrate-like ligands, electron transfer properties and features of their cofactors and cofactor-binding regions. For the research, recombinant proteins were normally expressed in *Escherichia coli* by growing in appropriate media. This chapter provides an exhaustive list of analytical methods that were used to characterize two cytochrome P450 enzymes as well as their redox partner proteins, including a full list of chemicals and reagents used.

### 2.1 Growth media for *E. coli*

#### **Luria-Bertani Medium (LB Medium)**

Per litre of distilled, deionized water (ddH<sub>2</sub>O), the following were added:

10 g Bacto-tryptone  
5 g Bacto-yeast extract  
10 g NaCl

#### **YT Medium**

Per litre of ddH<sub>2</sub>O, the following were added:

16 g Bacto-tryptone  
10 g Bacto-yeast extract  
5 g NaCl

#### **SOC Medium**

Per litre of ddH<sub>2</sub>O, the following were added:

20 g Bacto-tryptone  
5 g Bacto-yeast extract  
0.5 g NaCl

The media were sterilized at 121 °C for 20 minutes, and once media were cooled to 60 °C or below, 20 ml of sterile 1 M glucose was added. Prior to use, a sterile solution of magnesium chloride was added (5 ml, 2.0 M per litre of medium).

## Luria-Bertani Medium Agar Plates.

Per litre of ddH<sub>2</sub>O, the following were added:

- 10 g Bacto-tryptone
- 5 g Bacto-yeast extract
- 10 g NaCl
- 10 g Bacto-Agar

The media was sterilized at 121 °C for 20 minutes, the agar solution was cooled (to 50 °C), the appropriate antibiotic added (see table below) and the mixture poured into plates. Plates were stored (4 °C) for up to four weeks.

## 2.2 Antibiotics

Antibiotic	Stock solution preparation	Use in liquid culture	Use in agar plates
Ampicillin (Amp)	50 mg/ml in deionized water. Filter sterilized and stored at -20 °C	50 µg/ml	100 µg/ml
Tetracycline (Tet)	5 mg/ml in 50% EtOH. Stored at -20 °C. Protected from light	34 µg/ml	68 µg/ml
Carbenicillin (57)	50 mg/ml in deionized water. Filter sterilized and stored at -20 °C	50 µg/ml	100 µg/ml
Rifampicin (Rif)	10 mg/ml in 65% Methanol, 0.17 N NaOH. Stored at -20 °C and used within 2 weeks. Protected from light.	200 µg/ml	
Kanamycin (Kan)	30 mg/ml in deionized water. Filter sterilized and stored at -20 °C	30 µg/ml for cells containing kan <sup>R</sup> plasmid. 15 µg/ml for cells containing chromosomal kan <sup>R</sup> gene.	60 µg/ml for kan <sup>R</sup> gene on plasmid. 30 µg/ml for chromosomal kan <sup>R</sup> gene.
Chloramphenicol (159)	34 mg/ml in EtOH. Stored at -20 °C. Protected from light.	34 µg/ml	34-68 µg/ml

## 2.3 Bacterial Strains

*E. coli* strains used in cloning work and for recombinant protein expression were described below. Unless stated otherwise, all strains came from Novagen.

Strain	Genotype/description
BL21 (DE3)	<i>F' ompT hsdS<sub>B</sub>(r<sub>B</sub><sup>-</sup> m<sub>B</sub><sup>-</sup>) gal dcm (DE3)</i>
HMS174 (DE3)	<i>F' ompT hsdR(r<sub>K12</sub><sup>-</sup> m<sub>K12</sub><sup>+</sup>) (DE3) (Rif<sup>R</sup>)</i>
Rosetta (DE3)	<i>F' ompT hsdS<sub>B</sub>(r<sub>B</sub><sup>-</sup> m<sub>B</sub><sup>-</sup>) gal dcm (DE3) lacY1 pRARE2 (Cm<sup>R</sup>)</i>
Rosetta-Gami (DE3)	<i>Δara-leu 7697 ΔlacX74 ΔphoAPvull<sup>+</sup> phoR araD139 ahpC galE galK rspL (DE3) F'[lac (lacI<sup>q</sup>)pro] gor522::Tn10 trxB::kan pRARE (Cm<sup>R</sup>, Kan<sup>R</sup>, Str<sup>R</sup>, Tet<sup>R</sup>)</i>
Origami B (DE3)	<i>F' ompT hsdSB(rB<sup>-</sup> mB<sup>-</sup>)<sub>R</sub> gal dcm lacY1 ahpC (DE3) gor522::Tn10 trxB (Kan<sup>R</sup>, Tet<sup>R</sup>)</i>
JM101	<i>F' traD36 proAB lacI Δ(lacZ)M15/Δ(lac-proAB) glnV44 e14 gyrA96 recA1 relA1 endA1 thi hsdR17</i>
XL1-Blue	<i>supE44 hsdR17 recA1 endA1 gyrA46 thi relA1 lac<sup>-</sup> F' [proAB<sup>+</sup> lacI<sup>q</sup> lacZΔM15 Tn10] (Tet<sup>R</sup>)</i>
NovaBlue	<i>endA1 hsdR17 (r<sub>K12</sub><sup>-</sup> m<sub>K12</sub><sup>+</sup>) supE44 thi-1 recA1 gyrA96 relA1 lac F' [proA<sup>+</sup>B<sup>+</sup> lacI<sup>q</sup>ZΔM15::Tn10] (Tet<sup>R</sup>)</i>

*E. coli* cells were grown by inoculating a single colony into the appropriate broth. These cultures were then incubated (37 °C, 200 rpm) until the appropriate cell density was achieved.

Bacterial colonies were maintained on agar plates (up to 4 weeks at 4 °C). For long-term storage, a fresh overnight culture (80 ml) was mixed with sterile glycerol (80% v/v, 20 ml) then snap-frozen using a dry ice/ethanol bath and stored (-80 °C). Prior to use, these stocks were thawed and streaked onto fresh agar plates.

## 2.4 Molecular biology

### 2.4.1 PCR amplification of ferredoxin (*Rv1786*) from *Mycobacterium tuberculosis* (Mtb)

PCR for amplification of the 204 bp fragment of the Mtb ferredoxin (*Rv1786*) was performed in a 50 µl volume. The PCR mix was made up in a 0.5 ml thin walled tube containing 25 ng template DNA (*M. tuberculosis* genome cosmid I04 received from Pasteur Institute, Paris), 30 pmol primers (see table below for sequence), 0.2 mM dNTP mix (equimolar dATP, dCTP, dGTP and dTTP), 5 µl 10X *Pfu* buffer and ddH<sub>2</sub>O to make up to the final volume. In addition, 1 µl *Pfu* DNA polymerase was added to the mixture after a denaturation step at 100 °C (2 min). The PCR reaction was performed in a Genius Thermal Cycler (Techne) with a 105 °C heated lid. The cycling parameters were 30 cycles of 95 °C

for 45 s, 67 °C for 30 s, 72 °C for 30 s, terminated by a final 72 °C elongation step for 10 min.

Gene	Oligonucleotide sequence	T <sub>m</sub> (°C)
<i>Rv1786</i>	Forward: 5'- GAG GAA ATC ATA TGA AAG TCC GTC TCG ATC C – 3'	68.8
	Reverse: 5' - CGG GAT CCT CAG TCC GCG TCG TCC TCC TC – 3'	> 75

#### 2.4.2 PCR amplification of ferredoxin reductase (*Rv0688*) from *Mtb*

The ferredoxin reductase (FdR) was cloned by PCR from the cosmid I04 of the *Mtb* H37Rv genome library, which contains the *Rv0688* gene. The reaction contained a 50 µl volume with 30 pmol primers (see sequences below), 25 ng DNA template (cosmid I04), 0.2 mM dNTP mixture (dATP, dTTP, dCTP, dGTP), 5 µl 10X *Pfu* buffer, and ddH<sub>2</sub>O to make up the volume to 50 µl. The reaction was performed in a Genius Thermal Cycler (Techne) with a 105 °C heated lid and preheated for 2 min at 95 °C. Immediately, 1 µl *Pfu* Turbo DNA polymerase (Stratagene) was added to the mixture. Amplification conditions were 95 °C for 2 min, 30 cycles of 95 °C for 50 s, 68 °C for 30s, 72 °C for 1 min, followed by a final polymerization step of 72 °C for 10 min.

Gene	Oligonucleotide sequence	T <sub>m</sub> (°C)
<i>Rv0688</i>	Forward: 5' – GAT CGC ATA TGA ACG CAC ACG TGA CCA GTC G – 3'	70.8
	Reverse: 5' – GGT GGA TCC TAG GCC TGA GTT TGG TCT AAC – 3'	69.5

#### 2.4.3 Agarose gel electrophoresis

DNA fragments of both FdR and Fdx were separated by agarose gel electrophoresis. The agarose gel (1% w/v, electrophoresis grade) was made up in 1 × TAE buffer. Ethidium bromide (0.5 µg ml<sup>-1</sup>) was added for visualisation of the DNA. DNA samples (10 µl) were mixed with loading buffer (2 µl). The loading buffer consisted of Bromophenol blue (0.25% w/v), Xylene cyanol FF (0.25% w/v) and Ficoll Type 400 (Pharmacia) (15% w/v) in water. A 1 kb ladder (4 µl) (NEB) was used as a marker. Gels were run (60 mA for *ca* 30 minutes) and the DNA was visualised by UV illumination.

#### **2.4.4 Diagnostic restriction enzyme digests**

Restriction digests were performed using the applicable DNA (0.2 - 1 µg), 10 x Bovine Serum Albumin (BSA) (1.5 µl) if required, 10 x enzyme buffer (1.5 µl, from enzyme supplier), ~10 units of the enzyme and ddH<sub>2</sub>O (to 15 µl total volume). The digest mixture was incubated (37 °C, 1 hour).

#### **2.4.5 Extraction and purification of DNA from agarose gels**

DNA was extracted from ethidium bromide-stained agarose gels and purified using the QIAquick Gel Extraction kit (Qiagen), according to the manufacturer's instructions. Specifically, a slice of agarose gel containing the DNA fragment of interest was excised using a clean, sharp scalpel. The gel slice was then weighed and three volumes of QG Buffer were added to one volume of gel. The mixture was then incubated for 10 min at 50 °C with occasional inversion in order to facilitate the dissolution of the gel slice. When the gel was completely dissolved, a 1 gel volume of isopropanol was added, followed by mixing. The mixture was then transferred to a QIAquick column, which was placed in a 2 ml collection tube and centrifuged for 1 minute at maximum speed in a microcentrifuge. Following centrifugation, the flow-through was discarded and 0.5 ml of Buffer QG added, and the column centrifuged for 1 minute. Thereafter, 0.75 ml of Buffer PE was added to the column, which was left to stand for 5 minutes at room temperature. The column was then subjected to centrifugation, as previously. The resultant flow-through was then discarded and the column was centrifuged for an additional 1 min. Finally, the column was placed in a clean 1.5 ml tube (Eppendorf), and the DNA bound to the column membrane was eluted by applying 30 µl of Buffer EB to the membrane followed by centrifugation, as described above. Subsequently, the purified fragment of *Rv1786* was 'A' tailed.

#### **2.4.6 'A' tailing of PCR fragments**

The *Rv1786* fragment was 'A' tailed in a 10 µl reaction volume. The mix, made up in a 0.5 ml thin walled PCR tube, contained 1 µl of 5 mM dATP and 7 µl of fragment DNA (~10 ng). In addition, the mix contained 1 µl of 10 x Taq buffer (Promega) and 1 µl of Taq polymerase (1 U/ml). 'A' tailing was performed in a Genius Thermal Cycler (Techne) with the parameters of 70 °C for 30 min. Subsequently, the fragments were ligated into the pGEM-T Easy vector (Promega).

### 2.4.7 Cloning of PCR- and restriction digest-generated fragments into pGEM-T Easy and pET15b plasmid vectors

The PCR-generated *Rv1786* fragment was cloned using a pGEM-T Easy vector system, following the manufacturer's recommended instructions (Promega). A 10 µl ligation reaction was set up containing 1 µl of PCR product, 5 µl of 10 x T4 ligase buffer, 1 µl of pGEM-T Easy vector (50 ng) (Promega), T4 DNA ligase (3 Weiss units/µl) (Promega) and left overnight at 16 °C. Transformation of the ligated products was then carried out using competent *E. coli* Nova blue cells (Novagen). Successful cloning of the *Rv1786* fragment was established by screening for recombinant clones (white) directly by colour selection on X-gal/isopropyl-thiogalactoside (IPTG) indicator plates (blue/white screen). Recombinant clones were prepared using the mini-prep spin kit (Qiagen), following the manufacturer's guide (Promega). The resulting DNA preparations were verified by restriction digestion and then by DNA sequencing of the entire plasmid.

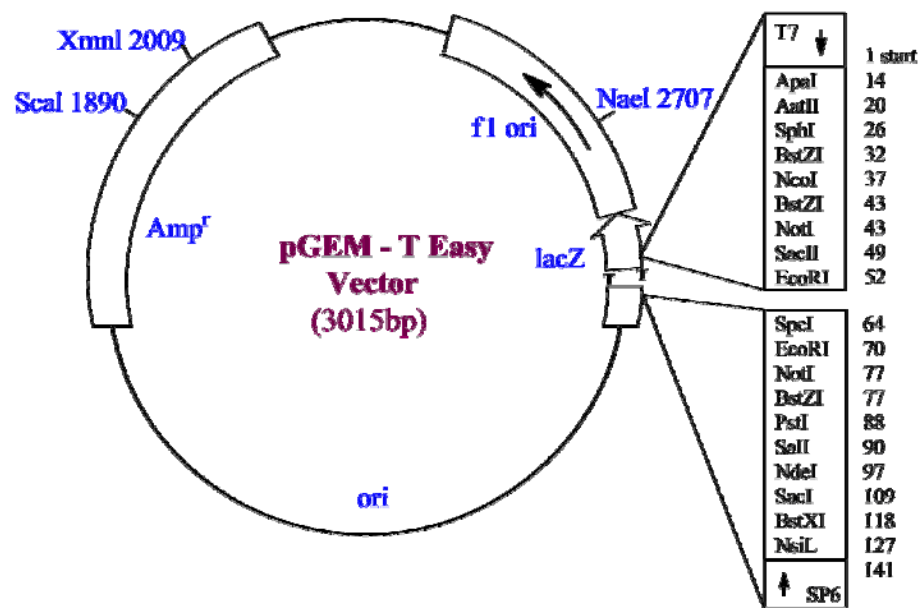


**Figure 2.1. Map of pGEM-T Easy vector.** pGEM-T carries “T” tailing cloning sites, which are available to ligate to “A” tailing sites on the PCR fragments of the *Rv1786* and *Rv0688* genes. Figure prepared based on image presented at <http://www.promega.com>.

The *Rv1786* gene fragment was cloned into pET15b pre-digested with *NdeI* and *BamHI*. A 20 µl ligation reaction was set up containing 2 µl of 10 x Ligase buffer (200 mM Tris-HCl, 100 mM MgCl<sub>2</sub>, 250 µg/ml acetylated BSA, pH 7.6), 2 µl 100 mM DTT, 1 µl 10 mM ATP, 2 µl prepared pET15b vector (100 ng), 2 µl *Rv1786* fragment (200 ng) and 1 µl T4 DNA Ligase (0.4 Weiss U/µL), and the mixture was incubated at 16 °C overnight. Transformation of the ligated products was then carried out using competent *E. coli*

NovaBlue cells (Novagen). Successful cloning of the *Rv1786* fragment was established by screening for recombinant clones on ampicillin-containing LB agar plates. Recombinant clones were prepared by the mini-prep spin kit (Qiagen), following the manufacturer's guide. The resulting DNA preparations were verified by restriction digestion and plasmid DNA sequencing. The cloning of the *Rv0688* gene was carried out using a similar protocol to that for the *Rv1786* gene.

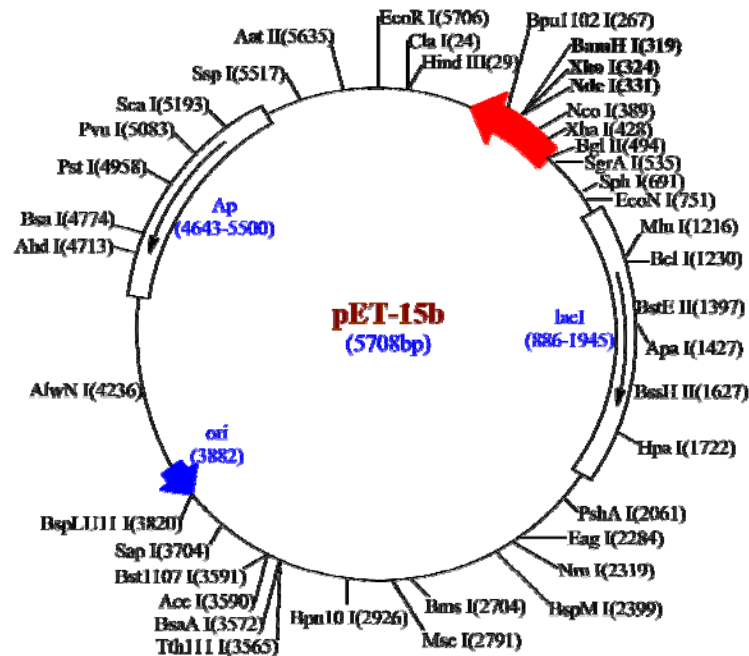


**Figure 2.2. pET15b vector map.** The pET15b plasmid contains an N-terminal His-tag and multiple cloning sites, including *NdeI* and *BamHI*. The *Rv1786* and *Rv0688* gene fragments and pET15b were pre-digested with *NdeI* and *BamHI*, and thereafter gene fragments were ligated to pET15b vector using the T4 DNA ligase enzyme. Figure was prepared based on image presented at [http://depts.washington.edu/bakerpg/plasmid\\_maps/pet15bm.pdf](http://depts.washington.edu/bakerpg/plasmid_maps/pet15bm.pdf).

#### 2.4.8 Transformation of competent cells with plasmid DNA

The competent cells were prepared by inoculating 5 ml of sterile LB media with the appropriate *E. coli* strain, from a glycerol stock or from a single colony picked from an agar plate, and incubated overnight at 37 °C and at ~220 rpm in a shaking incubator. 5 ml of fresh sterile LB medium was inoculated with 50 µl from the overnight culture, and the cells grown to an OD<sub>600</sub> of ~0.6. 1 ml per transformation was taken and put into 1.5 ml Eppendorf tubes, and the cells then pelleted in a microfuge at 13,000 rpm for 30 seconds. Pellets were resuspended in 0.5 ml of 50 mM CaCl<sub>2</sub> (sterile, pre-chilled, on ice). The cells were microfuged again at 13,000 rpm for 30 seconds. Pellets were resuspended a second time in 0.5 ml of 50 mM CaCl<sub>2</sub> (sterile, pre-chilled, on ice) and left for 1 hour on ice. At

this stage cells can be stored at  $-80\text{ }^{\circ}\text{C}$  for transformation at a later date. Bought in or pre-made competent cells were thawed on ice, and used by following the rest of this protocol.

$\sim 1\text{ }\mu\text{g}$  of plasmid DNA was added to the reaction tube. Cells were left on ice for a further hour. Cells were then heat shocked at  $42\text{ }^{\circ}\text{C}$  for 1 minute exactly. Cells were returned to ice for 2 minutes. 0.8 ml of SOC medium was added to each transformation. Transformants were incubated at  $37\text{ }^{\circ}\text{C}$  and at 220 rpm for 1 hour in a shaking incubator. Transformants were microfuged for 60 seconds at 13,000 rpm. The supernatant was decanted and pellets were resuspended in 100–200  $\mu\text{l}$  of fresh LB medium. Transformed cells were spread on agar plates using the technique described above.

#### **2.4.9 Isolation of plasmid DNA**

Qiagen kits were used for the extraction of plasmid DNA from transformed *E. coli* cultures. For small scale preparations, 5.0 ml of LB medium, containing the appropriate antibiotic was inoculated with a single colony of the plasmid-carrying strain and incubated overnight ( $37\text{ }^{\circ}\text{C}$ , 220 rpm). The culture was transferred to microcentrifuge tubes and pelleted (13,000 rpm, 1 minute). The resulting pellet was resuspended in the manufacturer's lysis buffer (TE [50 mM Tris.Cl, 1 mM EDTA, pH 7.5] containing RNaseA, 250  $\mu\text{l}$ , approximately 10 units) and treated in accordance with the manufacturer's protocol (for a microfuge scale preparation).

Larger scale preparations were carried out using a Qiagen midi-prep kit. An overnight culture (50 ml) was grown up as described above. The cells were collected by centrifugation (4000 rpm, 30 minutes) resuspended in lysis buffer (TE containing RNaseA, 2.0 ml) and treated in accordance with the manufacturer's protocol.

#### **2.4.10 Automated DNA sequencing**

The recombinant plasmids were isolated and sequenced in order to confirm the correct DNA sequence using the services of Eurofins MWG Operon. The DNA content was sequenced base on the Sanger method (160). For the pGEM-T vector system, sequencing was carried out by the use of oligonucleotide primers 5'-TGT AAT ACG ACT CAC TAT ACG G-3' and the Sp6 primer 5'-ATT TAG GTG ACA CTA AGA CAT A-3'. For the pET vector system, DNA sequencing was used two primers pETFor 5'-TAA TAC GAC

TCA CTA TAG GG-3' for T7 promoter and pETRev 5'-GCT AGT TAT TGC TCA GCG G-3' for T7 terminator.

## **2.5 Protein expression of histidine-tagged CYP126, CYP141, FdR, Fdx<sub>1,2</sub>, and non-histidine-tagged FLDR, and FLD**

The trial expressions of all proteins (in order to produce the highest levels of soluble protein) were done by transformation of the recombinant plasmids into different *E. coli* cell strains (BL21 (DE3), BL21 gold (DE3), HMS174 (DE3), Rosetta (DE3), Origami B (DE3)) and using cells grown in different media types (2xYT, TB, and LB). Expression of target genes was induced by addition of various concentrations of IPTG in a range of 0–1 mM at different temperatures (18–37 °C). The length of culture time post induction time was also investigated from 2 to 24 h. The expression cells were then collected by centrifugation at 6,500 rpm for 20 min. The levels of soluble proteins were compared by loading samples of supernatant and cell pellets of lysed cells (after centrifugation) on SDS-PAGE gels. The highest soluble protein levels were selected and the relevant cells and culture conditions then used for large scale culture for protein production. The descriptions below present the expression process using the optimized protocol for each protein.

Expression of N-terminal histidine-tagged CYP126 was performed using cell cultures of the *E. coli* strain BL21 gold (DE3) containing the *CYP126/pET15b* expression plasmid (previously developed by Dr. Kirsty McLean, University of Manchester), with cells grown at 37 °C in 10-20 litres of TB medium containing 100 µg/mL ampicillin, and in a refrigerated shaking incubator at 220 rpm. Twenty minutes prior to induction ( $OD_{600} = 0.5-0.6$ ) the temperature was reduced to 18 °C and the culture allowed to equilibrate, with shaking at 180 rpm. The induction of gene expression was carried out by the addition of 10 µM IPTG at  $OD_{600} = 0.7-0.9$ , and cells were grown for a further 18-24 hours at 18 °C, 180 rpm. Cells were harvested by centrifugation (6,500 rpm, 20 min).

Expression of CYP141 was also performed in the *E. coli* strain BL21 (DE3) containing the *CYP141/pET15b* construct (previously developed by Dr. Kirsty McLean, University of Manchester). As before, the cells were grown at 37 °C in 10-20 litres of TB medium containing 100 µg/ml ampicillin with vigorous agitation at 220 rpm. When the  $OD_{600}$  reached 0.6, the temperature was reduced to 18 °C, and after 20-30 minutes 100 µM IPTG was added to induce gene expression. The culture was prolonged for more than 20 h at 18 °C, 180 rpm. Cells were collected by centrifugation at 6000 rpm for 15 min.

Poly-histidine tagged recombinant FdR was constructed by insertion of a 1221 bp DNA fragment containing the *Rv0688* gene into the pET15b expression vector. HMS174 (DE3) *E. coli* cells were used for transformation with the FdR recombinant plasmid. The cells were grown at 37 °C until the OD<sub>600</sub> reached 0.6, and then cooled to 25 °C. Immediately, 1 mM IPTG was added to the culture. The culture was then extended for 24 h at the same temperature. The cells were harvested by centrifugation as before.

For the production of the Fdx<sub>1</sub> and Fdx<sub>2</sub> proteins, the recombinant pET15b plasmids were transformed into the *E. coli* strain HMS174 (DE3). Cells were grown in 10-20 litres of TB medium containing 100 µg/ml ampicillin, and incubated at 37 °C, 220 rpm. Once OD<sub>600</sub> reached ~0.8, the temperature was decreased to 25 °C. The culture was extended for 24 h at 20 °C, 180 rpm without IPTG induction. The collected cells were stored at -20 °C until lysed.

The non-histidine tagged plasmid construct containing the *fprA* gene (*Rv3106*) was a gift from Dr Kirsty McLean (University of Manchester). The *fprA* gene was expressed from the pKM3b vector (*161*) and transformed into HMS174 (DE3). The cells were grown at 37 °C until the OD<sub>600</sub> reached ~0.8 in TB medium. The temperature was then decreased to 25 °C and gene expression induced by the addition of 1 mM IPTG. The culture was extended for 24 h at the same temperature and cells harvested by centrifugation as above. The collected cells were stored at -20 °C until lysed.

The production of the *E. coli* flavodoxin reductase (FLDR) and flavodoxin (FLD) proteins were done by strictly following the expression protocol from the paper of McIver *et al.* (*162*). The plasmid constructs contain the *FLDR* and *FLD* genes were kindly supplied by Dr Kirsty McLean (University of Manchester). For *FLDR* expression, the recombinant plasmid pCL21 was transformed into the HMS174 (DE3) strain, and the transformants were grown in 10 litres of TB medium at 37 °C until the OD<sub>600</sub> was ~1.0. At this time, expression of the *FLDR* gene was induced by the addition of 1 mM IPTG. The cells were grown for a further 3 h and the cells were then centrifuged at 6000 rpm for 15 min at 4 °C, and collected cells stored at -20 °C until lysed. For the expression of *FLD*, the plasmid pDH1 was transformed into JM101 cells. When the OD<sub>600</sub> reached 0.8, the production of *FLD* was induced by the addition of 100 µM IPTG and 5 mg/ml riboflavin. The culture was harvested 6 h after induction by centrifugation as described above. The collected cells were stored at -20 °C until lysed.

## 2.6 Cell Lysis

The cell pellet was washed by resuspension in ice-cold lysis buffer (50 mM potassium phosphate [KPi], 300 mM NaCl, 10 % glycerol, pH 8.0), centrifuged (as above) and then resuspended in the lysis buffer containing a complete<sup>TM</sup> protease inhibitor tablet (EDTA-free) (Roche). PMSF and benzamidine hydrochloride (~1 mM) were added to all buffers and the cell extract was kept on ice at all times to minimise proteolysis.

Cells expressing each of the proteins studied were lysed by intermittent sonication, using a Bandelin Sonoplus GM2600 sonicator with an Ultrasonic Homogeniser HG2600 probe. Sonication was performed by 8-10 x 20 second bursts at full power, with 1 minute breaks between each burst, keeping the suspension on ice at all times. The cell suspension was also subjected to further lysis using a French Press (2 passes, 960 lb/inch<sup>2</sup>) to improve the efficiency of cell lysis. The lysate was centrifuged (18,000 rpm, 30 mins, 4 °C) to remove cellular debris, and the supernatant was filtered, and (for all proteins except FprA, FLDR and FLD) diluted in Nickel buffer (50 mM KPi, 300 mM NaCl, 10 % glycerol, pH 8.0) and then loaded directly onto a nickel column for purification. For the cell supernatants containing FprA, FLDR and FLD, dilution was instead in ice cold buffer Q (50 mM Tris-HCl, 1 mM EDTA, pH 7.2), leading to loading onto a Q-Sepharose column.

## 2.7 Protein Purification

For the purification of N-terminal histidine tagged CYP141 and CYP126, the protein solutions were loaded onto a nickel affinity column (Qiagen, Valencia, CA), pre-equilibrated with Nickel buffer. The loaded columns were washed with 50-100 column volumes of Nickel buffer containing 20 mM imidazole. The proteins were eluted with the same buffer containing 60 mM imidazole. The eluted proteins were then dialysed against two changes of buffer containing 2 L of buffer Q. Thereafter, these protein solutions were loaded onto a Q-Sepharose column (30 cm x 5 cm), which had been equilibrated with buffer Q, and the column was then washed extensively with buffer Q. For the CYP126 purification, the loaded column was washed with 50-100 volumes of buffer Q containing 30 mM sodium chloride (NaCl), and then the protein was eluted using 80 mM NaCl in buffer Q. For the CYP141 purification, the loaded column was washed with 50-100 volumes of buffer Q containing 140 mM NaCl and then eluted with 200 mM NaCl in the same buffer. The intensely red-coloured fractions were pooled and concentrated by ultrafiltration (3,500 rpm, 4 °C) to a final volume of  $\leq 0.5$  ml using Centriprep ultrafiltration devices, with a 30 kDa MWt cut-off (Millipore). For a final purification step, 0.5 ml concentrated proteins

were mixed with 0.5 ml glycerol. Thereafter they were loaded onto a gel filtration column (Sephacryl S-200), and run at a flow rate of 0.1 ml/min. The proteins were collected and concentrated by ultrafiltration (3,500 rpm, 4 °C) to a final concentration of 30-100 mg/mL using Centripreps with a 30 kDa MWt cut-off. The purified proteins were dialysed overnight in 10 mM Tris-HCl buffer, pH 7.5 containing 50% (v/v) glycerol and then stored at -80 °C.

In the case of FdR and Fdx<sub>1,2</sub> protein purifications, these proteins were purified by a single step using a Ni-NTA column. The crude extract was loaded onto Ni columns which were pre-equilibrated with Nickel buffer. The loaded column with Fdx<sub>1</sub> was then washed with 100 column volumes of Nickel buffer containing 12 mM imidazole, and protein eluted from the column in a concentration of 50 mM imidazole in Nickel buffer. The loaded column with Fdx<sub>2</sub> was washed with 100 column volumes of Nickel buffer containing 20 mM imidazole, and then protein eluted with 60 mM imidazole. The loaded column with FdR was washed with 10 mM imidazole in Nickel buffer and then FdR was eluted with 50 mM imidazole. The proteins were dialyzed in 10 mM Tris-HCl buffer (pH 7.5) and thereafter concentrated by ultrafiltration (Centriprep with 5 kDa MWt cut-off) to a concentration of ~2 mM. The protein was stored frozen at -80 °C after the addition of ~50 % glycerol (v/v).

For the purification of non-histidine tagged proteins (FprA, FLDR and FLD), the cell lysate collected after centrifugation was loaded directly onto a Q-Sepharose column (40 cm x 5 cm), which had been pre-equilibrated in buffer Q. The proteins were eluted from the columns in a gradient of 0-1 M sodium chloride (1000 ml) in buffer Q. The yellow coloured fractions were collected and checked on SDS-PAGE gels to identify pure fractions. All pure fractions were then dialyzed in 10 mM Tris-HCl buffer (pH 7.5) and concentrated by ultrafiltration (Centripreps with 30 kDa MWt cut-off). Lastly, ~50 % glycerol was added to the protein sample and they were stored frozen at -80 °C.

## **2.8 Spectrophotometric analysis of purified proteins**

UV-visible absorption spectra of the P450s were recorded at 25 °C over a wavelength range from 250-800 nm using a Cary-50 UV-visible scanning spectrophotometer (Varian) and a 1 cm pathlength quartz cuvette. Purity of protein samples was assessed by comparison of the P450 Soret band (~A<sub>418</sub>, depending on the particular P450 absorbance) to the aromatic amino acid absorption band (A<sub>280</sub>). The ratio of the two peaks A<sub>418</sub>/A<sub>280</sub> is a convenient indicator of P450 purity, with a ratio value of ~ 2.3 (although the value can vary due to the

aromatic amino acid content of the particular P450 protein) indicating highly pure P450 protein. For the ferredoxins, the absorption spectra were recorded at a wavelength range from 250-800 nm, with the oxidized cofactor absorbance peak in the UV-visible wavelength range at 412 nm. For the flavin proteins (FdR, FprA, FLDR and FLD), the flavin absorbance spectra in their oxidized forms exhibited two major peaks between 300 and 500 nm, with the absorbance maxima at 455, 454, 458, and 467 nm, respectively.

## 2.9 Carbon monoxide and nitric oxide binding

Binding of carbon monoxide (CO) to the CYP126 and CYP141 proteins was performed following reduction of the oxidized protein using a few grains of solid sodium dithionite. CO was then bubbled slowly through the ferrous P450 solution for 1 minute inside a fume hood. Spectra of the oxidised, reduced and reduced/CO-bound forms were recorded. P450 difference spectra were generated by the subtraction of the spectrum for the reduced form from that for the reduced/CO-bound adduct. Nitric oxide (NO) complexes of CYP126 and CYP141 were obtained by brief bubbling of the buffered oxidized enzyme solution with NO gas. Care was taken to avoid excessive addition of NO given its ability to form nitrous acid in solution, with consequent effects on protein denaturation.

## 2.10 Concentration determination

The concentration of P450 samples was determined spectroscopically using the method of Omura and Sato (54).

$$A = \epsilon cl \quad \text{Equation 2.1}$$

Equation 2.1: The Beer-Lambert law used for the calculation of cytochrome P450 concentration

Where **A** is absorbance;  $\epsilon$  is the extinction coefficient for the protein; **c** is the sample concentration; and **l** is the pathlength of the sample cuvette.

The P450 concentration was calculated by subtraction of the ferrous P450 spectrum from that for the ferrous/CO-bound adduct, and the absorbance difference calculated between a peak value and a wavelength where negligible absorption change is observed ( $A_{448}$  minus  $A_{490}$ ). The Beer-Lambert law ( $A = \epsilon cl$ ) was then applied, using the P450 molar extinction coefficient  $\Delta\epsilon_{448-490} = 91,000 \text{ M}^{-1} \text{ cm}^{-1}$  (54).

Due to incomplete conversion of the P450s to the reduced/CO-adduct at 450 nm (i.e. P420 formation, likely reflective of protonation of the heme thiolate ligand, was typically observed and was considered likely to be due at least partially to the reductive process involved in forming the adduct), the concentration was also estimated directly using the Soret maximum of the oxidised enzyme in the resting (low-spin state) by using an extinction coefficient of  $95 \text{ mM}^{-1} \text{ cm}^{-1}$  (138).

### **2.11 Hemoprotein concentration determination using the pyridine hemochromagen method**

The heme concentration of P450 enzymes was also calculated using the method of Berry and Trumpower (163). The oxidized spectra were measured using  $5 \mu\text{M}$  protein in 1 ml potassium phosphate buffer (100 mM, pH 7.5) containing 100 mM NaOH, 400 mM potassium ferricyanide [ $\text{K}_3\text{Fe}(\text{CN})_6$ ], and 20% (v/v) pyridine (164). The sample was thereafter reduced by an appropriate amount of sodium dithionite. The heme concentration was calculated based on the difference between oxidized and reduced forms using the Beer-Lambert law (equation 2.1) with the extinction coefficient of  $\Delta\epsilon_{556,4-540 \text{ nm}} = 23.98 \text{ mM}^{-1} \text{ cm}^{-1}$  for heme *b*.

### **2.12 Redox potentiometry**

All redox titrations were performed in a glove-box (Belle Technology) under a nitrogen gas atmosphere. All solutions were degassed under vacuum with nitrogen prior to use in the glove-box. Oxygen levels were maintained at less than 5 ppm. The concentrated CYP126 and CYP141 proteins were passed through an anaerobic Sephadex G25 column (1 x 20 cm) (10DG column, Bio-Rad) immediately on admission to the glove-box to remove all traces of  $\text{O}_2$ . The column was pre-equilibrated and proteins were buffer-exchanged into anaerobic 100 mM potassium phosphate pH 7.0, which was used throughout the experimental procedures. The buffer also contained glycerol at 10% v/v to aid stability of the proteins throughout the process. The protein solution ( $\sim 10\text{-}20 \mu\text{M}$  enzyme in 5 ml buffer), was titrated electrochemically according to the method of Dutton (165) using sodium dithionite as reductant and potassium ferricyanide as oxidant. The communication of enzyme and electrode was facilitated by addition of mediators. Typically,  $2 \mu\text{M}$  phenazine methosulfate (PMS) ( $E^\circ = +80 \text{ mV}$ ),  $5 \mu\text{M}$  2-hydroxy-1,4-naphthoquinone (HNQ) ( $E^\circ = -145 \text{ mV}$ ),  $1 \mu\text{M}$  methyl viologen (MV) ( $E^\circ = +430 \text{ mV}$ ), and  $1 \mu\text{M}$  benzyl viologen (BV) ( $E^\circ = +311 \text{ mV}$ ) were introduced to mediate within the full experimental range of the titration (166, 167). At least 10-15 minutes were allowed to elapse between each addition of reductant/oxidant to

ensure equilibration of the solution and stabilization of the electrode. Spectra (250-800 nm) were recorded using a Cary UV-50 Bio UV-Visible scanning spectrophotometer coupled to a fibre optic probe. The potential of protein was measured using a Mettler Toledo SevenEasy S20-K meter coupled to a Calomel electrode (ThermoRussell Ltd.) at 25 °C. The calibration of the electrode was done by using the Fe<sup>3+</sup>/Fe<sup>2+</sup> EDTA couple as a standard (+108 mV). The calomel electrode was corrected by +244 mV ± 2 mV relative to the standard hydrogen electrode. Spectral data at wavelengths maximal for the optical (Soret) transition between oxidised (Fe<sup>3+</sup>) and reduced (Fe<sup>2+</sup>) forms of P450 heme iron were plotted *versus* the applied potential, and the data fitted to the Nernst function using Origin 7.0 (OriginLab, Northampton MA).

### 2.13 pH titration

The ferrous P450 pH titrations were conducted within a Belle Technology glove-box under a N<sub>2</sub> atmosphere with oxygen maintained at less than 5 ppm. Degassed, concentrated protein samples (CYP126 and CYP141) were loaded through an anaerobic Sephadex G25 column (1 x 20 cm) immediately on admission to the glove box to remove all traces of O<sub>2</sub> and to exchange into the appropriate buffer: 100 mM potassium phosphate, pH 6.0, containing 10% v/v glycerol. A small amount of sodium dithionite was added to the protein solution to reduce the ferric P450 heme iron to ferrous, and then the sample volume of 5 ml was titrated between pH 6.0 and 10.6 using potassium hydroxide. After 3-5 minutes equilibration at each titration point, spectra were recorded (typically between 250 nm and 800 nm) using a Cary UV-50 Bio UV-Visible scanning spectrophotometer coupled to a fibre optic probe. Spectral data at wavelengths maximal for the optical transition between the pH 6.0 and 10.6 forms of the ferrous P450 heme iron were collated and data were analysed and fitted using Origin 7.0 (OriginLab, Northampton MA). The pK<sub>a</sub> value was generated by fitting to equation 2.2:

$$y = A_0 + (A_{\max} - A_0)/(1 + 10^{(pK_a - x)}) \quad \text{Equation 2.2}$$

Where: y = absorbance value determined at pH value x, A<sub>0</sub> = minimum value of absorbance, A<sub>max</sub> = maximum value of absorbance.

## 2.14 Inhibitor binding

The P450 inhibitors; imidazole, clotrimazole, econazole, ketoconazole, miconazole, fluconazole and voriconazole were used. These were prepared as stock solutions in DMSO. In contrast, 2-phenylimidazole, and 4-phenylimidazole were prepared in potassium phosphate buffer (100 mM, pH 7.5). Additions of the inhibitors was done in 0.1-0.2  $\mu\text{l}$  aliquots using a Hamilton syringe, titrating a final volume of not more than 2  $\mu\text{l}$  into the total assay volume of 800  $\mu\text{l}$ . Spectra were recorded after each addition of ligand, and difference spectra were computed by subtraction of the starting (ligand-free) spectrum from those generated at each point in the titration. The apparent maximum absorbance change induced at each point in the titration was determined by subtraction of the minimum absorption value at the trough in each difference spectrum from the maximum value at the peak (using data at the same wavelengths in each titration). Dissociation constants ( $K_d$  values) were determined by plotting the maximum differential changes in absorption *versus* the relevant ligand concentration. Data were fitted either to a rectangular hyperbola (Equation 2.4) or, where ligands bound very tightly to the P450 enzyme, to a quadratic function (Equation 2.3) that accounts for the quantity of enzyme consumed in the enzyme-substrate complex at each point in the titration.

$$A = ((A_{\max} / (2 \times E)) \times (L + E + K_d)) - ((L + E + K_d)^2 - (4 \times L \times E))^{0.5} \quad \text{Equation 2.3}$$

Equation 2.3. Quadratic function for ligand binding analysis.

$A$  is the observed absorption difference at eachazole titration point,  $A_{\max}$  is the maximal absorption difference atazole saturation,  $E$  is the total enzyme concentration,  $L$  is the ligand concentration used to obtain  $A$ , and  $K_d$  the dissociation constant for the ligand.

$$Abs = \frac{A_{\max} [L]}{K_d + [L]} \quad \text{Equation 2.4}$$

Equation 2.4. Hyperbolic function for ligand binding analysis.

$A_{\max}$  is the maximal absorbance change at ligand saturation,  $K_d$  is the dissociation constant for the ligand binding to the P450,  $L$  is the ligand concentration used and  $Abs$  is the observed absorption difference generated at the ligand concentration  $L$ .

### **2.15 Differential Scanning Calorimetry**

DSC was used to examine the stability of CYP126, CYP141, and FdR proteins in order to obtain data on melting temperatures ( $T_m$  values). The protein solution was dialysed against several changes of potassium phosphate buffer (10 mM Kpi, pH 7.5), which was used throughout the experimental procedures for DSC reference, equilibration and dilution. Purified proteins were prepared at a final concentration of 0.4 mg/ml. A baseline scan was collected by loading DSC sample and reference cells with degassed buffer using an appropriate temperature and scan rate (typically 20-90 °C, 60 °C /h). The DSC scans were repeated several times using the same parameters to establish reversibility and reproducibility. This repetition minimises baseline artifacts that can be induced by the thermal shock involved in loading the sample or reference cells. The protein solution was added to the DSC sample cell after final cooling and scanned using the same program as in the reference scan. All thermal transitions were recorded by a VP-DSC instrument (MicroCal Inc., Amherst, MA). Data were analysed using Origin software (OriginLab).

### **2.16 Light scattering**

Light scattering was performed at the University of Manchester Biomolecular Analysis facility by Mrs Marj Howard. Prior to the light scattering experiments, concentrated protein was dialysed into 10 mM Tris-HCl buffer containing 150 mM NaCl, pH 7.5, and then diluted to 200  $\mu$ M in 500  $\mu$ l in the same buffer. The protein samples were gel filtered using a Superdex-200 10/300 GL column and directly passed through a Wyatt EOS 18-angle laser photometer with the 13<sup>th</sup> detector replaced with Wyatt QELS detector for the simultaneous measurement of hydrodynamic radius. This was coupled to Wyatt Optilab rEX refractive index detector and the hydrodynamic radius, molecular mass moments and concentration of the resulting peaks were analysed by using Astra 5.3.2 software.

### **2.17 Mass spectrometry**

Electrospray mass spectrometry was carried out on a Waters LCT Mass Spectrometer and a Waters Alliance autosampler, running Waters MassLynx 4.0 software, and run by Dr Reynard Spiess (MIB, University of Manchester). The cone voltage was set to 45 V and source temperature to 80 °C. The system was calibrated using horse heart myoglobin. The protein samples were washed and exchanged into ddH<sub>2</sub>O several times to remove all salts using a Centricon ultrafiltration device (30 kDa cut off, Millipore), and then concentrated to 4 mg/ml in 250 ml of a 50/50 mixture of acetonitrile (ACN)/H<sub>2</sub>O, 0.1% formic acid. Thereafter, the samples were injected into a mobile phase of 50/50 ACN/H<sub>2</sub>O, 0.1 % formic

acid. The 1 s scan and the average molecular mass were calculated using the MaxEnt algorithm of MassLynx 4.0 software.

### 2.18 Steady-state kinetics

Steady-state kinetic measurements of Mtb ferredoxin reductase (encoded by *Rv0688* gene) were carried out by following the reduction of potassium ferricyanide using both NADH and NADPH as electron donors. Kinetic parameters ( $k_{\text{cat}}$ ,  $K_m$ ) for ferricyanide reduction were determined in 100 mM potassium phosphate buffer (pH 7.5) at 25 °C. Enzyme concentration was used at 100 nM. Ferricyanide concentration was maintained at 1.0 mM (near-saturating) in reactions where NAD(P)H concentrations were varied (from 0–1 mM) to establish  $K_m$  values for the coenzymes. In reactions where the concentration of NAD(P)H was maintained at near-saturating concentrations, ferricyanide concentrations were varied (0-1 mM) to determine the  $K_m$  for ferricyanide. Ferricyanide reduction was determined at 420 nm ( $\epsilon_{420} = 1020 \text{ M}^{-1} \text{ cm}^{-1}$ ). Reaction progress was monitored over 1 min and reaction measurements were repeated at least three times, and all data points varied < 5 % from the mean. The observed rate against substrate concentration data were fitted to the Michaelis-Menten function to establish relevant the  $K_m$  and  $k_{\text{cat}}$  parameters.

### 2.19 Circular dichroism

The protein samples for CD measurement were prepared at concentration of 2  $\mu\text{M}$  for far-UV CD and 50  $\mu\text{M}$  for visible region CD. The CD spectra were recorded on a JASCO J-810 spectropolarimeter. The far-UV spectra were recorded over the wavelength range of 190–260 nm in a 0.1 cm pathlength quartz cuvette with a scan rate of 10  $\text{nm min}^{-1}$ . The CD spectrum of the baseline (buffer) was then subtracted from the measured spectrum to give the corrected spectrum. In the visible region (260–600 nm), the CD spectra were recorded by using a 0.5 cm pathlength quartz cuvette and with a scan rate of 20  $\text{nm min}^{-1}$ . The molar ellipticity per residue values were calculated using equation 2.5 (see below). The secondary structural content was analyzed by fitting using the Selcon program (168). The CD spectra in both the far-UV and visible regions were generated using Origin software.

$$[\theta] = \frac{100 \times \theta}{(C \times l)} \quad \text{Equation 2.5}$$

Where:  $[\theta]$  = molar circular dichroism per residue,  $\theta$  = measured ellipticity,  $C$  = molar concentration of protein, and  $l$ : cell pathlength in cm.

## **2.20 Magnetic circular dichroism**

Magnetic circular dichroism spectra were recorded by Dr Hazel Girvan (University of Manchester) and Dr Myles Cheesman (School of Chemistry, University of East Anglia). The protein samples were prepared to concentrations between 50–200  $\mu\text{M}$ , and the spectra for ligand-free CYP126 and CYP141 were recorded on a Jasco circular dichrograph model J-810 for the UV-visible and model J730 for the near-infrared regions. MCD spectra in the UV-visible region were recorded using a 0.1 cm pathlength quartz cuvette with sample concentration around 50-200  $\mu\text{M}$ . Spectra in the near-infrared region were recorded in a 0.2 cm pathlength quartz cuvette with the same sample concentration. MCD signals were recorded at a magnetic field of 8 Tesla.

## **2.21 Electron paramagnetic resonance**

EPR spectra were collected by Dr Stephen Rigby (University of Manchester). The concentration of purified proteins used was 200  $\mu\text{M}$  in 50 mM potassium phosphate buffer (pH 7.5) containing 10% glycerol. For inhibitor-bound CYP126 and CYP141 spectra, 100  $\mu\text{l}$  of native enzyme solutions (at 200  $\mu\text{M}$ ) were mixed with 2  $\mu\text{l}$  of saturated ketoconazole (CYP126) and clotrimazole (CYP141) stocks. In the case of reduced ferredoxins, the protein solution was reduced by the addition of sodium dithionite until the red-brown colour was lost. X-Band EPR spectra of samples were collected on a Bruker ELEXSYS E500 series electromagnet and microwave source interfaced to a Bruker EMX control unit, and temperature control was effected using an Oxford Instruments ESR900 cryostat linked to an ITC503 controller. The protein samples were rapidly frozen in liquid nitrogen before reading.

## **2.22 Stopped-flow kinetic studies**

Multiple-wavelength scanning absorption studies of FdR were measured by using a PDA (photodiode array) detector attachment in rapid mixing experiments. Reactions were typically performed using an enzyme concentration of 50  $\mu\text{M}$  (25  $\mu\text{M}$  in the final mixture) in 100 mM potassium phosphate (pH 7.5). NADH and NADPH (at concentrations up to 250  $\mu\text{M}$  in the final mixture) were mixed with oxidized enzyme. Spectra were collected over extended time periods after the mixing event. Spectra collected were then analyzed globally using the Applied Photophysics ProKin software package to determine the kinetics of the process and to identify any intermediate species forming between oxidized and 2-electron reduced (hydroquinone) states, and their rates of formation and decay.

To investigate the ability of sodium dithionite-reduced FdR to deliver electrons to electron acceptors ( $\text{NAD}^+$  and  $\text{NADP}^+$ ), the protein sample was reduced by addition of excess dithionite under anaerobic conditions (in glove-box). The excess dithionite was then removed by passing reduced enzymes through a BioRad Econo-Pac 10DG desalting column (pre-equilibrated with degassed 100 mM potassium phosphate buffer, pH 7.0) in the anaerobic environment. The reduced enzymes were diluted to a concentration of 50  $\mu\text{M}$  and mixed with  $\text{NAD}^+$  or  $\text{NADP}^+$  (up to final concentration of 250  $\mu\text{M}$ ) in the stopped-flow apparatus. Reoxidation of FdR was recorded by accumulation of both single wavelength data (at 455 nm) and entire spectra using a PDA detector. The rates of FdR reoxidation in the presence of  $\text{NAD}^+$  and  $\text{NADP}^+$  were analyzed as described above.

### 2.23 Crystallization

Purified proteins were concentrated to 20-40 mg/ml (in case of CYP126, CYP141) and 80 mg/ml (in case of ferredoxin ( $\text{Fdx}_1$ ) – encoded by *Rv1786* gene), and then subjected to automated screening of crystallization conditions using a nanolitre drop setter Mosquito robot (TTP LabTech) using the Nextal screening JCSG, Classics Lite suite, and PEGs suite solutions (Qiagen). Equal volumes of protein and precipitant solution (0.1  $\mu\text{l}$ ) were mixed in 96-well intelliplates using sitting drop vapour diffusion and incubated at 4 °C. Small crystals were observed in a number of conditions within 2 days (for CYP126 and  $\text{Fdx}_1$ ), and at 40-60 days (for CYP141). The most promising conditions in JCSG, Classics Lite suites, and PEGs suites were focused on, and screening around these conditions was performed by varying the concentration of PEG (4k, 6k, and 8k), sodium acetate, protein/crystallization solution ratios, different pH values, and increasing drop size to yield larger, more suitable crystal forms. Streak-seeding was also used to obtain improved crystals suitable for data collection. For the CYP126 ketoconazole-bound complex, the protein solution (at a concentration of 20 mg/ml) was prepared by the addition of 2  $\mu\text{l}$  of a saturated ketoconazole solution. Thereafter, sitting drop drops were prepared by mixing 1  $\mu\text{l}$  of ketoconazole-bound CYP126 with 1  $\mu\text{l}$  mother liquid (40% sodium sulfate, 0.1 M Tris pH 7.0) and incubating at 4 °C. The sodium phosphate conditions only generated low-quality crystals, and then streak-seeding was used to generate crystals in the sodium acetate conditions (38% sodium acetate, 0.1 M sodium cacodylate, pH 6.5).

Seeded crystals were placed in cryoprotectant, and flash-frozen in liquid nitrogen for X-ray diffraction experiments. Data for CYP126, CYP141, and  $\text{Fdx}_1$  were collected from a single cryofrozen crystal at the Diamond Light Source, Oxford, with processing by the XDS

program package and subsequent handling in the CCP4 program suite (169-172). The structure of ligand-free CYP126 and ketoconazole-bound CYP126 were solved by Dr Colin Levy and Dr David Leys (University of Manchester) using molecular replacement (MR), and utilising a homology model derived from the structure of P450eryF (CYP107A1), with a PDB code of 1OXA for CYP126. The CaspR pipeline was utilised in conjunction with Phaser to generate the initial model. Rebuilding and refinement were carried out using ArpWarp, COOT and Phenix in conjunction with Molprobit to validate the structure (173-175).

#### 2.24 Reconstitution of a Mtb P450 redox partner electron transport chain

Redox systems for Mtb P450s were constructed by combinations of three protein components in a 1:1:4 ratio (P450:reductase:ferredoxin) prior to diluting in 50 mM potassium phosphate buffer (pH 7.5). The concentration of P450 was typically 4-5  $\mu$ M. The reactions were done in 1.0 ml sealed cuvettes for spectral measurements (at 25 °C). The buffer was deaerated and saturated with CO by bubbling with CO gas in sealed quartz cuvette for at least 5 min. Thereafter, the protein components were injected through the rubber septum (less than 30  $\mu$ l additions). The redox reactions were initiated by the addition of 200  $\mu$ M NADPH and the spectra (300-700 nm) were recorded regularly (1.30 min intervals) until there was no further change in the P450 Fe(II)CO complex formation. The rates of Fe(II)CO complex formation were determined by plotting of  $A_{450}$  versus time, and data were fitted using an exponential function to generate  $T_{1/2}$  values. The rate constants were then calculated using equation 2.6.

$$k = \frac{\ln 2}{T_{1/2}} \quad \text{Equation 2.6}$$

Where  $k$  = the rate constant determined for Fe(II)CO complex formation and  $T_{1/2}$  = the time at which the Fe(II)CO complex reaches half of its maximum formation.

### 3 EXPRESSION, PURIFICATION AND CHARACTERIZATION OF CYP126

#### 3.1. Introduction

As was described in chapter 1, there has been much interest in the number of cytochrome P450 enzymes in the pathogenic bacterium *Mycobacterium tuberculosis* (Mtb), with 20 putative CYP enzymes that are of interest as potential drug targets (44, 51). To understand fully the roles of all CYPs for the growth and viability of *M. tuberculosis*, many research groups in the world have extensively studied these P450 systems over the 12 years that have elapsed since the sequencing of the Mtb genome in 1998 by Cole *et al* (42). However, to date there are only seven CYP enzymes (CYP51B1, CYP121, CYP125, CYP130, CYP124, CYP142 and CYP144) among the 20 putative enzymes that have been reported as characterised in a purified form (119, 121, 124, 135-138). Catalytic activities for CYP51B1 (sterol 14 $\alpha$ -demethylation), CYP125 (cholesterol 27-hydroxylation), CYP124 (branched chain fatty acid  $\omega$ -oxidation), CYP121 (C-C bond coupling of the cyclodipeptide cYY), and CYP142 (cholesterol 27-hydroxylation) have been defined, helping to define their roles in the growth and viability of *Mycobacterium tuberculosis* in the human body. Therefore, the continuing research on the remaining CYPs of Mtb is an area to reveal the full biochemical functions and enzyme mechanisms of the P450s in Mtb.

CYP126 (*Rv0778*) is found widely in *M. tuberculosis* strains and other pathogenic mycobacteria, which suggests that it has an important catalytic activity. CYP126 is located adjacent to *purB* – adenylosuccinate lyase (*Rv0777*) and *purC* – phosphoribosylaminoimidazole succinocarboxamine synthase (*Rv0780*). These proteins are suggested to have roles in intermediary (purine) metabolism. Therefore, *CYP126* is possibly part of a functional operon along with *purB* and *purC* (Figure 3.1). *PurB* is involved in *de novo* purine biosynthesis at the ninth step (Figure 3.0), likely catalysing the conversion of 1-(5-phosphoribosyl)-4-(N-succino-carboxamine)-5-aminoimidazole to fumarate + 5'-phosphoribosyl-5-amino-4-imidazolecarboxamine. *PurB* is also predicted to catalyse the conversion of N<sup>6</sup>-(1, 2-dicarboxyethyl) AMP to fumarate + AMP (176). *PurC* is likely involved in the *de novo* purine biosynthesis at the eighth step (Figure 3.0), catalysing conversion of ATP + 1-(5-phosphoribosyl)-4-carboxy-5-aminoimidazole + L-aspartate to ADP + phosphate + 1-(5-phosphoribosyl)-4-(N-succino-carboxamine)-5-aminoimidazole (177).

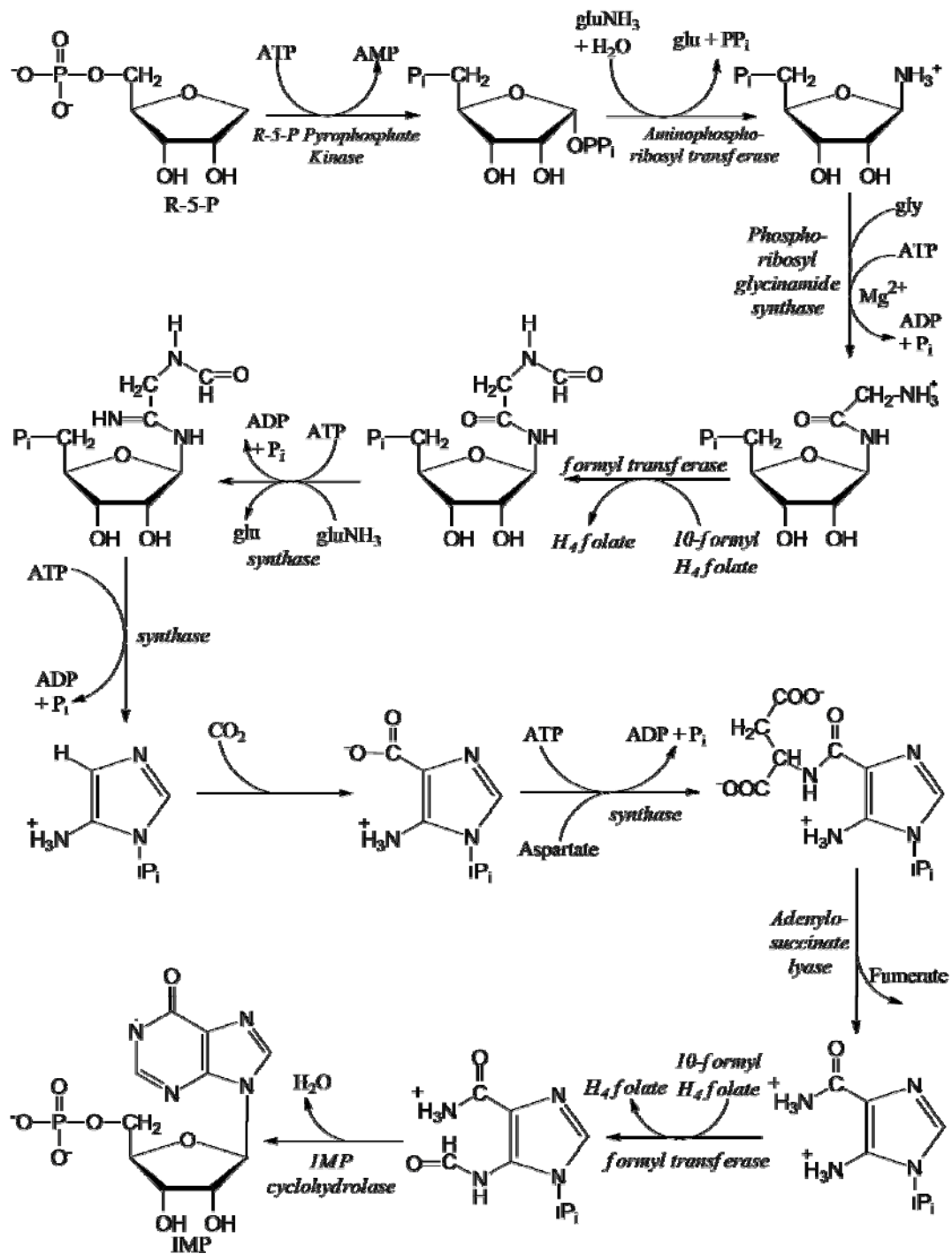


**Figure 3.0.** A diagram of the predicted purine biosynthesis pathway in *E. coli*. All components, 11 reactions, and many enzymes involved in the catalytic steps are detailed and identified in the figure. Figure prepared based on image presented at: [http://users.humboldt.edu/rpaselk/C432.S09/C432Notes/C432nLec13\\_slide.htm](http://users.humboldt.edu/rpaselk/C432.S09/C432Notes/C432nLec13_slide.htm).

Data from gene disruption analysis confirms that *purC* is an essential gene by Himar1-based transposon mutagenesis in the H37Rv strain (178). The position of *CYP126* might indicate that this P450 is involved in some aspect of purine biosynthesis or modification, due to its predicted position in an operon with *purB* and *purC*. However, no evidence has yet been presented for a functional link between *CYP126* and *PurB/PurC*. While *Mtb*

H37Rv genome-wide transposon mutagenesis revealed that several P450 genes were not essential for viability or optimal growth *in vitro* (179), no data have been presented to date regarding the gene essentiality of *CYP126* in either this strain or in the other virulent Mtb strain CDC1551.

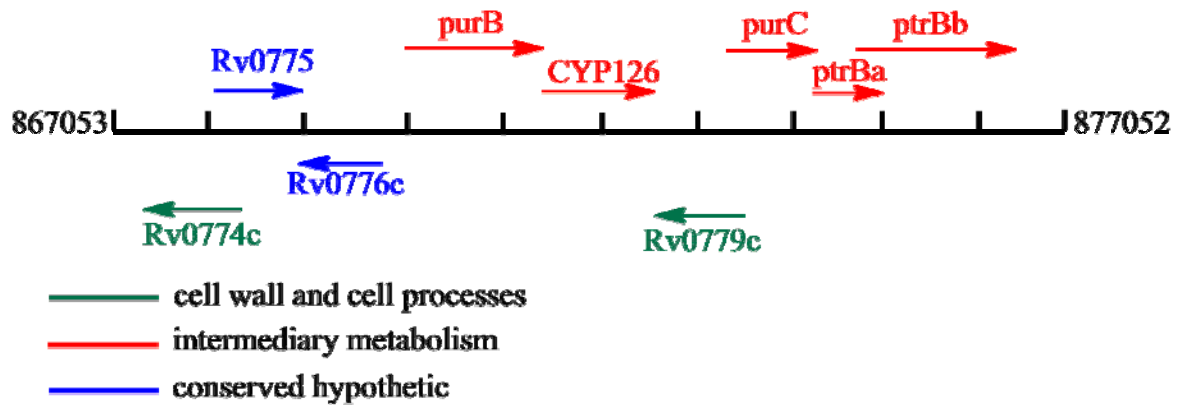


**Figure 3.1. Organization of *CYP126* and its adjacent genes in the chromosome of *Mtb* H37Rv.** *CYP126* is next to the *purB* and *purC* genes which are coloured in red, and is predicted to be in the same operon. Image prepared based on image presented at <http://genolist.pasteur.fr/TubercuList/>.

In addition, other genes in the “operon” here, particular the *Rv0775c* gene and *ptrBb* genes between *purB* and *purC* may have functions related to those of *CYP126*. However, *Rv0775c* is a non essential gene by Himar1-based transposon mutagenesis in H37Rv and CDC1551 strains (180), and codes for an enzyme of unknown function. The *ptrBb* gene encodes an enzyme involved in cleavage of peptide bonds on the C-terminal side of lysyl and arginanyl residues (181). Therefore, it is predicted to be the second part of protease II, equivalent to the C-terminus of protease II from *Mycobacterium leprae* (182), and also to be highly similar to the N-terminus of protease II enzymes from *E. coli* strains K12 and HB101 (183) Although these genes may share the same operon with *CYP126*, no evidence has yet been provided for a functional link between these proteins and *CYP126*.

The Mtb genome sequence revealed a particularly high density of CYP genes, and the large number of distinct cytochrome P450 enzymes and the apparent susceptibility of *M. tuberculosis* to azole agents (that bind tightly to many of the Mtb P450s) suggests essential function of these enzyme for Mtb physiology, and hence their potential use as therapeutic targets (105). At the time of submission of this thesis, only seven Mtb CYP genes have been studied as individually expressed recombinant proteins. All of these P450s were shown to tightly bind econazole, the agent of the azole class with highest known

antimycobacterial activity (184-186), as well as other azole and triazole drugs such as ketoconazole, clotrimazole, fluconazole, miconazole and itraconazole (187-192). The  $K_d$  values for azole binding to these seven Mtb P450s are detailed in Table 3.1.

Ligand	CYP51B1 $K_d$ ( $\mu$ M)	CYP121 $K_d$ ( $\mu$ M)	CYP130 $K_d$ ( $\mu$ M)	CYP124 $K_d$ ( $\mu$ M)	CYP125 $K_d$ ( $\mu$ M)	CYP144 $K_d$ ( $\mu$ M)	CYP142 $K_d$ ( $\mu$ M)
Econazole	$0.77 \pm 0.04$	< 0.2	$1.93 \pm 0.03$	$2.1 \pm 0.1$	$11.7 \pm 0.7$	$0.78 \pm 0.29$	$4.6 \pm 0.2$
Fluconazole	$19.0 \pm 1.9$	$9.7 \pm 0.1$	$48.0 \pm 1.5$	-	$43.2 \pm 0.8$	> 10,000	$860 \pm 108$
Ketoconazole	-	$3.3 \pm 0.3$	-	-	$27.1 \pm 0.9$	$134 \pm 5$	$21 \pm 4$
Itraconazole	-	-	-	-	$30.2 \pm 4.3$	-	-
Miconazole	$0.59 \pm 0.03$	< 0.2	$1.70 \pm 0.21$	$1.9 \pm 0.2$	$4.6 \pm 0.4$	$0.98 \pm 0.22$	$4.0 \pm 0.5$
Clotrimazole	< 0.1	< 0.2	$13.3 \pm 0.6$	$2.5 \pm 0.1$	$5.3 \pm 0.6$	$0.37 \pm 0.08$	$3.8 \pm 0.9$
Voriconazole	-	-	-	-	-	$6510 \pm 470$	-
2-phenylimidazole	-	-	-	-	$345 \pm 4$	-	-
4-phenylimidazole	-	-	-	-	$216 \pm 5$	$280 \pm 18$	$12.0 \pm 1.5$
Imidazole	-	-	-	-	$536 \pm 7$	$2965 \pm 275$	-

**Table 3.1.  $K_d$  values for the binding of various azole drugs to the seven Mtb P450s characterized to date (119, 121, 124, 135-138).**

In order to contribute to our understanding of the structure/function and biochemical properties of cytochrome P450s in Mtb, In this chapter, initial studies are reported analysing the biochemical and biophysical properties of CYP126 using a range of techniques, including gene cloning and expression, DSC, light scattering, redox titration, pH titration, EPR, CD, MCD and mass spectrometry, as well as crystallography to explore heme iron coordination and environment as well as the overall conformational and structural features of CYP126, and to enable a more detailed understanding of the properties of this novel Mtb P450 in order to design a potent drug for TB treatment. CYP126 was successfully expressed, purified and characterized by those methods mentioned above and the crystal structures were also obtained in both ligand-free and azole bound forms, revealing many properties that are common among P450 enzymes. The detailed results are presented below.

## 3.2. Results

### 3.2.1. Expression and purification of CYP126

The soluble protein produced by the histidine-tagged CYP126 gene (six histidines at the N-terminal) was expressed using the strict conditions optimised, and as described in the Methods chapter (section 2.5). Numerous conditions were investigated to optimise expression of soluble protein, including investigations of temperature, concentration of IPTG inducer, time of induction, host strains and media types. CYP126 has a predicted molecular weight of 45,954 Da, and the His-tag has a molecular weight of approximately 2,181 Da. Therefore, the expressed protein retaining its His-tag has a predicted molecular weight of 48,135 Da. The trial expression studies by SDS-PAGE showed that there was a large protein band that was over-expressed during induction using 0.1 mM IPTG (Figure 3.2). The apparent molecular mass of this species (~48 kDa) corresponds to the predicted molecular weight. In order to determine the length of time to optimise the expression of CYP126, the trial expression was extended from 2 h to 24 h. The results of this expression trial showed that CYP126 expression increased over time and that the best time for expression was 24 h (Figure 3.2).

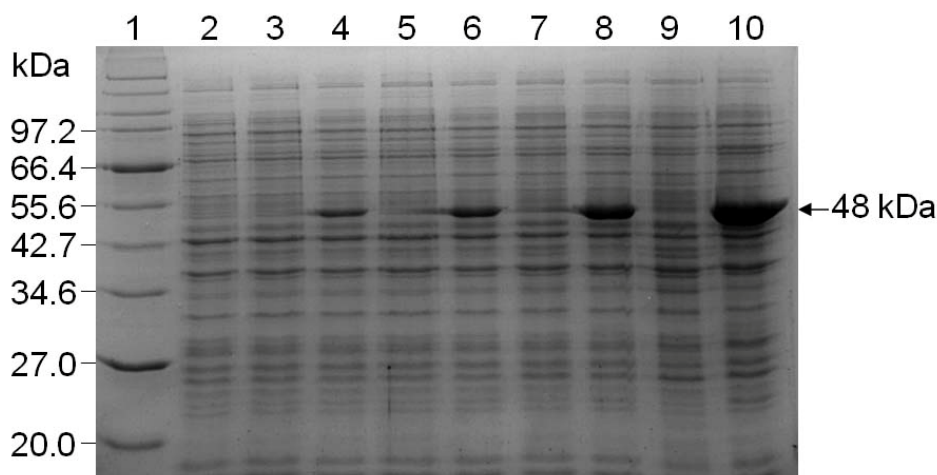


**Figure 3.2.** SDS gel of CYP126 expression trial in *Escherichia coli* BL21 (DE3). Cells were induced by 0.1 mM IPTG at different times ranging from 0 to 24 h. Lane 1: Molecular mass standard (97 200, 66 400, 55 600, 42 700, 34 600, 27 00, 20 000 Da); lane 2: total protein at time T=0; lanes 3-4: total protein of control (uninduced) and induced samples at T= 2 h; lanes 5-6: total protein of control and induced samples at T= 4 h; lanes 7-8: total protein of control and induced samples at T= 6 h; lanes 9-10: total protein of control and induced samples at T= 24 h.

The preliminary expression trials indicated that CYP126 could be expressed to high levels under control of the T7 RNA polymerase promoter system in pET15b, using the *E. coli* BL21 Gold (DE3) strain. Analysis by SDS-PAGE showed that the heterologously expressed CYP126 was produced at higher levels than any host proteins. In Figure 3.2, the protein was notably expressed at 2 h, but it was shown that the protein quantity was relatively low at this time, and that the amount of expressed protein increased over time. The maximum protein production was obtained at 24 h compared to other time points. Therefore, these results suggested that CYP126 protein was successfully expressed and might be purified, and that growth of cells for ~24 hours should produce substantial amounts of CYP126 under these conditions.

To determine the yield of soluble protein, an efficient cell lysis process was used to analyse the ratio of soluble to insoluble protein. Despite high expression levels of CYP126 in the *E. coli* host cells, analysis from the trial expression culture revealed that a significant proportion of the expressed protein was in the insoluble fraction. Expression of CYP126 was measured on SDS-PAGE gels by comparison of soluble and insoluble fractions from lysed cells. The soluble fractions were collected from the supernatant after centrifugation of lysed cells, and the insoluble fractions were collected from the cell pellet. These fractions were then diluted in appropriate concentrations, denatured at 95 °C for 5 min and run on SDS-PAGE gels (see Methods section 2.6). The results indicated that the bulk of the CYP126 protein was located in inclusion bodies (Figure 3.3).

Furthermore, solubilisation of protein from the insoluble fraction using denaturant (guanidinium chloride and Bugbuster protein extraction reagent from Novagen) and CO-binding analysis produced exclusively the “inactive” form of CYP126 that arises from protonation of the heme cysteine thiolate ligand (P420, data not shown). The native soluble expression of CYP126 was optimised using various conditions as described in chapter 2 (section 2.5). The analysis of a variety of data indicated that addition of small amounts of detergent in the growth step and lysis buffers (e.g. 0.1% Tween 20) was not beneficial for soluble protein recovery. However, low temperature and mild induction with a low concentration of IPTG (0.1 mM) were found to be essential to promote overproduction of the soluble form of CYP126. The optimised soluble CYP126 production was achieved by using host strain *E. coli* BL21 Gold (DE3), and with induction at the mid logarithmic phase of growth at 18 °C, and with cell culture continued for approximately 24 h post induction at the same temperature. Under these conditions, the total protein expression of CYP126 was

lower than at higher temperatures, but the recovery of soluble CYP126 was higher (Figure 3.4A, lanes 6, 7, 8).

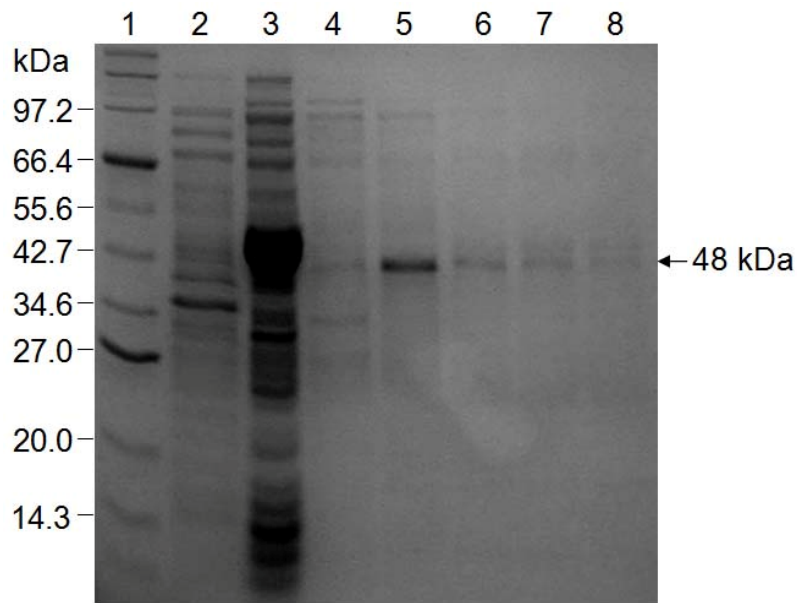


**Figure 3.3. SDS PAGE gel of CYP126 purification trial.** Growth was at 37 °C and used 0.1 mM IPTG induction. Lane 1: Molecular mass standard (97 200, 66 200, 55 600, 42 700, 34 600, 27 00, 20 600, 14 300 Da); lane 2: flow through after Ni-NTA column; lane 3: cell pellet after centrifugation; lane 4: 20 mM imidazole wash; lane 5: elution with 50 mM imidazole; lane 6-8: elution with 100 mM imidazole.

In order to purify homogenous histidine-tagged CYP126 protein, two different columns were used to enable isolation of soluble protein. The Ni-NTA affinity column was used to bind the histidine tag part of the CYP126 protein. This resin is very specific for binding of proteins containing histidine tags, while other proteins from host cell will flow through during loading and washing steps with buffer containing small amounts of imidazole. However, many *E. coli* proteins which also possess histidine-rich regions can bind to the column, such as *E. coli* proteins consisting of a domain homologous to FK506 binding proteins (FKBPs) that were detected as a persistent contaminant in immobilized metal affinity chromatography of recombinant proteins expressed in *E. coli* (193). The analysis of the elution fractions on an SDS-PAGE gel showed other small bands along with the CYP126 band (Figure 3.4 A, lane 6, 7)). Therefore, an ion-exchange column (Q-Sepharose) was applied to separate CYP126 protein from the mixture. Following the final step of purification, the fraction which contains pure protein was checked by running on an SDS-PAGE gel to demonstrate the homogeneity of the protein (Figure 3.4 B).

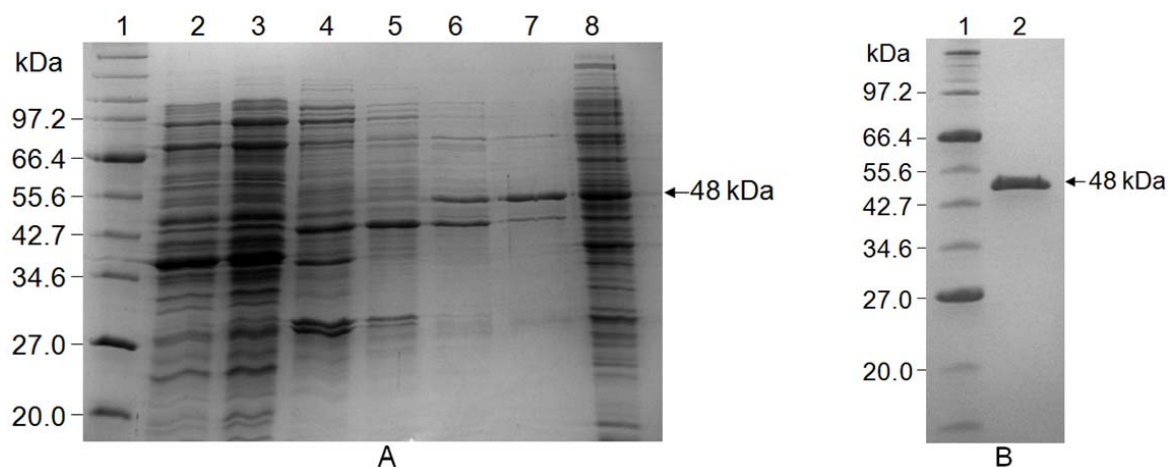


**Figure 3.4. Purification steps of CYP126.** (A) SDS-PAGE of Mtb CYP126 purification steps using a Ni-NTA column. Lane 1, molecular mass standards (97 200, 66 200, 55 600, 42 700, 34 600, 27 00, 20 600 Da); lane 2, total protein after loading; lane 3, 10 mM imidazole wash; lane 4, 15 mM imidazole wash; lane 5 20 mM imidazole wash; lane 6, elution with 40 mM imidazole; lane 7, elution with 60 mM imidazole; lane 8, total protein of cell pellet after sonication and centrifugation. (B) Further CYP126 purification using a Q-Sepharose column; lane 1, molecular mass standard marker; lane 2, Q-Sepharose elution with 80 mM NaCl for a sample loaded following Ni-NTA purification.

Purification stage	Total protein (mg)	Total P450 (mg)	Ratio ( $A_{418}/A_{280}$ )	P450 Yield (%)	Purification fold
Lysate	1020	14	0.014	100	1
Ni-NTA	12	8	0.67	57	47.9
Q-Sepharose	0.6	1.4	2.3	10	164.3

**Table 3.2. Summary purification steps for native CYP126 in 1 litre culture.** At each stage, the total amounts of protein and P450 are given. The relative ratios of  $A_{418}/A_{280}$  are also detailed in the table. The total protein was calculated by the overall protein absorbance (assuming  $A_{280} = 1 = 1 \text{ mg mL}^{-1}$ ), and the total P450 was determined by using the Beer-Lambert equation (section 2.10 – chapter 2) using the extinction coefficient  $A_{418} = 100 \text{ mM}^{-1} \text{ cm}^{-1}$ .

According to those results above, it was shown that the intact CYP126 was successfully expressed and purified by column chromatography. Following each round of purification, the enzyme purity was assessed by measuring the ratio of heme-specific absorbance at 418 nm and total protein content with absorbance at 280 nm. This Rz (Reinheitzahl) ratio of a pure sample showed a value of approximately 2.3, with purity also verified by SDS-PAGE as shown in Figure 3.4 B. A final Q-Sepharose step was introduced where necessary to obtain highly-purified CYP126 protein for further experiments, including crystallization screens. The measurements typically showed that soluble CYP126 was purified approximately 53-fold from the original cell extract and recovered in yields of around 1.2-

1.4 mg pure CYP126 per litre of cell culture. The purification data for amounts of CYP126 (from 1 litre culture) in extract and after Ni-NTA and Q-Sepharose columns are detailed in Table 3.2.

### 3.2.2 Spectrophotometric analysis of CYP126

UV-visible spectroscopy is a useful technique to analyse and characterise cytochrome P450 enzymes, due to the specific absorption properties of the bound heme cofactor in the UV-visible wavelength range. The UV-visible spectrum of the oxidised CYP126 shows typical characteristic features of a heme-containing protein. In Figure 3.5, the major Soret band (gamma or  $\gamma$  band) was located at 418 nm, with the lower intensity  $\alpha$  and  $\beta$  bands at 568 nm and 535 nm (also known as Q-bands), respectively. These features are similar to the other well-characterized P450 enzymes from Mtb such as CYP121 ( $\gamma$  band at 416.5 nm,  $\alpha$  and  $\beta$  bands at 565 and 538 nm, respectively (138), CYP124 ( $\gamma$  band at 421 nm,  $\alpha$  and  $\beta$  bands at 571 and 538 nm, respectively (136), CYP130 ( $\gamma$  band at 418 nm,  $\alpha$  and  $\beta$  bands at 567 and 535 nm, respectively (137), and CYP144 ( $\gamma$  band at 420.5 nm,  $\alpha$  and  $\beta$  bands at 568 and 538 nm, respectively (135). The pure enzyme was reduced with sodium dithionite, showing the Soret band shifts to 411 nm and decreases in intensity (Figure 3.5).

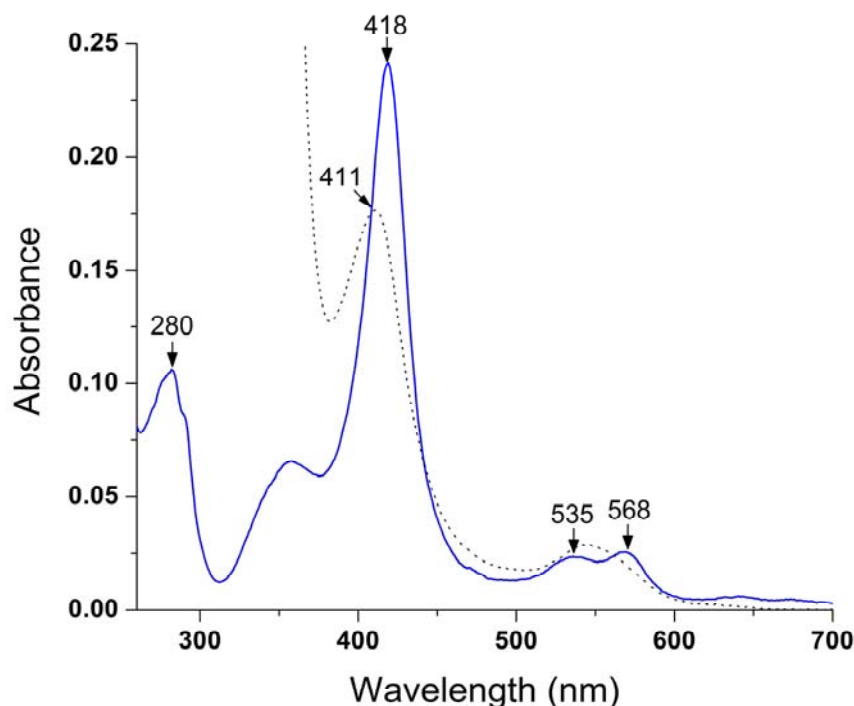


**Figure 3.5. UV-visible absorbance spectrum of pure CYP126.**

The absorbance of CYP126 (~2.5  $\mu$ M) was recorded in 100 mM potassium phosphate (pH 7.5). The CYP126 protein absorbs at 280 nm, whilst the bound heme cofactor absorbs maximally at 418 nm (Soret band) with the  $\alpha$  and  $\beta$  bands at 568 nm and 535 nm. The ratio of the heme-specific absorbance at 418 nm to the protein absorbance at 280 nm is ~2.3. The dithionite-reduced enzyme has Soret band at 411 nm (black dotted line).

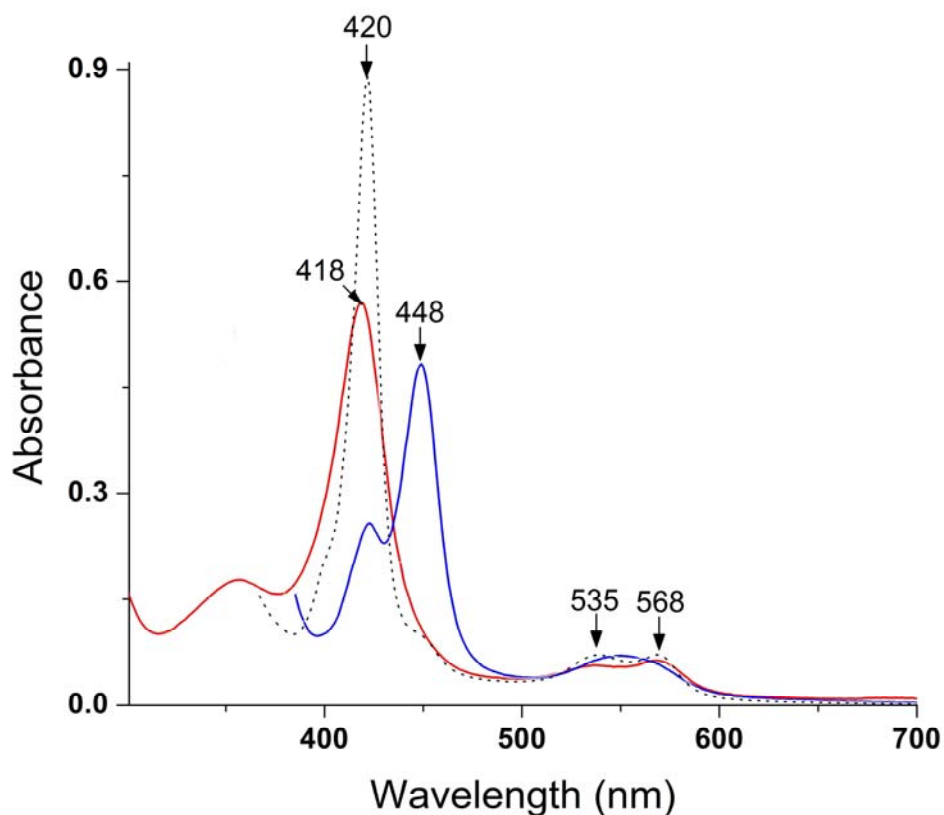


**Figure 3.6. UV-visible spectrum of Mtb CYP126 on reaction with carbon monoxide.**

CYP126 ( $\sim 5 \mu\text{M}$ ) has ferric heme iron in the oxidised form, and possesses maximal absorbance at 418 nm (red line). After reduction and reaction with CO, the absorption maximum shifts to 448 nm (blue line). This P450 species quickly collapsed to the P420 form (dotted black line) after 10 minutes.

Binding of CO to the dithionite-treated CYP126 leads to formation of an Fe(II)-CO complex, with a major absorption maximum at 448 nm and a minor Soret maximum at 420 nm (close to that for the oxidized form of the enzyme, and due to the heme thiol-coordinated P420 form) (Figure 3.6). The shift of the Soret band to 448 nm strongly indicates that CYP126 is a cytochrome P450 with a cysteinate thiolate-ligated heme. Under aerobic or anaerobic conditions, CYP126 proved difficult to completely reduce to the ferrous form, indicative of a quite negative potential of the heme iron (and probably also to some extent reflecting the fast re-oxidation of the heme iron), but the tight binding of CO ensures that the equilibrium is pulled over to the Fe(II)CO species once heme iron reduction is achieved.

In addition, large excesses of dithionite also caused aggregation and precipitation of CYP126 (and thus were avoided), and bubbling of CO through the dithionite-treated

CYP126 invariably generated a mixture of spectral species with absorption maxima at 448 and 420. However, the P450 form was not stable and quickly collapsed to P420 within 10 minutes (Figure 3.6, black dotted line). This likely indicates that dithionite-mediated reduction of CYP126 results in a mixture of thiol- and thiolate-coordinated ferrous heme iron, resulting in a mixture of P450/P420 CO-bound species. Over time, more heme thiolate protonation occurs causing the further shift of the Soret band from 450 nm to 420 nm. Similar phenomena have been observed for other Mtb P450s (e.g. CYP51B1 and CYP121) (138, 194).

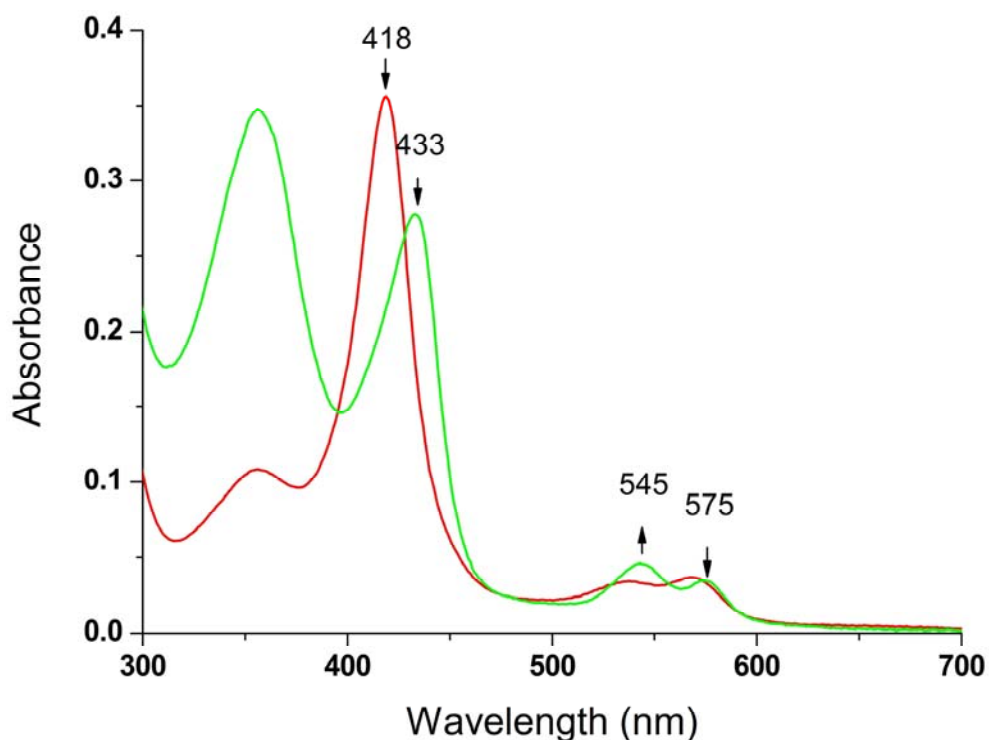


**Figure 3.7. UV-visible spectrum of CYP126 bound to NO.**

The ferric form ( $\sim 3.5 \mu\text{M}$ ) again has its Soret band at 418 nm (red line), with a Soret shift to 433 nm, and that of the  $\alpha$  and  $\beta$  bands to 575 nm and 545 nm, respectively, when NO complexes the heme iron (green line).

Similar to CO-binding, binding of nitric oxide (NO) to the ferric CYP126 leads to formation of a distinctive Fe(III)-NO (or Fe(II)-NO<sup>+</sup>) species, and resulted in decrease in the CYP126 Soret intensity, with a shift of the Soret band to 433 nm, and of the  $\alpha$  and  $\beta$  bands to 575 nm and 545 nm, respectively (Figure 3.7). This result again demonstrates that CYP126 was successfully expressed and purified as a homogeneous P450 enzyme with a cysteinyl thiolate-ligated heme.

### 3.2.3 Pyridine hemochromagen of CYP126

The Beer-Lambert law provides an efficient tool to calculate the concentration of most proteins (195). Often, the protein concentration for a P450 is calculated spectroscopically using the Beer-Lambert law by the method of Omura and Sato (54), and applying the extinction coefficient  $\Delta\epsilon_{450-490}$  of  $91 \text{ mM}^{-1} \text{ cm}^{-1}$  for data for the absorbance difference between reduced ( $\text{Fe}^{2+}$ ) and reduced/CO-bound ( $\text{Fe}^{2+}\text{-CO}$ ) spectral forms of the P450. However, the unstable CO-complex for CYP126 did not allow useful application of this method to calculate the P450 concentration, due mainly to the variable amounts of P420 formed and uncertainties as to whether this reflected heme thiolate protonation due simply to the experimental approach (as opposed to genuine thiol-coordinated P450 in the oxidised enzyme). Therefore, CYP126 heme concentration was calculated by using spectral data with the pyridine hemochromagen technique (Berry and Trumpower method) (163), thereafter using the Beer-Lambert law (equation 2.1 – section 2.10, chapter 2) to convert these data into a useful extinction coefficient value for CYP126 in its oxidised form.

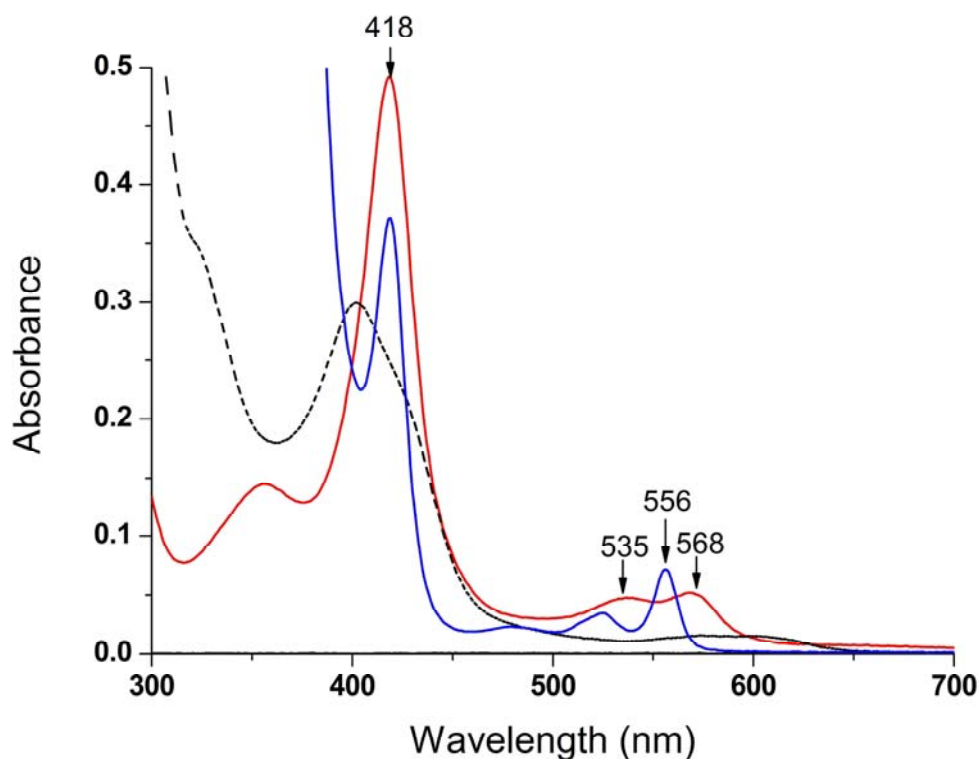


**Figure 3.8. Pyridine hemochromagen spectra of CYP126.**

The red line shows the oxidised form of CYP126 heme (ferric form) with the Soret band at 418 nm. The dashed black line shows the dithionite-reduced form of the heme (ferrous form). The blue line represents the pyridine hemochromagen spectrum with a maximum in the Q-band region at 556 nm, which is indicative of heme *b*. The heme concentration of CYP126 was calculated based on the Beer-Lambert equation, using an extinction coefficient of  $\Delta\epsilon_{556,4-540 \text{ nm}} = 23.98 \text{ mM}^{-1} \text{ cm}^{-1}$ , as  $4.9 \text{ }\mu\text{M}$ . The extinction coefficient of oxidised CYP126 at 418 nm was also then calculated as  $100 \text{ mM}^{-1} \text{ cm}^{-1}$  using the above coefficient.

When extinction coefficients of the native P450s are not known, it is possible to calculate the total concentration of heme from the spectra of hemochromes formed from cytochromes. In reaction with pyridine done using the Berry and Trumpower method, the heme iron is completely dissociated from protein. Figure 3.8 shows the pyridine hemochromagen spectrum used for the calculation of the CYP126 P450 concentration. The Soret band starts at 418 nm at  $\sim 5 \mu\text{M}$  concentration of CYP126, with the Q-bands at 535 and 568 nm. The mixture of CYP126 and pyridine shows an absorbance maximum in the Q-band region at 556 nm, which is typical of heme *b*, and the reduced form shows that CYP126 was completely reduced by dithionite. The difference between the oxidised and reduced forms was 0.118 for the wavelength pair 550 minus 570 nm. Therefore, the total heme concentration of CYP126 was calculated, using the heme *b* extinction coefficient of  $\Delta\epsilon_{556,4-540 \text{ nm}} = 23.98 \text{ mM}^{-1} \text{ cm}^{-1}$ , as  $4.9 \mu\text{M}$ .

In addition, the extinction coefficient ( $\epsilon$ ) of CYP126 was calculated for oxidised CYP126 at the Soret peak (418 nm) via the Beer-Lambert equation, using data from the pyridine hemochromagen spectra, indicating a value of  $100 \text{ mM}^{-1} \text{ cm}^{-1}$ . This value is in a typical range for oxidised P450 heme Soret coefficients (194). In a recent report, Driscoll *et al.* determined the extinction coefficient for CYP144 using the pyridine hemochromagen method, and this also resulted in determination of a coefficient of  $\Delta\epsilon_{420,5} = 100 \text{ mM}^{-1} \text{ cm}^{-1}$  at the Soret peak for the oxidized enzyme (135). Other P450s were also determined for a heme Soret extinction coefficient by using the pyridine hemochromagen method, including CYP121 ( $\Delta\epsilon_{416,5} = 110 \text{ mM}^{-1} \text{ cm}^{-1}$ ), CYP51B1 ( $\Delta\epsilon_{419} = 134 \text{ mM}^{-1} \text{ cm}^{-1}$ ) (194, 196), and P450cam ( $\Delta\epsilon_{417} = 115 \text{ mM}^{-1} \text{ cm}^{-1}$ ) (196).

### 3.2.4 Circular Dichroism

Circular Dichroism (CD) spectroscopy reports on the three-dimensional arrangement of polymers. Therefore, it is extremely useful in the study of the three-dimensional structure of proteins and nucleic acids (197). Each of the three major basic secondary structural elements of a polypeptide chain (including alpha helix, beta sheet, and random coil structures) shows a characteristic shape and magnitude of CD spectrum in the far UV region. Analysis of the CD spectra for proteins can provide estimates of the relative contents of the secondary structural features, such as the proportions of alpha helical, beta-sheet, or random coil structures (198).

The secondary structure of the proteins can be estimated from CD measurements in the far UV spectral region (190-260 nm). At these wavelengths the peptide bond acts as the chromophore, and the CD signal arises when it these are located in a regular, folded environment. Normally, an  $\alpha$ -helix gives a strong CD signal with minima at approximately 208 nm and 222 nm, whereas a  $\beta$ -sheet gives a rather weaker intensity spectrum with a single minimum at  $\sim$ 217 nm. Computational tools are often used to estimate secondary structural composition of a protein, by simulating the observed spectrum using different proportions of the individual CD spectra for alpha helix, beta sheet, random coil and other protein structural elements (199, 200). The tertiary structure can be analysed in the near UV spectral region (260-320 nm), since at these wavelengths the aromatic amino acids and disulfide bonds act as the chromophores to give a rise to broad signals throughout the near UV spectrum. In this region, the CD signals are predominantly attributable to phenylalanine, tyrosine and tryptophan residues, and disulfide bonds only contribute weak signals (201). For the P450s, the CD spectra normally report on heme environment in the visible region (320-600 nm), relating to e.g. the redox state of the heme iron and the presence of ligands or substrates. The CD spectra of CYP126 are shown in Figure 3.9 and Figure 3.10.

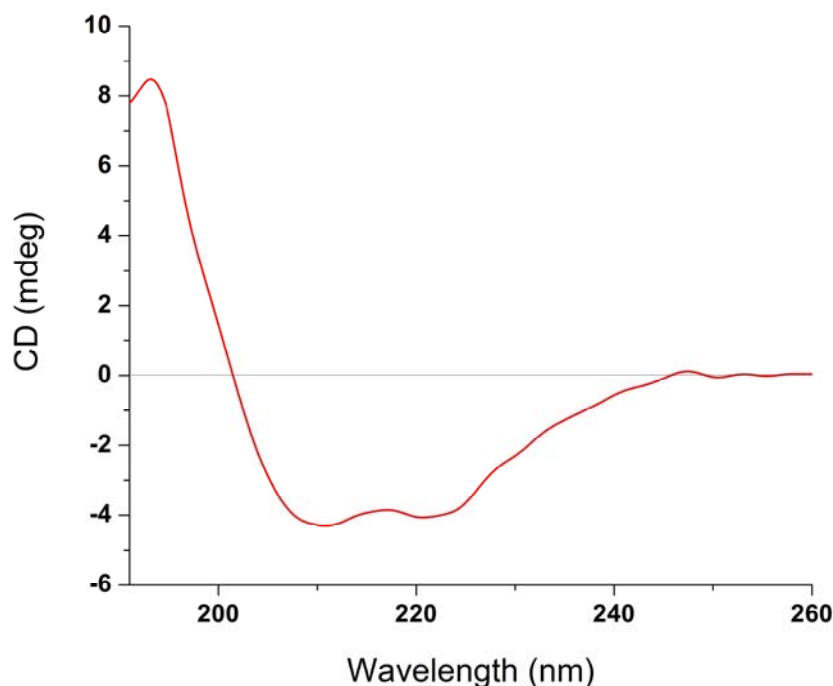


**Figure 3.9. Far UV CD spectrum for CYP126.**

The oxidised form of CYP126 (2.0  $\mu$ M) is shown as a red line. The spectrum was recorded at 25  $^{\circ}$ C in 10 mM potassium phosphate (pH 7.5) as described in chapter 2 (section 2.19). Minima in the spectrum are located as 210.8 nm and 221 nm.

The CD spectra of CYP126 were collected on a Jasco spectropolarimeter, in both the far UV and near UV-visible regions. Ellipticity data were analyzed using the Selcon program to obtain a secondary structural prediction (202). The far UV CD spectrum of CYP126 reveals a mainly alpha helical structure with approximately 50 %, as expected for a cytochrome P450 enzyme. All P450 structures solved to date are predominantly alpha helical (203). Figure 3.9 presents the far UV CD spectrum of Mtb CYP126 with a strong positive maximum at 190 nm, and minima at 210.8 nm and 221 nm. The spectrum is highly similar to that of other well-characterised P450s such as P450 BM3 and CYP121 (82). Using the equation described in the Methods chapter (equation 5, section 2.19) to calculate the value of the molar ellipticity per residue, and inputting these data into the Selcon prediction program, the prediction is that greater than 50 % of CYP126 is alpha helical, 16 % is beta sheet, and around 5 % is random coil for CYP126. Based on studies of other P450 enzymes, the amount of alpha helix is typically >50%, indicating that the secondary structure of CYP126 is quite similar to other P450 enzymes. Hence, the CD (in the far UV) spectra show that CYP126 has a folded conformation with a spectrum typical of P450, thus pointing to the importance of structural data to obtain a relative estimate of secondary structural content in CYP126.

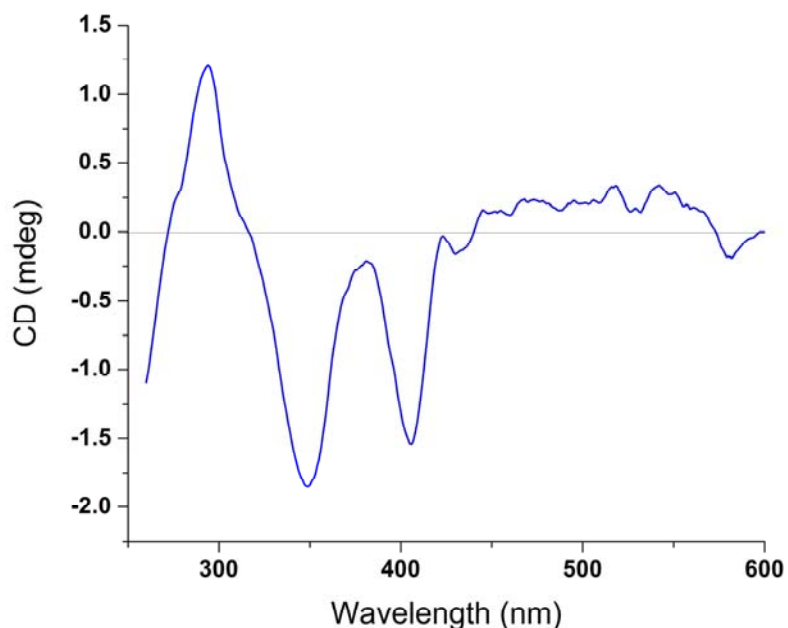


**Figure 3.10. Near UV-visible CD spectrum for CYP126.**

The spectrum for the oxidised form of CYP126 (20  $\mu$ M, blue line) is shown in the near UV-visible CD region.

Interestingly, in the near UV-visible spectral region, CYP126 shows similarity to spectra of other reported P450s (Figure 3.10) (138). In the near UV region (260-320 nm), signals

report on mainly aromatic amino acid side chains, and CD spectra in this region are characteristic of individual P450 isoforms. In the visible region (320-600 nm), the CD spectrum of CYP126 is highly similar to other P450s characterized to date, which are dominated by a large signal of negative sign, with a minimum near the position of the Soret band in the electronic absorption spectrum. However, for CYP126 the Soret visible CD band suggested subtly different changes to the chirality and/or electronic properties of the heme compared to the visible CD bands of P450 BM3 and CYP121 (138). In addition, the Soret CD features in CYP126 also exhibited a distinct signal of negative sign from CYP121, which revealed the Soret visible CD band of positive sign at 419 nm, close to the Soret maximum in the electronic absorption spectrum at 416.5 nm. The P450 BM3 heme domain revealed a similar intensity of the negative band to CYP126 at 417 nm. The reason for the differences in CD spectra between CYP126/BM3 and CYP121 may relate to small changes in heme conformation (138).

### **3.2.5 Azole inhibitor binding**

Previous studies of seven CYPs in *Mycobacterium tuberculosis* (CYP51B1, CYP121, CYP130, CYP125, CYP124, CYP144 and CYP142) have demonstrated the capability of commercially available anti-fungal azoles to bind tightly to these enzymes, and such drugs display an inhibitory potential against the latent and multidrug-resistant strains of *M. tuberculosis* (105, 137, 138, 204). As described in the chapter 1, the azole antifungals include two classes, the imidazoles and triazoles. Both share the same mechanism of action (205, 206). The imidazole derivatives include clotrimazole, econazole, ketoconazole and miconazole. Triazoles include posaconazole, fluconazole, voriconazole and itraconazole (207, 208).

The binding of azole inhibitors to CYP126 was recorded at 25 °C by UV-vis absorption spectroscopy, as previously described in the Materials and Methods (section 2.14). Azole compounds were seen to induce red (type II) shifts in the absorbance maximum of the Soret band of CYP126. Titrations with the azole anti-fungals ketoconazole, econazole and miconazole indicated tight binding to CYP126, although imidazole itself showed only weak binding. The summary of azole inhibitor binding to CYP126 is shown in Table 3.3.

#### **3.2.5.1 Ketoconazole binding**

There was a large change in absorbance between each titration point by using a ketoconazole solution at 18.82 mM. Therefore, ketoconazole was diluted to a concentration

of 1.882 mM, and then 1  $\mu$ l was used for each titration point (1.882  $\mu$ M per addition). The typical azole-induced changes in the absorbance of CYP126 are displayed in Figure 3.11 upon addition of successive amounts of ketoconazole. There was a general spectral decrease in intensity and shift in the absorbance maximum of CYP126 from 418 nm to 424 nm (Figure 3.11 main). Also seen upon ketoconazole binding was the spectral decrease in intensity of the  $\alpha$  and  $\beta$  bands at both the wavelengths of 568 nm and 535 nm, respectively.

In order to analyse these titration data, a set of difference spectra was constructed at each point by the subtraction of the spectrum for the inhibitor-free form from each successive inhibitor-bound spectrum in the titration. This spectra displayed minima and maxima values at approximately 415 nm and 434 nm, respectively (Figure 3.11, inset).

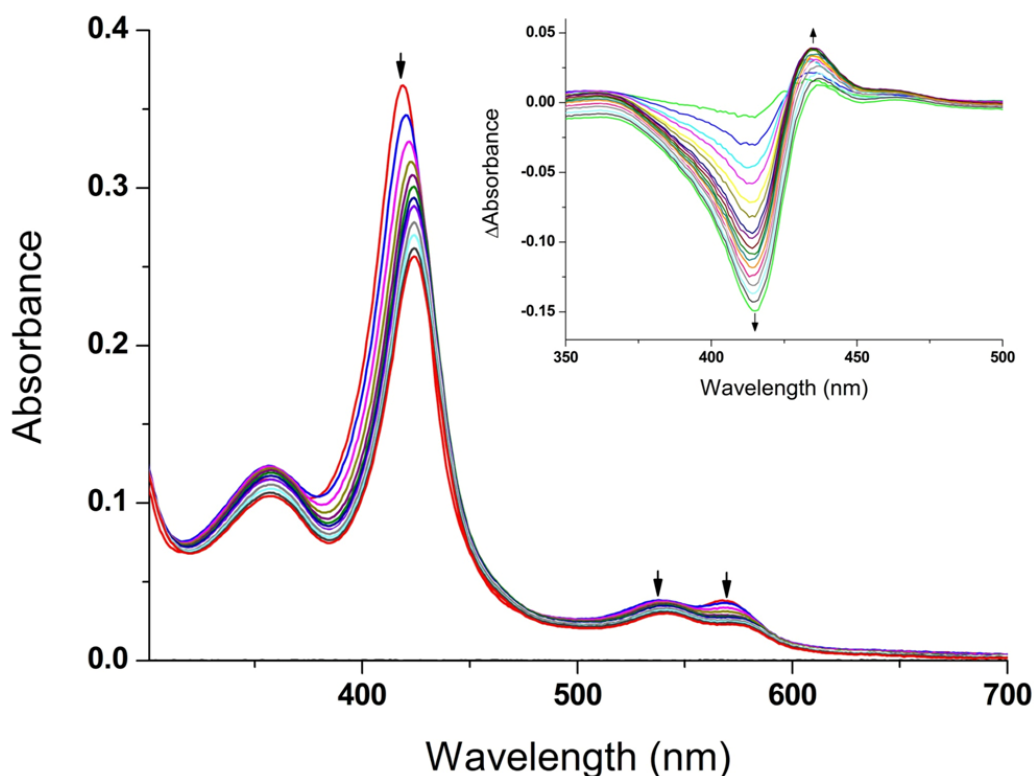


**Figure 3.11. Binding of ketoconazole to CYP126.**

Main figure: shown in the higher red spectrum is the starting spectrum, containing  $\sim 3.7 \mu$ M CYP126, with a Soret maximum at 418 nm. The lower spectrum is the final spectrum (near the ligand saturation point) which has a Soret maximum at 424 nm. The arrows indicate directions of absorption change on ligand addition. Shown inset are the difference spectra generated from the data collected, and the maximal absorbance changes derived from these data. Difference spectral maxima and minima are at 434 nm and 415 nm, respectively.

For each ketoconazole concentration, the maximal absorbance change induced was calculated by subtraction of the absorbance value at the trough from that at the peak in each difference spectrum (using the same wavelength pair in each case). These values were then

plotted against the corresponding concentration of ketoconazole, and the data were fitted using equation 3 (detailed in section 2.14 of chapter 2) to generate a dissociation constant value ( $K_d = 1.4 \pm 0.1 \mu\text{M}$ ) (Figure 3.12).

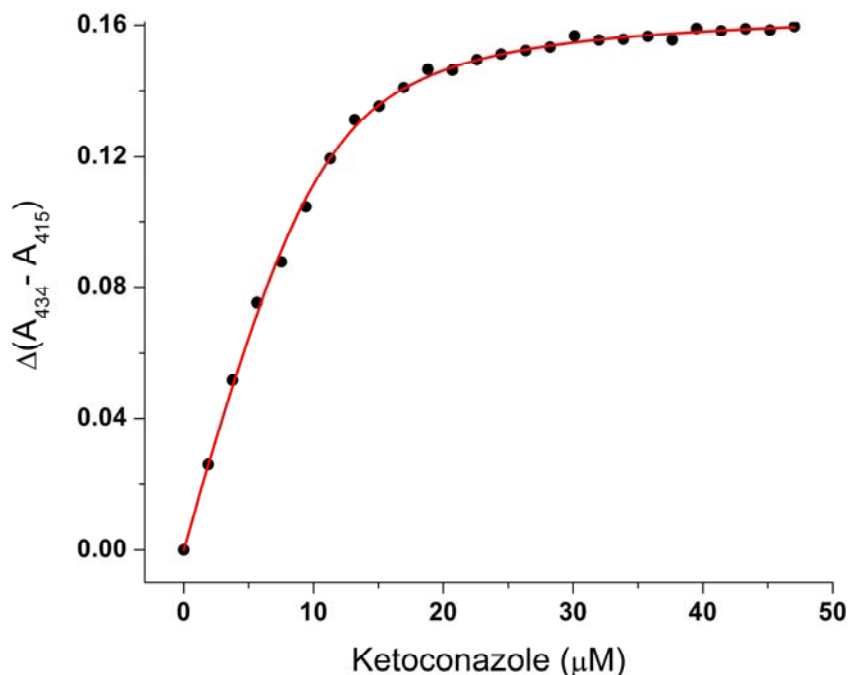


**Figure 3.12. Titration curve for the binding of ketoconazole to CYP126.**

Data from the difference spectra ( $\Delta(A_{434}-A_{415})$ ) were fitted to equation 2.3 (section 2.14 - chapter 2), yielding a  $K_d = 1.4 \pm 0.1 \mu\text{M}$ .

### 3.2.5.2 Miconazole binding

Miconazole again showed distinct type II spectral interactions with CYP126, having a final maximum absorbance at 422 nm, (Figure 3.13, main). These data were processed as described for the ketoconazole titration. These indicated maximum and minimum absorbance at approximately 434 and 414 nm in the difference spectra, respectively (Figure 3.13 inset). Data were fitted as described above to determine the  $K_d$  value for miconazole binding of  $1.3 \pm 0.2 \mu\text{M}$  (Figure 3.14).

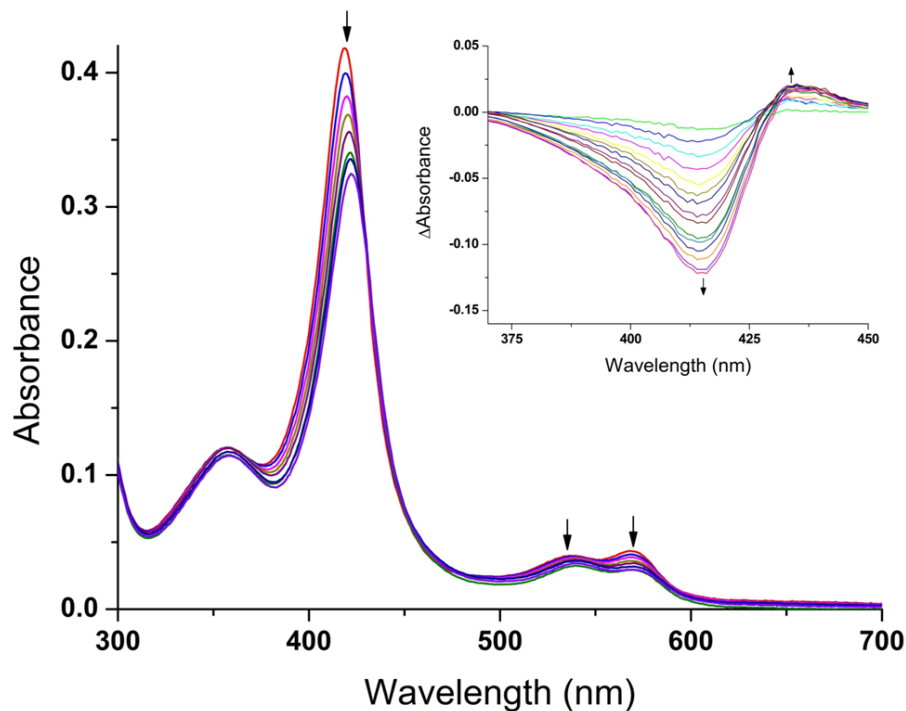


**Figure 3.13. Binding of miconazole to CYP126.**

Main figure: UV-vis spectra displaying titration of CYP126 ( $\sim 4.25 \mu\text{M}$ ) with miconazole, with arrows indicating directions of absorption change on ligand addition. Shown inset are the difference spectra generated from the data collected, and the maximal absorbance changes derived from these data at the peak and trough. Arrows again indicate directions of absorption change on ligand binding.

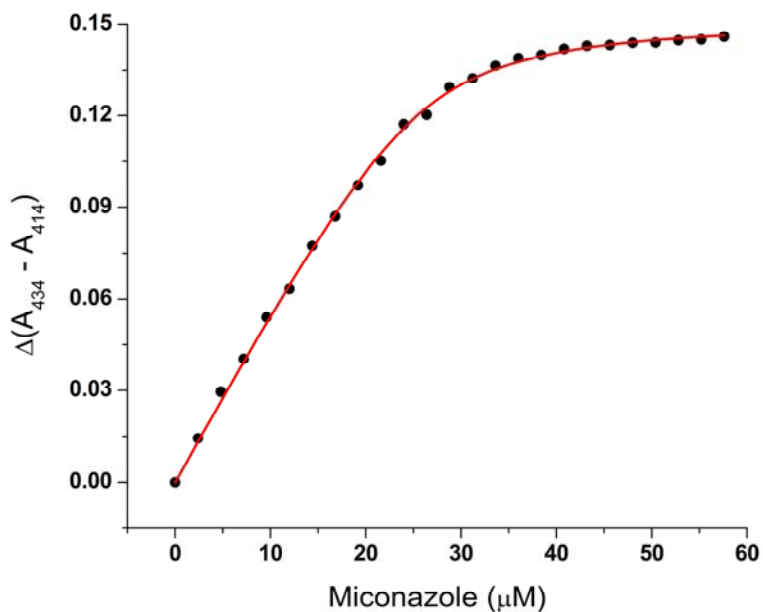


**Figure 3.14. Titration curve for the binding of miconazole to CYP126.**

Data from the difference spectra ( $\Delta(A_{434} - A_{414})$ ) were fitted to equation 2.3, yielding a  $K_d = 1.3 \pm 0.2 \mu\text{M}$ .

### 3.2.5.3 Econazole binding

Econazole bound to CYP126 exhibited a distinct type II spectral interaction, shifting the Soret band from 418 nm to 423 nm (Figure 3.15, main). Data were processed as before

(Figure 3.15 inset). Data were fitted to equation 2.3 to generate the dissociation constant. The results reveals a  $K_d$  value =  $5.05 \pm 0.3 \mu\text{M}$  (Figure 3.16).

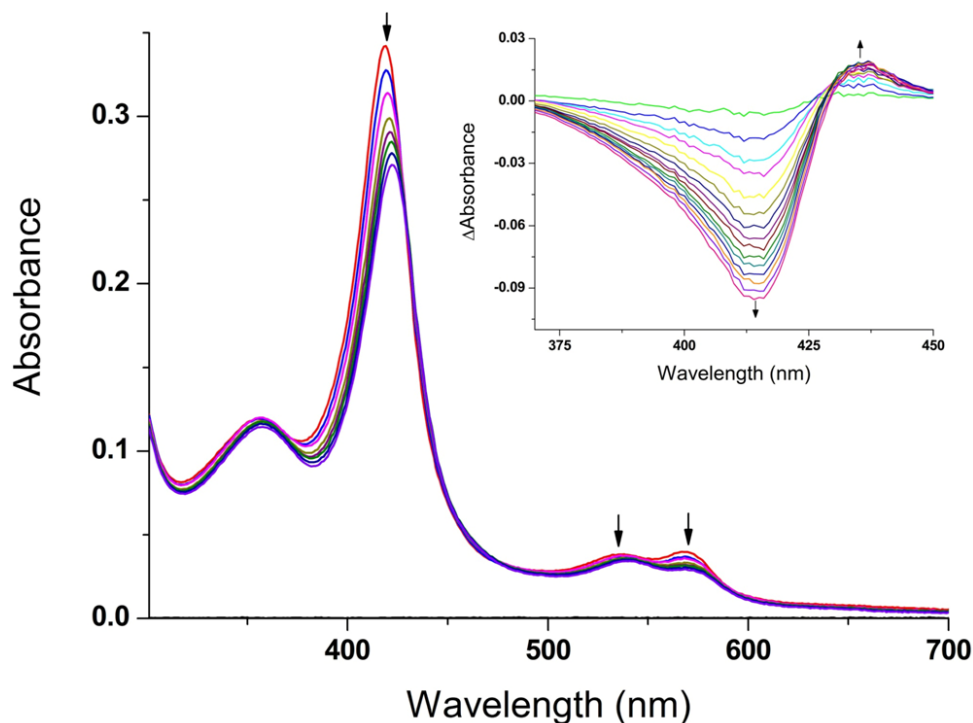


**Figure 3.15. Binding of econazole to CYP126.**

Main figure: UV-vis spectra of the binding of econazole to CYP126 ( $3.5 \mu\text{M}$ ), with arrows indicating directions of absorption change on ligand addition. Inset: the difference spectra generated from the data collected and the maximal absorbance changes derived from these data. Arrows indicate directions of absorption change on ligand binding.

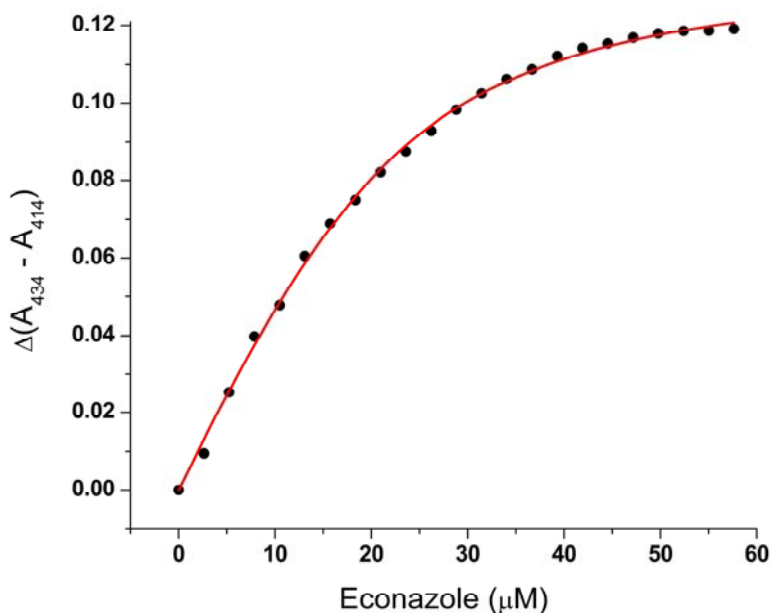


**Figure 3.16. Titration curve for the binding of econazole to CYP126.**

Data from the difference spectra ( $\Delta(A_{434}-A_{414})$ ) were fitted using equation 2.3, yielding a  $K_d$  =  $5.05 \pm 0.3 \mu\text{M}$ .

### 3.2.5.4 Imidazole binding

Imidazole induced a shift of the Soret maximum to  $\sim 423$  nm (Figure 3.17 main). Maxima and minima in the difference spectra were at 435 and 416 nm, respectively (Figure 3.17 inset) and the dissociation constant was  $2591 \pm 59$   $\mu\text{M}$  (Figure 3.18).

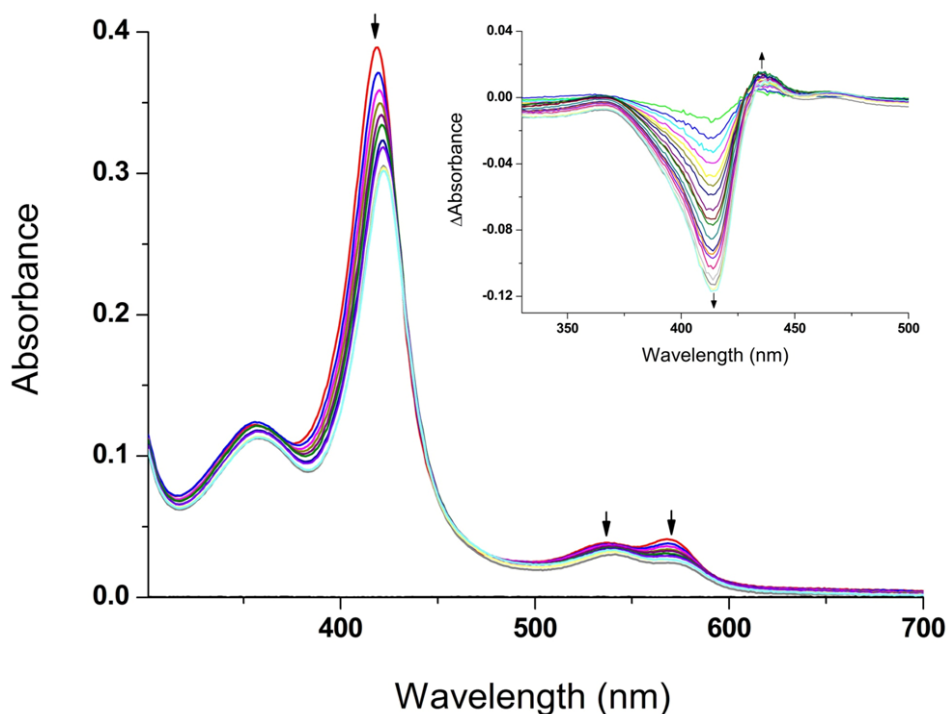


**Figure 3.17. Binding of imidazole to CYP126.**

Main figure: UV-vis spectra of the binding of imidazole to CYP126 ( $\sim 4$   $\mu\text{M}$ ), with arrows indicating directions of absorption change on ligand addition. Inset: the difference spectra generated from the data collected and the maximal absorbance changes derived from these data.

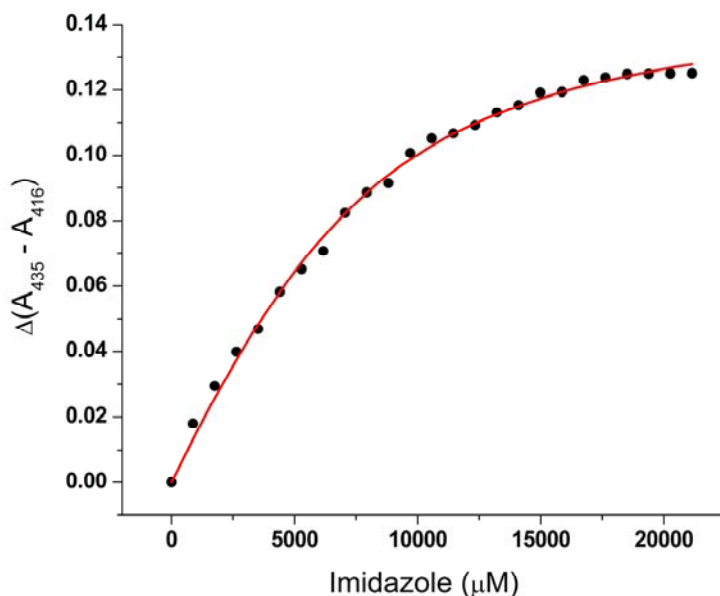


**Figure 3.18. Titration curve for the binding of imidazole to CYP126.** The difference spectra ( $\Delta(A_{435}-A_{416})$ ) were fitted to equation 2.3, yielding a  $K_d$  value =  $2591 \pm 59$   $\mu\text{M}$ .

Ligand	$K_d$ ( $\mu\text{M}$ )
Ketoconazole	$1.4 \pm 0.1$
Miconazole	$1.3 \pm 0.2$
Econazole	$5.05 \pm 0.3$
Imidazole	$2591 \pm 59$

**Table 3.3. Dissociation constants for azole drugs binding to CYP126.**

The  $K_d$  values for azoles drug binding were determined by optical titration and data were fitted by using equation 2.3 (detailed in section 1.14 of chapter 2).

### 3.2.6 Redox potentiometry

Determination of the heme iron reduction potential of cytochromes P450 is fundamental in terms of understanding electron transfer between NAD(P)H and P450s via redox partner enzymes, and the driving force for this process (166, 209, 210). A practical technique to determine reduction potentials is potentiometry by spectroelectrochemistry, and this is conveniently done using a calomel electrode to measure the reduction potential changes that are associated with alterations in electronic absorption spectrum (measured using a spectrophotometer) on the progressive reduction and oxidation of the heme using chemical reductant and oxidant (typically sodium dithionite and potassium ferricyanide, respectively), and mediators which function as electron carriers to expedite equilibration (211, 212). The heme redox centres of P450s are frequently buried in the hydrophobic core of the protein and quite well insulated. These factors, likely together with absence of appropriate protein surface-orientated amino acid side chains that might bring parts of the heme cofactor close to the electrode, probably explain the rather poor electronic interaction of P450s with an electrode surface. Thus, to create good conditions for the electronic communication of P450s, small amounts of organic and inorganic redox mediator agents were used in the redox potentiometry experiments reported here (213, 214). These help to facilitate electronic equilibration between the P450 heme and the electrode, thus expediting the process of redox potential determination. Mediators such as phenazine methosulphate (PMS, midpoint potential +80 mV vs. normal hydrogen electrode, NHE), benzyl viologen (BV, -358 mV), methyl viologen (MV, -450 mV) and 2-hydroxy-1,4-naphthoquinone (HNQ, -152 mV) are commonly used for determination of redox potentials of cofactor-containing proteins (215).

The redox potential of the CYP126 heme was determined by titration of small amounts of sodium dithionite, with simultaneous recording of applied potential and induced spectral change once the system reached equilibrium. The spectral changes observed during the

redox titration of CYP126 are displayed in Figure 3.19. During titration with sodium dithionite, a decrease and shift of heme absorption at the Soret maximum from 418 nm to 414 nm was observed, along with the development of a prominent shoulder at 402 nm. In addition, there was an increase in the absorption intensity in the visible region with the development of a strong feature for the ferrous heme iron at 550 nm, where the  $\beta$  and  $\alpha$  bands absorb at 535 and 568 nm in the oxidized P450 (Figure 3.19). The spectral changes suggest that the enzyme converts from a dominant single species in the oxidised form to (probably) a pair of species in the reduced form (see “splitting” in the Soret feature for the reduced enzyme).

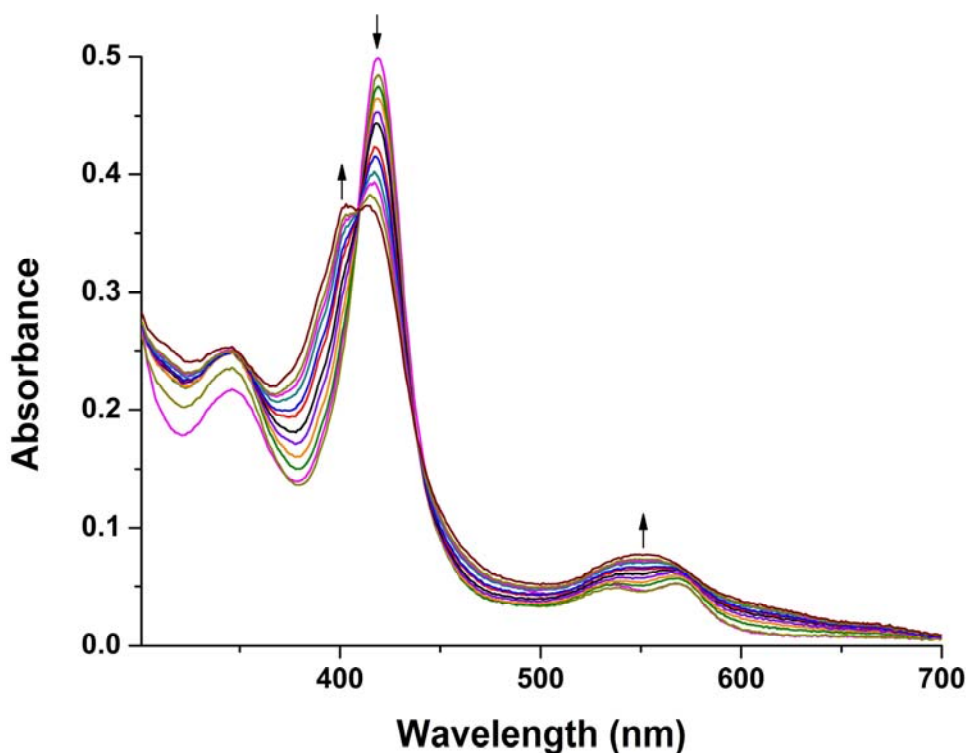


**Figure 3.19. Spectroelectrochemical redox titration of CYP126.**

Spectral changes observed for the CYP126 during redox titration in 100 mM potassium phosphate, 10% glycerol, pH 7.0. The starting spectrum is that of the oxidized (magenta line), ferric form of CYP126 with Soret maximum at 418 nm and  $\alpha$ - and  $\beta$ -bands at 565 and 533 nm, respectively. Arrows indicate direction of spectral changes during the reductive reaction. Increases in intensity are observed in the long wavelength region for the reduced enzyme, and there are blue shifts in the Soret region.

These absorption changes in the potentiometric studies of CYP126 are consistent with previous reports on the redox potential of CYP121 (82), which showed a shift of the Soret band from 416.5 to 407 nm during reduction of the heme, and similar shifts were also observed in previous studies on P450 BM3 and P450cam enzymes (216, 217). However, in recent studies on the reduction of CYP144 (135), the enzyme exhibited a red shift for heme

absorption from 420.5 to 425 nm, accompanied by development of a shoulder at 395 nm, and a strong band at 560 nm in visible region. Similar to CYP144, reductive titration of ligand-free CYP51B1 also revealed a Soret shift from ferric to ferrous with absorption switch from 419 to 423 nm, and with accumulation of a strong band at 558.5 nm in the reduced form. Thus, the changes in absorbance of heme features are consistent with the conversion of the heme thiolate to thiol in this P450 enzyme (59). Since sodium dithionite's own potential is  $\sim -420$  mV, the complete reduction of CYP126 was not achieved until an excess of reductant was added, leading to a small accumulation of a dithionite optical signal with maximum at 346 nm towards the end of the reductive titration. There was development of a prominent shoulder at 402 nm during reduction, indicating that some of the protein still retains heme thiolate-coordinated in the ferrous CYP126 enzyme. However, the spectral changes during reduction of CYP126 indicate that a proportion of the heme iron was also protonated in order to convert it from the thiolate-bound form to become thiol-coordinated in the ferrous state. The formation of the CYP126  $\text{Fe}^{2+}$ -CO complex with absorption maximum at 450 nm is also consistent with the reduction of the heme iron of the CYP126 enzyme to a thiolate-coordinated form, with subsequent protonation of the thiolate forming P420.

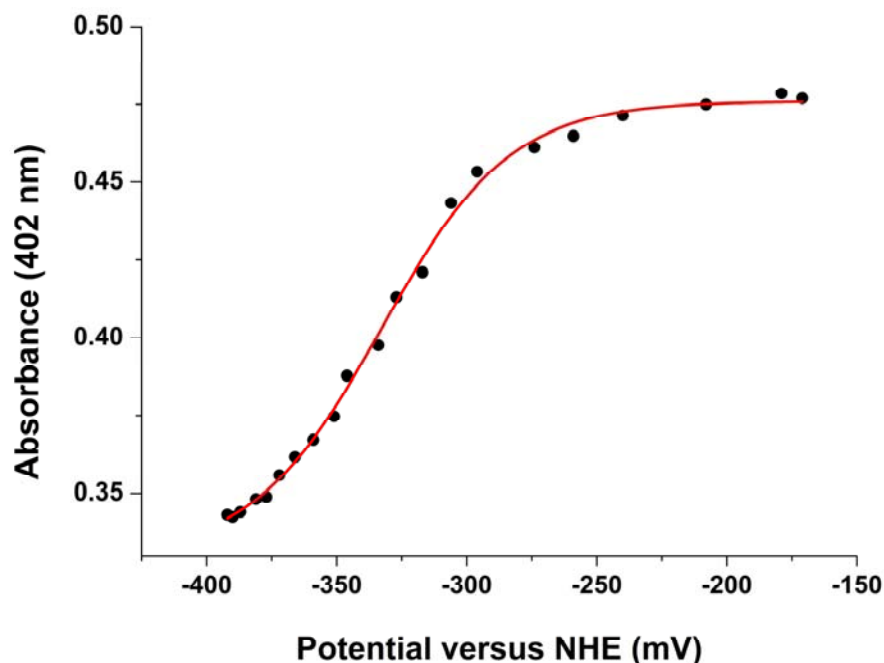


**Figure 3.20. Plot of change in Soret absorbance against applied potential (vs NHE) for CYP126.**

The data at 402 nm (near the absorbance maximum for the reduced state of the CYP126 heme) were fitted using a single electron Nernst function and the end-point absorption values predicted to allow an estimation of the heme iron mid-point potential for the enzyme. The potential determined was  $-332 \pm 4$  mV.

The redox potential of CYP126 was calculated by fitting data at the prominent reduce peak (402 nm), at which the minimal and maximal values are 0.35 (-392 mV) and 0.5 (-178 mV), respectively. By using the Nernst equation to generate a single electron fit to the data, it was feasible to calculate the mid-point reduction potential for the CYP126 heme iron. This method produced a potential for CYP126 of  $-332 \pm 4$  mV (Figure 3.20). This value indicates a moderately negative potential, suggesting that CYP126 probably needs substrate binding to elevate its heme potential in order to facilitate heme iron reduction by redox partner enzyme(s) (120). The electron donor – NAD(P)H has a midpoint reduction potential of -320 mV, a slightly more positive reduction potential than that of substrate-free CYP126.

In recent studies, McLean *et al.* showed a very positive reduction potential (-31 mV) of a ferredoxin (*Rv0763c*), which is located adjacent to CYP51B1 and is probably a true redox partner for at least this Mtb P450. The potential values of NAD(P)H and this ferredoxin suggest that CYP126 may be unable to receive electron(s) directly from this particular redox partner protein. However, recent studies on substrate (cYY) binding to CYP121 demonstrated that the binding of cYY to CYP121 induced a conversion of this P450's heme iron from a low-spin to a high-spin state, accompanied by a positive shift in the heme iron potential. This potential shift leads to CYP121's heme iron becoming able to obtain electron(s) from NAD(P)H via Mtb redox partner enzymes, even though the redox potential of substrate-free CYP121 shows a very negative value (-467 mV) (82). The substantial positive shift in heme iron potential was also observed on substrate binding to CYP51B1 (estriol binding causes a potential shift from -375 to -225 mV) (194), and P450 BM3 (arachidonate binding leads to change in redox potential from -427 to -289 mV) (167). Therefore, it is likely that when a substrate binds to CYP126 it may increase the redox potential of the enzyme (i.e. make it more positive) by ~130 mV. The details of P450 redox potential shifts are shown and discussed further in chapter 5.

### 3.2.7 pH effects on spectral properties of CYP126

Of particular interest is the nature of the reduced form of heme ( $\text{Fe}^{\text{II}}$ ). This form normally associates with CO to form  $\text{Fe}^{\text{II}}\text{-CO}$ , which has its main absorption maximum at a wavelength close to 450 nm when a thiolate ligand from the protein is *trans* to the CO. The Soret shift from 418 nm (oxidized, low-spin form) to 450 nm ( $\text{Fe}^{\text{II}}\text{-CO}$  complex) is a hallmark of P450s (218). Normally, the  $\text{Fe}^{\text{II}}\text{-CO}$  complex is associated with a thiolate proximal ligand to the heme iron (cysteinate). In this case, CYP126 possesses Cys<sup>363</sup> as the proximal ligand to the ferric heme iron. The protonation of the thiolate leads to formation

of the thiol form and is generally associated with a shift of  $\text{Fe}^{\text{II}}\text{-CO}$  complex at 450 nm to an “inactivated” P420 form of P450 enzymes (218). The protonation process can occur in the presence of chaotropic agents such as guanidinium chloride, leading to disruption of enzyme structure on the proximal side of the heme that favours protonation (59, 219). However, recent studies of CYP167A1 (P450epoK) from *Sorangium cellulosum* and CYP51B1 from Mtb demonstrated that the binding of substrate (epothilone D for CYP167A1 and estriol for CYP51B1) to P450 enzymes can retard the protonation of the thiolate, or even lead to deprotonation of heme thiol in the former P450 (194, 220).

In order to examine the thiol/thiolate transition in the ferrous enzyme, a pH titration was done using KOH to examine the conversion of CYP126  $\text{Fe}^{\text{II}}$  at different pH values, and in view of the potential effects of pH on the reduced form of CYP126 mediated through protonation/deprotonation of the proximal cysteinate. The titration was performed by measurement of the absorption spectrum as described in the Methods chapter (section 2.13).

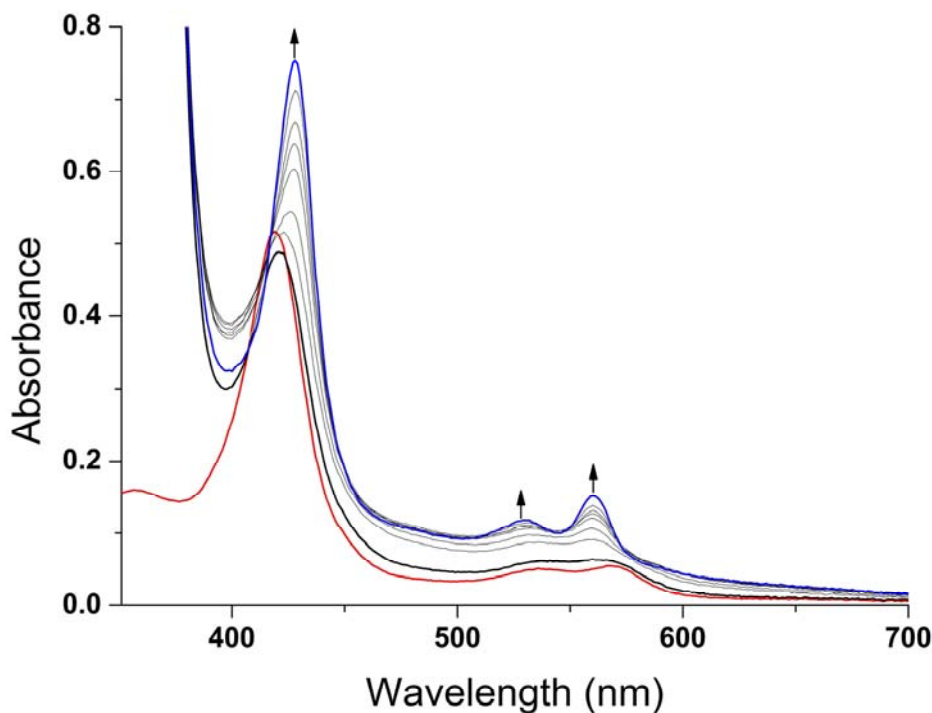


**Figure 3.21. pH dependence of the UV-visible spectrum of CYP126 in the ferrous ( $\text{Fe}^{\text{II}}$ ) state.**

$\text{Fe}^{\text{III}}$  CYP126 (red line) was reduced by sodium dithionite to  $\text{Fe}^{\text{II}}$  at pH 6.0 (black line). The starting spectrum is the oxidized form of CYP126 with Soret maximum at 418 nm and  $\alpha$ - and  $\beta$ -bands at 559 and 530 nm, respectively (red line). Addition of dithionite at the same pH leads to a shift of the Soret to ~421 nm (thick black line). Arrows indicate the direction of spectral changes during pH changes induced by KOH addition. At pH 8.73, the spectrum reaches a maximal absorption at 428 nm (blue line).

As shown in Figure 3.21, oxidized CYP126 (with absorption maximum at 418 nm) was reduced by sodium dithionite at pH 6.0. This ferrous species absorbed maximally at a wavelength close to 421 nm. During a subsequent pH titration of the ferrous form of the enzyme, the reduced form reached a maximum absorption at 428 nm at pH 8.73. Other changes were also observed in the Q-band region with an increase in intensity of  $\alpha$  and  $\beta$  bands at 560 and 530 nm, respectively. The Soret absorption shift to longer wavelength (from 422 to 428 nm) and changes in the Q-band region probably indicates heme thiolate (Cys<sup>363</sup>) protonation to thiol, since a red shifted Soret band is a feature of such a transition. Another explanation could be that a hydroxide ligand is bound to the ferrous iron at higher pH. However, such evidence for a change of distal ligand binding in the pH titration is not clear, and has not been reported previously. For this reason, changes in cysteine thiolate/thiol status are the most likely explanation for the absorbance changes observed.

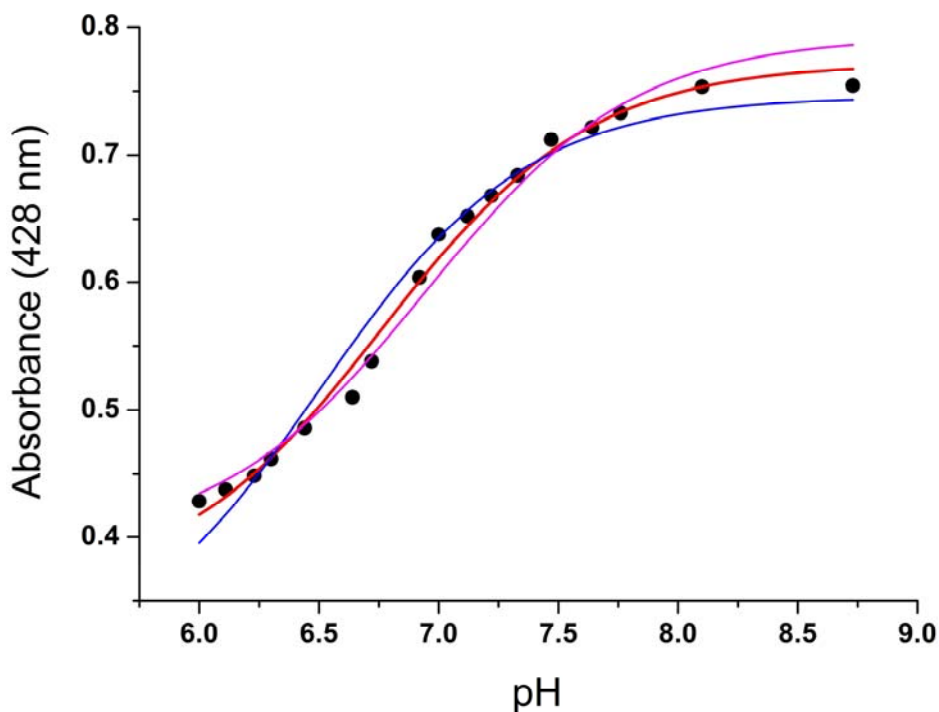


**Figure 3.22. Plot of data from pH titration of the CYP126 Fe<sup>II</sup> form.**

The spectral absorption data at 428 nm were fitted accurately to a single  $pK_a$  equation (equation 2.2, chapter 2) as shown for the red line, generating a  $pK_a$  value of  $6.8 \pm 0.1$ . The blue and magenta lines show the effects of constraining the  $pK_a$  values to 6.5 and 6.95, respectively, resulting in poorer fits to the data.

Figure 3.22 shows a plot of the data from the pH titration of the CYP126 thiolate/thiol transition in the range of pH 6.0 – 10.63. The  $pK_a$  value was generated by fitting data at the main peak (428 nm), with maximal and minimal values of 0.75 at pH 8.1 and 0.43 at pH 6.0, respectively. The data were fitted accurately to a single  $pK_a$  equation (see details of the  $pK_a$  equation 2.2 in section 2.13, chapter 2) to give a  $pK_a$  value of  $6.8 \pm 0.1$  (red line). This

$pK_a$  value is lower than that for CYP121, which showed a midpoint value of  $7.2 \pm 0.1$  (218). The  $R^2$  value in the case of CYP126 (a measure of the goodness of fit to the data points) was 0.99266 (where a perfect fit would give a  $R^2$  value of 1.0). To illustrate the effects of fit quality with small alterations in the  $pK_a$ , the blue and magenta lines show fits to the same data set with the  $pK_a$  values fixed at 6.5 and 6.95, respectively. These show inferior quality fits with  $R^2$  values of 0.97542 and 0.98317, respectively. The fact that the  $A_{428}$  value increases (indicating greater levels of heme thiolate protonation at Cys<sup>363</sup>) at higher pH seems inconsistent with the expectation that thiol formation should occur more readily at lower pH values. Since the spectral features observed clearly appear to be due to heme thiol accumulation at high pH values, it is likely that the  $pK_a$  value obtained is instead that for a different residue. It thus appears to be the case that the addition of base can induce structural rearrangements and/or altered hydrogen and other bonding interactions in the vicinity of the proximal cysteinate (as a consequence of deprotonation of a different, proximal amino acid), and in this way give rise to greater protonation of the cysteinate at more basic pH values.

### 3.2.8 Differential Scanning Calorimetry

Differential scanning calorimetry (DSC) (17, 221) is a technique able to measure melting temperatures of samples by controlling (increasing or decreasing) the environmental temperatures of the sample (222, 223). In addition, it is also possible to determine thermal transition (melting) temperatures of the samples in solution. DSC can provide useful information about protein-protein and protein-ligand binding because the basic mechanism of DSC is direct measurement of sample thermal properties (224, 225). Heat denaturation associates with enthalpy ( $\Delta H$ ) of folding. The transition midpoint  $T_m$  is the determined temperature at which 50% of the protein retains its native conformation and the other 50% is denatured (unfolded). The higher the  $T_m$ , the more stable the molecule. The change of heat capacity ( $\Delta C_p$ ) is also measured by DSC, and heat capacity changes are relatively consistent with protein unfolding due to exposure and hydration of protein side chains that are buried in the native state of the protein (226, 227).

#### 3.2.8.1 DSC of CYP126 in the ligand-free state

To investigate temperature effects on CYP126, DSC was done on highly purified CYP126 to estimate the temperature at which the protein unfolds in the presence and absence of ligand. Ligand binding may stabilize the protein, and hence studies were also done for the

ketoconazole-bound form, which showed the tightest binding to the CYP126 enzyme (see detailed data in section 3.2.5.1 – Figure 3.11 and 3.12).

In the absence of ligand, CYP126 was found to have a midpoint melting temperature (113) of 54.73 °C. The peak contains two separate unfolding temperatures, which are consistent with the unfolding of C- and N-terminal domains at different temperatures. One domain unfolds at 52.58 °C with enthalpy values of  $3.85 \pm 1.87$  kcal/mole and the other at 55.22 °C with enthalpy of  $3.93 \pm 1.54$  kcal/mole (Figure 3.23). As mentioned in chapter 1, the P450 structure is composed of two major domains; the smaller is the  $\beta$  domain (composed mainly of  $\beta$ -sheet) and the larger is the  $\alpha$  domain (composed mainly of  $\alpha$  helices) (see detailed structure in Figure 1.5 – chapter 1). The protein unfolding at different temperatures may relate to the unequal melting temperature of these domains. It can be supposed that the larger domain ( $\alpha$  domain) might be the one with the largest enthalpy and the  $\beta$  domain may possess lower enthalpy values. However, no evidence has yet been presented for a temperature-enthalpy link between  $\alpha$  and  $\beta$  domains in a P450 structure, and therefore it was not possible to determine which domain unfolds first.

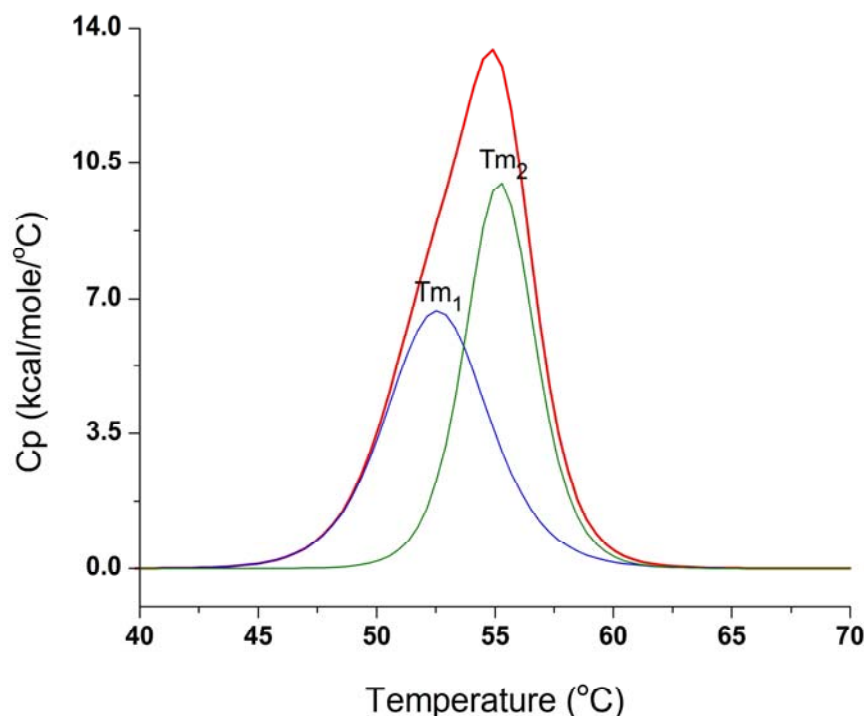


**Figure 3.23. DSC analysis of ligand-free CYP126.**

Protein sample in the absence of ligand was dialysed in 10 mM potassium phosphate buffer, pH 7.5 and heated from 20 °C to 90 °C with a scan rate of 60 °C/h. The experimental raw data were fitted to deconvolute melting temperatures using Origin software (Microcal). For clarity, two  $T_m$  values are indicated with  $T_{m1}$  at 52.58 °C and  $T_{m2}$  at 55.22 °C.

### 3.2.8.2 DSC of CYP126 with ketoconazole bound

In the presence of ketoconazole, prepared in DMSO to a concentration of 10 mg/ml, with 5  $\mu$ l added to the protein solution (400  $\mu$ g/ml final concentration – equivalent to 100  $\mu$ M ketoconazole), the midpoint  $T_m$  of CYP126 was increased to 60.8  $^{\circ}$ C, an increase of 6.3  $^{\circ}$ C, revealing a considerable increase of unfolding temperature of the protein structure in the presence of the ligand (Figure 3.24). The fitting results also indicated two distinct and separate unfolding events, again likely corresponding to the N- and C-terminal domains ( $\beta$  and  $\alpha$  domains) of the protein unfolding at different temperatures. One domain unfolds at 59.33  $^{\circ}$ C and the other at 61.49  $^{\circ}$ C (Figure 3.24). The increase of unfolding temperatures is consistent with a shift of enthalpy to higher values of  $8.8 \pm 5.29$  kcal/mole and  $5.56 \pm 5.21$  kcal/mol, respectively. The superimposed DSC data are presented to indicate the  $T_m$  transitions to higher temperature (6.3  $^{\circ}$ C) between ligand-free and ligand-bound forms (Figure 3.25), suggesting that ketoconazole binding to CYP126 does indeed result in the formation of a structure stabilized at higher temperature. In this chapter, the structure of CYP126 ketoconazole-bound complex was also determined, revealing several changes in conformation, especially in the active site cavity (see section 3.2.13). These changes might relate to the more stable conformation of CYP126 protein, but to date there has been no evidence indicating a link between structural change and stable conformation in P450 enzymes.

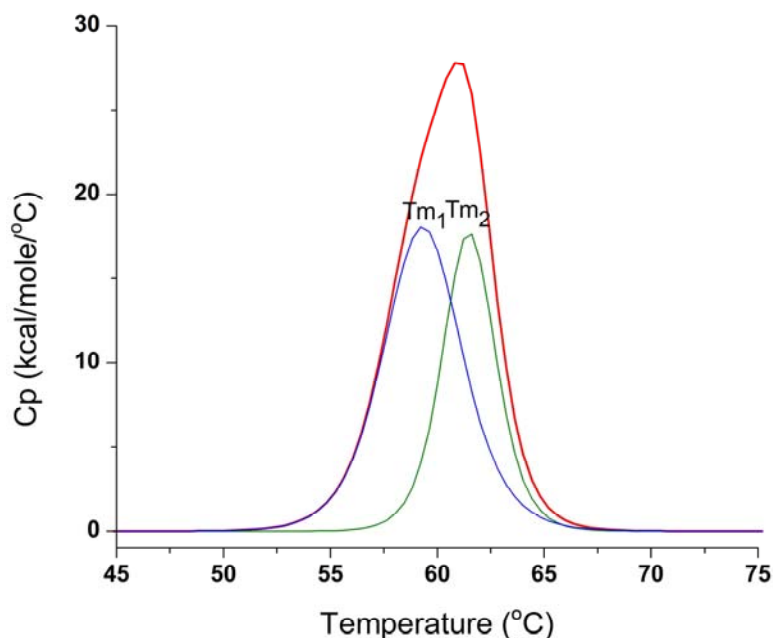


**Figure 3.24. DSC analysis of ketoconazole-bound CYP126.**

Protein (0.4 mg/ml) in the presence of ligand (ketoconazole, 20  $\mu$ M) was heated from 20 to 90  $^{\circ}$ C with a scan rate of 60  $^{\circ}$ C/h. The data were fitted by using Origin software. The fitting results indicated that there were two distinct unfolding events with  $T_m$  values of 59.33  $^{\circ}$ C and 61.49  $^{\circ}$ C.

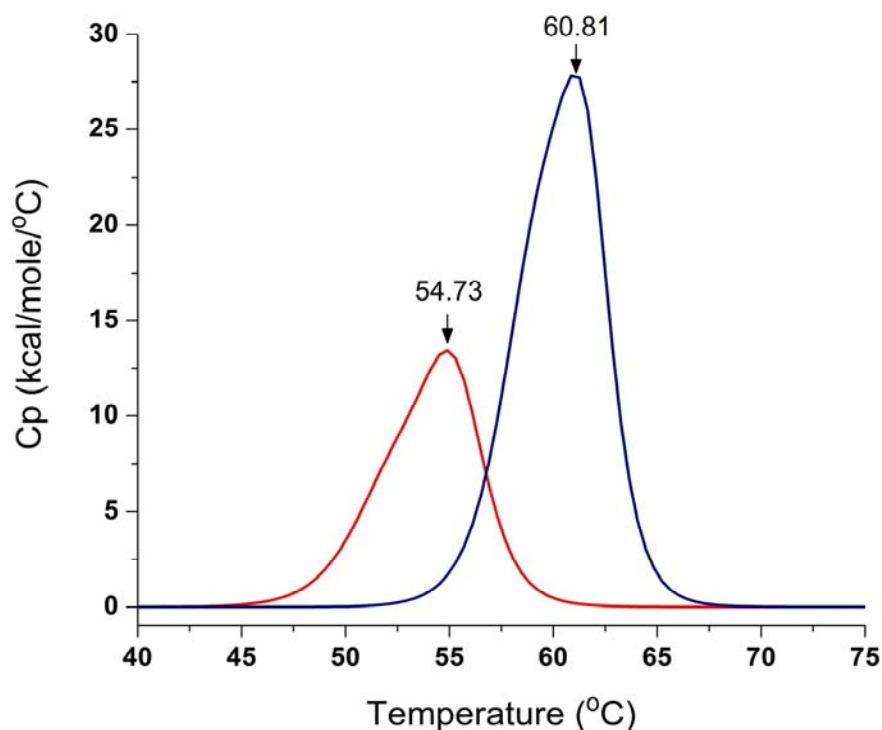


**Figure 3.25. Superimposed DSC curves for CYP126 in ligand-free and ketoconazole-bound forms.** Protein samples in the absence (red) and presence of ketoconazole (blue) were heated from 20 to 90 °C, showing the maximum of the thermal transition ( $T_m$ ) and the  $\Delta H_v$  in each case. For clarity, only the midpoint  $T_m$  is indicated. Full details of the  $\Delta H_v$  values are shown in the Table 3.1.

Sample	$T_m$ (°C)	$T_{m1}$ (°C)	$\Delta H_1$ (kcal/mol)	$T_{m2}$ (°C)	$\Delta H_2$ (kcal/mol)
CYP126	$54.73 \pm 0.05$	$52.58 \pm 0.82$	$3.85 \pm 1.57$	$55.22 \pm 0.20$	$3.93 \pm 1.54$
CYP126-ketoconazole	$60.81 \pm 0.05$	$59.33 \pm 1.02$	$8.80 \pm 5.29$	$61.49 \pm 0.37$	$5.86 \pm 5.21$

**Table 3.4. Summary of the thermodynamic data for CYP126.**

$T_m$  studies by DSC revealed the unfolding temperatures of CYP126 in ligand-free and ketoconazole-bound forms.  $T_{m1}$  and  $T_{m2}$  present the melting temperatures in each case, fitted by Origin software. The enthalpy of unfolding ( $\Delta H$ ) is also presented.

### 3.2.9 Electron paramagnetic resonance spectroscopy

EPR provides very distinctive signals for ferric heme proteins in low-spin and high-spin forms, as well for samples with different ligands to the heme iron (228, 229). EPR spectroscopy is also a tool well suited for investigation of structural changes of heme active sites in enzymes (i.e. those impinging on the heme environment and its ligands) and the electronic nature of the redox intermediates formed during enzyme catalysis (230). EPR spectroscopy is frequently used to study metalloproteins such as hemoproteins and proteins with iron-sulfur clusters in an appropriate “EPR active” redox state. EPR active molecules have one or more unpaired electrons. EPR is similar to NMR in principle, but while the

latter involves excitation of atomic nuclei, EPR uses microwave energy to excite unpaired electron spins (231). Under influence of an external magnetic field, the electron's magnetic moment aligns either parallel or antiparallel to the applied field, with the parallel alignment being the lower energy state. The energy difference between these states increases according to the strength of the applied magnetic field. In EPR measurements, absorption of microwave energy leads to the unpaired electron moving from the lower to the higher energy level. Spectra are usually collected at a constant microwave frequency, with the magnetic field being varied (232). Absorption of microwave energy occurs at one or more points where the energy difference between the two states matches that of the microwaves. In the case of ferric hemes, there are three resonant absorptions, relating to the three non-equivalent components of the g tensor (x, y and z), which is a term controlling interactions between unpaired electron spins and the applied magnetic field. The anisotropy in the ferric heme g tensor is due to axial (tetragonal) and rhombic distortions caused by the heme iron axial ligand(s) and the porphyrin ring, and results in heme EPR spectra of the type shown for e.g. CYP126 in Figure 3.26 (233).

Equation 3.1

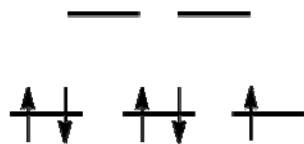
$$g = \frac{h\nu}{\beta b}$$

g: g factor  
 ν: frequency of radiation  
 h: Planck's constant ( $6.626 \times 10^{-34} \text{ J s}^{-1}$ )  
 β: electron Bohr magneton ( $9.274 \times 10^{-24} \text{ J T}^{-1}$ )  
 b: strength of magnetic field in Tesla

The g factor for anisotropic species breaks down into three values following a Cartesian coordinate system which is symmetric along the diagonal:  $g_x$ ,  $g_y$ , and  $g_z$  (234). EPR samples are normally frozen, so the many molecules in the sample will be locked into many different individual orientations relative to the magnetic field. Since the unpaired electron(s) is/are not distributed spherically over the molecule, in each of these orientations the interaction between unpaired electron(s) and the magnetic field will be different. In the ferric iron ( $\text{Fe}^{\text{III}}$ ), there are 5 electrons in its 3d orbital set (235, 236). These could be arranged in two ways, depending on the respective energies of the different orbitals. These energies depend on the ligand arrangement around the metal ion (237). The two most common types of spectra for iron-containing cytochromes are axial high spin and rhombic low spin (238). Axial high-spin systems have characteristic g-values of ~2 and ~8, whereas rhombic low-spin systems have three distinct g-values between 1.0 and 3.8. The model of the spin states of heme iron in its 3d orbital is presented in the graph below (239).



High-spin: five unpaired electrons per 3d orbital, total spin,  $S = 5/2$



Low-spin: only one unpaired electron in total, rest paired. Two empty orbitals,  $S = 1/2$

The spin state of ferric iron is determined by two factors: spin pairing energy (energy needed to pair two electrons in one orbital) and relative energy levels. If the balance of the energies is altered, it may lead to split energy levels and produce spin state changes (240). In P450 proteins, there are two axial ligands ligated to the heme iron: typically a cysteine thiolate and a water molecule (241). The binding of water or other molecules directly to heme iron causes the lowest energy (low-spin, LS) with one unpaired electron in a total 5 electrons (85). Once substrate binds, the axial water molecule is expelled from heme iron, leading to generation of the higher energy level and producing 5 unpaired electrons (high-spin, HS) (242). The typical P450 has an EPR spectrum with  $g$  values around  $g_z = 2.42$ ,  $g_y = 2.25$ ,  $g_x = 1.91$  for LS and  $g_z = 8.0$ ,  $g_y = 3.5$ ,  $g_x = 1.68$  for HS (243).

In order to determine the rhombic spectrum, EPR spectroscopy was used to study the heme iron coordination state of the CYP126 heme domain in the inhibitor-free and ketoconazole-bound forms, in collaboration with Dr Stephen Rigby (Faculty of Life Sciences, University of Manchester).

### 3.2.9.1 EPR spectrum of ligand-free CYP126

In the ligand-free form, the X-band EPR spectrum for oxidized (ferric) CYP126 was recorded and is shown in Figure 3.26. The major signals in the spectrum arise from the five 3d-electrons in three  $t_{2g}$  orbitals:  $d_{xy}$ ,  $d_{xz}$ , and  $d_{yz}$ . The spectrum shows a single set with a rhombic trio of  $g$ -tensor elements that is typical for low-spin ferric P450 enzymes, which all give rise to spectra with  $g_z$  in the range of  $\sim 2.40 - 2.45$  in low-spin, inhibitor-free forms (244). In this case, the ligand-free CYP126 EPR spectrum displayed features at  $g_z = 2.40$ ,  $g_y = 2.24$ ,  $g_x = 1.92$ , with  $g$ -values indicating that thiolate coordination has been maintained in this form. This species is thus assigned to a hexa-coordinated low-spin species with water as sixth ligand, suggesting interaction between the Cys<sup>363</sup> side chain (in its thiolate

form) and the heme iron. The  $g$ -values from the CYP126 EPR spectrum are also very similar to those reported for different isoforms of nitric synthase (NOS), which also have cysteinate- and water-ligated heme iron (245). The CYP126 EPR spectrum is virtually identical to those reported previously for well-characterized P450s such as P450cam ( $g = 2.46, 2.26, \text{ and } 1.91$ ) (246), P450 BM3 ( $g = 2.42, 2.26, \text{ and } 1.92$ ) (247), CYP51B1 ( $g = 2.44, 2.25, \text{ and } 1.91$ ) (194), and CYP121 ( $g = 2.47, 2.25, \text{ and } 1.90$ ) (82).

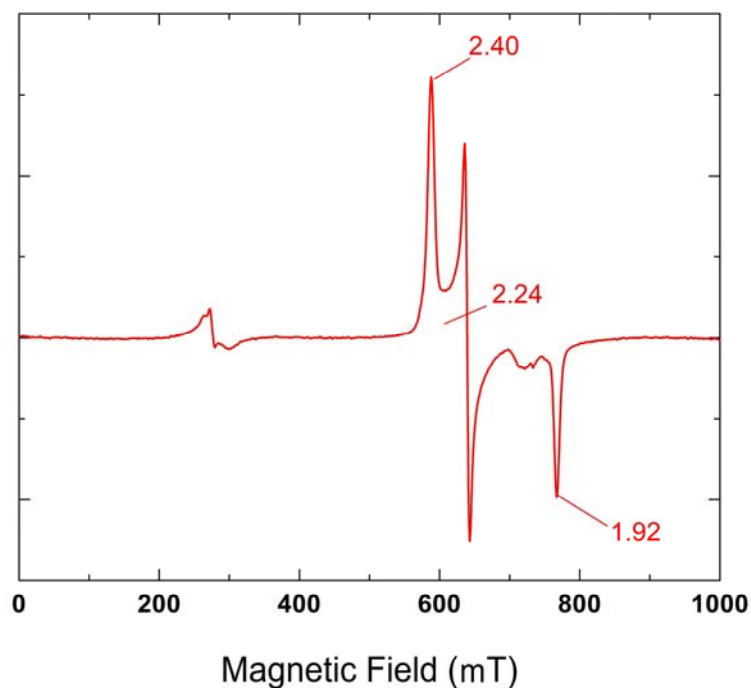


**Figure 3.26. EPR spectrum obtained for ligand-free CYP126.**

The EPR spectrum was collected with a protein concentration of 200  $\mu\text{M}$  in 50 mM potassium phosphate, pH 7.5 including 10% glycerol. EPR conditions were as follows: microwave frequency, 9.67 GHz; power, 2 milliwatts; temperature, 10.0 K; modulation amplitude, 10 G.  $g$ -values are detailed in the figure.

### 3.2.9.2 EPR spectrum of ketoconazole-bound CYP126

Addition of inhibitor (ketoconazole at a concentration of 100  $\mu\text{g/ml}$ ) to CYP126 provided data further consistent with the assignments described, with a rather increased complexity of the EPR signal and new low-spin heme iron features arising. Thus complex mixture of ketoconazole-bound CYP126 species may be a consequence of different orientations of the distal nitrogen or proximal cysteinate ligands. In addition, there was no significant switch to a high-spin form. Instead, changes in the EPR spectrum for ketoconazole-bound CYP126 indicate differences in the distribution of the low-spin species. As shown in Figure 3.27, it is clearly seen that a rhombic spectrum is obtained that is shifted to higher  $g_z$  values with respect to the ligand-free enzyme. The  $g$ -values for this complex are  $g_z = 2.44$ ,  $g_y = 2.24$ , and  $g_x = 1.90$ . The shift in  $g_z$  is typical for such complexes in other P450s, which are

commonly in the range from  $\sim 2.43$  to  $2.48$  (159). Moreover, the peaks widths are larger, and the amplitudes are less intense than for ligand-free CYP126. However, the peaks at  $g_z$  and  $g_x$  indicated that there was likely around 2/3 of the P450 in the complex with ketoconazole bound to the heme iron of CYP126. Residual material is clearly seen with  $g$ -values similar to that for the ligand-free CYP126 (Figure 3.26).

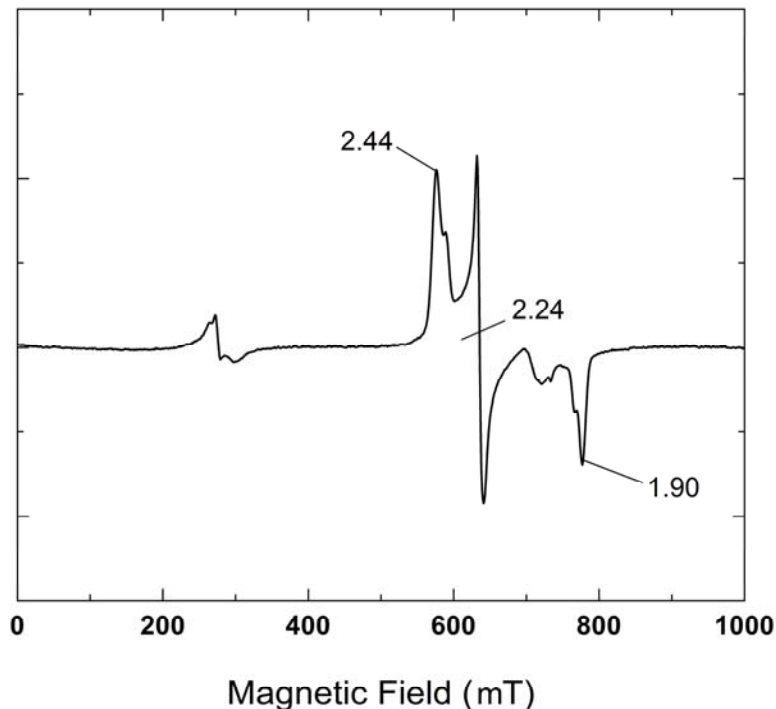


**Figure 3.27. EPR spectrum obtained for ketoconazole-bound CYP126.**

EPR spectra were collected with a protein concentration of  $200 \mu\text{M}$  in  $50 \text{ mM}$  potassium phosphate,  $\text{pH } 7.5$  including  $10\%$  glycerol and with a final ketoconazole concentration of  $100 \mu\text{g/ml}$  ( $\sim 0.2 \text{ mM}$ ). EPR conditions were as follow: microwave frequency,  $9.67 \text{ GHz}$ ; power,  $2 \text{ milliwatts}$ ; temperature,  $10.0 \text{ K}$ ; modulation amplitude,  $10 \text{ G}$ . The major set of  $g$ -values is detailed in the Figure.

The solubility of ketoconazole is rather limited in water, but CYP126 displayed tight binding to CYP126 with a  $K_d = 1.4 \pm 0.1 \mu\text{M}$ . The result of a ketoconazole titration binding curve indicated that at a lower protein concentration ( $\sim 4 \mu\text{M}$ ) than used for EPR, addition of  $\sim 4 \mu\text{M}$  ketoconazole resulted in near-complete saturation within the soluble range of the inhibitor. However, when the EPR sample was prepared with a higher protein concentration ( $200 \mu\text{M}$ ), much more ketoconazole is required in solution (at least  $200 \mu\text{M}$ ) to saturate the enzyme. In the experiment, the inhibitor was added at an equal concentration ( $\sim 200 \mu\text{M}$ ) in attempts to ensure that CYP126 could be near-saturated with the ligand. However, the EPR signals indicated that around 2/3 of CYP126–ketoconazole bound complex was formed, producing a rhombic triplet of signals with  $g$ -values of  $2.44$ ,  $2.24$ , and  $1.90$  (Figure 3.27).

Other signals were identical to those of the ligand-free form, suggesting that the ketoconazole was not soluble enough to near-saturate CYP126 under these conditions.

On the other hand, the crystal structure analysis of CYP126 reveals a narrow active site cavity. Therefore, it might be possible that, since ketoconazole is quite a large molecule, it may encounter difficulty in accessing the narrow active site cavity of the enzyme, and perhaps bind tightly to only particular conformations of the enzyme. The EPR spectra recorded from the complex revealed that only  $\sim 2/3$  of the species were in a form that could be immediately recognized as being due to nitrogenous heme iron ligation from the azole. While one explanation for this observation is that limited solubility of the drug prevents near-complete iron coordination (despite its low  $K_d$  value), other possibilities could be considered. Overall, the EPR spectral features are consistent with a mixture of species in which a substantial proportion of the heme iron is axially coordinated by cysteinate and an oxygen donor ligand (i.e. the resting form). However, it is impossible to eliminate the possibility that this residual species is not one that has ketoconazole bound to the enzyme, perhaps having instead the azole ligating to the iron indirectly via the water molecule retained on the heme iron, as was observed for CYP121 in its fluconazole complex (149).

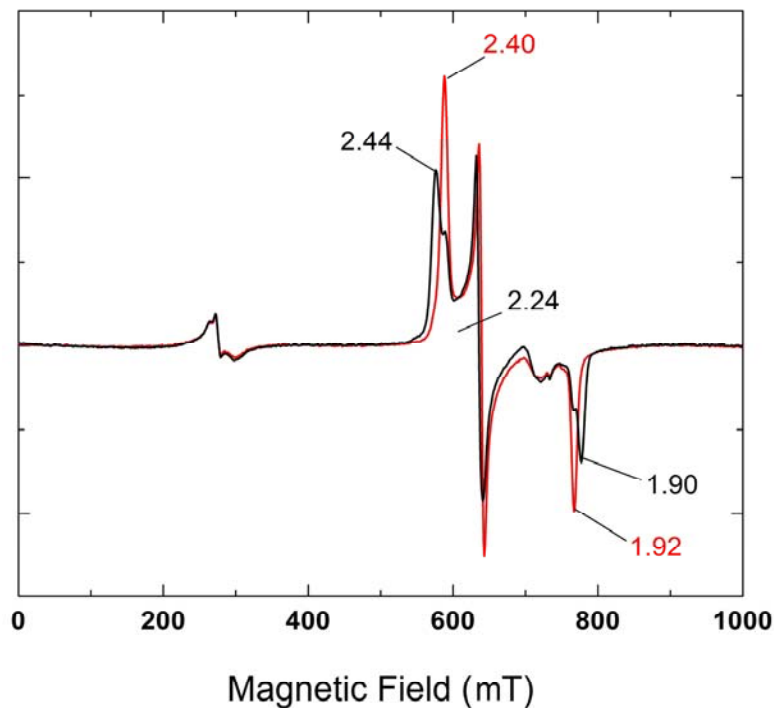


**Figure 3.28. Divergent EPR signals observed in overlaid spectra for ligand-free and ketoconazole-bound forms of CYP126.**

The EPR spectrum obtained for ligand-free CYP126 (red) is overlaid with that for the ketoconazole-bound form (black). The major sets of g-values are detailed in the appropriate colour codes.

The EPR spectra for the ketoconazole-bound form and for the ligand-free CYP126 show minor differences in  $g$ -values, which are highlighted in the spectral overlay in Figure 3.28. In the ligand-free form, there appears to be one predominant species in CYP126, with  $g$ -values at 2.40, 2.24, and 1.92, and these values are consistent with a low-spin ferric heme species with cysteinate and water axial ligands. The spectrum is comparable with those previously reported for other Mtb P450s, including CYP121 and CYP51B1 (82, 194). However, in the azole-bound CYP126 complex, there are changes in  $g$ -values at  $g_z$  and  $g_x$  that correspond to the ligation of the azole nitrogen to the heme iron, indicative of displacement of the coordinate axial-water in the distal pocket. As described above, it appears that in  $\sim 2/3$  of the observed species there is ligation of heme iron by the ketoconazole nitrogen. Other signals still remained at  $g = 2.40$  and 1.92, and may reflect a proportion of enzyme retaining an aqua distal ligand, or else perhaps indirect azole coordination of the heme iron, as described above.

### 3.2.10 Magnetic circular dichroism

Magnetic circular dichroism (MCD) is a useful tool in elucidating the geometric and electronic structures of the metal centre in metalloproteins such as heme iron- and iron sulfur cluster-binding proteins. MCD relies on the measurement of the differential absorption of left (LCP) and right (RCP) circular polarised light, which is induced in a sample by application of a strong magnetic field that is oriented parallel to the propagation of the light. In particular, MCD can differentiate between structures with different symmetry of axial ligation in cytochrome P450 proteins, and identify the cluster types of iron-sulfur proteins (248). Generally, UV-vis absorption and MCD spectra have the same set of spectral bands, but the band morphologies are different due to the effect of the applied magnetic field and the use of differential absorbance intensity (249).

The MCD spectra of heme protein are sensitive to the redox and spin states of the metal and to the nature of its axial ligands, as well as to proximity of a second heme group and to the nature of the protein environment (250, 251). The spectral properties of cytochrome P450 are believed to be associated with the presence of an axial thiolate ligand from a cysteine residue occupying the fifth axial position. The ferrous-CO form exhibits a Soret maximum at an unusually long wavelength (450 nm), indicating that the state of the heme is considerably different from other hemoproteins. In MCD spectroscopy, different wavelengths from the UV-visible range and the near infrared region can be used to probe

the structure of heme iron and its ligands in various redox and ligand-bound states (252, 253).

The UV-visible MCD spectra for oxidised CYP126 are shown in Figure 3.29. It is clearly seen that the MCD spectra reported in this region are similar to the electronic absorbance spectrum and reveal the properties of the spin- and oxidation-states of the CYP126 heme iron. The MCD signals at wavelengths between 250 and 600 nm are due to  $\pi$ - $\pi^*$  transitions of the porphyrin ring (254).

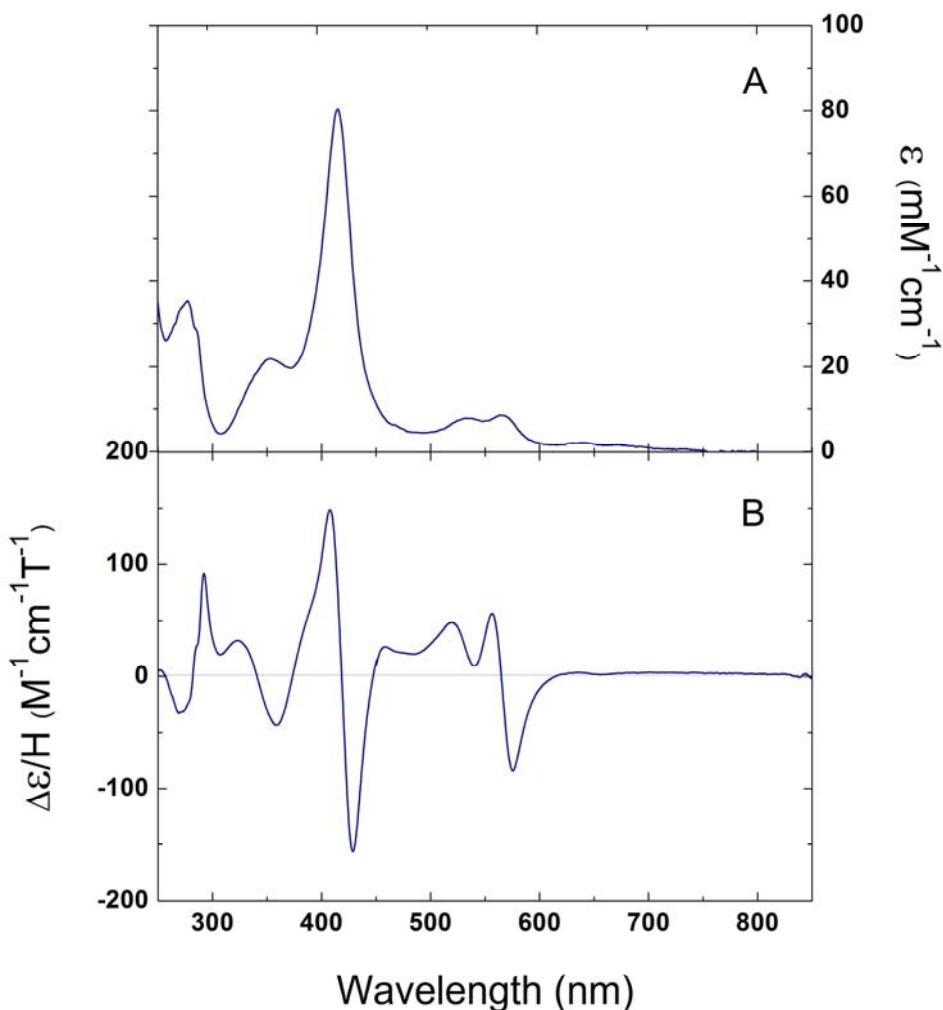


**Figure 3.29. MCD spectra for CYP126.**

The UV-visible absorption spectrum for CYP126 (panel A) is compared with the MCD spectrum in the same region (panel B). Protein concentration for MCD measurement is 200  $\mu\text{M}$ . MCD spectra were generated by subtraction of the baseline from +8 Telsa.

Similar to UV-visible spectroscopy, the UV-visible MCD spectra present information on spin- and oxidation-state of the iron. According to the signals from Figure 3.29, the features in the MCD spectrum revealed typical properties of low-spin ferric heme with intensities in  $\epsilon$ : 359 nm (-43.4), 407.7 nm (+148.8); the crossover at 418.3 nm (0). Additional bands are

found at 520 nm (+48.7); 556.5 nm (+56.5); 564.7 nm (0); and 575.5 nm (-83.8). As described above, the electronic absorption spectrum of ferric CYP126 has characteristic bands at 418, 535 and 568 nm (Figure 3.29, panel A). A comparison of these bands (Figure 3.29, panel A) with the MCD spectrum (Figure 3.29, panel B) indicates that the major features are relatively similar, and present as typical of low-spin ferric hemes. In addition, a medium intensity positive band at 292 nm is contributed by tryptophan residues of CYP126. Compared to the MCD features of CYP121, which has bands at 357 nm, 406 nm, 416.4 nm, 522 nm, 554.5 nm, 563.2 nm, and 576 nm (138), the MCD properties of CYP126 are highly similar.

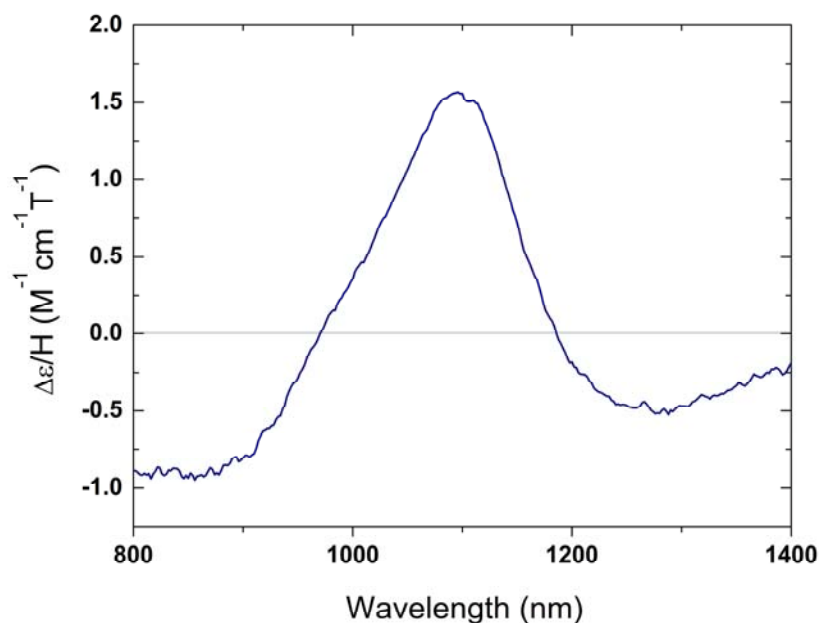


**Figure 3.30. The MCD spectrum for CYP126 in the near IR region**

MCD spectra were recorded at room temperature as described in the Materials and Methods section. Protein concentration was 200  $\mu\text{M}$ .

Additional MCD spectra were also recorded in the near-infrared region (near IR or NIR region), in which spectra contain a ligand-to-metal charge-transfer (CT) transition. The CT transition is sensitive to the energies of the d-orbitals, which change according to alterations in the axial heme ligation. Therefore, it is immensely useful to diagnose the nature of the heme ligation in the ligand-free and ligand-bound forms. The MCD spectrum of CYP126 in the ligand-free form is presented in Figure 3.30. A CT band is located at approximately 1097 nm, which is in the region associated with cysteinate/water ligation of the heme iron. This feature is similar to the position of this CT band in other P450s such as P450 BM3 (1060 nm) (247), P450 BioI (1090 nm) (255), and CYP121 (1125 nm) (138). The intensity and position of the CT band suggest that the cysteinate/water ligation occurs in CYP126.

### 3.2.11 Mass spectrometry

To determine accurate molecular masses of peptides and proteins, Electrospray ionization mass spectrometry (ESI-MS) is often used to verify the desired mass of e.g. the intact protein (256). In order to obtain high resolution structures using methods such as X-ray crystallography, it is important to work with intact and homogeneous proteins. Hence, ESI-MS could be used to confirm the precise mass of the protein that has been successfully expressed – i.e. to show that the primary structure of the protein construct is correct and that the protein is intact (257, 258). Therefore, in this case, ESI-MS was used to analyze purified CYP126, to verify its integrity and the absence of any sample heterogeneity after expression in *E. coli*.

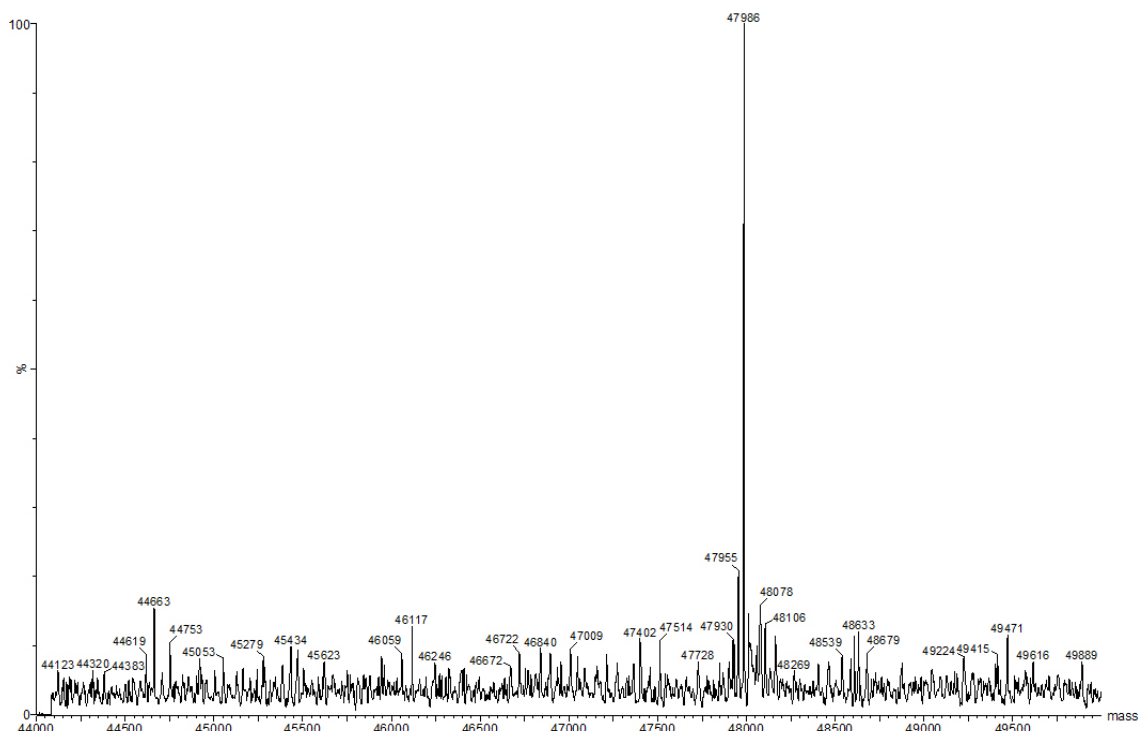


**Figure 3.31. Mass spectrometry of CYP126 using a Waters LCT Mass spectrometer.**

Protein was eluted from an ESI-TOF instrument (LCT, Waters UK) in 50/50 acetonitrile/H<sub>2</sub>O, 0.1 % formic acid at a final concentration of 4 mg/ml. All data were collected and analysed by MaxEnt 4.0 software. The result from electrospray mass spectrometry revealed CYP126 to be a single, intact species of molecular mass 47986 Da.

The amino acid sequence of the CYP126 from *Mtb* was determined by translation of the corresponding gene. The protein is composed of 415 amino acids. Figure 3.31 shows the result of electrospray mass spectrometry of the CYP126 protein. In the ESI mass spectra there is a single, intact species of molecular mass = 47986 Da. The measured molecular mass of the main component (47986 Da) is in good agreement with the predicted mass of CYP126 based on translation of its gene sequence, once the mass of the initiator

methionine has been subtracted (the predicted mass is calculated from the amino acid sequence to be 48135 Da). Therefore, the result suggests that no modification was detected during the expression of the *CYP126* gene in *E. coli* cells and that the protein was not proteolytically processed.

### 3.2.12 Light scattering

In order, to determine the state of the native form of a protein, laser light scattering provides a direct measure of molecular mass (259). This method is useful to determine the native state of a protein (e.g. monomer or oligomer), revealing any different aggregation states of the sample (260). The sample (protein) is measured by light scattered at different angles that relate to the incident laser beam (261). In case of a globular protein with molecular mass below 500 kDa, the scattered light intensity is uniform in all directions, and therefore the sample is usually only measured with scattered light at a single angle (normally 90°). The molecular mass is the calculated base on the scattered light intensity and protein concentration (262).

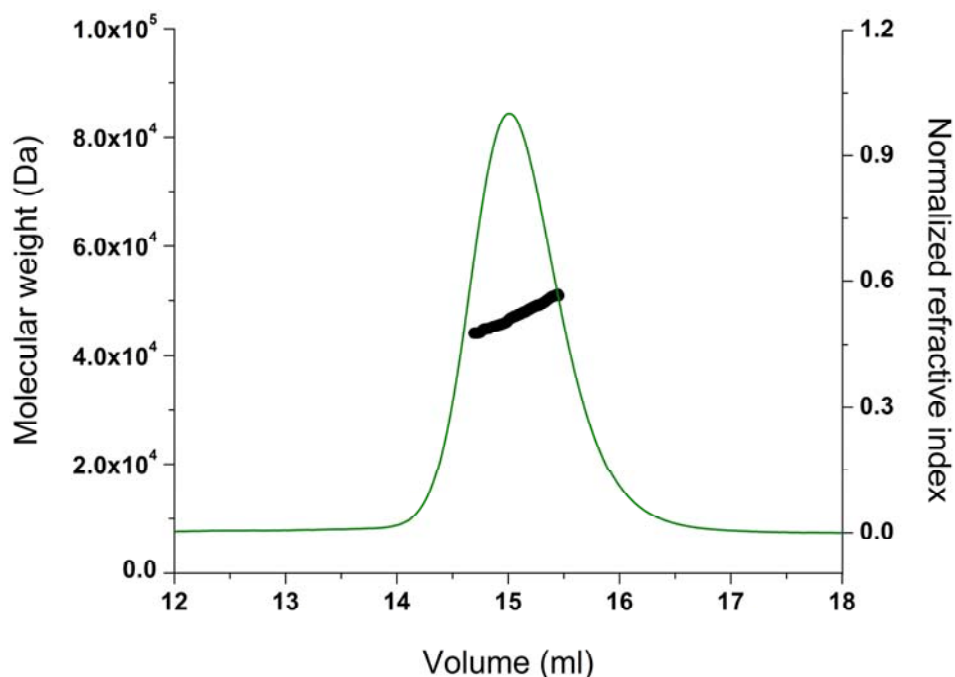


**Figure 3.32. Superdex – 200 10/300 GL gel filtration chromatography and MALLS analysis of CYP126.**

A summary of MALLS data for the ligand-free form of CYP126 is presented. The protein is predicted to have a molecular mass of  $48100 \pm 1200$  Da. When the mass of the initiator methionine is included (and considering the experimental errors from polydispersity measurement), this is almost identical to that expected for a monomer of the protein (48135 Da).

The size and oligomeric status of CYP126 was first analysed by multiangle laser light scattering (MALLS). Figure 3.32 shows the native form of CYP126 that was analyzed by MALLS (following gel filtration) to yield a molecular mass. As can be seen from Figure 3.32, the chromatogram contains a major species eluting at ~15 ml without any minor species. The molecular mass value of CYP126 was measured based on the angular dependence of the scattered light, allowing a weight-average molecular mass of  $48.1 \pm 1.2$  kDa to be calculated for CYP126. From this experimentally determined value, and assuming that monomer of CYP126 has a molecular mass of ~ 48 kDa (from SDS-PAGE or amino acid sequence), it can be concluded that CYP126 appears to behave as a monomer under this condition. Similar experiments were repeated at least 6 times, but no dimeric or higher order oligomeric forms were found in any case. The mass value from light scattering is similar to that measured by ESI-mass spectrometry. Therefore, it can be concluded that the monomeric form of the recombinant CYP126 is representative of the protein in the conditions used (10 mM Tris-HCl, 150 mM NaCl, pH 7.5). In recent studies on the oligomerization of CYP144 (135), it was also reported as a single monomeric species, and similar results were also obtained for CYP125 and CYP121 (121, 138).

### 3.2.13 Crystallography

Cytochrome P450 proteins are involved in various metabolic reactions, with different sets of substrate specificities and metabolic transformations catalysed (68). Substrate specificity and oxidative mechanism are controlled by the active site structure. Therefore, the biological properties of P450s cannot be fully understood without detail knowledge of their 3D structure. The increasing number of P450 crystal structures solved over the past twenty two years, allows us to study the relationship between structure and function of this enzyme class. Typically, to determine the 3D structure of a protein at an atomic level, an experimental technique such as X-ray crystallography is used (263, 264). Thus, this technique has been proved to be useful in resolving structural features of several P450s (265, 266).

The available P450 structures from a wide variety of sources reveal that the overall structural fold of P450 is highly preserved during evolution from bacteria through to mammals (267, 268). The analysis of the structures of P450s also indicated that there are highly variable regions that appear to be associated with recognition and binding of a diverse range substrates and redox partners (99, 269-271). Therefore, it is necessary to

study the overall structure to gain information on the active sites of P450s, which will be immensely useful for understanding how the individual P450s work.

### 3.2.13.1 Crystallization of ligand-free CYP126

CYP126 was expressed and purified as described in the Methods section (section 2.23). The purity of the protein is important for crystallization screening. The protein has a molecular weight of ~48 kDa and contains one cysteine-ligated *b*-type heme (C363), and another cysteine at position 159. Figure 3.33A shows the results obtained from the original screen (using the JCSG core II as the screening kit). The results indicated that CYP126 was quite easy to crystallize in a ligand-free state. However, the crystals were quite small and spherical. Following identification of initial crystal conditions, larger and better shaped crystals were obtained by screening around the original conditions using small variations in a range of 36-42% precipitants (sodium sulfate and sodium acetate). Drops were made by mixing 1  $\mu$ l of 20 mg ml<sup>-1</sup> CYP126 protein with 1  $\mu$ l of reservoir solution (38% saturated sodium sulfate, 10% 1 M Tris-HCl, pH 6.5 and 54% H<sub>2</sub>O) and by incubating at 4 °C for 24-48 hrs. The crystals of CYP126 formed within 48 hrs and these were observed under a microscope. The crystals in Figure 3.33 B appeared as tetragonal trapeziums of typical dimensions ~ 0.9 x 0.3 x 0.2 mm.

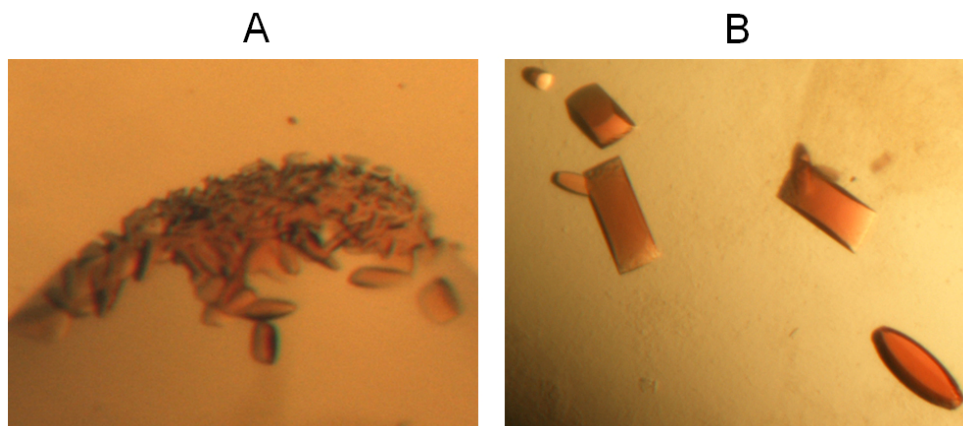


**Figure 3.33. Native crystals of CYP126**

(A) Preliminary crystals were obtained from small tray growth with a nanolitre drop setter Mosquito using JCSG core II as the screen. (B) Crystals obtained following optimization by the sitting-drop method with conditions of 38% saturated sodium sulfate, 10% 1 M Tris-HCl, pH 6.5 and 54% H<sub>2</sub>O.

Prior to data collection, CYP126 crystals were soaked for 5-10 s in a cryoprotectant solution consisting of mother liquor supplemented with 10% polyethylene glycol 200. The crystal was then attached to a cryoloop and put in a 100 K nitrogen stream. Diffraction data were collected and are presented in Figure 3.34. Data were scaled, integrated and the

structure solved by Dr. Colin Levy (University of Manchester). Structures were solved by molecular replacement using Phaser (272). Refinement and model building were carried out using ArpWarp, Phenix and COOT in conjunction with Molprobity to validate the structure (273). The detailed data and final refinement statistics are given in Table 3.5. The crystals were found in space group  $P2_12_12_1$ , with unit cell parameters  $a = 58.9$ ,  $b = 69.9$ ,  $c = 233.4$  Å (Table 3.5).

	Ligand-free protein Data bank code 1OXA
<b>Data collection</b>	
Resolution	1.7 Å
X-ray wavelength	1.069800
Space group	19 P212121
Cell dimension	
a, b, c	233.438, 58.910, 69.974 Å
$\alpha$ , $\beta$ , $\gamma$	90.0, 90.0, 90.0°
solvent content	54%
$R_{sym}^{a, b}$	7.8% (33.5%)
$I/\sigma$	13.4 (3.9)
Unique reflections	395462
Completeness	95.9% (93.6%)
Multiplicity	3.7
$R_{cryst}/R_{free}^c$	17.3/20.9 %
Bond angles	1.49°
Bond length	0.015 Å

**Table 3.5. X-ray data collection and refinement statistics for ligand-free CYP126.**

The unit cell dimensions are given as three lengths: a, b, and c; and three angles:  $\alpha$ ,  $\beta$ , and  $\gamma$ .

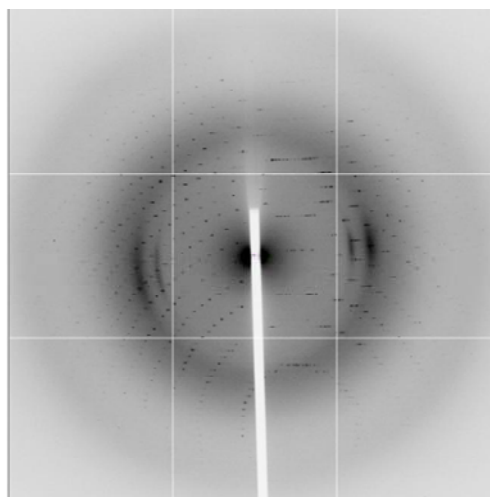


**Figure 3.34. A representative X-ray diffraction image obtained from CYP126 crystals.** The data were collected at 100 K on an R-AXIS IV image plate.

The crystal structure was determined for the ligand-free form of CYP126 at 1.7 Å. The overall structure of CYP126 has the characteristic fold common to all structurally defined cytochromes P450. Figure 3.35 shows that the structural features of CYP126 commonly involved in heme binding, substrate recognition, and formation of the active site cavity are readily distinguished and are comparable with other P450 proteins for which structures are known, such as the I helix and heme sixth ligand. The orientations of the BC and FG loops are highly similar to the other Mtb P450s like CYP121, CYP125, CYP130 and CYP124 (121, 136, 137, 149). However, CYP126 does exhibit some conformational and oligomerization differences when compared to many other P450 structures. The CYP126 structure contains four  $\beta$ -sheets ( $\beta$ 1,  $\beta$ 2,  $\beta$ 3,  $\beta$ 4) and 13  $\alpha$ -helices, with a structural core consisting of a four helix bundle (L, I, E, D). There is an absence of the  $\beta$ 5 sheet section observed in many other P450s (Figure 3.35).

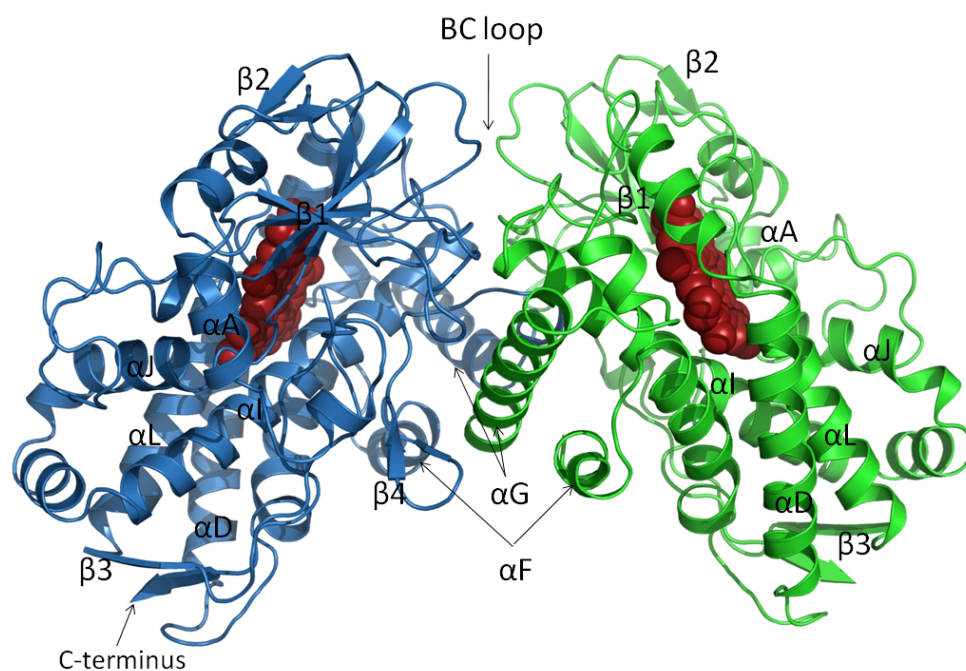


**Figure 3.35. Overall view of CYP126.**

A ribbon diagram of the substrate-free CYP126 crystal dimer is shown. The dimer interface is formed largely via interactions between the G helices and multiple contacts in the BC-loop regions. The monomers are shown in green and blue, heme is in firebrick. The BC-loop region is well structured having two short alpha helices. The I helix N terminus locates near the heme iron.

The region of the active site cavity of CYP126 is formed by heme that is positioned between the I and L helices, with the proximal Cys-363 (in its thiolate form) anchoring the cofactor to the L helix. Several components such as F, G, and C helices and residues from the BC and FG loops build one half of the active site cavity. In addition, the other half is

composed of the C-terminal loop that trails the L helix, and  $\beta$ -sheet 1 (four anti-parallel strands) (Figure 3.35).

Substrate-free CYP126 crystallized as a dimer in the asymmetric unit, with one monomer apparently bound to imidazole (derived from the purification procedure) (274), while the other monomer is ligand-free. This difference in ligation state appears associated with large differences in the structure of selected loop regions. It is clearly seen that the F helix in the “open form” (the imidazole-bound state) of CYP126 loses one helical turn, and at the same time the G helix also loses one helical turn. Therefore the FG $\alpha$  loop is missing from the open form, whereas this is present in the closed form (the ligand-free state). Conformational mobility of the FG region has been observed previously in other structurally defined P450 enzymes, and this may serve to enable substrate access and product release from the active site (275, 276).

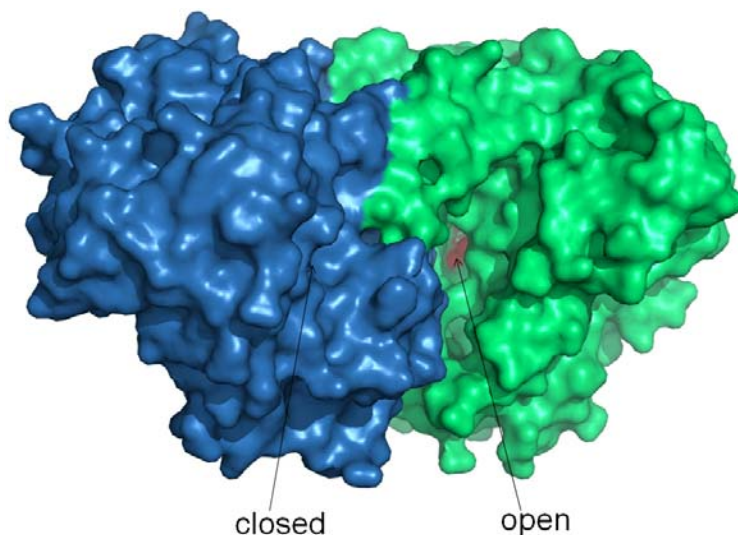


**Figure 3.36. A surface representation of CYP126.**

The dimeric form of CYP126 presents both the closed and open forms of the P450 (with respect to active site cavity access). The open form is coloured in green and reveals the access channel to the active site (the heme is coloured in red). The closed form (coloured in blue) lacks any such channel.

In the open form, the heme appears directly accessible from the surface due to the mobility of the FG $\alpha$  region (Figure 3.36). This is similar to what has been observed in certain other P450s, for instance CYP130 (137). However, in the closed form, the FG-loop closes the access gate of the active site cavity. The crystallographic data suggest that the oligomerization of CYP126 seen in the crystal can also occur even in the absence of bound imidazole, as the presence of imidazole in the active pocket does not appear to directly

affect the dimer interface. As reported in other P450s, the transitions between open and closed forms are often related to binding of the native ligand. The first crystal structure of an antifungal inhibitor-bound form of Mtb CYP51B1, in complex with fluconazole, was determined at 2.2 Å resolution and revealed that the triazole ring is positioned perpendicular to the porphyrin plane with a ring nitrogen atom coordinated to the heme iron. This interaction is associated with conformational changes, which are seen to occur after binding of larger ligands like fluconazole to CYP51B1. The fluconazole-bound conformational changes involve a transition of the C helix, accompanied with BC loop movement to close the access channel to the substrate-binding site (119). In addition, the crystal structure of econazole-bound CYP130 (3.0 Å) also showed that the protein crystallizes in a closed conformation as a dimer. The conformational changes in the open-closed transition involve repositioning of the BC and FG loops.

Whether the dimeric form of CYP126 is physiologically relevant remains to be established. However, it is tempting to speculate that the enzyme could operate as a dimer, with different monomers reacting in sequence. However, multi angle laser light scattering (MALLS) studies did not reveal a large proportion of the dimeric form of CYP126 in solution, and there have been no functional data to indicate the link between protein oligomerization and the activity of CYP126.

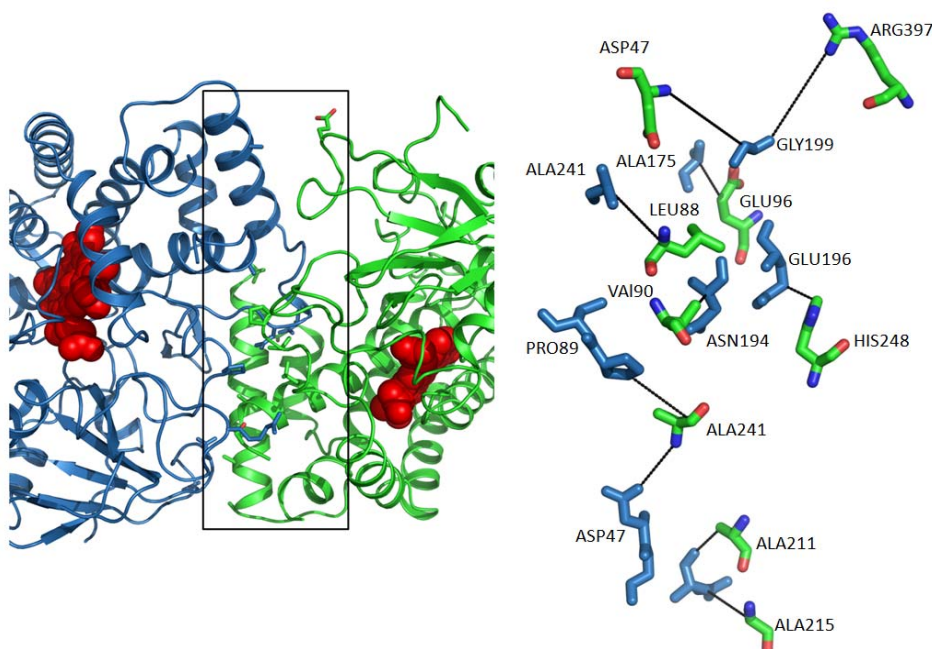


**Figure 3.37. A detailed view of the dimerization interface of CYP126.**

Approximately 800 Å<sup>2</sup> in size, the interface between both CYP126 monomers is formed largely via interactions between the G helices of the open form (green colour) and other loops and helices of the closed form (blue colour). The multiple contacts are shown in sticks. The key interactions of amino acids were measured at close distances for several amino acids from chain A (open-form – green) and chain B (closed-form – blue).

The native crystal was formed at 20 mg/ml (420  $\mu$ M), and crystallographic analysis revealed the dimeric form in ligand-free CYP126. The dimer in the crystal is stabilized, and analysis of the interactions between the two monomers shows that dimer formation involves specific hydrophobic interactions and salt bridges (Figure 3.37). These types of interactions are also observed in the CYP130-econazole complex, indicating several hydrophobic and H-bonding interactions that stabilize the dimeric form of this P450 of uncertain catalytic function (137). In recent studies of CYP130, it was also reported that the stable dimer form of the protein in solution, if formed, is not sufficiently populated to detect it by equilibrium techniques, including gel filtration coupled with MALLS or native gel electrophoresis at protein concentrations up to 100  $\mu$ M (137). Therefore, it is possible also that the CYP126 dimeric form might be found in native conditions (see section 3.2.12), but not at a level at which it can be detected by MALLS.

Therefore, these data suggest that the CYP126 protein may be able to form a dimer in solution, but that such a form could not be detected by MALLS, which shows only the monomer at a concentration of 8  $\mu$ M. In addition, the data from previous studies of CYP130 indicated that the dimerization of protein may be formed by non-specific interactions, and in the presence of higher salt concentrations. However, the crystallographic data suggest that the oligomerization of CYP126 seen in the crystal might also occur in solution, and that there might exist an equilibrium between the open-closed and open-open forms in such a dimer, even though the oligomeric form does not appear to be highly populated in solution.

The crystal structure of CYP126 reveals different structural features between the closed and open forms, and it furthermore demonstrates that the ligation of the imidazole to the heme iron of CYP126 occur concomitantly with changes in the I helix conformation. A comparison of the closed and open forms of CYP126 was made by superimposing these structures using the Pymol program (141) to reveal the different structural changes in the absence and presence of imidazole ligand. Figure 3.38 presents such an overlay and highlights changes in the closed and open forms of the dimer.

It is clear that the direct coordination of the CYP126 heme iron by imidazole leads to an altered position of threonine 257 and alanine 253 on the I helix, as compared to the closed form of the P450. In addition, the alpha F and alpha G helices show significant differences in their respective positions, and the FG-loop in the open form loses one helical turn,

whereas the closed form gains one helical turn, leading to its covering the access to the active site cavity. The conformational mobility of the FG region may serve to enable substrate access and product release from the active site pocket. This conformational mobility has been previously observed in other structurally defined P450 proteins, such as the phytanic acid-bound CYP124 structure, which showed that substrate binding induces the FG loop to move inwards, making the structure more “closed” (with respect to active site access) by  $\sim 3.0 \text{ \AA}$  (136). In addition, in the active site in the closed form, there may also be a more dramatic reshaping of the active site. The best representatives of such changes include the FG-loop and the B' helix. However, such changes do not fully explain how a P450 protein can accommodate a variety of different substrates.

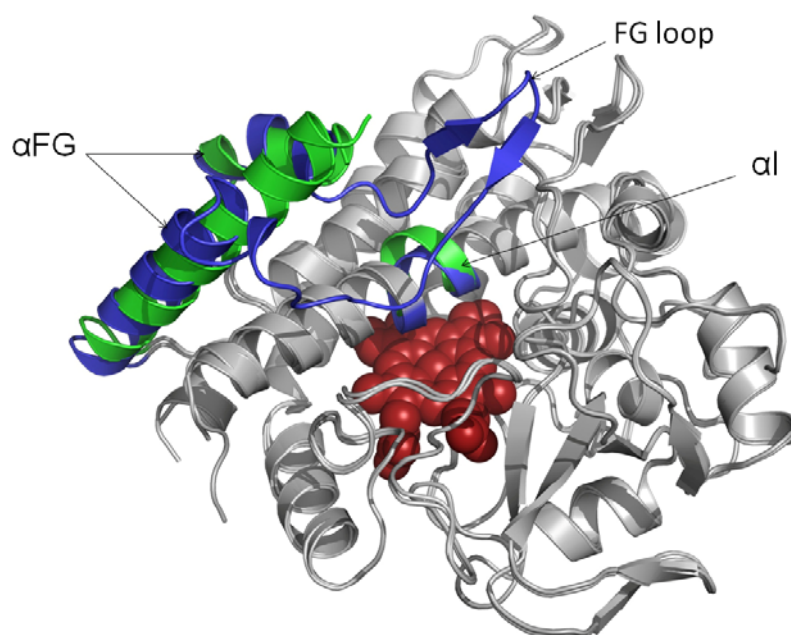


**Figure 3.38. Superimposition of the ligand-free (closed) and imidazole-bound (open) CYP126 monomers.** Areas with distinct differences are colour coded, with the ligand-free (closed form) coloured in green, and the imidazole-bound (open form) in blue. Structures are shown with the common P450 secondary structure elements labelled. Heme is in firebrick spacefill representation.

The dimer of CYP126 in the crystal might be formed in different conformational states such as open-closed, open-open, and closed-closed forms. In order to determine how the new set of the CYP126 dimers form, an alignment was done with one open monomer overlaid on a closed monomer to produce a new model of the open-open dimer form. Figure 3.39 presents the conformational features of an open-open form. It is clearly seen that the G helices are located opposite one another at the interface. The F helices are also packed in parallel orientations on both sides of the G helices. The two G helices are

stabilized by partial overlap (about three residues - aspartic acid 195 – valine 197, shown in red in Figure 3.39) and the model suggests that the FG region of the open-open form is involved in the dimerization of CYP126.

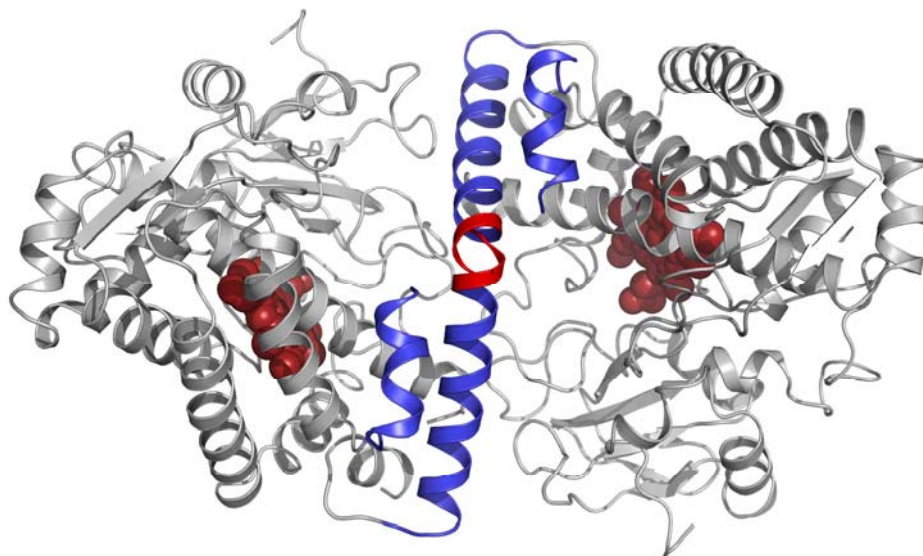


**Figure 3.39. Open-open conformational form of CYP126**

The open monomer of the dimer was superimposed on the closed form, leading to a new dimer structure of open-open forms. The heme irons are marked in firebrick, the FG loops are coloured in blue, and the overlapped residues on the G helix are in red.

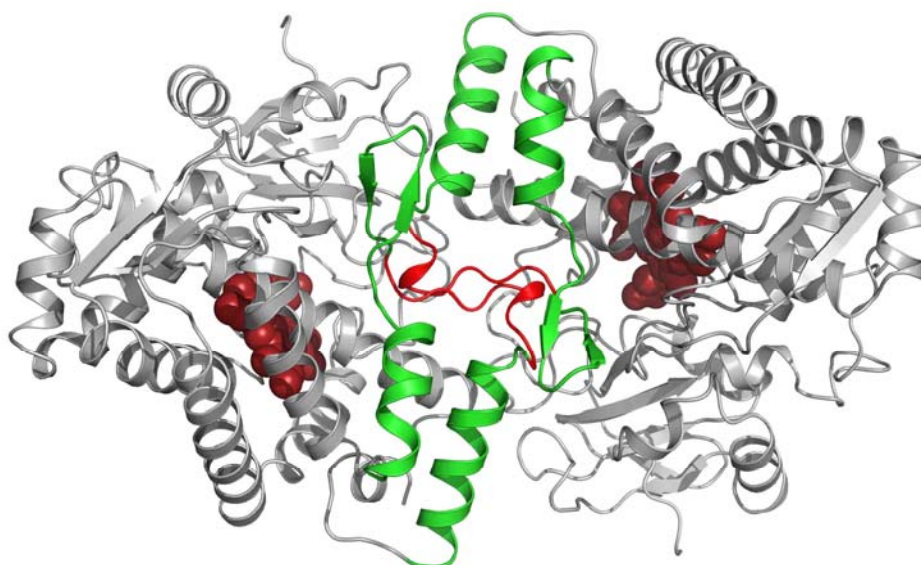


**Figure 3.40. Closed-closed conformational form of CYP126**

The closed form of the dimer was superimposed on the open form, leading to formation of a new dimer structure. The heme irons are marked in firebrick, the FG loops are coloured in green, and the overlapped residues on the FG loop are in red.

In addition, a new model of a closed-closed form of the dimer exhibits different position of the FG helices, in which both of the helices are packed in parallel orientations (Figure 3.40). The F helices are located in the same position at both sides of the G helices compared to the open-open form. However, the G helices are not in opposite positions, instead they are in parallel. Figure 3.40 presents the conformational features of the closed-closed form with the interactions of a part of the FG loop in this dimer. It is clearly seen that the FG loops of the dimer interact through several residues (about nine residues, Met<sup>190</sup> – Gly<sup>199</sup>), which form a part of the FG loop. Therefore, the interactions between FG loops are believed to be involved in stabilizing the crystallographic dimer interface.

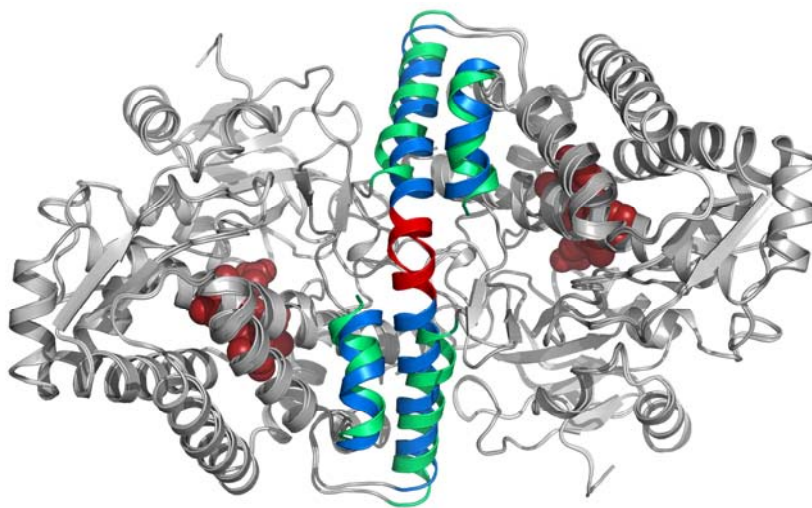


**Figure 3.41. Divergent stereo view of an overlay of both open–open and closed–closed forms of CYP126.** The CYP126 heme irons are shown in firebrick, whereas the corresponding FG helices are shown in blue for the open-open form, and in green for the closed-closed form. The red colour on the G helices indicates the distinct features of the G helix in different forms.

A comparison of the open-open and closed-closed forms revealed that almost all conformational features are in the same positions, except for the F and G helices. It is clearly seen in the Figure 3.41 that the G helices of the closed form shift 4.8 Å upward to the heme iron plane, whereas the G helices in the open form extend to form a longer helix, which shows the partial overlap of residues (in red colour, starting at Met<sup>190</sup>). On the other hand, the F helices also reveal a slight change, shifting 2.0 Å inwards to the heme iron plane. The changes and movements of the FG helices in the closed form lead to the formation of a longer loop, and this loop is appropriate to, and responsible for, closing the active site of the protein. However, the open-open form is unlikely to form in crystals due to steric clashes of G helix with several residues being overlapped.

Despite their divergence in sequence, the P450 structural fold has remained the same throughout evolution, and the determination of an increasing number of P450 crystal structures indicates that the unusual variability in sequences does not preclude a high degree of conservation of their general topography and structural fold (80). Among the multiple well-known Mtb P450 proteins, CYP126 has relatively modest levels of amino acid identity with other Mtb P450s, for instance, 35%, 37%, 33%, 27% and 25% with CYP125, CYP124, CYP130, CYP121 and CYP51B1, respectively. Therefore, to compare the conserved P450 structural fold of the CYP126 crystal structure with the other well-defined Mtb P450s, the structure of CYP126 was superimposed with those Mtb P450s for which crystal structures have been determined (Figure 3.42).

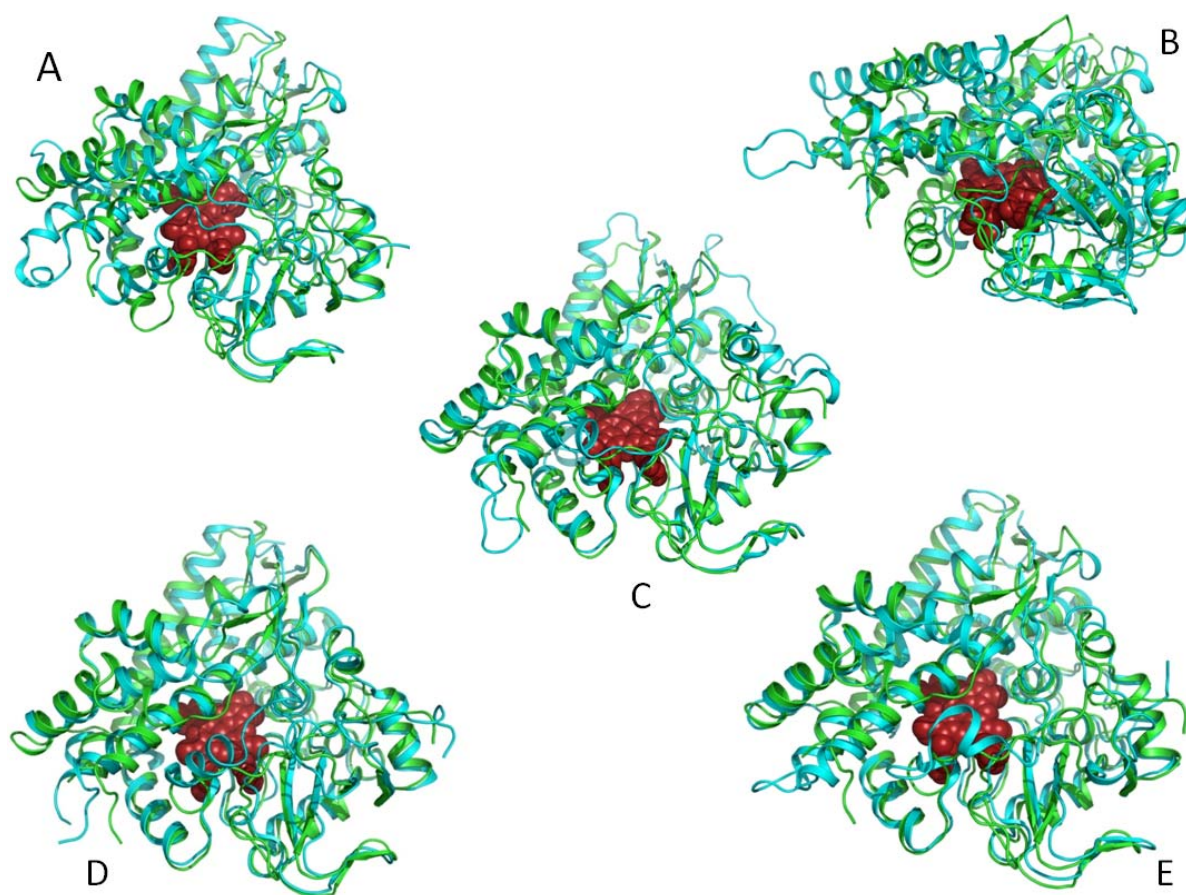


**Figure 3.42. Structural alignment of the CYP126 closed form with CYP51B1, CYP121, CYP130, CYP124 and CYP125 crystal structures.** The ribbon representation of the CYP126 closed form structure is shown (in green) with the CYP121 ligand-free form (in cyan, PDB code-1N40), with an RMSD of 3.1 Å. (B) The CYP51B1 ligand-free form (in cyan, PDB code-1H5Z), with an RMSD of 5.6 Å. (C) The CYP124 ligand-free form (in cyan, PDB code-2WM4), with an RMSD of 1.9 Å. (D) The CYP125 ligand-free form (in cyan, PDB code-3IVY), with an RMSD of 1.8 Å. (E) The CYP130 ligand-free form (in cyan, PDB code-2UUQ), with an RMSD of 2.3 Å (277).

It is clearly seen that the fold of the CYP126 structure is highly conserved in other Mtb P450s, presented in Figure 3.42. Interestingly, CYP126 shares only 35% amino acid sequence identity with CYP125 (PDB code 3IVY), but the alignment (Figure 3.42D) reveals the highest similarity of the structural fold between these two proteins. The I, L, F, G, and C helices are located in the same position, with an RMSD of 1.8 Å. However, CYP125 shows a slight difference at the FG-loop, with a shorter loop compared to CYP126.

CYP124 (PDB code 2WM4) shares the highest sequence identity with CYP126 (37% identity), but shows a higher RMSD of 1.9 Å (Figure 3.42C). CYP124 has a longer G-helix than CYP126, but the FG-loop is likely quite similar. In comparison with CYP51B1 (PDB code 1H5Z), the alignment shows significant differences in positions of structural elements between CYP126 and CYP51B1 (Figure 3.42B). The FG-helix is longer and is located at a more than 30 degrees deviation from the FG-loop in CYP126. Although CYP51B1 shows a nearly identical position of the C-terminal portions of the I helix, the N-terminal half deviates significantly from that of CYP126. Therefore, the I helix is bent away from the heme. However, the open position of the BC loop in CYP51B1 reveals a similar conformational structure to that in CYP126. In addition, CYP51B1 possesses a bent I helix and an open BC loop to define a large access channel, which runs roughly parallel to the heme (119). In contrast, the access channel in CYP126 runs perpendicular to the heme.

Despite sharing a lower identity of amino acid sequence (27%), the general structural fold of CYP121 (PDB code 1N40) shows high similarity to CYP126 (Figure 3.42A). The alignment of the two proteins reveals an RMSD of 3.1 Å. In addition, CYP126 also shows a closed structural fold, as seen in CYP130 (Figure 3.42 E) with an RMSD of 2.3 Å. The alignments of these enzymes reveal a similar position at the FG and BC loops, and even in the conformation of the I helix. According to the RMSD values from the structural alignments, the closest structural fold to CYP126 is that of CYP125, with an RMSD of 1.8 Å.

In the closed form, (Figure 3.43) the CYP126 active pocket contains a water molecule acting as the distal axial ligand to the heme iron (bond distance 2.36 Å). The axial water is additionally stabilized via a H-bond to the carbonyl group of Ala-253 (distance 3.08 Å) and a H-bonding network is formed by a cluster of water molecules bound in the proximity. In order to provide a H-bond to the axial water, the I helix closely approaches the porphyrin

(distance 4.99 Å between the Ala-253 carbonyl group and the heme iron) at A253. This imposes steric constraints on the binding of potential ligands in the active site, and at the same time obstructs the axial water from release. It might be expected that the substrate binding event occurs with displacement of both the axial water ligand and the proximal A253 residue from their positions in the substrate-free P450.

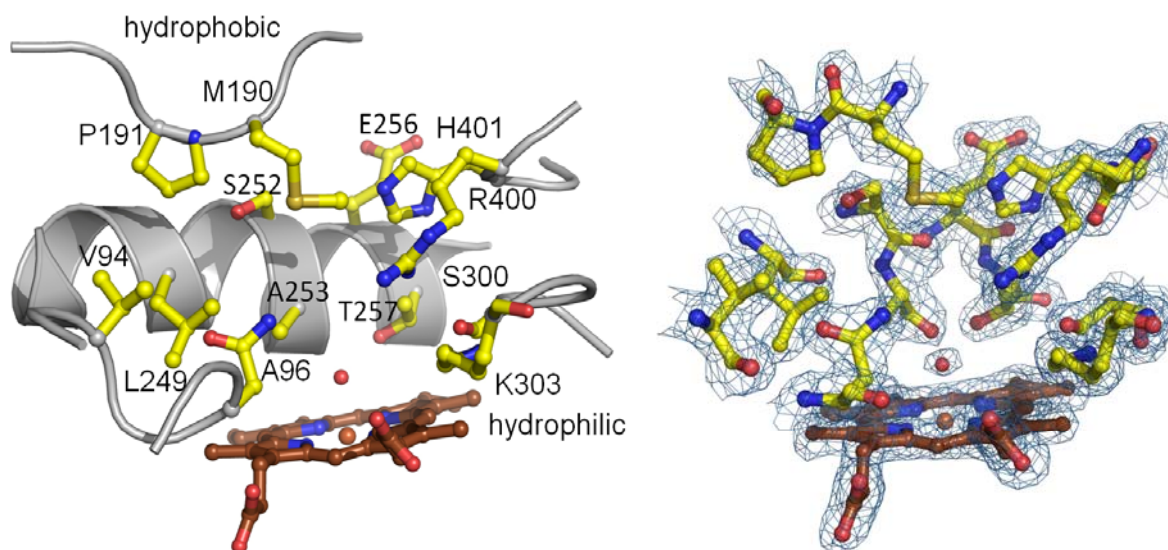


**Figure 3.43. Active site pocket of CYP126 (closed form)**

The amino acids around the active site are shown as sticks with the portion of the I helix of the protein depicted as a gray ribbon. The heme prosthetic group is shown as sticks, with nitrogen and carbon atoms coloured in blue and firebrick, respectively. The ferric iron and oxygen of the distal water molecules are marked in brown and pink, respectively. Fragments of the  $F_o - F_c$  electron density composite omit map contoured at 1.0  $\sigma$  are in blue. The electron density image was generated using the CCP4 and Pymol programs (141).

An entrance to the active site cavity is clearly defined by the B', L and F  $\alpha$  helices and their preceding loop regions (Val<sup>176</sup> – Arg<sup>201</sup>, Arg<sup>383</sup> – Val<sup>409</sup>, and Arg<sup>65</sup> – Pro<sup>101</sup>, respectively). In addition, there are contributions by the I helix (Leu<sup>245</sup> – Asn<sup>260</sup>) and Ser<sup>300</sup> – Lys<sup>303</sup> from the J helix loop region. The entire pocket is lined by hydrophobic residues and resembles a letterbox shape with the B', L and F helices. The position of the I helix residue Ala<sup>253</sup>, that is located in the immediate vicinity of the heme distal pocket, and the orientation of the Ala<sup>253</sup> side chain is linked to the coordination state of the heme iron. The electron density for the ligand-free form of CYP126 is unambiguously defined in each of two monomers in the asymmetric unit (Figure 3.43, right hand panel).

When comparing the open, imidazole-bound form to the closed structure, the most significant feature of the active site cavity in the open form structure is a large open cleft

between the FG-loop and the heme iron. This cleft is wide and is formed primarily by the disorder of the FG-loop. The orientation of the FG-loop is defined as the “open” form of CYP126 (Figure 3.44). Reorganization of conserved secondary structures leads to formation of the cleft, and does not break the general structural fold of the P450. A PDB search confirmed that the open form structure of CYP126 is most similar to that of CYP125 (136), which demonstrated that the cleft arises from the dissociation of contacts between the loop of the F–G helices and the heme.

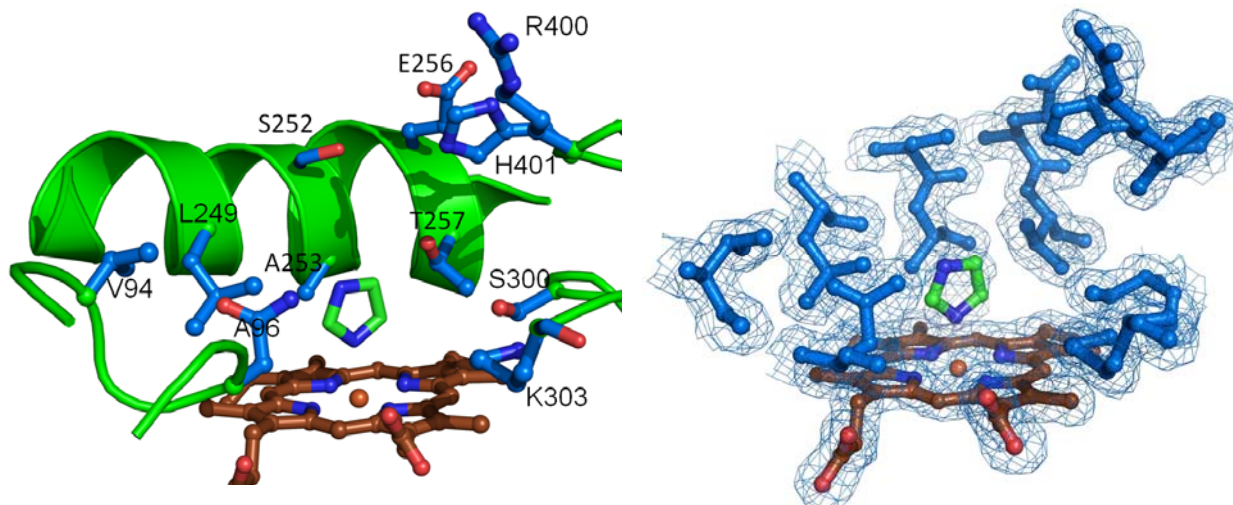


**Figure 3.44. Detailed view of the active site of the open form of CYP126**

Residues responsible for forming the active site are shown in sticks (blue) with the portions of the secondary structure of the protein depicted as a ribbon and coloured in green (I-helix). The heme prosthetic groups are shown in sticks, with carbon atoms coloured in firebrick. The ferric iron and water oxygen molecules are in brown and pink, respectively. The  $2F_o - F_c$  omit map is contoured at  $1 \sigma$  and shown in light blue (right hand panel).

As shown in Figure 3.43 and Figure 3.44, the precise conformational differences between the open and closed forms extend to the proximal heme face. Both Pro<sup>191</sup> and Met<sup>190</sup> on the FG-loop move away from the heme in the open conformation, making a cleft between FG helices and heme iron. Other changes occur in the position of Arg<sup>400</sup> on the L helix, which moves sharply upward from the heme distal plane by approximately 8.5 Å. In addition, the Glu<sup>256</sup> on the I helix also shifts about 0.6 Å upwards from the heme plane. The differences between closed and open active sites are distinguished in the Figure 3.45, which shows the alignment of two active site forms. The superposition of the crystal structures of the closed and open forms in the CYP126 dimer reveals that there are two different conformations for this protein in the unbound state, involving a movement of the FG loop.

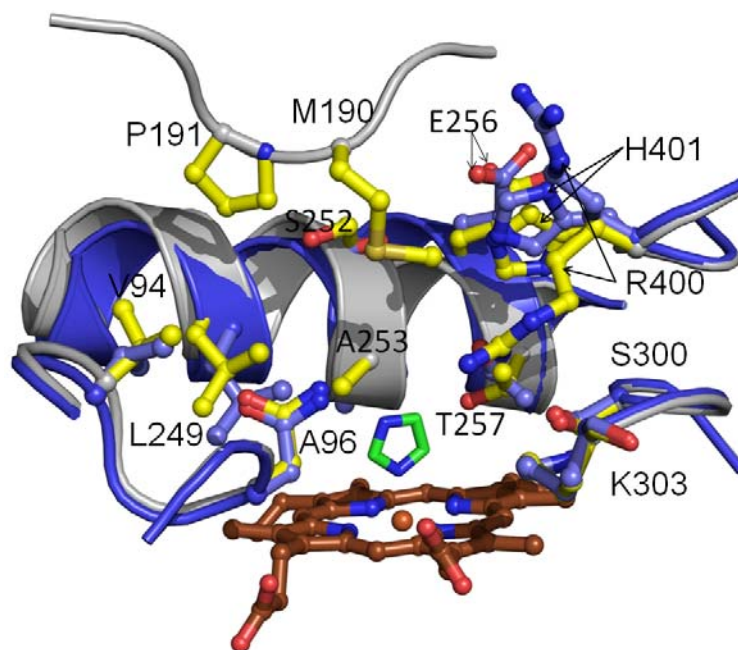


**Figure 3.45. An overlay of the active sites of the closed and open CYP126 monomers**

The movement of the FG-loop and nearby residues in the open conformation compared to the closed form. The closed and open forms are coloured in grey and blue, respectively. The relative residues are presented in sticks in yellow for the closed, and in blue for the open conformation. The imidazole is coloured in green/blue, and induces Arg<sup>400</sup> and Glu<sup>256</sup> to move upwards from the heme plane.

The partial orientation of the FG-loop and the bracketing helices BC and L is strongly conserved, with coordination of iron to the protein through Cys<sup>363</sup>. This conserved residue (in its thiolate form) is imperative for the generation of activated oxygen at the sixth coordination site on the iron. However, comparison of the active site in the closed and open conformations reveals differences in the interactions between the protein and the heme propionates (Figure 3.45). In the open form, helix I exhibits a distinct bend over the heme group at the position of Glu<sup>256</sup>. This orientation is a likely consequence of the presence of imidazole in the active site, and cannot be directly linked to the open conformation itself.

Larger bends than that in helix I of the CYP126 open form have been observed in azole complexes of other P450s such as CYP51B1, which showed the N-terminal I helix bent away from the heme and enlarging the space available for econazole (and other azole) binding. This indicates that the orientations of the imidazole group bound to CYP126 affect the angle of the bend observed in the I helix (Figure 3.45). Significant changes of several amino acids in the active site relate to the accommodation of a new imidazole ligand on the heme iron. The nitrogen atom of the imidazole ring directly coordinates to the heme iron,

showing a distance of about 2.25 Å, and in the open form complex with the inhibitor imidazole it is seen that the ring of the nitrogen ligand is approximately perpendicular to the I helix.

### 3.2.13.2 Crystallization of ketoconazole-bound CYP126

As mentioned previously, azole and triazole drugs are cytochrome P450 inhibitors widely used as fungal antibiotics, and are also potent inhibitors of cell growth in mycobacteria and other actinobacteria (105, 150). For the pathogen *M. tuberculosis*, several azoles have been shown to bind the CYP51B1, CYP121, CYP130, CYP125 and CYP124 proteins (119, 121, 136, 137, 149). Currently, several structures of P450-antifungal azole complexes are available, most showing direct coordination of heme iron by azole nitrogen, e.g. in case of Mtb CYP51B1 with fluconazole and CYP130 with econazole. In addition, fluconazole binding in absence of direct ligation (i.e. with an axial water ligand on the heme iron interstitial between the triazole nitrogen and the heme) is observed for CYP121, while econazole is bound to CYP125 at the mouth of the active site and distant from the heme (121). Therefore, the detailed molecular interactions of azole inhibitor in the active site of P450s will provide key data for designing more potent inhibitors (azole-based inhibitors) and also avoiding drug resistance development (149). Therefore, we aimed to obtain a crystal structure of a ketoconazole:CYP126 complex, with ketoconazole being one of the tightest binding ligands to the enzyme, with a  $K_d = 1.4 \mu\text{M}$ .

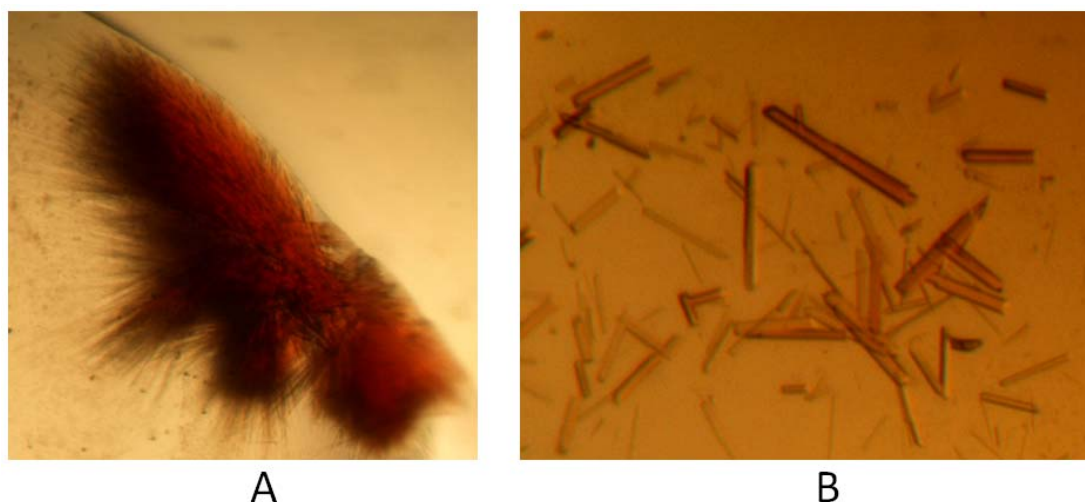


**Figure 3.46. Native crystals of ketoconazole-bound CYP126**

(A) The crystals were obtained from growth (using sodium sulfate with a range of 38–42%) by the sitting-drop using sodium sulfate as precipitant. (B) Larger crystals obtained by seeding with the crystals shown in panel A.

In work leading up to the crystallization of the ketoconazole complex of CYP126, it was established that the previously identified crystallization conditions are compatible with the co-crystallization experiment (278, 279). As described in the experimental section, CYP126 was crystallized in both sodium acetate and sodium sulfate conditions within a range of 38-42%. The results from co-crystallization with ketoconazole inhibitor indicated that CYP126 could be crystallized in sodium sulfate, but that the crystals show a low-quality of appearance, with multiple “fibres” formed (Figure 3.46 A). This kind of shape is different from the crystals of the ligand-free form, which appeared as tetragonal trapeziums. Therefore, it could be the case that ketoconazole binding causes low-quality crystal formation under the conditions used. Also, the protein did not crystallize well and formed precipitates in sodium acetate, suggesting that the protein does not go to the nucleation zone, the prerequisite condition for forming crystals (280). Therefore, to achieve successful crystallization, the seeding method was used to transfer some small crystals formed in the sodium sulfate conditions to the sodium acetate conditions. Instead, a longer incubation (~2 weeks) under the same set of conditions was required to generate ketoconazole-bound crystals. (Figure 3.46, Table 2)

The co-crystallized CYP126 crystals with ketoconazole produced a complex that was solved to a resolution of 1.8 Å (Figure 3.47). It is clearly seen that the molecule is no longer dimeric in this particular crystal packing, and instead a monomer was presented as the native form of the ketoconazole-bound crystal structure. The I helix along with the F and G helices are visible in the monomer as the comparable features seen in other Mtb P450s for which structures are known, e.g. CYP121, CYP125 and CYP124 (121, 136, 149). These characteristics for CYP126 are quite opposite to the crystal structure of the CYP130 econazole-bound complex. Thus, the ligand-free CYP130 crystallizes in an open conformation as a monomer, whereas the econazole-bound form revealed a closed conformation as a dimer (137). In contrast, the ligand-free CYP126 presents as a dimer form, with different closed-open or open-open conformations seen (Figure 3.35), but is a monomer when bound to ketoconazole. The transition between dimer and monomer conformations might be associated with producing an inactive CYP126 on inhibition by one of the azole class drugs. It may thus be hypothesized that CYP126 could be “activated” in the absence of an inhibitor, and that this active form is composed of two monomers in order to form a catalytically competent dimer form. With inhibitor bound, CYP126 could become inactive when the dimer is separated into monomers. However, this proposition

needs to be further investigated by doing substrate oxidation experiments using both monomeric and dimeric forms of CYP126.

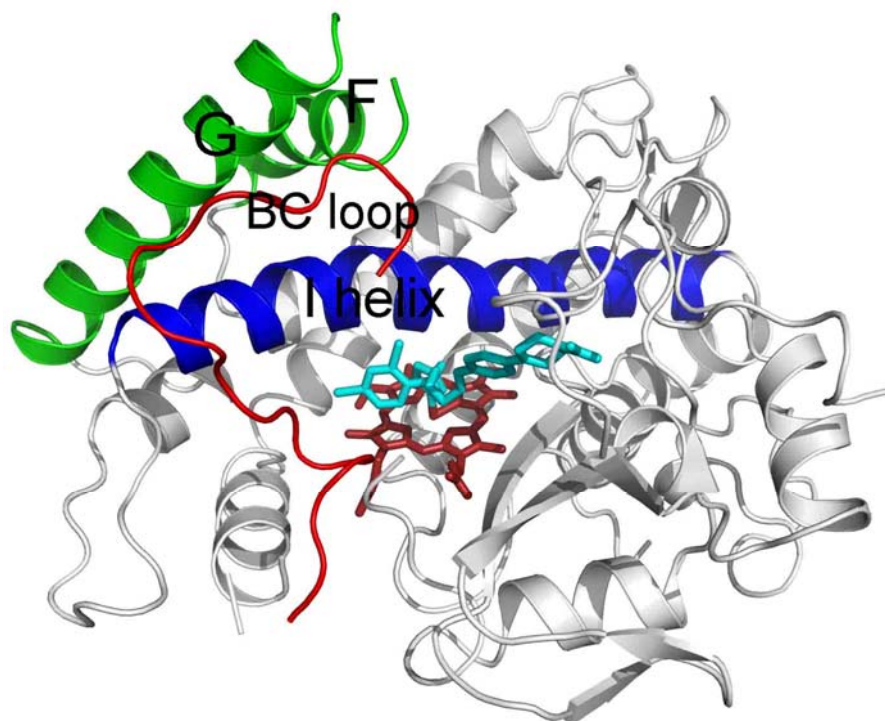


**Figure 3.47. Overall view of CYP126 ketoconazole-bound complex**

The structure is shown of ketoconazole in complex with CYP126, with the FG helices, I helix, and BC loop coloured in green, blue, and red, respectively. Ketoconazole is highlighted in cyan with the heme iron in firebrick.

There are significant differences between the ligand-free and ketoconazole-bound CYP126 structures. As expected, ketoconazole binding induced a reorganization of secondary structure elements, which are highlighted by different colours in Figure 3.48. Like imidazole binding, ketoconazole binding also exhibits a similar change in FG helices, with a longer G helix and the FG loop invisible, suggesting that the protein is in the “open” form. The positions of both FG helices are also not coincident, and the G helix at position Leu<sup>202</sup> shifts  $\sim 1.27$  Å inwards towards the active site. In addition, the loop connecting the I helix with the H helix is also observed in the ketoconazole-bound form, whereas it disappears in the ligand-free form. The biggest difference is observed in the BC loop region, where it presents in different directions for the ligand-free and ketoconazole-bound forms. In the ligand-free form, residues of the BC loop (Val<sup>73</sup>–Gln<sup>93</sup>) surround the active site cavity in parallel with the I helix. However, in the ketoconazole-bound conformation, the BC loop (at the same residues) moves  $\sim 8.8$  Å upward and towards the I helix, making a lid over the active site. However, only a half of the BC loop is visible in the ketoconazole-

bound CYP126 structure. Other important changes are also seen in the I helix, with a bend at the positions of residues Ala<sup>253</sup> and Leu<sup>249</sup> upwards of the proximal side of the heme.

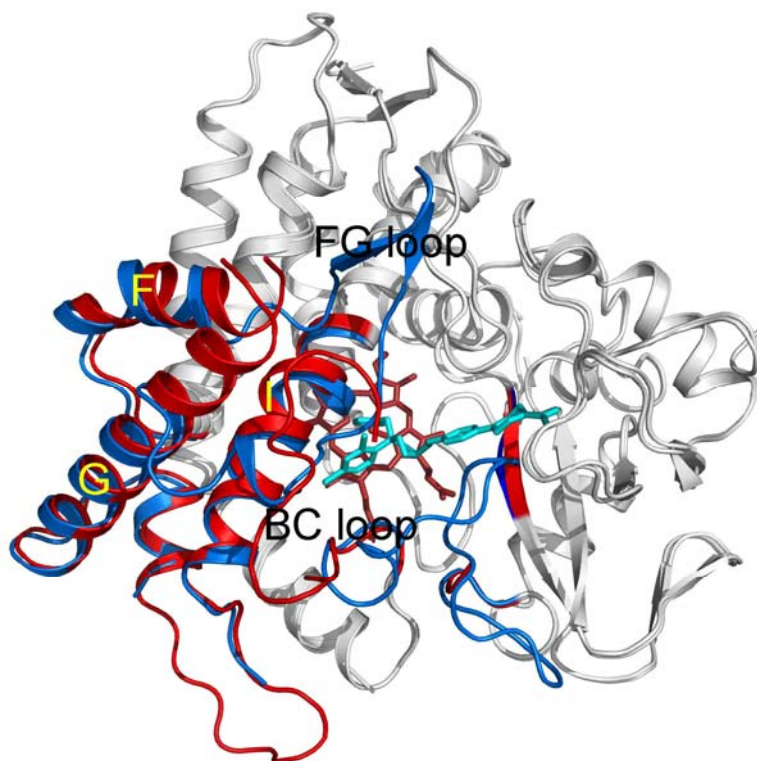


**Figure 3.48. Superimposition of the ligand-free (closed) and ketoconazole-bound (open) CYP126 monomers.** Both structures of CYP126 are shown with the common P450 secondary structure elements. The protein backbone is depicted in cartoon (white colour), with significant changes seen upon inhibitor binding in the F, G and I helices, BC loop, and  $\beta$ 1. Ligand-free CYP126 is in blue and ketoconazole-bound CYP126 is in red. Heme is in firebrick, and ketoconazole is in cyan.

Inhibitor binding also causes one of  $\beta$  sheet residues (Lys<sup>303</sup>) in the  $\beta$ 1 bundle to change in position, moving backwards in the active site. The movements of residues Ala<sup>253</sup> and Leu<sup>249</sup> on the I helix and residue Lys<sup>303</sup> on  $\beta$ 1 away from the active site enlarge the space available for accommodation of the ketoconazole molecule. These changes in FG helices and BC loop accompany the relocation of these regions as they gather around the active site.

Figure 3.49 shows a comparison of the active site cavity in the absence and presence of inhibitor. It is clearly seen that there are several changes induced by the binding of ketoconazole in the active site cavity. In detail, the binding of ketoconazole to CYP126 heme iron is made by a ligation of nitrogen azole atom to the heme iron with a distance of 1.99 Å, whereas the distance of the water molecule from the heme iron in ligand-free CYP126 is 2.36 Å (see detail in Figure 3.43).

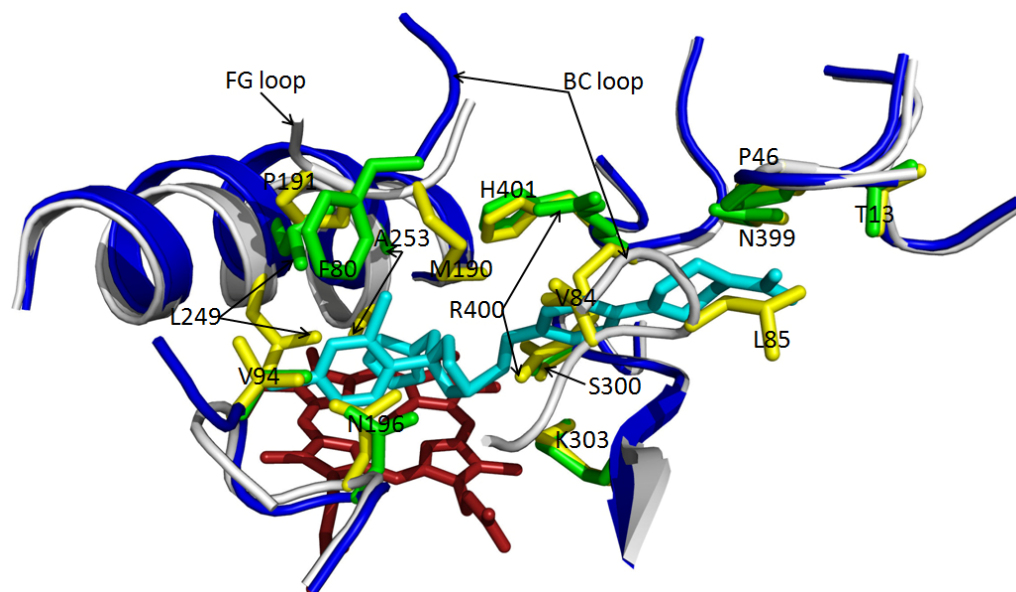


**Figure 3.49. An overlay of the active sites of the ligand-free and ketoconazole-bound CYP126 monomers.** Expanded stereoscopic view of CYP126 with ketoconazole bound (blue) in the active site compared with its ligand-free form (white). The relative residues are highlighted in sticks in yellow for the ligand-free and green for the ketoconazole-bound forms. The ketoconazole is coloured in cyan, inducing several movements of Leu<sup>249</sup>, Ala<sup>253</sup>, Arg<sup>400</sup> and Asn<sup>196</sup>, and a different position of the BC loop.

This displacement introduces several changes in location of amino acids on the I helix and the BC loop, as well as in the F and G helices. The I helix is bent outwards from the active site at amino acid positions Ala<sup>253</sup> and Leu<sup>249</sup>. While the Leu<sup>249</sup> side chain moves  $\sim 5.7$  Å upwards in the active site, the Ala<sup>253</sup> side chain shifts a shorter distance of approximately 3.6 Å. Similar to Leu<sup>249</sup>, Arg<sup>400</sup> on the L helix also shifts about 8 Å upwards from the floor of the active site cavity. The other major change was observed for Asn<sup>96</sup>, which moves slightly backwards from the heme plane. It is clearly seen that these relocations of several residues around the active site are required in order to make a larger space to accommodate the ketoconazole molecule, as well as to provide more space for the ligation of anazole ring nitrogen to the heme iron. In addition, the BC loop shifts 16.5 Å toward a newly ordered turn, forming a lid functioning as a door to close the active site. Moreover, the FG loop (with two residues, Met<sup>190</sup> and Pro<sup>191</sup>) and the BC loop (with two residues, (Val<sup>84</sup> and Leu<sup>85</sup>) move away from the active site when ketoconazole binds.

### 3.2.14 Identification and characterization of inhibitors and substrates binding to CYP126 from a compound library screen

In the hope of finding substrates and new types of inhibitors, there have been increased investigations into identifying P450 isoform-specific substrates/inhibitors, sometimes

leading to the discovery of new potent, effective drugs for blocking P450 catalytic activity, such as azole antifungal drugs. In recent years, compound libraries containing vast numbers of molecules have been developed (e.g. the library used contains approximately 20,000 synthetic organic compounds) and these provide extremely useful means to screen for potential drug leads against P450 enzymes. In previous reports, screening of a compound library against the Mtb CYP51B1 P450 (which functions in Mtb sterol demethylation, possibly in relation to Mtb membrane function) revealed several type I and type II binding hits, providing information suggesting one or more new sets of inhibitor classes that might abolish activity of CYP51B1 and impair *M. tuberculosis* infectivity (140). In addition, screens of the same library against Mtb CYP130 revealed several type II hits with the typical shift of the Soret band to longer wavelength, but no type I hits for CYP130 (155). All of the type II hits identified for CYP130 are related to heterocyclic arylamines, the chemical structures of which are different from the azole class. These data indicate that potent inhibitors against P450s could come from other sources than azole (antifungal) drugs, pointing towards the possibility of identifying novel, potent and selective inhibitory compounds for blocking specific P450 enzyme activity.

The function of the cytochrome P450 CYP126 has not been determined and its catalytic activity remains unknown. In previous sections, CYP126 was reported to be a potential drug target enzyme due to the tight binding of antifungal azole drugs. Although this azole class exhibits good activity in binding CYP126, the screening of CYP126 against compound libraries may also detect new inhibitor classes that are more potent inhibitors of CYP126. This screening may also identify substrate-like compounds in order to determine the function of the CYP126 enzyme. The changes in CYP126 spectral properties provide specific characterization for either substrate binding (type I - blue shift) or inhibitor binding (type II – red shift). In this section, I report on screening of a library of 20,000 organic molecules against CYP126, leading to the isolation of potent candidate drug leads and substrate-like molecules for the CYP126 protein.

#### **3.2.14.1 Identification of binding hits**

The library binding hits for CYP126 were isolated based on the change in P450 spectral properties for both type I and type II binding events. Type I binding was identified by the shift of the Soret band from 418 nm to ~393 nm. This indicates that the distal water molecule is expelled from the heme iron, leading to the conversion of the LS to the HS form. Type II binding generally shifts the Soret band from 418 nm to longer wavelength

(425-436 nm), indicating the water molecule is replaced by the direct ligation of another (stronger) ligand to the heme iron. The spin state of enzyme (LS) is unchanged in type II binding. The shape of the induced difference spectra were evaluated as: type I spectra exhibit a minimum at ~420 nm and a maximum at ~390 nm, whereas type II spectra exhibit a minimum at ~390 nm and a maximum at ~430 nm) (Figure 3.50).

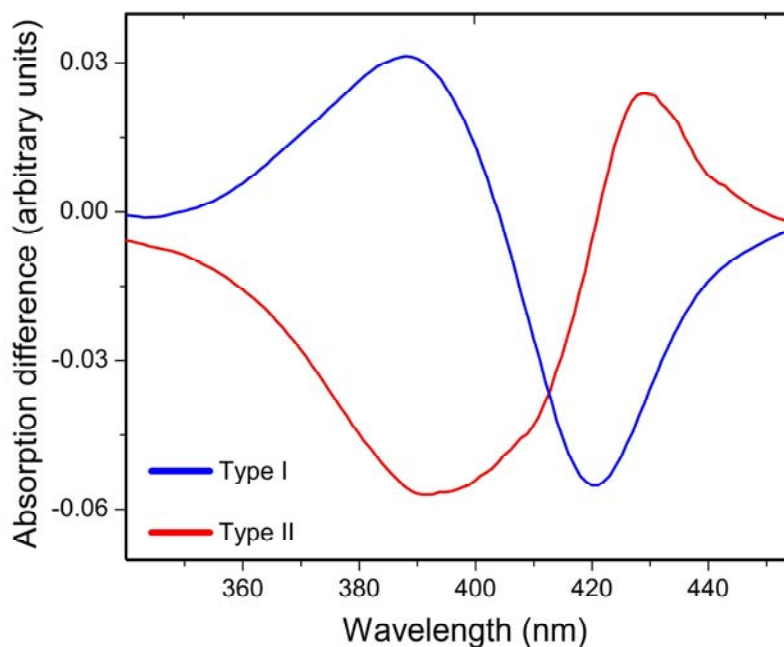


**Figure 3.50.** The difference spectra produced by subtraction of the ligand-free CYP126 spectrum from successive spectra for both type I and type II bound species. The red line presents a common feature for type II binding with a minimum at ~390 nm and maximum at ~430 nm. The solid blue line shows the difference spectrum for type I binding, exhibiting a minimum at ~420 nm and maximum at ~390 nm. Data were created using the binding spectra for ketoconazole (type II) and library compound 32027 (type I).

The screening results of the library against the CYP126 enzyme show hundreds of type II and type I binding hits. The primary screen analysis based on spectral changes initially identified 190 high-spin and 339 low-spin hits (type I- or type II-difference spectra, respectively). The corresponding difference spectra of the 190 high-spin and 339 low-spin hits from the primary screen were therefore inspected visually by checking the shape of the difference spectra (calculated as presented in Figure 3.50). The resultant difference spectra for 63 compounds recorded at different compound concentrations (ranging from 20  $\mu\text{M}$  to 0.48  $\mu\text{M}$ ) were inspected visually for shape and concentration-dependent behaviour. As a result, 33 of 63 compounds did not show any significant signal. From the residual 30 compounds, 15 type I- and 15 type II-difference spectra passed the validation screen for CYP126 (see Figures 3.51 and 3.52).

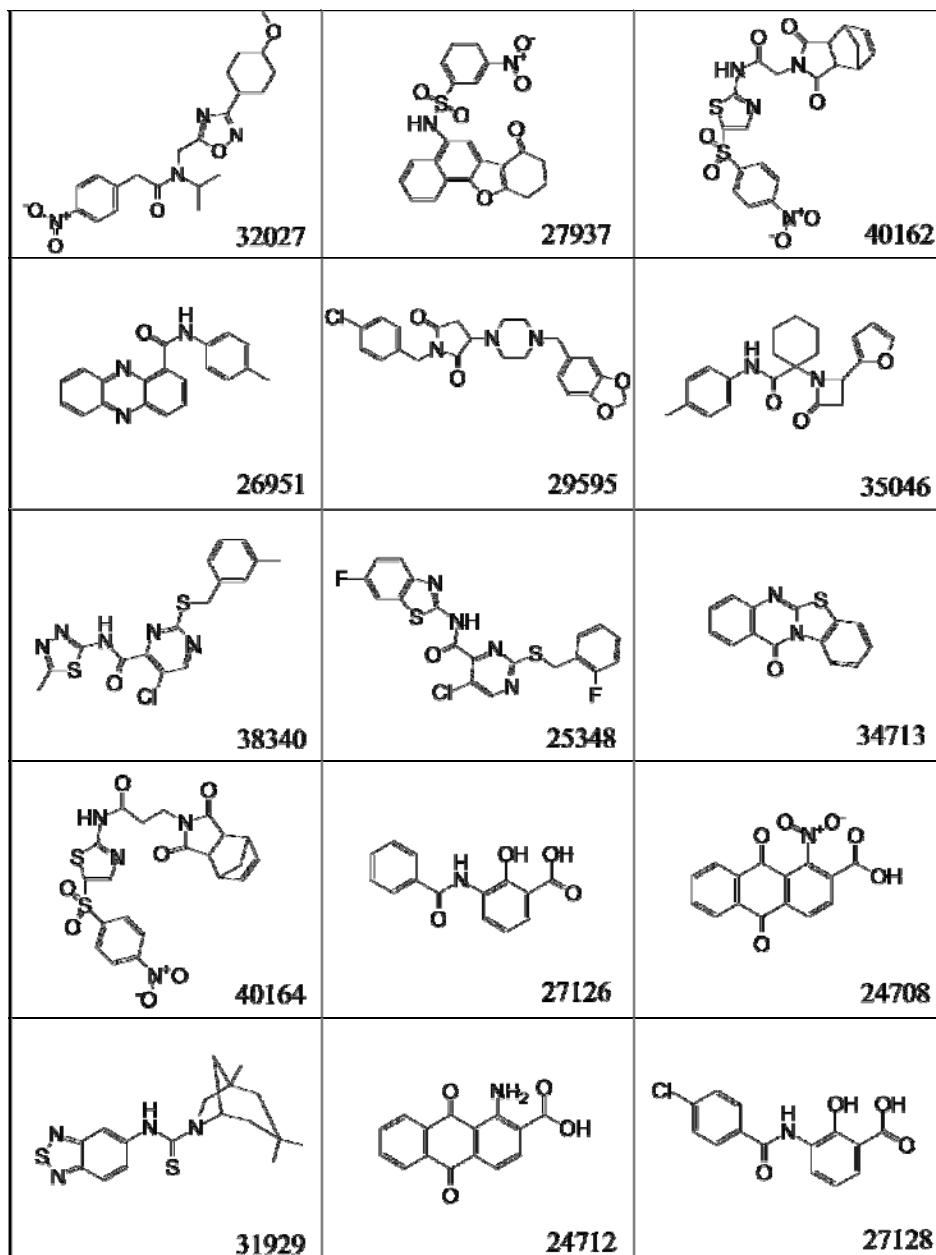


**Figure 3.51. Type I high throughput screen hits for CYP126.**

The spectra measured with CYP126 and compounds were recorded automatically for changes in absorption spectra (310-450 nm). The statistical values were calculated by the average of the measured values from 420-430 nm minus the measured values from 390-400 nm, giving the value term signal. The z-scores were calculated over the compound sample signal values; z scores > 3 yielded high-spin hits, and z scores < -3 yielded low-spin hits. The screen analysis based on z-scores identified 15 top hits, and the type I chemicals are ranked above for the biggest change to the smallest change, going from left to right from the top of the page. In descending order, these hits are 32017, 27937, 40162, 26951, 29595, 35046, 25348, 34713, 40164, 27126, 24708, 31929, 24712, and 27128.

The type I binding hits for CYP126 are the most helpful in defining the function and catalytic activity of the protein. Among the 15 selected hits, the three top hit compounds

were selected for further investigation, these being compounds 32027, 27937, and 29595, respectively. Binding affinity of these compounds to CYP126 was examined by the spectral titration and the  $K_d$  values were obtained from fitting curves, as described in section 2.14, and with data summarized in Table 3.6. It is clearly seen from Table 3.6 that the compound 27937 is the tightest type I binder, with a  $K_d$  value of  $2.85 \pm 0.15 \mu\text{M}$ . This  $K_d$  is lower than the values for compounds 32027 ( $5.63 \pm 0.67 \mu\text{M}$ ) and 29595 ( $65.19 \pm 16.6 \mu\text{M}$ ). Although the  $K_d$  value of compound 27927 is 2-fold lower than for compound 32027, compound 27927 does not induce as extensive a HS shift as does compound 32027 (Fig. 3.53). Compound 320207 induces highest accumulation of HS CYP126, suggesting that compound 32027 may represent the most “substrate-like” molecule for CYP126 in terms of occupancy of active site space immediately adjacent to the heme iron. In comparison with other Mtb P450s, the binding affinity of compounds 32027 and 27937 to CYP126 is lower than that for the binding of cholesterol to CYP142 ( $1.65 \pm 0.10 \mu\text{M}$ ) (124) and phytanic acid to CYP124 ( $0.22 \pm 0.01 \mu\text{M}$ ) (136), but higher than that for the binding of cYY to CYP121 ( $21.3 \pm 3.5 \mu\text{M}$ ) (120). However, compound 2959 binds more weakly to CYP126 than all the aforementioned substrates do to their target P450s.

Interestingly, the three top type I hits for CYP126 share a similar nitrobenzene functional group structure, which is identical to a functional group found in chloramphenicol and azidamphenicol (Figure 3.52). This might suggest that compound 32027 could have similar activity to antibiotics like chloramphenicol.

	<b>32027</b>	<b>27937</b>	<b>29595</b>
<b><math>K_d</math> (<math>\mu\text{M}</math>)</b>	<b><math>5.62 \pm 0.67</math></b>	<b><math>2.85 \pm 0.15</math></b>	<b><math>65.19 \pm 16.6</math></b>

**Table 3.6. The values of dissociation constants of the three selected library compounds for type I binding to CYP126.**

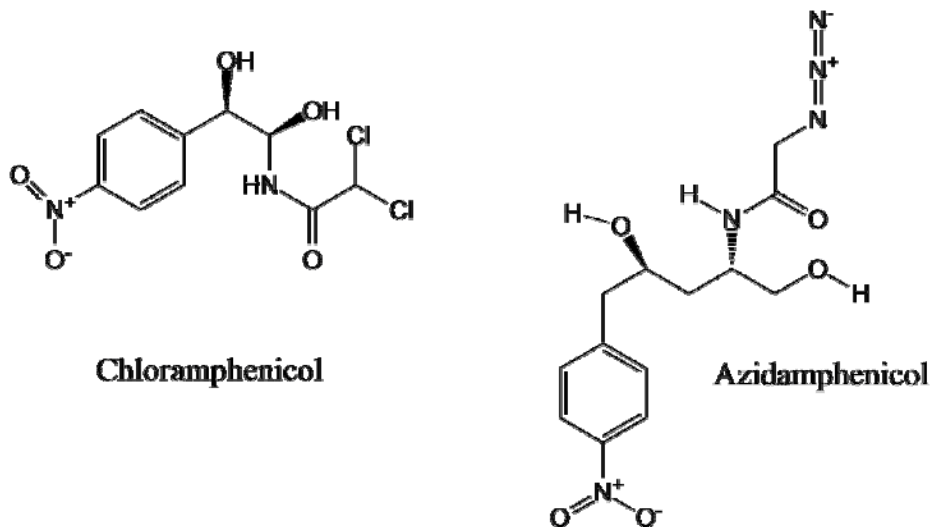


**Figure 3.52. Chemical structures of Chloramphenicol and Azidamphenicol.** These molecules contain nitrobenzene functional groups. Image prepared based on image presented at <http://en.wikipedia.org/wiki/>.

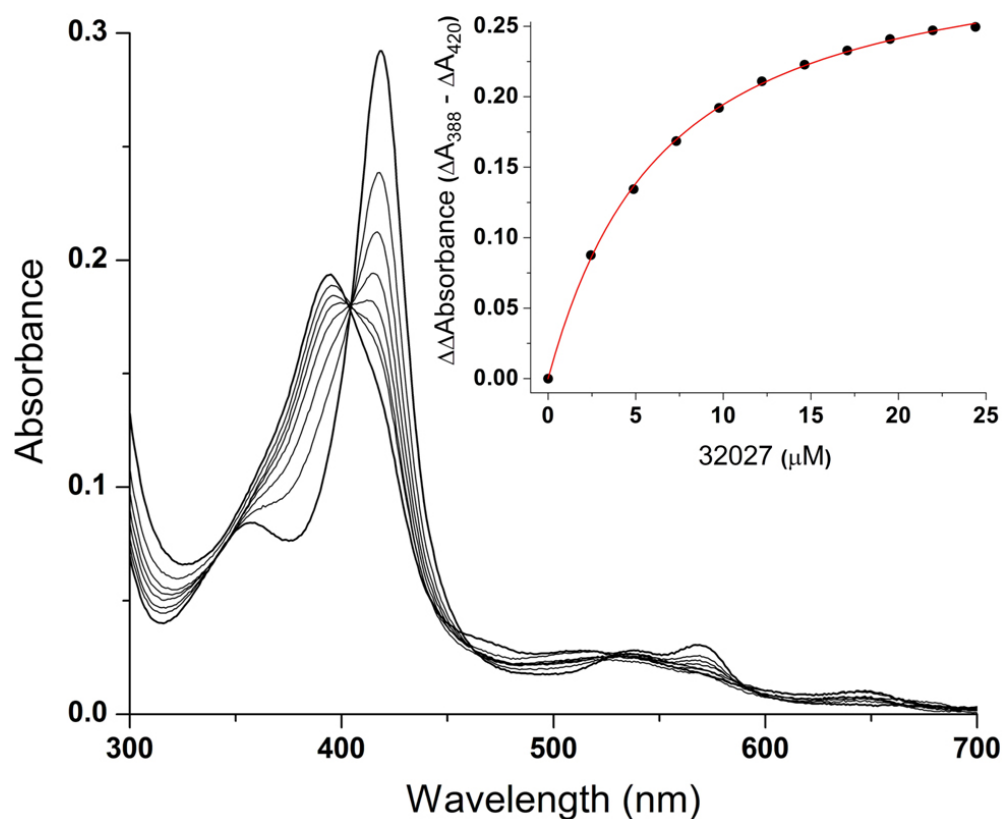


**Figure 3.53. CYP126 spectral titration with compound 32027.**

The main figure shows recorded spectra during titration of CYP126 (~3 μM) with compound 32027. The Soret band shifts from 418 nm to 393 nm, indicating a high spin shift in the ferric heme iron. An increase of absorption intensity at a wavelength of 648 nm also suggests a substrate-like event. The inset shows maximal induced absorption changes from the CYP126 titration plotted against compound 32027 concentration, with data fitted using equation 3 to generate a  $K_d$  value of  $5.6 \pm 0.6$  μM.

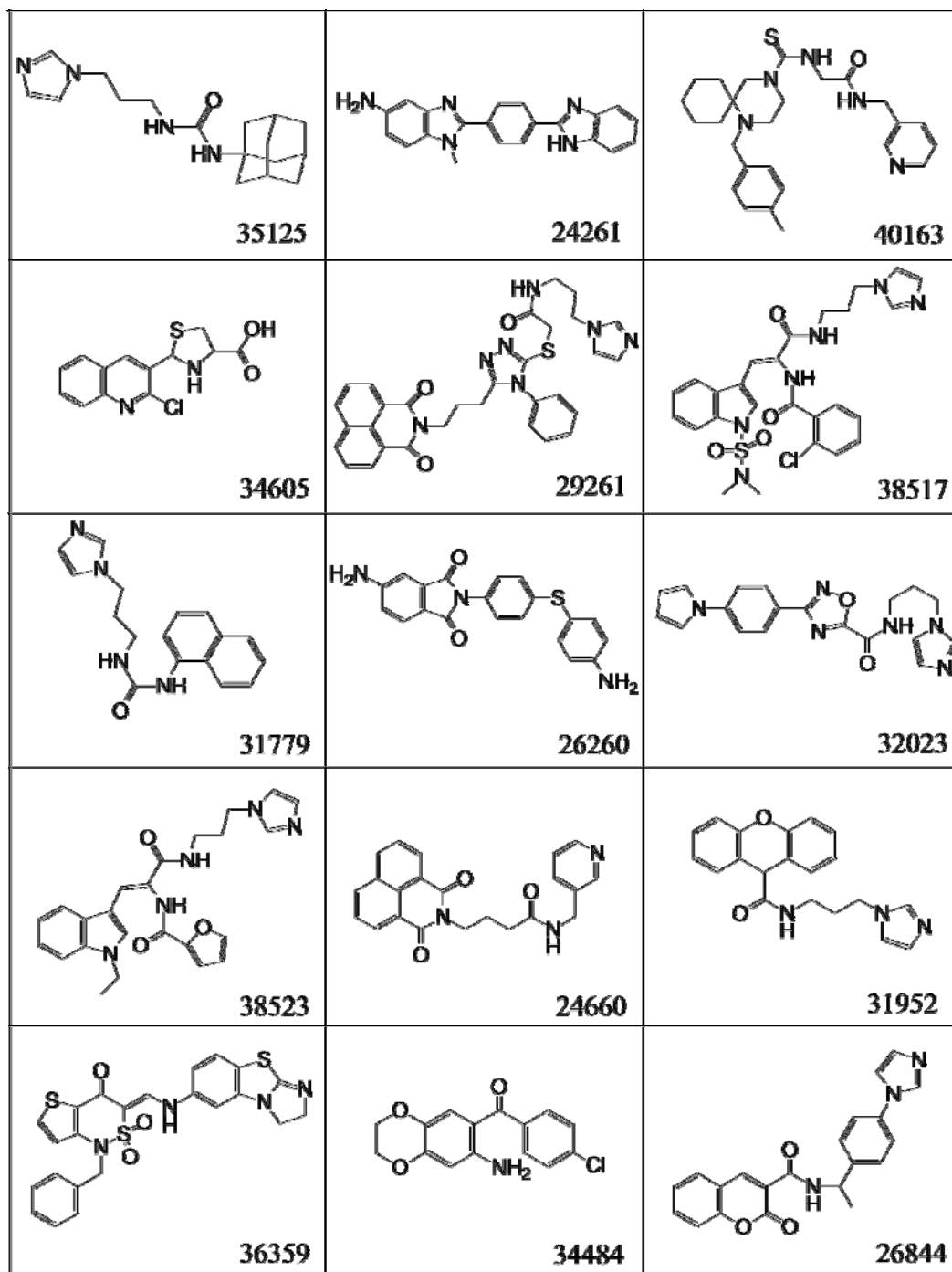


**Figure 3.54. Type II high throughput screen hits for CYP126**

The 15 top hits were selected from 339 low-spin hits from the screen. According to the z-scores, the compounds were classified from the biggest change to smallest change. These are shown in descending order from top left to bottom right in the figure: 35125, 24621, 40163, 34605, 29261, 38517, 31779, 26260, 32023, 38523, 24660, 31952, 36359, 34484, and 26844.

The top 15 type II hits are presented in Figure 3.54, according to the structure of these compounds, it is seen that most of these molecules (35125, 29261, 38517, 31779, 32023, 38523, 31952, 36359 and 26844) contain 1,3-diazole in a five membered aromatic ring,

which is the same as seen in the structure of imidazole derivatives such as ketoconazole, clotrimazole, miconazole and econazole, suggesting the binding mode of these compounds might be similar to azole drugs where the nitrogen atom ligates directly to heme iron. Three of the top type II hits were selected for further investigation, these being compounds 35125, 24621 and 34605. As expected, the binding mode of these three molecules was similar to azole inhibitors, where the Soret band shifts from 418 nm to ~422-423 nm, and decreased intensity at both the Soret band and  $\alpha/\beta$  band region is observed (Figure 3.55). The  $K_d$  values of these compounds are presented in Table 3.7. It is clearly seen that the compound 35125 has the tightest binding to CYP126 with a  $K_d = 4.13 \pm 0.61 \mu\text{M}$ , followed by compound 24261 ( $K_d = 10.92 \pm 0.53 \mu\text{M}$ ) and compound 34605 ( $K_d = 16.32 \pm 0.66 \mu\text{M}$ ). Compared to the  $K_d$  values for azole drugs, these data indicates that compound 35125 has a CYP126 binding affinity slightly higher than for econazole ( $K_d = 5.05 \mu\text{M}$ ), but lower than that for ketoconazole ( $K_d = 1.4 \mu\text{M}$ ) and miconazole ( $K_d = 1.3 \mu\text{M}$ ). In contrast, both compound 24261 and 34605 have lower affinity than those of these azole inhibitors. However the differences in affinity are small.

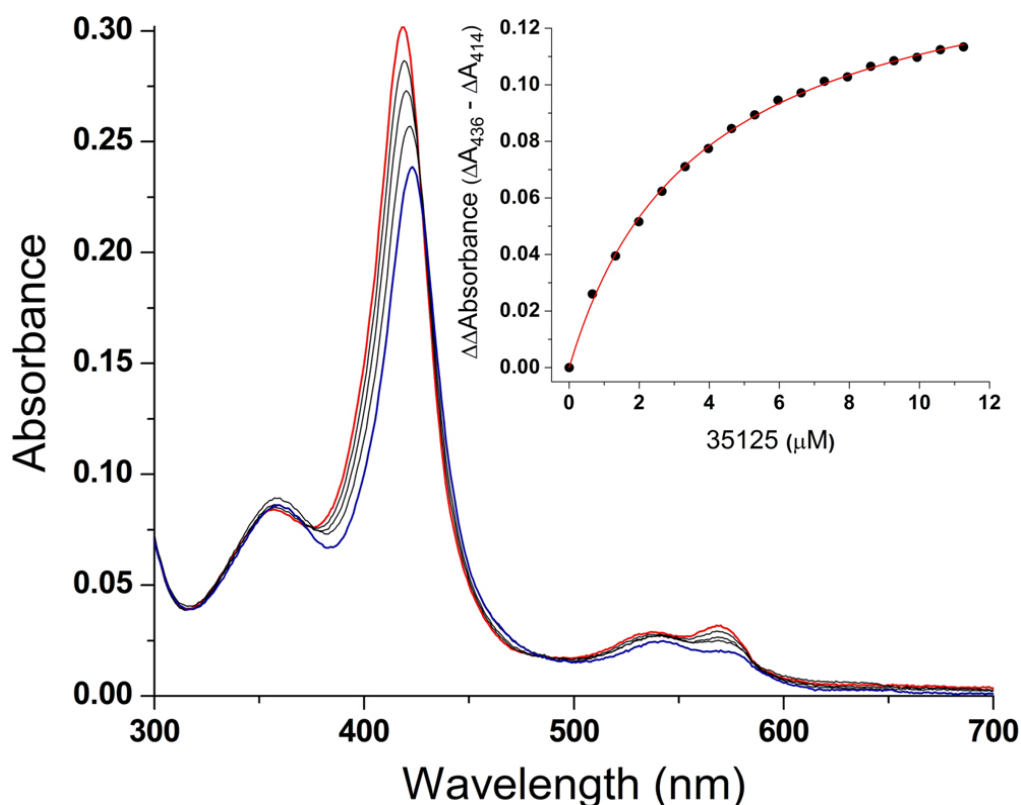


**Figure 3.55. CYP126 spectral titration with compound 35125.**

Main figure: Type II spectral changes as a result of binding of compound 35125 to CYP126, where the Soret band shifts from 418 nm (red line) to 423 nm (blue line). Inset: the maximal absorbance change data were plotted versus concentration of compound 35125, and data were fitted using equation 3 to generate a  $K_d$  value of  $4.13 \pm 0.61 \mu\text{M}$ .

	35125	24621	34605
$K_d$ ( $\mu\text{M}$ )	$4.13 \pm 0.61$	$10.92 \pm 0.53$	$16.32 \pm 0.66$

**Table 3.7. The values of dissociation constants of the three selected library compounds for type II binding to CYP126.**

### 3.2.14.2. Redox potentiometric analysis for CYP126 bound to a substrate-like compound from the library screen (compound 32027)

Substrate binding normally shifts the P450 ferric heme LS form to a ferric HS form, consistent with a shift of Soret band from  $\sim 418$  nm to a shorter wavelength ( $\sim 393$  nm). In addition, the binding of substrate also elevates the reduction potential of P450s, revealing a more positive reduction potential of the heme iron in the substrate-bound form. This has been shown in several P450s. For example, Mtb CYP51B1 has a heme iron reduction potential of  $-375$  mV in the ligand-free form, rising to  $-225$  mV for the estriol-bound form (194). The ligand-free form of CYP142 has a potential of  $-416$  mV, but this increases to  $-192$  mV when bound to cholesterol (124). Similarly, *Bacillus subtilis* P450 BioI showed a difference of  $130$  mV between the heme iron potential for the ligand-free form and for the fatty acid-bound form (255). Here, the heme iron reduction potential of CYP126 was determined in the presence of compound 32027, which shows a type I binding (substrate-like) spectrum with CYP126.

Binding of compound 32027 to CYP126 produced a blue shift of the Soret band from  $418$  nm to  $393$  nm, along with decreases in intensity in the alpha and beta band region, and the development of a charge transfer band at  $\sim 647$  nm (Figure 3.56), all indicative of a transition of the CYP126 ferric LS form to the ferric HS form on binding substrate-like compound 32027. On the addition of sodium dithionite, reducing the heme iron from the ferric to the ferrous state, there was a decrease of intensity at  $393$  nm and accumulation of intensity at  $420$  nm, along with the loss of absorption in the  $\alpha$  and  $\beta$  band region on heme iron reduction. Simultaneously, the charge transfer band at  $647$  nm also collapsed, suggesting a complete conversion of the ferric to the ferrous heme iron in the substrate-like compound-bound enzyme form.

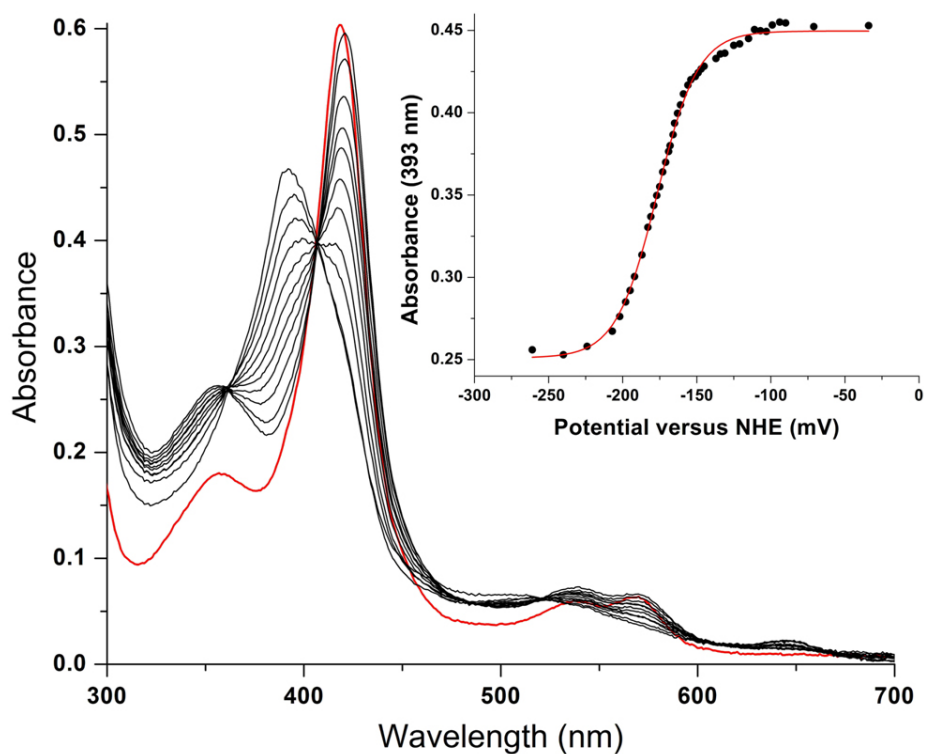


**Figure 3.56. Potentiometric titration for CYP126 bound to substrate-like compound 32027.** The main panel shows spectral data from the redox titration of CYP126 (6  $\mu\text{M}$ ) bound to compound 32027 ( $\sim 6 \mu\text{M}$ ). The substrate-free enzyme is shown in the red spectrum, and compound 32027 binding induces an absorbance shift of the ferric LS heme iron to the ferric HS form at  $\sim 393 \text{ nm}$  (black spectrum with highest intensity at 393 nm). The progressive addition of sodium dithionite reductant leads to decreases in intensity of the Soret band at 393 nm, accompanying increases in intensity of Soret band at 420 nm (the ferrous LS form). The inset presents a plot of heme absorbance change at 393 nm against applied potential. The data were fitted using the Nernst equation to produce a midpoint potential of  $-176 \pm 2 \text{ mV}$  for the Fe(III)/Fe(II) transition of the compound 32027-bound CYP126 heme iron.

The fitted data indicate that the redox potential of 32027-bound CYP126 is substantially increased to  $-176 \pm 2 \text{ mV}$ , with a positive shift of potential of  $>155 \text{ mV}$  compared to substrate-free CYP126. This shift is a little more than observed for arachidonic acid binding to P450 BM3 ( $\sim 130 \text{ mV}$ ), estriol binding to CYP51B1 ( $\sim 150 \text{ mV}$ ), and fatty acid binding to P450 BioI ( $\sim 130 \text{ mV}$ ), but lower than the change reported for cholest-4-en-3-one binding to CYP142 ( $\sim 192 \text{ mV}$ ) (124, 247, 255). The elevation of the CYP126 redox potential from  $-332 \text{ mV}$  to  $-176 \text{ mV}$  is due to changes in enzyme conformation on “substrate” binding, inducing a different environment of the heme iron (and most notably an extensive shift in heme iron spin-state to high-spin with distal water ligand removal). These changes mean

that the heme iron is more favourable to reduction by NAD(P)H via redox partner proteins in the compound 32027-bound form of CYP126.

### 3.2.14.3 EPR analysis of type I and type II binding to CYP126

The binding of type I and type II compounds to CYP126 is clearly seen by UV-visible spectrometry (Figures 3.55 and 3.56). In addition, EPR examination of the heme coordination of CYP126 in complex with substrate- and inhibitor-like compounds from the compound screening studies could give further detailed evidence of changes in heme iron ligation. EPR spectra for native CYP126, and for (compound screening derived) substrate-bound and inhibitor-bound forms were collected, and are presented in Figure 3.57.

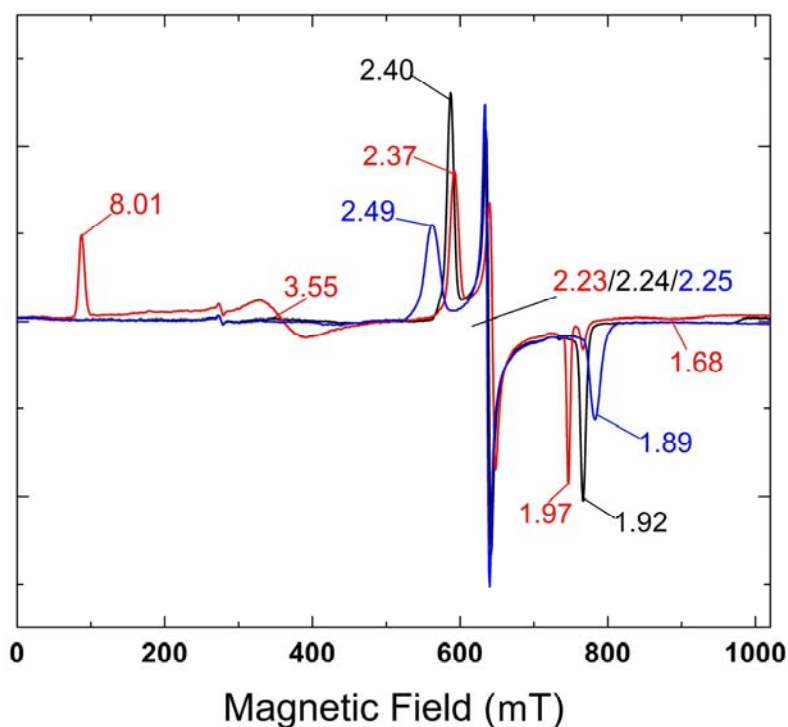


**Figure 3.57. EPR spectra of CYP126 in complex with compounds 32027 and 35195.**

Ligand-free CYP126 has g-values at 2.40, 2.24 and 1.92 for the low-spin  $\text{H}_2\text{O-Fe-Cys}$  state (black line). There are two species seen in the substrate-like 32027-bound CYP126 enzyme, a low-spin species with g-values at 2.37, 2.23 and 1.97, and a high spin species with g-values at 8.01, 3.55 and 1.68 (red line). A small proportion of substrate-free LS CYP126 remains visible at a g-value of 1.92. The blue line shows features of the inhibitor-like 35195-bound CYP126 complex as a low spin species with g values at 2.49, 2.25 and 1.89.

Figure 3.57 presents overlaid X-band EPR spectra of CYP126 in complex with its substrate-like compound (32027) and inhibitor-like (35195) compounds. For ligand-free CYP126, the g-values ( $g_z = 2.40$ ,  $g_y = 2.24$ ,  $g_x = 1.92$ ) indicate that the protein is in a LS

thiolate-coordinated state. These values are similar to well-characterized P450s such as CYP142 ( $g_z = 2.40$ ,  $g_y = 2.23$ ,  $g_x = 1.92$ ) (124), CYP125 ( $g_z = 2.40$ ,  $g_y = 2.25$ ,  $g_x = 1.94$ ) (121), and P450 BM3 ( $g_z = 2.42$ ,  $g_y = 2.26$ ,  $g_x = 1.92$ ) (247). However, in complex with the inhibitor (compound 35195), the spectra were changed with a new species having g-values at  $g_z = 2.49$ ,  $g_y = 2.25$ ,  $g_x = 1.89$ , which are consistent with the direct coordination of a nitrogen atom from compound 35195 to the heme iron of CYP126. Compared to ketoconazole-bound CYP126 ( $g_z = 2.44$ ,  $g_y = 2.24$ ,  $g_x = 1.90$ ), a difference is revealed with the compound 35195, with a new set of g-values. Possibly this reflects a more complete coordination of the heme iron in the 35195-bound CYP126 than in the ketoconazole complex. In the substrate-like compound 32027-bound CYP126 sample, there are two novel species, a low-spin species with g-values at 2.37, 2.23 and 1.97, and a high-spin species with g-values at 8.01, 3.55 and 1.68. A small amount of unconverted CYP126 seems to be present with a g-value at 1.92. The HS set of values are comparable with those for CYP142 bound to its substrate cholest-4-en-3-one ( $g_z = 7.87$ ,  $g_y = 3.65$ ,  $g_x = 1.71$ ) (124). The difference in g-values between native and the substrate-like compound 32027-bound CYP126 is consistent with changes to the 6<sup>th</sup> ligand environment of the CYP126 heme iron, indicating that compound 32027 is able to displace the axial water ligand to the heme iron and to induce accumulation of the 5-coordinate HS form of CYP126.

#### **3.2.14.4 Crystal structures of CYP126 in complex with compound 32027 and compound 35125.**

Crystals were obtained by co-crystallizing CYP126 with compounds 32027 and 35125 using screening kits (Morpheus and Premier pact – Molecular dimensions). Contrary to the CYP126 ligand-free and ketoconazole-bound crystals, CYP126-32017 and -35125 complexes were neither crystallized in sodium sulfate nor sodium acetate conditions. Screening results indicated that CYP126 in complex with these compounds was crystallized in new conditions. The CYP126-32027 complex formed crystals in solution 1 (0.1 M carboxylic acids (acetic acid, acetate, acetyl), 0.1 M imidazole-MES, pH 6.5 and 30% ethylene glycol-PEG 8K) (Figure 3.58A), and the CYP126-35125 complex formed crystals in solution 2 (0.2 M sodium sulfate, 0.1M Bis Tris propane pH 7.5, and 20% PEG 3350). However, crystals of the CYP126-35125 complex showed a very low-quality of appearance with multiple fibred forms. Therefore, to obtain higher quality of crystals, a seeding method was used to transfer small pieces of these crystals to sodium acetate conditions, where the CYP126-35125 complex was initially unable to crystallize. This appeared to be successful and a crystal was produced within 3 days of incubation at 4 °C (Figure 3.58 B). Both

crystals of the CYP126 complexes appeared as tetragonal trapeziums, which are highly similar to those formed by the ligand-free CYP126.

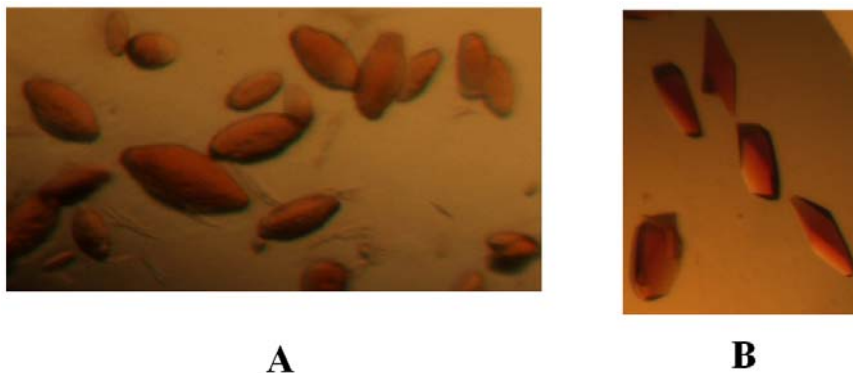


**Figure 3.58. Co-crystallization of CYP126 with compound 32027 and compound 35125.** (A) The crystals of the substrate-like CYP126-32027 complex were obtained by the sitting drop method using 0.1 M carboxylic acids (acetic acid, acetate, acetyl), 0.1 M imidazole-MES, pH 6.5 and 30% ethylene glycol-PEG 8K. (B) The crystals of the inhibitor-like CYP126-35125 complex were produced by seeding with crystals obtained from condition 2 (0.2 M sodium sulphate, 0.1M Bis Tris propane pH 7.5, and 20% PEG 3350).

### 3.3 Discussion

Since the *M. tuberculosis* genome sequence revealed a large number (20) of cytochrome P450–encoding genes (CYPs), this indicated that there are likely essential roles for these enzymes in the physiology of the pathogen. However, the current database of knowledge on Mtb P450 functions is not extensive, and relatively little is known about their enzymology or the biophysical features of these enzymes. The first Mtb P450 studied, CYP51B1, has been the most intensively characterized (119, 140), and is encoded by the *Rv0764c* gene. CYP51B1 is a sterol demethylase, and in yeasts and fungi this function is related to the synthesis of the essential membrane sterol ergosterol. However, this is unlikely to be the function in Mtb.

Biochemical analysis of the Mtb membrane showed that it is composed of up to 60% lipids, compared to 10-20% that is typical of many other organisms (281). The very high lipid component may partly explain why Mtb can survive during antibiotic treatment (282-285). The inhibition of *M. tuberculosis* growth in response to treatment with CYP51-inhibiting azole drugs has been investigated, and it was shown that these validated antifungals could be effective antitubercular drugs (119). Antifungals such as econazole, ketoconazole, clotrimazole, itraconazole, miconazole etc could provide an attractive new antibiotic therapy for Mtb, although there are issues with azoles as systemic drugs (208). In the past ten years, six other Mtb P450s, CYP121 CYP130, CYP124, CYP144, CYP125, and CYP142 were cloned, expressed and characterized in detail (121, 124, 135-138). Their analysis also revealed their enormous potential for azole drug-binding. Moreover, the crystal structures of the Mtb CYP51B1, CYP121, CYP130, CYP124, CYP142 and CYP125 P450s revealed several stabilizing interaction between protein side chains and the aromatic rings of the inhibitors, as well as the ligation of the ferric heme iron to the azole groups of the inhibitors.

Preliminary expression studies with CYP126 demonstrated that it could be produced at medium levels of soluble protein in *E. coli* strain BL21 gold (DE3) and by using relatively low concentrations of inducer (0.1 mM IPTG) to stimulate T7 RNA polymerase-driven transcription of the target gene. However, large amounts of inclusion bodies formed during expression of the protein in *E. coli*, regardless of concentrations of inducer. This problem was largely overcome by slowing bacterial growth (by low growth temperature). Comparisons of the levels of expression of CYP126 and CYP141 (see section 4.2.1, chapter 4) indicated that much less P450 was produced for CYP126 than for CYP141 in

their respective expression systems. Alignment of the amino acid sequence of CYP126 with those of other members of the Mtb P450 family (286) shows similarity between CYP126 and numerous P450s in Mtb over the entire length of the protein, and it shows that even for the most closely related P450s, sequence identity is less than 24%. However, this is typical among the P450s, with few completely conserved amino acids and only the heme binding motif around the cysteine, which ligates the heme iron, showing very strong identity in all P450s. Although overall sequence identity is rather low, several key amino acids are retained in CYP126. These including cysteine 363 – which provides the proximal sulfur ligand to the heme iron, threonine 229 – which may participate in a proton transfer pathway to the heme iron, and phenylalanine 338 – implicated in regulation of thermodynamic properties of the P450 heme iron.

Biophysical studies of CYP126 indicated that it exhibits many properties that are typical of the P450 class. As shown by UV-vis absorption, CYP126 is predominantly low-spin in its resting, oxidised state. The spectra reporting CO-binding all indicate that a considerable amount of P420 forms during bubbling of dithionite-reduced CYP126 with carbon monoxide. This may result from the sensitivity of the enzyme to the reduction required to form a carbon monoxide adduct, i.e. that there is a tendency for the thiolate ligand to be protonated in the reduced, substrate-free form. This is confirmed by the studies of the pH dependence of this process in reduced CYP126 (Figure 3.21). Moreover, the carbon monoxide complexes of CYP126 are not stable over the time, and collapse within 2-3 minutes in air to the P420 form. Detailed results of the unstable  $\text{Fe}^{\text{II}}\text{-CO}$  complex of CYP126 are presented and discussed in section 5.2.7, chapter 5. Compared to the previous studies of Mtb CYP121 (138, 194), this suggest that these P450 complexes in CYP126 are unstable, and that the P450 form converts to the inactive P420 form within a few minutes of formation of the CO complex of CYP126, as a consequence of heme thiolate protonation.

Several polycyclic azoles are used as antifungal antibiotics, and also display potent activity against latent and multidrug-resistant forms of *M. tuberculosis* (105, 150). Mtb P450s which bind tightly to these drugs, including CYP126 (which is potentially an essential *CYP* gene for Mtb viability in absence of further data from gene knock-out) are therefore plausible Mtb drug targets for the azole class of antibiotics (287). Type II azole binding (288) has been demonstrated clearly for CYP51B1, CYP121, CYP130, CYP125, and CYP124. However, CYP125 was reported to exhibit a peculiar type I binding of econazole, which is normally the case for the binding of substrate (121). However, McLean *et al.* also

reported type II binding of econazole following conversion of the extensively high spin CYP125 to a low spin form (121). Generally, CYP126 shows strong binding to a selection of azole antifungal inhibitors such as econazole, ketoconazole, miconazole, as well as (more weakly) to imidazole, and with typical type II binding (heme coordination). CYP126 also has poorer affinity for fluconazole, voriconazole, itraconazole, 2-phenylimidazole and 4-phenylimidazole. Among these azole drugs, imidazole, 2-phenylimazole and 4-phenylimdazole are the most water-soluble, and among the weakest binding. This may indicate that the active site of CYP126 is highly apolar in nature, as is common among P450s. In comparison with the other seven best characterized *M. tuberculosis* P450s (CYP51B1, CYP121, CYP130, CYP124, CYP125, CYP142 and CYP144), CYP126 displays a tighter binding constant with ketoconazole than any of the other P450s (Table 3.8). Novel drugs and drug targets are desperately needed due to the prevalence of drug-resistant strains of the pathogen. Preliminary work suggests that azole drugs are effective in preventing growth of mycobacteria (185). The binding of azole inhibitors to CYP126 is relatively tight ( $K_d$  values in  $\mu\text{M}$  range), raising the possibility that the CYP126 could be a new anti-Mtb drug target.

Ligand	CYP51B1	CYP121	CYP130	CYP124	CYP125	CYP144	CYP142	CYP126
Econazole	$0.77 \pm 0.04$	<0.2	$1.93 \pm 0.03$	$2.1 \pm 0.1$	$11.7 \pm 0.7$	$0.78 \pm 0.29$	$4.6 \pm 0.2$	$5.05 \pm 0.3$
Fluconazole	$19.0 \pm 1.9$	$9.7 \pm 0.1$	$48.0 \pm 1.5$	-	$43.2 \pm 0.8$	> 10,000	$860 \pm 108$	-
Ketoconazole	-	$3.3 \pm 0.3$	-	-	$27.1 \pm 0.9$	$134 \pm 5$	$21 \pm 4$	$1.4 \pm 0.1$
Itraconazole	-	-	-	-	$30.2 \pm 4.3$	-	-	-
Miconazole	$0.59 \pm 0.03$	<0.2	$1.70 \pm 0.21$	$1.9 \pm 0.2$	$4.6 \pm 0.4$	$0.98 \pm 0.22$	$4.0 \pm 0.5$	$1.3 \pm 0.2$
Clotrimazole	<0.1	<0.2	$13.3 \pm 0.6$	$2.5 \pm 0.1$	$5.3 \pm 0.6$	$0.37 \pm 0.08$	$3.8 \pm 0.9$	-
Voriconazole	-	-	-	-	-	$6510 \pm 470$	-	-
2-phenylimidazole	-	-	-	-	$345 \pm 4$	-	-	-
4-phenylimidazole	-	-	-	-	$216 \pm 5$	$280 \pm 18$	$12.0 \pm 1.5$	-
Imidazole	-	-	-	-	$536 \pm 7$	$2965 \pm 275$	-	$2591 \pm 59$

**Table 3.8. Summary of a comparison of the CYP126 dissociation constant values ( $K_d$ ) for several azoles and azole antifungal inhibitors with CYP51B1, CYP121, CYP130, CYP125, CYP124, CYP142 and CYP144 (82, 119, 121, 124, 135-137). Values are in  $\mu\text{M}$ . - indicates “not determined”.**

Potentiometric data have important implications relative to the mechanism of the reduction of cytochromes P450. Two electrons are required for P450 catalysis and must be delivered through two consecutive single electron transfers from redox partners. Potentiometry enables the determination of the midpoint reduction potential of the heme iron and thus the energetic requirements for the first of these electron deliveries. This thesis presents the first

report of the determination of the reduction potential of CYP126. Thermodynamically, the reduction potential of the P450 heme iron is often responsive to substrate binding, with the potential becoming more positive. For soluble bacterial P450s characterised to date, substrate binding may elicit a positive shift in redox potential of ~130 mV, perhaps taking the potential to around -250 mV, reflecting the different midpoint potentials between low-spin and high-spin forms of the enzyme (289). The data collected for substrate-free CYP126 displayed a midpoint reduction potential of -332 mV. Such a potential is far more typical of a substrate-free P450 enzyme in the low-spin state, and would make electron transfer via a NADPH-driven system slightly disfavoured due to adverse thermodynamic properties ( $E^{\circ} = -320$  mV for the NAD(P)H/NAD(P)<sup>+</sup> couple). Thus, substrate binding is predicted to cause a large increase in redox potential in the case of CYP126. In a previous report, McLean *et al.* demonstrated that the reduction potential of the iron sulfur cluster in Fdx<sub>1</sub> (one of two ferredoxins located adjacent to Mtb P450s, in this case CYP51B1, with the other [Fdx<sub>2</sub>] next to CYP143) is -31 mV. This is considerably more positive than that for ligand-free CYP51B1 heme iron (-375 mV) (194). However, the reduction potential for estriol-bound CYP51B1 is much more positive (-225 mV). Despite the apparent thermodynamic barrier to electron transfer, Fdx<sub>1</sub> can clearly reduce CYP51B1 (albeit slowly) and sterol substrates were demethylated in a NADPH-dependent manner using a plant ferredoxin reductase to mediate electron transfer from NADPH (-320 mV) to Fdx<sub>1</sub>. The study with cytochrome P450 BioI from *Bacillus subtilis* (255) also indicated that there is a ~130 mV difference in the reduction potentials of the low-spin and high-spin (substrate-bound) forms of the enzyme, and this shift in spin state and potential of the heme iron as substrate binds occurs *in vivo* and precedes electron transfer from redox partners.

Through pH titration of the reduced (ferrous) CYP126, it was found that increasing the pH of the buffer solution produced spectral changes suggestive of an increased proportion of the thiol-coordinated form of the cytochrome heme iron, with a Soret shift from shorter (420 nm) to longer wavelength (428 nm), and spectral increases in the Q-band region. In ferrous P450s, the thiolate-coordinated form often has its Soret maximum at ~ 410-412 nm. The thiol-coordinated form has the Soret at longer wavelengths (~420-425 nm) (59). The spectral shift at higher pH (from both Soret and alpha/beta region changes) is clearly consistent with the formation of a thiol-coordinated reduced heme in the case of CYP126. This being the case, the transition monitored at 428 nm likely reflects mainly the transition between Fe<sup>II</sup>-thiolate and Fe<sup>II</sup>-thiol coordinated hemes. The successful formation of ferrous CYP126 (with at least some of the heme apparently in the thiolate-coordinated form) in

redox titrations at neutral pH are likely a consequence of the neutral pH used with respect to the  $pK_a$  determined for the thiol/thiolate transition ( $pK_a = 6.8 \pm 0.1$ ). The fact that there is apparent accumulation of thiol-coordinated heme iron as the pH is increased is, of course, counter-intuitive in view of the fact that increased acidity (not basicity) would be expected to result in greater heme thiolate protonation. A logical explanation for the phenomenon observed would be that the  $pK_a$  observed here is actually one for a different amino acid side chain (likely proximal to the cysteine), and that its deprotonation is linked to conformational rearrangements that result ultimately in the protonation of the cysteinate ligand to the heme iron. The identity of the amino acid side chain titrated here with a  $pK_a$  of  $\sim 6.8$  thus still requires identification in further studies on CYP126.

Through analysis of the conformational stability of CYP126 by DSC to determine the temperature at which the protein structure was disrupted in the presence and absence of ligand, it was found that ligand binding induced the stabilization of CYP126, with the  $T_m$  increasing by 6.3 °C in the presence of ketoconazole. This demonstrates that the ligand inhibits protein unfolding at a temperature at which the ligand-free P450 unfolds. The ligand-bound conformation of the protein in solution clearly has greater thermal stability than the ligand-free species. Analysis of the thermal transition obtained when the protein unfolded showed that the protein unfolds as two distinct events that likely represent the separate unfolding of the N- and C-terminal domains of the protein. Despite the fact that the entire protein is stabilized by the presence of ligand, the domains unfold (from their individual  $T_m$  values) at nearly the same temperature, and so it is conceivable that only one domain is stabilized substantially in the presence of ligand. However, it is impossible to define whether the N- (alpha) or C-terminal (beta) domain unfolds first. The crystal structure of CYP126 was solved in the open and closed forms, with imidazole bound in the open form and clear structural differences observed between forms. This indicates that ligand binding produces a conformational change in order to stabilize the protein structure. Therefore, from the data presented in these studies, which indicate that a ligand binding event stabilizes the structure of the protein, there is the suggestion that a conformational change induced on azole inhibitor binding occurs, similar to that observed for CYP51B1, CYP121, CYP130, CYP125 and CYP124.

EPR studies of ligand (ketoconazole)-bound CYP126 reveal spectral homogeneity in the low-spin form of protein, without evidence of any high-spin form of the enzyme. The results of this study demonstrated that the protein exhibits spectral properties consistent

with cytochrome P450 enzymes such as CYP121 (149). CYP126 interacts with the azole ketoconazole *in vitro* with the tightest  $K_d$  among azoles tested, producing typical type II binding absorption spectra and characteristic EPR spectra. The EPR spectrum for ketoconazole-bound CYP126 revealed that the  $g_z$  did not move out past 2.5, a value that would very clearly indicate nitrogenous axial ligation, as found in other well characterized P450s such as CYP51B1 and CYP121 in their interactions with various azole ligands (119, 149). One model explaining the CYP126-ketoconazole EPR spectrum is that, in solution, coordination occurs via the interstitial 6<sup>th</sup> water ligand. However, this would mean that this situation is different from the crystal structure form. The  $K_d$  value of ketoconazole for CYP126 is extremely tight (1.4  $\mu$ M) and comparable with that for another lipophilic azole, miconazole (1.3  $\mu$ M). It is also tighter than for econazole (5.05  $\mu$ M) (Table 2). The ketoconazole-bound form of CYP126 does show some heterogeneity in the EPR spectrum, possibly indicative of two states of the enzyme in which there is both direct N-Fe binding and indirect coordination of the heme iron via the distal water molecule. However, the limited solubility of the azole is also an issue and likely results in inability of the drug to completely saturate CYP126 at a protein concentration of 200  $\mu$ M used for EPR.

MCD studies provide important reference spectra, including in the near UV-visible and NIR CT regions, that can be important in identifying similarly ligated hemoproteins elsewhere in nature. Specific and potentially diagnostic MCD spectral features are also reported here, with the strong Soret band at 418 nm for ligand-free CYP126 showing a similar intensity to the typical band observed for other thiolate-ligated heme systems (59). In brief, the MCD features of the wild-type CYP126 in the UV-visible region indicate that the protein has a monosignate MCD spectrum typical of a low-spin ferric heme with cysteinate- and water-ligation to the heme iron. In the NIR region, the heme iron of this enzyme was found to possess a cysteinate MCD CT<sub>LS</sub> band. Comparative studies for the MCD features of the ligand-free CYP126 indicate similar spectral properties and wavelength maximum of this band to those obtained previously for other P450s such as CYP121 (138, 194) and P450 BM3 (247).

The molecular mass estimate obtained from MALLS analysis demonstrated that virtually all the CYP126 eluted as a single species with a molecular weight corresponding to 48.1 kDa. Compared to the molecular weight of CYP126 predicted from the gene sequence, these data suggest that the protein was monomeric in solution, and that significant amounts of the dimer (or higher oligomeric forms) were not found under standard conditions. The

results of the MALLS studies shows that the molecular mass of CYP126 is very similar to that expected for the theoretical calculation based on the amino acid sequence. Therefore, it is believed that proteolysis was effectively inhibited during purification and that the intact, monomeric protein was successfully isolated.

Measurement of the accurate molecular mass of proteins or peptides is necessary for defining protein structure and any covalent modifications or proteolytic events. To define intact protein, an accurately measured mass should also allow us to pinpoint the precise sites of any e.g. translational errors, covalent modifications and individual proteolytic events. The measured mass of the recombinant CYP126 purified from *E. coli* is almost identical to the one expected from the amino acid sequence with one heme iron bound. The purified, native CYP126 protein showed a peak at 47986  $m/z$ , identical to the theoretical calculation based on the amino acid sequence. The observed mass of 47986 Da is the monomeric molecular weight of CYP126. Therefore, the value determined from mass spectrometry of CYP126 is exactly that predicted from the amino acid sequence translated from the sequenced DNA. It is worthy of note, also, that the mass determined for CYP126 indicates that significant proportion of the purified protein retains its initiator methionine residue, and that there are no covalent modifications of the cytochrome P450 protein in the heterologous host (as might be expected).

The overall ligand-free structure of CYP126 at high resolution (1.7 Å) exhibits a dimeric form with a narrow active site-access channel. Like a number of other P450s, CYP126 also displays the longest helix (the I helix) disrupted such that the N-terminal portion bends away from the structural core, making an angle with the C-terminal part. The structure also reveals several water molecules providing H-bonds to peptide groups in the active site. The I helix movement away from heme releases the inter-helix BC loop from a closed conformation, and this enlarges the space available for substrate or inhibitor binding to the P450. However, the dimeric structure of CYP126 also displays an unusual feature in which one monomer is in an “active” (closed) form and the other is in an “inactive” (open) form. These forms can be seen clearly in the model structure. The BC loop in one monomer is closed suggesting that the active site is primed.

In contrast, the other monomer shows the movement of the BC loop, revealing an open active site that is presumably available for substrate entry and thus in an “inactive” state. In addition, the binding of the imidazole in the “open” form exhibits a steric constraint

imposed by the I helix, which bends over the heme group at the position of Glu<sup>256</sup>. This makes the active site cavity larger than is required to accommodate imidazole and provides space for the ligation of theazole nitrogen to the heme iron. Similar to the binding of imidazole, the ketoconazole-bound CYP126 crystal structure reveals a larger active site than the ligand-free form in order to support room for possible alternative ligation modes to the heme iron. However, the new movement of the BC loop upwards in the active site to form a lid over the cavity might be a barrier to preclude further entry of ketoconazole to coordinate heme iron. The ligation of ketoconazole (in the crystal structure) also changes the oligomerization state of CYP126 from dimer to monomer, which relates to the production of the “inactive” conformation once inhibitor binds.

By screening the library of 20,000 organic compounds against CYP126 to identify substrate-like and inhibitor-like compounds for this P450, dozens of type I and type II hits were identified via the spectral shift of the P450 heme Soret band. The top type I hits share a similar structure with a nitrobenzene ring, which is also found as a functional group in several antibiotics, such as like chloramphenicol and azidamphenicol. This could suggest that CYP126 might have a function related to detoxification of xenobiotic compounds containing such groups. Binding of these type I compounds induced a Soret shift from 418 nm to 393 nm, consistent with the shift from LS ferric heme to HS ferric heme, which was verified by UV-visible spectroscopy and EPR, suggesting that these compounds could be real substrates for CYP126. In previous studies of Mtb P450s, CYP51B1, CYP124, CYP125 and CYP142 were reported to be involved in sterol (CYP51B1), fatty acid (CYP124) and cholesterol (CYP125/142) metabolism, while CYP121 was reported to be involved in the biosynthesis of a secondary metabolite, the cross-linked derivative of the cyclodipeptide cYY (120). Therefore, an involvement of CYP126 in a detoxification process would show a distinct function from these other Mtb P450s, and also reveal a diversity of activity of the Mtb P450 enzyme system.

Among the 15 selected type II hits for CYP126, 9 compounds exhibited a similar structure with a 1,3 diazole five membered aromatic ring similar to various P450 inhibitor imidazole derivatives. These compounds also revealed an identical binding mode (i.e. heme coordination via a nitrogen atom on the ring), indicating that they probably have a similar inhibitory mechanism as theazole drugs. Only 6 compounds revealed distinct structures from the others, thus they may have different binding modes and possibly different potencies against CYP126. Clearly, new inhibitory classes for CYP126 were determined

alongside the known azole antifungal drugs, providing us with more options and new chemical scaffolds for elaboration to generate more potent inhibitors to block CYP126 (and possibly other Mtb P450) catalytic activity.

Future work will focus on the determination of CYP126 structure with compound 32027 (substrate-like) and compound 35125 (inhibitor). Further work relates to the identification of products formed by substrate oxidation in CYP126.

## 4 EXPRESSION, PURIFICATION, AND CHARACTERIZATION OF CYP141

### 4.1 Introduction

CYP141 is one of twenty P450 enzymes in Mtb and there is no further information on this protein regarding characteristic functional and structural properties, excepting that the gene is missing from the virulent *Mycobacterium bovis* strain and from its avirulent counterpart *M. bovis* BCG (51, 290). Therefore, the uncharacterized CYP141 becomes an interesting target to investigate further in order to determine its role in the biology of Mtb. The relevant CYP141 (*Rv3121*) gene possesses 1201 base pairs, coding for the CYP141 protein with 401 amino acids. Blast searches indicated that the amino acid sequence of CYP141 shows similarity to the various cytochrome P450 of *Streptomyces* species. A comparison of the homologue, CYP141 shows 33.35 % amino acid sequence identity with CYP107N1 from *Streptomyces lavendulae* (401 aa) with a 396 amino acid overlap (291). The CYP107N1 enzyme is involved in the biosynthesis of mitomycin C in *S. lavendulae*, which has activity as an inhibitor against a variety of solid tumours. In fact, to have anticancer activity, this bacterial product must be activated by a number of other enzymes (291). In addition, CYP141 has similar levels of identity with CYP107D1 from *Streptomyces antibioticus* (407 aa), CYP107M1 from *Actinomadura hibisca* (411 aa), and CYP112A1 from *Rhizozium* sp. strain NGR324 (400 aa), with 34.85%, 31.05% and 33.0% identity, respectively. Unfortunately, there is no specific information on substrate selectivity related to these enzymes (292-294). Therefore, studies on CYP141 should reveal more detailed information about the functional properties of this (and possibly other) P450 enzymes in Mtb, and could show if it is a good target for the design of selective inhibitors.

In this chapter, studies are reported on the expression and purification of CYP141, leading to the biochemical and biophysical characterization of this P450 enzyme. The P450 exhibits several interesting features, including some unique spectroscopic properties and a mixture of low-spin and high-spin forms. CYP141 also displays high affinity for azole antifungal drugs, which bind to the CYP141 heme iron, suggesting it could be a drug target enzyme. Furthermore, this study provides fundamental new data relating to the redox potential and optical pH dependence properties of CYP141, and its properties by MCD, EPR, DSC, MALLS and CD spectroscopy. This chapter also reports crystal trials in order to determine the structure for ligand-free Mtb CYP141.

## 4.2 Results

### 4.2.1 Expression and purification of CYP141

Preliminary expression trials indicated that CYP141 could be expressed to very high levels under control of the T7 RNA polymerase promoter system in pET15b, using *Escherichia coli* BL21 (DE3) under regular growth conditions as described in the Methods chapter (section 2.5). Analysis by SDS-PAGE showed that the heterologously expressed CYP141 was produced at high levels, and cell pellets were relatively red in colour, indicating high levels of CYP141 enzyme was accumulated, as shown in Figure 4.1.1. However, the subsequent breakage of these cells revealed that the bulk of CYP141 was located in inclusion bodies and only a small amount was in the soluble form (Figure 4.1.2).

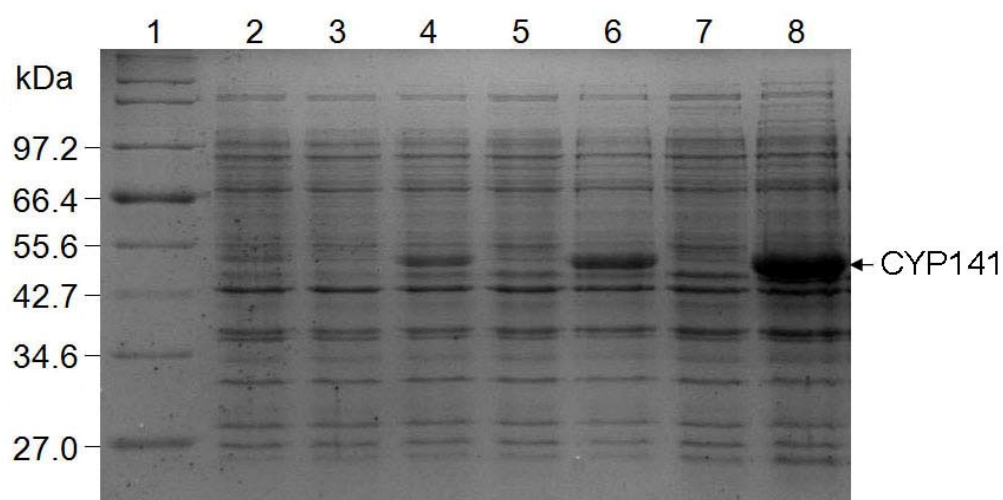


**Figure 4.1.1. SDS PAGE gel of CYP141 trial expression in *Escherichia coli* BL21 (DE3) cells.** *CYP141* was expressed with induction by 1 mM IPTG at different times, ranging from 0 to 24 h; lane 1: Molecular mass standard marker (97 200, 66 400, 55 600, 42 700, 34 600, 27 000 Da); lane 2: total protein at T = 0; lane 3-4: total protein of control (uninduced) and induced samples at time T=2 h; lane 5-6: total protein of control and induced samples at T = 6 h; lane 7-8: total protein of control and induced samples at T= 24 h. The band at approximately 46 kDa is due to production of CYP141 protein.

To optimise the expression conditions for gaining higher levels of the soluble form of CYP141, a variety of other growth conditions and host strains were investigated. Inclusion of small amounts of detergent (e.g. 0.1 % Tween 20) in the growth medium was without beneficial effect on soluble protein recovery. However, low temperature was found to be essential to promote overproduction of soluble CYP141. The optimal soluble CYP141 production was obtained in *E. coli* strain BL21 (DE3), with IPTG induction (1 mM) in the mid-logarithmic phase of growth, and with cell culture continued at low temperature (18

°C) for approximately 20-24 hours post-induction. Under these conditions, the overall expression of CYP141 was lower, but the recovery of soluble CYP141 protein much higher.

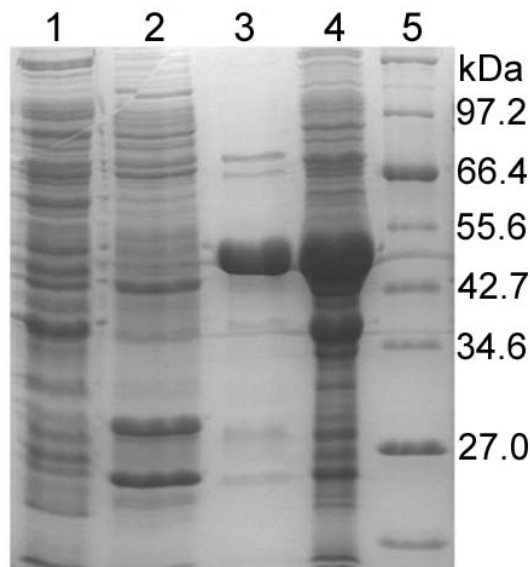


**Figure 4.1.2. SDS PAGE gel of CYP141 trial purification in *Escherichia coli* BL21 (DE3) cells.** The cells were suspended in 50 mM KPi buffer containing 300 mM NaCl, 10% glycerol, pH 8.0, and a Complete EDTA-free protease free inhibitor tablet (Roche). The cells were broken by sonication. The disrupted cell extract was centrifuged at 20,000 rpm for 20 min. The supernatant was then loaded onto a nickel-NTA resin column, the column was washed with 10 volumes of the same buffer containing 20 mM imidazole. Finally, the protein was eluted using 80 mM imidazole in the same buffer. Lane 1: the supernatant after loading; lane 2: post washing with 20 mM imidazole; lane 3: protein elution from column with 80 mM imidazole; lane 4: total protein from cell pellet after disruption; lane 5: molecular mass standard markers.

For protein purification, CYP141 was purified to homogeneity using two different columns as described in the Methods chapter (section 2.7). Initially, CYP141 was purified by Ni-NTA column chromatography, due to this protein containing a histidine tag at the N-terminal (6 histidine residues), which is specific for binding to the Ni resin. The result of SDS-PAGE analysis showed that CYP141 was faithfully expressed and purified as a mainly soluble protein (Figure 4.2). However, it was still contaminated by other proteins from the host cells after purification by Ni-NTA column chromatography. Therefore, the protein was then applied to a Q-Sepharose anion exchange column to separate further contaminant proteins from CYP141. The relative purity of CYP141 was measured during purification by comparing the heme specific absorption (at 417.5 nm) with the total protein at 280 nm at different stages of purification. The ratio of heme-specific to total protein

absorption ( $A_{417.5/280}$ ) gives a measure of purity, with a value of approximately 2.3 indicating homogenous CYP141, as verified by SDS-PAGE (Figure 4.3). Samples with a  $A_{418/280}$  ratio of  $>1.7$  were considered to be sufficiently pure for further analysis, including spectroscopic studies.

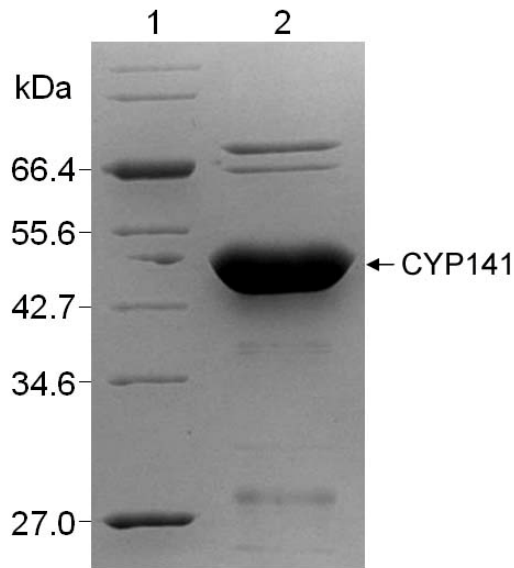


**Figure 4.2. SDS PAGE gel of CYP141 expression and purification by Ni-NTA column chromatography.** Lane 1: Protein marker (relevant size markers indicated); lane 2: protein elution from column with 60 mM imidazole, demonstrating isolation of the CYP141 protein.

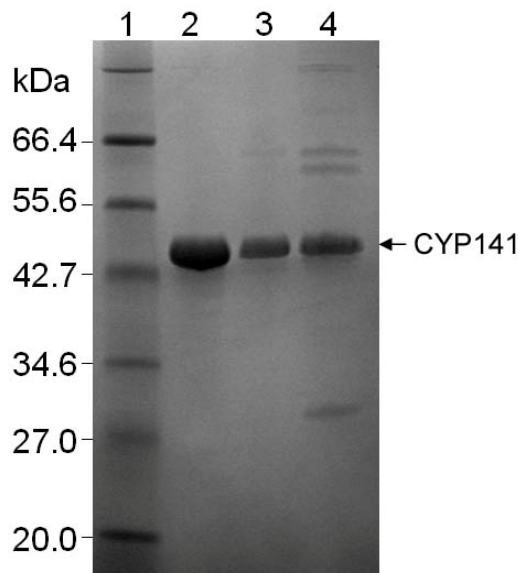


**Figure 4.3. SDS PAGE gel analysis of CYP141 protein purification steps using a Q-Sepharose column.** Lane 1: protein marker; lane 2: protein elution from Q-Sepharose with 200 mM NaCl; lane 3: protein elution with 250 mM NaCl; lane 4: protein elution with 300 mM NaCl. The collected protein band (lane 2) demonstrated very high purity of CYP141 ( $A_{418}/A_{280} = \sim 2.3$ ).

#### 4.2.2 Spectrophotometric characterization

The pure sample of CYP141 in its oxidised form reveals spectral properties typical for a ferric P450 protein, but with the heme iron in a mixture of high spin and low spin states, exhibiting the minor Soret ( $\gamma$ ) band feature at 393 nm and the major Soret band feature located at 417.5 nm, and with the smaller  $\alpha$  and  $\beta$  bands located at 574 and 537 nm, respectively (Figure 4.4). The ratio between the heme spin states varied somewhat between different concentrations and preparations of protein samples. The mixture of low and high spin states feature is similar to the well-characterized CYP170A1 from *Streptomyces coelicolor* A3 (295). The reduction of CYP141 with sodium dithionite results in a Soret band shift to 403 nm with a decrease of intensity (Figure 4.4). Generally, with the exception of the mixture of spin states (bacterial P450s are usually extensively low-spin), other features of CYP141 are typical of P450s, and similar to most of the other Mtb P450s, although the spectral maxima for both oxidised and reduced forms are both at slightly longer wavelengths (by approximately 1 nm) for CYP141 than for CYP121, another structurally characterized P450 enzyme from Mtb.

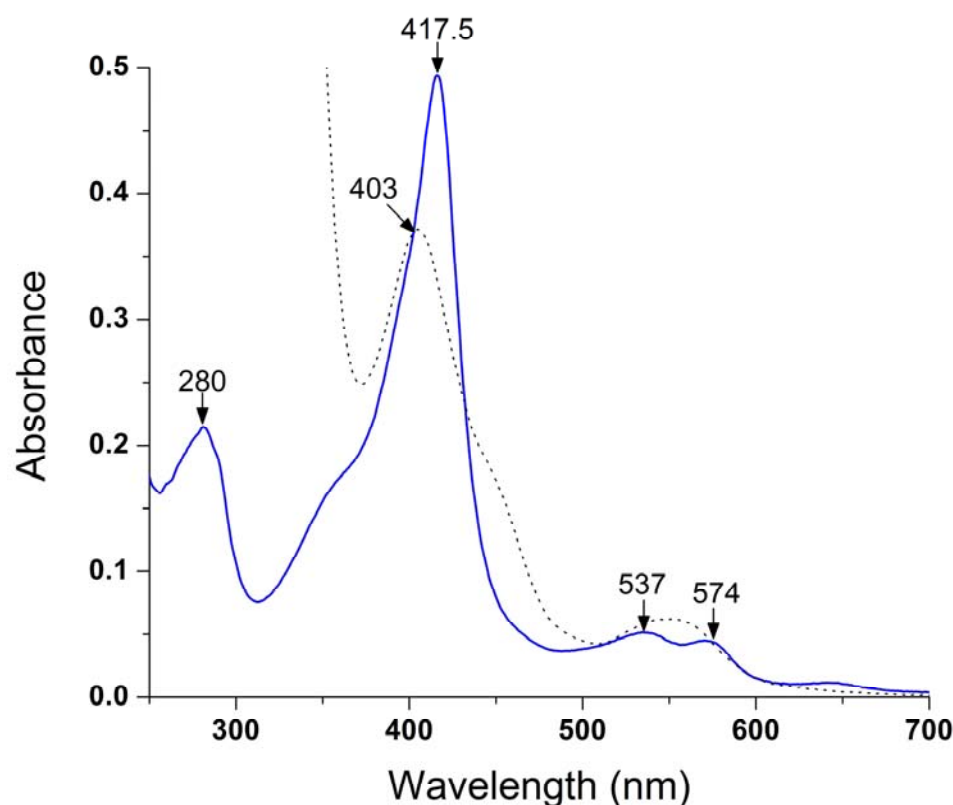


**Figure 4.4. Electronic absorption spectra for pure CYP141.**

The UV-visible absorption spectrum for pure CYP141 (ca. 5  $\mu$ M) in the oxidised form. The absorbance was recorded in 100 mM potassium phosphate, pH 7.5. The protein absorbs maximally at 280 nm, whilst the heme absorption maximum is located at 417.5 nm with  $\alpha$  and  $\beta$  bands at 574 nm and 537 nm (blue line). The dithionite-reduced enzyme has its Soret band at 403 nm (black dotted line).

Surprisingly, the purified CYP141 displays a unique reduced carbon monoxide different spectrum, with a maximum at ~440 nm, instead of the typical P450 absorption maximum at ~450 nm (Figure 4.5). This characteristic was reported previously for CYP170A1 (295), which also indicated a similar spectrum at 440 nm. In the oxidized form, CYP170A1 exhibits a mixture of high-spin and low-spin state at 393 and 417 nm, and in the reduced, carbon monoxide-bound form the Soret band shifts to 440 nm, which is different from a typical P450, but very similar to CYP141.

Under aerobic conditions, CYP141 was relatively easy to reduce completely to the ferrous form, and this was proved by bubbling of carbon monoxide through the dithionite-treated CYP141. This invariably generated a species with absorption maximum at 440 nm (i.e. the P450  $\text{Fe}^{2+}$ -CO form with the cysteine ligand in this thiolate form), and with a very small spectral species at ~420 nm. The latter P420 species likely indicates that a small proportion of the enzyme has lost thiolate ligation in favour of the thiol form following dithionite reduction and exposure to the gas. However, this amount is very small.

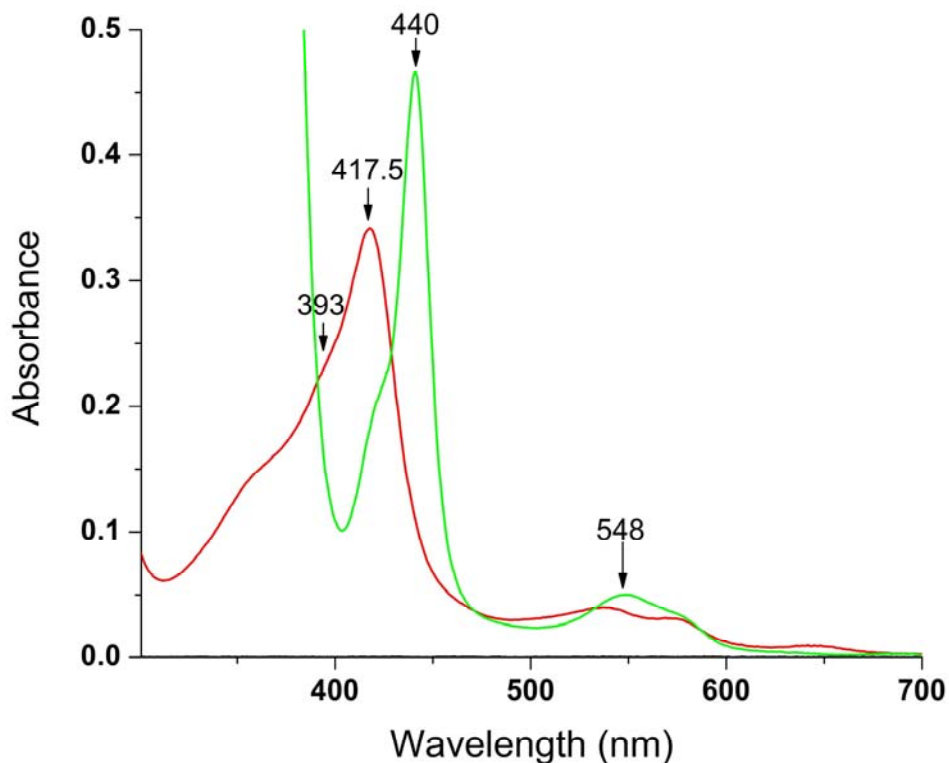


**Figure 4.5. UV-visible spectrometry of CO-bound CYP141.**

The CYP141-CO complex with Soret peak at 440 nm is shown. The red spectrum is that for the oxidised enzyme (*ca.* 4  $\mu\text{M}$ ), and the green spectrum is that for the (sodium dithionite-reduced) ferrous-CO complex. The latter shows a Soret feature split between a thiol-coordinated CO-bound form (minor feature at ~420 nm) and the thiolate-bound form at 440 nm.

Addition of nitric oxide to the ferric CYP141 resulted in a shift of Soret band to ~431 nm (Figure 4.6). Production of a nitrosyl adduct generates a spectral maximum at 431 nm that is consistent with a cysteinyl-ligated nitrosyl complex. The ligation of NO to the heme results in the conversion to a single spectral species typical for those seen in other P450s, such as NO-bound CYP144 (Soret at 436 nm) (135), and NO-bound CYP121 (Soret at 437 nm) (138).

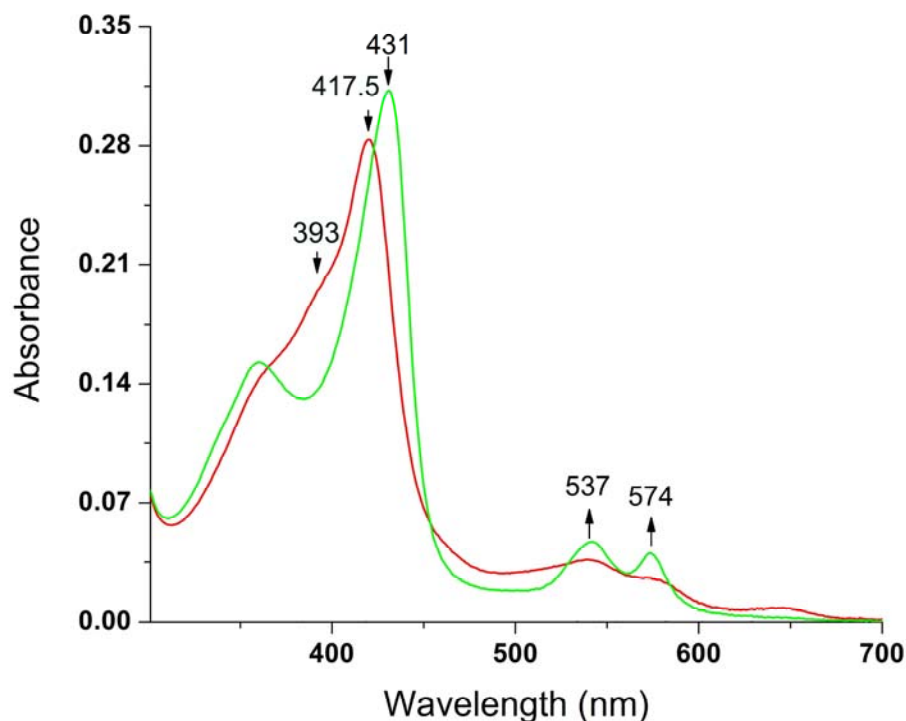


**Figure 4.6. UV-visible spectrometry of NO-bound CYP141.**

The CYP141-NO complex has its maximum at 431 nm. The red spectrum is for oxidised CYP141 (*ca* 3.5  $\mu$ M) and the green spectrum is for the complex formed with nitric oxide (NO). Arrows highlight major absorption features on NO complex formation. The small feature at ~350 nm is due to oxidation of NO to nitrous acid.

#### **4.2.3 Determination of heme absorption coefficient using the pyridine hemochromagen method.**

Correia *et al.* (296) reported that the concentration of a P450 enzyme can be determined via a stable Fe(II)-CO adduct using the extinction coefficient  $\Delta\epsilon_{450-490}$  of  $91 \text{ mM}^{-1} \text{ cm}^{-1}$  for data from the reduced/CO-bound minus reduced P450 difference spectrum. However, an alternative method to determine an extinction coefficient for a hemoprotein (CYP141 in this case) is to estimate heme concentration by generating pyridine hemochromagen spectra using the method of Berry and Trumpower (163), as was also used to calculate the extinction coefficient of CYP126 in its oxidized form (see section 3.2.3).

Figure 4.7 shows the pyridine hemochromagen spectrum used for the calculation of the CYP141 heme concentration. The Soret band for oxidized CYP141 is at 417.5 nm ( $\sim 5 \mu\text{M}$ ), with Q-bands having absorbance maxima at 537 and 574 nm. The mixture of oxidized CYP141 and pyridine shows an absorbance maximum in the Q-band region at 556 nm, which is typical of heme *b*, and the reduced form shows that CYP141 was completely reduced by dithionite. The difference in absorbance between oxidised and reduced forms (at 556 nm) was 0.137. Therefore, the total heme concentration of the CYP141 sample was calculated, using the heme *b* extinction coefficient of  $\Delta\epsilon_{556,4-540\text{nm}} = 23.98 \text{ mM}^{-1} \text{ cm}^{-1}$  (from the difference spectrum) as  $5.7 \mu\text{M}$  for this sample. The usefulness of the pyridine hemochromagen method for analysis of CYP141 concentration becomes clear when one considers that the spin-state of CYP141 is variable between samples, and with temperature pH etc – and thus the pyridine methods provides a consistent way of establishing heme concentration for samples with different heme absorption properties.

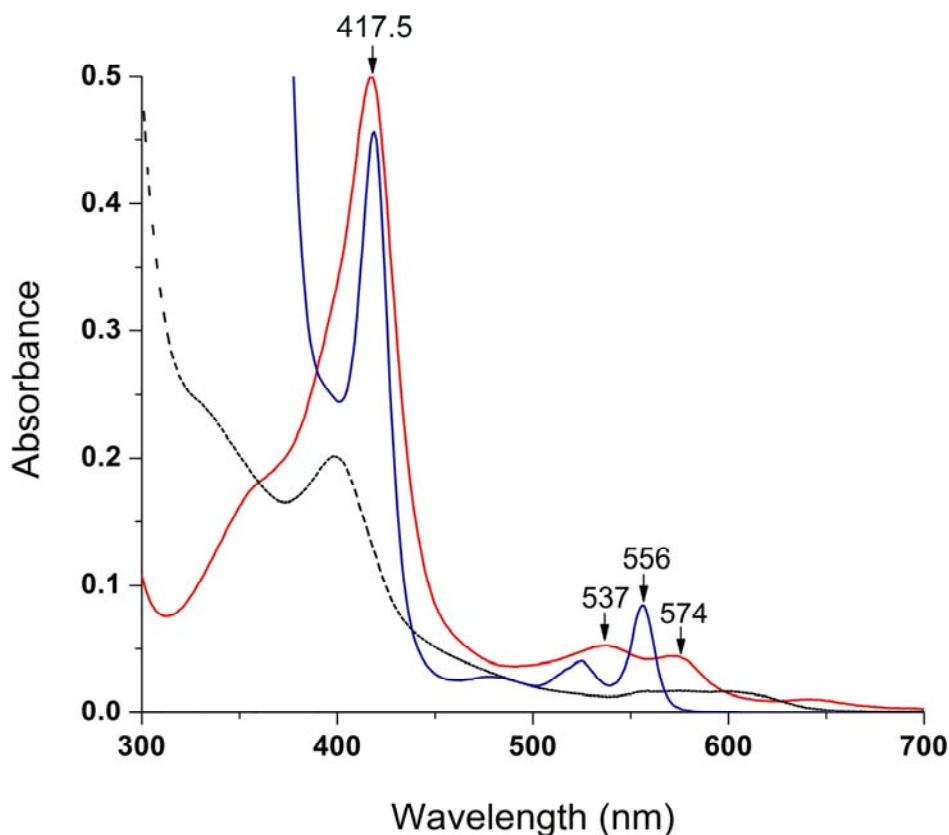


**Figure 4.7. Pyridine hemochromagen spectra of CYP141.**

The red line shows the oxidised form of CYP141 (ferric form) with the Soret band at 417.5 nm. The dashed black line presents the reduced form of CYP141 (ferrous form) with dithionite. The blue line presents the pyridine hemochromagen spectrum with a maximum in the Q-band region at 556 nm, and indicative of heme *b*. Using the extinction coefficient ( $\Delta\epsilon_{556,4-540\text{nm}}$ ) of  $23.98 \text{ mM}^{-1} \text{ cm}^{-1}$ , the heme concentration of CYP141 was calculated as  $5.7 \mu\text{M}$ .

#### 4.2.4 Circular dichroism

The CD spectra for CYP141 were collected on a Jasco spectropolarimeter, in both the far UV and near UV-visible regions, and then ellipticity data in the far UV region were analyzed using the Selcon program (168). The far UV (190-260 nm) CD spectrum of CYP141 exhibited CD minima at 222 and 208 nm, and a strong CD maximum at 190 nm, which indicates a mainly alpha helical structure with a value of >60% helix estimated by the Selcon program.

All P450 crystal structures solved to date are predominantly alpha helical (297-299). Figure 4.8 presents the far UV CD spectrum of Mtb CYP141, which is highly similar to the CD spectrum of other well-characterised P450 enzymes such as P450 BM3 and CYP121 (138, 300). Using the equation described in section 2.19 to calculate the value of the molar ellipticity per residue, and analysing the data with a prediction program, the Selcon3 method estimated approximately 60%  $\alpha$  helix, 15%  $\beta$  sheet and around 3% random coil contents for CYP141.

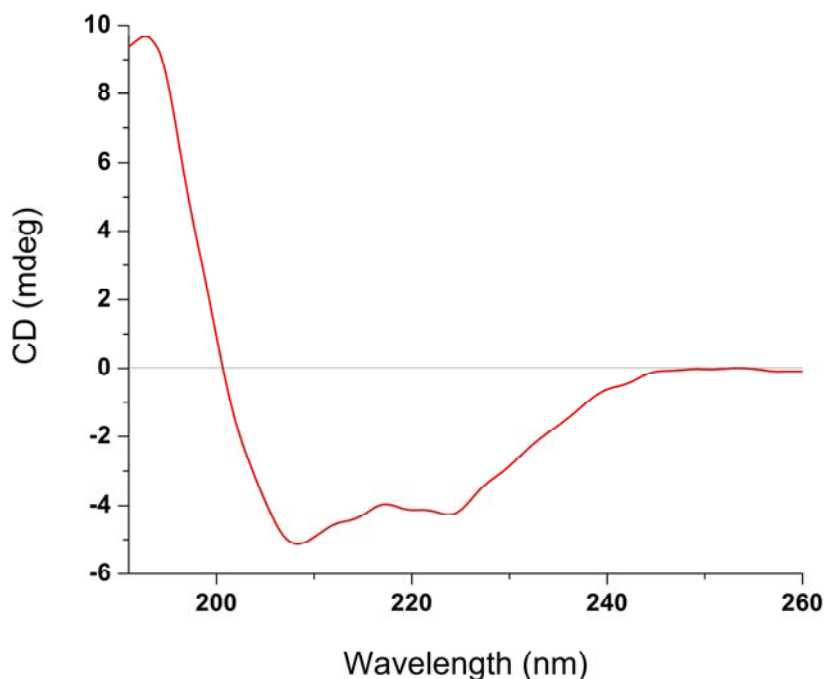


**Figure 4.8. Far UV CD spectrum for CYP141.**

The far UV CD spectrum of CYP141 is shown at a concentration of 2.0  $\mu$ M. The protein was in 10 mM potassium phosphate, pH 7.5. The CD spectrum of CYP141 (red line) exhibited minima at 222 and 208 nm, and a strong maximum at ~191 nm. The secondary structural composition was calculated as described in the Methods section (section 2.19).

Figure 4.9 exhibits the CD spectrum of the oxidised form of CYP141 in the near UV-visible region (260-600 nm). Signals in the 260-320 nm region arise mainly from aromatic amino acid side chains, and CD spectra in this region are characteristic of individual P450 isoforms, meaning that each protein has a specific near UV CD spectrum. In the visible region (320-600 nm), the CD spectrum of CYP141 is dominated by a large signal of negative sign with a minimum near the position of the Soret maximum in the electronic absorption spectrum. This characteristic is highly similar to those of other P450s characterized to date, such as CYP121 and P450 BM3 (138, 300).

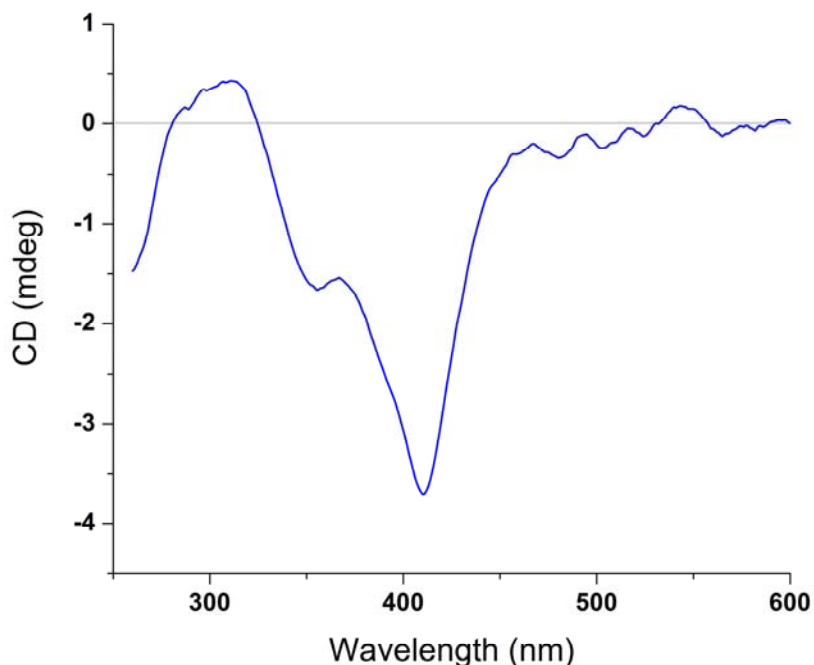


**Figure 4.9. Near UV-visible CD spectrum of CYP141.**

The sample (20  $\mu$ M) was in 10 mM potassium phosphate, pH 7.5. The blue line presents the CD spectrum of CYP141 in the near UV-visible region. The spectral minimum is at 410.5 nm.

#### 4.2.5 Azole inhibitor binding

Tests of CYP141 to determine its affinity for members of the class of azole drugs were performed, following the protocol described in the Methods chapter (section 2.14). The azole antifungal agents (including miconazole, ketonazole, fluconazole and econazole) were found to bind tightly to CYP141. Binding of each of the azole antifungal drugs to CYP141 was monitored via the type II shift of the heme Soret band caused by coordination of the inhibitors to the heme iron atom. The results are presented in individual sections below, and the summary of azole inhibitors binding to CYP141 is shown in Table 4.1.

#### 4.2.5.1 Fluconazole binding

Fluconazole has good antifungal activity and is less toxic to the human cells than many other azoles (164, 301). It binds in the P450 active site such that the triazole ring is (ideally) positioned perpendicular to the porphyrin plane with a ring nitrogen atom coordinated to the heme iron. This leads to a shift of the major (Soret) absorbance band to ~424-425 nm (288). The binding of fluconazole to the heme iron of CYP141 was monitored via the type II shift of the heme Soret band from ~418 nm to 421 nm (Figure 3.10 main). The Soret band for the fluconazole complex is located at ~ 421 nm, suggesting that there may be an altered ligation mode compared to most other P450s and that the formation of a low spin hem iron complex may not involve exclusively direct iron-nitrogen ligation. Similar characteristics of fluconazole binding were also described in CYP121, for which structural data indicated that indirect coordination of heme iron can occur via an interstitial water molecule (82).

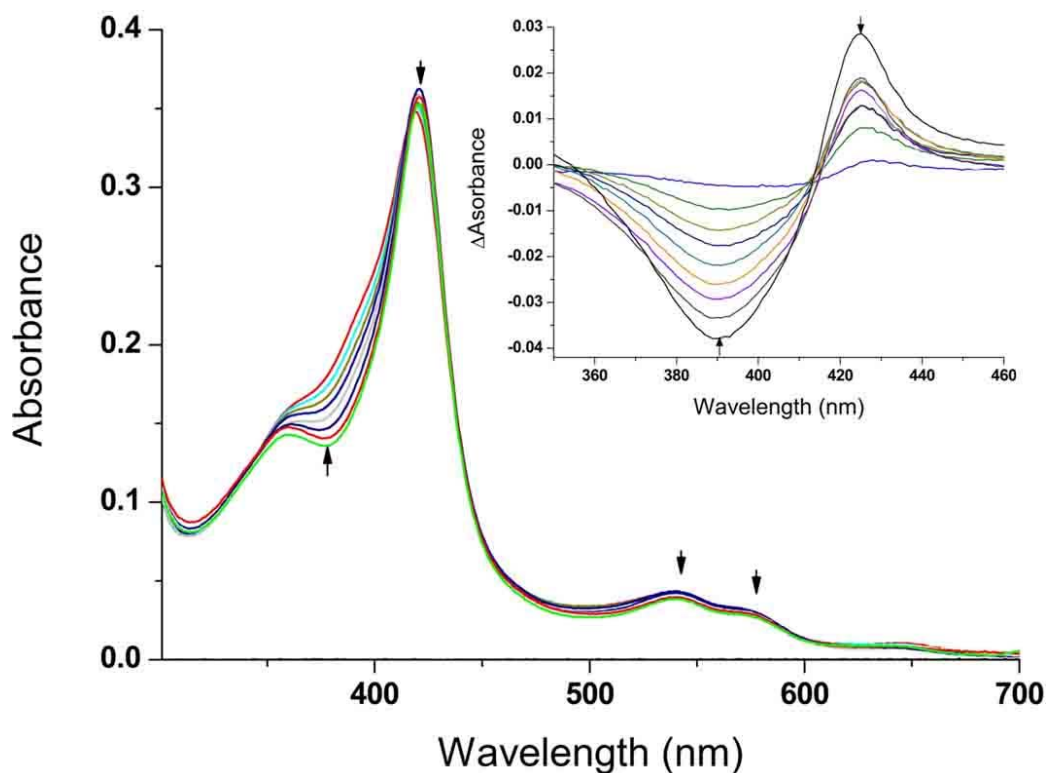


**Figure 4.10. Binding of fluconazole to CYP141.**

Main figure: shown in the red line is the starting spectrum, containing ~4  $\mu\text{M}$  CYP141, with a Soret maximum at 418 nm. The green line is the final spectrum which has a Soret maximum at 421 nm. The arrows indicate directions of absorption change on ligand addition. The binding of fluconazole to the heme of CYP141 induces a shift in the UV-visible absorption spectrum. Shown inset are the difference spectra generated from the data collected and the maximal absorbance change derived from these data. Arrows indicate directions of absorption change on ligand addition. Difference spectral maxima and minima are at 425 nm and 390 nm, respectively.

Type II spectra were produced with a broad trough at ~389-390 nm (Figure 3.10 main) and changes at the Soret peak that suggest azole coordination to the heme iron through a nitrogen atom. There are also changes in the spectral characteristics of the  $\alpha$  and  $\beta$  bands in the absolute spectrum on fluconazole binding, suggesting reinforcement of the low spin heme state of CYP141. In order to analyse further, a difference spectrum was constructed at each titration point by the subtraction of the spectrum for the inhibitor-free form from each successive inhibitor-bound spectrum in the titration. These spectra displayed minima and maxima at approximately 390 nm and 425 nm, respectively (Figure 4.10 inset). For each fluconazole concentration, the maximal absorbance difference was calculated by subtraction of the absorbance value at the trough from that at the peak in each difference spectrum. These values were then plotted against the corresponding concentration of fluconazole, and the data were fitted to a standard hyperbolic function to determine the dissociation constant value. The result of the fluconazole titration is shown in Figure 4.11 with a  $K_d$  value of  $25.2 \pm 3.6 \mu\text{M}$ .

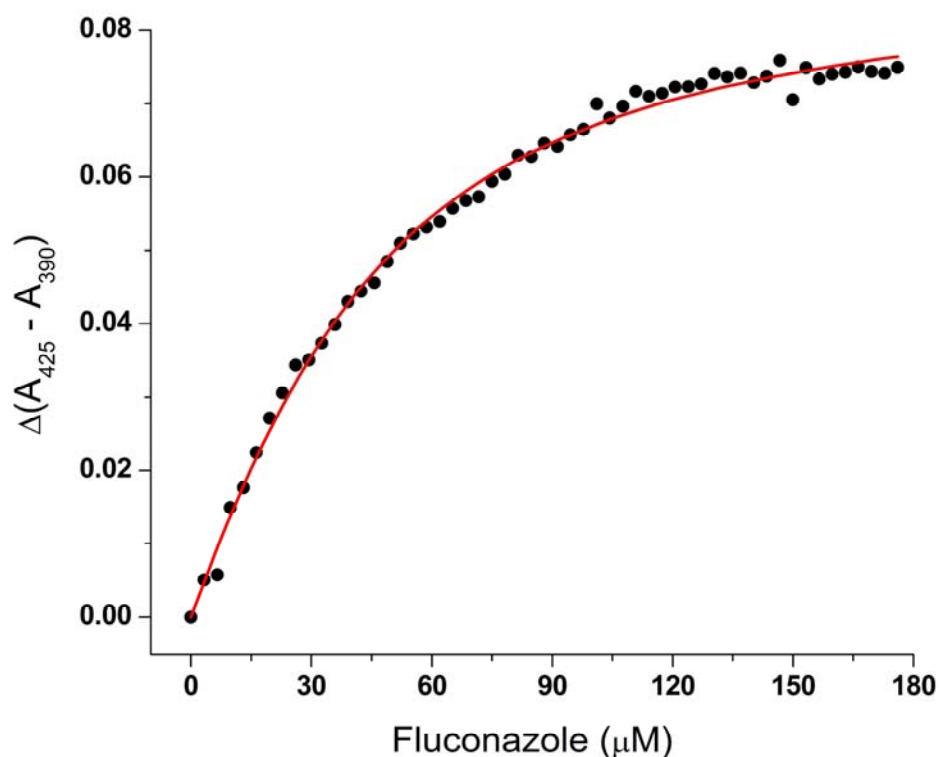


**Figure 4.11. Titration curve for the binding of fluconazole to CYP141.**

Data from the difference spectra ( $\Delta(A_{425}-A_{390})$ ) were fitted to equation 2.3 (section 2.14), yielding a  $K_d$  value =  $25.2 \pm 3.6 \mu\text{M}$ .

#### 4.2.5.2 Econazole binding

The absolute spectrum of CYP141 displayed a low-spin Soret band with an absorption maximum of 418 nm. A slight shoulder on the right side of this peak (at ~396 nm) was presumed to be the small percentage that exists in the high spin state (Figure 4.12 main). The type II ligand econazole bound to the heme iron of CYP141 and also showed a distinct type II spectral interaction with a shifting of the Soret band from 418 nm to 422 nm (Figure 4.12 main), suggesting that the binding of econazole displaced a water molecule with a basic nitrogen from azole ring (or possibly that ligation of the drug occurred via the interstitial water, given the rather small absorption change). The shift in the visible absorption spectrum of the P450s caused by azole inhibitors is most notable through the shift of the Soret absorption maximum to a longer wavelength. However, in the case of CYP141, the Soret band shifted with econazole was again from 418 to 422 nm, suggesting that it may involve an altered ligation mode and the formation of a low spin heme iron complex in which there is not exclusively direct iron-nitrogen ligation.

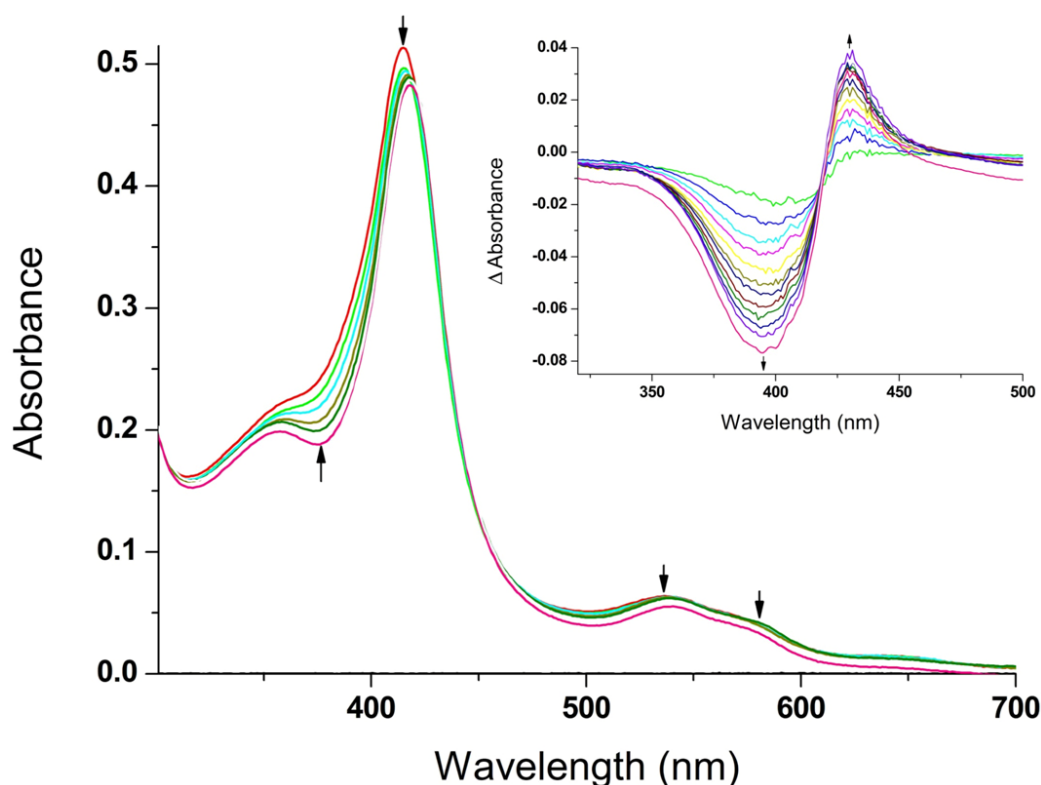


**Figure 4.12. Binding of econazole to CYP141.**

Main figure: shown in the higher red spectrum is the starting spectrum, containing ~5  $\mu\text{M}$  CYP141 and with a Soret maximum at 418 nm. The lower spectrum is the final ligand-bound spectrum which has a Soret maximum at 422 nm. The arrows indicate directions of absorption change on ligand addition. Shown inset are the difference spectra generated from the data collected and the maximal absorbance change derived from these data. Arrows indicate directions of absorption change on ligand addition. Difference spectral maxima and minima are at 430 nm and 396 nm, respectively.

As can be seen in Figure 4.12 inset, binding of econazole to the CYP141 leads to difference spectra with maxima and minima at approximately 430 nm and 396 nm, respectively. The  $K_d$  value for inhibitor was obtained from the spectral titration curve. The results show that the  $K_d$  value is  $14.2 \pm 1.7 \mu\text{M}$  (Figure 4.13). The binding affinity of econazole to the heme iron of CYP141 is about an order of magnitude lower than for CYP130 ( $K_d = 1.93 \pm 0.03 \mu\text{M}$ ) (137), CYP124 ( $K_d = 2.1 \pm 0.1 \mu\text{M}$ ) (136), CYP51B1 ( $K_d = 0.77 \pm 0.04 \mu\text{M}$ ) (119), CYP121 ( $K_d < 0.2 \mu\text{M}$ ) (82) and CYP144 ( $K_d = 0.78 \pm 0.29 \mu\text{M}$ ) (135).

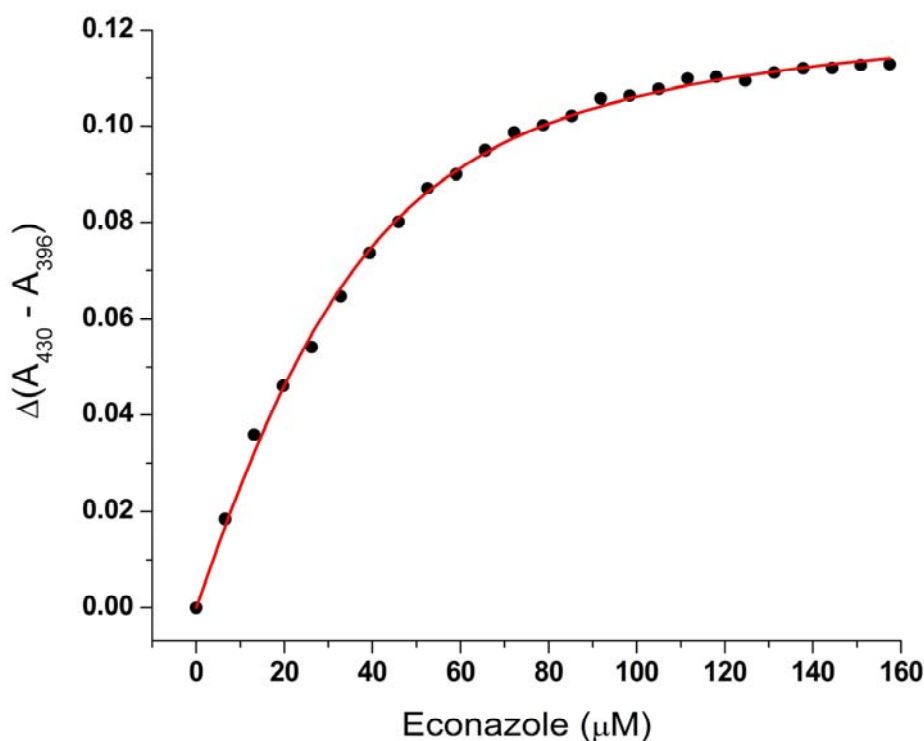


**Figure 4.13. Titration curve for the binding of econazole to CYP141**

Following titration of econazole against CYP141, the data from the difference spectra ( $\Delta(A_{430}-A_{396})$ ) were fitted to equation 2.3 (section 2.14), yielding a  $K_d$  value =  $14.2 \pm 1.7 \mu\text{M}$ .

#### 4.2.5.3 Ketoconazole binding

Experimentally, the inhibition of CYP141 was also measured as the ability to bind ketoconazole. The results showed that ketoconazole was a type II ligand for the CYP141 isoform, as described for the other inhibitors above. The binding of ketoconazole to the pentacoordinate heme iron atom of the CYP141 enzyme causes a complete spin shift of the iron from the mixed spin to the low spin state. This spectral shift is characterized by the Soret band shifting from 418 nm to 422 nm, with a trough at 392 nm (Figure 4.14 main). Difference spectra were also computed for ketoconazole binding to CYP141, displaying maxima and minima at approximately 429 nm and 392 nm (Figure 4.14 inset).

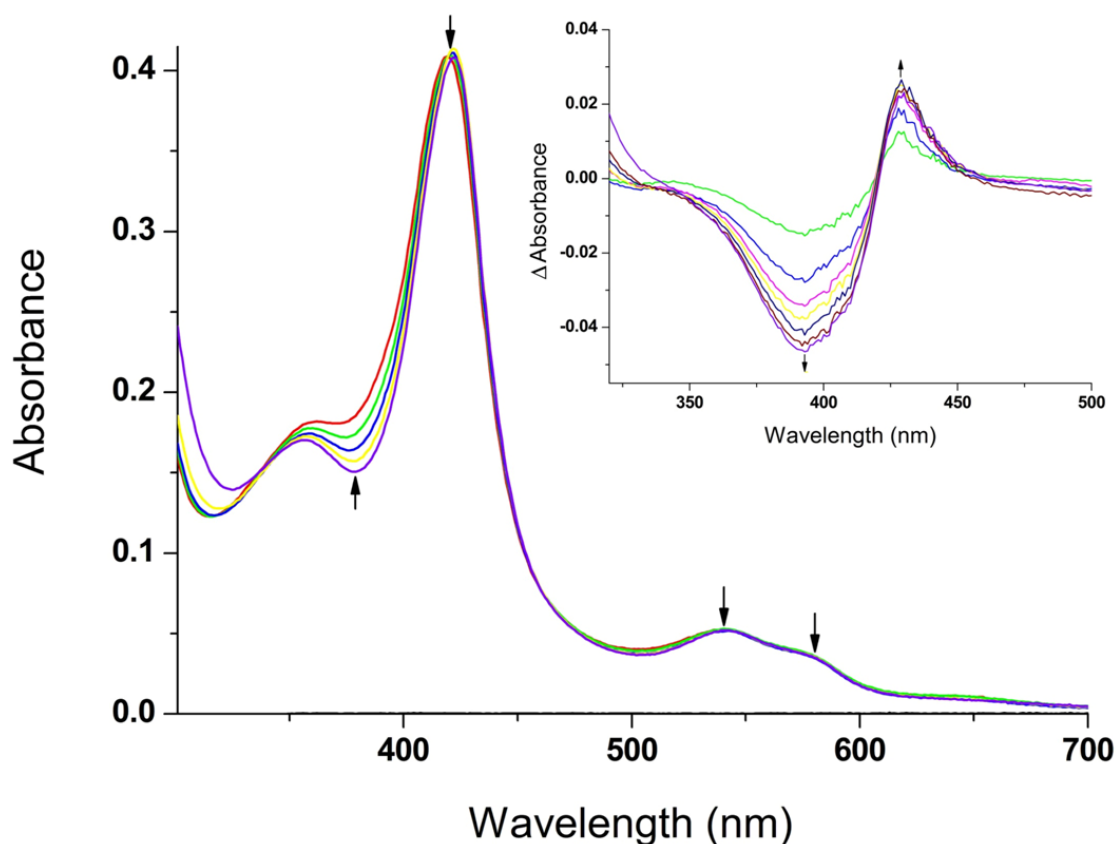


**Figure 4.14. Binding of ketoconazole to CYP141.**

Main figure: shown in the red spectrum is the starting ligand-free form, with  $\sim 4 \mu\text{M}$  CYP141. The CYP141 Soret maximum is at 418 nm. The final spectrum (purple) has a Soret maximum at 422 nm. The arrows indicate directions of absorption change on ligand addition. Shown inset are the difference spectra generated from the data collected and the maximal absorbance changes derived from these data. Arrows indicate directions of absorption change on ligand addition. Difference spectral maxima and minima are at 429 nm and 392 nm, respectively.

The dissociation constant value of ketoconazole was determined from the derived absorbance difference data by plotting inhibitor concentration versus the change in absorbance between the peak and trough in the different spectra. The  $K_d$  value for ketoconazole binding was determined as described in the Methods section (section 2.14) and was  $18.4 \pm 3.2 \mu\text{M}$  (Figure 4.15). Comparisons with other  $K_d$  values for ketoconazole binding to different Mtb P450s reveal that the affinity of binding of ketoconazole to the heme iron of CYP141 is apparently similar to or tighter than to several Mtb P450s (CYP130:  $48.0 \pm 1.8 \mu\text{M}$ , CYP51:  $19.0 \pm 0.9 \mu\text{M}$ , CYP125:  $27.1 \pm 0.9 \mu\text{M}$ ) (121), but weaker than to CYP121:  $3.3 \pm 0.3 \mu\text{M}$  (138).

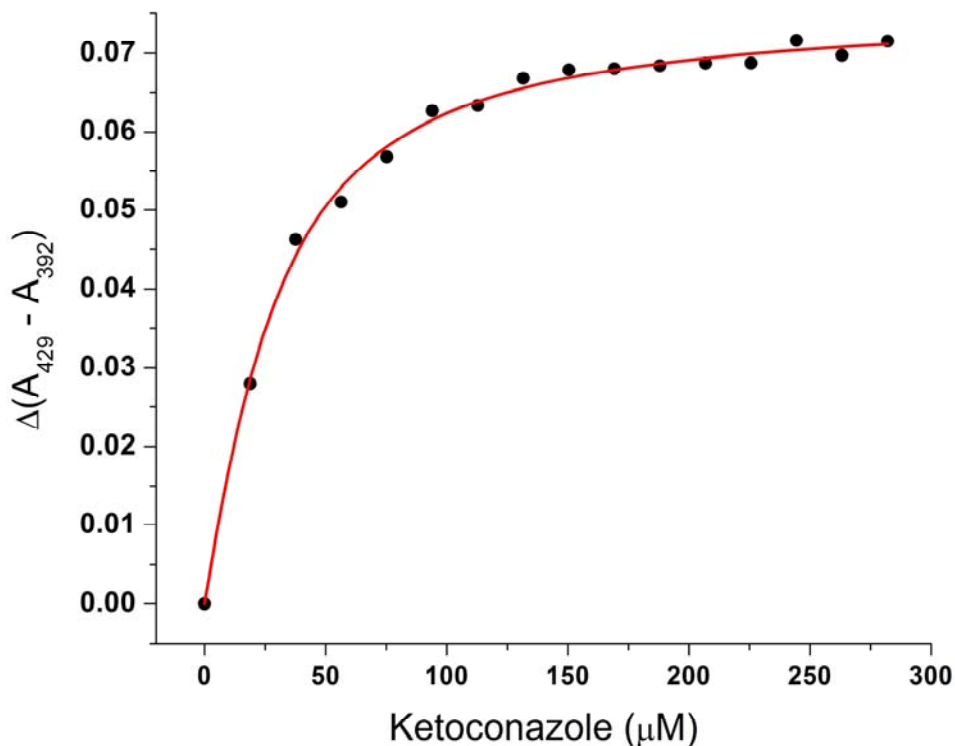


**Figure 4.15. Titration curve for the binding of ketoconazole to CYP141.**

Data from the difference spectra ( $\Delta(A_{429}-A_{392})$ ) were fitted to equation 2.3 (section 2.14), yielding a  $K_d$  value =  $18.4 \pm 3.2 \mu\text{M}$ .

#### 4.2.5.4 Miconazole binding

As with the other azoles, miconazole binds to the heme iron of CYP141, causing a similar shift of the Soret band as seen with the otherazole inhibitors tested (i.e. type II spectral shifts). Miconazole binding leads to a Soret band shift from 418 nm to 422 nm (Figure 4.16 main). The type II spectrum centred at 422 nm is consistent with coordination of a nitrogen atom of the miconazole molecule to the heme iron of CYP141 (either indirect or direct), leading to the red shift of the Soret band. The peak and trough for the type II miconazole-induced CYP141 difference spectra were at approximately 430 nm and 394 nm, respectively (Figure 4.16 inset).

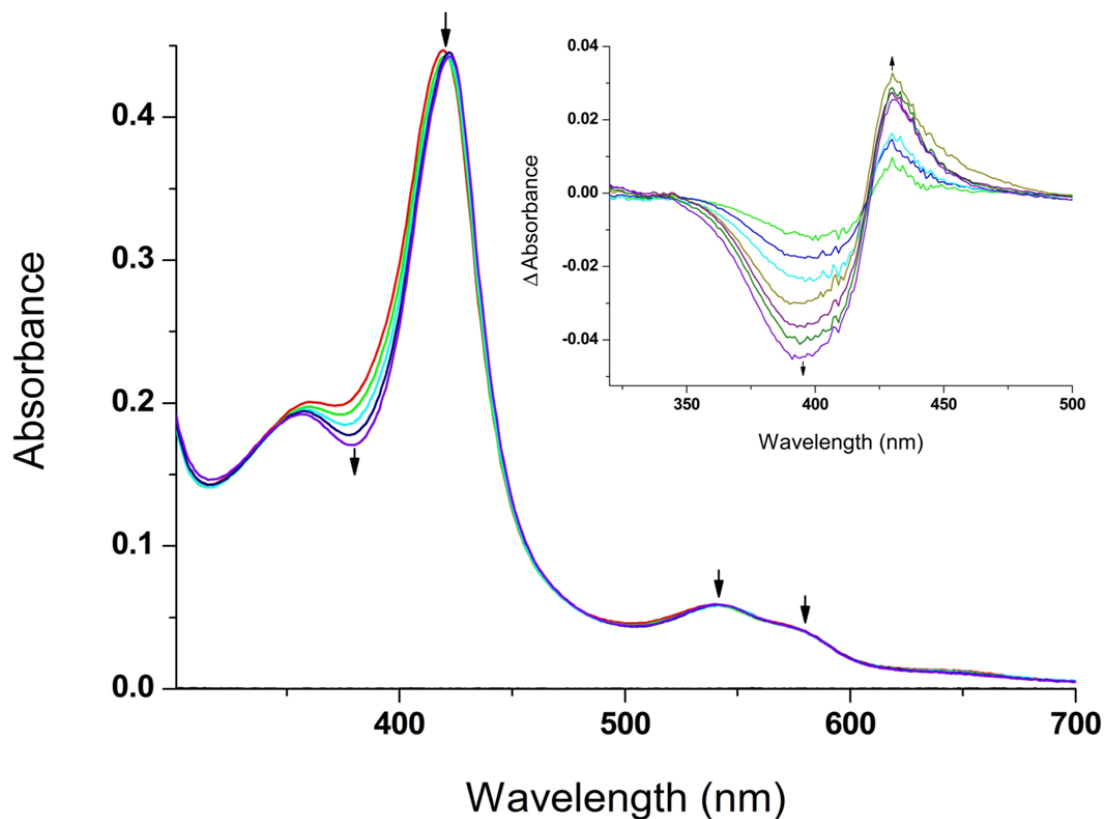


**Figure 4.16. Binding of miconazole to CYP141**

Main figure: shown in the red spectrum is the ligand-free CYP141 enzyme ( $\sim 4.5 \mu\text{M}$ ) with a Soret maximum at 418 nm. The purple spectrum is the final spectrum, which has a Soret maximum at 422 nm. The arrows indicate directions of absorption change on miconazole addition. In the inset are difference spectra generated from the data collected, and show maximal absorbance changes derived from these data. Arrows indicate directions of absorption change on ligand addition. Difference spectral maxima and minima are at 430 nm and 394 nm, respectively.

The data for spectral changes induced on miconazole addition allow determination of a binding constant value for the interaction between miconazole and CYP141: this was  $7.0 \pm 2.1 \mu\text{M}$  (Figure 4.17). The  $K_d$  value for miconazole is higher than the respective values for CYP130 ( $1.70 \pm 0.21 \mu\text{M}$ ) (137), CYP51B1 ( $0.77 \pm 0.04 \mu\text{M}$ ) (119), CYP125 ( $4.6 \pm 0.4 \mu\text{M}$ ) (121), CYP124 ( $1.9 \pm 0.2 \mu\text{M}$ ) (136), and CYP121 ( $< 0.2 \mu\text{M}$ ) (138).

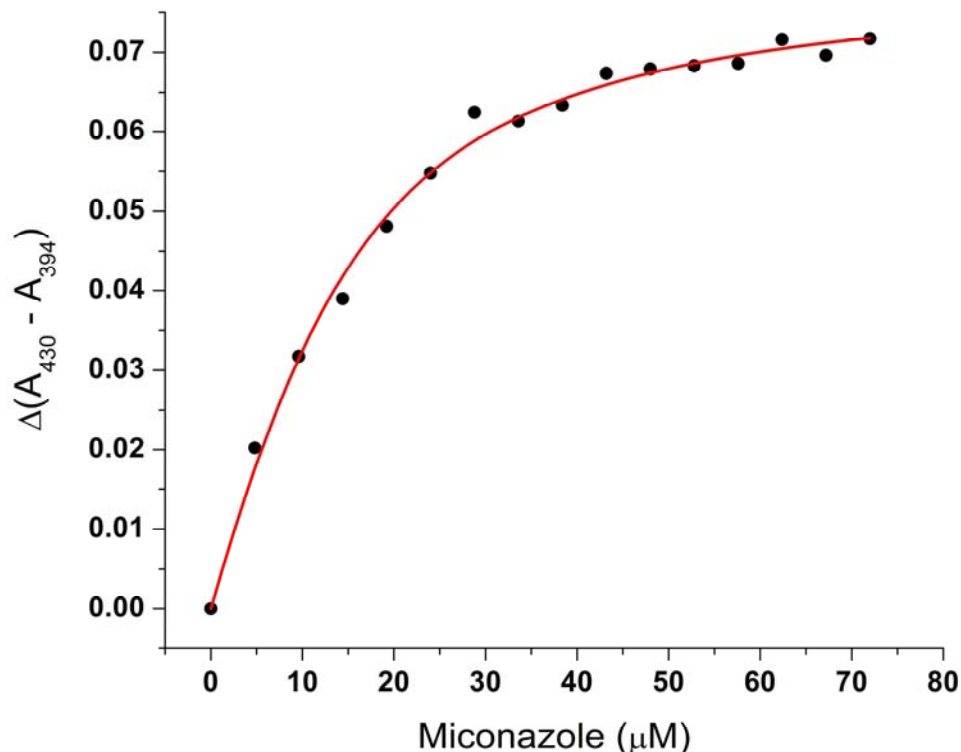


**Figure 4.17. Titration curve for the binding of miconazole to CYP141.**

Data from the difference spectra ( $\Delta(A_{430}-A_{394})$ ) were fitted to equation 2.3 (section 2.14), yielding a  $K_d$  value =  $7.0 \pm 2.1 \mu\text{M}$ .

#### 4.2.5.5 Itraconazole binding

Unusual binding properties were observed for itraconazole ligating to the CYP141 heme iron, with only small type II shifts, suggesting only ~ 10-20% heme iron coordination. Figure 4.18 (main) presents the spectra associated with the binding of itraconazole to the heme iron of CYP141, leading to a shift of the  $\gamma$  band from 418 nm to 420 nm. A more extensive Soret shift is typically observed for azole coordination to P450 heme (to 424-425 nm, but only to 422 nm in the case of e.g. miconazole binding to CYP141), which suggests that the nature of the heme iron coordination is unusual (perhaps via a water ligand, as observed for CYP121(*I49*)) or else that coordination of heme iron is not completed at saturation (e.g. a mixture of populations of CYP141 might exist, where only certain forms are capable of binding the ligand). The difference spectra obtained with CYP141 are clearly consistent with itraconazole being a type II ligand, and displayed maxima and minima at ~439 and 410 nm (Figure 4.18 inset). However, the type II-like absorbance changes are also accompanied by turbidity due to increasing volumes of DMSO solvent and insolubility of itraconazole, meaning that an isosbestic point is not observed.

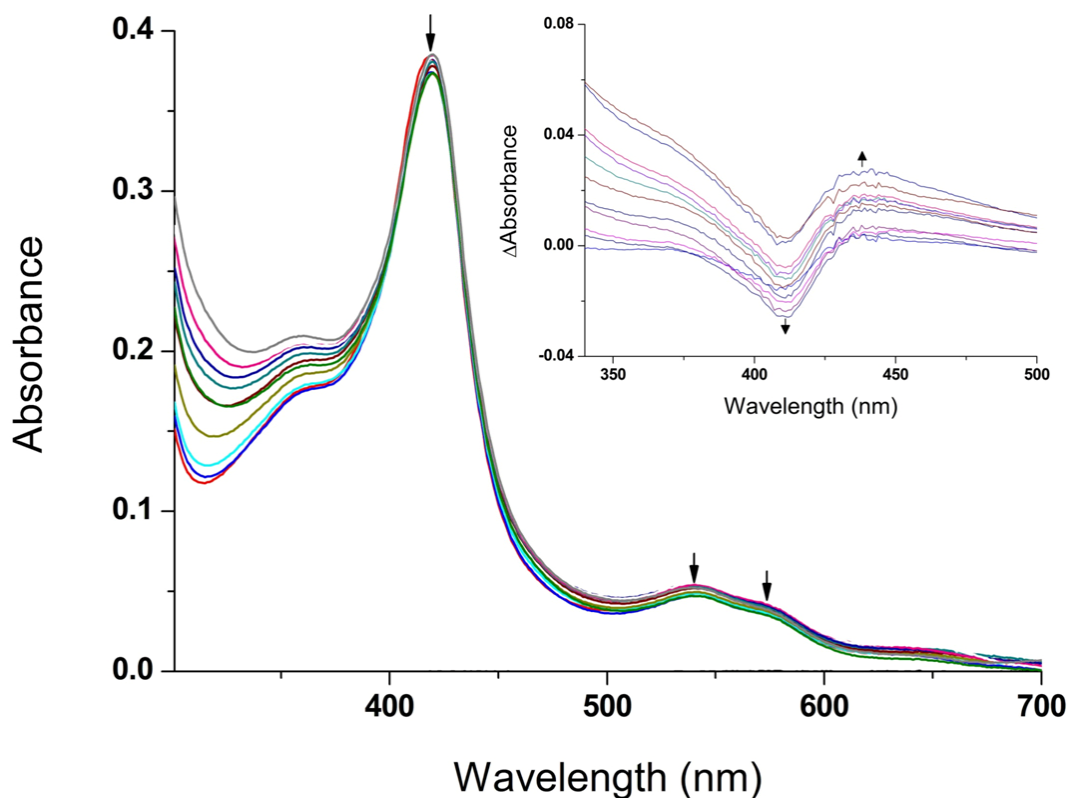


**Figure 4.18. Binding of itraconazole to CYP141.**

Main figure: shown in red spectrum (with highest Soret intensity) is the starting spectrum, containing  $\sim 4 \mu\text{M}$  CYP141, with a Soret maximum at 418 nm. The lowest spectrum is the final spectrum with a Soret maximum at 420 nm. The arrows indicate directions of absorption change on ligand addition at various points in the spectrum. Shown inset are the difference spectra generated from the data collected and the maximal absorbance changes derived from these data. Arrows indicate directions of absorption change on ligand addition. Difference spectral maxima and minima are at 439 nm and 410 nm, respectively.

The binding constant value for the interaction of itraconazole with the CYP141 heme iron was determined by plotting itraconazole concentration versus the change in absorbance between the peak and trough in the difference spectra. The apparent  $K_d$  generated was  $0.27 \pm 0.19 \mu\text{M}$  (Figure 4.19). This apparent  $K_d$  is  $> 100$ -fold lower in CYP141 than in CYP125 ( $30.2 \pm 4.3 \mu\text{M}$ ) (121), suggesting that itraconazole may bind extremely tightly, even though (at apparent saturation) only a small proportion of itraconazole might ligate directly to the CYP141 heme iron. An alternative model could be that CYP141 is heterogeneous in conformation, and that there is selective heme ligation by itraconazole in only a sub-population of the enzyme (and with high affinity). The binding of itraconazole to the heme iron of CYP141 only shifts the Soret band from 418 nm to 420 nm, not to 422 nm like the other drugs, which could be consistent with these models. The crystal structure of the CYP121-fluconazole complex revealed that a predominant drug binding mode was with the azole coordinated to the heme iron via a bridging water 6<sup>th</sup> ligand. This was accompanied

by a shift of the Soret absorbance band in the fluconazole complex to 421 nm, rather than to 425 nm, as is seen in “typical” distal coordination of P450 heme iron with azoles (77, 105, 150, 302). Therefore, there is a previous example of a P450 enzyme which binds an azole drug tightly, but without complete azole coordination directly to its heme iron. The data collected here show that the binding of itraconazole to CYP141 causes a similar extent of red shift of the Soret band as was seen for CYP121/fluconazole, and thus could reflect a similar mode of indirect iron-nitrogen interaction, formed via the distal water molecule. Clearly, a structure of the CYP141-itraconazole complex would be highly informative in clarifying the mode of binding of this azole drug.

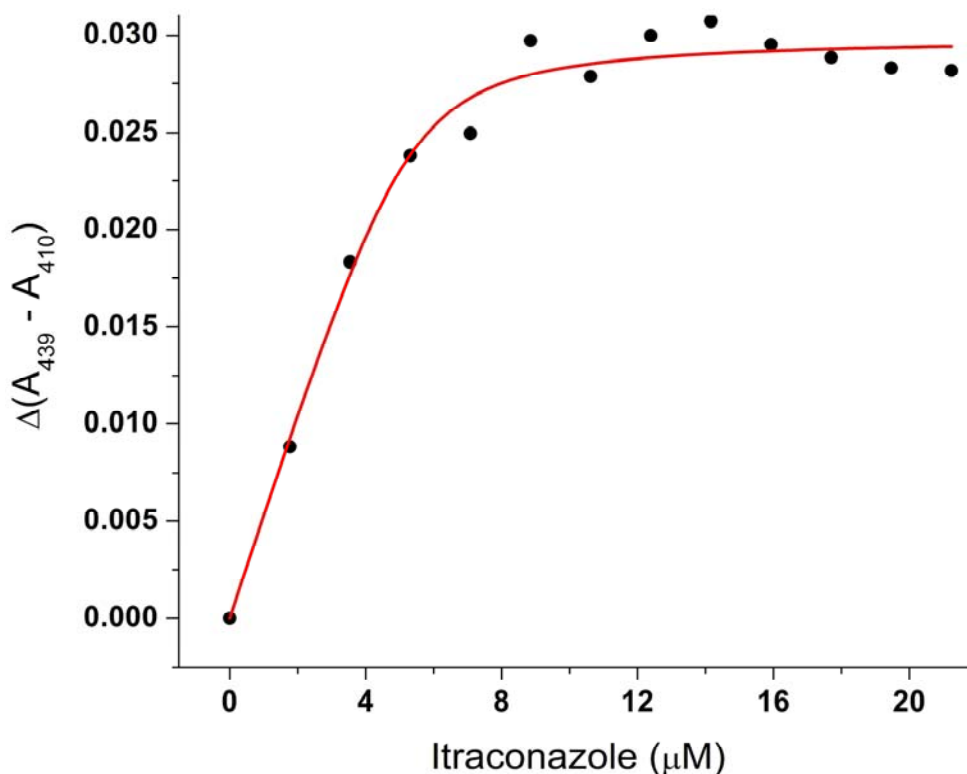


**Figure 4.19. Titration curve for the binding of itraconazole to CYP141.**

Data from the difference spectra ( $\Delta(A_{439}-A_{410})$ ) were fitted to equation 2.3 (section 2.14), yielding a  $K_d = 0.27 \pm 0.19 \mu\text{M}$ .

#### 4.2.5.6 Clotrimazole binding

The azole antifungal drug clotrimazole was also tested for binding to CYP141 to clarify the type of binding for this inhibitor. Experimentally, the addition of clotrimazole to the heme iron induced a shift in the Soret band from 418 nm to 422 nm, due to the replacement of the sixth water ligand to the ferric heme iron by the azole moiety of the drug and/or indirect coordination via the retained water ligand. Smaller intensity changes were also observed in the  $\alpha$  and  $\beta$  bands of the heme at 578 and 542 nm, respectively (Figure 4.20, main panel).

The wavelength shift at the  $\gamma$  band was similar to that given by fluconazole, econazole, ketoconazole, and miconazole. The low-spin Soret band intensity was not affected much by clotrimazole compared with other azoles listed above (i.e. intensity was not decreased). Titration with clotrimazole indicated that the degree of the shift of the low-spin Soret in CYP141 is the same as that found for the triazole-containing drugs, as were the maxima and minima at 427 nm and 391 nm in the difference spectra, respectively (Figure 4.20 inset).

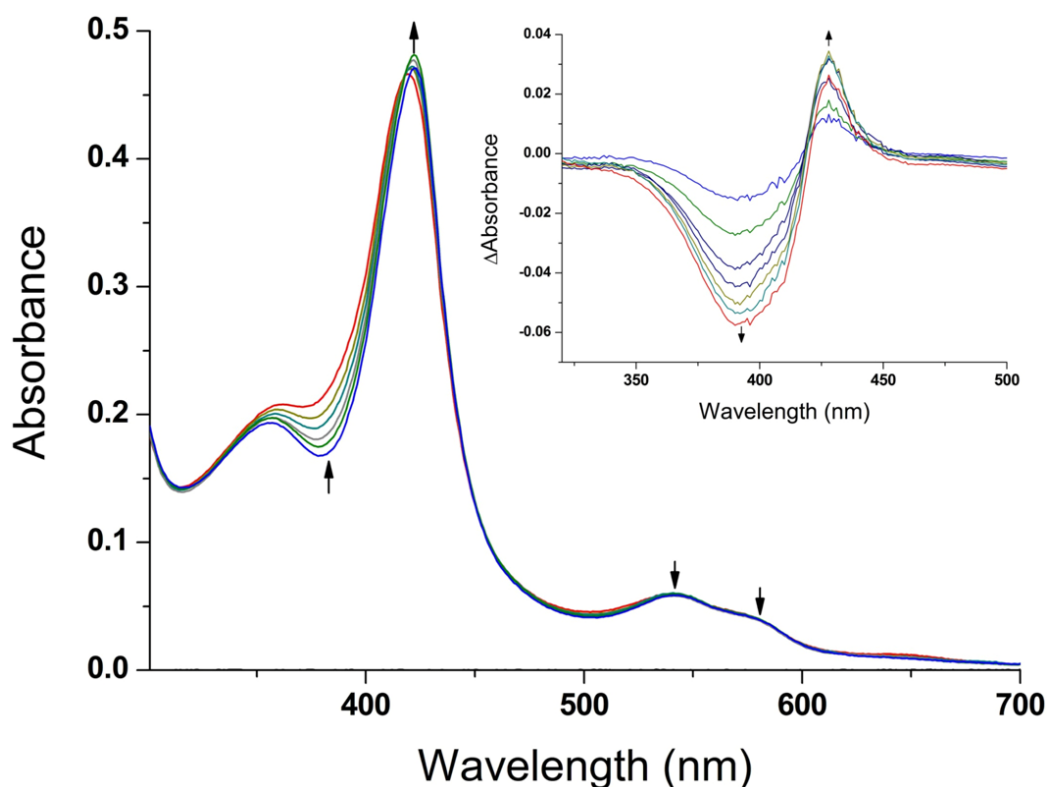


**Figure 4.20. Binding of clotrimazole to CYP141.**

Main figure: shown in the red spectrum is the starting ligand-free spectrum, containing  $\sim 4.5$   $\mu\text{M}$  CYP141, with a Soret maximum at 418 nm. The lower spectrum (blue line) is the final spectrum at near-saturation with clotrimazole, which has a Soret maximum at 422 nm. The arrows indicate the directions of absorption change on ligand addition. Shown inset are the difference spectra generated from the data collected and the maximal absorbance changes derived from these data. Arrows indicate directions of absorption change on ligand addition. Difference spectral maxima and minima are at 427 nm and 391 nm, respectively.

The binding of clotrimazole gave a  $K_d$  value =  $1.08 \pm 0.27$   $\mu\text{M}$  (Figure 4.21), which was considerably stronger than the binding of clotrimazole to CYP125 ( $5.3 \pm 0.6$   $\mu\text{M}$ ) (121), CYP130 ( $13.3 \pm 0.6$   $\mu\text{M}$ ) (137) and CYP124 ( $2.5 \pm 0.1$   $\mu\text{M}$ ) (136), indicating the high affinity of the clotrimazole antifungal for CYP141.

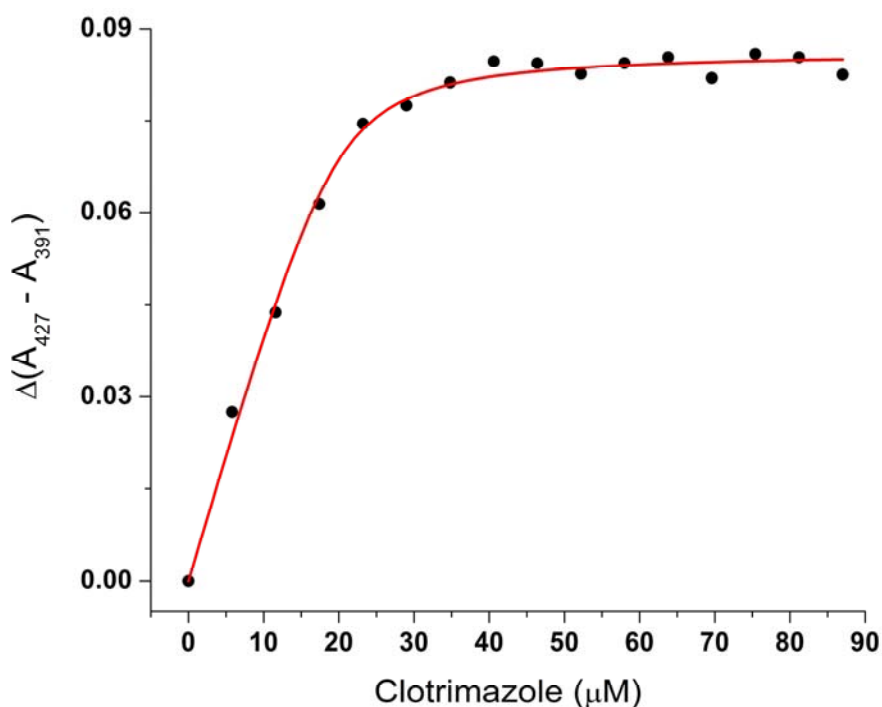


**Figure 4.21. Titration curve for the binding of clotrimazole to CYP141.**

Data from the difference spectra ( $\Delta(A_{427}-A_{391})$ ) were fitted to equation 2.3 (section 2.14), yielding a  $K_d$  value =  $1.08 \pm 0.27 \mu\text{M}$ .

Ligand	$K_d$ ( $\mu\text{M}$ )
Fluconazole	$25.2 \pm 3.6$
Econazole	$14.2 \pm 1.7$
Ketoconazole	$18.4 \pm 3.2$
Miconazole	$7.03 \pm 2.1$
Itraconazole	$0.27 \pm 0.19$
Clotrimazole	$1.08 \pm 0.27$

**Table 4.1. Summary of dissociation constants for azole drugs binding to CYP141.**

#### 4.2.6 Redox potential determination

Potentiometry was applied to CYP141 using a calomel electrode to measure the reduction potential associated with changes in electronic absorption spectrum on progressive reduction of the protein using sodium dithionite, with mediators added to expedite electrical communication between electrode and protein, as described in the Methods (section 2.12). The protein was completely stable during the titration experiment, leading to collection of good spectra in order to generate an accurate midpoint potential value. The spectrum of

fully oxidized CYP141 has a Soret band at 416 nm. Reduction of CYP141 caused a shift of the Soret band to longer wavelength (422.5 nm) (Figure 4.22, inset), this is likely due to the fully reduced form of CYP141. There were also increases in the absorption intensity in the visible region, where the  $\beta$  and  $\alpha$  bands absorb at 529 nm and 557 nm, respectively, in the reduced enzyme (Figure 4.22, main).

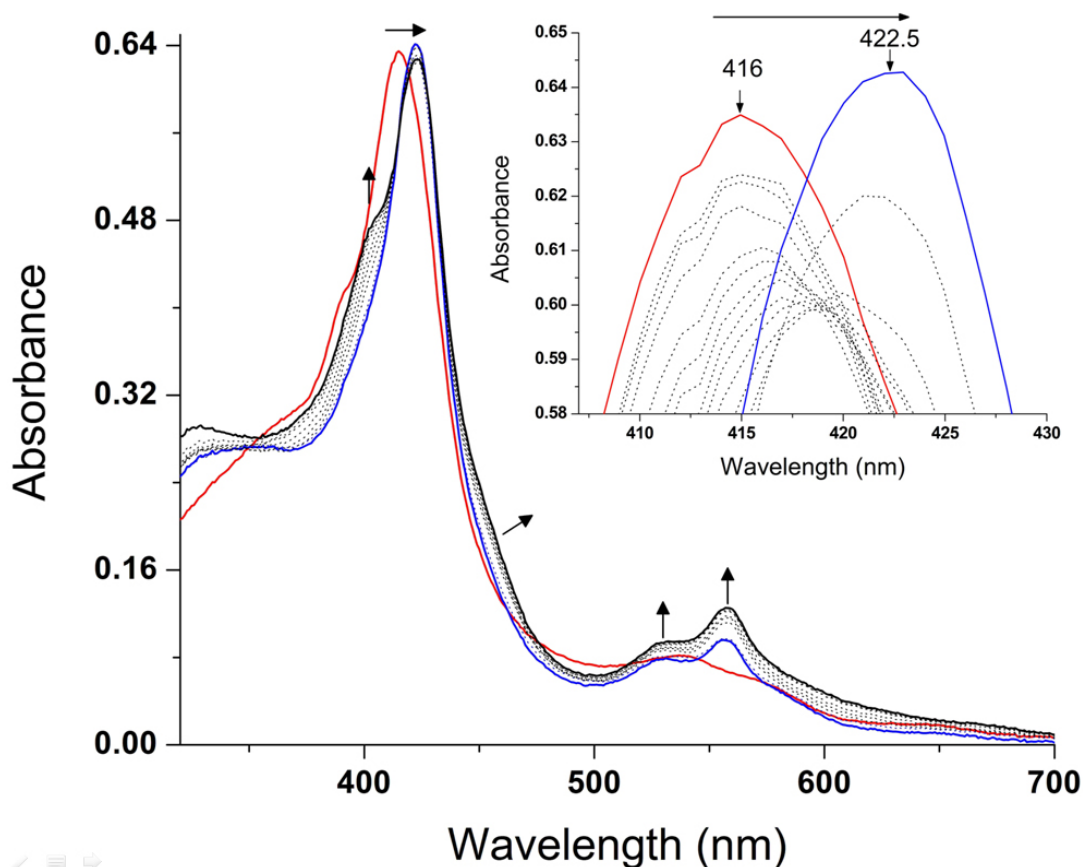


**Figure 4.22. UV-vis spectra of CYP141 during redox titration.**

Main figure: Spectral changes observed for CYP141 ( $\sim 7 \mu\text{M}$ ) collected in 100 mM potassium phosphate (pH 7.0) at 25 °C during a reductive titration as described in the Methods section. The starting spectrum is that of the oxidised, ferric form of CYP141 with Soret maximum at 416 nm and  $\alpha$ - and  $\beta$ -bands at 576 and 538 nm, respectively (red line), taken at a potential = -42 mV vs. NHE. After adding small amounts of sodium dithionite, the Soret shifts to longer wavelength (422.5 nm) with a measured value = -150 mV vs. NHE (blue line). The black line shows the final species formed during reduction at an applied potential of -364 mV vs. NHE. Arrows indicate direction of spectral changes for the major absorption bands as the titration progresses in the reductive direction. Inset shows the expanded spectral changes of the Soret band region during CYP141 reduction.

However, on further reduction by sodium dithionite, the Soret band decreases its intensity at 422.5 nm and development of prominent shoulder at 402 nm, accompanies with

accumulation of reduced mediators at 325 nm. This indicates that the reductive progress is probably showing only reduction of mediators after the heme reduction is completed. In comparison with other P450s such as CYP126, which show the reduced Soret band shifting to shorter wavelength (see section 3.2.6), CYP141 show a distinct Soret feature that is observed in the reduced state at longer wavelength (422.5 nm). However, this characteristic is quite similar to CYP144, which exhibits a reduced heme Soret band with decreased intensity and shifted from 420.5 nm (ferric) to 425 nm (ferrous) (135).

The heme Soret band was restored to original wavelength and intensity by addition of appropriate amounts of ferricyanide (on reoxidation, data not shown). The spectral changes observed during the redox titration of CYP141 are displayed in Figure 4.22. Ferric CYP141 was consistently found to be in a mixed spin state form, with proportions of both low- and high-spin forms of the heme iron. However, the low-spin form predominates (see the red spectrum in Figure 4.22).

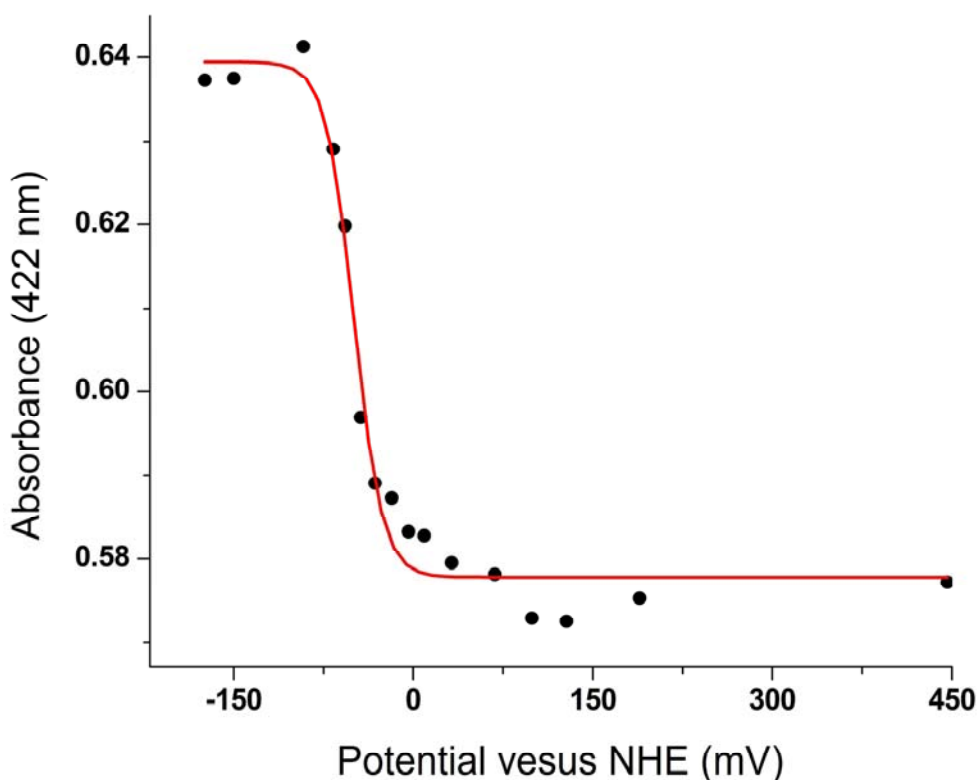


**Figure 4.23. Plot of absorbance change versus potential ( $E'$ , mV versus NHE) during reductive titration.** The data at 422 nm (reflecting a major change in absorption between oxidized and reduced enzymes) versus reduction potential were fitted to a single electron Nernst function, as described in the Methods (section 2.12). The midpoint reduction potential for the CYP141 heme iron  $\text{Fe}^{3+}/\text{Fe}^{2+}$  transition was determined from the data fit. The potential determined was  $-50 \pm 2$  mV.

All data were recorded across the range from oxidized to reduced heme cofactor, and were then analyzed by plotting the absorbance at 422 nm, which correlated with substantial absorption changes that occurred during the apparent conversion between oxidized and reduced forms. The data for the plot is fitted well to the Nernst equation as described in the Methods (section 2.12). A plot of the normalized absorbance at this wavelength as a function of potential is shown in Figure 4.23. The collected data were fitted to the Nernst equation (for a single electron process), indicating that the CYP141 heme iron possesses a very positive redox potential of  $-50 \pm 2$  mV (Figure 4.23).

#### **4.2.7 pH dependence of heme ligation in CYP141**

To understand the nature of the reduced form of ferrous CYP141 in the formation of a ferrous-thiol coordinated form (suggested by the development of a Soret feature that is at 422.5 nm in the reduced spectrum, together with the features in the 500-600 nm region, see Figure 4.24), a pH titration was done to examine the conversion of CYP141 between ferrous thiol-coordinated and thiolate-coordinate forms. The titration was performed by measurement of the absorption spectrum in 100 mM potassium phosphate, pH 6.0, with the pH titrated between 6.0 and 10.32 using potassium hydroxide. As shown in Figure 4.24, through the pH titration of CYP141, it was found that the absorption maximum of the Soret band was very sensitive to pH changes in the range between 6 and 10.32. At pH 6.0, the oxidized form absorbed at a wavelength maximum of 415 nm. However, after reduction by sodium dithionite, the Soret peak shifted to 417 nm. At pH 8.14, the reduced Soret maximum was located at 423 nm (Figure 4.24).

As the pH was lowered (pH 6.0) the absorption maximum of the Soret band was consistently shifted toward shorter wavelengths (417 nm). In addition, the absorption maximum of the Soret band moved toward longer wavelengths (423 nm) at higher pH values (e.g. pH 8.14). Moreover, increasing the pH also produced an increase of intensity of the CYP141 Soret band. These data suggest that at lowest pH tested (6.0) the ferrous P450 formed at least some of the thiolate-coordinated species which often has a Soret maximum at ~410-412 nm. In contrast, at high pH (8.14) the reduced form reached a maximum absorption at 423 nm, more typical of a near-completely thiol-coordinated P450.

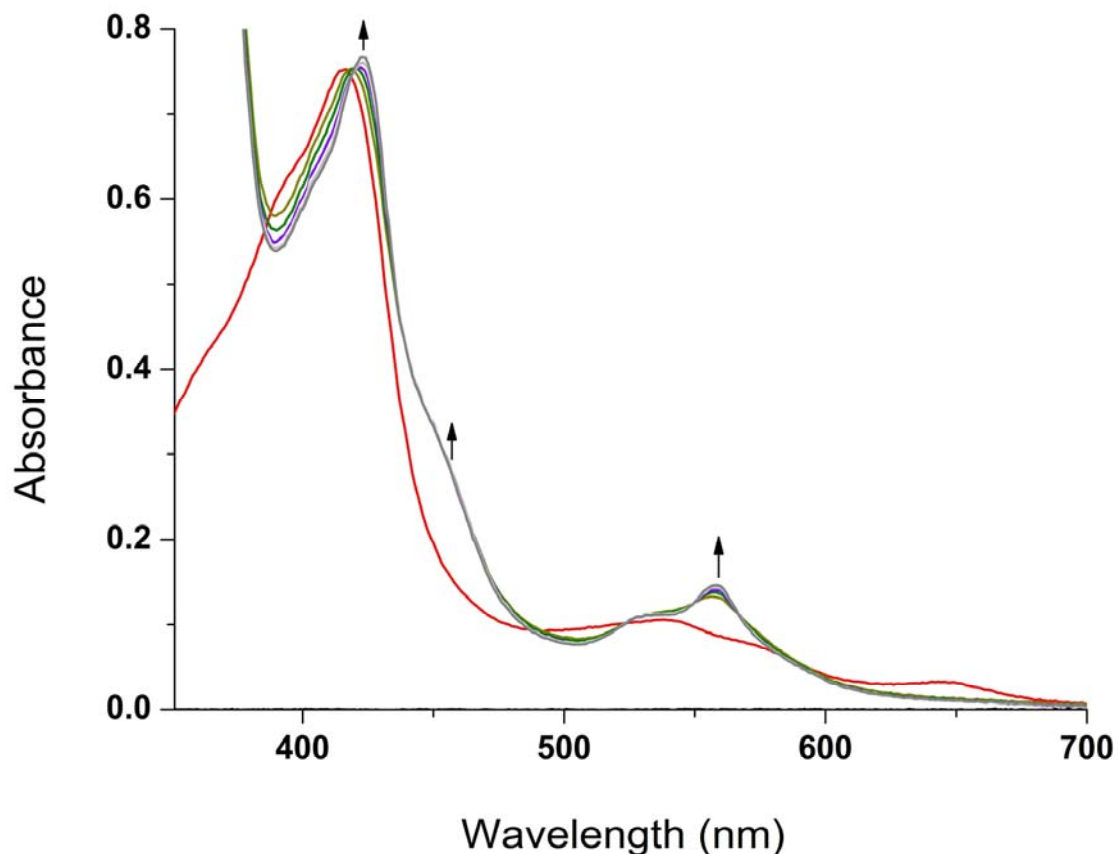


**Figure 4.24. pH dependence of the optical properties of CYP141 in its reduced form.**

The  $\text{Fe}^{\text{III}}$  CYP141 ( $\sim 7.8 \mu\text{M}$ ) was reduced by sodium dithionite to the  $\text{Fe}^{\text{II}}$  form at pH 6.0. The starting (red) spectrum is the oxidized form of CYP141 with Soret maximum at 415 nm and  $\alpha$ - and  $\beta$ -bands at 557 and 528 nm, respectively. Arrows indicate direction of spectral changes during pH changes (increases). At pH 9.0, the Soret band reaches an absorption maximum at 423 nm. The spectra shown were collected at pH values 6.0, 6.56, 7.08, 7.71, and 9.0.

The oxidized Soret absorption is also clearly affected by buffer pH. Oxidized CYP141 was prepared in different pH buffers, and exhibited Soret band maxima at different wavelengths. For instance, at pH 7.5, the Soret band was at 417-418 nm. However, at lower pH values, such as pH 7.0 and pH 6.0, Soret absorption maxima were at 416 and 415 nm, respectively. In addition, the mixture of spin states (high-spin and low-spin) is a specific characteristic of this enzyme, and is also apparently affected by pH (detailed in Figure 4.25).

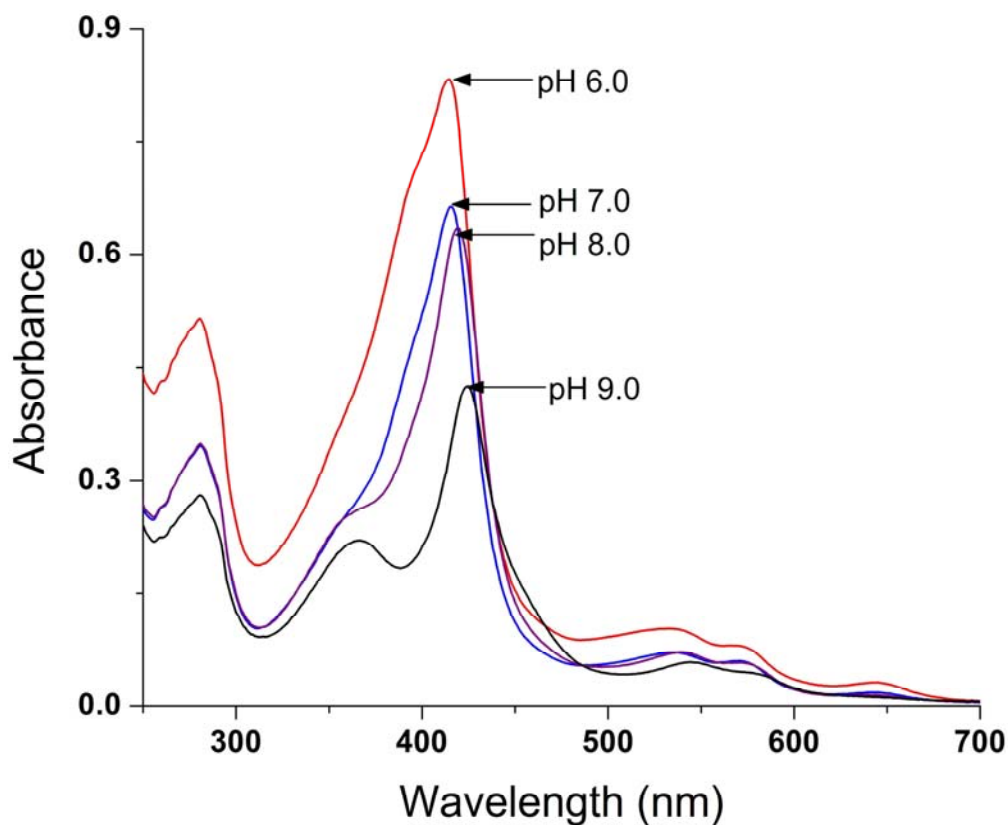


**Figure 4.25. The influence of pH on the spectrum of the ferric CYP141 enzyme.**

The red line shows the ferric heme spectrum at pH 6.0, the blue line at pH 7.0, the purple line at pH 8.0, and the black line at pH 9.0.

Figure 4.26 shows a plot of the data from the pH titration of the ferrous CYP141. The data were fitted accurately using a single  $pK_a$  equation to generate a midpoint ( $pK_a$ ) value of  $6.6 \pm 0.1$  (Figure 4.26). This data fit was associated with a  $R^2$  value of 0.98186. Also shown in Figure 4.26 are fits to the data with the  $pK_a$  value constrained to 6.4 (blue line,  $R^2$  value of 0.97558) and 6.8 (magenta line,  $R^2$  value of 0.97075). While these data reinforce that the fits become poorer with deviation of the  $pK_a$  from 6.6, the changes in the  $R^2$  values are not as large as were observed for the CYP126 refitting shown in Figure 3.22, which likely reflects the fact that the  $A_{423}$  data do not reach a plateau at the lower pH values for CYP141. As was also observed for CYP126, there are apparent increases in heme thiolate protonation at basic pH. This is counter-intuitive, and may (as was discussed in chapter 3 for CYP126) indicate that the group titrated is another amino acid, and that basic pH-induced structural rearrangements of uncertain nature result in altered environment of the CYP141 heme thiolate, and a greater tendency for it to become protonated. Further spectroscopic and structural studies are clearly required to discover the origins of the unusual pH dependence of ferrous heme spectral changes in both CYP141 and CYP126.

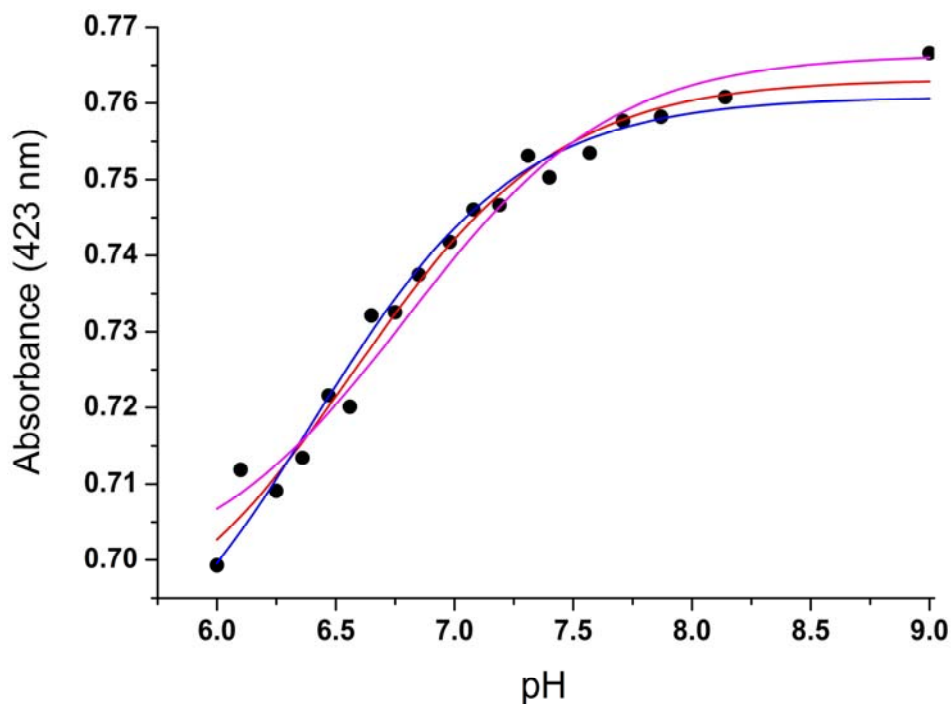


**Figure 4.26. Determination of the midpoint pH ( $pK_a$ ) for the ferrous heme optical transition in CYP141.**

The figure shows a plot of data from the pH titration of CYP141 ( $\sim 7.8 \mu\text{M}$ , Figure 4.24) with spectra for the  $\text{Fe}^{\text{II}}$  species collected across the pH range from 6.0 to 10.32 (data up to pH 9.0 are shown). The data at 423 nm were fitted to a single  $pK_a$  equation producing a  $pK_a$  value of  $6.6 \pm 0.1$  (red line). The fits shown in blue and magenta were done with  $pK_a$  values constrained at 6.4 and 6.8, respectively.

#### 4.2.8 Differential Scanning Calorimetry

In initial attempts to understand the stability of CYP141 under conditions of increasing temperature, DSC studies were performed with the enzyme in its native form and in complex with clotrimazole, which showed the tightest binding (lowest  $K_d$ ) to this P450 while producing a near-complete conversion to a ligand-bound species.

##### 4.2.8.1 DSC analysis of ligand-free CYP141

Investigations of thermal stability of CYP141 were carried out using DSC to determine the unfolding temperature ( $T_m$  or multiple  $T_m$  values) of the native, ligand-free CYP141. DSC data provide information of the folded state of the protein, revealing the melting temperature at which protein becomes unfolded and loses activity. Figure 4.27 shows the results of DSC scans conducted with native CYP141 isolated from *E. coli* in the absence of anyazole inhibitor. The scans were carried out from  $20^\circ\text{C}$  to  $90^\circ\text{C}$  with a scan rate of  $60^\circ\text{C/h}$ , and the transition was fitted with non-two-state model as described in the Methods chapter (section 2.15).

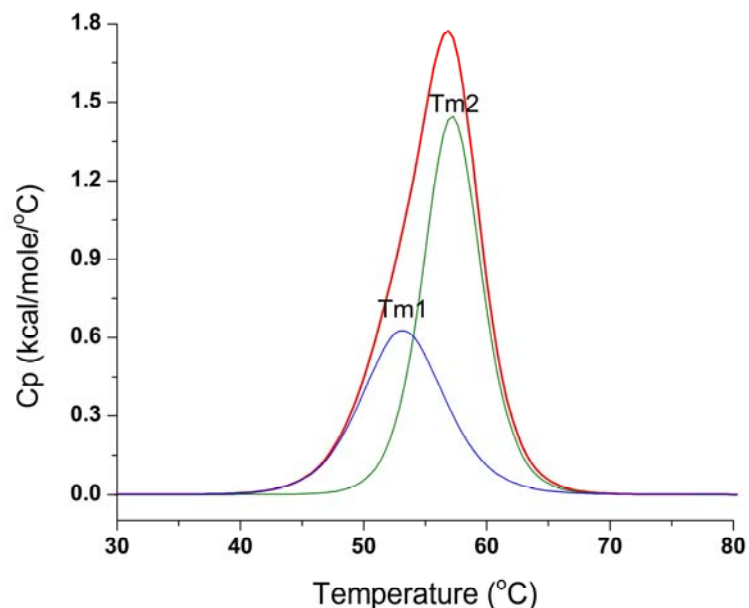


**Figure 4.27. DSC analysis of ligand-free CYP141.**

The protein sample in the absence of ligand was dialysed in 10 mM potassium phosphate, pH 7.5 and heated from 20 °C to 90 °C with a scan rate of 60 °C/h. A buffer baseline was subtracted from the raw data, and the scans were normalized for molar concentration and scan rate. The experimental raw data were fitted to deconvolute the melting temperatures using Origin software (OriginLab, Northampton MA). Two  $T_m$  values are indicated with  $T_{m1}$  at 53.2 °C and  $T_{m2}$  at 57.2 °C.

The thermal denaturation of the protein was found to have a melting transition with a midpoint peak at 56.6 °C. The peak contains two separate  $T_m$  values that are consistent with the different unfolding temperature of C- and N-terminal domains. One domain unfolds at 53.2 °C and the other at 57.2 °C (Table 4.2). The typical structure of P450 enzymes is with two domains, an alpha domain and a beta domain. The DSC data for CYP141 revealed two distinct unfolding temperatures, and it is predicted that the distinct unfolding of the two domains of the enzyme may relate to these unfolding temperatures. However, to date there are no data to indicate the link between alpha/beta domain structural disruption and the two melting temperatures occurring during DSC scans.

#### 4.2.8.2 DSC analysis of clotrimazole-bound CYP141

Similar experiments were performed with highly purified CYP141 in the presence of clotrimazole inhibitor, which was shown previously to binding very tightly to the heme iron of CYP141, with a  $K_d$  value of 1.08  $\mu$ M from optical titration (Figure 4.21). In Figure 4.28, the DSC thermogram fits best to a non-two-state model with two peaks using standard equilibrium equations. The binding of clotrimazole causes the midpoint thermal peak of CYP141 to increase from 56.6 °C to 57.5 °C, an increase of 0.9 °C. In addition, it also revealed two distinct and separate unfolding transitions with  $T_m$  values at 55 °C and at

58.3°C (Table 4.2). The CYP141-clotrimazole complex DSC measurements were repeated several times to confirm that these small changes in unfolding temperatures occurred on binding clotrimazole. It is likely, therefore, that clotrimazole ligand binding results in only a small change in stabilization of the protein structure (Figure 4.29), demonstrating that this enzyme adopts a slightly more stable conformation upon clotrimazole binding.

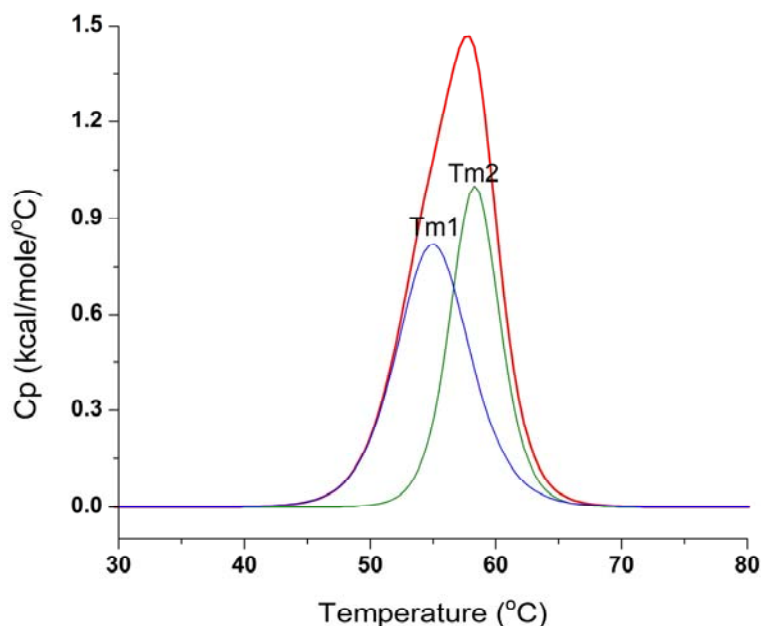


**Figure 4.28. DSC analysis of the clotrimazole-bound form of CYP141.**

The CYP141 protein in the presence of clotrimazole (50  $\mu$ M) was heated from 20 to 90 °C with a scan rate of 60 °C/h. The data were fitted using Origin software. The fitting results indicate that there are two distinct unfolding events with  $T_m$  values of 55 °C and 58.3 °C.

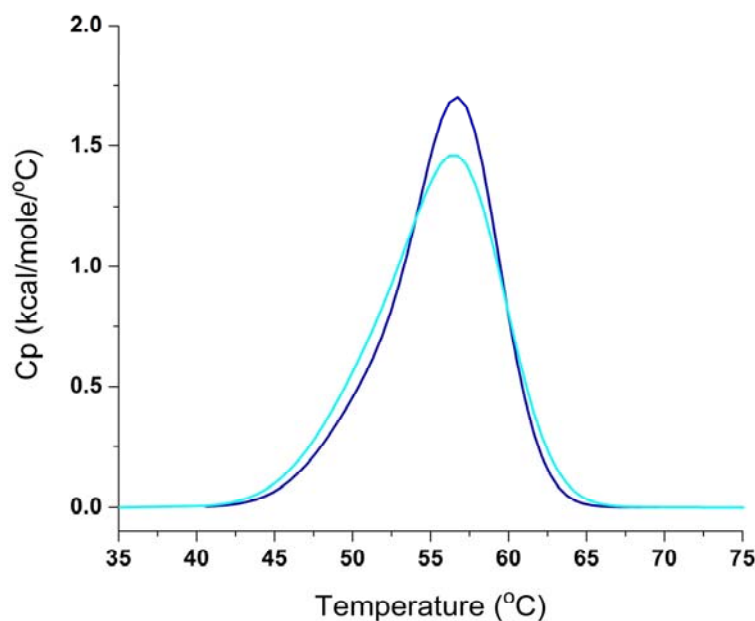


**Figure 4.29. Superimposed DSC thermograms for ligand-free and clotrimazole-bound CYP141.** Protein samples in the absence (blue) and presence of clotrimazole (cyan) were heated from 20 to 90 °C, showing the thermal transitions and  $\Delta H_v$  in each case. Full details of the  $T_m$  and  $\Delta H_v$  values are shown in Table 4.1.

Sample	$T_m$	$T_{m1}$	$\Delta H1$	$T_{m2}$	$\Delta H2$
	$^{\circ}C$	$^{\circ}C$	<i>kcal/mol</i>	$^{\circ}C$	<i>kcal/mol</i>
CYP141	56.6 ± 0.06	53.23 ± 0.98	5.58 ± 1.85	57.20 ± 0.16	9.06 ± 1.81
CYP141-clotrimazole	57.5 ± 0.07	55.04 ± 0.64	6.34 ± 1.56	58.34 ± 0.17	5.22 ± 1.53

**Table 4.2. Summary of the thermodynamic data for CYP141 from DSC analysis.**

$T_m$  indicates the midpoint melting temperature of CYP141 in presence and absence of clotrimazole.  $T_{m1}$  and  $T_{m2}$  indicate the two component melting temperatures identified from the two deconvoluted curves. The enthalpy of unfolding ( $\Delta H$ ) for the deconvoluted curves is also shown. The data were fitted using Origin software.

#### 4.2.9 Electron paramagnetic resonance spectroscopy

In order to examine the electronic state of the CYP141 heme iron in the absence or presence of a ligand (ketoconazole), EPR was used to report on the spin state of the CYP141 ferric heme iron, and on the nature and orientation of the heme iron ligand(s).

The EPR spectrum of the inhibitor-free form of the wild-type CYP141 heme domain is shown in Figure 4.30. Clearly discerned are the signatures of the low-spin form of cytochrome P450, with  $g$ -values of 2.44 ( $g_z$ ), 2.25 ( $g_y$ ), 1.91 ( $g_x$ ). Of interest, however, is that there is a proportion of the enzyme present as high-spin ferric P450 heme iron, with  $g$  values at 7.95, 3.59, 1.70, and assigned to a penta-coordinated heme iron with a cysteinate fifth ligand and the sixth aqua ligand displaced. The zero-field splitting parameters for the high-spin species with the above  $g$ -values indicates some heterogeneity of this species, as does the minor structural heterogeneity observed at the other  $g$ -values. This particular combination of high-spin and low-spin forms is also observed for the cysteinate coordinated hemes of selected other cytochromes P450 (303, 304). Other work in this chapter highlights the modulation of the spin-state of CYP141 by pH, reinforcing the sensitivity of the CYP141 heme to spin-state change.

The mixture of both the high- and low-spin forms of P450 was also found in microsomal preparations and in liver slices (305), with comparable  $g$  values to those of CYP141, revealing some similarities in heme coordination between CYP141 and eukaryotic P450s. Therefore, the data from the EPR spectra of CYP141 indicates that thiolate coordination has been maintained to the heme iron, and the EPR spectrum is virtually identical to those reported previously for other well-characterised P450s, including Mtb CYP51B1 (sterol demethylase) ( $g$  – 2.44, 2.25, 1.91) (218), Mtb CYP121 ( $g$  – 2.47, 2.25, 1.90) (138), P450 cam ( $g$  – 2.46, 2.26, 1.91) (246), P450 BM3 ( $g$  – 2.42, 2.26, 1.92) (247) for the low-spin

components, and for liver cytochrome P450 from rabbit liver (low-spin:  $g = 2.44, 2.26, 1.91$ ; high-spin:  $g = 8.0, 3.70, 1.70$ ) (306), and CYP120A1 from *Synechocystis* sp. PCC 6803 (rhombic signal at  $g = 2.41, 2.24, 1.91$  for low-spin ferric heme and at  $g = 7.97, 3.54, 1.68$  for high-spin ferric heme) (307) for both low-spin and high-spin components.

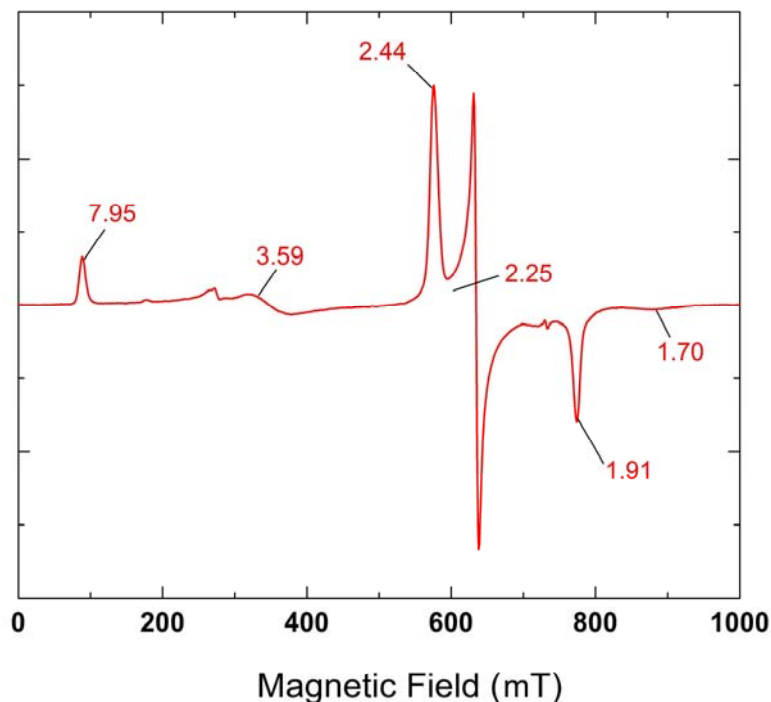


**Figure 4.30. EPR spectrum obtained for solution state ligand-free CYP141.**

EPR spectra were collected with a protein concentration of 200  $\mu\text{M}$  in 100 mM potassium phosphate, pH 7.5 including 10% glycerol. EPR conditions were as follows: microwave frequency, 9.67 GHz; power, 2 milliwatts; temperature, 10.0 K; modulation amplitude, 10 G.  $g$ -values are detailed on the figure.

On binding of clotrimazole to CYP141, a rhombic spectrum is obtained that is shifted and sharpened with respect to the ligand-free enzyme. The high-spin form(s) were no longer present in the EPR spectrum (Figure 4.31). When clotrimazole binds, the  $g$  values were significantly altered from those of the ligand-free form (2.44, 2.25, 1.91 for ligand-free, compared with 2.50, 2.26, 1.87 for clotrimazole-bound CYP141) (Figure 4.31). The  $g_z$  value has reached the “threshold” value of 2.50, and in this case there appears clear evidence that this species arises from distal coordination of the CYP141 heme iron by a nitrogen atom from clotrimazole.

In addition, the  $g_y$  peak widths are similar, and amplitudes are less intense than for the ligand-free CYP141 at the  $g_z$  and  $g_x$  values (Figure 4.32). Normally, the binding of substrate causes a change of the heme iron from the low-spin to the high-spin form (type I

shift). In contrast, the binding of clotrimazole (an inhibitor) to CYP141 has collapsed the high-spin form and this correlates with an increase in the low-spin character of the heme iron (type II shift). These features indicate that clotrimazole coordinates to the iron, replacing the water molecule as the sixth axial ligand.

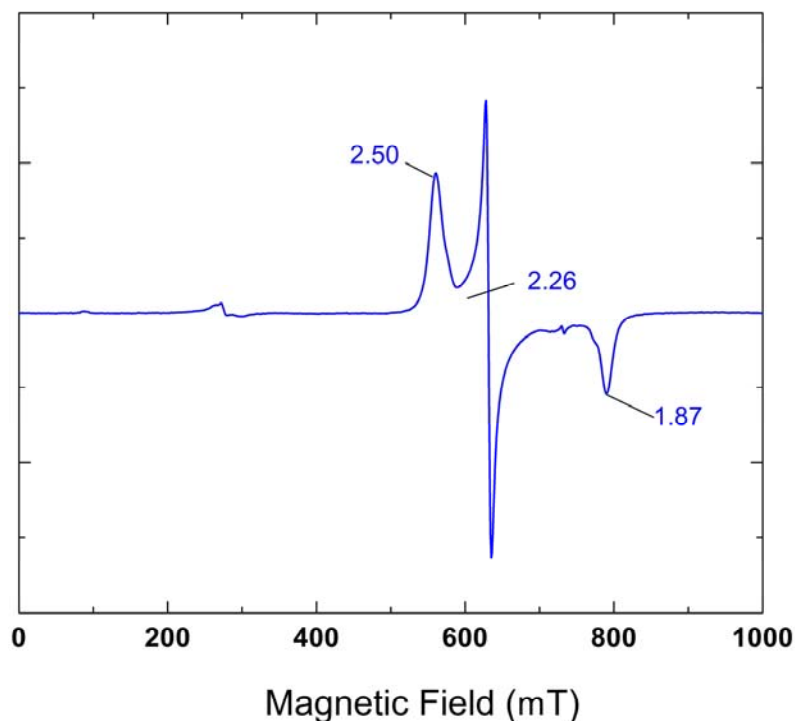


**Figure 4.31. EPR spectrum obtained for solution state clotrimazole-bound CYP141.**

EPR spectra were collected with a protein concentration of 200  $\mu\text{M}$  in 100 mM potassium phosphate, pH 7.5 including 10% glycerol and with the final clotrimazole concentration of 200  $\mu\text{M}$ . EPR conditions were as follows: microwave frequency, 9.67 GHz; power, 2 milliwatts; temperature, 10.0 K; modulation amplitude, 10 G.  $g$ -values are detailed in the figure.

A comparison of the EPR spectra of the clotrimazole-bound form of wild-type CYP141 and the ligand-free CYP141 is shown in Figure 4.32. It can be seen clearly that signals for the high-spin form(s) of CYP141 observed in the ligand-free spectrum virtually disappear in the clotrimazole-bound form. In the clotrimazole-bound complex, there appears to be one predominant species with the  $g_z$  and  $g_x$  signals broadened. The homogenous spectrum of the CYP141-clotrimazole sample indicates that the ligation of azole to the heme iron was apparently near-complete. Clotrimazole produces a type II optical shift, and the EPR spectrum observed here is similar to that described recently for azole inhibitors binding to other P450s such as CYP144 (ligand-free:  $g_z - 2.42$ ,  $g_y - 2.25$ ,  $g_x - 1.93$ , and in complex with clotrimazole:  $g_z - 2.44$ ,  $g_y - 2.26$ ,  $g_x - 1.92$ ) (135). This is explained by thiolate/azole ligation of the CYP144 heme iron with clotrimazole as the 6<sup>th</sup> ligand.

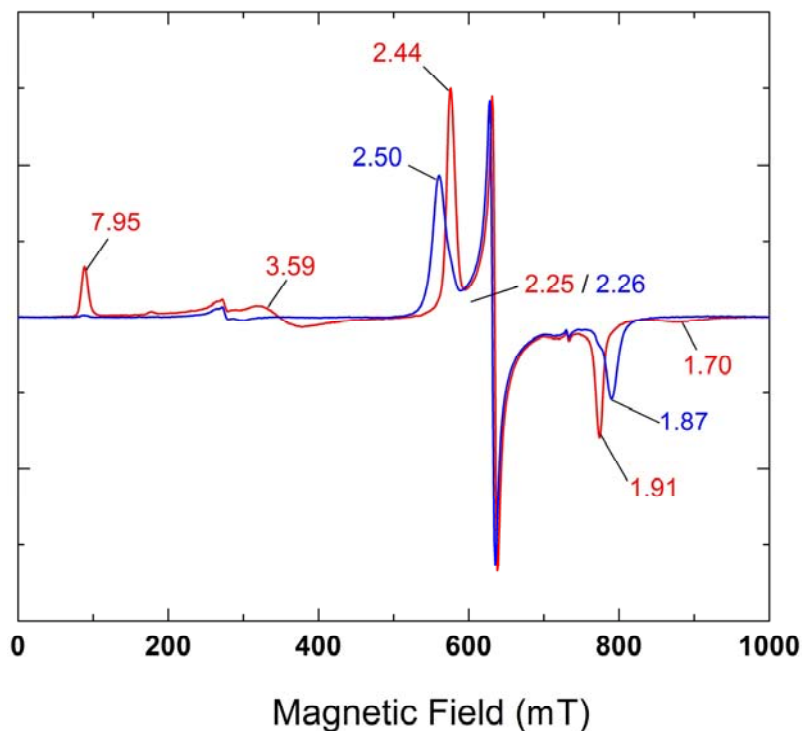


**Figure 4.32.** EPR spectra overlaid for solution state ligand-free CYP141 (red) and for the clotrimazole-bound form (blue). Protein concentration was 200  $\mu\text{M}$ . EPR conditions were: microwave frequency, 9.67 GHz; power, 2 milliwatts; temperature, 10.0 K; modulation amplitude, 10 G. *g*-values are detailed in the appropriate colour code.

#### 4.2.10 Magnetic circular dichroism of CYP141

MCD provides detailed information on the cysteine status (e.g. cysteine thiolate versus cysteine thiol), as well as on the transition of the spin state on the binding of substrate/inhibitor (308-310). Therefore, to study the axial coordination in the ferric heme of CYP141, MCD spectroscopy was used to investigate CYP141 heme iron. The experiments were done in collaboration with Dr Myles Cheesman at the University of East Anglia.

Figure 4.33 (panel A) shows that the electronic absorption spectrum of ferric CYP141 has characteristic bands at 417.5, 537 and 574 nm, and a small peak corresponding to a minor proportion of high-spin state CYP141 was observed at  $\sim 650$  nm. The major features in the UV-visible MCD spectra of CYP141 state in the same sample were obtained as follows, with intensities in  $\epsilon$ : 359.6 nm (-57.9); 408 nm (+136.2); the crossover at 420 nm (0); and the small band found at 390 nm (+15.9). Additional bands are found at 523 nm (+49.7); 557 nm (+27.3); 564 nm (0); 577 nm (-90.2). The 420 nm crossover (zero point of the derivative-shaped feature) in the Soret region of the MCD spectrum is close to the Soret

peak in the absorption spectrum at 417.5 nm as are analogous features of P450cam (254, 311), P450 BM3 (312), and CYP121 (138). In the visible region, the MCD spectrum of CYP141 has a second derivative-shaped feature with a peak at 557 nm, a trough at 577 nm, and a crossover at 564 nm. This feature and its band positions correspond with analogous features in the MCD spectra of ferric P450s such as CYP121, which displays a UV-visible absorption spectrum with peaks at 416.5, 565 and 538 nm (138). These data are unique to low-spin hemes with thiolate ligation.

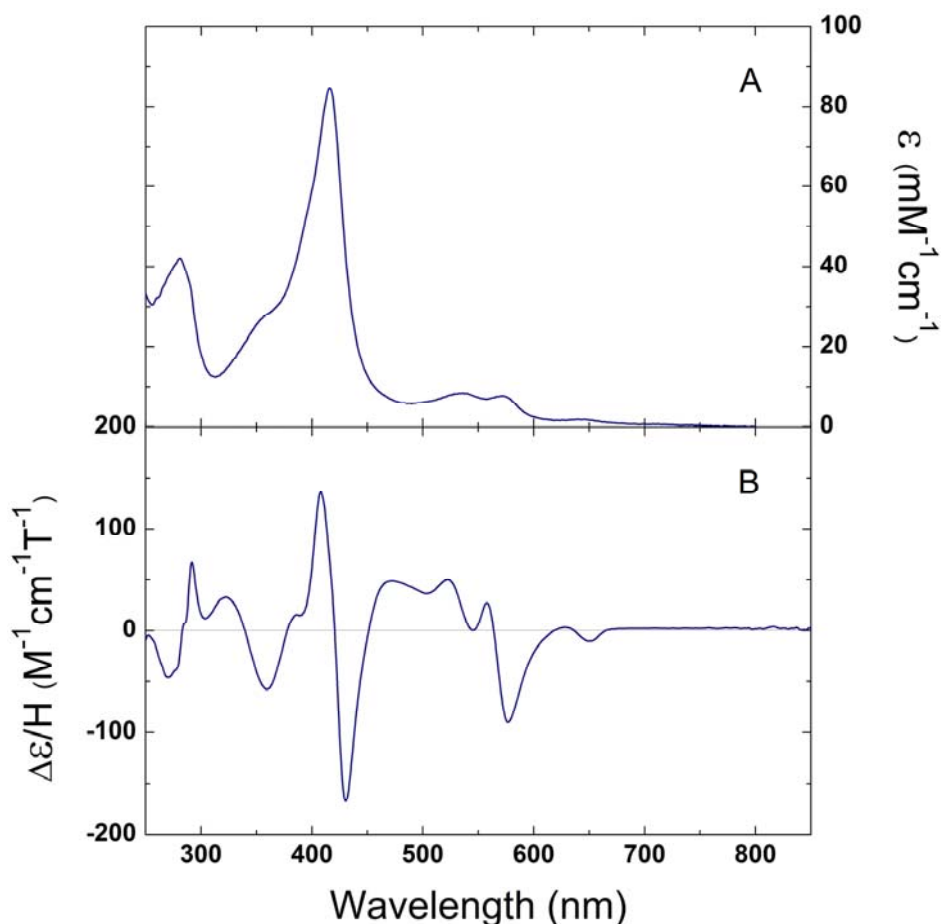


**Figure 4.33. MCD and optical spectra for CYP141.**

The UV-visible absorption spectrum for CYP141 (panel A) is compared with the MCD spectrum in the same region (panel B). Protein concentration for MCD measurement was 200  $\mu$ M. MCD spectra were generated at +8 Tesla.

It is clearly seen that the electronic absorption spectrum of CYP141 in the UV-visible region is typical in wavelength for a low-spin ferric heme. In addition, the tryptophan residues of the protein produce a positive signal at 290 nm, but less sharp when compared to CYP121, which shows a very strong positive peak at 290 nm (138). The band at  $\sim$  390 nm with an intensity ( $\epsilon$ ) of +15.3 and a second negative feature at  $\sim$ 650 nm are high-spin marker bands. This latter band is typical of the five-coordinate, high-spin P450 enzymes

and is known to be charge transfer in origin. The properties of this feature are similar with respect to shape, intensity, and position for the substrate-bound forms of P450s (254, 313, 314). This is consistent with the presence of high-spin heme iron in the sample, as also observed in UV-visible absorption and EPR analysis of CYP141.

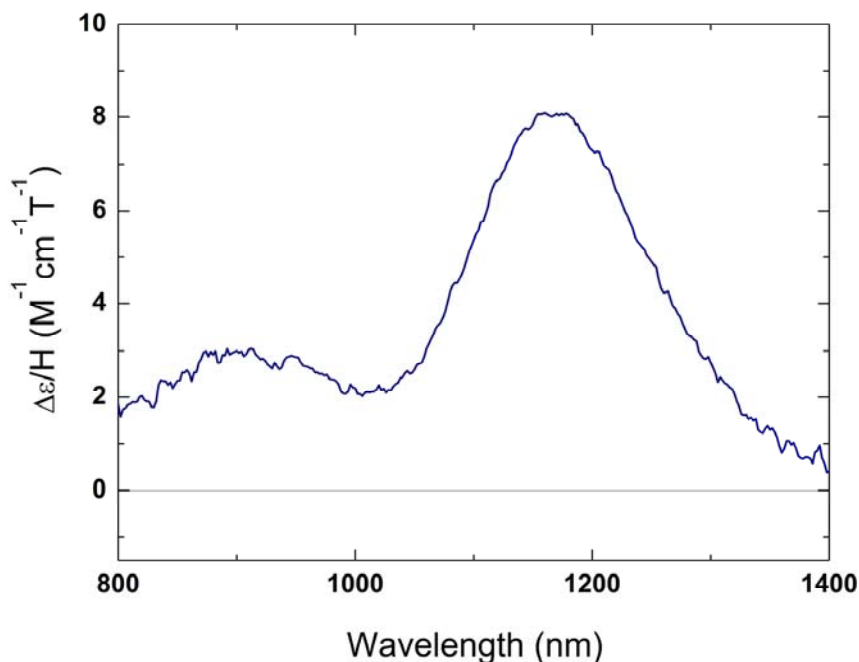


**Figure 4.34. The MCD spectrum for CYP141 in the near IR region.**

Room temperature near-infrared MCD spectra were recorded as described in the Methods (section 2.20). Protein concentration was 200  $\mu\text{M}$ .

At near-infrared wavelengths (Figure 4.34), low-spin ferric hemes give rise to a porphyrin-to-ferric charge transfer transition which appears in the MCD spectrum as a positive band, the exact energy of which is diagnostic of heme ligation. This near-infrared charge-transfer band appears at  $\sim 1168$  nm for the heme in CYP141, providing evidence for cysteinate-water ligation (254). In addition, there is a weak positive band at  $\sim 900$  nm, with this feature attributable to a high-spin heme iron component of the sample.

#### 4.2.11 Mass spectrometry of CYP141

ESI-MS may be used to characterize post-translational modifications, and also to identify errors in cDNA sequences. Therefore, to determine the mass of CYP141 protein and to confirm that the protein is intact, the ESI-MS technique was used. A sample of CYP141 was analyzed on a Waters LCT Mass Spectrometer and a Waters Alliance autosampler, running Waters MassLynx 4.0 software as described in Materials and Methods (section 2.17).

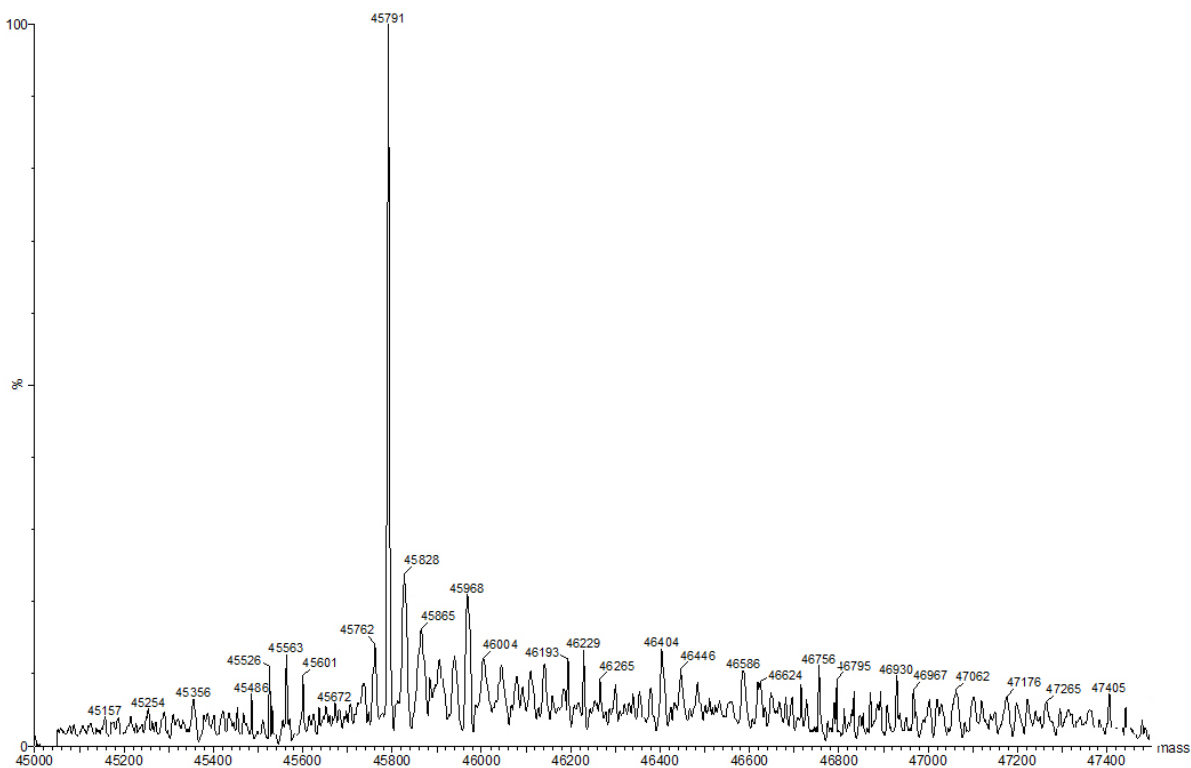


**Figure 4.35. Mass spectrum of CYP141 using a Waters LCT Mass spectrometer.**

Protein was eluted in 50/50 acetonitrile/H<sub>2</sub>O, 0.1% formic acid, with a final protein concentration of 4 mg/ml. All data were collected and analysed by MaxEnt 4.0 software. The result from electrospray mass spectrometry of CYP141 showed a single, intact species of molecular mass 45,791 Da.

Figure 4.35 shows the results of electrospray mass spectrometry of the CYP141 protein. It indicates a single, intact species of molecular mass = 45791 Da. As mentioned above, the mass of CYP141 with its native his tag is 45610 Da. Comparing this value with the molecular mass from ESI-MS data reveals a near-exact correlation with the predicted mass of CYP141 based on translation of its gene sequence. This indicates that there was no modification of the CYP141 during translation in the host cells (*E. coli*) and that the protein remained intact during purification.

#### 4.2.12 Light scattering analysis of CYP141

To determine the native form of CYP141 protein (monomer or oligomer), laser light scattering was used to analyse the system and to provide a direct measure of molecular mass. Figure 4.36 shows data for the native form of CYP141 analyzed by multi-angle laser light scattering (MALLS) coupled to gel filtration to yield a molecular mass measurement.

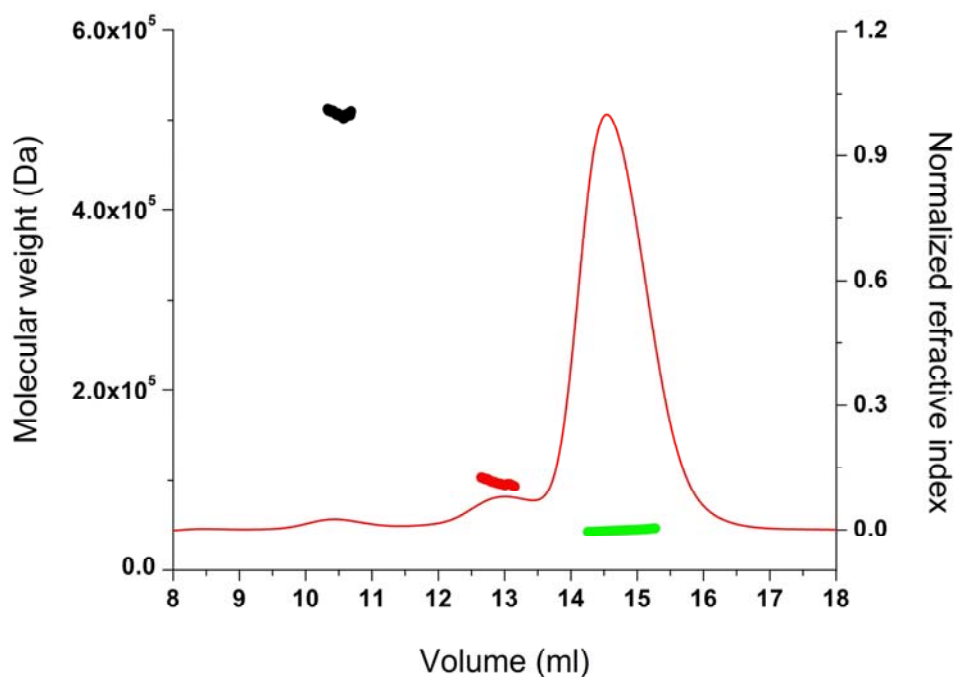


**Figure 4.36. Superdex–200 10/300 GL gel filtration chromatography and MALLS analysis of CYP141.** CYP141 produced three refractive index peaks with elution volumes centred at ~10.5, 12.9 and 14.8 ml. The light scattering and the refractive index are used by the instrument software to calculate molecular mass. Material eluting centred at 10.5, 12.9, and 14.8 ml was found to have apparent masses of  $512.1 \pm 6.2$  kDa,  $91.8 \pm 1.7$  kDa, and  $45.5 \pm 1.3$  kDa, respectively, masses that might be expected for an ~11-mer, dimer and monomer species of CYP141.

The ligand-free form of CYP141 at a concentration of 400  $\mu\text{g/ml}$  produced three refractive index peaks eluting at ~10.5, 12.9 and 14.8 ml, respectively (Figure 4.36). Based on the intensity of scattered light angular dependence, molecular mass of the protein was measured across these peaks. The flat trace of calculated mass (black, red and green lines, Figure 4.36) showed that the peak 1 corresponds to a mass of 512.1 kDa, the peak 2 located at ~12.9 ml elution corresponds to a molecular mass of 91.8 kDa, and the peak 3 centred at ~14.8 ml corresponds to 45.5 kDa. Based on the calculated mass of the polypeptide along with the mass of the histidine-tag, a monomer molecular mass is ~45.6 kDa (from SDS-PAGE or compositional analysis). Therefore, it can be concluded that CYP141 appears to behave as a monomer, dimer, and an approximate 11-mer under the conditions used (10 mM Tris, 150 mM NaCl, pH 7.5). In addition, the analysis of the refractive index was also determined to establish the percentage of the CYP141 forms (monomer, dimer and ~11-mer) in the mixture. From this experiment, the monomer is predominant, accounting for approximately 94.6% of the total protein, whereas the minor species (~11-mer and dimer) account for approximately 1% and 4.4%, respectively.

### 4.2.13 Crystallography of CYP141

CYP141 was expressed and purified to homogeneity enzyme as described in the Methods section (section 2.5), since the purity of the protein is important for successful crystal screening. Crystallization trials for purified CYP141 were carried out using a nanolitre drop dispenser Mosquito (TTP LabTech) and used a range of screening kits including Classics Lite Suites and pH clear suites. The trial crystallization screens indicated that CYP141 was crystallized and that two initial hits could be obtained, each showing what appeared to be very high quality crystals with pentagonal pyramid appearance.

Figure 4.37A shows the result of a small tray using Classics Lite Suites as the screening reagents. The results indicated that CYP141 crystals were obtained when using 0.2 mM MgCl<sub>2</sub>, 0.1 M Tris-HCl, pH 8.5, 15% Polyethylene Glycol (PEG) 4000 as precipitant. The crystals had a high quality of appearance and shape, but were quite small. Therefore, it was decided to scale up the procedure, using a larger tray and the sitting-drop vapour-diffusion method to develop the size of the crystals. Drops were made by mixing 1 µl of 40 mg ml<sup>-1</sup> CYP141 protein with 1 µl of reservoir solution (0.2 mM MgCl<sub>2</sub>, 0.1 M Tris-HCl, pH 8.5, 15% PEG 4000) and by incubating at 4 °C. Under these conditions, the crystals of CYP141 formed within 1-2 days, and this was observed by microscopy. The crystals in Figure 4.37B were faintly red in colour and appeared as tetragonal pyramids of typical dimension 0.8 x 0.4 x 0.4 mm.

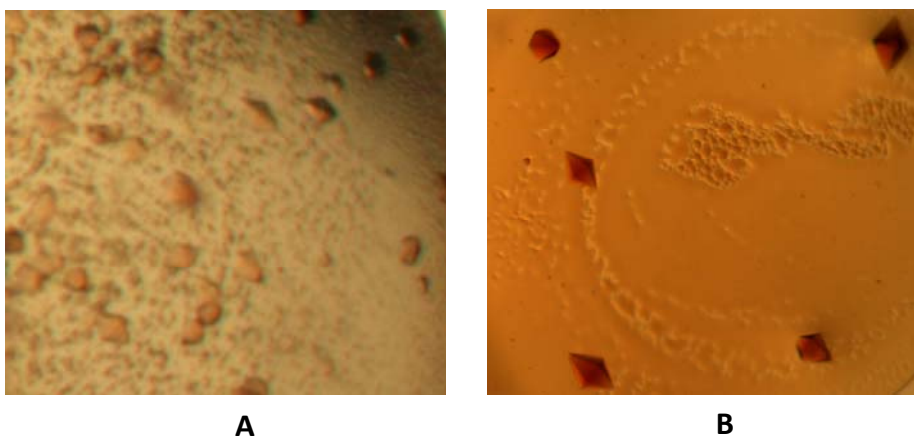
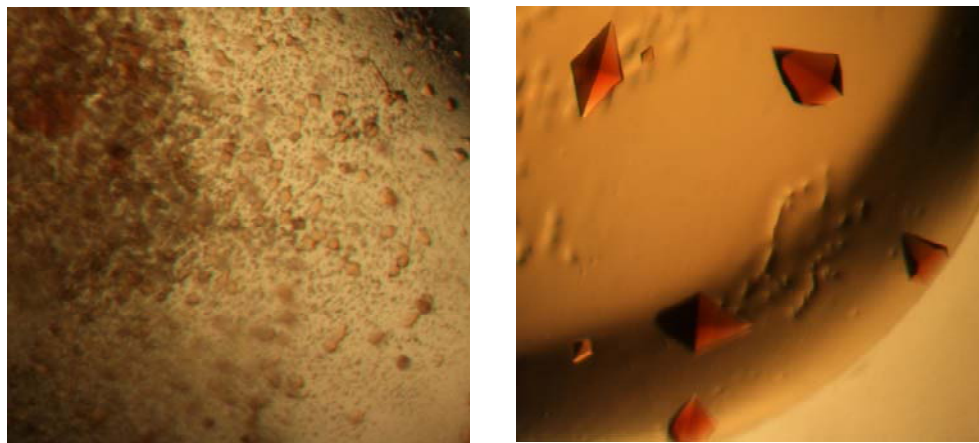


**Figure 4.37. Crystals of CYP141 grown in 0.2 M MgCl<sub>2</sub>, 0.1 M Tris-HCl, pH 8.5, 15% (w/v) PEG 4000.** (A) The crystals were obtained from small tray growth by nanolitre drop setter Mosquito, using Classics Lite Suites screen. The crystals were formed at position of 88 – H4 (location of refill-hit solutions in 96-well plate format). (B) The crystals from a large tray growth formed by the sitting-drop method, using 1 µl enzyme at a concentration of 40 µg ml<sup>-1</sup> mixed with an equal volume of reservoir solution and equilibrated against 100 µl reservoir solution. The mixture was incubated at 4 °C for 24-48 h, and the crystals were observed and photographed using microscopy.



A

B

**Figure 4.38. Crystals of CYP141 grown in 1 M lithium chloride, 0.1 M Bicine, 10% (w/v) PEG 6000.** (A) The crystals were crystallized in pHClear II suites screen at position of 12 – A12 (location of refill-hit solutions in 96-well plate format). (B) The crystals were obtained from a large tray using the sitting-drop method, and with 2  $\mu\text{l}$  of protein at a concentration of 45  $\mu\text{g ml}^{-1}$  mixed with 1  $\mu\text{l}$  reservoir solution and equilibrated against 100  $\mu\text{l}$  reservoir solution. The mixture was incubated at 4 °C for ~40 days.

In the second condition, the crystals grew from 1 M lithium chloride, 0.1 M Bicine, 10% (w/v), PEG 6000. In this condition, the crystal growth was slow, but showed improved crystal properties and shape such as larger dimensions and tight crystals. Figure 4.38A displays crystals obtained from a small tray using pHClear II suites as the screen regents after ~40 days incubation at 4 °C. The crystals had a good shape but were quite small. To improve the dimensions of the crystals, the large tray and sitting-drop method were scaled-up, as described in the Methods chapter (section 2.23). For obtaining crystals from large trays, longer incubation times were required compared to the initial trial conditions. Normally, the CYP141 protein crystallized after ~40 days, but still showed very small crystals. Therefore, the tray was incubated for 5-10 days to get larger crystals that were easier to pick up and appropriate for diffraction studies and data analysis. The larger crystals of CYP141 are shown in Figure 4.38B. These have a similar shape and other properties to the first crystals above, but show larger dimensions of 1.2 x 0.6 x 0.6 mm.

For diffraction, crystals were soaked in 10% PEG 200 solution and were flash-frozen at 100 K in a stream of nitrogen gas. Complete sets of diffraction data were collected at 100 K on an R-AXIS IV<sup>++</sup> image plate. Diffraction data only extended (at best) to ~3.2 Å resolution for a variety of the crystals tested, and from crystals derived from both conditions (Figure 4.39). All crystals belonged to space group 178, with unit cell parameters  $a = b = 96.75$ ,  $c = 270.87$  Å,  $\alpha = \beta = 90^\circ$ ,  $\gamma = 120^\circ$ . Although a complete data set was obtained to ~3.2 Å, the

structure could not be solved using molecular replacement methods. One possibility is heavy metal soaks, and another solution is to instead attempt to get crystals of a ligand-bound complex (again probably a tight-binding azole).

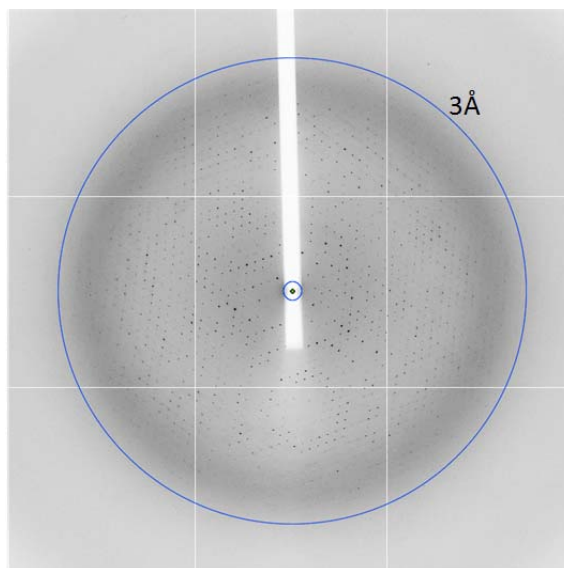


**Figure 4.39.** A representative X-ray diffraction pattern of CYP141 crystals. The diffraction data only extend to  $\sim 3.2\text{\AA}$ .

### 4.3 Discussion

The analysis of Mtb and *M. bovis* genome sequences shows that both CYP141 (in region f deletion 12, RD12) and CYP130 (in RD13) are missing from *M. bovis* (155). In the last two years, CYP130 was characterized by Ortiz de Montellano's group, while CYP141 has not been characterized to date at the protein level. The CYP141 is absent from the virulent *M. bovis* strain and its counterpart *M. bovis* BCG, suggesting that it is not essential for growth, but that it may be relevant for virulence and infectivity of Mtb towards the human host. Preliminary expression studies with CYP141 demonstrated that it could be produced at very high levels in *E. coli* BL21 (DE3) strain and the *CYP141* gene generated higher levels of soluble protein at high concentrations of IPTG (1 mM) compared to CYP126 expression (section 2.5). However, large amounts of inclusion bodies formed during expression of both proteins in *E. coli*, regardless of concentrations of inducer. This problem was largely overcome by slowing bacterial growth (at low growth temperature).

Spectroscopic analyses performed on CYP141 expressed as a recombinant protein in *E. coli* are consistent with the present of a cysteine thiolate coordinated heme iron. The oxidised absolute spectrum of CYP141 reveals Soret band features at 393 nm and 418 nm that likely indicate a mixture of spin states, varying somewhat between different preparations of the P450, but with the latter band being more prominent. It could be that some very hydrophobic ligand from *E. coli* remains bound in the heme pocket during CYP141 purification, and that this leads to the partial high spin state of CYP141. The positions of these Soret band features are typical for high and low spin P450 forms. Surprisingly, CYP141 displays a unique reduced/CO-bound spectrum, with a maximum at ~440 nm instead of the typical P450 Fe<sup>2+</sup>-CO absorption maximum at ~450 nm. In a previous report, Lamb *et al.* (315) indicated that a specific reduced P450 enzyme could bind to CO, producing a spectral maximum around or below 450 nm. The carbon monoxide binding experiments of CYP141 were performed on more than 50 preparations of purified enzyme, and the absorption maximum of the Soret band was consistently seen at 440 nm in all preparations.

Almost all other P450s reported to date reveal the Soret maximum of the reduced CO spectrum at about 450 nm, from which the name of these monooxygenases arises. However, cytochrome P450 170A1 (CYP1701A1) from *Streptomyces coelicolor* A3 (295) shows similar characteristics to CYP141 with a reduced carbon monoxide spectrum at 440

nm. CYP170A1 is involved in the biosynthesis of epi-isozizaene, which has been reported to exhibit antibacterial activity (316). The protein sequence alignment indicated CYP141 has ~30% identity with CYP170A, suggesting a relatively high amino acid sequence similarity, and possibly indicating that CYP141 may have a similar substrate selectivity to CYP170A1. However, there are no data to indicate a similar function between CYP141 and CYP170A1, due to absence of data for substrate selectivity for the former and since the crystal structure of CYP141 is still unknown. The ~10 nm hypsochromic shift of the absorbance maximum in the ferrous-CO form (i.e. to ~440 nm) compared to most P450s also occurred if the reduction was carried out with redox proteins (*E. coli* flavodoxin and flavodoxin reductase, or Mtb ferredoxins and ferredoxin reductases, see next chapter) rather than dithionite. The molecular formation of the Soret maximum at 440 nm is still not clear, but could have its origins in altered properties of the thiolate ligand compared to other P450s. In addition, the studies on CO binding to CYP141 also revealed that the P440 complex is very stable, and that there was only a very small amount of P420 formed. The equilibrium of P420/P440 is stable over time and the P440 did not convert to P420. This characteristic is dissimilar to certain other Mtb P450s such as CYP126 (see section 3.6) and CYP51B1 (218), both of which show a rapid conversion of P450 (active form) to P420 (inactive form).

The CD spectrum of the purified CYP141 in the far UV region (190 – 260 nm) exhibited minima at 222 and 208 nm, and a strong positive maximum at 190 nm, which are consistent with CYP141 having a high  $\alpha$  helix content. Consistent with this, the crystal structures available for mammalian, bacterial and fungal P450s all show a high  $\alpha$  helical content (71, 317). The analysis of secondary structural composition by the Selcon3 method gave >60%  $\alpha$  helix content, 15%  $\beta$  sheet and around 3% turn. These values are similar to two characterized P450s, CYP121 and P450 BM3 (138, 300), which also showed >50% alpha helical content. However, > 60% helix is almost certainly an overestimate of the true value. In the near UV-visible region (260–600 nm), which reports on contributions from aromatic amino acids and on the heme environment, there is a negative sign in the Soret region of the CYP141 visible CD spectrum. This result shows the similarity of CYP141 to other well-characterized bacterial P450s such as CYP51B1 and P450 BM3.

Spectroscopic analysis of azole binding to CYP141 revealed high affinity for azole antifungal drugs, and there is thus potential for CYP141 as an azole drug target in Mtb. The differences in the molecular structure of azole compounds used affects their solubility and

their ability to bind and to inhibit the CYP141 enzyme. While imidazole derivatives contain two nitrogen atoms in the five-membered ring, triazoles possess three nitrogen atoms (see Figure 1.14 and Figure 1.15). A nitrogen atom in the azole ring coordinates to the heme iron in CYP141, giving type II spectral interactions. The azole antifungals examined in this study almost all showed type II spectral interactions with CYP141, characterized by an increased Soret intensity at >422 nm. The shift of the Soret band on the binding of azole drugs indicated that the ligands were co-ordinated to the heme iron and replaced the distal water molecule.

Analysis of azole binding indicated that CYP141 binds to a number of antifungal drugs, including econazole, miconazole, itraconazole, clotrimazole, ketoconazole, fluconazole (and with poorer affinity to voriconazole, data not shown). The weakest affinity shown is for the drug fluconazole, which is the most water soluble of these drugs. This again is possibly partly due to the apolar nature of the active site of CYP141. In comparison with the other eight best characterized *M. tuberculosis* P450s (CYP51B1, CYP121, CYP130, CYP125, CYP124, CYP142, CYP144, and CYP126), CYP141 shows tight azole binding ability, with low  $K_d$  values comparable to those previously determined for CYP121, and generally tighter  $K_d$ 's than those for the other 5 P450s (Table 4.3) (119, 121, 135-137, 149).

ligand	CYP51B1	CYP121	CYP130	CYP124	CYP125	CYP144	CYP142	CYP126	CYP141
Econazole	0.77 ± 0.04	<0.2	1.93 ± 0.03	2.1 ± 0.1	11.7 ± 0.7	0.78 ± 0.29	4.6 ± 0.2	5.05 ± 0.3	14.2 ± 1.7
Fluconazole	19.0 ± 1.9	9.7 ± 0.1	48.0 ± 1.5	-	43.2 ± 0.8	> 10,000	860 ± 98	-	25.2 ± 3.6
Ketoconazole	-	3.3 ± 0.3	-	-	27.1 ± 0.9	134 ± 5	21 ± 4	1.4 ± 0.4	18.4 ± 3.2
Itraconazole	-	-	-	-	30.2 ± 4.3	-	-	-	0.27 ± 0.19
Miconazole	0.59 ± 0.03	<0.2	1.7 ± 0.21	1.9 ± 0.2	4.6 ± 0.4	0.98 ± 0.22	4.0 ± 0.5	1.3 ± 0.2	7.03 ± 2.1
Clotrimazole	<0.1	<0.2	13.3 ± 0.6	2.5 ± 0.1	5.3 ± 0.6	0.37 ± 0.08	3.8 ± 0.9	-	1.08 ± 0.27
Voriconazole	-	-	-	-	-	6510 ± 470	-	-	-
2-phenylimidazole	-	-	-	-	345 ± 4	-	-	-	-
4-phenylimidazole	-	-	-	-	216 ± 5	280 ± 18	12 ± 1.5	-	-
Imidazole	-	-	-	-	536 ± 7	2965 ± 275	-	2591 ± 59	-

**Table 4.3. Comparison of the azole dissociation constant values for Mtb P450s.**

The  $K_d$  values ( $\mu\text{M}$ ) for seven azole drugs are compared for CYP51B1, CYP121, CYP130, CYP124, CYP125, CYP144, CYP142, CYP126 and CYP141. (-) indicates “not determined” or (in case of CYP141) no spectral binding signal observed. Data for binding of 2-phenylimidazole, 4-phenylimidazole and imidazole are also compared between CYP141, CYP144 and CYP125/CYP126.

Potentiometric studies have provided the first description of the reduction potential of the P450 CYP141 heme iron in the ligand-free form. The knowledge of the reduction potential

for the heme iron in the P450 is central to our understanding of the role of the heme iron in an electron transport pathway in which electrons are delivered from NAD(P)H via redox partners (ferredoxin reductase and ferredoxin). Redox potential measurements of the substrate-free CYP141 enzyme revealed a midpoint reduction potential of -50 mV vs NHE. This is a very positive potential for a likely substrate-free P450, and this is approximately 300 mV higher than those of other Mtb P450 enzymes such as CYP51B1 (-375 mV) CYP121 (-467 mV) CYP144 (-355 mV) and CYP126 (-332 mV) (135, 138, 194).

It has been suggested that the redox potential of P450 is dependent on the nature and strength of the sixth ligand to the iron, as well as on electrostatic, hydrophobic and hydrogen bonding interactions within the heme cavity (99, 318, 319). The positive shift of the reduction potential of a P450 heme iron often occurs on substrate binding (320-322). For soluble bacterial P450s characterised to date, substrate binding is often associated with an increase in the heme iron redox potential, and a positive shift in redox potential of ~130 mV may be elicited, perhaps taking the potential to around -250 mV, and reflecting the different midpoint potentials between low-spin and high spin forms of the enzyme (61, 289, 323, 324). The data collected for substrate-free CYP141 indicate a very positive heme iron potential, with a value that is more typical of a substrate-bound P450 and at the positive end of the spectrum for such a species. It cannot be discounted at present that there is some substrate-like molecule co-purified with CYP141, but the positive potential may also be related to unusual heme ligation, as is suggested from its unusual P440 reduced/CO-bound spectrum.

Through pH titration of the reduced form of CYP141, it was found that increasing the pH of the buffer solution produced spectral changes indicative of an increased proportion of an unusual low-spin form of the cytochrome, with a Soret shift from shorter (417 nm) wavelength in the oxidized enzyme to a longer wavelength (423 nm) in the reduced state. In ferrous P450s, the thiolate-coordinated form often has its Soret maximum at ~410-412 nm. The thiol-coordinated form has the Soret at longer wavelengths (~420-425 nm), as seen in CYP121 and CYP51B1, which show the protonation of the thiolate to a thiol associated with a shift of the Soret band to ~420 nm (218, 325). The spectral shift at higher pH (also seen in diagnostic features in the alpha/beta region) is clearly consistent with formation of a reduced heme in a thiol-coordinated state in the case of CYP141. Thus, the spectra are consistent with formation of a ferrous-thiol coordinated CYP141 at the higher pH. This being the case, the transition monitored from 417 and 423 nm may reflect mainly the

transition between Fe<sup>II</sup>-thiolate and Fe<sup>II</sup>-thiol coordinated hemes. These results indicate that thiolate-coordinated enzyme (active form) was protonated at higher pH to become the thiol-coordinated (inactive form), the conversion from Fe<sup>II</sup>-thiolate to Fe<sup>II</sup>-thiol coordinated heme occurs at an apparent p*K*<sub>a</sub> value of 6.57, and more thiol-coordinated protein appears to be formed at the higher pH, with the conversion process completed at approx. pH 8.14.

Wild-type CYP141 was examined by DSC in the ligand-free and clotrimazole-bound forms to establish whether there were measurable effects on thermal stability induced by binding of the inhibitor. It was found that clotrimazole binding induced the stabilization of CYP141, with the *T*<sub>m1</sub> increasing by ~2 °C, and *T*<sub>m2</sub> increasing by ~1 °C in the presence of clotrimazole. The midpoint unfolding temperatures are likely related to the two domains of the protein. However, it is not possible to determine the unfolding of which domain (alpha and beta domain) corresponds to *T*<sub>m1</sub> or *T*<sub>m2</sub>. These data demonstrate that ligand binding stabilized CYP141 to protein unfolding and precipitation by a small amount over the ligand-free P450. The stabilization event may relate to the association of ligand with, and stabilization of, one particular conformation of the protein in solution. The protein unfolds with two distinct *T*<sub>m</sub> events that likely represent the separate unfolding of the N- and C-terminal domains of the protein.

According to the general structure of a P450 enzyme, the N-terminal domain corresponds to the beta domain (smaller domain) and C-terminal is the alpha domain (larger domain). Although the entire protein is more stable in the presence of inhibitor, the domains unfold at nearly the same temperature, and it is suggested that only one CYP141 domain may be stabilized to some degree in the presence of the ligand. It is predicted that the domain with the lower change in heat capacity should be the smaller domain – i.e. the beta domain, and that the alpha domain (with the larger heat capacity change) corresponds to the higher *T*<sub>m</sub> change. Unfortunately, the crystal structure of CYP141 could not be determined due to poor diffraction quality, and therefore it is not yet possible to analyse the conformational characteristics of the enzyme in its interactions with the inhibitor. However, several reports have indicated that ligand binding results in conformational changes that stabilize the structure of a P450 protein (223, 326, 327).

The presence of a minor Soret band feature at 393 nm in the UV-visible absorption spectrum of the ferric CYP141 substantiates assignment of this proportion of the enzyme as a thiolate-ligated pentacoordinate high-spin complex. The mixture of the spin-states of

CYP141 was confirmed in the EPR spectrum, with a distinguishing characteristic of pentacoordinate high-spin ferric thiolate-bound heme displayed as  $g_z$ ,  $g_y$ ,  $g_x$  values of 7.95, 3.59, 1.70, respectively. A major portion of the protein displays a signal with  $g$ -values at 2.44, 2.25 and 1.91, which correspond to a low-spin state. The similarity of these  $g$ -values with those for other well-characterized Mtb P450 enzymes (124, 135, 138) suggests that a water molecule is coordinated to the distal position of the heme iron in this portion of CYP141. The fact that no high-spin signal was observed with ketoconazole bound to CYP141, accompanied by a different set of  $g$ -values at 2.50, 2.26 and 1.87, indicates that a more homogeneous 6-coordinate low-spin form was generated in the azole complex. This change demonstrates that the heme protein has a proximal cysteinate ligand with a nitrogen from ketoconazole as the 6<sup>th</sup> ligand to the heme iron.

The MCD spectroscopic analysis of CYP141 sample in both regions also indicated highly similar characteristics to those observed previously for other bacterial P450 enzymes, as well as for Mtb P450s (138, 300). The MCD spectra in the UV-visible region indicate that CYP141 is predominantly low-spin form in its resting oxidized state. A small high-spin component (<10%) was also recorded by MCD with the troughs at ~390 nm and ~650 nm. The mixture of low-spin and high-spin forms of CYP141 was also indicated by EPR studies, which showed the high-spin  $g$ -values at 7.95, 3.59 and 1.70. Perhaps the most intriguing spectroscopic property of CYP141 is its MCD signal in the near-infrared region (~800-1400 nm). Other P450s characterized to date show a charge transfer (CT) band for the low-spin P450 heme iron (CT<sub>LS</sub>) at around 1100 nm, such as CYP121 (1125 nm), CYP51B1 (1110 nm), P450 BM3 (1080) and P450 BioI (1090 nm) (138, 255, 300), which is in the region associated with cysteinate/water ligation of heme iron.

CYP141 also revealed a band in the near-infrared region at ~1170 nm, indicating that CYP141 likely also has typical P450 cysteinate- and water-ligation to the heme iron. However, the CT<sub>LS</sub> band of CYP141 at 1170 nm is at a somewhat higher wavelength than for these other P450s, possibly reflecting the alterations in heme coordination that give rise to its P440 form. Previous studies on binding of inhibitors to CYP121 and CYP51B1 indicated a clear shift on fluconazole binding with CT<sub>LS</sub> bands at 1180 nm and 1165 nm, respectively, and the imidazole complex of P450 BM3 also reveals the CT<sub>LS</sub> band at 1180 nm (138, 300). Therefore, the unusual CT<sub>LS</sub> band of CYP141 in the ligand-free form indicates a remarkable difference from other P450s and the biological significance for this unusual MCD shift to longer wavelength deserves further investigation. At this stage, there

is no reason to conclude that the 1170 nm CYP141 band results from azole ligation to the heme iron, since imidazole was removed from samples prior to spectroscopic analysis.

The oligomerization states probed for Mtb CYP141 by MALLS analysis demonstrated that virtually all the CYP141 eluted as a mixture of three distinct peaks with the molecular weights corresponding to  $512.1 \pm 2.2$  kDa,  $91.8 \pm 1.7$  kDa, and  $45.5 \pm 1.3$  kDa. Compared to the theoretical calculation of the molecular weight of CYP141, based on its amino acid sequence, these data suggest that protein was oligomerized as an ~11-mer and a dimer, as well as being present in a monomeric form. The protein is predominantly in the monomeric form (~ 94.6 %), while dimer and 11-mer forms are present at ~4.4% and 1%, respectively. This may suggest that the biological function of CYP141 relates to its oligomerization, at least with respect to the monomer/dimer equilibrium. In previous studies on Mtb P450s, none revealed formation of higher oligomers under native conditions, and in chapter 3, CYP126 was also revealed a monomeric form as the native condition of this enzyme. In addition, CYP130 only exhibits the dimeric form in the presence of econazole, but in the absence of inhibitor it shows a monomeric form (137). Therefore, the presentation of the oligomerization of CYP141 in the absence of ligand may show a distinct physical characteristic from the other Mtb P450s, although the relevance of such oligomerization to any biochemical function of CYP141 still remains obscure and the proportions of dimer are small.

In the present study, Mtb CYP141 was overexpressed in *E. coli* cells, and followed by purification to homogeneous enzyme. The authenticity of the expressed native protein is crucial to any structure/function interpretations. Toward this end, the cloned DNA sequence was confirmed in its entirety before use and, as a final confirmation, the determination of the intact protein molecular weight of CYP141 was done by ESI-mass spectrometry. An accurately measured mass is capable of revealing any gross abnormalities, such as truncated protein, and also can pinpoint the precise sites of errors, modifications and individual proteolysis of peptides. The molecular weight of the purified native CYP141 protein showed a peak for the native protein at 45791 *m/z*. Upon comparison of the measured mass with the theoretically calculated mass based on the amino acid sequence without the heme (45610 Da), the observed mass of 45791 Da corresponded closely to the predicted monomeric molecular weight of CYP141, and it was thus confirmed that the protein integrity was conserved during expression. In addition, posttranslational modifications and other alterations were not detected in this case, since the molecular mass

is highly similar between the determined mass and theoretical mass. Therefore, these results suggest that CYP141 recombinant protein from *Mycobacterium tuberculosis* was fully and exclusively expressed as an intact protein.

Despite several efforts to reveal atomic structures of P450s, it is sometimes difficult to produce suitable crystals for analysis by x-ray diffraction. To date, the crystal structure of CYP121 from Mtb, determined at 1.06 Å, is the highest level of resolution available for a P450 structure, and reveals novel information relating to P450 architecture. However, it is clear that the crystal form and the diffraction quality are different between various P450s. This chapter has reported the crystallization of CYP141. Preliminary work showed that the crystals of this protein could be grown under very different conditions, though the crystals themselves have very similar morphology, symmetry, and limits of diffraction. The crystallization of CYP141 appears to be sensitive to the concentration of PEG (PEG 4000 and PEG 6000). It is also interesting to note that the optimal concentration of protein used for crystallogenesis is very high (compared with various other crystallization reports).

However, the crystals consistently yielded a poor and weak diffraction pattern at 100 K. A resolution of 3.5 Å was collected for first data set, and indicated that the crystals contain a high solvent content. Therefore, to improve quality of the diffraction, a dehydration method was used by soaking crystals in precipitant such as glycerol. This method improved diffraction to resolution of 3.2 Å. A complete data set was obtained to ~3.2 Å, but the structure could not be solved using molecular replacement methods. To investigate further to enable the determination of the crystal structure of CYP141, it will be necessary to improve the resolution of diffraction data to around 2.0 Å, since at this resolution the structure could likely be solved using one of the other available P450 structures by molecular replacement. Unfortunately, many efforts in using a heavy metal derivative to solve the structure of this enzyme also failed. Of course, if this was successful it could improve the resolution of existing crystals to better than 3.2 Å. Another solution could be to useazole derivatives and solve the structure of a drug complex. Theseazole drugs may prove an effective new class of drugs against the multidrug resistant strains of the tuberculosis pathogen. Therefore, attempting to co-crystallize CYP141 with clotrimazole, which showed the best binding (lowest  $K_d$ ) to this enzyme, might allow us to establish the structural basis for the tight binding of this drug to this important pathogen P450. However, attempts to co-crystallise CYP141 were unsuccessful even when the protein was screened across a range of differentazole concentrations.

Future work will focus on attempts to determine the CYP141 structure by X-ray crystallography, as well as to address the substrate specificity profile of the protein. The structure and function of this protein may thereafter suggest novel targets for therapeutic intervention and, in addition, new insights into this class of protein.

## 5 CLONING, EXPRESSION, PURIFICATION, CHARACTERIZATION AND FUNCTIONAL ANALYSIS OF P450 REDOX PARTNERS

### 5.1 Introduction

The monooxygenation reaction requires two distinct electron transport processes, with electrons derived from NAD(P)H and delivered to P450s by redox partner proteins (89, 290, 328, 329). In the first reductive process, the heme iron of P450 is in the ferric state ( $\text{Fe}^{3+}$ , resting state), and accepts one electron from the redox partner to reduce the ferric iron to the ferrous form (330). In the ferrous state, the heme iron binds dioxygen to form a semi-stable low-spin, hexacoordinate ferrous- $\text{O}_2$  (or ferric superoxy) form. The binding of molecular oxygen to the ferrous heme iron initiates the second reductive process to produce a ferric peroxy species. Two further protonation reactions occur in order to protonate the bound dioxygen molecule, and then leads to heterolytic O-O bond cleavage releasing water, and generating the oxo-ferryl porphyrin radical intermediate that catalyses oxygen transfer to the substrate. It is clear to recognize that the monooxygenase reaction could not be accomplished in the absence of electron transfer proteins, which deliver two electrons for the P450 catalytic cycle. Therefore, the electron transport reactions between P450 and the redox partner play critical roles in the catalytic cycle of P450 (331).

The vast majority of P450s catalyze oxidation of chemical compounds using the successive delivery of two electrons provided by one or more redox partners (271, 332, 333). Different P450 classes have different interactions with their redox partners (334). Generally, classification of P450 redox systems can be divided neatly into two broad classes (269): class I and class II. The class I systems are mainly found in eukaryotic mitochondrial membranes and in bacteria, consisting of two electron transfer proteins: a flavoprotein reductase and a ferredoxin. These function in electron transfer from NAD(P)H to flavoprotein reductase, and then to the P450 via the ferredoxin. Class II systems use a diflavin reductase (NADPH-cytochrome-P450 reductase – CPR), which possesses both flavin adenine dinucleotide (FAD) and flavin mononucleotide (FMN) binding domains. The class II redox systems are widely used in eukaryotes (335-337).

The function of redox partners in electron transfer chains to P450 has been widely investigated and there are reports of systems used by several bacterial P450s, such as CYP106A2 from *Bacillus megaterium* ATCC 13368 (338) and CYP105D5 from *Streptomyces coelicolor* A3 (84). The amino acid sequences of well characterized P450s

reveal several positively charged residues such as Lys, Arg, and His, which are critical for interactions with conserved negatively charged residues (Asp and Glu) of the redox partners, leading to protein docking and electron transfer from NAD(P)H to P450s (99, 270, 271). Crystal structures of many P450s has revealed that the positively charged residues cluster at the proximal surface (around the heme iron), and the negative residues are present in the distal face of the protein, forming a dipole molecule (154). On the binding of a redox partner to P450s, the electrostatic nature of positive residues on the proximal face helps recognition of negative residues on the relevant face of the redox partner, leading to the formation of an interaction between P450 and redox partner protein (269, 333).

The deciphering of the Mtb genome showed several genes coding for ferredoxins and ferredoxin-like proteins, which could provide electrons for the catalytic activity of the 20 P450 enzymes (89, 290). Among them, four obvious candidates are of particular interest for P450 redox partners, these being ferredoxins encoded by the *Rv0763c* gene (adjacent to the P450 *CYP51B1*), the *Rv1786* gene (adjacent to *CYP143*), and two uncharacterized ferredoxins: FdxA (encoded by *Rv2007c*) and FdxC (encoded by *Rv1177*) are other potential redox partners of P450s. To date, the ferredoxin product of the *Rv0763c* gene is the only Mtb ferredoxin that has been biochemically and catalytically characterized, including its use in reconstitution of the redox pathway of CYP51B1 (194). This ferredoxin (*Rv0763c*) contains one [3Fe-4S] cluster per monomer and, when reconstituted with an endogenous redox partner (FdR, the ferredoxin reductase product of *Rv0688*), was shown to deliver electrons to Mtb CYP51B1, demonstrating that this pathway could support electrons for the demethylation of sterols by this P450 (153, 194). The further investigation of redox reactions was carried out on CYP121, indicating that exogenous redox partner proteins (from spinach) could also drive Mtb CYP121 catalytic activity in the formation of C-C bond within the cyclodipeptide cYY (120).

The genome sequence of Mtb shows that 20 P450 enzymes were encoded, but several ferredoxins and putative ferredoxin reductases are also distributed in the genome, making it difficult to identify categorically which P450 might interact with which partner system. The question is thus raised as to which redox partners supply electrons for which of the 20 P450s using the class I system identified as NAD(P)H → ferredoxin reductase → ferredoxin → P450 (339). It is likely that various Mtb redox proteins may be promiscuous in their ability to deliver electrons from NAD(P)H to the large number of Mtb P450s (290). To date, the only ferredoxin analysed has been Fdx1 – the product of the *Rv0763c* gene

(194). This has been cloned, expressed, and characterized in its redox function for supporting electron transfer for CYP51B1 sterol demethylation. This P450 is encoded by the adjacent *Rv0763c* gene. The limited information on redox reactions of P450s with redox partner proteins is a major barrier to our understanding of Mtb P450s in physiology and pathogenicity.

To provide more information on Mtb redox systems, experiments here have examined and established functional partner proteins for the novel Mtb P450s CYP126 and CYP141, as well as providing partner proteins to support the well-established catalytic activities of other Mtb P450s such as CYP51B1, CYP121, CYP142 and CYP125. In this chapter, initial studies are reported for the cloning, expression, purification, and characterization of the Mtb ferredoxin encoded by the *Rv1786* gene, the Mtb ferredoxin reductase encoded by the *Rv0688* gene, and their biophysical, thermodynamic, and spectroscopic features. Moreover, the Mtb flavoprotein reductase A (FprA) encoded by the *Rv3106* gene, the Mtb ferredoxin encoded by the *Rv0763c* gene, and two genes encoding the *Escherichia coli* flavodoxin NADP<sup>+</sup> oxidoreductase (FLDR) and flavodoxin (FLD) were also expressed and purified as both host (homologous) and heterologous proteins to serve as redox partners for the electron transport pathway of various P450s. In addition, the data collected also report on the interactions between CYP126, CYP141 and these redox partners, providing fundamental new information relating to the properties and molecular interactions of P450 enzyme systems in the pathogen *Mycobacterium tuberculosis*.

## 5.2 Results

### 5.2.1 Cloning, expression, purification and characterization of Mtb ferredoxin reductase (*Rv0688*)

#### 5.2.1.1 Cloning, expression and purification of a Mtb ferredoxin reductase

Ferredoxin reductase (FdR) from Mtb is an FAD-associated flavoprotein (153), encoded by the *Rv0688* gene, and which shows very high similarity of amino acid sequence to ferredoxin-NAD(P)<sup>+</sup> reductases from *Mycobacterium parascrofulaceum* and *Rhodococcus jostii* RHA1, with 82.3% and 61.8% identity, respectively (123, 340). In addition, FdR also has similar levels of identity with FAD-dependent pyridine nucleotide-disulfide oxidoreductases from *M. vanbaalenii* PYR-1, *M. gilvum* PYR-GCK, and *Gordonia bronchialis* DSM 43247, with 71.2%, 70%, and 51.9% identity, respectively (341-343). The sequence of the *Rv0688* gene from the tuberculist website (180) reveals that this gene contains 1206 base pairs, coding for 401 amino acids, and with a predicted molecular mass of ~43 kDa. The primers for amplifying the *Rv0688* gene were designed based on the complementary sequences at both the 5' and 3' ends of the gene, and by attaching the recognition sequences of the restriction enzymes *Bam*HI and *Nde*I to the ends of the primers to enable cloning of the PCR products. The gene was initially cloned using the polymerase chain reaction to amplify *Rv0688* from the original cosmid sequence, as described in the Methods section (section 2.4.2).

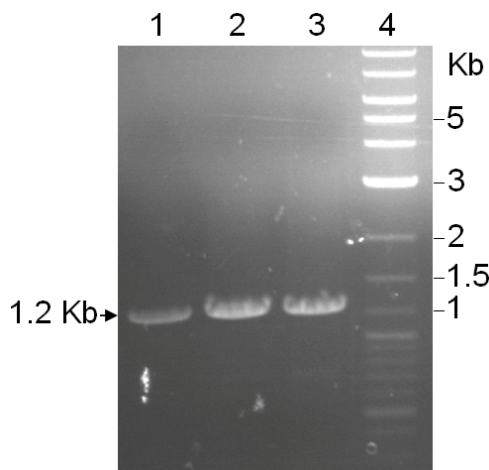


**Figure 5.1. PCR amplification of *Rv0688*.**

The gene was cloned from *M. tuberculosis* H37Rv cosmid I04. The PCR product was resolved on an ethidium bromide-stained 0.8% agarose gel. Bands displayed are those of *Rv0688* in the presence and absence of DMSO. Lane 1: PCR product in the absence of DMSO, lane 2: PCR product in presence of DMSO, lane 3: PCR product from reaction in the presence of MgCl<sub>2</sub>, lane 4: Molecular mass standards (5000, 3000, 2000, 1500 and 1000 bp fragments are indicated).

The analysis of an agarose gel electrophoresis experiment for the PCR production of the *Rv0688* gene indicates that the reactions in the absence and presence of DMSO and  $MgCl_2$  were successful with a product size corresponding to ~1.2 kb. Compared to the theoretical calculation from the DNA sequence, the size of PCR product is correct. In addition, to insert the gene into an expression vector, as described in the Methods section (section 2.4.7), genes and vectors were digested with the same restriction enzymes (*Bam*HI and *Nde*I), and then ligated overnight. The ligations thereafter were transformed into the *Escherichia coli* NovaBlue strain to propagate the recombinant plasmid. The isolated plasmids were then digested and sequencing performed to confirm the successful cloning of the *Rv0688* gene. As shown in Figure 5.2, agarose gel electrophoresis reveals bands in both lanes 1 and 2, which correspond to the size of the pET15b vector (~5.7 kb) and the *Rv0688* gene (~1.2 kb). Moreover, the DNA sequencing results also indicated that the sequences of the amplified and theoretical gene sequences are absolutely identical (data not shown). Therefore, these results suggest that the cloning and insertion of the *Rv0688* gene into a pET15b expression vector were successful.

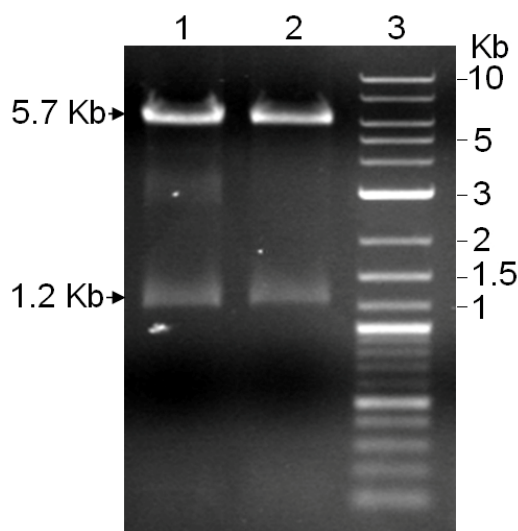


**Figure 5.2. Digestion products of a recombinant pET15b vector containing the *Rv0688* gene.** Lane 1-2: digestion of pET15b with restriction enzymes (*Nde*I and *Bam*HI - see detailed vector pET15b map in Figure 2.2, section 2.4.7, demonstrating that the clone contains the *Rv0688* gene corresponding to ~1.2 kb. Lane 3: Molecular mass standards (10000, 5000, 3000, 2000, 1500 and 1000 bp fragments indicated).

For the expression of the Mtb gene *Rv0688* (FdR), the gene was expressed from an inducible T7 promoter system in the plasmid vector pET15b. The soluble protein of the histidine tagged FdR was produced as described in the Methods chapter (section 2.5). The FdR protein has a predicted molecular weight of 43017.8 Da, and its His-tag has a molecular weight of approximately 2181.3 Da. Therefore, the expressed protein should

have a molecular mass of ~45.2 kDa. The trial expression showed that there was a large protein band which was overexpressed during induction with 1 mM IPTG (Figure 5.3). This molecular mass corresponds well to the original molecular mass calculated based on the amino acid sequence. The total protein at each different time point was compared by a SDS-PAGE gel, and results indicated that the expression levels of target protein (FdR) was slightly different between 2 h, 8 h, and 24 h time points. However, the induced cells grew slowly after IPTG induction, and therefore the cell culture was extended to 24 h in order to obtain higher biomass.

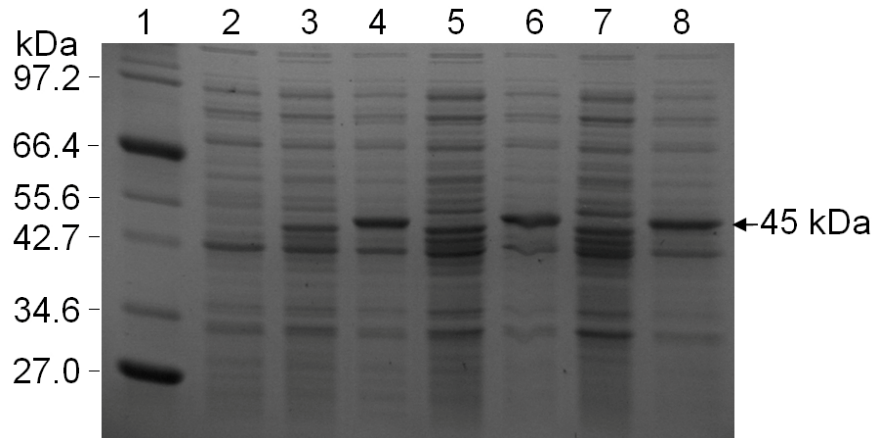


**Figure 5.3. SDS-PAGE gel of FdR trial expression in *Escherichia coli* HMS174 (DE3) cells.** Cells were induced using 1 mM IPTG at different times, ranging from 0 to 24 h. Lane 1: Molecular mass standards (97200, 66400, 55600, 42700, 34600, 27000 Da); lane 2: total protein at time T=0; lane 3-4: total protein of control (uninduced) and induced samples at T= 2 h; lane 5-6: total protein of control and induced samples at T= 8 h; lane 7-8: total protein of control and induced samples at T= 24 h.

From the trial expression results, it was shown that FdR could be expressed to high levels under control of the T7 RNA polymerase promoter system in pET15b, using the *E. coli* HMS174 (DE3) strain, and cell pellets of the induced *E. coli* transformants were markedly green/yellow in colour, suggesting high levels of production of the flavin-containing protein. Analysis of the trial expression of FdR by SDS-PAGE showed that the heterologously expressed FdR was produced at higher levels than any of the host proteins. In Figure 5.4, the protein was expressed as a soluble form, and after induction by IPTG the cells did not grow well, so that it was necessary to extend the culture to 24 h to obtain higher density of cells.

In addition, this protein also presented an easy purification process by using a Ni-NTA column. Moreover, SDS-PAGE analysis of the cell pellet after sonication also revealed that a large amount of FdR was located in inclusion bodies (Figure 5.4, lane 8). However, the

expression of FdR in the *E. coli* HMS174 (DE3) strain is very good, with large amounts of soluble protein also obtained in 10 litre culture growth, thus making it unnecessary to recover further protein by solubilization of inclusion bodies. Therefore, these results suggest that the FdR protein was successfully expressed at very high levels and could be used for further experiments. The large scale purification of the FdR protein (from 10 litres of culture) also indicated that the protein could be isolated as a homogeneous form with a large amount of soluble, purified protein recovered, resulting in production amounts of ~2.6 mg/litre culture (Figure 5.5).

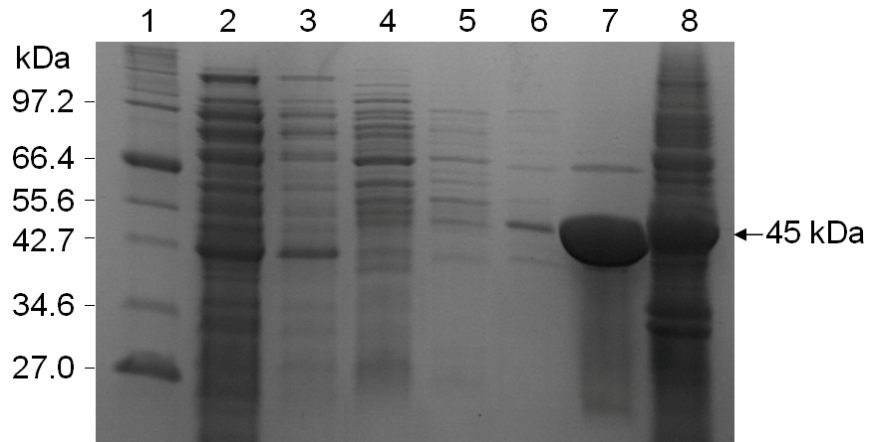


**Figure 5.4. SDS-PAGE gel of FdR trial purification in HMS174 (DE3).**

Cells were grown at 37 °C with 1 mM IPTG induction. Lane 1: Molecular mass standards (97200, 66400, 55600, 42700, 34600, 27000 Da); lane 2: flow through after Ni-NTA column; lane 3: buffer wash; lane 4-5: 5 mM imidazole wash; lane 6: 10 mM imidazole wash; lane 7: elution with 120 mM imidazole; lane 8: cell pellet after centrifugation.

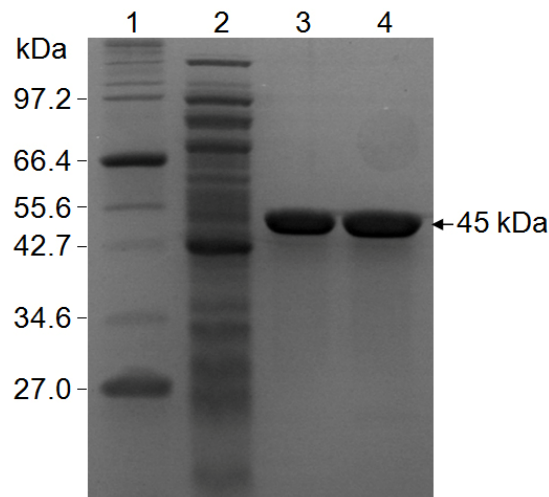


**Figure 5.5. SDS-PAGE gel of large scale purification scheme for FdR.**

An SDS/PAGE gel is shown (12% acrylamide) indicating the purification of Mtb FdR from *E. coli* HMS174 (DE3) using a Ni-NTA column. Lane 1: molecular mass standards (97200, 66200, 55600, 42700, 34600, 27000 Da); lane 2: total protein after loading column; lane 3-4: elution of column with 50 mM imidazole.

### 5.2.1.2 General properties of FdR

The UV-visible spectrum of recombinant FdR displays characteristic flavoprotein absorbance maxima at 272, 365, and 455 nm (Figure 5.6), and the ratio of total protein to flavin-specific absorption ( $A_{272}/A_{455}$ ) was 7.3. The pure oxidized FdR enzyme possesses spectral features typical of flavin-containing enzymes with the two characteristic flavin absorbance bands between 300 and 500 nm. Shoulders on the longer wavelength band are located at 428 and 479 nm. The protein/flavin absorption ratio ( $A_{272}/A_{455} = 7.3$ ) compares favourably with values reported previously for FprA from Mtb ( $A_{274}/A_{452} = 6.8$ ) (161), and with ADR purified from bovine adrenal gland ( $A_{272}/A_{450} = 8.4$ ) (344) and from rat liver ( $A_{269}/A_{450} = 7.25$ ) (345). Addition of excess sodium dithionite under anaerobic conditions induced full reduction of the FAD, with complete bleaching of the flavin spectrum and without formation of spectral signals attributable to flavin semiquinone species. Addition of excess NADPH or NADH (20-fold) resulted in complete flavin reduction (see details in section 5.2.1.3). Only for NADH reduction was there a small proportion of semiquinone (SQ) formed during the reductive reaction, with the development of an absorption band located at 584 nm. This SQ disappeared when the FAD was fully reduced to its hydroquinone form by NADPH (Figure 5.8 A, B).

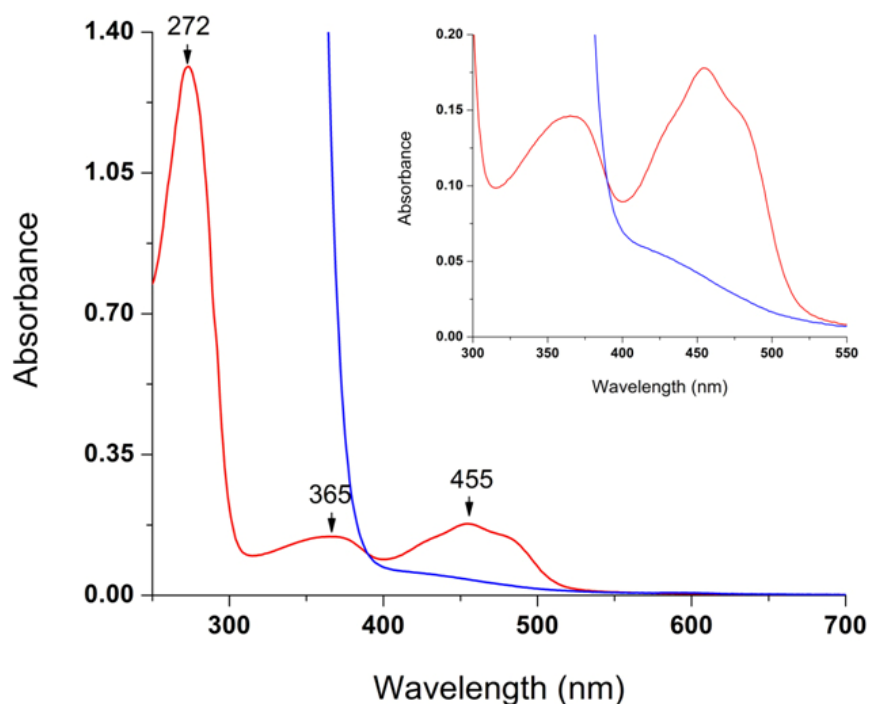


**Figure 5.6. Ultraviolet-visible absorbance spectra of pure FdR.**

The absorbance was recorded in 100 mM potassium phosphate (pH 7.5) at a protein concentration of  $\sim 20 \mu\text{M}$ . The protein absorbs at 272, 365, and 455 nm, with the inset showing an expanded scale spectrum of the characteristic flavin absorbance region between 300 and 550 nm. The sodium dithionite-reduced FdR is shown in a blue line with completely hydroquinone flavin.

In addition, aerobic oxidation experiments of FdR also indicated that the reduced enzyme is sensitive to oxygen, even in the presence of a small amount of oxygen in the buffer. To confirm the sensitivity of FdR to oxygen, the spectrum of the oxidized state of the enzyme was recorded and the protein was titrated with appropriate amounts of sodium dithionite to obtain approximately 80% reduced enzyme in anaerobic conditions. Thereafter, the mixture was bubbled with air. Absorbance scans were recorded every two minutes, and the results showed that under aerobic conditions there was a significant rate of reoxidation of FdR (23  $\mu\text{M}$ ). The reoxidation progress was completed within  $\sim 24$  minutes, with the calculated reoxidation rate of  $9.51 \pm 0.44 \times 10^{-4} \text{ s}^{-1}$  ( $0.057 \pm 0.003 \text{ min}^{-1}$ ) (Figure 5.7). This was compared to the reoxidation rate of NADH- and NADPH-reduced FprA enzyme samples ( $1.26 \pm 0.06 \text{ min}^{-1}$  and  $0.043 \pm 0.004 \text{ min}^{-1}$ , respectively) (161), indicating that the reoxidation rate of FdR is much slower than for NADH-reduced FprA, but slightly higher than for NADPH-reduced FprA. In addition, the reoxidation of FdR occurs without any accumulation of flavin SQ, and only oxidized and hydroquinone forms of the protein are present throughout the experiment. This suggests that the semiquinone is destabilized in favour of the hydroquinone and oxidized forms, and the one-electron reduced form of FAD was not stabilized on oxygen reduction, due either to electronic comproportionation between semiquinones or direct two electron reduction of oxygen.

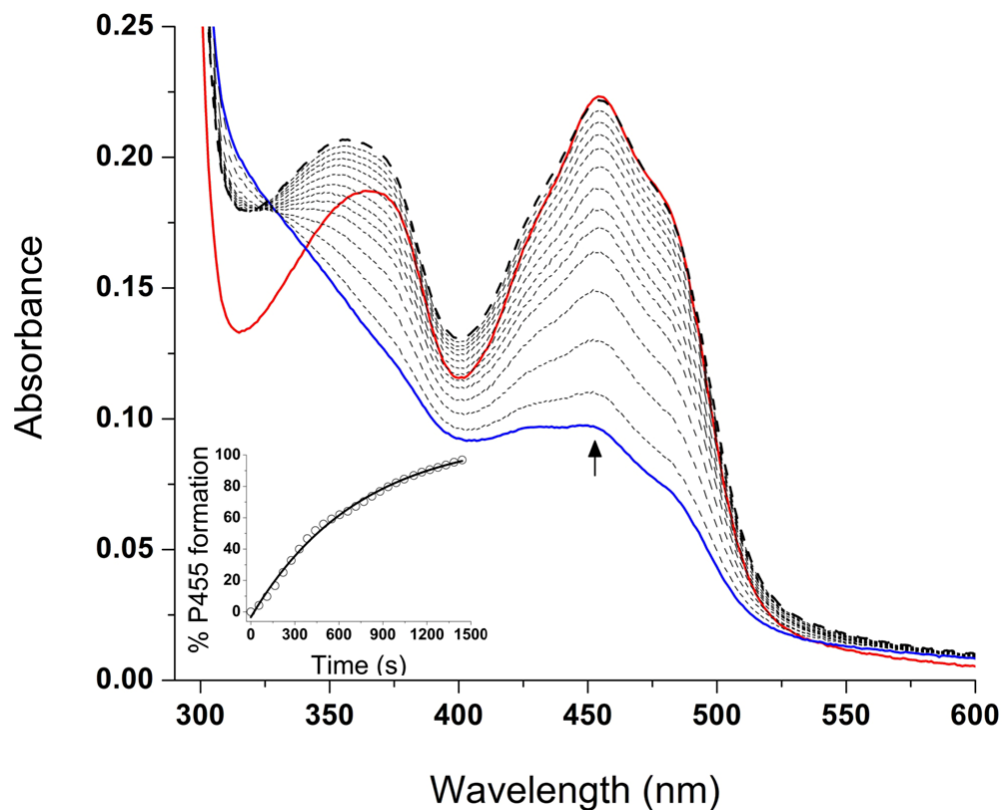


**Figure 5.7. Re-oxidation of FdR under aerobic conditions.**

A representative spectrum for the oxidized state of FdR at a concentration of  $\sim 23 \mu\text{M}$  is shown in the red line, and titration was performed using sodium dithionite to obtain  $\sim 80\%$  reduced FdR (shown in the blue line). A scan was recorded every two minutes, and the recovery of the fully oxidized form of FdR was obtained after approximately 24 minutes (shown as a black dashed line). The spectrum showed that the  $\sim 80\%$  reduced FdR re-oxidized fully within  $\sim 24$  minutes. The inset shows a plot of  $A_{455}$  versus time (named P455 for recovered flavin) and the rate constant was determined as  $9.51 \pm 0.44 \times 10^{-4} \text{ s}^{-1}$  by using a single exponential function.

### 5.2.1.3 Reduction of FdR by NAD(P)H

Bacterial P450 redox systems consist of at least two redox partner proteins involving two electron delivery steps, and using ferredoxin reductase and ferredoxin proteins. Initially, oxidation of NAD(P)H releases two electrons, which will reduce oxidized ferredoxin reductase to its hydroquinone form. In this form, the ferredoxin reductase has ability to donate  $2 \times 1e^-$  to ferredoxin proteins, which transfer electron(s) to P450 for its substrate oxidation function. Therefore, ferredoxin reductase is defined as the first electron carrier, which can directly receive electron(s) from donor (NADH or NADPH) and then transfer them to ferredoxin and then onto the final target P450. In order to test the electron accepting ability of FdR, the protein was mixed with 20-fold excess concentrations of NADH and NADPH in presence and absence of oxygen. The results are detailed in Figure 5.8.

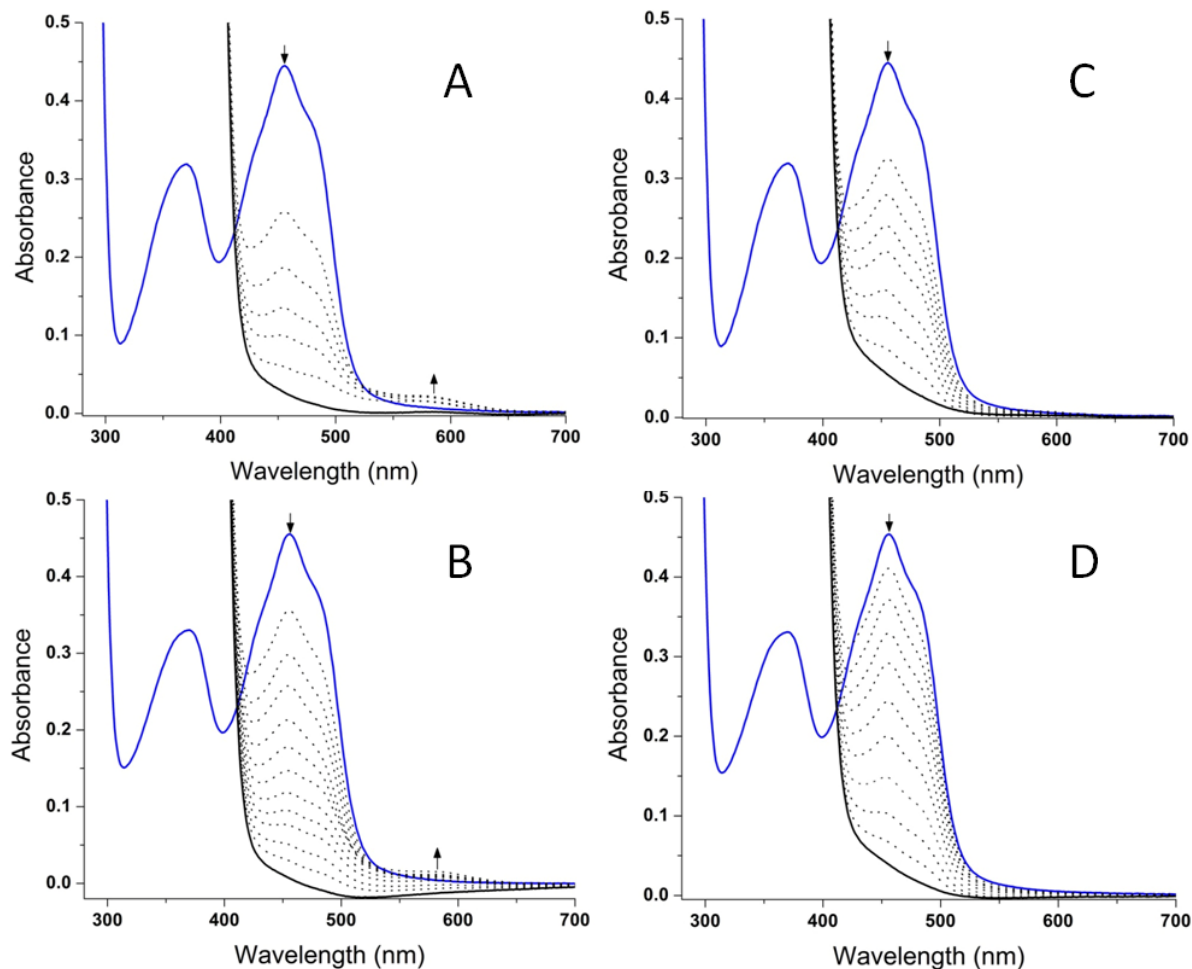


**Figure 5.8. UV-visible spectra of Mtb FdR (45  $\mu$ M) during reduction by NAD(P)H.**

The reduction spectra of FdR with NADH (1 mM) and NADPH (0.5 mM) were recorded under anaerobic (upper row) and aerobic (lower row) conditions. (A) Representative spectra for the reduction of FdR with NADH under anaerobic conditions. The upper blue line is the oxidized form, the solid black line is the fully reduced form collected at 20 minutes. (B) Reduction of FdR with NADH under aerobic conditions, the blue line is oxidized FdR, the solid black line is the fully reduced FdR collected at 37 minutes. (C) Reduction of FdR with NADPH under anaerobic conditions, the upper blue line is oxidized FdR, the lower solid black line is the fully reduced FdR collected at 31 minutes. (D) Reduction of FdR with NADPH under anaerobic conditions. The solid black line is the fully reduced FdR obtained after 58 minutes.

Overall results indicated that NADH showed more efficient reductive activity than NADPH, which revealed a slower rate of flavin reduction. Figure 5.8A presents the reduction of FdR (45  $\mu$ M) with NADH under anaerobic conditions. The UV-visible spectrum of full oxidized enzyme (quinone form) shows a maximum absorbance peak of FAD at 455 nm. The reductive reaction occurs after addition of a 20-fold excess of NADH ( $\sim$ 1 mM), leading to loss of the yellow colour and to bleaching of the spectrum at 455 nm. In addition, at longer wavelength ( $\sim$ 550-600 nm), FdR exhibits increased absorption in the

reduced form, with a low intensity absorption peak at ~584 nm, suggesting that the reductant NADH produced a species with a spectral signature characteristic of the neutral blue FAD semiquinone state during the titration. The reaction progressed to full reduction of the FAD at 20 minutes, showing that the flavin absorbance was bleached and the semiquinone form also disappeared, with FAD converted to its hydroquinone state.

Similar characteristics were also obtained in the presence of oxygen. However, the reduction time was very different from anaerobic conditions. The reduction was completed after 20 minutes anaerobically, whereas in aerobic conditions with NADH it was completed after 37 minutes (Figure 5.8B). In the case of NADPH (0.5 mM), the reductive reaction under anaerobic conditions proceeded slower than with NADH, with the reductive reaction completed at 31 minutes without formation of neutral blue semiquinone form (Figure 5.8C). Under aerobic condition, the reaction was extended to a longer time, and completed at 58 minutes (Figure 5.8D). Compared with the reductive potency of NADH, it appears that NADPH is less effective. The conclusions from these results are that FdR protein could be reduced by both NADPH and NADH, but that NADH is a more efficient reductant of FdR than is NADPH.

#### **5.2.1.4 Kinetic properties of FdR**

Flavoprotein reductases can often catalyze electron transfer from NADH or NADPH to artificial electron acceptors such as ferricyanide (346). Therefore, steady-state kinetic studies of such flavoproteins often use ferricyanide as an electron acceptor substrate. Many flavoproteins use either or both the NADPH and NADH coenzymes as their natural electron donors (312). As shown in section 5.2.1.3, FdR was able to receive electrons from both NADH and NADPH. Therefore, in this study, the reductase activities of FdR were determined in steady-state assays by using the electron acceptor ferricyanide, and electron donor NAD(P)H. The  $K_m$  (affinity for substrate) and  $k_{cat}$  (limiting reaction rate) values for electron acceptors were calculated by fitting of the data to the Michaelis-Menten function. The electron donor NAD(P)H was used at near-saturating concentrations of ~1 mM (Figure 5.9).

Reactions with ferricyanide obeyed Michaelis-Menten behaviour and fits of data to rectangular hyperbolae yielded the relevant kinetic parameters. The reduction of ferricyanide generated  $k_{cat} = 466 \pm 9 \text{ min}^{-1}$  and  $K_m = 136 \pm 11 \text{ } \mu\text{M}$  (Table 5.1) – using NADPH as the electron donor at a concentration of 1 mM.

NADH and NADPH  $K_m$  values were obtained by re-determining ferricyanide reduction rates at a fixed saturating concentration of the electron acceptor (1 mM) and by varying the concentration of NADH/NADPH (0-1 mM) electron donors in the assays. The  $K_m$  values obtained for NADH/NADPH were  $80 \pm 17 \mu\text{M}/788 \pm 72 \mu\text{M}$  respectively, and the  $k_{\text{cat}}$  values were  $200 \pm 7/327 \pm 61 \text{ min}^{-1}$ , respectively (Table 5.1). The data reveal that the  $k_{\text{cat}}$  value for wild-type FdR with NADPH as reducing coenzyme ( $327 \pm 61 \text{ min}^{-1}$ ) is greater than with NADH ( $200 \pm 7 \text{ min}^{-1}$ ), possibly reflecting higher affinity for  $\text{NAD}^+$  product in the FdR. The  $K_m$  value for NADPH was much higher than that for NADH, reflecting the weaker apparent binding of NADPH to the enzyme. In addition, the specificity constant ( $k_{\text{cat}}/K_m$  ratio) showed a higher value for NADH than for NADPH, suggesting that FdR operates more efficiently with NADH.

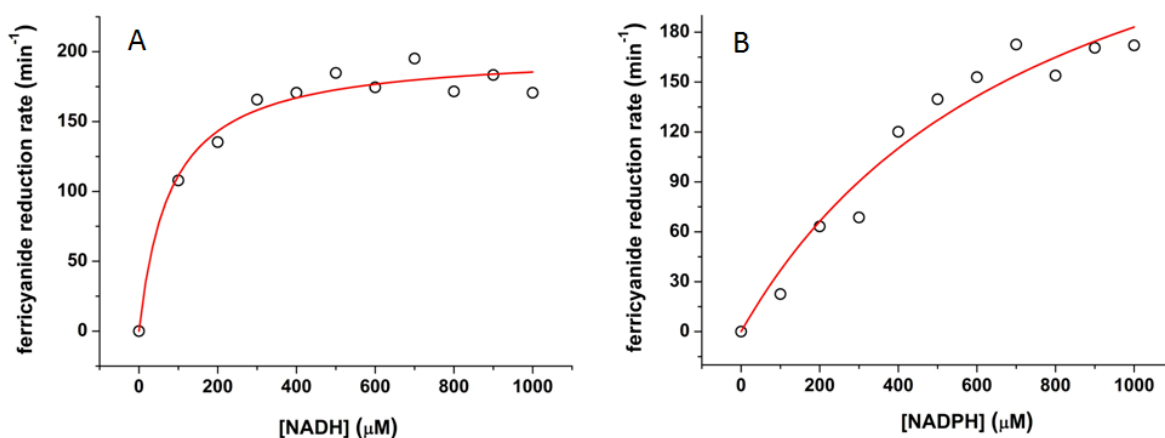


**Figure 5.9. Steady-state kinetics of NADH- and NADPH-dependent ferricyanide reduction in FdR.** Michaelis–Menten plots for Mtb FdR–catalyzed NADH- (panel A) and NADPH-dependent (panel B) reduction of potassium ferricyanide, as monitored at by the loss of ferricyanide absorbance at 420 nm on its reduction.

$k_{\text{cat}}$ ( $\text{min}^{-1}$ )			$K_m$ ( $\mu\text{M}$ )			$k_{\text{cat}}/K_m$ ( $\mu\text{M}^{-1} \cdot \text{min}^{-1}$ )			
Fe(CN) $_6^{3-}$	NADH	NADPH	Fe(CN) $_6^{3-}$	NADH	NADPH	Fe(CN) $_6^{3-}$	NADH	NADPH	$k_{\text{cat}}/K_m$ NADH
									$k_{\text{cat}}/K_m$ NADPH
466 $\pm$ 9	200 $\pm$ 7	327 $\pm$ 61	136 $\pm$ 11	80 $\pm$ 17	788 $\pm$ 72	3.4 $\pm$ 0.8	2.5 $\pm$ 0.4	0.4 $\pm$ 0.8	6.25 $\pm$ 0.5

**Table 5.1. Steady-state kinetic parameters for wild-type FdR.**

Steady-state assays and kinetic parameters were performed as described in the Methods section (section 2.18). Reaction rate data were calculated using an extinction coefficient of  $\Delta\epsilon_{420} = 1020 \text{ M}^{-1} \cdot \text{cm}^{-1}$  to generate  $k_{\text{cat}}$  and  $K_m$  parameters using a hyperbolic function. Values in the final column indicate the relative efficiency with NADH versus NADPH, based on the ratio of specificity constants using the two coenzymes.

### 5.2.1.5 Stopped-flow (PDA) studies of FdR

As mentioned in section 5.2.1.3, both reductants NADH and NADPH are able to reduce the FdR flavin cofactor. Steady-state kinetic studies of FdR activities with ferricyanide showed that the  $k_{\text{cat}}$  values are lower than those of other flavoproteins such as Mtb FprA ( $k_{\text{cat}}^{\text{NADH}} = 2720 \pm 100 \text{ min}^{-1}$ ,  $k_{\text{cat}}^{\text{NADPH}} = 2070 \pm 90 \text{ min}^{-1}$ ) (161) and *Plasmodium falciparum* ferredoxin-NADP<sup>+</sup> reductase (PfFNR) ( $k_{\text{cat}}^{\text{NADH}} = 96 \pm 4 \text{ s}^{-1}$ ,  $k_{\text{cat}}^{\text{NADPH}} = 250 \pm 7.7 \text{ s}^{-1}$ ) (347, 348). A comparison with several sequences of FNR-like proteins, such as spinach leaf FNR, maize root FNR, and *T. gondii* FNR, indicated that they all possess two basic residues (Arg<sup>235</sup> and Lys<sup>244</sup>) in their NADP<sup>+</sup> binding motifs. These amino acids are thought to stabilize the 2' phosphate of NADP(H) and are highly conserved within FNR family (349). In addition, the comparison of the Mtb FdR (*Rv0688*) amino acid sequence with those sequences of the FNR proteins above indicate that FdR lacks these two basic residues, and that this could explain the observed lower affinity for NADP(H) (350, 351). Moreover, studies of flavin reduction suggested that the reductive half-reaction of the FdR catalytic cycle was probably responsible for the low values of  $k_{\text{cat}}$  for ferricyanide reductase activity (352). To prove this hypothesis and to analyse further this catalytic step in FdR, the process of reduction and re-oxidation of the protein by NADH, NADPH, NAD<sup>+</sup>, and NADP<sup>+</sup> was investigated by stopped-flow diode array spectrophotometry.

The spectra of FdR (50  $\mu\text{M}$ ) reacting with either NADH or NADPH (stoichiometric or 20-fold excess) were recorded by stopped-flow absorbance spectroscopy using a photodiode array (PDA) attachment on the Applied Photophysics instrument, over a variety of time scales following the mixing event. The data for NADH confirm the findings from the UV-visible spectrometry study that the reductive reaction proceeds faster than that of NADPH over the time regimes used (1000 s), as shown in Figures 5.10 A, B. Furthermore, the PDA spectra of FdR also indicated that the reaction did not progress to reach full reduction of FAD (~90%) within 1000s (~16.7 min), similar to the other reduction studies of FdR reported in section 5.2.1.3 (Figure 5.8A). In this time regime, the data for reduction by stoichiometric NADH fit to a biphasic expression and a single step model ( $A \rightarrow B$ ) for the best fit to the data, with approximately 90% of the amplitude in the initial (fast) phase and a slow phase consistently occurring at  $9.53 \pm 0.64 \times 10^{-4} \text{ s}^{-1}$  (Figure 5.10 A).

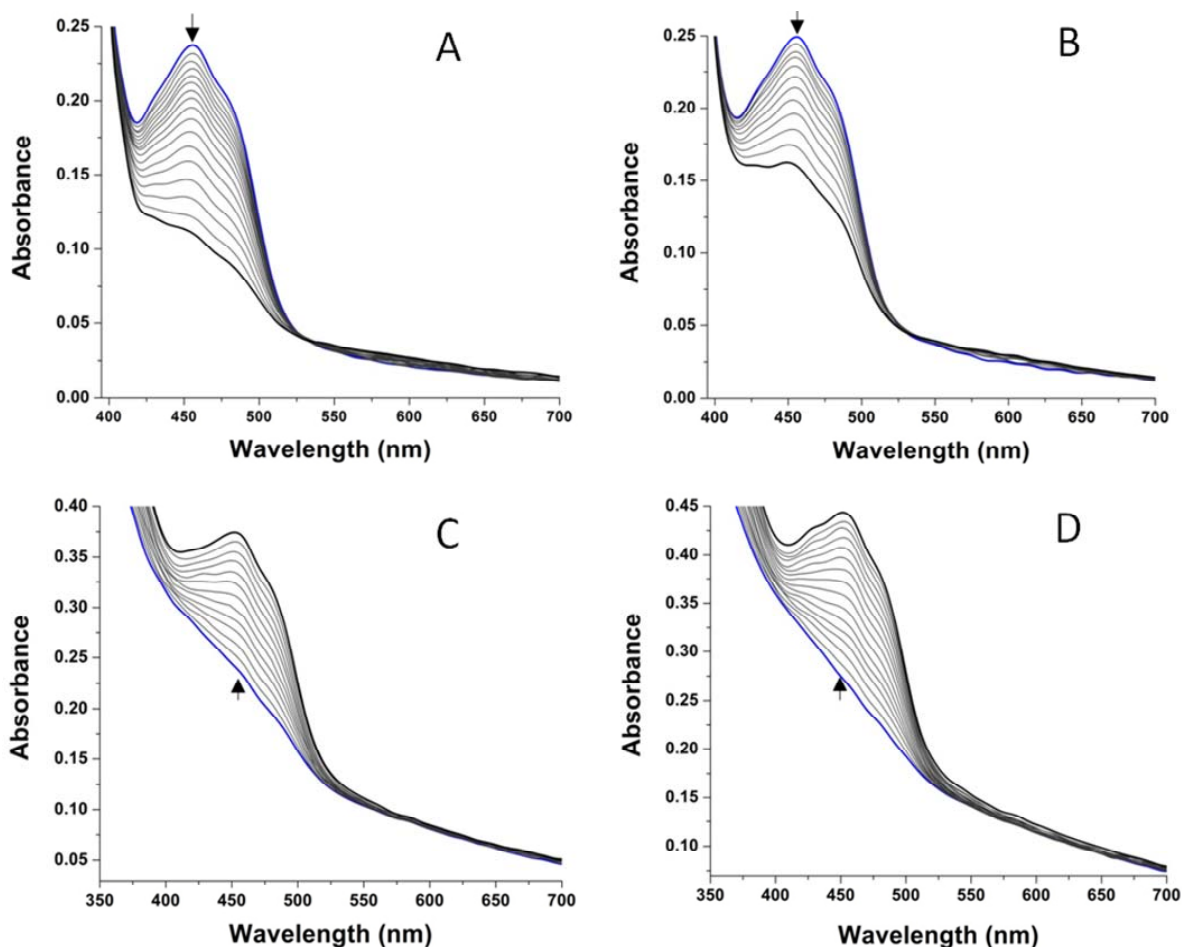


**Figure 5.10. PDA UV-visible absorption spectra for oxidative and reductive reactions of FdR.** Reaction of Mtb FdR with NADH (1 mM) and NADPH (0.5 mM) monitored by stopped-flow photodiode array spectroscopy during the anaerobic reduction and reoxidation of FdR were collected as described in the Methods section (section 2.22). Time-dependent spectral changes occurring over 1000 s following rapid mixing of FdR with NADH/NADPH were recorded. Data were analyzed using the Photophysics Prokin software package to identify distinct spectral intermediates in the reactions. Spectra are shown for the reductive half reaction of FdR (11  $\mu\text{M}$ ) with a 10-fold excess of NADH (**A**) and NADPH (**B**). The upper blue thick line is the first spectrum collected (at 0.00771 s) and the lower black thick line the spectrum collected at approx. 0.584 s. Intermediate spectra are shown in thinner lines. Arrows indicate direction of absorbance change at the flavin maximum at 455 nm. (**C**) and (**D**) show reoxidation of dithionite-reduced FdR (11  $\mu\text{M}$ ) with 500  $\mu\text{M}$   $\text{NAD}^+$  and 250  $\mu\text{M}$   $\text{NADP}^+$  respectively. In (**C**), the lower blue thick line is the first spectrum collected at 0.00325 s and the upper black thick line the spectrum collected at 0.214 s. Intermediate spectra are shown in thinner lines. Arrows indicate direction of absorbance change at the flavin maximum at 455 nm. In (**D**), the lower blue thick line is the first spectrum collected (0.00348 s) with upper black thick line showing the spectrum collected at 1000 s.

Using stoichiometric NADPH, reduction was slower than with NADH and did not progress to full reduction of FAD. At 20-fold excess NADPH, approximately 70% FAD was converted to the hydroquinone form after 1000 s following the mixing event. Over the time frame, the NADPH reduction data fit best to a model (A $\rightarrow$ B) with approximate 90% of the

amplitude in the rapid first phase and the slow phase again occurring consistently at  $2.47 \pm 0.28 \times 10^{-4} \text{ s}^{-1}$  (Figure 5.10 B). The rate constants measured in the PDA mode for the fast phases in both NADH and NADPH-dependent FdR reductions are similar.

PDA detection was also used to follow the spectral changes occurring following mixing of dithionite-reduced (in hydroquinone form) FdR with  $\text{NAD}^+$  and  $\text{NADP}^+$ . The PDA data collected in these experiments were consistent with single-wavelength studies at 455 nm, showing slow flavin reoxidation in the FdR, and revealed an oxidation rate at  $3.34 \pm 0.1 \times 10^{-2} \text{ s}^{-1}$  on mixing with  $\text{NAD}^+$  (Figure 5.10 C) and  $1.43 \pm 0.03 \times 10^{-2} \text{ s}^{-1}$  with  $\text{NADP}^+$  (Figure 5.10 D). The final spectra collected for oxidized FdR reduced with NADH and NADPH (to hydroquinone FdR) and those for hydroquinone FdR that were fully reoxidized with the same  $\text{NAD}^+$  and  $\text{NADP}^+$  concentrations (1 mM  $\text{NAD}^+$  and 0.5 mM  $\text{NADP}^+$ ) showed that the same spectral end points are reached in either oxidative (hydroquinone FdR plus  $\text{NAD}^+/\text{NADP}^+$ ) or reductive (oxidized FdR plus NADH/NADPH) directions.

#### **5.2.1.6 Light scattering analysis of FdR**

The size and oligomeric status of FdR was first analysed by multi-angle laser light scattering (MALLS). Figure 5.11 shows the native form of FdR that was analyzed by MALLS coupled to gel filtration to yield a molecular mass. Two refractive index peaks were observed, eluting centered at  $\sim 12.5$  and  $14.7$  ml, respectively. The flat trace of calculated mass shows that the peak 1 corresponds to a molecular mass of  $92.2 \pm 2.2$  kDa, the peak 2 located at  $\sim 14.7$  ml elution has a corresponding molecular weight of  $45.6 \pm 1.2$  kDa. These two distinct species have molecular mass estimates of 92 and 45 kDa, respectively, in agreement with dimer and monomer masses as predicted from amino acid sequence. In addition, the analysis of refractive index indicated that the monomer species is predominant with  $\sim 92\%$  of total protein, whereas the minor species of dimer accounts for  $\sim 8\%$ . Moreover, the two major refractive index peaks observed at  $\sim 12.5$  and  $14.7$  ml were pooled and analyzed by SDS-PAGE (12% acrylamide), and the results indicated that these peaks both contained the FdR protein (data not shown).

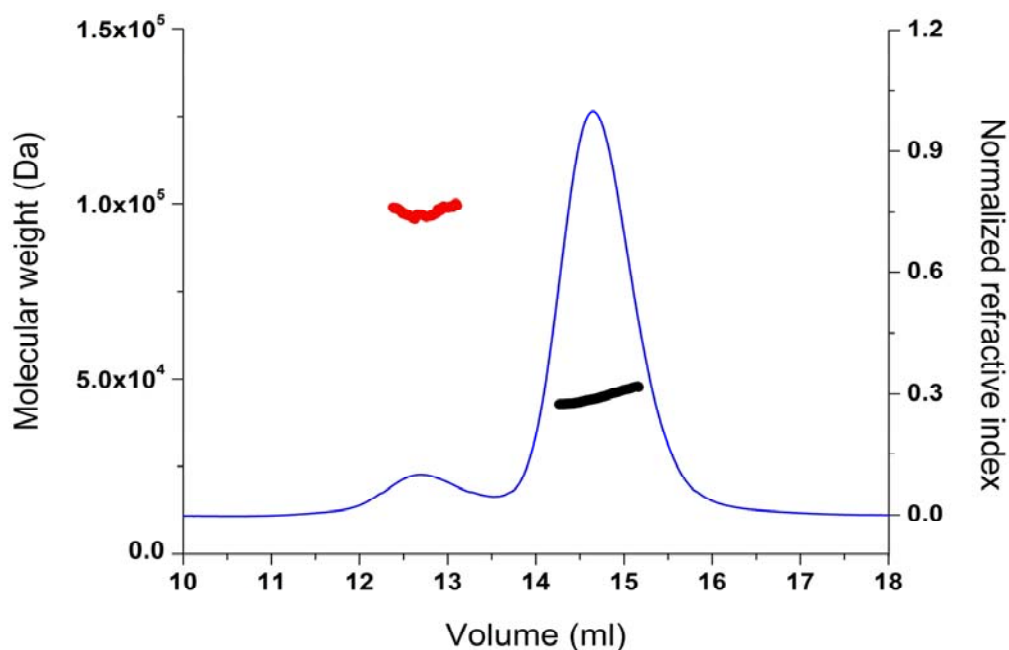


**Figure 5.11. Superdex–200 10/300 GL gel filtration chromatography and MALLS analysis of Mtb FdR.** The chromatograms were baseline corrected and the differential refractive index (a measure of protein concentration) was normalized to 1.0 for each peak maximum. Two refractive index peaks were observed eluting at ~12.5 and 14.7 ml. The light scattering and the refractive index are used by the instrument software to calculate molecular mass. Material eluting at 12.5 and 14.7 ml was found to have apparent mass of  $45.6 \pm 1.2$  kDa and  $92.2 \pm 2.2$  kDa, respectively.

### 5.2.1.7 Differential Scanning Calorimetry analysis of FdR

To investigate structural stability of FdR to temperature denaturation, DSC scans were performed with highly purified FdR to estimate the temperature at which the protein unfolds. Figure 5.12 shows the result of DSC scans conducted with native FdR. During initial heating scans, the experiment was terminated shortly after the  $T_m$  had been reached. The scanning result indicated that unfolding of this ferredoxin reductase occurs at temperatures rather lower than some other flavoproteins such as ferredoxin-NADP<sup>+</sup> reductase from spinach chloroplast ( $T_m = 66$  °C) (353). The data shown in Figure 5.12 are for the initial scan that was collected beyond the  $T_m$  so that adequate post-transition baselines were collected for data analysis.

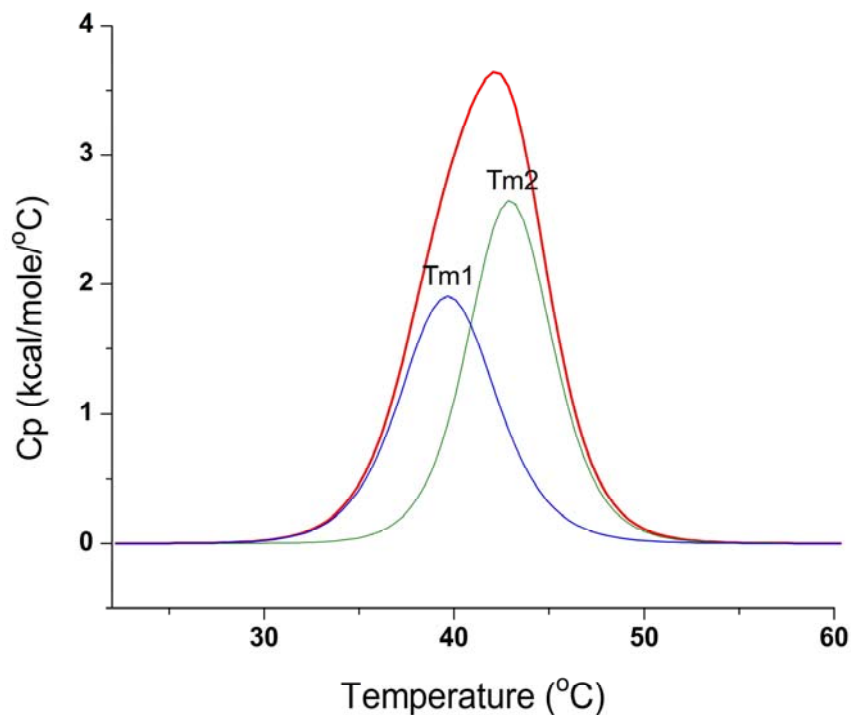


**Figure 5.12. DSC analysis of Mtb FdR.**

A DSC scan for Mtb ferredoxin reductase FdR is shown. Protein sample was in 10 mM potassium phosphate (pH 7.5) and heated from 20 °C to 90 °C with a scan rate of 60 °C/h. In the scan the solid red line is the experimentally measured unfolding endotherm, and the blue and green lines are nonlinear least-squares best fits to the data obtained using a non-two-state unfolding model incorporated in Origin software (OriginLab). For clarity, two  $T_m$  values are indicated with  $T_{m1}$  at 39.71 °C and  $T_{m2}$  at 42.97 °C.

It is clear from Figure 5.12 that the protein was found to have a midpoint melting temperature (*113*) of 42.06 °C. The peak contains two distinct unfolding events that possibly relate to the unfolding temperatures of the C- and N-terminal domains of the protein. In this scenario, one domain unfolds at 39.71 °C and the other at 42.97 °C. The unfolding temperatures and enthalpy values of FdR are summarized in Table 5.2. Structurally, the FNR-like protein is comprised of two domains, including a N-terminal domain, which binds FAD, and a C-terminal domain, which binds NADP<sup>+</sup>/NADPH. Therefore, perhaps the two unfolding  $T_m$  of FdR at 39.71 °C and 42.79 °C are associated with NADP<sup>+</sup>-binding and FAD binding domains unfolding sequentially. In comparison with another flavin protein, FdR reveals a lower  $T_m$  than the spinach chloroplast ferredoxin NADP<sup>+</sup> reductase, which shows an unfolding temperature at 66.3 °C (*353*).

Sample	$T_m$ ( $^{\circ}C$ )	$T_{m1}$ ( $^{\circ}C$ )	$\Delta H1$ (kcal/mol)	$T_{m2}$ ( $^{\circ}C$ )	$\Delta H2$ (kcal/mol)
Mtb FdR	42.06 $\pm$ 0.12	39.71 $\pm$ 0.23	1.29 $\pm$ 1.57	42.97 $\pm$ 0.11	1.56 $\pm$ 1.35

**Table 5.2. Calorimetrically derived thermodynamic parameters for unfolding of Mtb FdR.** The parameters derived from DSC studies on the FdR are shown. Data were collected as described in the Methods section (section 2.15). The  $T_m$  encompasses two melting temperatures.  $T_{m1}$  and  $T_{m2}$  indicate the melting temperatures from the two deconvoluted curves. The enthalpy of unfolding ( $\Delta H$ ) for the deconvoluted curves is also shown. The data were analyzed using Origin software (OriginLab).

### 5.2.1.8 Potentiometric analysis of FdR

The reduction potential of the flavin in the FdR protein was determined by titration of small amounts of sodium dithionite with simultaneous recording of the applied potential and the induced spectral change. The spectral changes observed during the redox titration of Mtb FdR at  $\sim 78 \mu M$  were monitored by ultraviolet/visible spectrophotometry between 350 nm and 700 nm, and are displayed in Figure 5.13. During titration with sodium dithionite, it was clearly shown that there was negligible formation of any stable semiquinone intermediate with long-wavelength absorbance. The formation of semiquinone is destabilized compared to the hydroquinone under equilibrium titration with sodium dithionite (reductant) and ferricyanide (oxidant). The spectral changes suggest that the FAD flavin of the enzyme converts from an oxidized flavin form to its hydroquinone in the reduced form. Since sodium dithionite's own potential is  $\sim -420$  mV, the completed reduction of FdR was achieved with a small amount of reductant added. The midpoint potential was determined from the redox titration data using absorption change at the flavin peak at 455 nm.

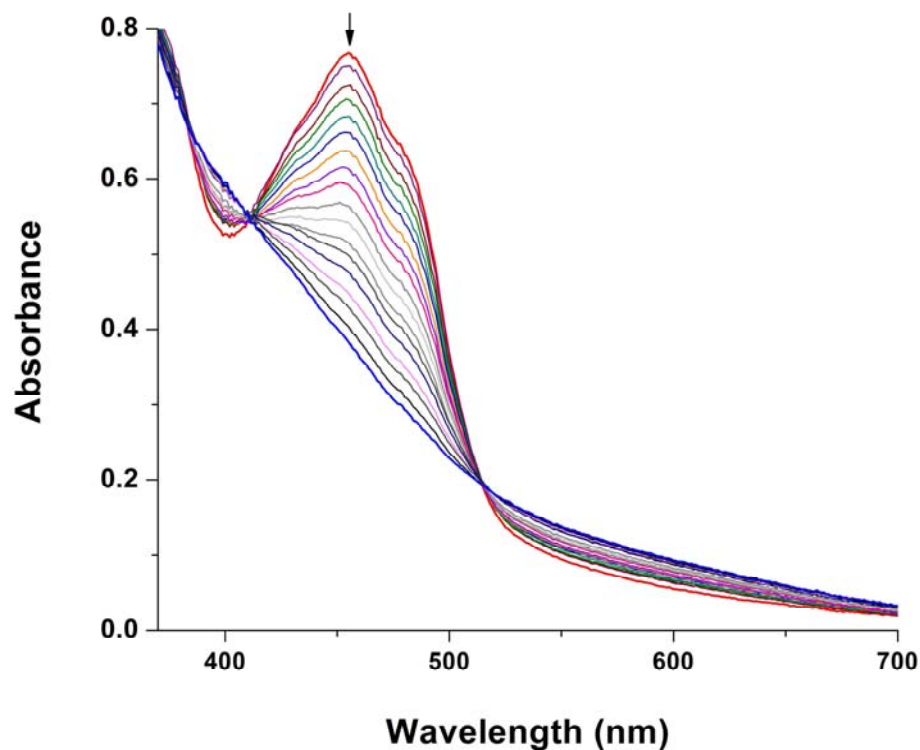


**Figure 5.13. UV-visible spectra of Mtb FdR during redox titration.**

A reductive (sodium dithionite) titration was performed anaerobically as described in the Methods section (section 2.12). Spectral changes accompanying reductive potentiometric titration of the ligand-free FdR ( $\sim 78 \mu\text{M}$ ) in 100 mM potassium phosphate, pH 7.0 are shown. The starting spectrum is that of the oxidized form of FdR with absorption maximum at 455 nm (thick red line). The spectra shown by other lines are those representing the conversion from the oxidized form to the hydroquinone form; with decreasing absorbance in the 455 nm region. The thick blue line shows the spectrum of the maximal hydroquinone species (fully reduced) with the bleaching of the flavin spectrum. The arrow indicates direction of spectral changes during the reductive reaction. Negligible spectral signals typical of the blue semiquinone form of the FAD flavin accumulate during reduction at longer wavelengths.

The absorbance versus potential data were fitted by using the Nernst equation to generate a 2-electron fit to the data, comprising the sum of two 1-electron redox function designed to model the absorbance of a flavin passing through different oxidation states. It was feasible to calculate the mid-point reduction potential for the Mtb FdR flavin domain. In this case, a fit of apparent absorption change at the flavin maximum ( $A_{455}$ ) against applied potential to a 2-electron Nernst function gave a midpoint potential of  $-252 \pm 3 \text{ mV}$  for the oxidized/hydroquinone transition (Figure 5.14). In preliminary redox titrations of FdR, it was found that the enzyme is very stable over the several hours required to complete the titration. Thus, this property aided accurate determination of the reduction potential of FdR. The redox titration was repeated in the same conditions, and the midpoint potential was found to be similar.

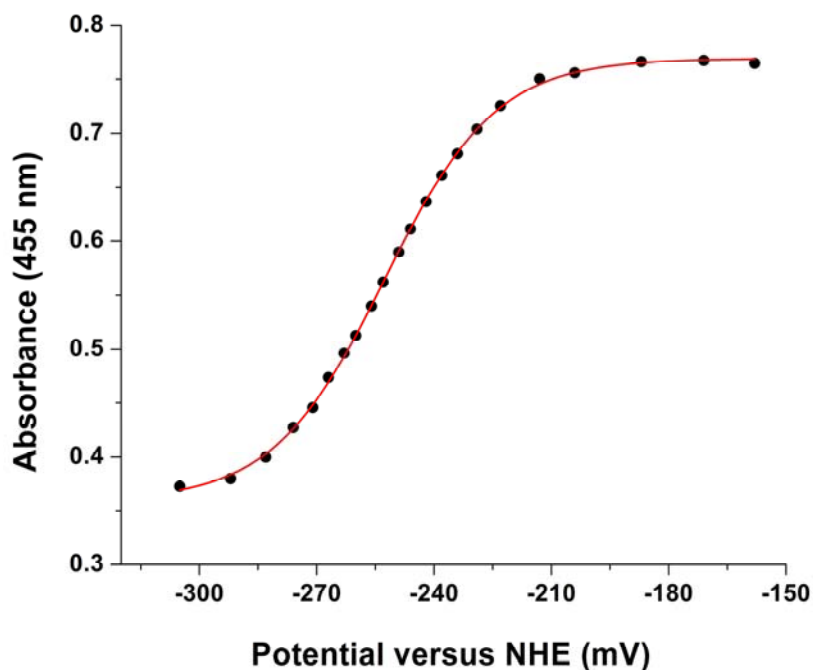


**Figure 5.14. Analysis of potentiometric data for FdR.**

An absorption versus potential plot of redox titration data is shown, with data fitted to a modified Nernst equation. The data at 455 nm (the maximal absorption of oxidized FdR) were fitted to a 2-electron Nernst function and the end-point absorption values predicted to allow an estimation of the mid-point potential for the enzyme. The potential determined was  $-252 \pm 3$  mV.

### 5.2.2 Expression and purification of flavodoxin $\text{NADP}^+$ oxidoreductase (FLDR)

In *Escherichia coli*, flavodoxin  $\text{NADP}^+$  oxidoreductase (FLDR) and flavodoxin (FLD) are two flavin-containing components of a short electron transfer chain from NADPH (162), which plays an important role as an electron donor system that functions in biotin synthesis (354). These enzymes are also involved in the crucial anaerobic generation of pyruvate for glycolysis, and in the generation of deoxyribonucleotides (355). A recent investigation has shown that the *E. coli* FLDR/FLD system can serve as a reductase system for heterologously expressed P450s, even though no endogenous P450s have yet been found in *E. coli* (356). Of particular interest is the analysis of the energetics of electron distribution between these two flavoproteins, since cytochromes P450 require two successive single electron transfers to perform their activation of molecular oxygen. In order, to study electron transfer from FLDR/FLD to P450s, these enzymes were over-expressed and purified.

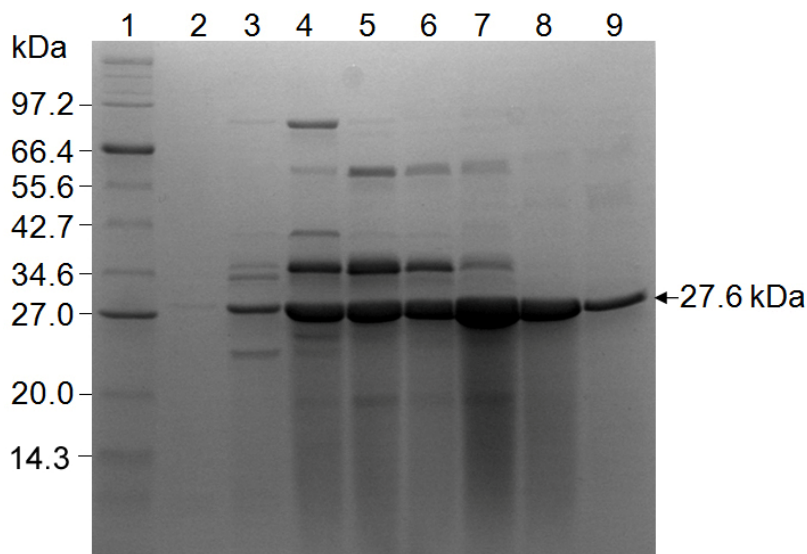


**Figure 5.15. SDS-PAGE analysis of *E. coli* flavodoxin NADP<sup>+</sup> oxidoreductase (FLDR) purification steps.** The protein was purified using a Q-Sepharose column. Lane 1, broad range molecular mass standards (97200, 66400, 55600, 42700, 34600, 27000, 20000, 14300 Da); lane 2-9, fractions 14, 19, 24, 27, 30, 33, 36, and 42 were eluted at different concentrations of sodium chloride in the range 0-1 M. The band at 27.6 kDa corresponds to the FLDR molecular weight.

For expression and purification of FLDR, The FLDR-encoding gene was constructed and kindly supplied by Dr. Kirsty McLean (The University of Manchester). The gene was expressed in the *E. coli* HMS174 (DE3) strain with a high level of soluble protein, as described in the Methods chapter (section 2.5). The wild-type FLDR was overexpressed successfully and purified to homogeneity in one chromatographic step (Q-Sepharose). The protein was eluted with the use of linear elution gradients (0-1 M) of sodium chloride, and FLDR (under the conditions used) started eluting from the column at fraction 14 (corresponding to a NaCl concentration of 30 mM in 50 mM Tris, 1 mM EDTA, pH 7.5). FLDR possesses a yellow colour, so that all fractions which are yellow were collected and analyzed on SDS-PAGE (12%) to check their purity. Figure 5.15 presents the purification process of FLDR using a Q-Sepharose anion exchange column with SDS-PAGE of various fractions shown on the gel. Interestingly, lanes 8 and 9 (fractions 36 and 42) indicated a purified protein corresponding to 27.6 kDa, and the gel also confirmed that the protein is purified as a unique species with no significant proteolysis evident. Finally, all fractions from 36 to the end were collected and concentrated as the purified protein for further experiments.

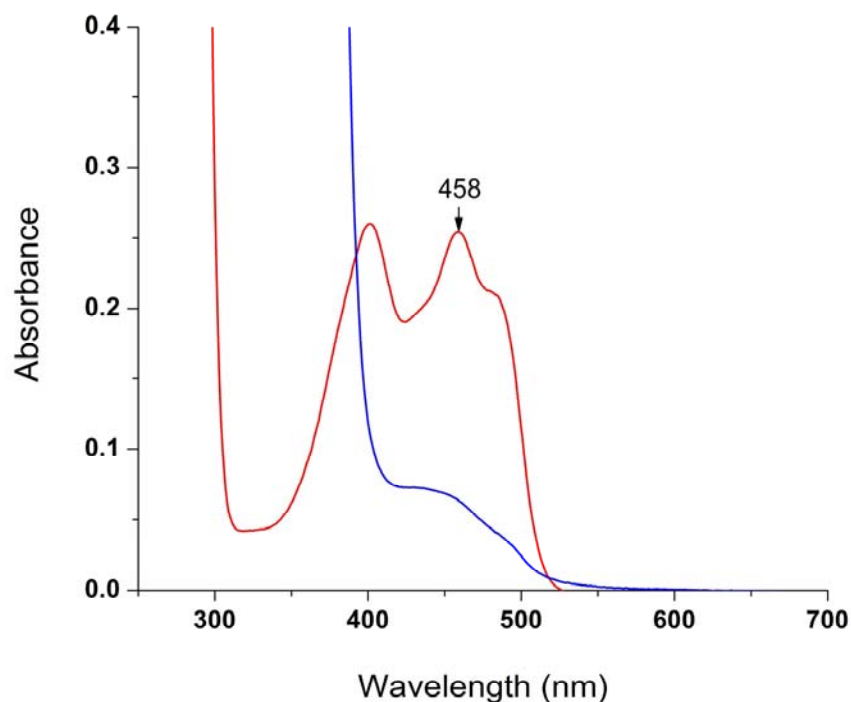


**Figure 5.16. UV-vis spectrum of *E. coli* FLDR.**

The protein ( $\sim 26 \mu\text{M}$ ) in its oxidized state is shown in the red line with spectral maxima at 458 nm and  $\sim 401$  nm. This double absorption feature is characteristic of an oxidized flavoprotein. The reduced state of FLDR is shown in the blue line following reduction with sodium dithionite.

To confirm that the purified protein was FLDR, UV-vis spectroscopy was used to determine the absorbance features, as presented in Figure 5.16. The FLDR spectrum has major absorption features corresponding to its bound FAD in the oxidized form. The UV-visible spectrum of recombinant FLDR displays characteristic flavoprotein absorbance maxima at 274, 401 and 458 nm, with shoulders at 424 and 482 nm. These spectra are distinct from that of free FAD, indicating that the flavin is associated with the FLDR protein. To obtain the hydroquinone species, FLDR was rapidly reduced using sodium dithionite. This experiment indicated that negligible 1-electron reduced (semiquinone) FLDR accumulated, and only hydroquinone was formed.

### 5.2.3 Expression and purification of FprA

The FprA ferredoxin reductase is encoded by *fprA* (*Rv3106*) in the Mtb genome, and is an adrenodoxin reductase homologue that is likely to transfer electrons to some or all of the P450 systems (357). The FprA protein of Mtb shares 40% identity with mammalian adrenodoxin reductases and is able to interact productively with iron-sulfur proteins, either adrenodoxin or plant ferredoxin (358). The enzyme also reduces various electron acceptors using either NADPH or NADH as the electron donor. In this section, FprA was expressed

and purified to homogeneity in order to combine the protein with other ferredoxins to reconstitute an electron transport chain for CYP126 and CYP141, as well as other Mtb P450s.

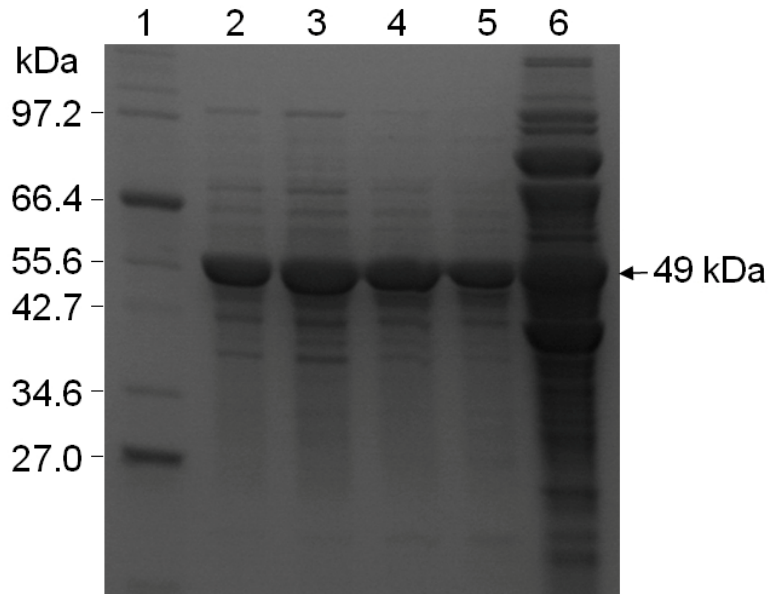


**Figure 5.17. SDS-PAGE analysis of FprA protein purification steps using a Q-Sepharose column.** Lane 1: protein marker (97200, 66400, 55600, 42700, 34600, 27000 Da); lane 2-5: protein elution from Q-Sepharose with gradient from 0 to 1 M NaCl. Fractions of 10, 20, 30, 40 (corresponding to NaCl concentrations of 40, 60, 80 and 120 mM) are presented as extensively purified protein; lane 6: the cell pellet after centrifugation. The band at 49 kDa corresponds to the molecular weight of FprA.

The gene was constructed and kindly supplied by Dr Kirsty McLean. For expression, FprA was successfully obtained in a soluble active form by expression of the gene in the *E. coli* strain HMS174 (DE3), following the protocol of McLean *et al.* (161). FprA was partially purified with a single step on a Q-Sepharose column, and eluted by the use of a linear elution gradient of NaCl (0-1 M) in 50 mM Tris, 1 mM EDTA, pH 7.5. Figure 5.17 shows the purification steps for FprA on a Q-Sepharose column. The protein band with a molecular mass of ~49 kDa was clearly visible in the SDS-PAGE gel, but a lot of the protein was present in an insoluble form. However, the expression of the protein was at very high levels, so a large amount of the pure, soluble protein was obtained. The purified fractions (10, 20, 30, 40) are shown on an SDS-PAGE gel (Figure 5.17), indicating that the enzyme was successfully expressed and partially purified.

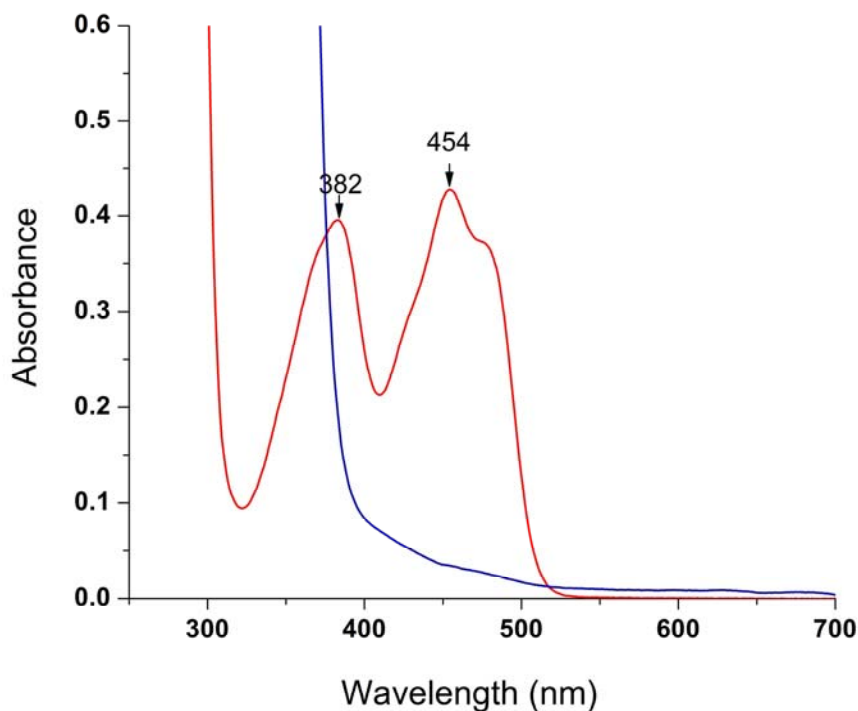


**Figure 5.18. Electronic absorption spectrum of purified FprA and its dithionite-reduced form.** FprA reveals typical features of flavin proteins. The Figure shows the visible absorption spectra for pure FprA (40  $\mu$ M) in its oxidized state (red line) with distinct absorption maxima at approximately 382 and 454 nm, and shoulders at 427 and 479 nm. The sodium dithionite-reduced FprA has absorption features indicative of a completely hydroquinone flavin (blue line).

The UV-visible spectrum shows that the oxidized FprA protein displays spectral maxima at 272, 382, and 454 nm (Figure 5.18), and shoulders on the longer wavelength band located at 427 and 479 nm. These spectral features indicate that the protein is a typical flavin-containing enzyme. In the reduced form, the protein was reduced by the addition of excess sodium dithionite, inducing full reduction of the flavin cofactor (FAD). The fully reduced FprA enzyme showed complete bleaching of the flavin spectrum without any accumulation of spectral signals attributable to a flavin semiquinone species. Therefore these characteristic properties suggest that the FprA enzyme was successfully expressed and purified to near-homogeneity as a potential electron carrier protein for Mtb P450 systems.

#### 5.2.4 Expression and purification of ferredoxin (Fdx<sub>1</sub> - *Rv0763c*).

The Mtb ferredoxin encoded by the *Rv0763c* gene is a small protein with a polypeptide chain composed of 69 amino acids, containing one Fe<sub>3</sub>S<sub>4</sub> cluster per monomer (194). Upon studying the redox cycle of this protein, McLean *et al.* reported the interaction of Fdx<sub>1</sub> with CYP51B1, which is located adjacent to the [3Fe-4S] ferredoxin (*Rv0764c*). By analogy

with other bacterial P450 redox systems, this ferredoxin is likely to be the redox partner for CYP51B1. In other work, Zanno *et al.* (153) established a reconstituted system consisting of ferredoxin reductase (FdR), ferredoxin (Fdx<sub>1</sub>) and CYP51B1 to demonstrate the sterol 14- $\alpha$  demethylase activity on lanosterol substrate. The results indicated that in the presence of Fdx<sub>1</sub> and FdR, CYP51B1 showed a conversion to the reduced CO-bound form 5 min after the addition of NADH. However, in the absence of Fdx<sub>1</sub> there was no observable CO complex at 450 nm from CYP51B1, indicating the essential role played by this Fdx<sub>1</sub> in the electron transfer system. Focusing on the function of Fdx<sub>1</sub> encoded by the *Rv0763* gene in *Mtb*, this gene was expressed and the encoded ferredoxin purified to homogeneity for reconstitution of an electron transfer chain in the redox system of other *Mtb* P450s, such as CYP126 and CYP141.

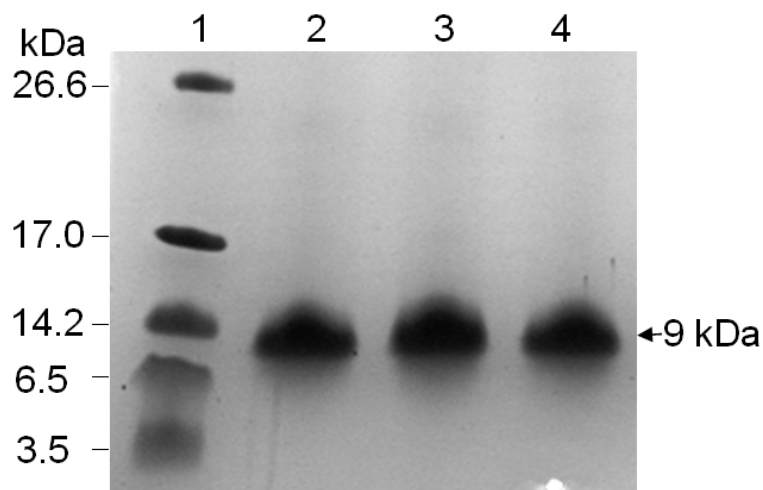


**Figure 5.19. Purification of recombinant Fdx<sub>1</sub> (*Rv0763c*) as analyzed by SDS-PAGE.** Lane 1, ultra low molecular mass markers (26600, 17000, 14200, 6500, 3500 Da); lanes 2–4, elution of Fdx<sub>1</sub> from Ni-NTA with 50 mM imidazole. A single band present on the gel indicates that this protein is pure.

The Fdx<sub>1</sub>-encoding gene (*Rv0763c*) was constructed and kindly supplied by Dr. Kirsty McLean (The University of Manchester). The gene was expressed in the *E. coli* HMS174 (DE3) strain with a high level of soluble protein, as described in the Methods chapter (section 2.5). Fdx<sub>1</sub> protein was purified using a nickel metal-affinity resin column for a single step purification of His-tagged ferredoxin. The wild-type protein was observed to have a green/brown color, indicating that the protein likely contains a [3Fe-4S] cluster that remains bound to the protein after purification. The extinction coefficient of 11 300 M<sup>-1</sup> cm<sup>-1</sup> at 412 nm was given by a previous publication (194), and therefore this was used to

calculate the Fdx<sub>1</sub> concentration as well as the level of purity of the sample during purification steps. As shown in Figure 5.19, the Tricine gel analysis for ultra low molecular mass proteins indicates that the purified Fdx<sub>1</sub> was obtained after the Ni-NTA column with one intense band presenting at an apparent molecular mass of ~9 kDa, which corresponds to the native molecular weight of His-tagged Fdx<sub>1</sub> (9862 Da).

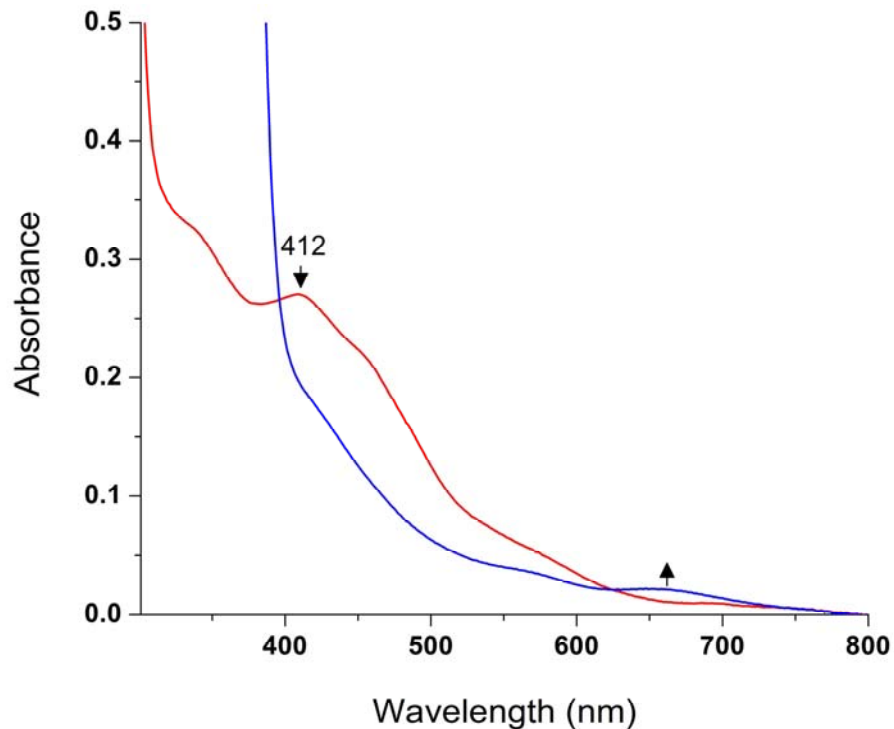


**Figure 5.20. Electronic absorption spectrum of purified Fdx<sub>1</sub>.**

The enzyme was at 28  $\mu$ M in 100 mM potassium phosphate (pH 7.5). UV-visible absorption spectra are shown for the oxidized form of Fdx<sub>1</sub> (red line) with a peak at 412 nm, and for the sodium dithionite-reduced form of Fdx<sub>1</sub> (blue line). Arrows indicate direction of absorption change on Fdx<sub>1</sub> reduction.

Spectroscopic analysis of Fdx<sub>1</sub> reveals that pure protein has a dark brown colour and possesses a broad UV-visible spectrum in its oxidized form, with a main peak at 412 nm and other absorption shoulders at ~460 and ~580 nm (Figure 5.20). Furthermore, reduction of Fdx<sub>1</sub> by sodium dithionite leads to loss of the native colour of the protein and to bleaching of the spectrum across the range from ~400 to 620 nm. However, at longer wavelengths (~620–720 nm), Fdx<sub>1</sub> exhibits increased absorption in the reduced form, with a low intensity absorption peak at 668 nm. These specific characteristics of Fdx<sub>1</sub> confirm that this ferredoxin was expressed successfully and purified to homogeneity for further experiments.

## 5.2.5 Cloning, expression, purification and characterization of another *Mtb* ferredoxin (Fdx<sub>2</sub> - *Rv1786*)

### 5.2.5.1 Cloning, expression and purification of Fdx<sub>2</sub>

To further analyze how electron transfer between redox partners and P450s occurs in the *Mtb* systems, the *Rv1786* gene, coding for a ferredoxin next to CYP143 on the genome, was cloned expressed and purified. The *Rv1786* gene contains 204 base pairs, encoding a 66 amino acid protein, with predicted mass of ~7.4 kDa. The primers were designed based on the complementary sequence at both the 5' and 3' ends of the gene. The cosmid I04 containing the *Rv1786* gene (obtained from Dr. Roland Brosch, Institut Pasteur, Paris) was used as DNA template for the cloning, and the *Rv1786* gene was amplified using PCR as described in the Methods section (section 2.4.1, Figure 5.21). The analysis of the PCR reaction by agarose gel electrophoresis shows that the PCR reaction was successful, with a product corresponding to 204 bp, i.e. the correct size compared to the theoretical calculation.

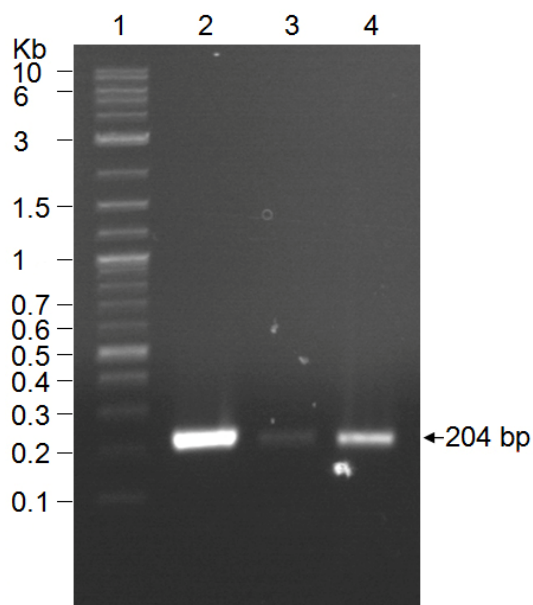


**Figure 5.21 . PCR products of the *Mtb Rv1786* gene.**

The *Rv1786* gene was amplified from *M. tuberculosis* H37Rv cosmid I04. The PCR product was resolved on an ethidium bromide-stained 1.5% agarose gel. Bands displayed are those of *Rv1786* in the presence and absence of DMSO. Lane 1: Molecular mass standards, lane 2: PCR product in presence of 20 mM MgCl<sub>2</sub>, lane 3: PCR product in the presence of 0.2% DMSO, lane 4: PCR product in the absence of DMSO.

The Fdx<sub>2</sub> (*Rv1786*) gene was cloned into the expression vector pET15b (Figure 5.22) using a similar protocol as described for FdR. The construction successfully added six continuous histidine residues to the N-terminal of the ferredoxin, which greatly accelerated the protein

purification process. Expression of the *Rv1786* gene in *E. coli* strains containing this construct was carried out successfully by growth in Terrific broth medium, at 25 °C overnight and without IPTG induction.

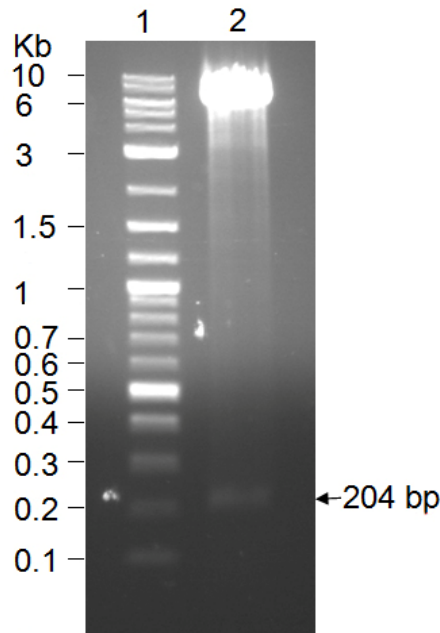


**Figure 5.22. Digestion products of a recombinant pET15b vector containing the *Rv1786* gene.** Lane 1, Molecular mass standards. Lane 2, digestion of pET15b with restriction enzymes (*Xho*I and *Bam*HI - see detailed vector pET15b map in Figure 2.2, section 2.4.7) demonstrating that the clone contains the *Rv1786* gene.

Expression of the *Fdx<sub>2</sub>* gene was successful under conditions similar to those described for *Fdx<sub>1</sub>* (359-363), and the desired protein was expressed to high levels with efficient assembly of the iron-sulfur cluster, as was evidenced from the dark brown colour of the isolated cell pellet. Tagged *Fdx<sub>2</sub>* has six additional histidines at the N-terminus plus 67 amino acids of the protein, giving a total molecular mass of 9,566 Da. The trial expression shown in Figure 5.23 indicated a leaky expression of the *Fdx<sub>2</sub>*. As is clearly seen on the SDS-PAGE gel, harvested *E. coli* cells showed a low molecular weight band of about 9 kDa that corresponds to that predicted from the *Fdx<sub>2</sub>* amino acid sequence. The protein band appeared over the course of the expression time, and could be considered as the recombinant ferredoxin. In addition, trial expression of *Fdx<sub>2</sub>* was also carried out on four different *E. coli* strains in order to test which strain has the strongest expression of the protein, including BL21 (DE3), Origami B (DE3), Rosetta (DE3), and HMS174 (DE3). The results of analysis by SDS-PAGE showed that the HMS174 (DE3) strain has the best

ability to express the *Rv1786* gene with the highest soluble protein amount compared with other *E. coli* strains (data not shown).

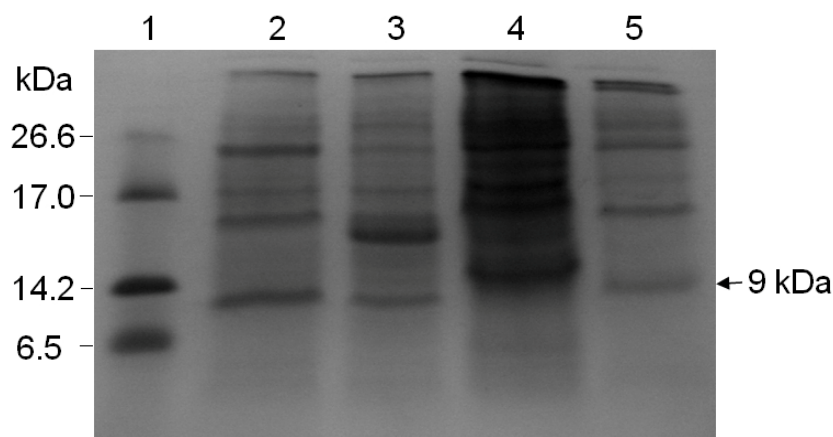


**Figure 5.23. SDS-PAGE of Fdx<sub>2</sub> trial expression in *Escherichia coli* HMS174 (DE3) cells.** The cells were expressed without induction by IPTG and samples were taken at different times, ranging from 0 to 24 h; lane 1: Molecular mass standard markers (26600, 17000, 14200, 6500 Da); lane 2: total protein at T = 2 h; lane 3: total protein T = 4 h; lane 4: total protein T = 8 h; lane 5: total protein at T= 24 h. The band at approximately 9 kDa corresponds to the native molecular mass expected for Fdx<sub>2</sub>.

To express the Mtb ferredoxin (Mtb-Fdx<sub>2</sub>) on a large scale, transformant HMS174 (DE3) cells were grown in 20 litres of TB medium, with the conditions for growth as described in the Methods section (section 2.5). The construction of the N-terminally histidine tagged form of the protein enabled its facile and rapid purification on Ni-NTA resin. For the purification process, Fdx<sub>2</sub> protein was purified by a single step of affinity chromatography on Ni-NTA resin (Novagen), based on the method previously described to isolate Fdx<sub>1</sub>. This enabled an easy purification step for obtaining purified protein from the crude extract. The ferredoxin appeared as a single band at a molecular mass appropriate for a protein of 9,566 Da, as calculated from the published gene sequence (Figure 5.24). The wild-type ferredoxin was observed to be green/brown in colour, indicating that the Fe-S cluster is still bound to the protein after purification. The final pure protein yield after affinity chromatography is around 5 mg per litre culture. The results suggest that the T7 polymerase promoter/BL21 (DE3) expression system used is a good one for expressing the ferredoxin in high yield, albeit using “leaky” expression.

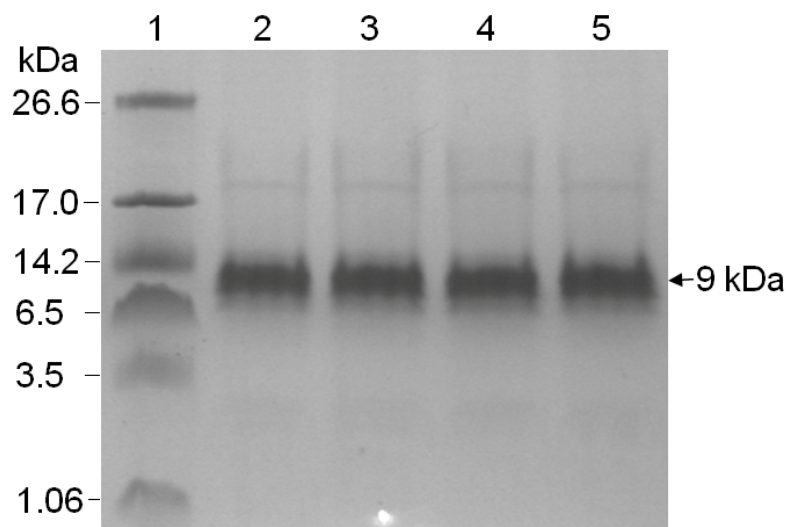


**Figure 5.24. SDS-PAGE of the purified Fdx<sub>2</sub>.**

The protein was purified to near-homogeneity after Ni-NTA column chromatography with washing using 21 mM imidazole. Purified samples were electrophoresed in a tricine gel (16.5%); lane 1, ultra low molecular mass standards (26600, 17000, 14200, 6500, 3500, and 1060 Da); lane 2, 3, 4, 5: eluted Fdx<sub>2</sub>-containing fractions with 50 mM imidazole.

#### 5.2.5.2 Spectrophotometric analysis of Fdx<sub>2</sub>

To confirm that Fdx<sub>2</sub> was expressed successfully in *E. coli*, UV-visible spectroscopy is a useful technique to analyze the protein and to identify the hallmark absorption features of the iron-containing cluster. Different types of iron-sulfur cluster have distinct absorption features, with many having broad absorption of low intensity across the UV-visible range. The spectrum of Mtb-Fdx<sub>2</sub> in Figure 5.25 shows that the absorption peak is at 412 nm, which is typical for proteins containing a Fe-S cluster. Reduction of Fdx<sub>2</sub> by dithionite leads to loss of the green/brown colour and to bleaching of the spectrum at 412 nm. In addition, at longer wavelengths (~600–700 nm) Fdx<sub>2</sub> exhibits increased absorption in the reduced form, with a low-intensity absorption peak at 670 nm. Those spectroscopic properties confirm that Fdx<sub>2</sub> was successfully expressed and purified as a cofactor-binding protein, and that the protein is pure enough for reconstitution of P450 redox reactions, as well as for crystal screening trials.

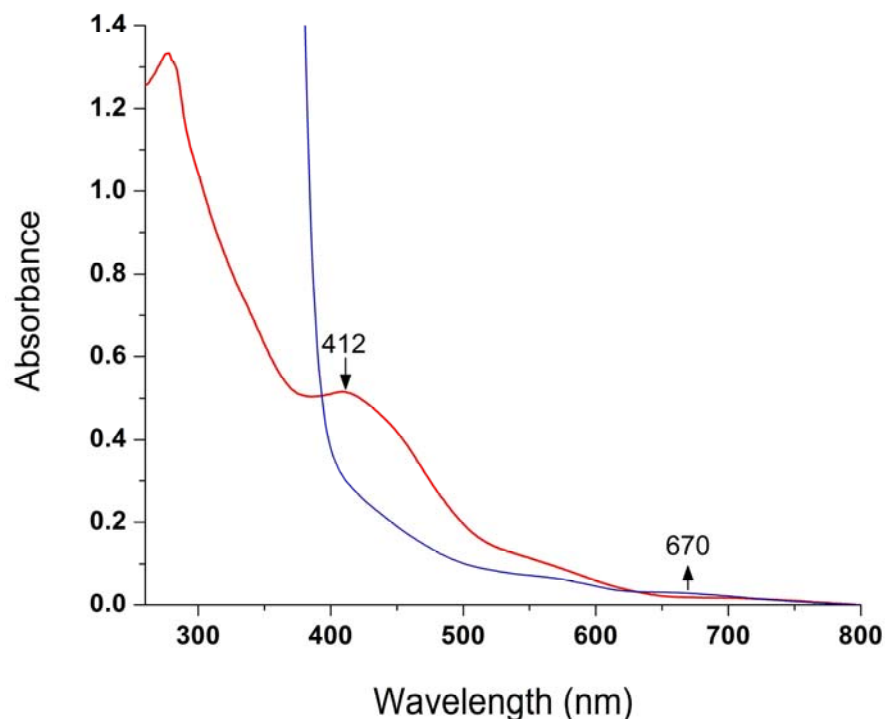


**Figure 5.25. UV-visible spectra of Mtb-Fdx<sub>2</sub> in its oxidized and reduced forms.**

Fdx<sub>2</sub> (60  $\mu$ M) was in 100 mM KPi buffer, pH 7.5, and exhibits an absorption maximum near 412 nm (red line), similar to the Fdx<sub>1</sub> UV-visible spectrum. The sodium dithionite-reduced Fdx<sub>2</sub> is shown in blue, with bleaching of the spectrum at 412 nm and increased intensity at 670 nm. Arrows indicate direction of absorption change on reduction.

### 5.2.5.3 Light scattering analysis of Fdx<sub>2</sub>

The size and oligomeric status of Fdx<sub>2</sub> were determined by laser light scattering. The recombinant Fdx<sub>2</sub> (400  $\mu$ g/ml) was subjected to Superose 12 size exclusion chromatography in TBS, and the column effluent passed in-line through a differential refractometer and multi-angle laser light scattering detector. The sample analysis was repeated at least three times to ensure there was no change in the MALLS data. Thereafter, the results were calculated to determine an average molecular mass. Figure 5.26 shows the native form of Fdx<sub>2</sub> that was analyzed by multi-angle laser light scattering coupled to gel filtration to yield a molecular mass.

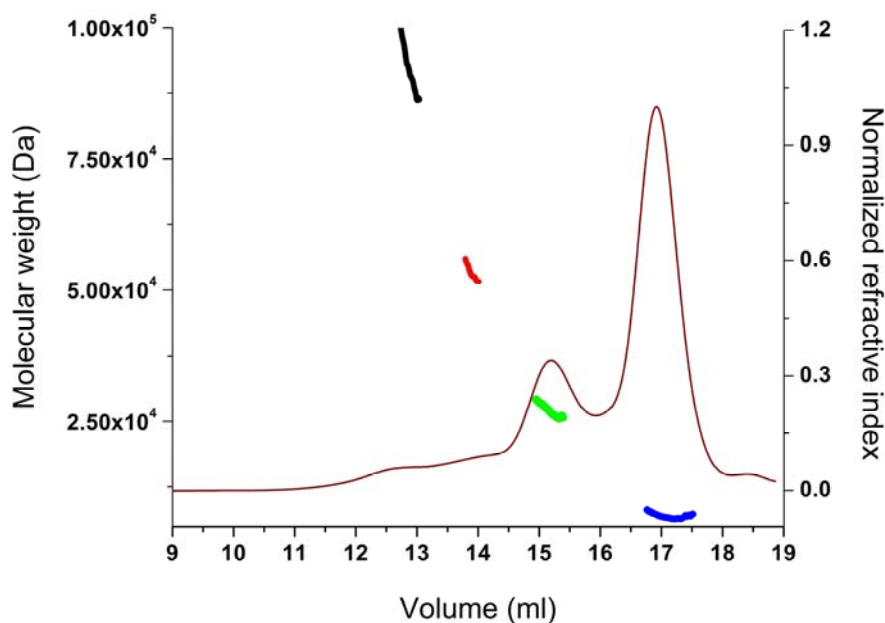


**Figure 5.26. Oligomerization status of Fdx<sub>2</sub>.**

The image shows a summary of MALLS data for Fdx<sub>2</sub>, with four refractive index peaks in agreement with masses expected for octamer (74.7 kDa), tetramer (40.3 kDa), dimer (21.2 kDa), and monomer (6.9 kDa) forms. The monomeric form is predominant.

The ligand-free form of Fdx<sub>2</sub> at a concentration of 400 µg/ml produced four refractive index peaks that eluted centred at ~12.3, 13.7, 15.3 and 17.5 ml, respectively (Figure 5.25). The average of the calculated mass shows that the peak 1 corresponds to a molecular weight of  $74.7 \pm 2.4$  kDa; peak 2 located at 13.7 ml elution corresponds to a molecular weight of  $40.3 \pm 1.3$  kDa; peak 3 centred at 15.3 ml corresponds to  $21.2 \pm 1.2$  kDa; and peak 4 has molecular mass of  $6.9 \pm 2.6$  kDa. These 4 distinct species have molecular mass estimates of 74, 40, 21 and 7 kDa, respectively, in agreement with octamer, tetramer, dimer and the monomer as predicted from the amino acid sequence. In addition, under the conditions used it was shown that the monomer species is predominant with ~51% of total protein, whereas, the minor species of octamer, tetramer and dimer account for 6, 15, and 28%, respectively. Moreover, samples at the four major refractive index peaks observed at ~12.3, 13.7, 15.3 and 17.5 ml were pooled and analyzed by SDS-PAGE (tricine gel) to ensure that these oligomeric forms are composed of Fdx<sub>2</sub>, and the results indicated that these peaks all contained Fdx<sub>2</sub> (data not shown).

#### 5.2.5.4 Circular dichroism analysis of Fdx<sub>2</sub>

To further analyze the Mtb Fdx<sub>2</sub>, CD spectroscopy was used to characterize the secondary and tertiary structure of Fdx<sub>2</sub>, with data collection in both the far UV and near UV-visible regions. The CD spectrum of the oxidized Fdx<sub>2</sub> is shown in Figure 5.27. The far UV CD

spectrum of Mtb Fdx<sub>2</sub> provided insight into the secondary structural constitution of a protein with both helical and  $\beta$ -sheet structure. The CD spectrum of Mtb Fdx<sub>2</sub> shows a strong minimum located at  $\sim$ 201 nm and another weaker minimum at  $\sim$ 226 nm, indicating the presence of both  $\beta$ -strand and  $\alpha$ -helical regions in the folded conformation. These properties indicate that the secondary structure of Fdx<sub>2</sub> is highly similar to those of other well characterized ferredoxin proteins such as *E. coli*, human, and *P. putida* ferredoxins (364-369). Using the equation for calculating the molar ellipticity per residue value and plotting the data on the Selcon program to analyse secondary structure, the prediction algorithm indicated approximately 37%  $\alpha$ -helix and 15%  $\beta$ -sheet, respectively. These estimates may not be accurate in order to provide a basis for comparison of the structure of Fdx<sub>2</sub> with other ferredoxin proteins. However, previous reports on the crystal structures of ferredoxins from *Chlorella fusca* (370), *Pseudomonas aeruginosa* (371), *Chromatium vinosum* (372), *Desulfovibrio africanus* (373), and *Desulfovibrio gigas* (374), revealed the  $\beta$ -sheet and  $\alpha$ -helix contents at 30%/17%, 28%/30%, 18%/35%, 22%/38%, and 24%/39%, respectively. Therefore, the estimated values of Fdx<sub>2</sub> secondary structure from CD analysis are likely within reasonable error of the true values.

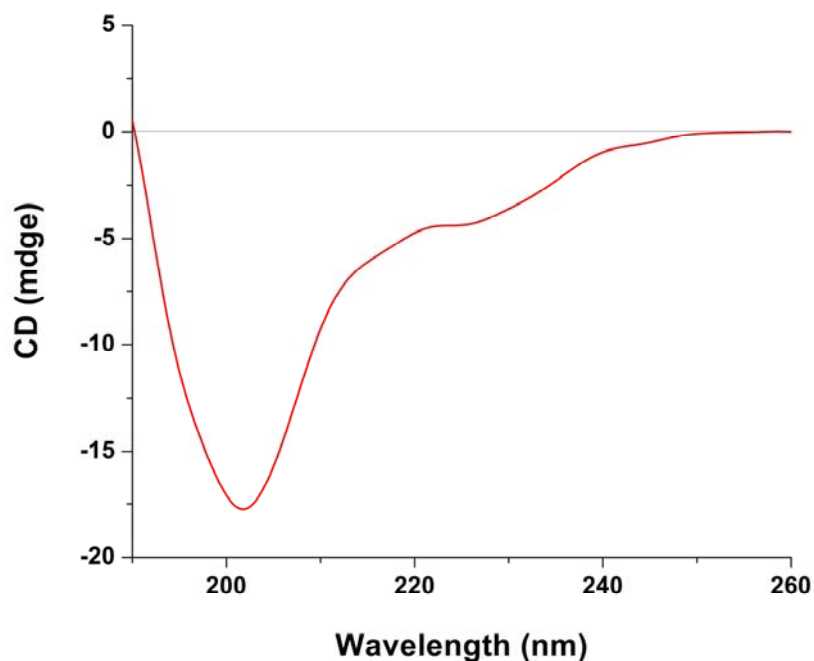


**Figure 5.27. CD spectroscopic analysis of Mtb Fdx<sub>2</sub> in the far UV region.**

The room-temperature (25 °C) spectrum of oxidized Fdx<sub>2</sub> (10  $\mu$ M) is shown in 50 mM potassium phosphate (pH 7.5). Spectra were collected on a Jasco spectropolarimeter (model J-810). The spectrum is presented with units of mean residue ellipticity in the far-UV region.

In the near UV-visible spectral regions, Mtb Fdx<sub>2</sub> displays a number of strong bands with positive and negative Cotton effects (Figure 5.28), which is a specific characteristic CD spectrum of the oxidized Fe-S cluster (364, 368). At wavelengths of 260 to 800 nm, CD spectral absorption features can be attributed to the Fe-S cluster of Fdx, with peaks at 278, 332, 472, 529 and 574 nm, and a minimum at 441 nm. The visible CD spectrum of oxidized Fdx<sub>2</sub> was distinct from that of the *Azotobacter* ferredoxin I, which revealed positive bands at 322, 387, 475 and 573 nm, and a small negative peak at 525 nm, without formation of a positive peak at 278 nm (375, 376). Apart from the difference in intensities of the negative and positive signals, the features in the Fdx<sub>2</sub> spectrum showed an almost one-to-one correspondence with features having a similar Cotton effect from the spectra of other Fe-S ferredoxins – i.e. the wavelengths and intensities of the corresponding maxima and minima were similar. Recent reports on the CD spectra of other Fe-S cluster Fdx proteins in this region also indicated similar absorption and CD properties (368, 377, 378).

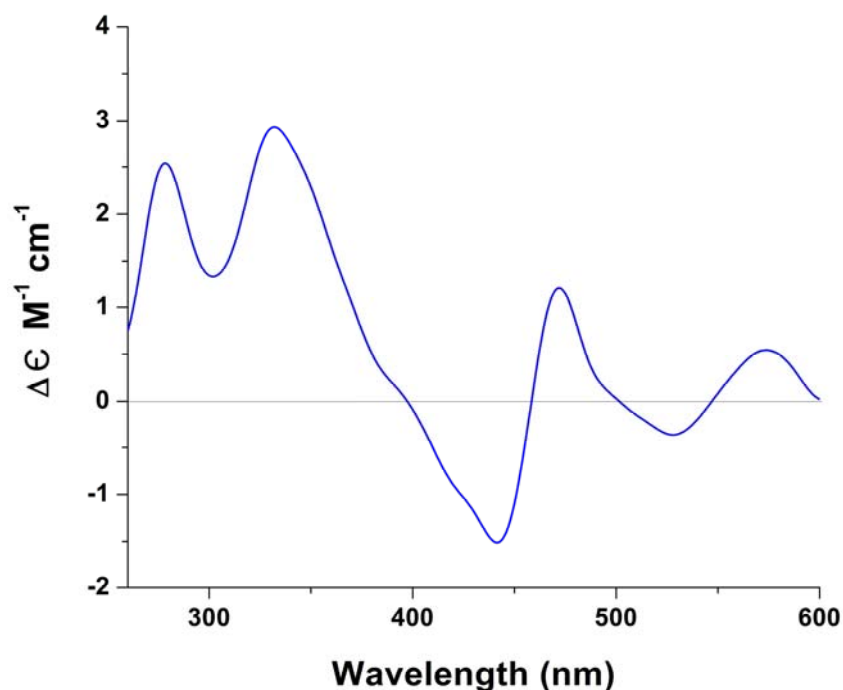


**Figure 5.28. CD spectrum of Mtb Fdx<sub>2</sub> in the near UV-visible region.**

The spectrum was recorded on a Jasco spectropolarimeter (model J810, cell pathlength 0.5 cm). The Fdx<sub>2</sub> (60 μM) was in 50 mM KPi (pH 7.5). The spectrum exhibit peaks at 278, 332, 472 and 574 nm, with a minimum at 441 nm. The spectrum is presented in units of molar coefficient.

#### 5.2.5.5 Electron paramagnetic resonance analysis of Fdx<sub>2</sub>

To confirm the presence of an iron-sulfur center in the Fdx<sub>2</sub>, X-band EPR spectra were recorded for oxidized and dithionite-reduced forms. With the exception of the background signal arising from the EPR resonator, which was subtracted for further spectral analysis,

no other EPR signals were observed within the spectral range from 0 to 1000 mT. The spectrum with a zero-crossing at 483.5 mT is clearly asymmetric due to an anisotropic  $g$ -matrix. It consists of a narrow peak at 445 mT and a broader trough at 528.3 mT. The  $g$ -principal values of the spectrum were obtained by a least-squares fitting routine reflecting axial symmetry of the  $g$ -matrix. Only oxidized Fdx<sub>2</sub> displayed an EPR spectrum (Figure 5.29, main). The oxidized Mtb Fdx<sub>2</sub> EPR signal has a strong  $g$ -value at 2.01 resonance, which is consistent with the presence of a [3Fe-4S]<sup>+</sup> cluster (194). This proved the presence of an oxidized [3Fe-4S]<sup>+</sup>  $S=1/2$  cluster with characteristic features in the Fdx<sub>2</sub> protein. A comparison of the Fdx<sub>1</sub> EPR spectrum with other [3Fe-4S]<sup>1+/0</sup> ferredoxins indicates that the spectrum of Fdx<sub>2</sub> had line shape and  $g$  value almost identical to those recorded for the Mtb Fdx<sub>1</sub> ( $g = 2.01$ ), *Methanosarcina thermophila* ferredoxin ( $g = 2.02$ ) (379), and *Azotobacter vinelandii* FdxI ( $g = 2.01$ ) (380). However, Fdx<sub>2</sub> also showed a distinct feature from Mtb Fdx<sub>1</sub> downfield of the main derivative ( $g = 2.14$ ), and different from the other iron-sulfur species that are mentioned above.

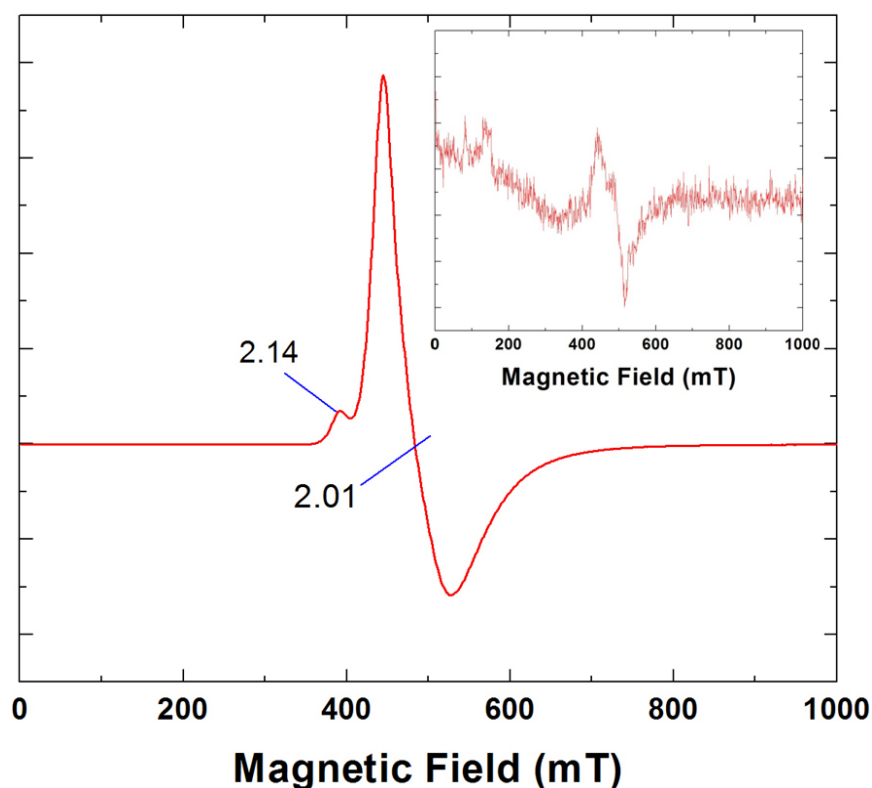


**Figure 5.29. EPR spectroscopic analysis of Mtb Fdx<sub>2</sub>.**

In the main figure, an EPR spectrum of oxidized Mtb Fdx<sub>2</sub> (600  $\mu$ M) was recorded in 50 mM potassium phosphate (pH 7.5) including 10% glycerol. The spectrum was measured at a microwave frequency of 9.67 GHz; power, 2 milliwatts; temperature, 10.0 K; modulation amplitude, 10 G. The oxidized protein spectrum with a  $g$ -value of 2.01 indicates that the protein sample contains a [3Fe-4S]<sup>+</sup> cluster. The inset figure indicates that no significant signal was detectable for the dithionite-reduced sample, which means that neither a [4Fe-4S] nor a [2Fe-2S] cluster is present.

Addition of excess sodium dithionite (DT) to Mtb Fdx<sub>2</sub> at pH 7.5 leads to the near complete loss of the EPR signal of Fdx<sub>2</sub> without appearance of any new signal, as shown in Figure 5.29 (inset). The disappearance of the  $g \sim 2.01$  EPR signal is consistent with conversion of the EPR-active [3Fe-4S]<sup>+</sup> form to the EPR-silent [3Fe-4S]<sup>0</sup> form (Figure 5.29, inset). The result indicates that DT reduction of Mtb Fdx<sub>2</sub> involves reduction of the [3Fe-4S]<sup>+</sup> cluster to the [3Fe-4S]<sup>0</sup> form, without reduction of any e.g. [4Fe-4S]<sup>+</sup> cluster. The reduction by DT resulting in the loss of the EPR spectrum was also observed for the Mtb Fdx<sub>1</sub> and *A. vinelandii* FdxI. In addition, the EPR signal and  $g$  value of Fdx<sub>2</sub> are distinct from those of [2Fe-2S] and [4Fe-4S] ferredoxins.

#### 5.2.5.6 Reduction potential determination

Potentiometry was used to measure the associated changes in electronic absorption spectrum on progressive reduction of the Fdx<sub>2</sub> using sodium dithionite. The protein was stable during the titration experiment, enabling collection of good quality sets of spectra. The Mtb Fdx<sub>2</sub> spectrum in the fully oxidized state has a maximal absorbance in the UV-vis range at 412 nm. Reduction of Fdx<sub>2</sub> caused a decrease of the intensity at the maximal absorbance from the oxidized state to the reduced state. There were also increases in the absorption intensity at a wavelength of 670 nm (Figure 5.30). The redox titration of Mtb Fdx<sub>2</sub> was completely reversible from oxidized to reduced states without development of turbidity due to enzyme aggregation and with no signal of hysteretical behaviour. The reaction was reversible as judged by restoration of the spectrum of the starting form at its original wavelength and intensity following reoxidation by ferricyanide (data not shown). The spectrum of the reduced [3Fe-4S]<sup>0</sup> form of Mtb Fdx<sub>2</sub> is nearly identical to that of the reduced [3Fe-4S]<sup>0</sup> cluster of Mtb Fdx<sub>1</sub> (194). The spectral changes observed during the redox titration of Mtb Fdx<sub>2</sub> are displayed in Figure 5.30.

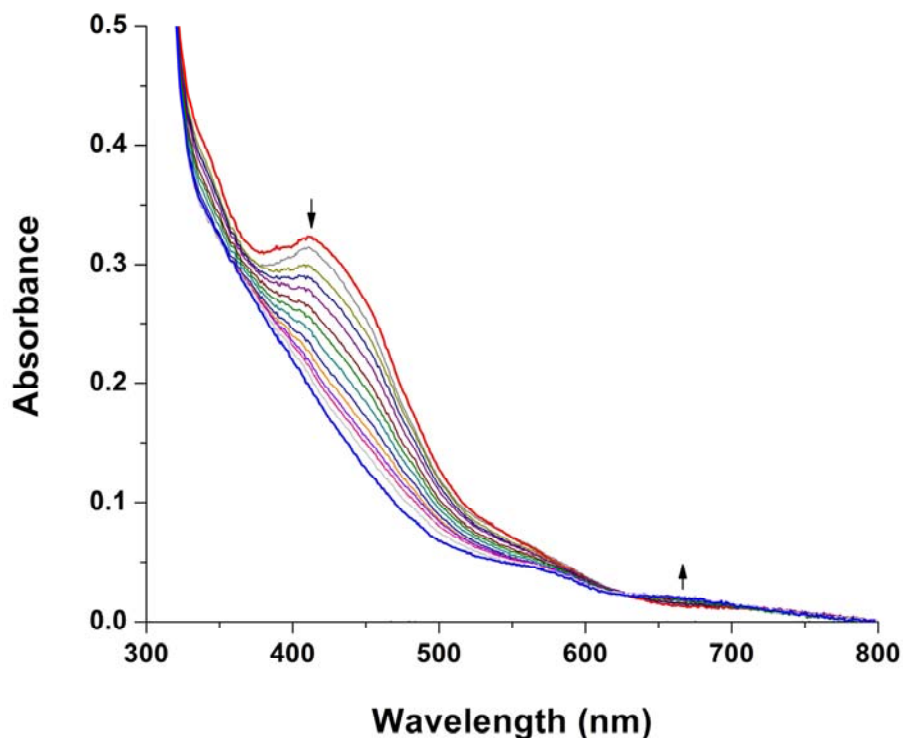


**Figure 5.30. Potentiometric titration of Mtb Fdx<sub>2</sub>.**

Spectral changes associated with the reductive titration of Mtb Fdx<sub>2</sub> are shown. The red line is that of fully oxidized Fdx<sub>2</sub> (~33 μM), the lowest blue line is that for fully reduced Fdx<sub>2</sub>. All data were recorded across the range from the oxidized to the reduced state, and were then analyzed by plotting the absorbance at 412 nm, which correlates with large absorption changes that occurred during the conversion between the oxidized and reduced forms of Fdx<sub>2</sub>.

All data were recorded across the range from oxidized to reduced forms, and were then analyzed by plotting absorbance at 412 nm, reflecting substantial absorption changes that occurred during the conversion between the oxidized and reduced forms. The data for the plot were fitted well to the Nernst equation as described in the Methods section (section 2.12). A plot of the normalized absorbance values at 412 nm as a function of potential is shown in Figure 5.31. The data were fitted to the Nernst equation, revealing that the protein has a midpoint reduction potential for the [3Fe-4S]<sup>+</sup> to [3Fe-4S]<sup>0</sup> transition of  $-30 \pm 2$  mV versus NHE (Figure 5.31), substantially more positive than that of the ligand-free heme iron potential of CYP126 and CYP141. However, the reduction potential of Mtb Fdx<sub>2</sub> (*Rv1786*) is similar to that of the other Mtb Fdx<sub>1</sub> (*Rv0763c*), which has a reduction potential of  $-31 \pm 5$  mV (194).

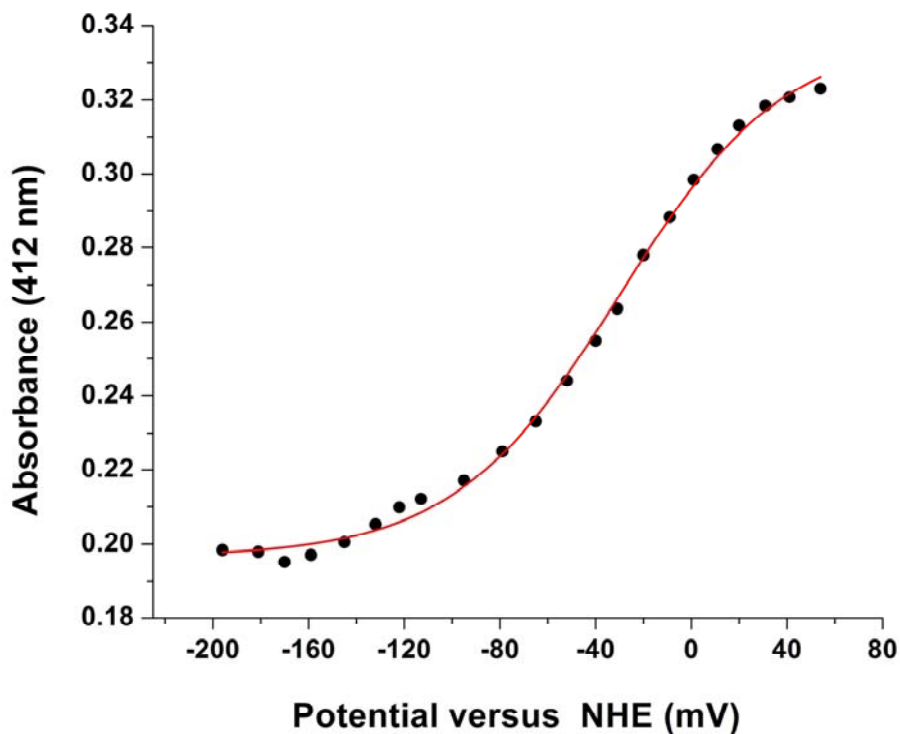


**Figure 5.31. Plot of proportion of Mtb Fdx<sub>2</sub> reduced versus potential (E', mV) during reductive titration.** The data at 412 nm (reflecting a major change in absorption between oxidized and reduced Fdx<sub>2</sub>) were plotted versus reduction potential and were fitted to a single electron Nernst function, as described in the Methods section (section 2.12). The midpoint reduction potential for the Mtb Fdx<sub>2</sub> was determined from the data fit. The potential for the Fdx<sub>2</sub> [3Fe-4S]<sup>+</sup> to [3Fe-4S]<sup>0</sup> transition was determined to be  $-30 \pm 2$  mV.

#### 5.2.5.7 Crystallography of Fdx<sub>2</sub>

A search from the protein data bank indicates that, to date, only two X-ray crystal structures of 3Fe Fdx proteins have been elucidated with high resolution. The first structure is the [3Fe-4S] Fdx from *Azotobacter vinelandii* (381) and a recent structure of another 3Fe Fdx from *Desulfovibrio gigas* (374) has also been reported. In addition, several 7Fe and 8Fe Fdx three-dimensional structures are also available (382-384). Structurally, 3Fe Fdx proteins can vary in their size from about 55 to 104 amino acids. However, they all share a very similar [Fe-S] cluster-binding core of about 55 amino acids folded according to a conserved  $(\beta\alpha\beta)_2$  structure topology (374). The location of the [Fe-S] cluster within the binding core is highly conserved in 3Fe Fdx proteins with the same  $\alpha$ - $\beta$ -fold retained. However, outside of the cluster binding core, Fdx proteins show a high level of structural variability.

To determine the crystal structure of Mtb Fdx<sub>2</sub> (Rv1786), as a first step the Fdx crystals were formed under the screening conditions of a PEGs suite kit. The crystals were formed

at locations 27 and 28 on the 96-well plate format. Well 27 contained 0.1 M sodium acetate, pH 4.5 and 25% (w/v) PEG 6000, whereas well 28 contained 0.1 M sodium acetate, pH 4.5 and 25% (w/v) PEG 8000. The crystals of Mtb Fdx<sub>2</sub> are shown in Figure 5.32. Crystals grown under these conditions are faintly brown in colour and appeared with a rod-like morphology from precipitate. The rods grew after around 1 day, with well defined edges appearing after a further 2 days incubation period. The length of the crystal is long but the width is smaller than a minimum measurement unit, and therefore these crystals were small and we were unable to measure the dimensions accurately. Unfortunately, although the crystals produced a good quality of diffraction (1.6 Å), but the structure was unable to be solved due to inability to determine the space group.

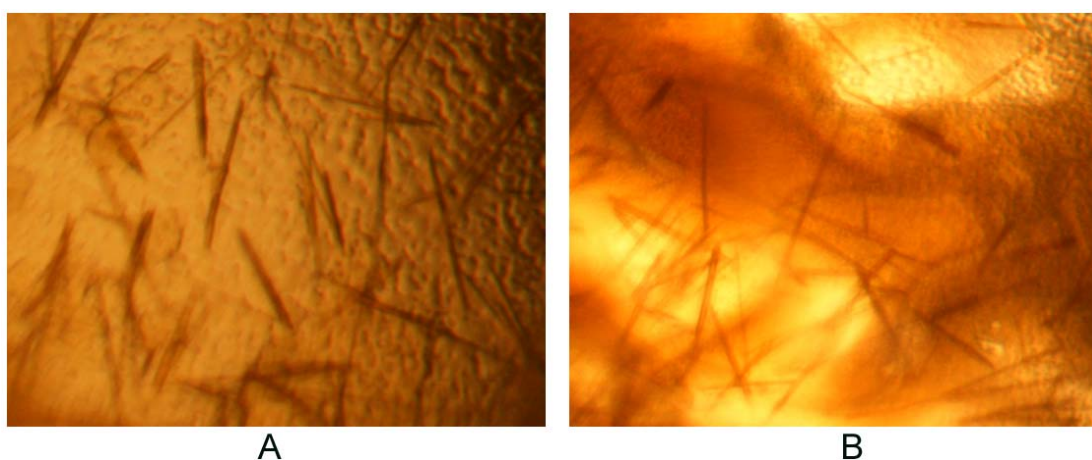


**Figure 5.32. Native crystals of Mtb Fdx<sub>2</sub>.**

The crystals were obtained from large tray growth by the sitting drop method. 1  $\mu\text{l}$  enzyme at a concentration of 45  $\mu\text{g ml}^{-1}$  was mixed with an equal volume of reservoir solution and equilibrated against 100  $\mu\text{l}$  of the reservoir solution. The mixture was incubated at 4 °C for 1-2 days, and the crystals were observed and photographed using microscopy. (A) The crystals were formed in 0.1 M sodium acetate, pH 4.5 and 25% (w/v) PEG 6000. (B) The crystals were formed in 0.1 M sodium acetate, pH 4.5 and 25% (w/v) PEG 8000.

### 5.2.6 Expression and purification of FLD

*E. coli* flavodoxin (FLD) is a flavin-containing component of a short electron-transfer chain from NADPH, and has been used to reconstitute an electron chain in cytochrome P450 reduction (162). The flavodoxin has been considered to function as single electron donor by cycling between the hydroquinone and semiquinone states. In a previous publication, McIver *et al.* (162) reported the redox properties of the FLD flavin cofactor. This indicated that the midpoint reduction potential values for FLD were -254 mV for the oxidized/semiquinone couple and -433 mV for the semiquinone/reduced couple. The latter value is some 100 mV more negative than that of the NADPH/NADP<sup>+</sup> couple (~ -320 mV),

and 165 mV and 125 mV more negative than those of FLDR oxidized/semiquinone and semiquinone/hydroquinone couples. However, data was also presented to show that the system can support an electron transfer chain to P450 as follows: NADPH-FLDR-FLD-P450. Therefore, to assemble a functional electron transport chain of *E. coli* FLD coupled with FLDR to support the redox system of P450 enzymes from *Mtb*, FLD was expressed and purified to homogeneity.

For the expression and purification of FLD (*E. coli* flavodoxin), the gene construct was kindly supplied by Dr Kirsty McLean (The University of Manchester). The transformant JM101 cells were grown and induced in similar fashion to HMS174 (DE3) for FLDR expression. A Q-Sepharose ion exchange resin column was used for single step purification of non His-tagged protein and FLD was eluted from the column in a linear gradient of sodium chloride (0-1 M). Due to its FMN content, FLD has a distinct bright orange colour expected for flavodoxin in its oxidized state. Therefore, all fractions which were an orange-yellow colour were collected and analyzed by SDS-PAGE (12%) to check the FLD purity.

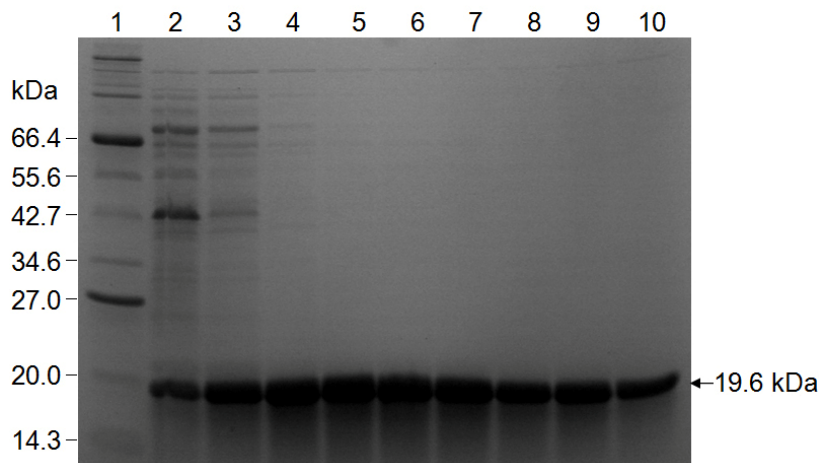


**Figure 5.33. SDS-PAGE of *E. coli* flavodoxin purification steps.**

Lane 1, broad range molecular mass standards (66400, 55600, 42700, 34600, 27000, 20000, 14300 Da); Lanes 2-10, Q-Sepharose NaCl gradient fractions of FLD, showing a band of the predicted mass (19.6 kDa). The proteins were eluted by a NaCl concentration range of 50 mM to 300 mM (lanes 2-10).

Figure 5.33 displays the purification process of the FLD protein by Q-Sepharose anion exchange chromatography. The lanes 5-10 (reflecting fractions from 25 to 50, representing a sodium chloride concentration range of 120 mM to 300 mM) show the FLD as a quite highly purified species which migrated to a level close to the 20 kDa molecular mass standard, consistent with the predicted mass for the FLD protein of ~19.6 kDa calculated from the published gene sequence. The results of expression and purification of FLD

indicated that a large amount of enriched protein was obtained after using Q-Sepharose ion exchange as a single purification step.

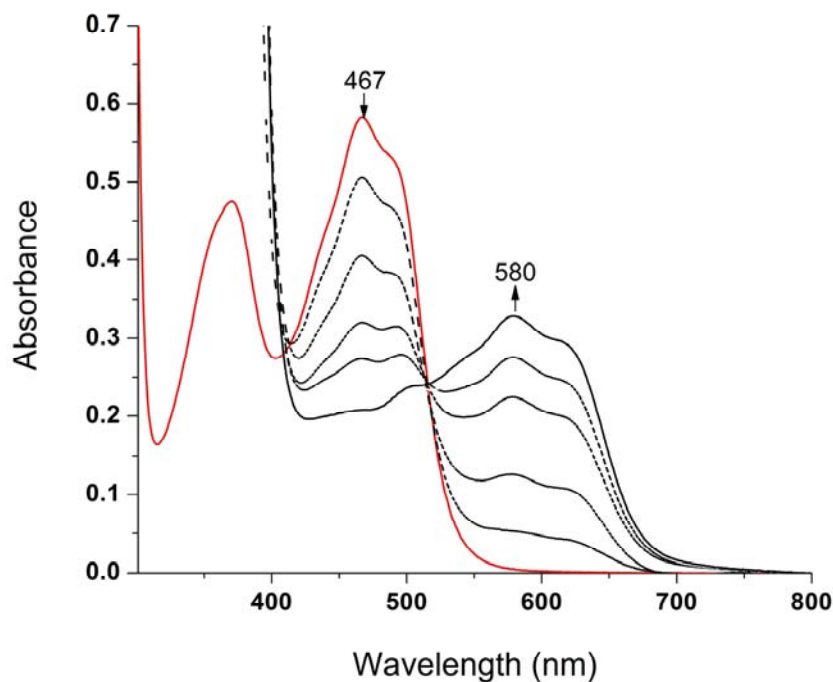


**Figure 5.34. Spectral properties of FLD in its different redox states.**

Electronic absorption spectra for *E. coli* FLD (~60  $\mu$ M) are shown. Spectra are presented for the flavodoxin in its oxidized form (solid, red line) with the major FMN absorption maximum at 467 nm for the oxidized protein, and the second FMN absorption band at 370 nm. The semiquinone species of the FLD (dashed, black lines) were generated by titration with various amounts of sodium dithionite reductant. An isosbestic point for the oxidized/semiquinone transition is observed at ~510 nm.

UV-vis spectroscopy was used to confirm the presence of the protein and to determine the maximum absorbance peak of the FLD. The protein was purified in its fully oxidized (quinone) form. The UV-visible spectrum of the oxidized flavodoxin shows features typical of this class of flavin-binding protein with the major oxidized flavin absorbance maxima at 467 nm and 370 nm, and shoulders at 403 and 492 nm. This corresponds to the known properties of *E. coli* FLD (Figure 5.34). In addition, partial reduction of FLD with the powerful reductant sodium dithionite produced species with spectral signatures characteristic of the neutral blue semiquinone state. This (blue) colour is also produced during expression of FLD in *E. coli*. This semiquinone species exhibits a broad absorption band at long wavelength with a maximum at ~580 nm and a shoulder at ~619 nm. From this evidence, it is clear that the flavodoxin from *E. coli* was successfully expressed and purified to near-homogeneity, and was ready for further experiments.

## 5.2.7 Electron transport pathway of CYP126

### 5.2.7.1 Spectroscopic interactions of CYP126 with FdR and Fdx proteins

CYP126 and various putative Mtb redox partner proteins were expressed and purified in order to analyze the P450 interactions with redox partner proteins. The three components (P450, reductase and ferredoxin/ flavodoxin) were combined in a 1:1:4 ratio prior to diluting in buffer. In these experiments, CYP126 is the electron acceptor, and its capacity to accept electrons was examined in saturated CO-buffer conditions, and by reconstituting CYP126 with either Mtb FdR, Mtb FprA or *E. coli* FLDR; and either Mtb Fdx<sub>1</sub>, Mtb Fdx<sub>2</sub> or *E. coli* FLD in a ratio of 1:1:4 (P450:reductase:ferredoxin/ flavodoxin), and using a single reductase and single ferredoxin/ flavodoxin in each case. Reduction of the heme in CYP126 was monitored by appearance of the characteristic absorbance at 450 nm (or 420 nm for the thiol-coordinated form) in the presence of carbon monoxide.

The first investigations of electron transport systems for the CYP126 protein were carried out anaerobically using Mtb redox partners FdR and Fdx<sub>1</sub>, typical of a strategy often used to reconstitute bacterial P450 systems proposed to involve ferredoxin proteins (153). As clearly seen in Figure 5.35, preliminary studies indicated that a combination of Mtb FdR and Fdx<sub>1</sub> and purified CYP 126 could support the NADPH-driven reduction of CYP126, detected by formation of the P450 Fe(II)CO product. As mentioned above, FdR is reduced very slowly by NAD(P)H, and therefore it was slow to reach its fully reduced form (~43 min) as gauged by the time taken for the spectral intensity to reach a minimum (the red spectrum in Fig. 5.35). In addition, the rate of electron transfer onwards through the system was likely also very slow, and the Fe(II)CO complex (P450) reached its maximal spectral development after ~65 min. Unfortunately, the P450 product of CYP126 is formed at only a small amount and is not stable over the time, quickly converting to the inactive P420 form, as previously reported (section 3.2.2 – Figure 3.6). Instead, and with the assumption that the failure to observe any considerable amount of P450 was a consequence of a faster rate constant for P450-to-P420 collapse compared to CYP126 reduction (forming P450), data were fitted at 422 nm (close to the peak of the P420 species in this and other CYP126 reduction experiments) in attempts to approximate the rate constant for CYP126 reduction by the various redox partner systems. In the case of P420 formation using FdR and Fdx<sub>1</sub> (and for each of the other redox systems),  $A_{422}$  changes for the formation of the P420 species were fitted using a monoexponential function and the rate constant is reported in Table 5.3. An independent measurement of the rate of the thiolate-to-thiol conversion (P450 to P420) in CYP126 was obtained through analysis of the rate of decay of the

dithionite-reduced Fe(II)CO complex (in presence of a substantial excess of reductant), giving an apparent rate constant of  $0.043 \pm 0.003 \text{ min}^{-1}$ .

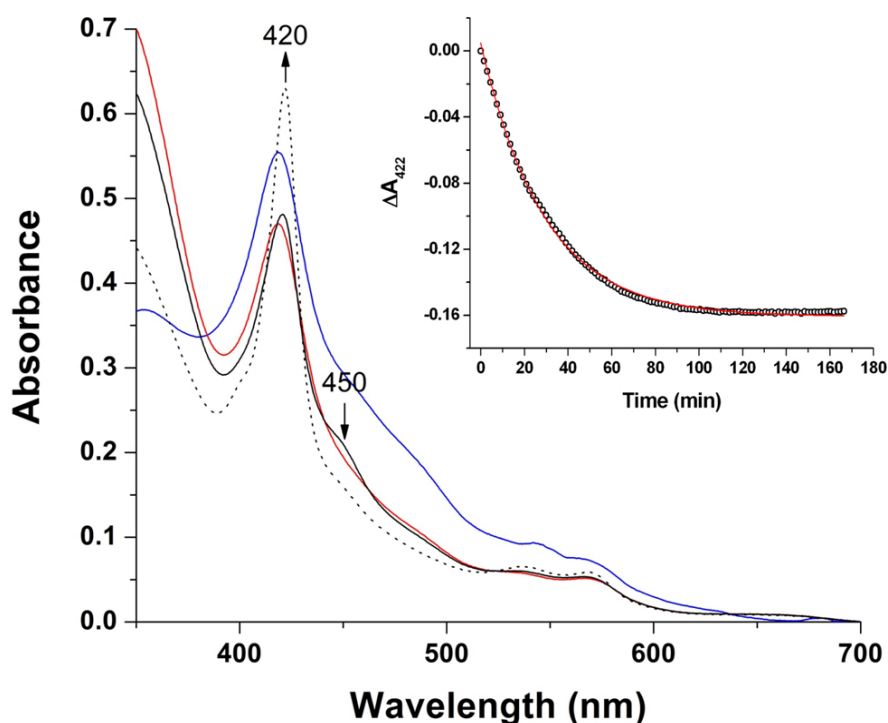


**Figure 5.35. Fe(II)CO complex formation in CYP126 with redox partners FdR and Fdx<sub>1</sub>.**

CO-bound spectra of CYP126 are shown. The reaction was done with a reconstituted system consisting of 5  $\mu\text{M}$  CYP126, 5  $\mu\text{M}$  Mtb FdR and 20  $\mu\text{M}$  Fdx<sub>1</sub>. The resting enzyme complex with its redox partner proteins is shown in blue. The red line is the spectrum recorded  $\sim 43$  min after the addition of NADPH. The black line is the maximum P450 obtained after 64.5 min. The black dotted line represents the conversion to the P420 form, which reached a maximum after 210 min. Arrows indicate the directions of absorption changes during the later phases of the reaction. The inset shows a fit of  $\Delta A_{422}$  data to a single exponential function, giving a rate constant of  $0.024 \pm 0.001 \text{ min}^{-1}$ .

Similar to the reconstitution of CYP126 using Fdx<sub>1</sub>, Fdx<sub>2</sub> was also used as a redox partner protein with FdR. As shown in Figure 5.36, similar characteristics of electron transfer within FdR and Fdx<sub>2</sub> were observed as seen with Fdx<sub>1</sub>, and the reduction of the P450 was very slow (as was also the case with Fdx<sub>1</sub>). Spectral changes indicative of the complete reduction of the redox partners occurred at  $\sim 49$  min, and the largest proportion of the P450 form was obtained at  $\sim 70$  min. The full P420 form was obtained after  $\sim 145$  min, indicating again that the P450 Fe(II)CO complex of CYP126 was converted to the inactive (thiol-coordinated) form. An additional experiment was done independently for the electron transport chain from  $\text{NADPH} \rightarrow \text{FdR} \rightarrow \text{CYP126}$  in the absence of ferredoxins (Fdx<sub>1</sub> and Fdx<sub>2</sub>). The results indicated that the P450 could receive electrons from FdR to produce

P420 species, but without any notable formation of the P450 form. The time for obtaining the maximum P420 content was at ~450 min. This result suggests that, in the absence of ferredoxin, the electron transfer rate is much slower than in the presence of either Fdx<sub>1</sub> or Fdx<sub>2</sub>, demonstrating the higher efficiency of electron transfer to CYP126 in the presence of Fdx<sub>1</sub> or Fdx<sub>2</sub>, and also (possibly) their requirement for maintaining at least some of the CYP126 heme in a thiolate-bound form.

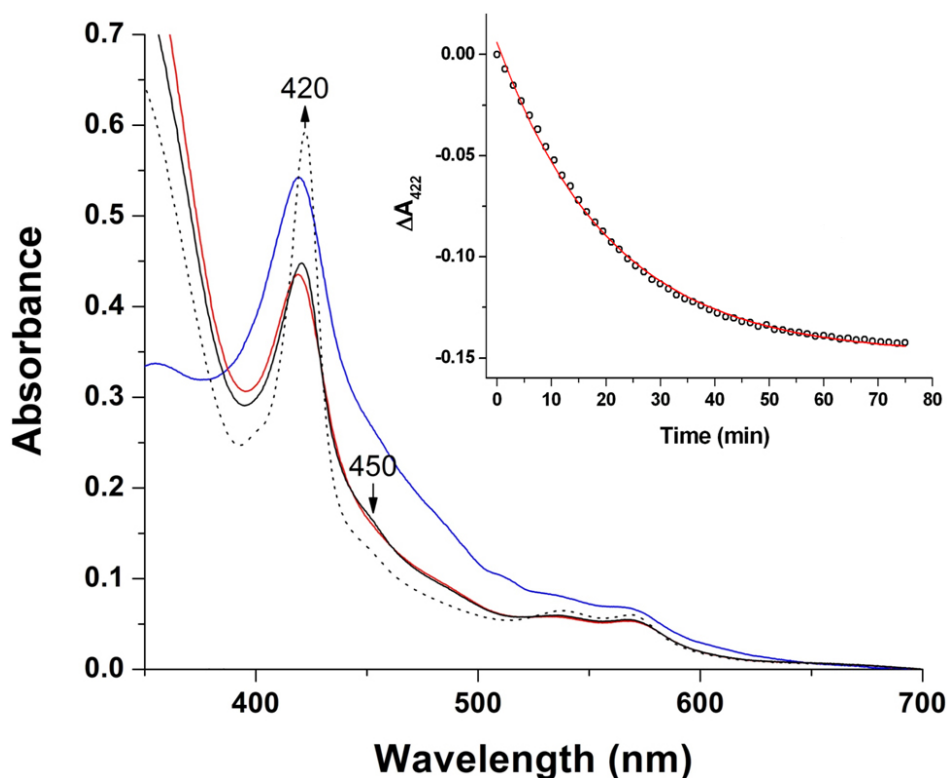


**Figure 5.36. Fe(II)CO complex formation in CYP126 with FdR+Fdx<sub>2</sub>.**

Spectra were recorded anaerobically to obtain the reduced/CO complex of CYP126. The reaction was done with a reconstituted system consisting of 5  $\mu$ M CYP126, and Mtb FdR and Fdx<sub>2</sub> in a molar ratio of 1:1:4. The resting enzyme complex with its redox partner proteins is shown in blue. The red line is the spectrum obtained 49 min after the addition of NADPH. The black line is the spectrum with maximal P450 (obtained at 70 min). The black dotted line represents the spectrum at which the P420 form is maximally converted (obtained at ~145 min). Arrows indicate the directions of absorption changes in the final phase of P450 to P420 conversion. The inset shows a fit of  $\Delta A_{422}$  data to a single exponential function, giving a rate constant of  $0.033 \pm 0.001 \text{ min}^{-1}$ .

### 5.2.7.2 Spectroscopic analysis of the interaction of CYP126 with FLDR, using FLD and Fdx partners

Early efforts with the *E. coli* flavodoxin reductase were successful in reconstituting a short electron transfer chain from NADPH, providing electrons for the biotin synthase system in *E. coli*, as well as supporting the function of heterologously expressed eukaryotic P450s

(255, 385-387). Thus, in this experiment, FLDR was also used to support Mtb cytochrome P450 reduction by reconstitution of a class I P450 redox chain.

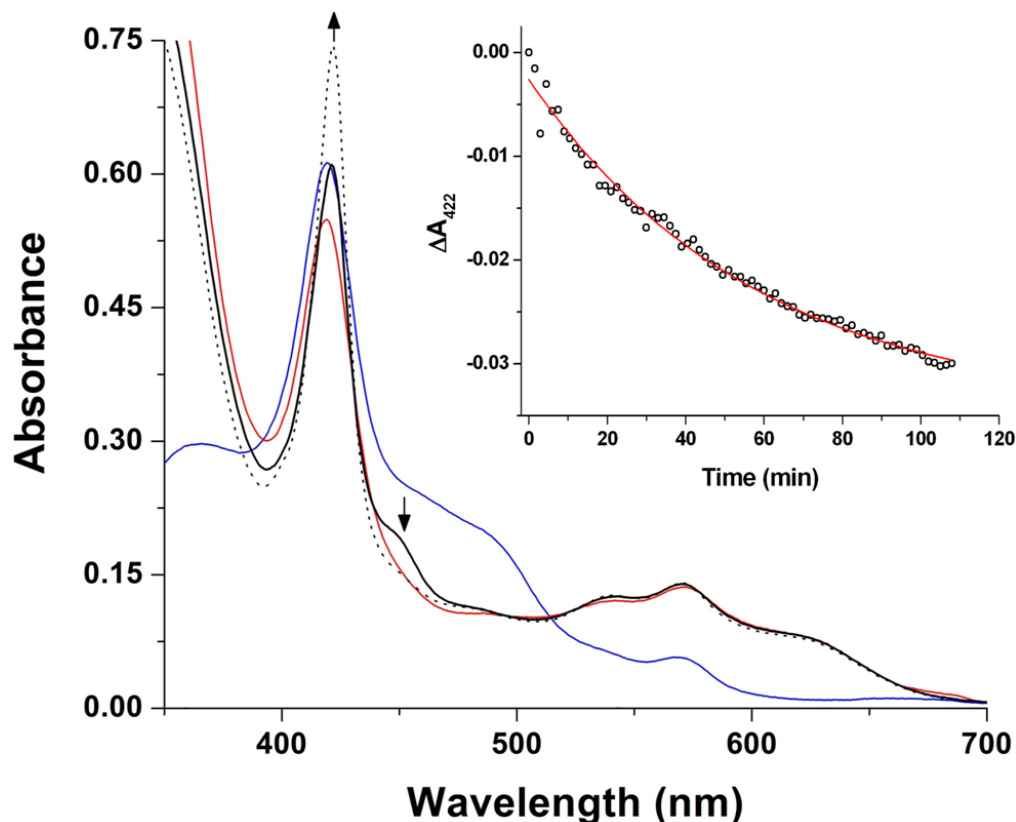


**Figure 5.37. Fe(II)CO complex formation in CYP126 with FLDR and FLD.**

The spectra show anaerobic CO spectral development in CYP126 using an *E. coli* redox partner system. The reaction was set up with a reconstituted system consisting of 4  $\mu\text{M}$  CYP126, and *E. coli* FLDR and FLD in a molar ratio of 1:1:4 (4 and 16  $\mu\text{M}$ , respectively). The resting enzyme complex with its redox partner proteins is shown in blue. The red line is the spectrum recorded immediately upon the addition of NADPH, and the black line is the spectrum obtained 18 min after the addition of NADPH, showing the maximal P450 conversion achieved. The black dotted line represents the P420 form, which reached a maximum after  $\sim 90$  min. Arrows indicate the directions of absorption changes at different points during the course of the experiment. The inset shows a fit of  $\Delta A_{422}$  data to a single exponential function, giving a rate constant of  $0.012 \pm 0.001 \text{ min}^{-1}$ .

Figure 5.37 shows the NADPH-reduced CO spectrum of CYP126 in the presence of FLDR and FLD with the electron donor NADPH. It is clearly seen that under saturated CO conditions a distinct absorbance band at 450 nm is observed at  $\sim 3$  min after addition of NADPH, and the maximum absorbance at 450 nm was observed after  $\sim 18$  min. The reduction of redox partner flavins is observed after the addition of NADPH, with accumulation of long wavelength signals that are likely derived mainly from FMN semiquinone in the FLD. The CO complex is formed to less than 20% of the total expected

intensity based on the concentration of CYP126 used in the experiment (4  $\mu\text{M}$ ). The trace taken 16.5 min after addition of NADPH shows a decrease in absorbance at 418 nm, also consistent with conversion of a fraction of the resting heme protein to the reduced CO complex at 450 nm. Moreover, subsequent traces collected >18 min after addition of NADPH showed an increase in the absorbance at 420 nm and a decrease in the absorbance at 450 nm. This suggests that there was conversion of CYP126 to the inactive P420 form of the enzyme (Figure 5.37 – black dotted line). This is in agreement with the results from chapter 3 (section 3.2.1) and in the reconstitution of CYP126 using Mtb FdR, which indicated that the P450 formation in CYP126 (obtained by the reduction of the enzyme by sodium dithionite or by NADPH/proteins in the presence of CO) is transient and that the protein rapidly converts to the P420 form.

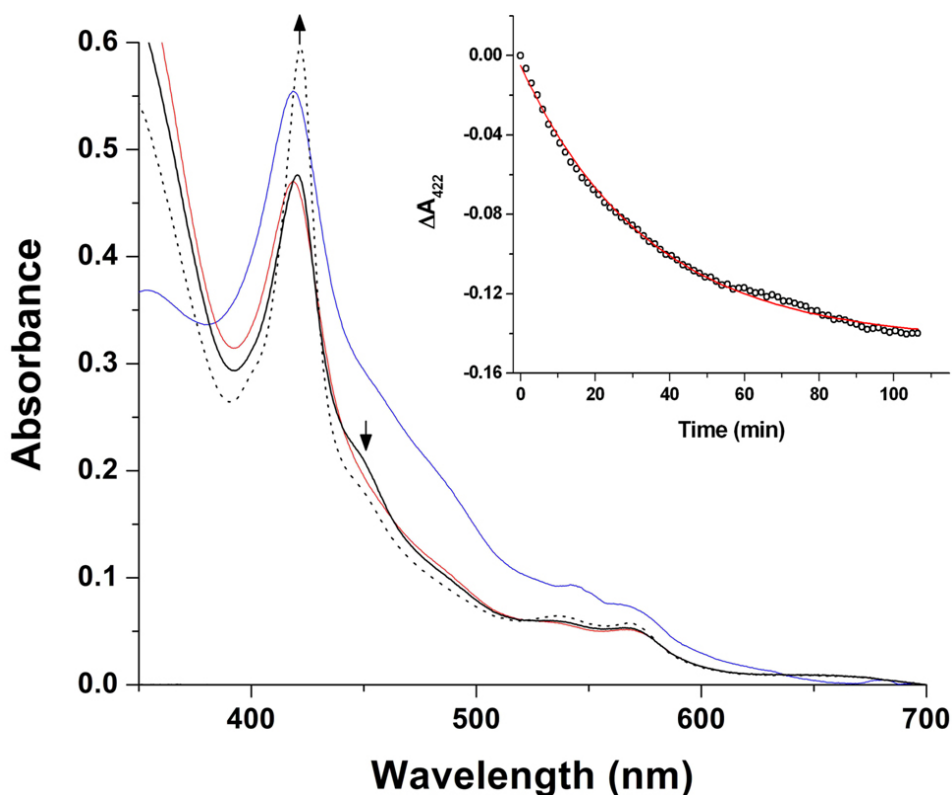


**Figure 5.38. Fe(II)CO complex formation in CYP126 (4  $\mu\text{M}$ ) with FLDR and Fdx<sub>1</sub>.** Collapse of the CYP126 ferrous–carbon monoxy complex from P450 to P420 occurs over time. The spectrum for the resting ferric heme and its redox partner proteins is shown in blue. The red line indicates the spectrum collected 1 min after addition of NADPH, and the black line (with the greatest absorption at 448 nm) was collected 19 min after addition of NADPH, and is the spectrum with largest P450 content. The black dotted line shows the maximum P420 spectrum collected at  $\sim 97$  min. The down arrow indicates the decreasing intensity at 448 nm (loss of the small amount of P450 stabilized) in the final stages of data collection, accompanying increased accumulation of the P420 species (up arrow). The inset shows a fit of  $\Delta A_{422}$  data to a single exponential function, giving a rate constant of  $0.02 \pm 0.001 \text{ min}^{-1}$ .

The reconstitution of the electron chain of CYP126 with FLDR and Fdx<sub>1</sub> revealed lesser development of the P450 form after reduction by NADPH than was seen in the reconstitution with FLDR/FLD, and the P450 form reached maximal occupancy at ~19 min. After this point, the P450 form converted to the inactive P420 form (Figure 5.38 – black dotted line). The conversion of thiolate-coordinated to thiol-coordinated (P450 to P420) heme is likely accompanied by the loss of activity of CYP126. The electron transfer rate computed for CYP126 reconstituted with FLDR-Fdx<sub>1</sub> (0.02 min<sup>-1</sup>) is a little faster than that measured for reconstitution with the FLDR-FLD system (0.012 min<sup>-1</sup>), but the maximal formation of P450 form is rather lower (albeit small in both cases). Possibly, this reflects a slightly greater stabilization of the P450 species in the presence of FLDR/FLD than using FLDR-Fdx<sub>1</sub>.

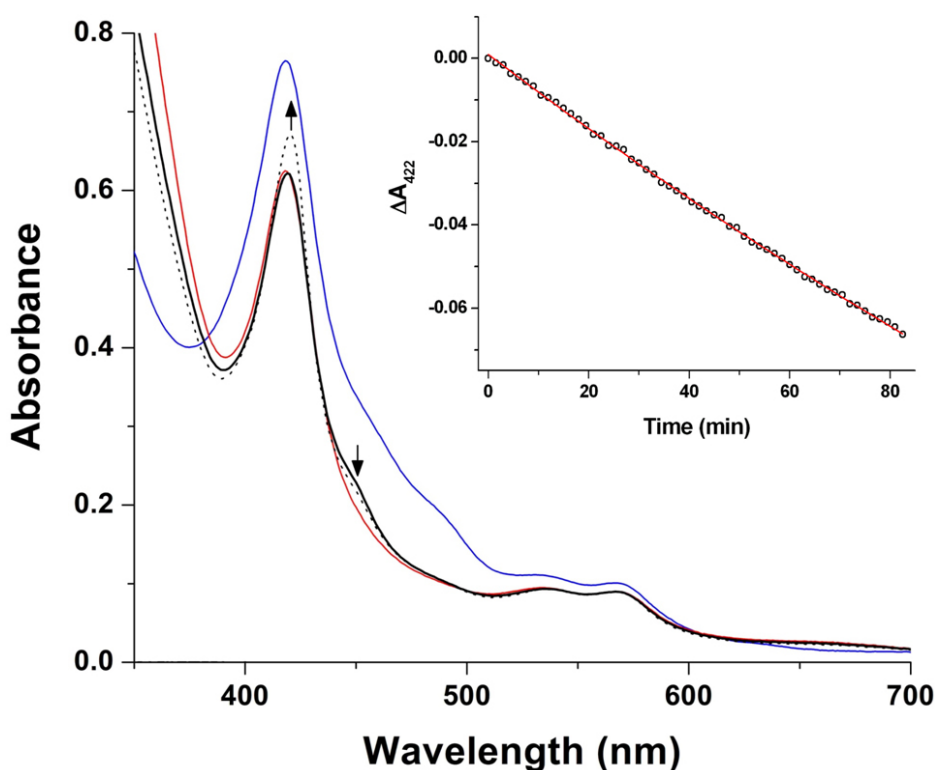


**Figure 5.39. Fe(II)CO complex formation in CYP126 with FLDR and Fdx<sub>2</sub>.**

Reduction of the Mtb P450 CYP126 (4 μM) by flavodoxin reductase and ferredoxin redox partners (in same molar ratios as described previously) is shown by the absorption change at 448 nm reflecting transient formation of the CO-bound P450 form of CYP126, preceding P420 formation. The spectrum for the oxidized enzyme and its redox partners is shown as a blue line. The red line is the spectrum collected after addition of NADPH (200 μM). The maximum P450 spectrum is shown in a solid black line for data collected at 18 min. The black dotted line shows the maximum P420 species obtained at ~75 min. The arrow directions indicate the conversion of P450 to the P420 form in the final stages of the titration. The inset shows a fit of  $\Delta A_{422}$  data to a single exponential function, giving a rate constant of  $0.0021 \pm 0.0002$  min<sup>-1</sup>. The very slow formation of P420 in this redox partner mixture produces a near-linear P420 formation curve.

The electron transfer system formed by FLDR and Fdx<sub>2</sub> also indicated that these partners were successful in delivery of electron(s) from NADPH to CYP126. As shown in Figure 5.39, a small amount of CO-bound P450 complex was observed as early as 1 min after reduction, but very slowly reached its maximal intensity (~18 min). At the same time, the spectral signal of the P420 form accumulated slowly, reaching its maximum intensity at ~75 min, accompanying a decrease of the P450 form (Figure 5.39). The final spectrum recorded did not show as intense a 420 nm peak as was observed in some of the other titrations, reflecting a slow electron transfer rate in this redox system. Interestingly, a small shoulder of P450 remained at ~75 min, indicating that there was still a minor species of thiolate-coordinated heme iron stabilized at this time, again possibly as a consequence of P450 stabilization by CYP126 docking with Fdx<sub>1</sub>.

An independent experiment was carried out with the same reconstitution system, but in absence of Fdx<sub>1,2</sub> or FLD. The electron transfer flow from NADPH → FLDR → CYP126 was then much slower than in the presence of Fdx<sub>1,2</sub> or FLD, with no measurable formation of P450. Only the P420 form was present, and reached its highest intensity after ~220 min. This is apparently confirmatory of the important role of this ferredoxin/flavodoxin protein in the electron transport chain of this bacterial P450 redox system (class I), and possibly also indicative of a slight stabilizing effect that Fdx/FLD proteins have on the CYP126 P450 form. Moreover, in the absence of both FLDR and Fdx<sub>1,2</sub>/FLD, CYP126 failed to receive electrons directly from NADPH, highlighting the importance of FLDR for electron transfer from NADPH.

### 5.2.7.3 Spectroscopic interactions of CYP126 with FprA and FLD/Fdx proteins

FprA was reported to reduce various electron acceptors using either NADPH or NADH as an electron donor (161). In order to establish an electron chain for CYP126, FprA was used as the reductase following the pathway NADPH → FprA → Fdx<sub>1,2</sub> or FLD → P450 + CO. Initial studies to reconstitute P450 CYP126 with Mtb FprA and FLD proteins from *E. coli* were successful, albeit showing a relatively slow rate. Figure 5.40 shows the CYP126 absorption changes observed during NADPH-dependent reduction, leading to the formation of the CO-bound heme iron complex of CYP126. This demonstrates that electrons from NADPH can be passed through FprA and FLD to give a CYP126 Fe(II)CO complex with absorbance maximum at 448 nm. However, similar to the results above, this P450 complex was unstable, and converted to P420, again with a very small amount of the P450 form remaining at the end of the reaction.

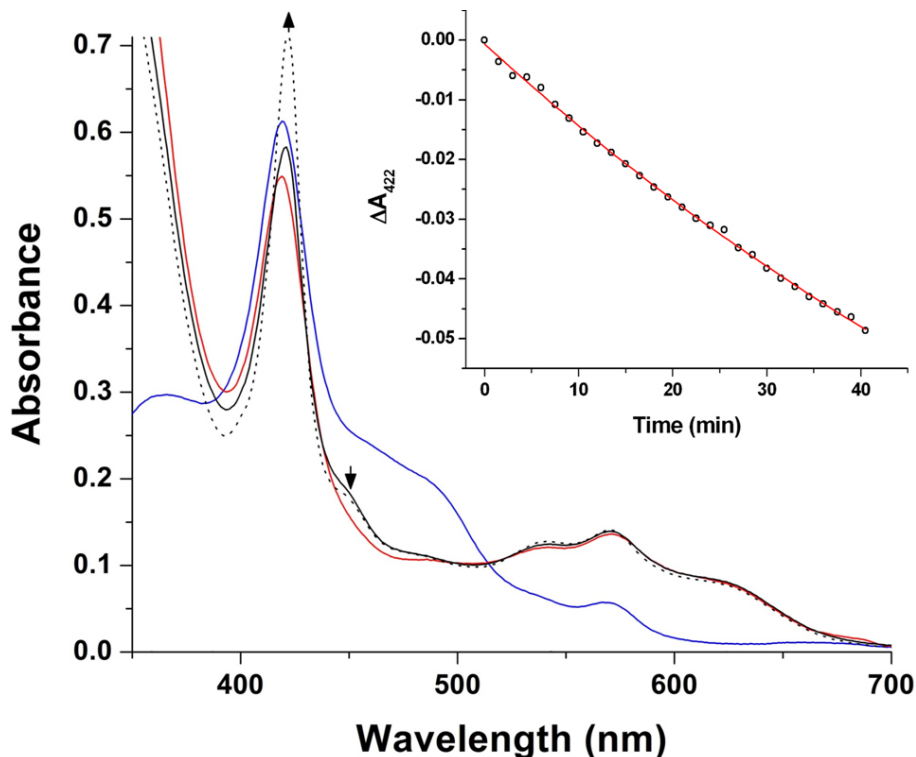


**Figure 5.40. Fe(II)CO complex formation in CYP126 with FprA and FLD proteins.** Spectra were recorded anaerobically using NADPH (200  $\mu\text{M}$ ) in a CO-saturated solution. The reaction was done with a reconstituted system consisting of 5  $\mu\text{M}$  CYP126, Mtb FprA and *E. coli* FLD in a molar ratio of 1:1:4. The resting enzyme complex with its redox partner proteins is shown in blue. The red line represents the spectrum recorded immediately upon the addition of NADPH, and the solid black line is the spectrum obtained 18 min after the addition of NADPH showing the maximum P450 species. The black dotted line is the maximum P420 species obtained at  $\sim 95$  min. Arrows indicate the directions of absorption changes in the final stages of the reaction as the P420 species accumulates. The inset shows a fit of  $\Delta A_{422}$  data to a single exponential function, giving a rate constant of  $0.0007 \pm 0.0009 \text{ min}^{-1}$ , with a near-linear progression curve over this timescale.

As indicated previously, either Fdx<sub>1</sub> or Fdx<sub>2</sub> could support electron transfer to CYP126. In the reconstitution with FprA–Fdx<sub>1</sub> and FprA–Fdx<sub>2</sub> systems, both Fdx<sub>1</sub> and Fdx<sub>2</sub> were apparently able to transfer electrons to the CYP126 heme iron. Figures 5.41 and 5.42 show the reduction of the heme iron of CYP126 in saturated CO buffer using these systems. The formation of the P450 (and then P420) species indicates that the CYP126 heme iron was reduced from Fe<sup>3+</sup> to Fe<sup>2+</sup> by electron transfer from Fdx<sub>1,2</sub>. Similar to the other redox systems, the P450 form reconstituted by FprA–Fdx<sub>1,2</sub> was quickly converted to the P420 form and reached its maximum at  $\sim 90$  min in both cases. It is clearly seen that the intensity of the P420 species is not comparable to the reconstitutions of FLDR–Fdx<sub>1,2</sub> and FdR–Fdx<sub>1,2</sub>. The reason for the low intensity of P420 form is not absolutely clear, but may relate in part to the more positive potential of the ferredoxin redox partners compared to the

CYP126 heme iron. In turn, this gives rise to a slower and less extensive electron transfer process in the timescale analysed, and possibly some competition from a slow breakdown of the Fe(II)CO complex to regenerate the ferric starting material. An additional reconstitution experiment in the absence of Fdx<sub>1,2</sub> indicated that CYP126 was able to accept electrons directly from FprA, mainly forming P420 (and with maximum absorbance obtained at ~350 min), but that the rate was much slower than that in the presence of either ferredoxin. This again demonstrates that the ferredoxin protein is a necessary component of the class I redox system, and may also result in some stabilization of the P450 form.

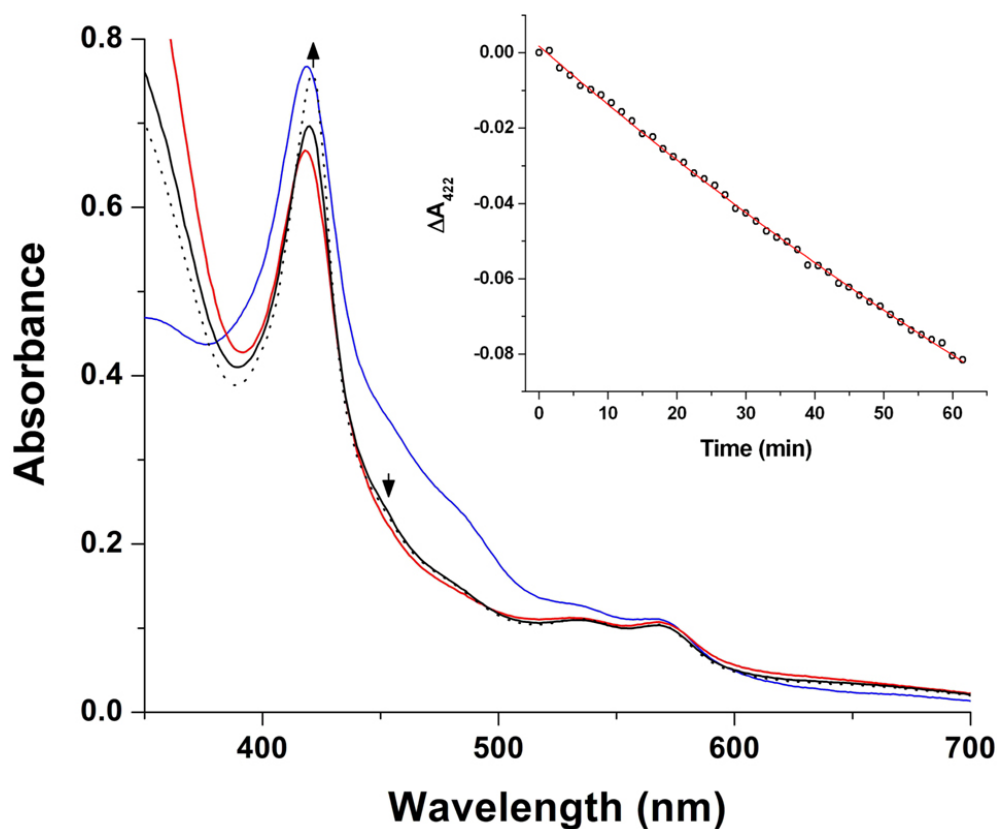


**Figure 5.41. Fe(II)CO complex formation in CYP126 with FprA and Fdx<sub>1</sub>.**

The reaction was done with a reconstituted system consisting of 5  $\mu\text{M}$  CYP126, Mtb FprA and Fdx<sub>1</sub> in a molar ratio of 1:1:4. The resting enzyme complex with its redox partner proteins is shown in blue. The red line represents the spectrum collected immediately upon the addition of NADPH (200  $\mu\text{M}$ ), and the solid black line is the maximum P450 spectrum obtained ~19 min after the addition of NADPH. The black dotted line shows the maximal P420 form collected at ~85 min. Arrows indicate the directions of absorption changes following conversion of P450 to P420 in the final stages of the reaction. The inset shows a fit of  $\Delta A_{422}$  data to a single exponential function, giving a rate constant of  $0.0036 \pm 0.0005 \text{ min}^{-1}$ , again with a near-linear progression curve over this timescale.

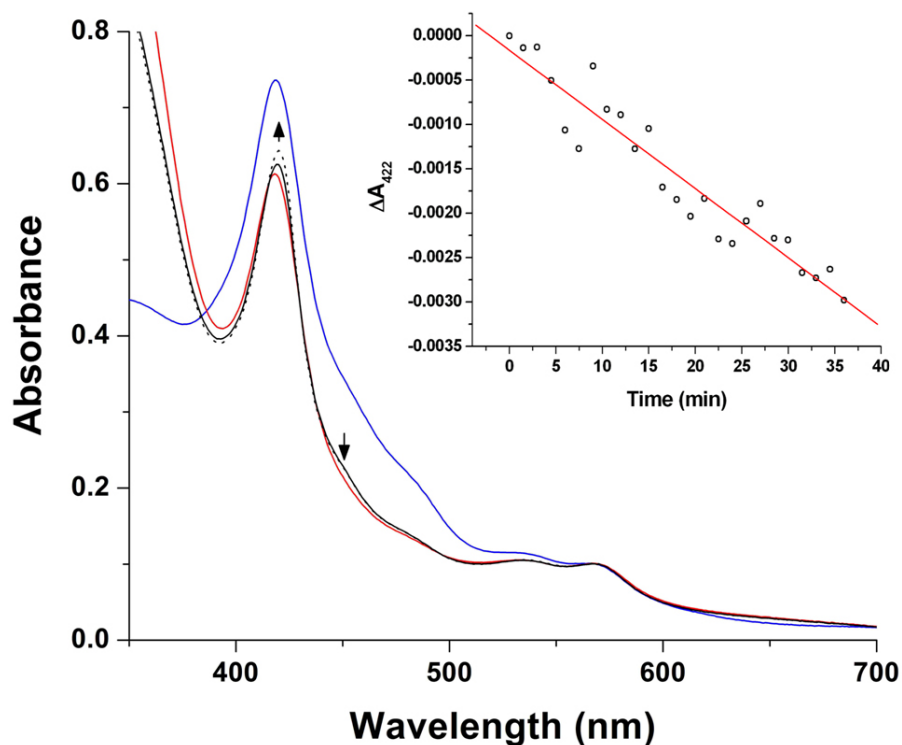


**Figure 5.42. Fe(II)CO complex formation in CYP126 with FprA and Fdx<sub>2</sub>.**

The reaction was done with a reconstituted system consisting of 5  $\mu\text{M}$  CYP126, Mtb FprA and Fdx<sub>2</sub> in a molar ratio of 1:1:4. The resting enzyme complex with its redox partner proteins is shown in blue. The red line represents the spectrum immediately upon the addition of NADPH (200  $\mu\text{M}$ ), and the solid black line is the spectrum obtained 17 min after the addition of NADPH when maximum P450 was obtained. The dotted black line shows the maximum P420 collected at  $\sim 90$  min. Arrows indicate the directions of absorption change at the end of the reaction and following conversion of P450 to P420. This reaction mixture gave the smallest overall conversion to a Fe(II)CO complex, and  $\Delta A_{422}$  data fitted best using a linear function. Under the reaction conditions used, an apparent rate constant of  $(6.24 \pm 4.12) \times 10^{-4} \mu\text{M CYP126 reduced min}^{-1}$  was derived (see inset), using  $125 \text{ mM}^{-1} \text{ cm}^{-1}$  as the extinction coefficient for the P420 form of CYP126.

These results prove that the reconstitution of FprA with both Fdx<sub>1</sub> and Fdx<sub>2</sub> results in the transfer of electrons from the donor (NADPH) to the heme iron of the CYP126 P450, suggesting that CYP126 is able to accept electrons from different partner ferredoxins. At this stage, it is not possible to conclude which redox proteins are the best for the electron delivery to CYP126, since all systems are rather slow, and there are not data for P450 product formation as yet. However, Table 5.3 indicates that the kinetics of electron transfer to CYP126 from the Mtb ferredoxin reductase FdR via Fdx<sub>1</sub> or Fdx<sub>2</sub> occurs somewhat faster than in the other systems. In the case of FprA and Fdx<sub>2</sub> (where the smallest amount of Fe(II)CO complex was formed) an exponential function could not accurately describe the P420 formation process, and in this case a second order rate constant derived from a linear fitting of the data is provided in Table 5.3.

## 5.2.8 Electron transport pathway of CYP141

Like CYP126, CYP141 is an enzyme of unknown function and the electron transfer pathway has not been extensively characterized. In order to determine the electron transfer chain for CYP141, *E. coli* FLDR and FLD, and Mtb FdR, FprA and Fdx<sub>1,2</sub> (as used to reconstitute the electron transfer pathway in CYP126) were used.

### 5.2.8.1 Establishment of FdR and Fdx systems for electron transfer to CYP141

As indicated previously, either FdR or Fdx could support the reduction of P450 heme iron. In these experiments, these systems were used to determine their ability to transfer electrons to CYP141.

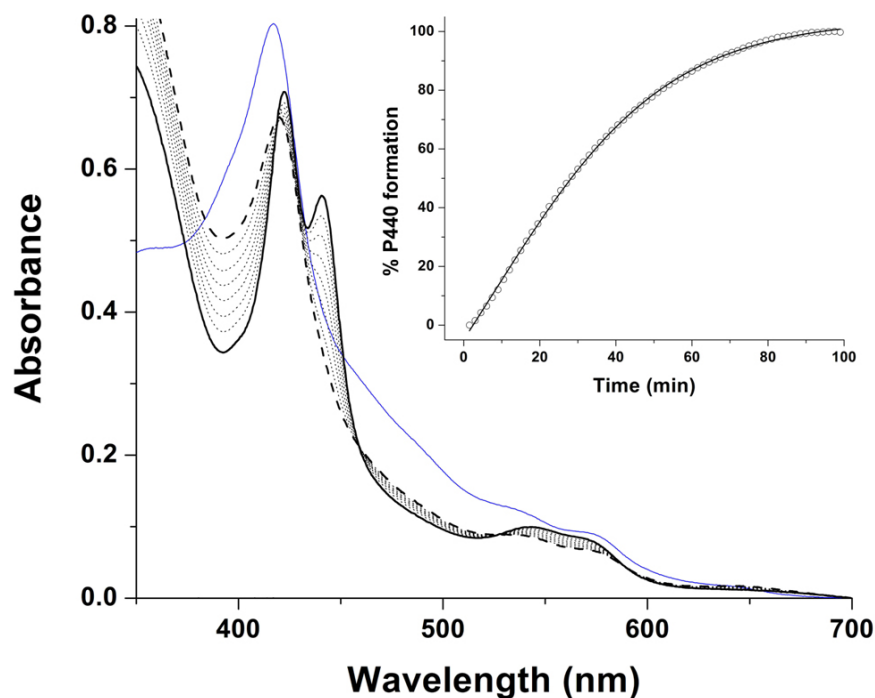


**Figure 5.43. Fe(II)CO complex formation in CYP141 using Fdx<sub>1</sub> and FdR.**

A Mtb redox system of FdR (5  $\mu$ M), Fdx<sub>1</sub> (20  $\mu$ M), and CYP141 (5  $\mu$ M) was set up in CO-saturated buffer. CYP141 complex formation was initiated by NADPH reduction (200  $\mu$ M). Shown is the spectral accumulation of the Fe(II)CO form of wild-type CYP141 over time. The initial spectrum (blue line) is prior to NADPH addition and has contributions from oxidized CYP141/FdR/Fdx proteins. The dashed line shows bleaching of reductase proteins (~63 min). Later spectra (dotted lines) were collected at 78, 93, 108, 123, 138, and 150 min. The final spectrum (dark solid line) at 162 min shows a predominantly thiolate-coordinated Fe(II)CO enzyme with Soret band at 440 nm. The inset shows a plot of  $A_{440}$  (percentage of P440 formed) versus time, with data fitted using an exponential function. The rate constant determined for Fe(II)CO complex formation was  $0.017 \pm 0.004 \text{ min}^{-1}$ .

As shown in Figure 5.43, Fe(II)CO complex formation occurred in CYP141, with an absorbance increase at 440 nm (indicative of the thiolate complex) driven by NADPH via FdR and Fdx<sub>1</sub>, and the P440 complex near-fully obtained ~162 min after addition of

NADPH (including 63 min for the complete formation of the reduced form of FdR). Interestingly, the CO complex of CYP141 was very stable, therefore enabling the calculation of the rate of electron transfer through to the Fe(II)CO complex formation by fitting absorbance change data at 440 nm (i.e. the peak for the Fe(II)CO heme thiolate complex) using a single exponential function, and as described in the Methods section (section 2.24). The apparent rate constant for electron transfer within the FdR-Fdx<sub>1</sub>-CYP141 complex was  $0.017 \pm 0.004 \text{ min}^{-1}$ .

Similar to Fdx<sub>1</sub>, Fdx<sub>2</sub> was used with FdR to reconstitute the electron transfer chain in CYP141 (Figure 5.44). However, the formation of the P440 was much slower, in addition to the slow reduction of the redox partner proteins. The calculated rate for the Fe(II)CO complex formation was  $0.006 \pm 0.001 \text{ min}^{-1}$ .

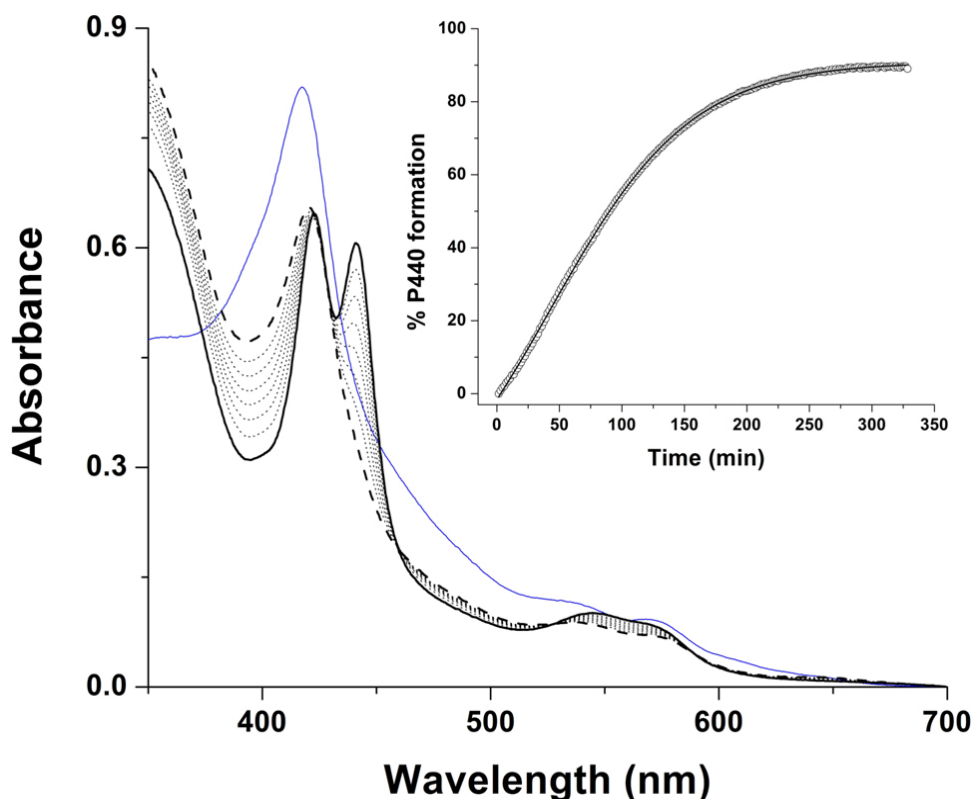


**Figure 5.44. Fe(II)CO complex formation in CYP141 using Fdx<sub>2</sub> and FdR.**

The redox system for CYP141 was formed by reconstitution of FdR (5  $\mu\text{M}$ ), Fdx<sub>2</sub> (20  $\mu\text{M}$ ), and CYP141 (5  $\mu\text{M}$ ) and was set up in CO-saturated buffer. Fe(II)CO complex formation was initiated by NADPH reduction (200  $\mu\text{M}$ ). The initial spectrum (blue line) is prior to NADPH addition and has contributions from oxidized CYP141/FdR/Fdx<sub>2</sub> proteins. The dashed line spectrum shows bleaching of reductase proteins (~238 min). Later spectra (dotted lines) were collected at ~284, 330, 376, 430, and 476 min. The final spectrum (dark solid line) at ~562 min shows the formation of Fe(II)CO complex with Soret maximum at 440 nm. The inset shows a plot of  $A_{440}$  versus time. The rate constant determined for electron transfer was  $0.006 \pm 0.001 \text{ min}^{-1}$ .

### 5.2.8.2 Use of FLDR-FLD/Fdx<sub>1,2</sub> as electron transport chains to CYP141

As mentioned above, some microbial P450s utilize flavodoxins and NADPH-FLD oxidoreductase as obligatory redox partners (388, 389). Therefore, FLDR and FLD from *E. coli* were used to reconstitute an electron chain for CYP141. Figure 5.45 shows the reduction of CYP141 in the presence of CO, indicated by the formation of 440 nm absorbance of the heme by electron donation from NADPH via FLDR and FLD electron carriers. The highest intensity of the 440 nm absorbance was collected at 109 min after addition of NADPH, showing near-complete conversion of oxidized enzyme to the P450 (i.e. P440) complex, but at a slow rate. However, the absence of FLD protein results in the failure to form any observable CO-bound heme iron spectrum at 440 nm. This result confirms that CYP141 strictly uses a “normal” bacterial redox system containing a ferredoxin or flavodoxin coupled with NADPH-FLDR (FdR) reductase for electron delivery from coenzyme donor to the heme iron of the P450 enzyme. The electron transfer to CYP141 is relatively slow (in the absence of an oxidizable substrate), with a rate constant for Fe(II)CO complex formation of  $0.024 \pm 0.001 \text{ min}^{-1}$  under the conditions used.

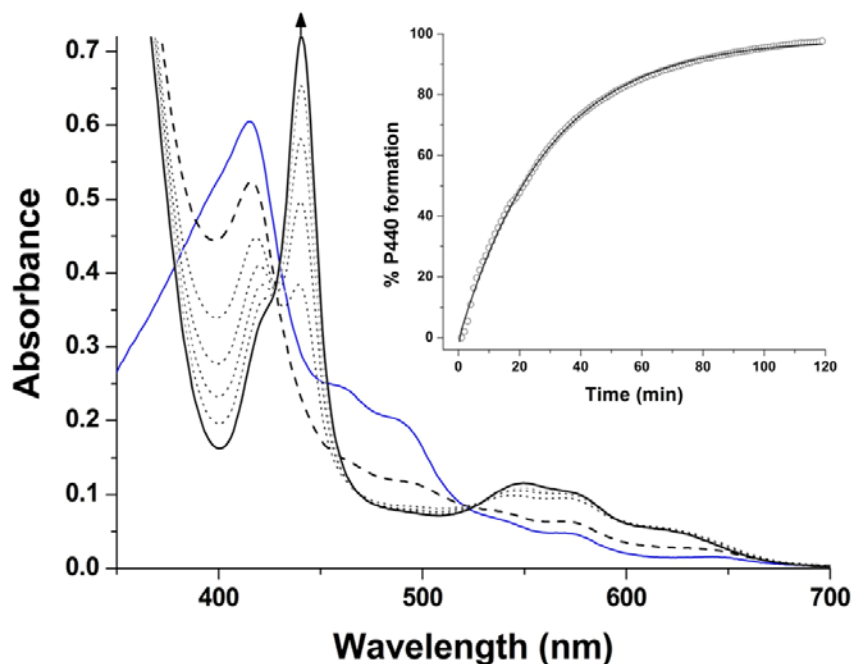


**Figure 5.45. Fe(II)CO complex formation in CYP141 with FLDR and FLD.**

The spectra shown report on the reduction of CYP141 (5  $\mu\text{M}$ ) in CO-saturated buffer in a system reconstituted with FLDR (5  $\mu\text{M}$ ) and FLD (20  $\mu\text{M}$ ) as electron carriers. An absorbance maximum at 440 nm appears after reduction by NADPH, which is typical for the CO-bound form of CYP141. The resting enzyme complex is shown in blue, the dashed line is the starting point of the experiment immediately following NADPH addition (200  $\mu\text{M}$ ). The solid black line represents the fully reduced CO-bound form, and the dotted lines indicate spectra collected at 11, 23, 35, and 35 min after addition of NADPH. The arrow indicates the direction of absorption change at 440 nm with time. The rate constant for P440 formation was  $0.024 \pm 0.001 \text{ min}^{-1}$ .

The electron transport pathway of CYP141 was examined when reconstituted with FLDR and Fdx<sub>1</sub> in a ratio 1:1:4. Figure 5.46 shows the CO-trapping when the heme iron of CYP141 was reduced by electron transfer from NADPH via FLDR-Fdx<sub>1</sub>. However, under similar conditions, the rate constant using FLDR-Fdx<sub>1</sub> was lower than that using FLDR-FLD. The highest intensity of the absorption at 440 nm was collected ~102 min after addition of NADPH, and did not show the full conversion to P440. The rate for electron transfer using this system was  $0.011 \pm 0.006 \text{ min}^{-1}$ .

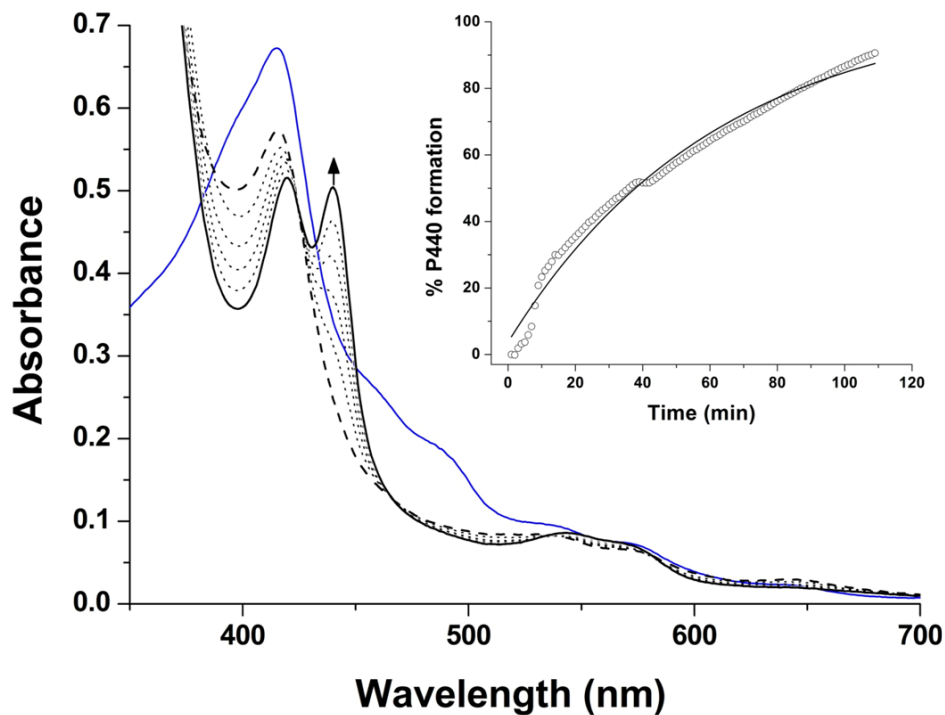


**Figure 5.46. Fe(II)CO complex formation in CYP141 with FLDR and Fdx<sub>1</sub>.**

A redox system was established by reconstitution of FLDR (5  $\mu\text{M}$ ), Fdx<sub>1</sub> (20  $\mu\text{M}$ ), and CYP141 (5  $\mu\text{M}$ ). CO-complex formation was initiated by NADPH reduction (200  $\mu\text{M}$ ). The initial spectrum (blue line) is prior to NADPH addition and has contributions from oxidized FLDR/Fdx<sub>1</sub> proteins. The dashed black line spectrum is after NADPH addition and shows bleaching of reductase proteins (after 1 min). Later spectra (dotted lines) were collected at 10, 28, 54 and 80 min. The final spectrum (dark solid line) at 102 min shows a predominantly thiolate-coordinated Fe(II)CO enzyme with Soret maximum at 440 nm. The inset shows a plot of  $A_{440}$  versus time, with data fitted using an exponential function. The rate constant determined for Fe(II)CO complex formation was  $0.011 \pm 0.006 \text{ min}^{-1}$ .

The CYP141 redox system was further investigated using a 1:4:1 molar ratio of FLDR/Fdx<sub>2</sub>/P450. CYP141 was clearly efficiently reduced by this electron transfer system. Both FLDR and Fdx<sub>2</sub> have a full complement of FAD and Fe-S clusters and are able to reconstitute an effective electron chain. However, the result showed a similarly slow transfer of electrons from NADPH through to the heme as was seen with FLDR/Fdx<sub>1</sub> partners, and the maximum intensity at 440 nm for the CO-complex absorbance was

slightly lower than that observed with FLD and Fdx<sub>1</sub>. Figure 5.47 presents the spectral detail for the anaerobic reduction of CYP141 coupled with FLDR/Fdx<sub>2</sub> as its electron transport system. The maximum intensity at 440 nm was achieved at 80 min, but the extent of formation of the P440 CO complex is only ~30% of the total expected intensity based on the concentration of CYP141 used in the experiment. The rate constant for electron transfer was calculated as  $0.011 \pm 0.001 \text{ min}^{-1}$  in this system. The less “complete” P440 formation observed using the FLDR/Fdx<sub>1</sub> and FLDR/Fdx<sub>2</sub> partners compared to FLDR/FLD likely occurs as a result of the rather positive reduction potential for the ferredoxins compared to that for the oxidized/semiquinone (or semiquinone/hydroquinone) couples of the FLD.

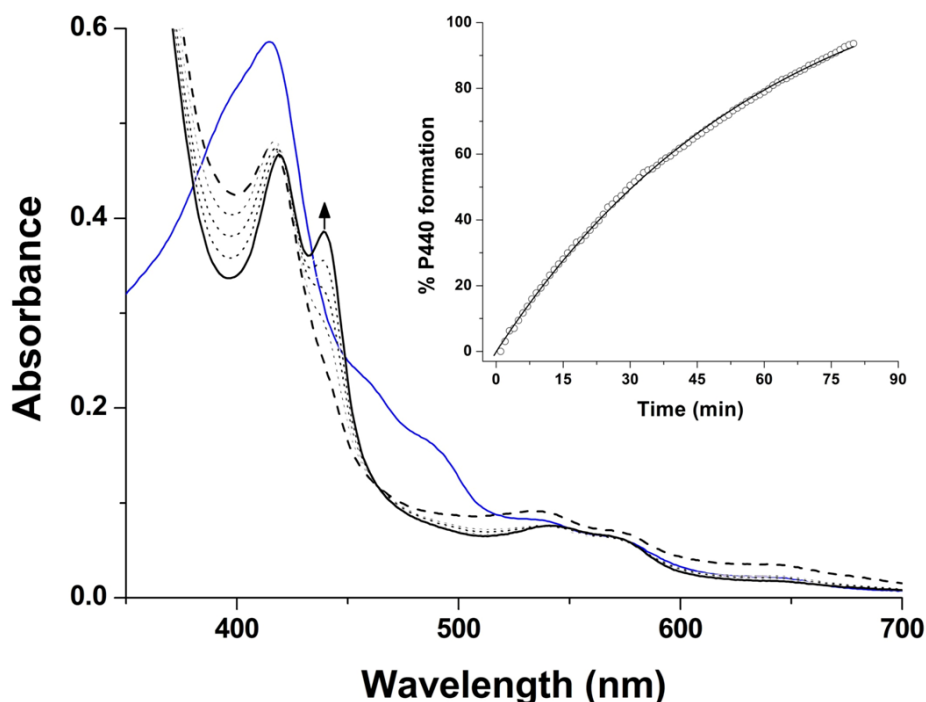


**Figure 5.47. Fe(II)CO complex formation in CYP141 with FLDR and Fdx<sub>2</sub>.**

A redox system for CYP141 was set up in CO-saturated buffer. Fe(II)CO complex formation was initiated by NADPH reduction (200  $\mu\text{M}$ ). The initial spectrum (blue line) is prior to NADPH addition and has contributions from oxidized CYP141 (5  $\mu\text{M}$ ), FdR (5  $\mu\text{M}$ ) and Fdx (20  $\mu\text{M}$ ) proteins. The dashed line spectrum shows bleaching of reductase proteins. Later spectra (dotted lines) were collected at 16, 31 and 53 min. The final spectrum (black solid line) at 81 min shows a Fe(II)CO complex with Soret maximum at 440 nm. The inset shows a plot of  $A_{440}$  versus time, with the rate constant determined for Fe(II)CO complex formation as  $0.011 \pm 0.001 \text{ min}^{-1}$ .

### 5.2.8.3 Use of FprA and FLD/Fdx<sub>1,2</sub> as an electron transport chain for CYP141

The reduction of CYP141 was also measured with a reconstituted FprA-FLD-CYP141 system at a ratio 1:4:1, and 200  $\mu\text{M}$  electron donor NADPH (Figure 5.48). Preliminary analysis showed that this system was the most efficient in supporting reduction of the heme

iron. This means that the FLD protein could stimulate the CYP141 reduction activity of FprA. Thus, the rates of CYP141 reduction by *E. coli* FLD using FLDR or FprA proteins appeared to be much higher than those using Fdx<sub>1</sub> or Fdx<sub>2</sub>. The rate of Fe(II)CO complex formation was  $0.025 \pm 0.004 \text{ min}^{-1}$  with FLD as the partner protein, and a near complete P440 formation was observed.

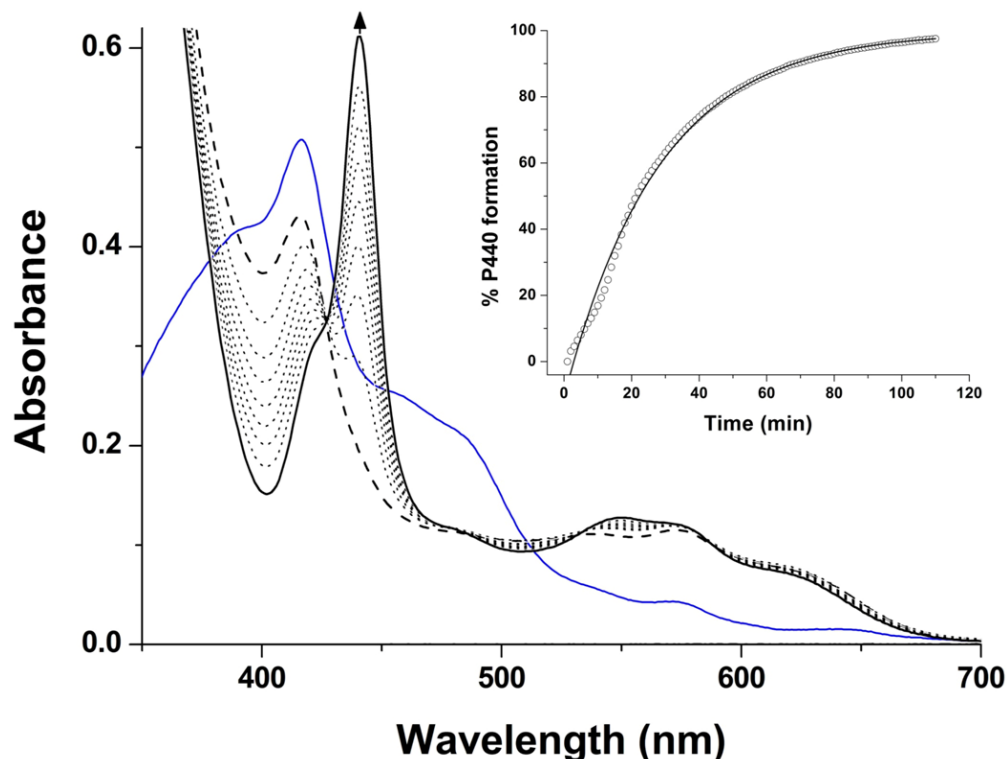


**Figure 5.48. Fe(II)CO complex formation in CYP141 with FprA and FLD.**

The redox system was set up in CO-saturated buffer. CYP141-CO complex formation was initiated by NADPH reduction (200  $\mu\text{M}$ ). Shown is the spectral accumulation of the Fe(II)CO form of wild-type CYP141 over time. The initial spectrum (blue line) is prior to NADPH addition and has contributions from the oxidized CYP141 (5  $\mu\text{M}$ ), FdR (5  $\mu\text{M}$ ) and FLD (20  $\mu\text{M}$ ) proteins. The dashed black line spectrum shows bleaching of the reductase proteins (1 min). Later spectra (dotted lines) were collected at 12, 17, 21, 27, 34, 43 and 58 min. The final spectrum (black solid line) at 111 min shows a predominantly thiolate-coordinated Fe(II)CO enzyme with Soret maximum at 440 nm. The inset shows a plot of  $A_{440}$  versus time with the rate constant determined for Fe(II)CO complex formation as  $0.025 \pm 0.004 \text{ min}^{-1}$ .

Reconstitution with FprA and Fdx<sub>1</sub> supported the reduction of CYP141, but this occurred at a very low rate (Figure 5.49). Although FprA and Fdx<sub>1</sub> from *Mtb* were demonstrated to support reduction of CYP126 (see section 5.2.7.3), the detailed structural and enzymatic properties of this system are not completely determined yet. Therefore, the reason for the low rates of CYP126 heme reduction when reconstituted with Fdx<sub>1</sub> and Fdx<sub>2</sub> is not clear

(although the positive reduction potentials of the ferredoxins are a likely explanation – i.e. thermodynamically restricted reduction of the P450 by the ferredoxin partner). In this experiment, the reduction of CYP141 was observed only when Fdx<sub>1</sub> was added in the assay, indicating that FprA was able to interact productively with this electron carrier protein and could not effectively reduced CYP141 in isolation. The highest intensity of the CYP141 Fe(II)CO absorption peak at 440 nm was obtained 90 min after addition of NADPH, but the conversion to P440 did not occur fully, and took place with a low apparent rate constant of Fe(II)CO complex formation of  $0.005 \pm 0.001 \text{ min}^{-1}$ . Here, and in other examples where incomplete P440 formation is observed towards the end of the experiment, it appears likely that the lower wavelength Soret feature is that of the ferric CYP141 (and not a P420 form), since absorption features in the  $\alpha/\beta$  region retain characteristics similar to those for the starting (ferric) enzyme form.

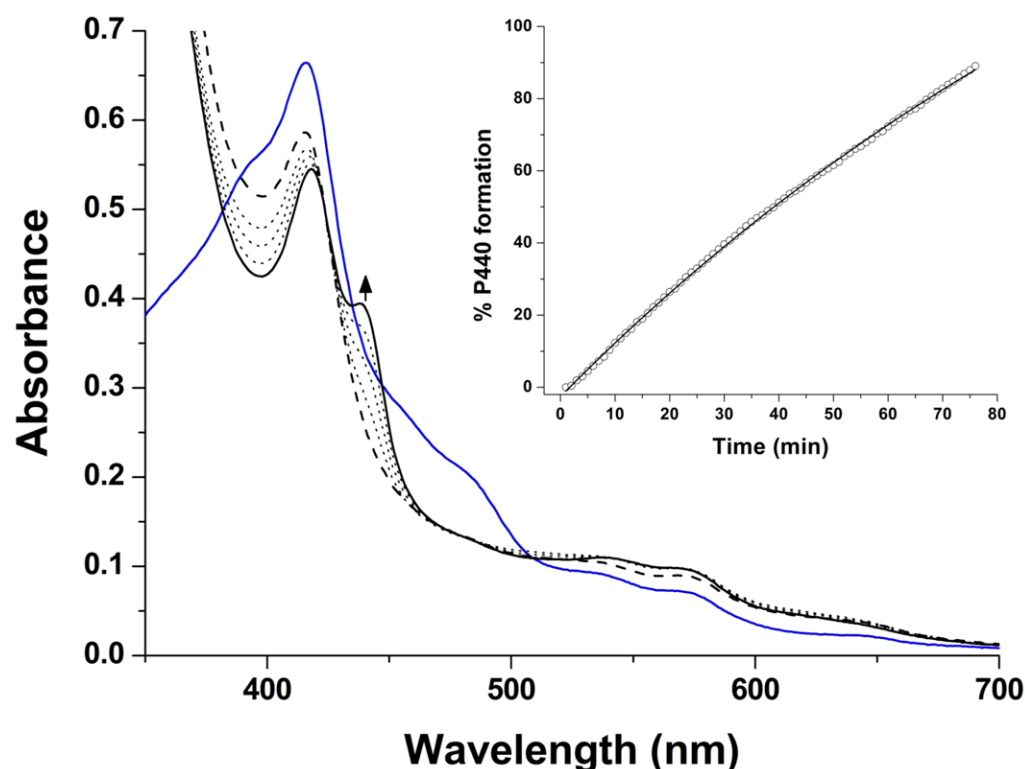


**Figure 5.49. Fe(II)CO complex formation in CYP141 with FprA and Fdx<sub>1</sub>.**

A Mtb redox system for CYP141 was set up using the Mtb partners. Shown is the spectral accumulation of the Fe(II)CO form of wild-type CYP141 (5  $\mu\text{M}$ ) over time in presence of FprA (5  $\mu\text{M}$ ) and Fdx<sub>1</sub> (20  $\mu\text{M}$ ). The initial spectrum (blue line) is prior to NADPH addition. The black dashed line spectrum shows bleaching of reductase proteins (1 min). Later spectra (dotted lines) were collected at 34, 54, and 78 min. The final spectrum (black solid line) at 97 min shows a partially formed Fe(II)CO complex with Soret maximum at 440 nm. The inset shows a plot of  $A_{440}$  versus time, with the rate constant determined for Fe(II)CO complex formation as  $0.005 \pm 0.001 \text{ min}^{-1}$ .

Similar to data using the *Mtb* ferredoxin Fdx<sub>1</sub>, combining FprA with Fdx<sub>2</sub> also yielded a stable complex of CO-bound CYP141 with a characteristic absorbance at 440 nm, providing a diagnostic test for the presence of thiolate-coordinated heme in the sample. However, the extent of overall conversion to the P440 form was low. In the absence of Fdx<sub>2</sub>, a CO spectrum was not observed at all, demonstrating that electrons are transferred in sequence from NADPH to FprA to Fdx<sub>2</sub>, and finally to CYP141 (Figure 5.50). The rate constant was calculated, as described in the Methods section (section 2.24), as  $0.005 \pm 0.001 \text{ min}^{-1}$ .

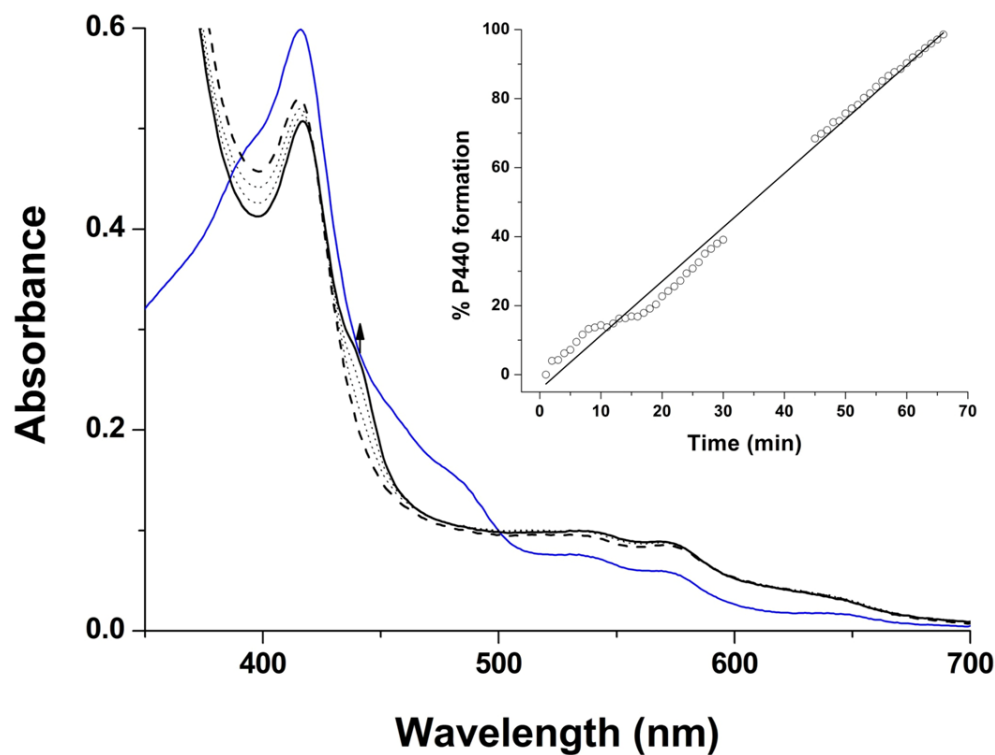


**Figure 5.50. Fe(II)CO complex formation in CYP141 with FprA and Fdx<sub>2</sub>.**

CYP141 complex formation was initiated by NADPH reduction (200  $\mu\text{M}$ ). Shown is spectral accumulation of the Fe(II)CO form of wild-type CYP141 (5  $\mu\text{M}$ ) over time in presence of FprA (5  $\mu\text{M}$ ) and Fdx<sub>2</sub> (20  $\mu\text{M}$ ). The initial spectrum (blue line) is prior to NADPH addition. The dashed black line is after NADPH addition. Later spectra (dotted lines) were collected at 26 and 31 min. The final spectrum (black solid line) was collected at 53 min. The inset shows a plot of  $A_{440}$  versus time and the rate constant determined for Fe(II)CO complex formation was  $0.005 \pm 0.001 \text{ min}^{-1}$ .

Redox system	Fe(II)CO formation rate constant (min <sup>-1</sup> ) <sup>a</sup>	
	CYP141	CYP126
FdR-Fdx <sub>1</sub>	0.017 ± 0.004	0.024 ± 0.001
FdR-Fdx <sub>2</sub>	0.006 ± 0.001	0.033 ± 0.001
FLDR-FLD	0.024 ± 0.001	0.012 ± 0.001
FLDR-Fdx <sub>1</sub>	0.011 ± 0.006	0.020 ± 0.001
FLDR-Fdx <sub>2</sub>	0.011 ± 0.001	0.0021 ± 0.0002
FprA-FLD	0.025 ± 0.004	0.0071 ± 0.0009
FprA-Fdx <sub>1</sub>	0.005 ± 0.001	0.0036 ± 0.0005
FprA-Fdx <sub>2</sub>	0.005 ± 0.001	*

**Table 5.3. Summary of the rate constants for CYP141/CYP126 Fe(II)CO complex formation using different redox partner systems.**

CYP141 and CYP126 were reduced in CO-saturated buffer by reconstituting with ferredoxin reductases (FdR, FLDR, FprA) and ferredoxins/flavodoxin (Fdx<sub>1</sub>, Fdx<sub>2</sub>, FLD) partner systems. <sup>a</sup>The kinetics of the complex formation (P450 [P440] formation in the case of CYP141, P420 formation for CYP126) were determined by plotting the extent of Fe(II)CO complex formation against reaction time and fitting the resultant data using a single exponential function with Origin software. \*The exception is for the data set describing the CYP126 P420 formation in the reaction with FprA/Fdx<sub>2</sub> partners. Here the linear reaction progress curve was used to calculate an apparent rate constant of  $(6.24 \pm 4.12) \times 10^{-4}$   $\mu\text{M P420 formed min}^{-1}$  under the conditions used.

It is clearly seen from Table 5.3 that CYP141 reduction occurs fastest when FLD is used, and when it is coupled with either of the two reductases, Mtb FprA or *E. coli* FLDR. The rate constants are much higher than on reconstitution using these reductases and Fdx<sub>1,2</sub>. Following this, the CYP141 reductase activities of Fdx<sub>1</sub> and Fdx<sub>2</sub> were roughly equivalent in the FprA/Fdx<sub>1,2</sub> and in the FLDR/Fdx<sub>1,2</sub> redox systems, but different rates were obtained for FdR/Fdx<sub>1,2</sub> (an ~3-fold difference in favour of Fdx<sub>1</sub>). Using the accumulation of P420 to follow electron transfer in the CYP126 system, the FdR/Fdx<sub>2</sub> system exhibited the fastest rate constant, followed by FdR/Fdx<sub>1</sub> and FLDR/Fdx<sub>1</sub>. The rate constant with FLDR/Fdx<sub>2</sub> partners was ~10-fold lower than with FLDR/Fdx<sub>1</sub>. In a previous report, Zanno *et al.* showed that FdR/Fdx<sub>1</sub> system is able to support electron transfer for Mtb CYP51B1-catalysed sterol demethylation (153). In view of the slow reduction of FdR by NAD(P)H, this catalytic activity is likely to be very low. The relatively low electron transfer activity of these systems toward CYP141 and CYP126 enzymes could mean that they are not the “native” redox systems for these P450s, particularly since the locations of the *Fdx*<sub>1,2</sub> genes

are adjacent to *CYP51B1* and *CYP143* genes, respectively. Potentially, CYP141 and CYP126 may preferentially select other Mtb redox partners for their catalytic activity.

## 5.2.9 Reconstitution of electron transport pathways for known-substrate P450s

### 5.2.9.1 Electron transport pathway for CYP51B1

The enzymatic activity of CYP51B1 was demonstrated *in vitro* (179). Recent reports also indicated electron transport systems for this enzyme (390). In this section, the ability of the newly cloned Mtb FdR and Mtb Fdx<sub>1,2</sub> proteins to transfer electrons to CYP51B1 from the coenzyme NADPH was investigated, in both the absence and presence of a substrate analogue (estriol).

Figure 5.51 presents the spectral changes accompanying the development of the Fe(II)CO complexes of active (P450) and inactive (P420) forms of CYP51B1 when reconstituted with FdR and either Fdx<sub>1</sub> or Fdx<sub>2</sub>. As reported previously, the reduced CO complex (absorbance band at 450 nm) was found to rapidly convert to the inactive P420 form of the enzyme due to heme thiolate protonation. The results indicated a very slow transfer of electrons from NADPH to FAD, as well as to the heme iron of CYP51B1. The rate of electron transfer from FdR via Fdx<sub>1</sub>/Fdx<sub>2</sub> to CYP51B1 was thus difficult to measure because of the formation of the inactive P420 form (i.e. the collapse of P450 into P420 with a rate competitive with those for heme reduction). This problem was overcome by following the progression of A<sub>420</sub> with time (following P420 formation) following the addition of NADPH to the system, and by fitting data using a single exponential function. This was done with the assumption that the rate of P450 to P420 collapse was faster (or at least similar) to the rate of electron transfer from Fdx<sub>1</sub>/Fdx<sub>2</sub> to CYP51B1. This assumption appears borne out by the fact that there is negligible accumulation of the P450 form of the Fe(II)CO complex in these systems. However, the addition of the substrate analogue (estriol) improved the rate of electron transfer between the redox partners as a consequence of its inducing a positive shift in the heme iron potential. The concomitant use of Mtb redox partners and estriol substrate analogue also stabilized the P450 form of CYP51B1. This enabled the determination of the rate constant for electron transfer to CYP51B1 by fitting of  $\Delta A_{450}$  versus time data to a single exponential function (using both FdR/Fdx<sub>1</sub> and FdR/Fdx<sub>2</sub> redox partner pairs).

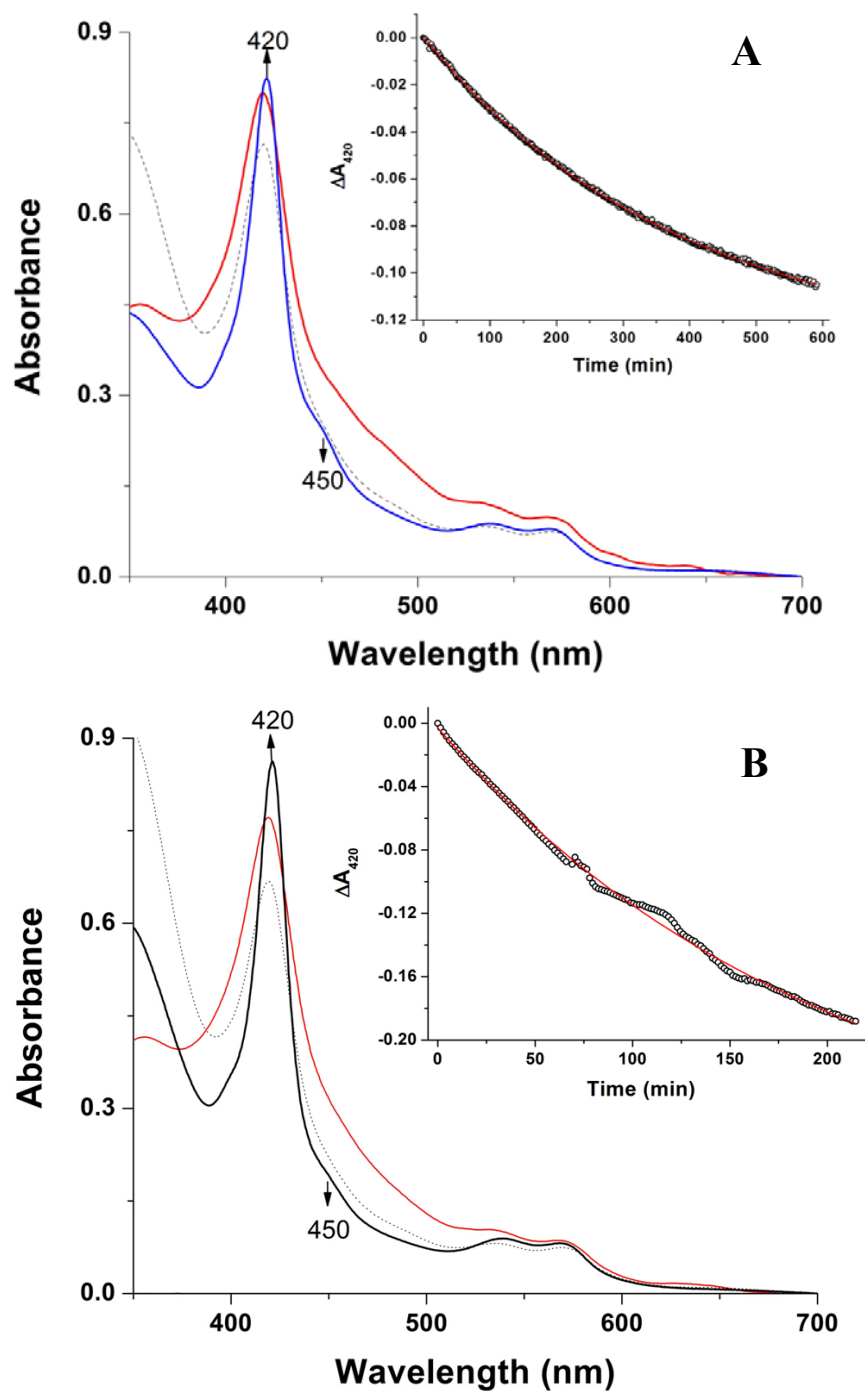


**Figure 5.51. Reconstitution of Mtb redox systems and electron transfer to CYP51B1.**

**A**, A Mtb redox system consisting of FdR (5  $\mu$ M), Fdx<sub>1</sub> (20  $\mu$ M) and CYP51B1 (5  $\mu$ M) was set up in CO-saturated buffer. The red line is the spectrum for the oxidized FdR/Fdx<sub>1</sub>/CYP51B1 proteins, the dotted line is the maximal P450 formed obtained at ~63 minutes, and the blue line is the maximal P420 formed once the P450 collapses, collected at ~600 minutes. **B**, A Mtb redox system consisting of FdR (5  $\mu$ M), Fdx<sub>2</sub> (20  $\mu$ M) and CYP51B1 (5  $\mu$ M) was set up as before. The red line is prior to NADPH addition (200  $\mu$ M), the dotted line the spectrum collected at maximal P450 accumulation, obtained at ~42 minutes, and the black line is at maximal P420 accumulation, collected at ~264 minutes. The insets show fits of  $\Delta A_{420}$  data using a single exponential function, giving apparent rate constants of  $0.0018 \pm 0.0001 \text{ min}^{-1}$  for electron transfer to the CYP51B1 heme iron using the FdR/Fdx<sub>1</sub> system (panel A), and of  $0.0035 \pm 0.0001 \text{ min}^{-1}$  for electron transfer using the FdR/Fdx<sub>2</sub> system (panel B).

As shown in Figure 5.52, a much faster reduction rate of CYP51B1 was obtained in a complete system containing 5  $\mu\text{M}$  FdR, 20  $\mu\text{M}$  Fdx<sub>1</sub>, 5  $\mu\text{M}$  P450 CYP51, 50  $\mu\text{M}$  estriol, and 200  $\mu\text{M}$  NADPH. Analysis was done by following the time-dependent accumulation of the P450 form of CYP51B1 at 450 nm, with this state stabilized in the presence of estriol. A rate constant of  $0.032 \pm 0.002 \text{ min}^{-1}$  was determined at 25 °C, indicating relatively rapid transfer of electrons to the CYP51B1 heme iron compared to the substrate-free form of the P450.

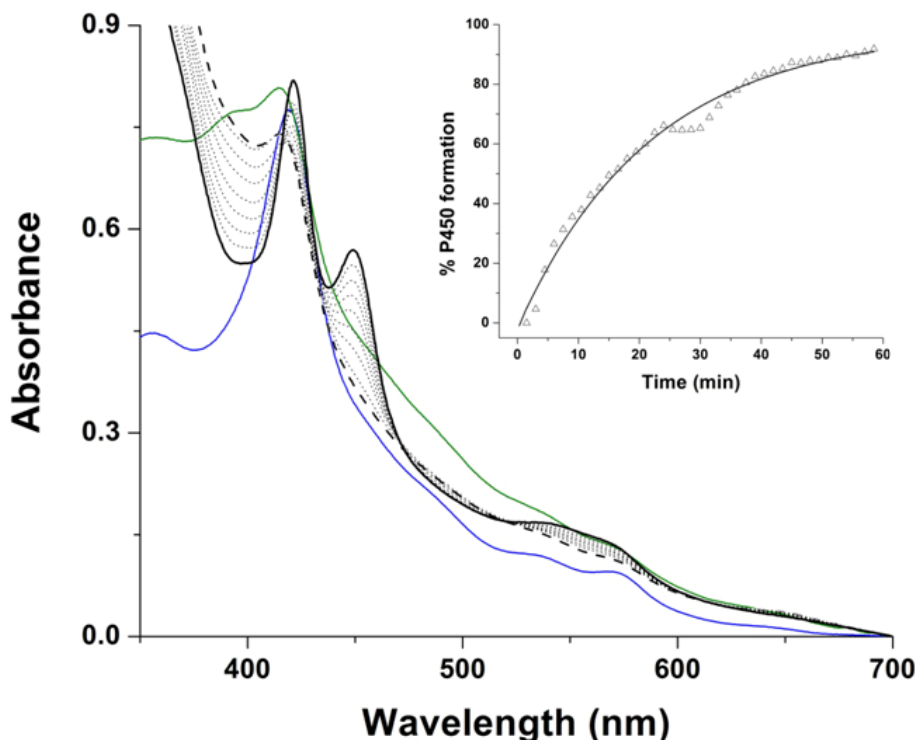


**Figure 5.52. The reduction of estriol-bound CYP51B1 using an FdR-Fdx<sub>1</sub> electron transfer system.**

The Mtb redox system comprising FdR (5  $\mu\text{M}$ ), Fdx<sub>1</sub> (20  $\mu\text{M}$ ), CYP51B1 (5  $\mu\text{M}$ ) and estriol (50  $\mu\text{M}$ ) was set up in CO-saturated buffer. The reduction of CYP51B1 was initiated by NADPH addition (200  $\mu\text{M}$ ). The blue line is the spectrum for the oxidized FdR/Fdx<sub>1</sub>/CYP51B1 proteins. The green line is after estriol addition. The dashed line is the apparent end point for the reduction of reductase proteins on NADPH addition. The dotted lines were collected at 5, 15, 25, 35, 45, 55, and 65 min. The final spectrum (black line) was collected at 75 min. The inset shows a plot of  $A_{450}$  versus time, and the rate constant was determined as  $0.032 \pm 0.002 \text{ min}^{-1}$  from data fitting using a single exponential function.

In addition, the rate of reduction was also measured with the reconstituted FdR-Fdx<sub>2</sub>-P450 CYP51B1 system, also using 50  $\mu\text{M}$  estriol. The rate of reduction of CYP51B1 was again estimated by measuring the increase in the absorbance ( $A_{450}$ ) after mixing with excess NADPH (200  $\mu\text{M}$ ) (Figure 5.53). The estimated rate was  $0.017 \pm 0.003 \text{ min}^{-1}$  at 25 °C,

showing a slower rate than that achieved by reconstitution using Fdx<sub>1</sub>. These results indicate that the reductive reaction of CYP51B1 could be supported by a combination of Mtb FdR and either of Fdx<sub>1,2</sub>. It was also found that enhanced CYP51B1 reduction occurred with substrate-bound (estriol) enzyme, at least in the case of the FdR/Fdx<sub>1</sub> system. However, electron transfer to CYP51B1 is relatively slow (even in the presence of an oxidizable substrate), but comparable to the rates determined above for reduction of CYP141. It is interesting to note that it was previously shown that estriol could retard (but not stop) P420 collapse in CYP51B1 (82). In these studies it appears that use of Fdx<sub>1,2</sub> along with estriol can effectively stop P420 collapse, producing a mixture of P450/P420 species at the final equilibrium point.

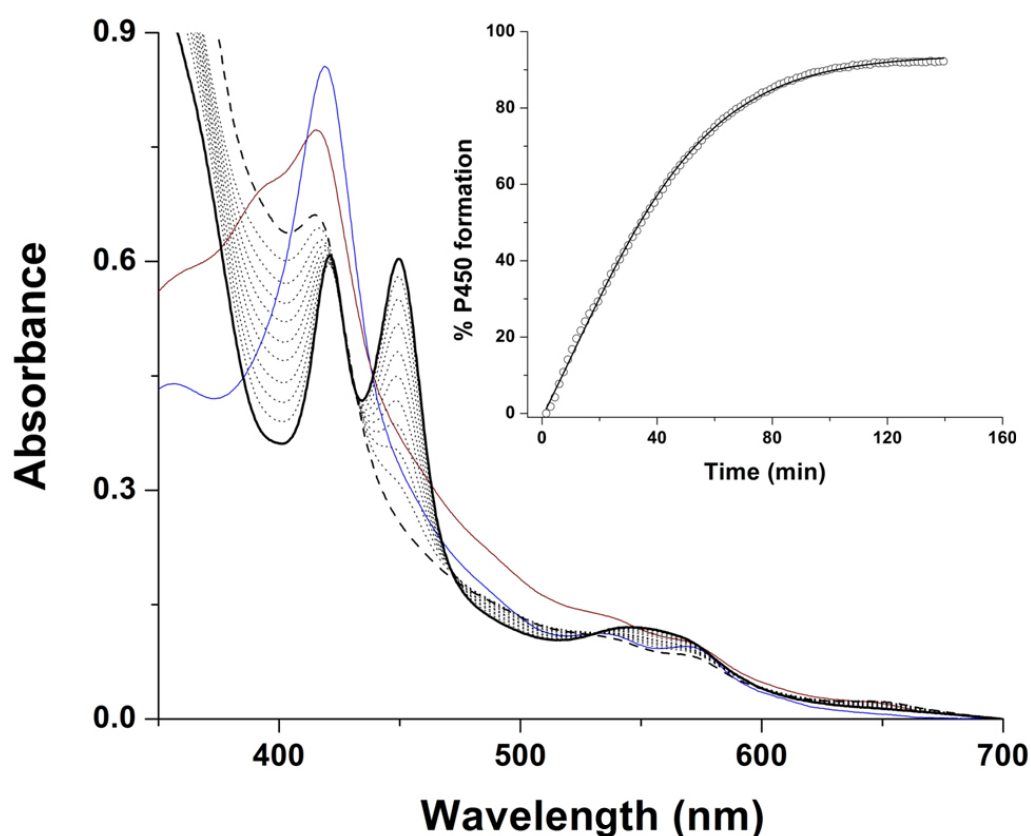


**Figure 5.53. The reduction of estriol-bound CYP51B1 using an FdR-Fdx<sub>2</sub> electron transfer system.**

A reconstitution system of FdR (5  $\mu$ M), Fdx<sub>2</sub> (20  $\mu$ M), CYP51B1 (5  $\mu$ M), and estriol (50  $\mu$ M) was set up in CO-saturated buffer. The reduction of CYP51B1 was initiated by NADPH addition (200  $\mu$ M). The blue line is for the oxidized FdR/Fdx<sub>2</sub>/CYP51B1 proteins. The brown line is after estriol addition. The dashed line is the apparent end point for the reduction of reductase proteins following NADPH addition. The dotted lines are for spectra collected at 20, 40, 60, 80, 100, 120, 140, 160 and 180 min. The final spectrum (black line) was collected at 195 min and shows extensive formation of both P450 and P420 species. The inset shows a plot of A<sub>450</sub> versus time and the rate constant was determined as  $0.017 \pm 0.003 \text{ min}^{-1}$  from data fitting using a single exponential function.

### 5.2.9.2 Electron transport systems for CYP121

Similar to the reconstitution of the electron transfer chain in CYP51B1, CYP121 reduction was also determined with the same set of redox systems as used for CYP51B1. As shown in Figure 5.54, a reductase system was successfully established to reduce CYP121 using a combination of the Mtb ferredoxin Fdx<sub>1</sub> and FdR. Using this system, the substrate-free enzyme gave a rate constant for Fe(II)CO complex formation of  $0.005 \pm 0.001 \text{ min}^{-1}$ . In other experiments, the combination of FdR and Fdx<sub>1</sub> together with cyclo-L-Tyr-L-Tyr (cYY substrate)-bound CYP121 enhanced the P450 reduction rate ( $0.042 \pm 0.004 \text{ min}^{-1}$ ) (Figure 5.55). An increase of reduction rate constant by 8-fold indicated that cYY binding likely increases the redox potential of the heme iron, therefore enabling faster electron transfer to the CYP121 heme iron as a consequence of a greater thermodynamic driving force.

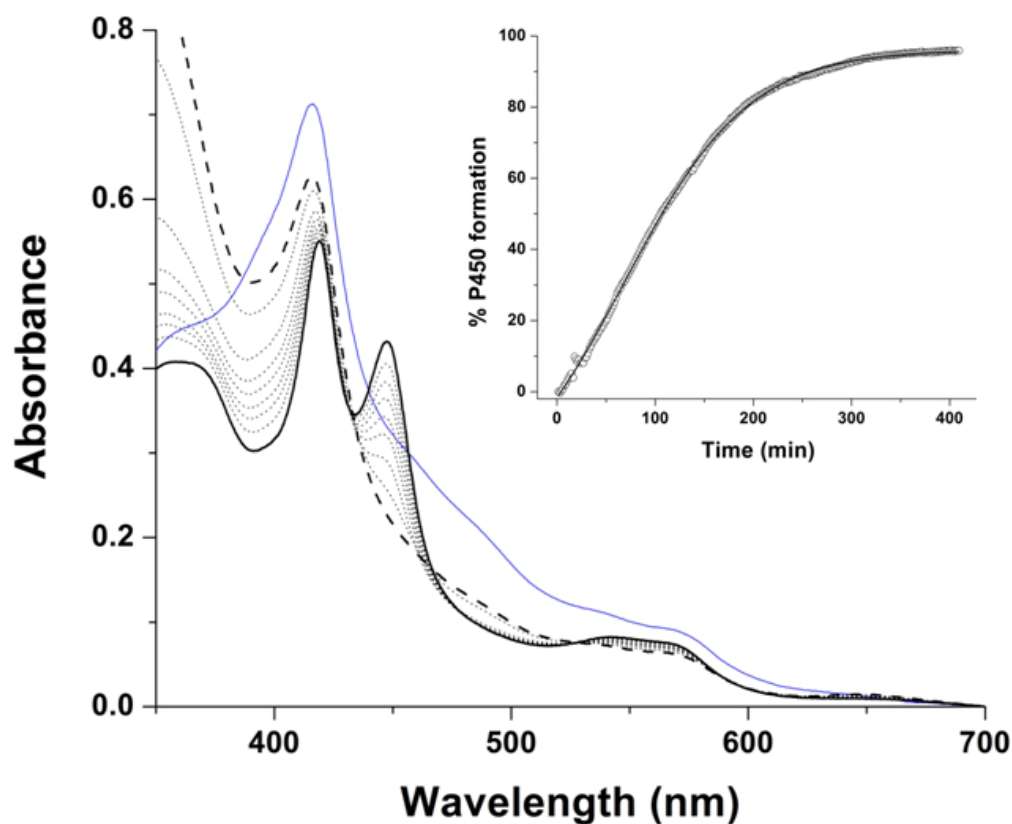


**Figure 5.54. A redox system for CYP121 using FdR-Fdx<sub>2</sub>.**

A combination of FdR (5  $\mu\text{M}$ ), Fdx<sub>2</sub> (20  $\mu\text{M}$ ) and CYP121 (5  $\mu\text{M}$ ) was set up as an electron transfer system to CYP121. The reduction of CYP121 was initiated by NADPH addition (200  $\mu\text{M}$ ). The blue line is for the oxidized FdR/Fdx<sub>2</sub>/CYP121 proteins. The dashed line is the apparent end point for the reduction of the reductase proteins. The dotted lines were collected at 50, 100, 150, 200, 250, 300 and 350 min. The final spectrum (black line) was collected at 412.5 min and shows extensive formation of both P450 and P420 species. The inset shown a plot of  $A_{450}$  versus time and the rate constant was determined as  $0.0053 \pm 0.001 \text{ min}^{-1}$  from data fitting using a single exponential function.

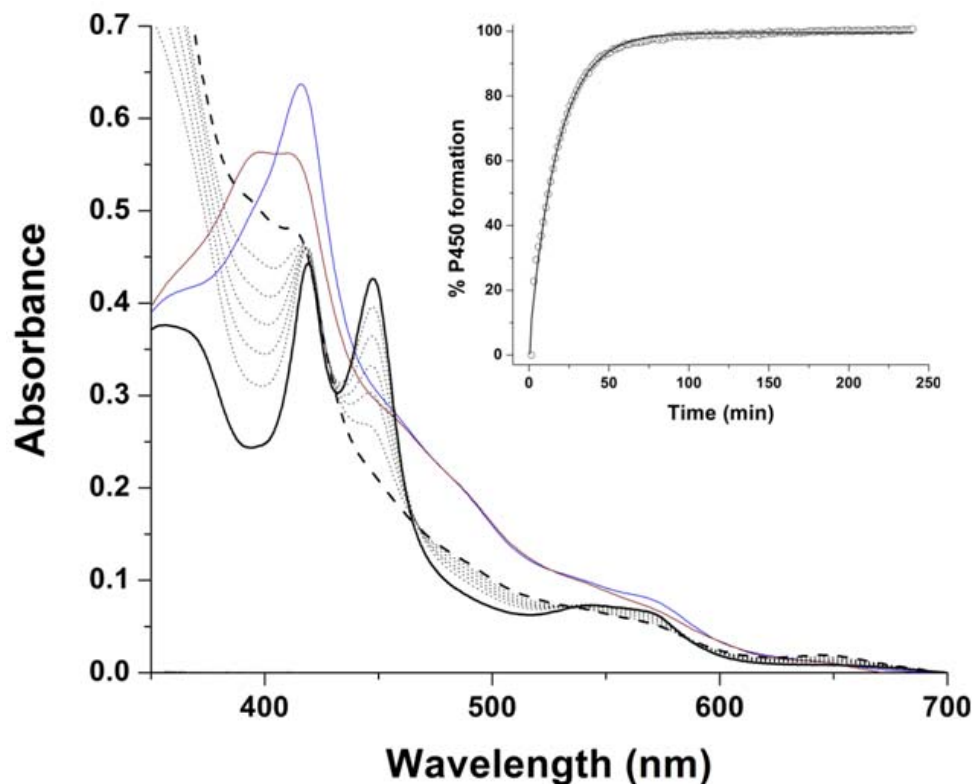


**Figure 5.55. Fe(II)CO complex formation in cYY-bound CYP121 using FdR and Fdx<sub>1</sub> redox partner enzymes.**

To reconstitute the electron transfer system, purified FdR (5  $\mu\text{M}$ ) was used with Fdx<sub>1</sub> (20  $\mu\text{M}$ ), CYP121 (5  $\mu\text{M}$ ), and cYY (50  $\mu\text{M}$ ) in the standard assay buffer (25 °C). The blue line is for the oxidized FdR/Fdx<sub>1</sub>/CYP121 proteins. The purple line is after cYY addition. The dashed line is the apparent end point for the reduction of the reductase proteins. The dotted lines were collected at 40, 80, 120, 160, 120, 140, 160 and 200 min. The final spectrum (black line) was collected at 246 min and shows extensive formation of both P450 and P420 species. The inset shown a plot of  $A_{450}$  versus time and the rate constant was determined as  $0.042 \pm 0.004 \text{ min}^{-1}$  from data fitting using a single exponential function.

The combination of FdR and Fdx<sub>2</sub> was also successful in supporting electron transfer for the reduction of CYP121 heme iron. Figure 5.56 presents the reduction of substrate-free CYP121 supported by FdR and Fdx<sub>2</sub> proteins. It is clearly seen that electron transfer to CYP121 via the redox system FdR/Fdx<sub>2</sub> enables Fe(II)CO complex formation with an absorbance maximum at 450 nm. The CO complex that is formed is less than 30% of the total expected intensity based on the concentration of P450 used in the experiment (5  $\mu\text{M}$ ), with the remainder being the P420 form. The rate constant determined was  $0.0072 \pm 0.0002 \text{ min}^{-1}$ . However, in the presence of cYY substrate, the rate of electron transfer in this system was increased approximately 16-fold compared to in absence of cYY, with a rate

constant of  $0.114 \pm 0.004 \text{ min}^{-1}$  determined (Figure 5.57). Similar to the electron transport chain in CYP51B1, the binding of cYY to the active site of CYP121 causes a positive change in redox potential and increases the driving force for electron transfer to the heme iron, thus accelerating reduction by the redox partners.

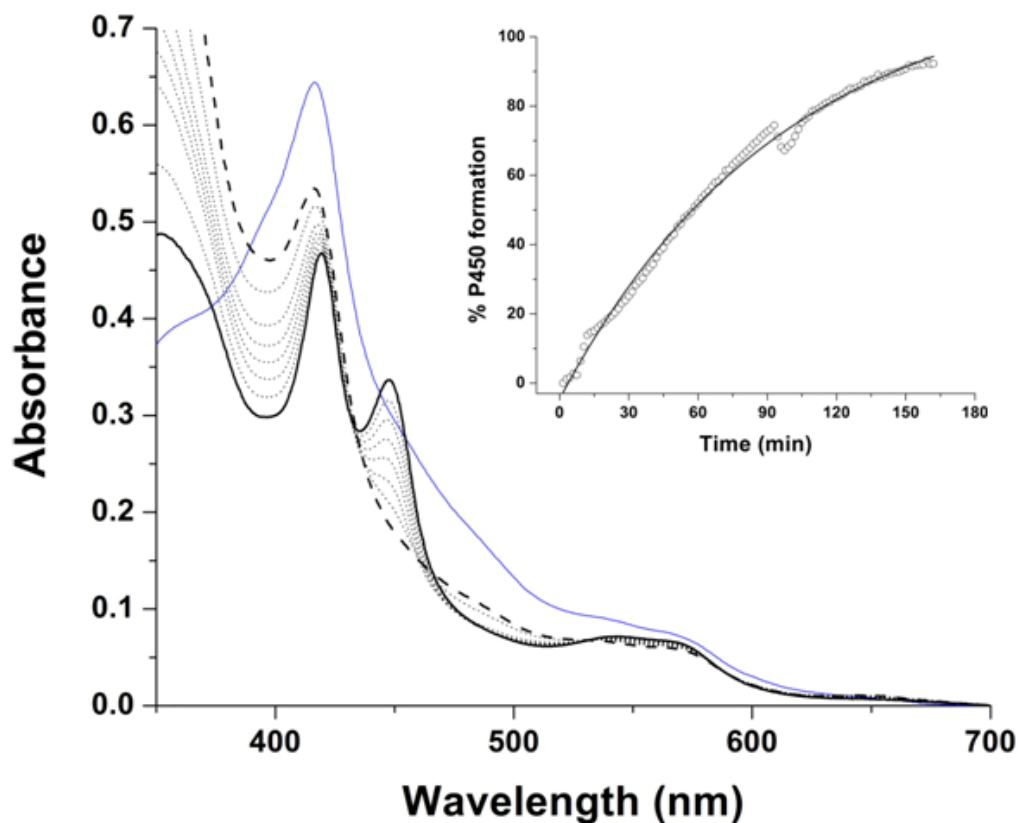


**Figure 5.56. Reduction of CYP121 by the FdR-Fdx<sub>2</sub> system.**

A mixture of FdR (5  $\mu\text{M}$ ), Fdx<sub>2</sub> (20  $\mu\text{M}$ ), CYP121 (5  $\mu\text{M}$ ) in 50 mM potassium phosphate buffer (pH 7.5) was deaerated and bubbled with CO for 10 min, and mixed with NADPH (200  $\mu\text{M}$ ). The blue line is the spectrum for the oxidized FdR/Fdx<sub>2</sub>/CYP121 proteins. The dashed line is the spectrum collected following addition of NADPH. The dotted lines were collected at 20, 40, 60, 80, 100, and 120 min. The final spectrum (black solid line) was collected at 160.5 min and shows extensive formation of both P450 and P420 species. The inset shows a plot of  $A_{450}$  versus time, and data were fitted using a single exponential function to give an apparent rate constant of  $0.0072 \pm 0.0002 \text{ min}^{-1}$  for CYP121 reduction.

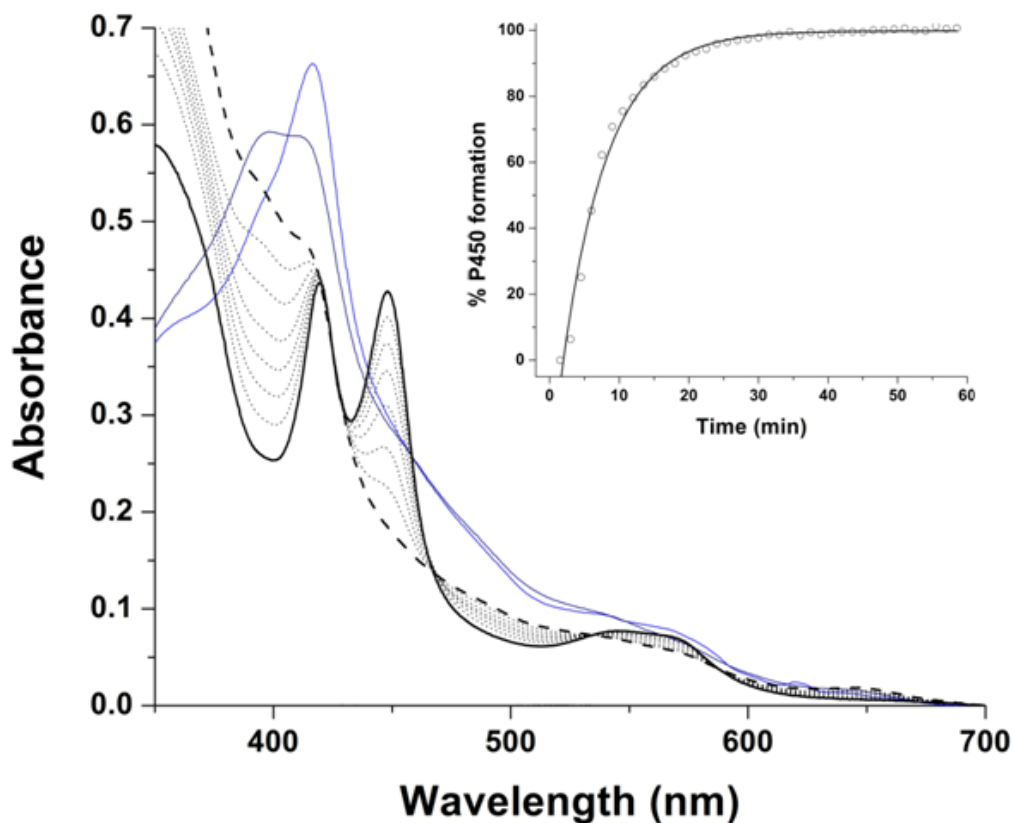


**Figure 5.57. Reduction of cYY-bound CYP121 by the FdR-Fdx<sub>2</sub> system.**

A reconstitution system of FdR (5  $\mu\text{M}$ ), Fdx<sub>2</sub> (20  $\mu\text{M}$ ), CYP121 (5  $\mu\text{M}$ ), and cYY (50  $\mu\text{M}$ ) was set up in CO-saturated 50 mM potassium phosphate buffer (pH 7.5). The reduction of CYP121 was initiated by NADPH addition (200  $\mu\text{M}$ ). The blue line is the spectrum for the oxidized FdR/Fdx<sub>2</sub>/CYP121 proteins. The purple line is after cYY addition. The dashed line is the apparent end point of reduction of the reductase proteins after NADPH addition. The dotted lines are for spectra collected at 9, 18, 27, 36, 40, and 50 min. The final spectrum (solid black line) was collected at 64.5 min and shows extensive formation of both P450 and P420 species. The inset shows a plot of A<sub>450</sub> versus time, and data were fitted using a single exponential function to give an apparent rate constant of  $0.114 \pm 0.004 \text{ min}^{-1}$ .

### 5.2.9.3 Electron transport pathway for CYP125

In order to reconstitute the electron transport pathway for the Mtb cholesterol hydroxylase CYP125, three ferredoxin and ferredoxin reductase proteins from Mtb were used to provide a redox system (FdR/Fdx<sub>1,2</sub>) that could deliver electron(s) to the CYP125 heme iron in both presence and absence of substrate. As done for the same set of redox reactions with other Mtb P450s above, the electron transfer between redox partners and the CYP125 heme iron was detected and measured by the formation of its Fe(II)CO complex. Figure 5.58 shows the electron transfer to substrate-free CYP125 driven by NADPH via the Mtb FdR/Fdx<sub>1</sub> redox system. The rate constant determined for Fe(II)CO complex formation was  $0.0065 \pm$

0.0002 min<sup>-1</sup>. Interestingly, addition of substrate (cholesterol) increased the electron transfer rate by approximately 7 fold ( $0.048 \pm 0.007$  min<sup>-1</sup>) (Figure 5.59). The relatively slow rate obtained for substrate-free CYP125 again likely reflects the thermodynamically unfavourable difference in the redox potential between the CYP125 heme iron (-305 mV) (121) and the ferredoxin (-30 mV) (194), and suggests that the binding of cholesterol to the heme iron of CYP125 elevates the potential to a more positive value, making it easier to drive electron transfer from the redox proteins to the substrate-bound P450 heme iron.

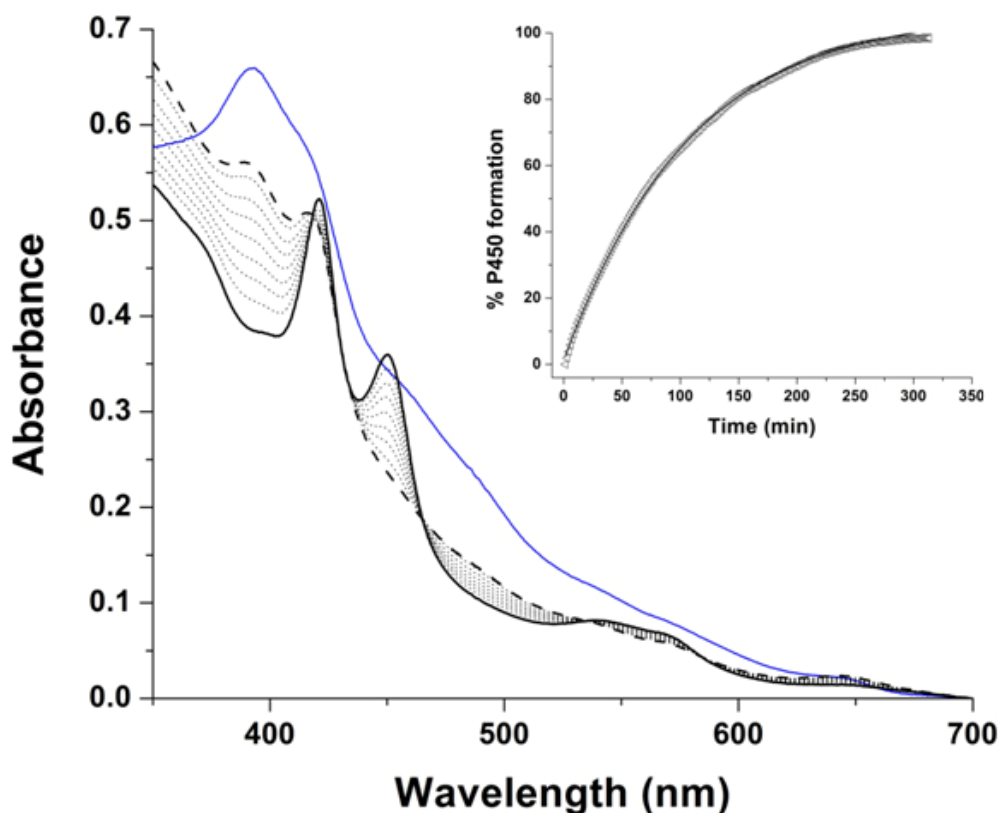


**Figure 5.58. Reduction of substrate-free CYP125 using the FdR-Fdx<sub>1</sub> electron transfer system.**

Purified FdR (5 μM) and Fdx<sub>1</sub> (20 μM) were used, together with CYP125 in its native, partially high spin form (5 μM). The reduction of CYP125 was initiated by NADPH addition (200 μM). The blue line is the spectrum for the oxidized FdR/Fdx<sub>1</sub>/CYP125 proteins. The dashed line is the apparent end point of reduction of the reductase proteins after NADPH addition. The dotted lines were collected at 35, 70, 105, 140, 175, 210 and 245 min. The final spectrum (black solid line) was collected at 307.5 min and shows extensive formation of both P450 and P420 species. The inset shows a plot of A<sub>450</sub> versus time and data were fitted using a single exponential function to give an apparent rate constant of  $0.0065 \pm 0.0002$  min<sup>-1</sup>.

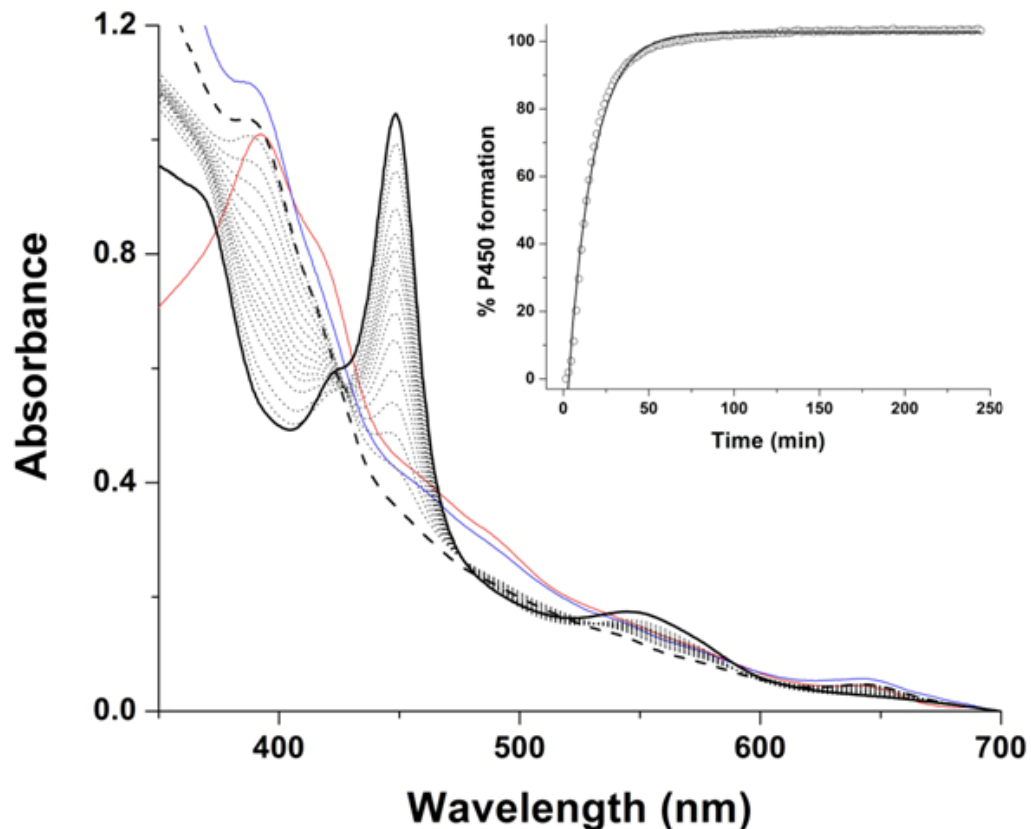


**Figure 5.59. Reduction of cholesterol-bound CYP125 using the FdR-Fdx<sub>1</sub> electron transfer system.**

A reconstitution system of FdR (5  $\mu\text{M}$ ), Fdx<sub>1</sub> (20  $\mu\text{M}$ ), CYP125 (5  $\mu\text{M}$ ), and cholesterol (50  $\mu\text{M}$ ) was mixed with NADPH (200  $\mu\text{M}$ ). The red line is the spectrum for the oxidized FdR/Fdx<sub>1</sub>/CYP125-cholesterol bound proteins. The blue line is after NADPH addition. The dashed line is the apparent end point of reduction of the reductase proteins. The dotted lines were collected at 18, 36, 54, 72, 90, 108, 126, 144, 162, 180, 198, 216 and 234 min. The final spectrum (solid black line) was collected at 265.5 min and shows extensive formation of the P450 species. The inset shows a plot of  $A_{450}$  versus time and data were fitted using a single exponential function to give an apparent rate constant of  $0.048 \pm 0.007 \text{ min}^{-1}$ .

In comparison, the combination of FdR and Fdx<sub>2</sub> improved the electron transfer rate in the reduction of substrate-free CYP125 compared to the FdR/Fdx<sub>1</sub> system. It is clearly seen in Figure 5.60 that the combination of FdR/Fdx<sub>2</sub> enables reduction of CYP125 heme iron by NADPH. The rate of reduction of CYP125 was again estimated by measuring the increase in the absorbance ( $A_{450}$ ) after mixing with excess NADPH (200  $\mu\text{M}$ ). The rate constant determined was  $0.017 \pm 0.001 \text{ min}^{-1}$  at 25 °C, approximately 2.6 fold higher than that obtained using FdR/Fdx<sub>1</sub>. The addition of cholesterol (Figure 5.61) elevated the apparent heme reduction rate constant approximately 2-fold higher than that for the substrate-free form using the same FdR/Fdx<sub>2</sub> redox system ( $0.032 \pm 0.006 \text{ min}^{-1}$ ). However, this is

slightly lower than obtained using the FdR/Fdx<sub>1</sub> combination with cholesterol-bound CYP125 ( $0.048 \pm 0.007 \text{ min}^{-1}$ ). These rate constants reflect the individual electron transfers from NADPH to FdR, from FdR to Fdx<sub>1/2</sub>, and from Fdx<sub>1/2</sub> to CYP125. The final step is likely to have the greatest control over the rate constant determined, but it is feasible (for example) that the rate constant for Fdx<sub>1/2</sub>-dependent reduction of cholesterol-bound CYP125 is somewhat faster than  $0.032 \text{ min}^{-1}$  given the slow NADPH-dependent reduction of FdR itself. It is also important to note that the formation of the P450 species was much more extensive for the cholesterol-bound CYP125 compared to that achieved for the substrate-free enzyme, possibly as a consequence of both heme potential shift and structural reorganization in CYP125 that favours redox partner docking.

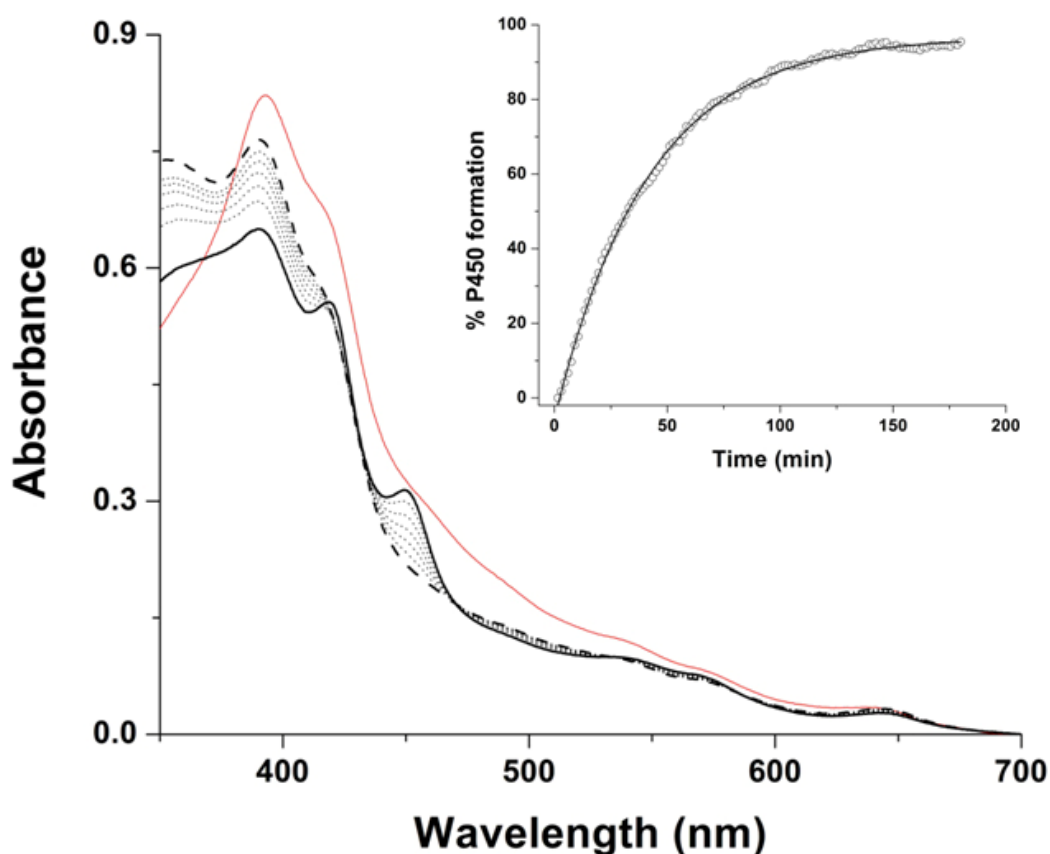


**Figure 5.60. Reduction of substrate-free CYP125 by the FdR-Fdx<sub>2</sub> system.**

A Mtb redox system of FdR ( $5 \mu\text{M}$ ), Fdx<sub>2</sub> ( $20 \mu\text{M}$ ), and CYP125 ( $5 \mu\text{M}$ ) was set up in 50 mM potassium phosphate (pH 7.5). The buffer then was deaerated and bubbled with CO gas, and mixed with NADPH ( $200 \mu\text{M}$ ). The red line is the spectrum for the oxidized FdR/Fdx<sub>2</sub>/CYP125 proteins. The dashed line is the apparent end point of reduction of the reductase proteins following NADPH addition. The dotted lines are spectra collected at 32, 64, 96, 128, and 160 min. The final spectrum (solid black line) was collected at 195 min and shows some formation of both the P450 and P420 species. The inset shows a plot of  $A_{450}$  versus time, and data were fitted using a single exponential function to give an apparent rate constant of  $0.017 \pm 0.001 \text{ min}^{-1}$ .

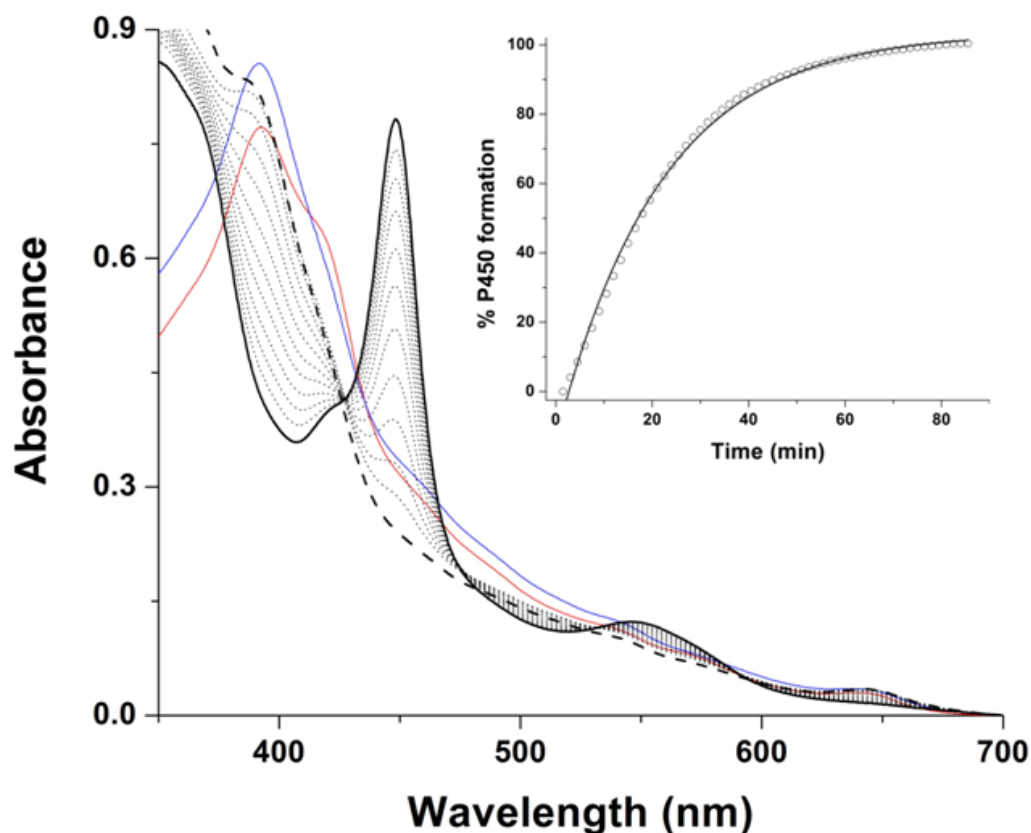


**Figure 5.61. Reduction of cholesterol-bound CYP125 by FdR-Fdx<sub>2</sub>.**

FdR (5  $\mu\text{M}$ ), Fdx<sub>2</sub> (20  $\mu\text{M}$ ), CYP125 (5  $\mu\text{M}$ ) and cholesterol (50  $\mu\text{M}$ ) were reconstituted in CO-saturated potassium phosphate, pH 7.5. The reduction of CYP125 was initiated by NADPH addition (200  $\mu\text{M}$ ). The red line is the spectrum for the oxidized FdR/Fdx<sub>2</sub>/CYP125 proteins. The blue line is after cholesterol addition. The dashed line is the apparent end point of reduction of the reductase proteins after NADPH addition. The dotted lines were collected at 15, 30, 45, 60, 75, 90, 105, 120, 135, and 150 min. The final spectrum (black line) was collected at 177 min and shows extensive formation of the P450 species. The inset shows a plot of  $A_{450}$  versus time, and data were fitted using a single exponential function to give an apparent rate constant of  $0.032 \pm 0.006 \text{ min}^{-1}$ .

#### 5.2.9.4 Electron transport pathways for CYP142

In order to examine the electron transfer systems that support electron transfer to the alternative Mtb cholesterol 27-hydroxylase CYP142, three ferredoxin reductase/ferredoxin proteins (FdR and Fdx<sub>1,2</sub>) were used to establish electron transfer systems that might be used by this P450 in the hydroxylation of cholesterol.

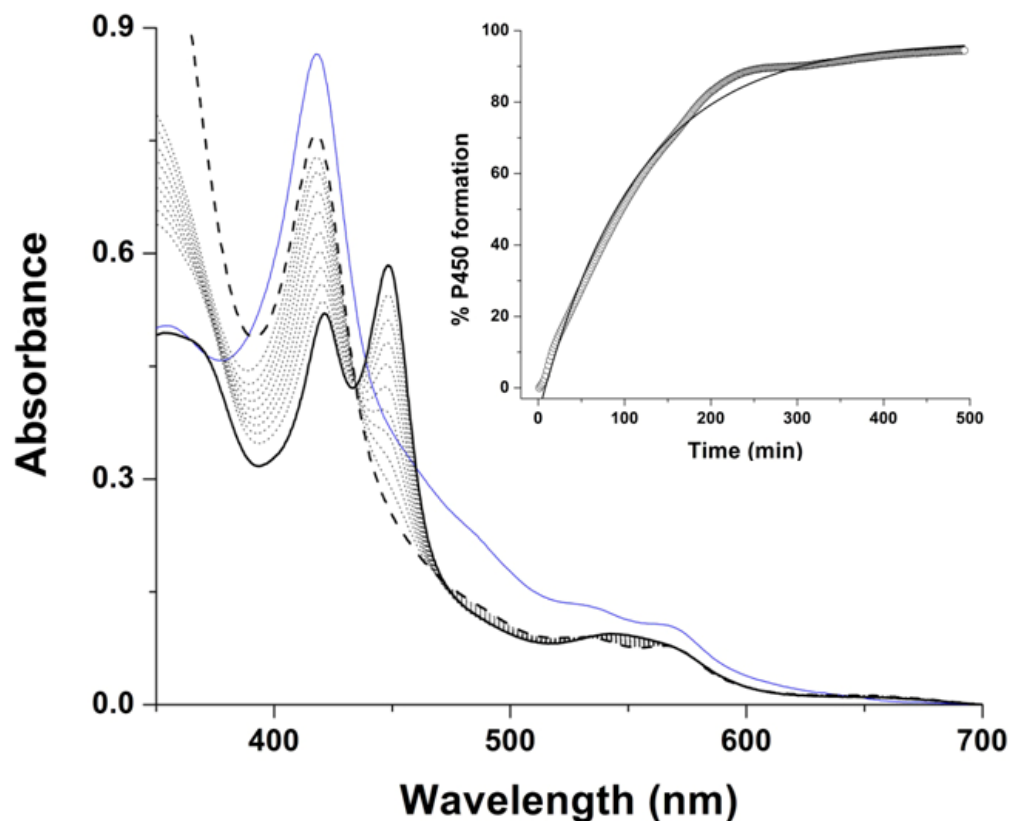


**Figure 5.62. Anaerobic reduction of substrate-free CYP142 by the FdR-Fdx<sub>1</sub> system in the presence of CO.**

The reduction of CYP142 was initiated by NADPH addition (200  $\mu\text{M}$ ). The blue line is the spectrum for the oxidized FdR (5  $\mu\text{M}$ )/Fdx<sub>1</sub> (20  $\mu\text{M}$ )/CYP142 (5  $\mu\text{M}$ ) proteins. The dashed line is the apparent end point of reduction of reductase proteins after NADPH addition. The dotted line spectra were collected at 55, 110, 165, 220, 275, 330, 385, 440 and 495 min. The final spectrum (solid black line) was collected at 567 min and shows extensive formation of the P450 species. The inset shows a plot of  $A_{450}$  versus time and data were fitted using a single exponential function to give an apparent rate constant of  $0.0063 \pm 0.0001 \text{ min}^{-1}$ .

As shown in Figure 5.62, a distinct absorbance band at 450 nm is observed after the addition of excess NADPH, indicating that FdR and Fdx<sub>1</sub> could support transfer of electron(s) for the reduction of the CYP142 heme iron. The reduction of CYP142 may not have been fully completed, although the absorption spectrum in the Q-band region at the end of the experiment did indicate that CYP142 was extensively reduced. Thus, it appears that a considerable proportion of the substrate-free CYP142 may have formed P420. The electron transfer rate constant underlying Fe(II)CO complex formation was  $0.006 \pm 0.0001 \text{ min}^{-1}$ . In contrast, in the presence of an oxidizable substrate (cholesterol) (Figure 5.63), the electron transfer rate constant was elevated approximately 8-fold higher than in the substrate-free form ( $0.046 \pm 0.002 \text{ min}^{-1}$ ). Thus, the more positive heme iron redox

potential for the cholesterol-bound CYP142 appears to be a dominant factor in enhancing electron transfer rate in the CYP142 redox system with FdR/Fdx<sub>1</sub>.

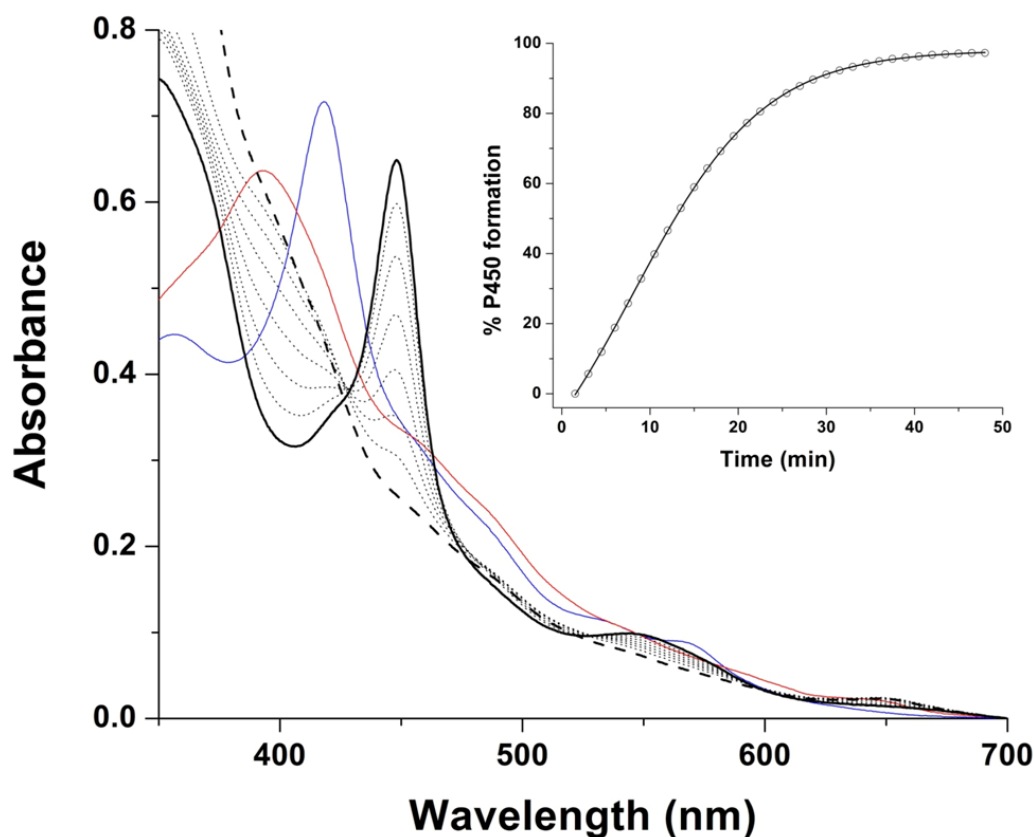


**Figure 5.63. Reduction of cholesterol-bound CYP142 by the FdR-Fdx<sub>1</sub> system.**

A reconstituted system of FdR (5  $\mu\text{M}$ ), Fdx<sub>1</sub> (20  $\mu\text{M}$ ), CYP142 (5  $\mu\text{M}$ ), and cholesterol (50  $\mu\text{M}$ ) was set up in CO-saturated potassium phosphate buffer. The reduction of CYP142 was initiated by NADPH addition (200  $\mu\text{M}$ ). The blue line is the spectrum for the oxidized FdR/Fdx<sub>1</sub>/CYP142 proteins. The red line is after cholesterol addition, showing an extensively high spin CYP142. The dashed line is the apparent end point of reduction of the reductase proteins post NADPH addition. The dotted line spectra were collected at 10, 20, 30, 40, 50, and 60 min. The final spectrum (solid black line) was collected at 79.5 min and shows extensive formation of the P450 species. The inset shown a plot of  $A_{450}$  versus time and data were fitted using a single exponential function to give an apparent rate constant of  $0.046 \pm 0.002 \text{ min}^{-1}$ .

The substrate-free form of CYP142 has a very negative redox potential (-416 mV), and therefore the rate constant for this species is likely retarded as a consequence of thermodynamic limitations to the Fdx-dependent electron transfer to the heme iron. As with CYP125, more extensive P450 formation was achieved for CYP142 when bound to cholesterol. Unfortunately, reconstitution of Fdx<sub>2</sub> with FdR for electron transfer to CYP142 (in both substrate-free and cholesterol-bound forms) was not successful, suggesting that

binding of Fdx<sub>2</sub> to the CYP142 was not compatible with efficient transfer of electrons to the CYP142 heme iron.

Table 5.4 summarises the apparent rate constants for Fe(II)CO complex formation during reduction of the Mtb P450s CYP51B1, CYP121, CYP125 and CYP142 (in presence and absence of substrates). It is clearly seen that, when using FdR as a reductase in the electron transport chain, Fdx<sub>1</sub> was clearly the most efficient in supporting P450 reduction for the estriol-bound form of CYP51B1, the cholesterol bound form of CYP125, and for CYP142 in both substrate-free and cholesterol-bound forms, with rate constants of 0.032 min<sup>-1</sup>, 0.048 min<sup>-1</sup>, and 0.046 min<sup>-1</sup>, respectively, for the substrate-bound forms of the three P450s. In contrast, Fdx<sub>2</sub> was the most efficient in supporting the reduction of CYP121, with a rate constant of 0.114 min<sup>-1</sup> in the presence of cYY. In conclusion, the genome of Mtb encodes several ferredoxin and ferredoxin reductase proteins, a combination of which, in principle, should support the catalytic activity of each of the 20 putative P450 enzymes. These redox proteins often display promiscuity in transferring electrons to P450 enzymes, and the ratio of P450 genes to the potential redox partners within the genome also suggests that this should be the case here. In this study (in addition to the *E. coli* FLDR and FLD proteins), the ferredoxin reductases FdR/FprA and ferredoxins Fdx<sub>1,2</sub> were expressed in *E. coli* and purified. All of these proteins showed catalytic activity in reducing the electron acceptor P450s, including CYP126, CYP141, CYP51B1, CYP121, CYP125 and CYP142. Fdx<sub>1</sub> was the most efficient in supporting electron transfer to CYP51B1, CYP125 and CYP142, whereas Fdx<sub>2</sub> showed stronger activity toward CYP121, but no measurable activity towards CYP142.

Redox system	Fe(II)CO complex formation rate constant (min <sup>-1</sup> ) <sup>a</sup>							
	CYP51B1		CYP121		CYP125		CYP142	
	Substrate-free	Estriol-bound	Substrate-free	cYY-bound	Substrate-free	Cholesterol-bound	Substrate-free	Cholesterol-bound
FdR-Fdx <sub>1</sub>	0.018 ± 0.001	0.032 ± 0.002	0.0053 ± 0.0008	0.042 ± 0.004	0.006 ± 0.0002	0.048 ± 0.007	0.006 ± 0.0001	0.046 ± 0.002
FdR-Fdx <sub>2</sub>	0.035 ± 0.001	0.017 ± 0.003	0.0072 ± 0.0002	0.114 ± 0.004	0.017 ± 0.001	0.032 ± 0.006	-----	-----

**Table 5.4. Rate constants for Fe(II)CO complex formation by the reconstituted FdR - Fdx<sub>1,2</sub> - P450 (CYP51B1, CYP121, CYP125, CYP142) systems.** <sup>a</sup>The kinetics of the complex formation (P450 formation, reflecting heme reduction rate) were determined by plotting the extent of Fe(II)CO complex formation against reaction time and fitting the resultant data using a single exponential function and Origin software. The combination of FdR and Fdx<sub>2</sub> showed negligible capacity to reduced CYP142 in substrate-free or substrate-bound forms.

### 5.3 Discussion

The genome sequence of Mtb H37Rv was determined in 1998 by Cole and co-workers (42), revealing 20 P450 enzyme-encoding genes. However, electron transport among Mtb P450s had not been extensively characterized, although several reports have elucidated some catalytic activities of three ferredoxin/ferredoxin reductase proteins - the two ferredoxin reductases (FdR and FprA) and one ferredoxin (Fdx<sub>1</sub>). The notable existence of two Fdx proteins adjacent to P450s and at least three prospective FDR proteins that could partner these P450s in *M. tuberculosis* provides some possible pathways for electron transfer to each P450. In addition, to understand the biochemistry and mechanistic details of the redox partners of the well characterized Mtb P450s, in this part of work I cloned and purified two Fdx and two FDR candidate proteins, plus several well-known P450s (CYP126, CYP141, CYP51B1, CYP121, CYP125, and CYP142) from Mtb, and was able to establish the primary pathway NAD(P)H → FDR → Fdx → P450 for the electron transfer chains in these enzymes.

In order to reconstruct the P450 redox systems and to examine how electron transfer to P450s is driven by NADPH via a Mtb class I-type redox system (these likely being the NAD(P)H-dependent reductases FdR/FprA and the two 3Fe-4S ferredoxins Fdx<sub>1</sub> and Fdx<sub>2</sub> in Mtb), studies were initialized to express homologous and heterologous redox partner systems. These redox partners were successfully expressed and purified with accurate molecular weights confirmed. The FLDR (flavodoxin reductase) and FLDA (FLD, flavodoxin) from *E. coli* were also expressed following methods from previous research papers, and purified by Q-Sepharose column chromatography. These systems are known to drive catalysis of several heterologous P450s produced in *E. coli*. SDS-PAGE and spectroscopic analysis indicated that these proteins were successfully expressed and purified sufficiently for use in redox reactions with Mtb P450s.

The location of the genes coding for FdR, Fdx<sub>1,2</sub> and P450s in Mtb may be consistent with their biological activity as P450 partners (e.g. *Fdx<sub>1</sub>* is adjacent to *CYP51B1* on the genome). In the first step, FdR was cloned, expressed and characterized as an individual protein to reveal those properties that are required for its reactions in Mtb electron transfer pathways. To this end, FdR was biochemically characterized, allowing us to expand our understanding of its properties and how the protein might interact with its redox partners. Preliminary expression studies with FdR demonstrated that the protein could be expressed at very high levels of soluble protein in *E. coli* strain HMS174 (DE3), although after addition of inducer

(1 mM IPTG) the cells did not grow well, and extending the culture time to 24 h was required to obtain higher biomass for protein production. In agreement with amino acid sequence analysis, FdR contains several charged residues (Glu<sup>168</sup>, Glu<sup>184</sup>, and Lys<sup>61</sup>), which are likely to be critical for NAD(P)H or FAD binding, and/or for hydride ion transfer from NAD(P)H.

Steady-state kinetic analysis showed that FdR prefers NADH as its reducing coenzyme with a  $K_m$  value ~10-fold lower than that of NADPH (Table 5.1). In addition, the specificity constant ( $k_{cat}/K_m$ ) of NADH is six times larger than that for NADPH. However, despite lower affinity, NADPH may also function as an electron donor for FdR, since the  $k_{cat}$  for ferricyanide reduction was approximately 1.6-fold higher affinity than that achieved using NADH (Table 5.1). The tighter binding of NADH may have important physiological implications, although the higher NADPH  $k_{cat}$  for ferricyanide reduction might indicate that NADP<sup>+</sup> is more efficiently dissociated than NAD<sup>+</sup> to enable faster steady-state catalysis. Anaerobic titrations of FdR with NAD(P)H revealed a completely different pattern from that obtained with sodium dithionite. Both NADPH and NADH produce a slow reduction of FdR, and negligible semiquinone was observed during the FAD reductive reactions (a small amount with NADH), with the FAD finally converted fully to its hydroquinone form. In the reoxidative reaction of reduced FdR with NADP<sup>+</sup>/NAD<sup>+</sup>, the enzyme completes its oxidative process to restore the fully oxidized form with maximum absorption of FAD at 455 nm. The reactions appear fully reversible in presence of excess of the relevant forms of the NAD(P)(H), and occur without formation of considerable amounts of semiquinone species. In contrast, reduction by dithionite is more efficient, and again produced the hydroquinone species.

To my knowledge, FdR is the first ferredoxin reductase protein from Mtb to be analyzed for its oligomeric status. The recombinant enzyme was shown to be a mixture of dimer and monomer forms in native conditions. The monomer is most likely the physiologically abundant form, with 92% population. However, FdR also forms a dimer, existing *in vitro* at low concentrations (~8%). It is important to note that the dimeric form may have important differences in biochemical properties and redox partner interactions. In addition, the calorimetry technique (DSC) used to investigate the thermal unfolding equilibrium of FdR revealed an apparent single major unfolding event, although the DSC data fitted best to a 2-transition process with quite closely spaced  $T_m$  values of 39.7 °C and 43.0 °C.

The calorimetric analyses shows good behaviour of the FdR protein and consistency in  $T_m$  and enthalpy values, with the melting temperature displaying a low thermal stability (around 42 °C) combined with a low enthalpy. This melting temperature is substantially lower than that for the ferredoxin-NADP<sup>+</sup> reductase (FNR) from spinach chloroplast (66 °C) (353), suggesting FdR is a relatively unstable protein. The thermal stability of a protein is reported to be enhanced by the formation of a few hydrogen bonds and salt bridges and by the occurrence of intra- and inter-molecular hydrophobic interactions (391, 392). Since spinach ferredoxin reductase has many lysine, tyrosine, and tryptophan residues, several such interactions may be formed to enhance its thermostability (393). However, the FdR amino acid sequence reveals only 11 lysine, 8 tyrosine, and 5 tryptophan residues in a total of 406 amino acids, perhaps pointing to key differences in stabilizing interactions in the FdR and FNR proteins.

Potentiometric studies of FdR reflected a relatively positive potential for a flavoprotein (-252 mV), compare to other FNR-like proteins such as ferredoxin-NADP<sup>+</sup> reductase from *Anabaena* PCC 7119 (-317 mV) (394), *A. variabilis* (-377 mV) (395), spinach chloroplast (-350 mV) (396), *Azotobacter vinelandii* (-327 mV) (397), and *B. subtilis yumC* (-385 mV) (398). However, a similar redox potential was obtained when FdR was compared to certain other ferredoxin-NADP<sup>+</sup> reductases from *Plasmodium falciparum* (-266 mV) (399), and *Rhodospseudomonas palustris* (-280 mV) (397, 400).

Thus, a redox potential characterization of the gene product is useful to establish the protein's function in that organism. This was particularly necessary in the case of the FdR gene product of Mtb, because of the presence in the Mtb genome of genes coding for [3Fe-4S] ferredoxins, expected electron transfer partners for a ferredoxin reductase enzyme. In a previous report, FdR was characterized as a recombinant protein, shown to contain bound FAD and also to have significant activity as a reductase for Mtb CYP51B1 (153). However, the reduction potential of FdR is considerably more positive than that of ligand-free CYP51B1 (-375 mV), therefore it might be considered unlikely to transfer electrons directly to the heme iron for the substrate-free enzyme, particularly since most bacterial P450 systems use a class I system that uses a ferredoxin to carry electrons from the reductase to the P450. Studies by McLean *et al.* showed a 150 mV increase in the CYP51B1 redox potential in the estriol-bound form, and this would undoubtedly be a more favourable form of the enzyme for electron transfer from FdR via a ferredoxin (194). However, a likely ferredoxin partner Rv0763c (Fdx<sub>1</sub>), which is also the ultimate donor for

the P450, has a much more positive potential than does even the substrate-bound CYP51B1 form. The fact that the Fdx<sub>1</sub> does participate in productive sterol demethylation reactions with CYP51B1 demonstrates that electron transfer to this P450 is feasible, despite the thermodynamic “hurdle”. It may well be the case that the ferrous-oxy complex of the P450 has a much more favourable potential, making the transfer of the first electron a key regulatory step in the CYP51B1 cycle, and perhaps enabling Mtb to finely control P450 reduction such that only substrate-bound P450 forms are competent electron acceptors from the high potential ferredoxins.

This is the first detailed characterization of the Mtb ferredoxin Fdx<sub>2</sub>, the gene for which (*Rv1786*) is located immediately downstream of *CYP143* (290). It is likely that the gene is physiological redox partner because, of the 20 P450s in the genome, only *CYP51B1* and *CYP143* are located adjacent to ferredoxins: *Rv0763c* and *Rv1786*, respectively. The studies on Fdx<sub>2</sub> presented in this chapter demonstrate that this protein is a [3Fe-4S] ferredoxin. Detailed spectroscopic, EPR, and CD analysis clearly indicate that the native Fdx<sub>2</sub> contains one [3Fe-4S] cluster per monomer. The light scattering analysis of its oligomeric status revealed a mixture of octamer, tetramer, dimer and monomer, possibly reflecting an important biological function of this enzyme with its redox partner proteins. Potentiometric analysis also indicates that the reduction potential of the iron-sulfur cluster of Fdx<sub>2</sub> is -30 mV, considerably more positive than that of P450s such as CYP126 (-332 mV), CYP141 (-50 mV) and four other well-characterized Mtb P450s in their substrate-free forms: CYP51B1 (-375 mV), CYP121 (-467 mV), CYP125 (-303 mV), and CYP142 (-416 mV) (121, 124, 135, 138). As discussed above, this presents a thermodynamic barrier that obstructs electron transfer between Fdx<sub>1/2</sub> and substrate-free P450, although the substantial positive shift in potential on P450 substrate binding and concomitant high-spin heme iron shift are likely to be major factors that facilitate electron flow to the heme and catalytic turnover.

Indeed, recent studies have demonstrated that the binding of substrate to P450 elevates the reduction potential to a much more positive value than that of the ligand-free form. Thus, the binding of estriol to CYP51B1 changes the reduction potential from -375 mV to -225 mV (194), cholesterol binding to CYP142 elevated the potential from -416 mV to -192 mV, and the P450 BioI from *Bacillus subtilis* exhibits behaviour typical of the soluble bacterial P450s with an elevation of ~130 mV in the heme iron reduction potential between the substrate-free low-spin form and the fatty acid-bound high-spin form (124, 326, 401).

Despite the apparent thermodynamic barrier to electron transfer, Fdx<sub>1</sub> can clearly reduce CYP51B1, and substrates (obtusifoliol, dihydrolanosterol and lanosterol) were demethylated in an electron transfer chain using a reductase from plant (spinach) combined with Fdx<sub>1</sub> to mediate electron transfer from NADPH ( $E_0 = -320$  mV) to the P450. The activity levels were also similar to those observed with *E. coli* flavodoxin reductase (FLDR) and flavodoxin (FLD) as redox partners. It is likely that substrate binding leads to displacement of a weakly bound aqua ligand at the distal coordination position on the low-spin heme iron ( $S = 1/2$ ) and produces a change in heme iron spin-state equilibrium in favour of the high-spin form ( $S = 2 1/2$ ). The high-spin form can then be more easily reduced by the physiological redox partner, so triggering electron transfer and productive catalysis. Therefore, the electron transfer process becomes thermodynamically favourable overall (i.e. from NADPH through to P450), and the intermediate Fdx<sub>1</sub>-to-P450 step (where there is still a thermodynamic barrier to ascend) may then be a major regulatory step that controls the catalytic activity of the P450 by modulating rate of electron transfer.

The existence of two ferredoxins, which are located adjacent to P450s, and some reductase proteins (including FprA and FdR) in *Mtb* provides several possible pathways for electron transfer to each P450, plus conceivable possibilities for direct transfer from reductases or other flavoproteins. In this project, four other candidate proteins were purified, plus some well-known P450s, and it was possible to establish the primary pathway of P450 reduction as NADPH → FDR → Fdx → P450 (i.e. reduction via NADPH/FDR or NADPH alone is very inefficient). The purification data for these candidate redox partner proteins suggest that all proteins were successfully expressed and isolated as homogeneous proteins. These redox proteins included FLDR and FLD from *E. coli*, which are known to support the function of heterologously expressed cytochromes P450 in this bacterium. The data presented demonstrate successful reconstitution of a class I P450 redox chain composed entirely of *Mtb* proteins, as well as ones using *E. coli* proteins, or mixtures thereof. The *Mtb* FdR and Fdx<sub>1,2</sub>, as well as *E. coli* FLDR and FLD systems, were shown to be viable redox partners for *Mtb* P450s in their ability to mediate electron transfer from NADPH to various characterized P450 enzymes. The reconstitution of *Mtb* FdR, Fdx<sub>1,2</sub>, *E. coli* FLDR, FLD and *Mtb* P450s (CYP126, CYP141, CYP51B1, CYP121, CYP125, and CYP142) resulted in a functionally active complex for electron transfer from NADPH to P450s, as evidenced by the binding of CO to the reduced P450s to form an absorption band at 450 nm (or at 420 nm in some cases where heme thiolate was prone to protonation). Detailed analysis indicated that many of the the *Mtb* P450s can accept electrons as effectively from

the heterologous *E. coli* FLD protein as from the Mtb Fdx proteins. Thus, the system appears to be relatively unselective among Mtb electron transfer proteins and proteins from a heterologous source (*E. coli*). However, in some cases the stabilization of the thiolate-coordinated (active) P450 form was noted with particular redox partners, pointing to the importance of specific redox partner interactions in the maintenance of the active form of the Mtb P450s.

The results of this study clearly identify the electron transfer pathway  $\text{NADPH} \rightarrow \text{FDR} \rightarrow \text{Fdx} \rightarrow \text{P450}$  in Fe(II)CO complex formation in Mtb, particularly since electron transfer to the Mtb P450s from (i) NAD(P)H directly or from (ii) NAD(P)H via FdR/FLDR/FprA is much less efficient than when Fdx<sub>1/2</sub> or FLD proteins are introduced (Figure 5.64). However, the electron transfer to P450 is relatively slow in both presence and absence of an oxidizable substrate. Recent studies have indicated that the electron transfer rate was relatively slow in some other reactions catalyzed by bacterial P450s, compared to high rates of oxidase reactions catalyzed by well studied bacterial P450 enzymes, such as *Pseudomonas putida* CYP101A1 (84), *Bacillus megaterium* CYP102A1 (402), and *Bacillus subtilis* P450 BioI (255). A number of questions remain to be addressed for the slow rate of electron transfer in the Mtb systems. An important question can be raised as to which step(s) are rate-limiting in reduction of the P450 within the Mtb systems identified in this study. The answer appears likely to be the first electron transfer from the Fdx<sub>1/2</sub> partners, which is at least partially thermodynamically redgulated. Arguably, the slow growing Mtb has evolved thermodynamic barriers for electron transport from redox partners to P450s as a mechanism for downregulating P450 activity, possibly in order to avoid over-accumulation of P450 products and/or to tune oxidase activities to the slow growth rate of the bacterium.

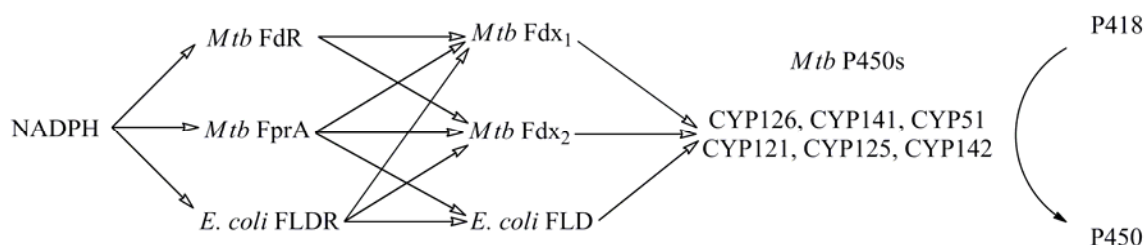


**Figure 5.64. Schemes of electron flow for Mtb P450s' Fe(II)CO complex formation.**

P418 refers to oxidized low-spin Mtb P450 with Soret maximum at ~418 nm. On binding substrate, the Soret typically shift to ~390 nm. P450 refers to the thiolate coordinated Fe(II)CO complex. The scheme shows both Mtb-specific and heterologous bacterial electron transfer pathways, featuring proteins used in this study.

Another major question is which proteins will be physiologically involved in electron transfer to different P450s in Mtb. The possibility exists that Fdx<sub>1</sub> and Fdx<sub>2</sub>, being in an operon with CYP51B1 and CYP143, respectively, could work selectively with CYP51B1, CYP143, or else more promiscuously with other remaining Mtb P450s. An interesting point to consider is that both Fdx proteins were relatively efficient in coupling Mtb FdR/FprA and *E. coli* FLDR to at least 6 P450s (in reduction of heme, enabling CO binding). These results may suggest that Fdx<sub>1,2</sub> could be promiscuous and function to support the inherent catalytic activities for many (or all) of the 20 P450s in Mtb. Unfortunately, in the current study I was unable to obtain all twenty P450 enzymes in order to test their electron transport chains. Therefore, in future it will be necessary to further characterize the electron delivery functions of Fdx<sub>1,2</sub> for the remaining Mtb P450s in order to address such a “promiscuous redox partner” hypothesis.

In summary, a number of Mtb and other potential P450 redox partners were expressed and characterized. The electron transport chain for Mtb P450s was identified as being NADPH → FDR → Fdx → P450 for the Mtb proteins examined. Measurable electron transfer rates were observed for all of the 6 Mtb P450 enzymes tested, and rate constants for electron transfer were enhanced for substrate-bound P450s, consistent with their more positive heme potential when substrate is associated. The Mtb P450s can use electrons almost as effectively from the homologous Fdx proteins as from the *E. coli* flavoprotein FLD when reconstituted with several FDR proteins. These studies provide some evidence of the approaches needed for elucidation of electron transfer pathways of Mtb P450s. However, additional work is needed to unravel the complex biochemistry of each of the potential redox systems, in order to indicate how the links are made and optimized from the various potential redox partner systems to the entire 20 P450 enzymes in Mtb, and how these links are associated with specific catalytic activities of the Mtb P450s.

## 6 CONCLUSIONS AND FUTURE WORK

This thesis has reported the detailed characterization of two *Mycobacterium tuberculosis* cytochrome P450 enzymes (CYP126 and CYP141) and two redox partner proteins from the same bacterium (FdR and Fdx<sub>2</sub>) using a number of spectroscopic, kinetic, thermodynamic, and structural methods. The main conclusions are categorized under four broad headings:

1. The properties and characteristics of CYP126, CYP141, FdR, and Fdx<sub>2</sub>.
2. Crystal structure of CYP126 and preliminary crystallization of CYP141 and Fdx<sub>1</sub>.
3. The reconstitution of electron transfer chain for CYP126, CYP141 and other Mtb P450s (CYP51B1, CYP121, CYP125, CYP142) using redox partner enzymes from *M. tuberculosis* (Mtb) and *E. coli*.
4. Substrate and inhibitor identification for CYP126 by screening a compound library and using P450-specific optical changes to identify these molecules.

### 6.1 Biochemical and biophysical properties of CYP126, CYP141, FdR, and Fdx<sub>2</sub>

Based on its spectral properties, CYP126 is a typical cytochrome P450 enzyme, possessing a Soret band at 418 nm along with  $\alpha/\beta$  bands at 568 nm and 535 nm in its oxidized form. The enzyme also showed a shift of its Soret band to 411 nm upon reduction by sodium dithionite, indicating that the ferric heme iron (Fe<sup>3+</sup>) accepts one electron to become ferrous heme iron (Fe<sup>2+</sup>) with cysteine thiolate as the 5<sup>th</sup> ligand. Reduced CYP126 can form a complex with CO (Fe<sup>II</sup>-CO) to produce an absorption maximum at 448 nm, confirming that CYP126 retains cysteine thiolate-ligation. However, this is followed by a slow collapse of the 448 nm feature to a species with Soret maximum at 420 nm. This indicated heme thiolate protonation (resulting in cysteine thiol-bound heme iron) and that the Fe<sup>II</sup>-CO complex is relatively unstable to this process compared with the CO-free ferrous form. Thiolate ligation of the ferric CYP126 was confirmed by EPR and MCD spectroscopy. Investigations into the redox potential of CYP126 demonstrated that the P450 has a moderately negative heme iron potential (-332 mV), making it rather difficult to facilitate heme iron reduction by various redox partner enzymes from Mtb and *E. coli*. However, upon binding of a substrate-like molecule (compound 32027), the CYP126 heme iron underwent a positive shift in redox potential of approximately 156 mV. This change means that the heme iron is more favourable to reduction by NAD(P)H via various redox partner proteins. The enzyme also showed strong binding to a selection of azole antifungal inhibitors, suggesting the possibility that the CYP126 could be a new anti-Mtb drug target.

Similar to CYP126, CYP141 has a Soret band feature located at 417.5 nm and with the smaller  $\alpha/\beta$  bands locate at 574 and 537 nm, respectively. This indicates that the protein is also a typical P450 enzyme. However, the heme iron of CYP141 is purified as a mixture of high spin and low spin states, distinct from most other Mtb P450s (which are low spin). Moreover, CYP141 displays a unique reduced/CO-bound absorbance spectrum, with a maximum at 440 nm, instead of the typical spectrum at  $\sim$ 450 nm. The formation of the P440 form in complex with CO was confirmed both with sodium dithionite reduction and NAD(P)H reduction (via redox partner proteins). The electronic structure and ligation of CYP141 heme iron was also explored using MCD and EPR. The results were in agreement with UV-visible spectroscopy, indicating that CYP141 likely also has typical P450 cysteinate- and water-ligation to the heme iron. A comparison of the CYP141 heme iron reduction potential with other P450s demonstrated that CYP141 possesses a much positive heme iron potential ( $\sim$  -50 mV), perhaps indicating unusual heme ligation, as is suggested from its unusual P440 reduced/CO-bound spectrum. Like CYP126, CYP141 binds to a number of antifungal drugs, with tight  $K_d$  values comparable to those previously determined for other Mtb P450s (e.g. CYP121, CYP126), and suggesting that this P450 could also be a drug target enzyme.

The ferredoxin reductase enzyme FdR displays characteristic flavoprotein absorbance maxima at 272, 365, and 455 nm in its oxidized state. The protein was shown to be reduced by both sodium dithionite and NAD(P)H, but NAD(P)H was a much less efficient reductant than was sodium dithionite. Both NADPH and NADH produce slow reduction of FdR flavin, and negligible semiquinone was observed during the FAD reductive reactions. In addition, the reduced FdR was quickly reoxidized when the enzyme was exposed to air, indicating that the protein is sensitive to oxygen. Investigations using stopped-flow (PDA), UV-visible spectroscopy, and steady-state kinetic analysis indicated that FdR operates more efficiently with NADH than it does with NADPH, possibly reflecting the weaker apparent binding of NADPH to the enzyme. FdR displays a low thermal stability compared to other FNR-like proteins, perhaps suggesting FdR is a relatively unstable protein. Potentiometric data for FdR showed a relatively positive 2-electron reduction potential for a flavoprotein (-252 mV). This potential therefore suggests that electron transfer from NAD(P)H to the substrate-bound form of CYP126 should be feasible (likely occurring via a ferredoxin protein) and that electron transfer to CYP141 (in both substrate-free and substrate-bound forms) is also likely to be thermodynamically favoured.

The spectral properties of the Mtb ferredoxin Fdx<sub>2</sub> showed a typical absorption for ferredoxins containing a [3Fe-4S] cluster, with an absorption peak at 412 nm. Relationships with other [3Fe-4S] ferredoxins were also confirmed by far UV CD and EPR spectroscopy. Reduction of Fdx<sub>2</sub> by sodium dithionite leads to a nearly complete bleach of the spectrum at 412 nm, indicating the conversion of the active [3Fe-4S]<sup>+</sup> form to a [3Fe-4S]<sup>0</sup> form, as confirmed by the loss of its EPR spectrum on reduction. Potentiometric studies revealed that the protein has a reduction midpoint potential for the [3Fe-4S]<sup>+</sup> to [3Fe-4S]<sup>0</sup> transition of -30 mV, substantially more positive than that of the redox potential of CYP126 and FdR, and slightly more positive than that of CYP141.

## **6.2. Crystal structure of CYP126 and crystallization of CYP141 and Fdx<sub>2</sub>**

The crystal structure of CYP126 was obtained at a resolution of 1.7 Å, revealing the characteristic fold common to all structurally defined P450s. However, CYP126 exhibits some conformational and oligomerization differences from many other P450 structures. The native CYP126 is a dimer, showing a narrow active site-access channel (which is composed of the I, L, F, G and C helices) and a mobile FGα loop that is likely to play an important function in enabling substrate access and product release from the active site. The dimer formation of CYP126 is related to specific hydrophobic interactions and salt bridges between monomers. However, laser light scattering (MALLS) analysis did not detect a large proportion of the dimeric form of CYP126 in solution, suggesting that the dimer may form at higher concentrations of the protein.

Upon binding of an azole drug (ketoconazole), the protein is no longer dimeric in this particular crystal packing, and instead a monomer was observed in the ketoconazole-bound crystal structure. The transition between dimer and monomer conformations might be associated with producing an inactive CYP126 on inhibitory binding by the ketoconazole molecule.

Preliminary work showed that crystals of CYP141 could be grown under two specific conditions, containing PEG 4K and PEG 6K, and that the crystals have a very good shape and size. Nevertheless, data indicated that these crystals have limits of diffraction which only extended to ~ 3.2 Å resolution for a variety of the crystals tested. Due to poor diffraction data, the structure therefore could not be solved using molecular replacement methods. Further investigations into the crystal structure of CYP141 were carried out using a heavy metal derivative, but this approach to solving the structure of this enzyme also

failed. An attempt was also made by co-crystallization of CYP141 with one of the best binding azole drugs (clotrimazole). However, this attempt was also unsuccessful, even when the protein was screened across a range of different concentrations of clotrimazole.

Crystals of the Mtb ferredoxin Fdx<sub>1</sub> were formed in two specific conditions, containing PEG 6K and PEG 8K. Although the crystals produced diffraction data extending to 1.6 Å, the diffraction data indicated that the space group of the crystals was not clear, and therefore the structure could not be solved using these data sets.

### **6.3. Electron transfer chain of Mtb P450s**

Electron transfer systems for the two novel P450 enzymes, CYP126 and CYP141, were successfully established using both endogenous and exogenous redox partner proteins. Data from chapter 5 indicated that combinations of ferredoxin and ferredoxin reductase proteins enabled Mtb P450 reduction through typical “class I” redox systems, as clearly observed by Fe<sup>II</sup>-CO complex formation. However, the electron transfer to the P450s is relatively slow, possibly suggesting that even the Mtb partners are not the native redox systems for CYP141 and CYP126, and that these P450s may preferentially select other redox partners for their catalytic activity. Alternatively, the slow-growing nature of the Mtb bacterium might have resulted in active selection of P450 partner systems that have modest electron transfer rates.

These redox systems were also applied to several other Mtb P450s of known substrate selectivity, including CYP51B1, CYP121, CYP125, and CYP142. The data indicated that all these partner systems were able to transfer electron from NADPH to these P450s. However, the electron transfer is relatively slow in both the presence and absence of an oxidizable substrate. Thus, it is proposed that the P450 systems examined appear to be relatively unselective among Mtb electron transfer proteins and proteins from a heterologous source.

### **6.4. Substrate and inhibitor identification for CYP126**

Screening a library of 20,000 organic compounds against CYP126 revealed at least 15 type I (substrate) and 15 type II (inhibitor) hits. Overall structures of the type I compounds reveals that several possessed a nitrobenzene ring, which is also found as a functional group in the antibiotics chloramphenicol and azidamphenicol. This could suggest that the function of CYP126 may relate to detoxification of xenobiotic compounds, or even to synthesis of

this type of molecule. Binding of these type I compounds induced a Soret shift from 418 nm to 393 nm, indicating that the 6<sup>th</sup> ligand water molecule is expelled from the heme iron, leading to the shift of a LS ferric heme to a HS ferric heme in order to make the redox potential more positive, and thereafter accelerate electron transfer from NAD(P)H to the P450 via redox partners.

Several (9) of the type II compounds recognized from the library screen had imidazole functional groups similar to those found in variousazole drugs, and all had a functional group that could potentially coordinate to a P450 heme iron. Trials with three of these compounds indicated a similar mode of binding involving direct interaction with the heme iron in CYP126, confirmed using both UV-visible and EPR spectroscopy. In conclusion, new inhibitor classes were identified for CYP126, providing scaffolds on which to build more potent inhibitors to block CYP126 and possibly other Mtb P450 activities.

## **6.5 Future work**

### **6.5.1 Identification of products formed by substrate oxidation in CYP126**

CYP126 is located adjacent to a gene cluster involved in *de novo* purine biosynthesis, suggesting that CYP126 may share the same operon with these genes. In fact, substrate and transformation reactions of a P450 enzyme can often be deduced by comparing its amino acid sequence with those of other P450s of known function. However, the sequence identity of CYP126 compared to other P450s proteins (in Mtb and other organisms) is relatively low (< 30%), and therefore it is not possible to predict a function for CYP126 with any confidence. By screening a library of 20,000 compounds against CYP126, several compounds were shown to be potential substrates for this enzyme. None of these resembled purine structures. In order to determine the products of substrate oxidation catalyzed by CYP126, it is necessary to obtain substrate turnover during a reaction with one or more of these molecules. This work is currently ongoing, and through position(s) of oxidation of substrate-like molecules tested, it is hoped that further insights into substrate specificity of CYP126 may be gained.

### **6.5.2 Determination of CYP126 structure with compounds 32027 and 35125**

Preliminary crystallization of CYP126 with selected substrate- (compound 32027) and inhibitor-like (compound 35125) compounds derived from the screening experiments showed that crystals could be obtained in different precipitants, and could produce high quality crystals. Previous studies showed that the ligand-free structure of CYP126 exhibits

a dimeric form, and that upon binding of an inhibitor (ketoconazole) there are changes to the oligomerization state of CYP126 from dimer to monomer. It is hypothesized that the ligand-free CYP126 could be activated in the absence of an inhibitor, and that this active form is composed of two monomers orientated to form a catalytically competent dimeric form. With ketoconazole bound, the protein could become inactive when the dimer is separated into monomers. Thus, the determination of the crystal structure of CYP126 with compound 32027 (substrate) and 35125 (inhibitor) will provide important evidence to support the hypothesis above.

### **6.5.3 Structural determination of CYP141 by X-ray crystallography**

Although CYP141 produced high quality crystals, the diffraction data only extended to 3.2 Å and a structure could not be solved from these data. Many efforts to make crystals providing better diffraction patterns also failed. Molecular replacement methods to solve crystal structures are generally only carried out if the crystal diffraction extends to around 2.0 Å. In order to produce better diffraction data for the solution of the CYP141 structure, it may be possible to obtain crystals from new conditions that may improve the quality of both the crystals and of the diffraction data.

CYP141 possesses many unusual features, such as the P440 Fe<sup>II</sup>-CO complex and its mixture of LS and HS forms (the equilibrium of which can be affected by both pH and temperature). These unusual properties may relate to some alterations around the heme iron in the active site cavity with respect to other P450 enzymes. Determination of a crystal structure for CYP141 provides the most likely route to establishing how CYP141 varies in structure in the heme pocket compared to other P450s. Thus, obtaining a crystal structure for this P450 remains a high priority to produce an exact explanation for the unusual features of CYP141.

### **6.5.4. Addressing the substrate specificity profile of CYP141**

By comparison of amino acid sequences of CYP141 with other cytochromes P450, a low degree of identity ( $\leq 34\%$ ) is revealed. Thus, it is impossible to deduce the substrate and chemical transformation catalysed by CYP141 based on sequence identity alone. Moreover, CYP141 showed similar characteristics to the well-characterized CYP170A1 from *Streptomyces coelicolor* A3, including the P440-like Fe<sup>II</sup>-CO complex and the mixture of spin states in the ferric form. However, the sequence identity between these two P440s is relatively low, and it is impossible to conclude that CYP141 may have a similar function to

CYP170A1 (synthesis of the antibiotic albaflavenone). In order to identify substrate(s) for CYP141, screening a library of compounds could provide some important information. This method has been widely used for analysis of various proteins and has proved to be a powerful tool in the field of substrate identification.

### **6.5.5 Determination of the crystal structure of Fdx<sub>2</sub>**

Although the crystals of Fdx<sub>2</sub> produced very good diffraction data, there were some problems in solving the crystal structure, including confusion of which space group was present. Fdx<sub>2</sub> is a small protein, composed of 66 amino acids, with a predicted mass of ~ 7.4 kDa. In the field of protein purification, a histidine tag (~2.1 kDa) is frequently added to the N- or C-terminal of a protein in order to provide an efficient purification step. By comparison of the Fdx<sub>2</sub> molecular mass with that of its N-terminal histidine tag, it is seen that the tag accounts for ~ 1/3 of the mass of the total protein. In the crystal structure, this tag may be a factor that affects the crystal packing and prevents structural elucidation. In order to improve the likelihood of structural resolution, removal of the histidine tag (either by selective proteolysis of the tagged Fdx<sub>2</sub> or by expression/purification of an untagged version) may enable production of better crystals from which a Fdx<sub>2</sub> crystal structure could be determined.

## **6.6. Conclusion**

The work undertaken in this thesis has revealed detailed biophysical and biochemical properties of two novel cytochrome P450s, CYP126 and CYP141. CYP126 is a “typical” P450 enzyme in terms of the optical properties of its Fe<sup>II</sup>-CO complex, and the structure of this protein was solved in both ligand-free and ketoconazole-bound forms. CYP141 is an “unusual” P450 in which the Fe<sup>II</sup>-CO complex is located at 440 nm, and in which heme ligation is clearly altered with respect to that of most other P450s. Future studies should be undertaken to further analyse substrate selectivity and the physiological reactions catalyzed by CYP126 and CYP141. This work will be aided by the identification of molecules that bind to CYP126 in a substrate-like manner through work presented in this thesis. However, studies are still required to enable substrate identification for CYP141 in order to reveal its general mechanism, and also to provide more detailed information on the activities performed by both these P450s in *Mycobacterium tuberculosis*.

Characterization of various exogenous and likely endogenous redox partner enzymes for the Mtb P450s has shown that all partner proteins characterized are relatively inefficient

electron transfer systems for CYP126 and CYP141, and for various other Mtb P450s (e.g. CYP121 and CYP125). This raises interesting questions as to whether slow-growing Mtb makes use of such slow electron transfer partners to suit its unusual physiology, or if more efficient redox partners are available in the Mtb genome. Clearly, further investigations into the isolation and reconstitution of Mtb electron transport proteins with Mtb P450s (including structural, biophysical and kinetic studies) are needed to identify “optimal” native redox partners for the catalytic cycles of CYP141 and CYP126.

## REFERENCES

1. Daniel, T. M. (2006) The history of tuberculosis, *Respir Med* 100, 1862-1870.
2. Mulder, K. (2001) Tuberculosis: a case history, *Lancet* 358, 766.
3. Teschner, M. (2006) [Tuberculosis in the old medical history of Greeks], *Pneumologie* 60, 401-407.
4. Houston, M. (1999) The white death: A history of tuberculosis, *BMJ* 318, 1705.
5. Welshman, J., and Bashford, A. (2006) Tuberculosis, migration, and medical examination: lessons from history, *J Epidemiol Community Health* 60, 282-284.
6. Grzybowski, S., and Allen, E. A. (1999) Tuberculosis: 2. History of the disease in Canada, *CMAJ* 160, 1025-1028.
7. Kaya, M., Nagoya, S., Yamashita, T., Niiro, N., and Fujita, M. (2006) Peri-prosthetic tuberculous infection of the hip in a patient with no previous history of tuberculosis, *J Bone Joint Surg Br* 88, 394-395.
8. Franco-Paredes, C., Roupahel, N., del Rio, C., and Santos-Preciado, J. I. (2006) Vaccination strategies to prevent tuberculosis in the new millennium: from BCG to new vaccine candidates, *Int J Infect Dis* 10, 93-102.
9. Iseman, M. D. (2002) Tuberculosis therapy: past, present and future, *Eur Respir J Suppl* 36, 87s-94s.
10. Martinez-Ramon, A. (1979) Effects of actinomycin D on ribosomal RNA and protein synthesis as revealed by high resolution autoradiography, *Virchows Arch B Cell Pathol Incl Mol Pathol* 31, 251-257.
11. Rao, V., Fujiwara, N., Porcelli, S. A., and Glickman, M. S. (2005) *Mycobacterium tuberculosis* controls host innate immune activation through cyclopropane modification of a glycolipid effector molecule, *J Exp Med* 201, 535-543.
12. Nahid, P., Pai, M., and Hopewell, P. C. (2006) Advances in the diagnosis and treatment of tuberculosis, *Proc Am Thorac Soc* 3, 103-110.
13. Cole, S. T. (1994) *Mycobacterium tuberculosis*: drug-resistance mechanisms, *Trends Microbiol* 2, 411-415.
14. Ahmad, S., and Mokaddas, E. (2009) Recent advances in the diagnosis and treatment of multidrug-resistant tuberculosis, *Respir Med* 103, 1777-1790.
15. Rastogi, N., Legrand, E., and Sola, C. (2001) The mycobacteria: an introduction to nomenclature and pathogenesis, *Rev Sci Tech* 20, 21-54.
16. Brosch, R., Gordon, S. V., Marmiesse, M., Brodin, P., Buchrieser, C., Eiglmeier, K., Garnier, T., Gutierrez, C., Hewinson, G., Kremer, K., Parsons, L. M., Pym, A. S., Samper, S., van Soolingen, D., and Cole, S. T. (2002) A new evolutionary scenario for the *Mycobacterium tuberculosis* complex, *Proc Natl Acad Sci U S A* 99, 3684-3689.
17. Smith, D. R., Richterich, P., Rubenfield, M., Rice, P. W., Butler, C., Lee, H. M., Kirst, S., Gundersen, K., Abendschan, K., Xu, Q., Chung, M., Deloughery, C., Aldredge, T., Maher, J., Lundstrom, R., Tulig, C., Falls, K., Imrich, J., Torrey, D., Engelstein, M., Breton, G., Madan, D., Nietupski, R., Seitz, B., Connelly, S., McDougall, S., Safer, H., Gibson, R., Doucette-Stamm, L., Eiglmeier, K., Bergh, S., Cole, S. T., Robison, K., Richterich, L., Johnson, J., Church, G. M., and Mao, J. I. (1997) Multiplex sequencing of 1.5 Mb of the *Mycobacterium leprae* genome, *Genome Res* 7, 802-819.
18. Garnier, T., Eiglmeier, K., Camus, J. C., Medina, N., Mansoor, H., Pryor, M., Duthoy, S., Grondin, S., Lacroix, C., Monsempe, C., Simon, S., Harris, B., Atkin, R., Doggett, J., Mayes, R., Keating, L., Wheeler, P. R., Parkhill, J., Barrell, B. G., Cole, S. T., Gordon, S. V., and Hewinson, R. G. (2003) The complete genome sequence of *Mycobacterium bovis*, *Proc Natl Acad Sci U S A* 100, 7877-7882.

19. Cavanagh, R., Begon, M., Bennett, M., Ergon, T., Graham, I. M., De Haas, P. E., Hart, C. A., Koedam, M., Kremer, K., Lambin, X., Roholl, P., and Soolingen Dv, D. (2002) *Mycobacterium microti* infection (vole tuberculosis) in wild rodent populations, *J Clin Microbiol* 40, 3281-3285.
20. Daffe, M., Lacave, C., Laneelle, M. A., and Laneelle, G. (1987) Structure of the major triglycosyl phenol-phthiocerol of *Mycobacterium tuberculosis* (strain Canetti), *Eur J Biochem* 167, 155-160.
21. Turenne, C. Y., Semret, M., Cousins, D. V., Collins, D. M., and Behr, M. A. (2006) Sequencing of hsp65 distinguishes among subsets of the *Mycobacterium avium* complex, *J Clin Microbiol* 44, 433-440.
22. Yew, W. W., and Leung, C. C. (2008) Update in tuberculosis 2007, *Am J Respir Crit Care Med* 177, 479-485.
23. Kim, T. H. (1977) High-viability lyophilized Bacille Calmette-Guerin vaccine produced by deep-culture technique, *Appl Environ Microbiol* 34, 495-499.
24. de Jonge, M. I., Brosch, R., Brodin, P., Demangel, C., and Cole, S. T. (2005) Tuberculosis: from genome to vaccine, *Expert Rev Vaccines* 4, 541-551.
25. Bong, C. N., Chen, S. C., Jong, Y. J., Tok, T. S., Hsu, C. F., Schouten, E. J., Makombe, S. D., Yu, J. K., and Harries, A. D. (2007) Outcomes of HIV-infected children with tuberculosis who are started on antiretroviral therapy in Malawi, *Int J Tuberc Lung Dis* 11, 534-538.
26. Cox, H. S., Orozco, J. D., Male, R., Ruesch-Gerdes, S., Falzon, D., Small, I., Doshetov, D., Kebede, Y., and Aziz, M. (2004) Multidrug-resistant tuberculosis in central Asia, *Emerg Infect Dis* 10, 865-872.
27. Jain, A. K. (2007) *Tuberculosis of the spine*, Lippincott Williams & Wilkins.
28. Cole, S. T. (1994) Mechanisms of drug resistance in *Mycobacterium tuberculosis*, *Immunobiology* 191, 584-585.
29. Zhang, Y., Heym, B., Allen, B., Young, D., and Cole, S. (1992) The catalase-peroxidase gene and isoniazid resistance of *Mycobacterium tuberculosis*, *Nature* 358, 591-593.
30. Chan, E. D., and Iseman, M. D. (2002) Current medical treatment for tuberculosis, *BMJ* 325, 1282-1286.
31. Makinoshima, H., and Glickman, M. S. (2005) Regulation of *Mycobacterium tuberculosis* cell envelope composition and virulence by intramembrane proteolysis, *Nature* 436, 406-409.
32. Garza-Gonzalez, E., Guerrero-Olazarán, M., Tijerina-Menchaca, R., and Viader-Salvado, J. M. (1998) Identification of mycobacteria by mycolic acid pattern, *Arch Med Res* 29, 303-306.
33. Brennan, P. J. (2003) Structure, function, and biogenesis of the cell wall of *Mycobacterium tuberculosis*, *Tuberculosis (Edinb)* 83, 91-97.
34. Attorri, S., Dunbar, S., and Clarridge, J. E., 3rd. (2000) Assessment of morphology for rapid presumptive identification of *Mycobacterium tuberculosis* and *Mycobacterium kansasii*, *J Clin Microbiol* 38, 1426-1429.
35. Radmacher, E., Stansen, K. C., Besra, G. S., Alderwick, L. J., Maughan, W. N., Hollweg, G., Sahm, H., Wendisch, V. F., and Eggeling, L. (2005) Ethambutol, a cell wall inhibitor of *Mycobacterium tuberculosis*, elicits L-glutamate efflux of *Corynebacterium glutamicum*, *Microbiology* 151, 1359-1368.
36. Tonge, P. J. (2000) Another brick in the wall, *Nat Struct Biol* 7, 94-96.
37. Guerrero, R. (2001) Bergey's manuals and the classification of prokaryotes, *Int Microbiol* 4, 103-109.
38. Tizard, M., Bull, T., Millar, D., Doran, T., Martin, H., Sumar, N., Ford, J., and Hermon-Taylor, J. (1998) A low G+C content genetic island in *Mycobacterium*

- avium* subsp. *paratuberculosis* and *M. avium* subsp. *silvaticum* with homologous genes in *Mycobacterium tuberculosis*, *Microbiology* 144 ( Pt 12), 3413-3423.
39. Fukunaga, H., Murakami, T., Gondo, T., Sugi, K., and Ishihara, T. (2002) Sensitivity of acid-fast staining for *Mycobacterium tuberculosis* in formalin-fixed tissue, *Am J Respir Crit Care Med* 166, 994-997.
  40. Kitamura, S., and Shibuya, Y. (1998) [Classification and concept of mycobacterial infections], *Nippon Rinsho* 56, 3036-3040.
  41. Kim, B. J., Lee, S. H., Lyu, M. A., Kim, S. J., Bai, G. H., Chae, G. T., Kim, E. C., Cha, C. Y., and Kook, Y. H. (1999) Identification of mycobacterial species by comparative sequence analysis of the RNA polymerase gene (*rpoB*), *J Clin Microbiol* 37, 1714-1720.
  42. Cole, S. T., and Barrell, B. G. (1998) Analysis of the genome of *Mycobacterium tuberculosis* H37Rv, *Novartis Found Symp* 217, 160-172; discussion 172-167.
  43. Camus, J. C., Pryor, M. J., Medigue, C., and Cole, S. T. (2002) Re-annotation of the genome sequence of *Mycobacterium tuberculosis* H37Rv, *Microbiology* 148, 2967-2973.
  44. Cole, S. T., Brosch, R., Parkhill, J., Garnier, T., Churcher, C., Harris, D., Gordon, S. V., Eiglmeier, K., Gas, S., Barry, C. E., 3rd, Tekaiia, F., Badcock, K., Basham, D., Brown, D., Chillingworth, T., Connor, R., Davies, R., Devlin, K., Feltwell, T., Gentles, S., Hamlin, N., Holroyd, S., Hornsby, T., Jagels, K., Krogh, A., McLean, J., Moule, S., Murphy, L., Oliver, K., Osborne, J., Quail, M. A., Rajandream, M. A., Rogers, J., Rutter, S., Seeger, K., Skelton, J., Squares, R., Squares, S., Sulston, J. E., Taylor, K., Whitehead, S., and Barrell, B. G. (1998) Deciphering the biology of *Mycobacterium tuberculosis* from the complete genome sequence, *Nature* 393, 537-544.
  45. Kato-Maeda, M., Rhee, J. T., Gingeras, T. R., Salamon, H., Drenkow, J., Smittipat, N., and Small, P. M. (2001) Comparing genomes within the species *Mycobacterium tuberculosis*, *Genome Res* 11, 547-554.
  46. Blattner, F. R., Plunkett, G., 3rd, Bloch, C. A., Perna, N. T., Burland, V., Riley, M., Collado-Vides, J., Glasner, J. D., Rode, C. K., Mayhew, G. F., Gregor, J., Davis, N. W., Kirkpatrick, H. A., Goeden, M. A., Rose, D. J., Mau, B., and Shao, Y. (1997) The complete genome sequence of *Escherichia coli* K-12, *Science* 277, 1453-1462.
  47. Bentley, S. D., Chater, K. F., Cerdeno-Tarraga, A. M., Challis, G. L., Thomson, N. R., James, K. D., Harris, D. E., Quail, M. A., Kieser, H., Harper, D., Bateman, A., Brown, S., Chandra, G., Chen, C. W., Collins, M., Cronin, A., Fraser, A., Goble, A., Hidalgo, J., Hornsby, T., Howarth, S., Huang, C. H., Kieser, T., Larke, L., Murphy, L., Oliver, K., O'Neil, S., Rabinowitsch, E., Rajandream, M. A., Rutherford, K., Rutter, S., Seeger, K., Saunders, D., Sharp, S., Squares, R., Squares, S., Taylor, K., Warren, T., Wietzorrek, A., Woodward, J., Barrell, B. G., Parkhill, J., and Hopwood, D. A. (2002) Complete genome sequence of the model actinomycete *Streptomyces coelicolor* A3(2), *Nature* 417, 141-147.
  48. Fleischmann, R. D., Alland, D., Eisen, J. A., Carpenter, L., White, O., Peterson, J., DeBoy, R., Dodson, R., Gwinn, M., Haft, D., Hickey, E., Kolonay, J. F., Nelson, W. C., Umayam, L. A., Ermolaeva, M., Salzberg, S. L., Delcher, A., Utterback, T., Weidman, J., Khouri, H., Gill, J., Mikula, A., Bishai, W., Jacobs Jr, W. R., Jr., Venter, J. C., and Fraser, C. M. (2002) Whole-genome comparison of *Mycobacterium tuberculosis* clinical and laboratory strains, *J Bacteriol* 184, 5479-5490.
  49. Quemard, A., Laneelle, G., and Lacave, C. (1992) Mycolic acid synthesis: a target for ethionamide in mycobacteria?, *Antimicrob Agents Chemother* 36, 1316-1321.
  50. Mawuenyega, K. G., Forst, C. V., Dobos, K. M., Belisle, J. T., Chen, J., Bradbury, E. M., Bradbury, A. R., and Chen, X. (2005) *Mycobacterium tuberculosis*

- functional network analysis by global subcellular protein profiling, *Mol Biol Cell* 16, 396-404.
51. McLean, K. J., Clift, D., Lewis, D. G., Sabri, M., Balding, P. R., Sutcliffe, M. J., Leys, D., and Munro, A. W. (2006) The preponderance of P450s in the *Mycobacterium tuberculosis* genome, *Trends Microbiol* 14, 220-228.
  52. Porter, T. D. (2004) Jud Coon: 35 years of p450 research, a synopsis of p450 history, *Drug Metab Dispos* 32, 1-6.
  53. Estabrook, R. W. (2003) A passion for P450s (remembrances of the early history of research on cytochrome P450), *Drug Metab Dispos* 31, 1461-1473.
  54. Omura, T., and Sato, R. (1964) The Carbon Monoxide-Binding Pigment of Liver Microsomes. Ii. Solubilization, Purification, and Properties, *J Biol Chem* 239, 2379-2385.
  55. Aldag, C., Gromov, I. A., Garcia-Rubio, I., von Koenig, K., Schlichting, I., Jaun, B., and Hilvert, D. (2009) Probing the role of the proximal heme ligand in cytochrome P450cam by recombinant incorporation of selenocysteine, *Proc Natl Acad Sci U S A* 106, 5481-5486.
  56. Hanson, L. K., Eaton, W. A., Sligar, S. G., Gunsalus, I. C., Gouterman, M., and Connell, C. R. (1976) Letter: Origin of the anomalous Soret spectra of carboxycytochrome P-450, *J Am Chem Soc* 98, 2672-2674.
  57. Deng, J., Carbone, I., and Dean, R. A. (2007) The evolutionary history of cytochrome P450 genes in four filamentous Ascomycetes, *BMC Evol Biol* 7, 30.
  58. Bernhardt, R. (1996) Cytochrome P450: structure, function, and generation of reactive oxygen species, *Rev Physiol Biochem Pharmacol* 127, 137-221.
  59. Perera, R., Sono, M., Sigman, J. A., Pfister, T. D., Lu, Y., and Dawson, J. H. (2003) Neutral thiol as a proximal ligand to ferrous heme iron: implications for heme proteins that lose cysteine thiolate ligation on reduction, *Proc Natl Acad Sci U S A* 100, 3641-3646.
  60. Werck-Reichhart, D., and Feyereisen, R. (2000) Cytochromes P450: a success story, *Genome Biol* 1, REVIEWS3003.
  61. Green, M. T. (2009) C-H bond activation in heme proteins: the role of thiolate ligation in cytochrome P450, *Curr Opin Chem Biol* 13, 84-88.
  62. Whalen, K. E., Starczak, V. R., Nelson, D. R., Goldstone, J. V., and Hahn, M. E. Cytochrome P450 diversity and induction by gorgonian allelochemicals in the marine gastropod *Cyphoma gibbosum*, *BMC Ecol* 10, 24.
  63. van den Brink, H. M., van Gorcom, R. F., van den Hondel, C. A., and Punt, P. J. (1998) Cytochrome P450 enzyme systems in fungi, *Fungal Genet Biol* 23, 1-17.
  64. Tijet, N., Helvig, C., and Feyereisen, R. (2001) The cytochrome P450 gene superfamily in *Drosophila melanogaster*: annotation, intron-exon organization and phylogeny, *Gene* 262, 189-198.
  65. Nelson, D. R. (1999) Cytochrome P450 and the individuality of species, *Arch Biochem Biophys* 369, 1-10.
  66. Shimizu, H., Park, S., Lee, D., Shoun, H., and Shiro, Y. (2000) Crystal structures of cytochrome P450nor and its mutants (Ser286-->Val, Thr) in the ferric resting state at cryogenic temperature: a comparative analysis with monooxygenase cytochrome P450s, *J Inorg Biochem* 81, 191-205.
  67. Graham, S. E., and Peterson, J. A. (1999) How similar are P450s and what can their differences teach us?, *Arch Biochem Biophys* 369, 24-29.
  68. Bernhardt, R. (2006) Cytochromes P450 as versatile biocatalysts, *J Biotechnol* 124, 128-145.
  69. Hasemann, C. A., Kurumbail, R. G., Boddupalli, S. S., Peterson, J. A., and Deisenhofer, J. (1995) Structure and function of cytochromes P450: a comparative analysis of three crystal structures, *Structure* 3, 41-62.

70. Peterson, J. A., and Graham, S. E. (1998) A close family resemblance: the importance of structure in understanding cytochromes P450, *Structure* 6, 1079-1085.
71. Denisov, I. G., Makris, T. M., Sligar, S. G., and Schlichting, I. (2005) Structure and chemistry of cytochrome P450, *Chem Rev* 105, 2253-2277.
72. Poulos, T. L. (1988) Cytochrome P450: molecular architecture, mechanism, and prospects for rational inhibitor design, *Pharm Res* 5, 67-75.
73. Sligar, S. G., Cinti, D. L., Gibson, G. G., and Schenkman, J. B. (1979) Spin state control of the hepatic cytochrome P450 redox potential, *Biochem Biophys Res Commun* 90, 925-932.
74. Ikeda-Saito, M., Hori, H., Andersson, L. A., Prince, R. C., Pickering, I. J., George, G. N., Sanders, C. R., 2nd, Lutz, R. S., McKelvey, E. J., and Mattera, R. (1992) Coordination structure of the ferric heme iron in engineered distal histidine myoglobin mutants, *J Biol Chem* 267, 22843-22852.
75. Denisov, I. G., Baas, B. J., Grinkova, Y. V., and Sligar, S. G. (2007) Cooperativity in cytochrome P450 3A4: linkages in substrate binding, spin state, uncoupling, and product formation, *J Biol Chem* 282, 7066-7076.
76. Das, A., Zhao, J., Schatz, G. C., Sligar, S. G., and Van Duyne, R. P. (2009) Screening of type I and II drug binding to human cytochrome P450-3A4 in nanodiscs by localized surface plasmon resonance spectroscopy, *Anal Chem* 81, 3754-3759.
77. Balding, P. R., Porro, C. S., McLean, K. J., Sutcliffe, M. J., Marechal, J. D., Munro, A. W., and Visser, S. P. (2008) How Do Azoles Inhibit Cytochrome P450 Enzymes? A Density Functional Study, *J Phys Chem A*.
78. Degtyarenko, K. N., and Archakov, A. I. (1993) Molecular evolution of P450 superfamily and P450-containing monooxygenase systems, *FEBS Lett* 332, 1-8.
79. Urlacher, V., and Schmid, R. D. (2002) Biotransformations using prokaryotic P450 monooxygenases, *Curr Opin Biotechnol* 13, 557-564.
80. Poulos, T. L. (2003) Cytochrome P450 flexibility, *Proc Natl Acad Sci U S A* 100, 13121-13122.
81. Inoue, K. (2005) [Cytochrome P450 enzymes in biosyntheses of some plant secondary metabolites], *Yakugaku Zasshi* 125, 31-49.
82. McLean, K. J., Carroll, P., Lewis, D. G., Dunford, A. J., Seward, H. E., Neeli, R., Cheesman, M. R., Marsollier, L., Douglas, P., Smith, W. E., Rosenkrands, I., Cole, S. T., Leys, D., Parish, T., and Munro, A. W. (2008) Characterization of active site structure in CYP121. A cytochrome P450 essential for viability of *Mycobacterium tuberculosis* H37Rv, *J Biol Chem* 283, 33406-33416.
83. Hanley, S. C., Ost, T. W., and Daff, S. (2004) The unusual redox properties of flavocytochrome P450 BM3 flavodoxin domain, *Biochem Biophys Res Commun* 325, 1418-1423.
84. Chun, Y. J., Shimada, T., Sanchez-Ponce, R., Martin, M. V., Lei, L., Zhao, B., Kelly, S. L., Waterman, M. R., Lamb, D. C., and Guengerich, F. P. (2007) Electron transport pathway for a Streptomyces cytochrome P450: cytochrome P450 105D5-catalyzed fatty acid hydroxylation in *Streptomyces coelicolor* A3(2), *J Biol Chem* 282, 17486-17500.
85. Hamdane, D., Zhang, H., and Hollenberg, P. (2008) Oxygen activation by cytochrome P450 monooxygenase, *Photosynth Res* 98, 657-666.
86. Makris, T. M., Davydov, R., Denisov, I. G., Hoffman, B. M., and Sligar, S. G. (2002) Mechanistic enzymology of oxygen activation by the cytochromes P450, *Drug Metab Rev* 34, 691-708.
87. Fabian, P., and Degtyarenko, K. N. (1997) The directory of P450-containing systems in 1996, *Nucleic Acids Res* 25, 274-277.

88. McLean, K. J., Girvan, H. M., and Munro, A. W. (2007) Cytochrome P450/redox partner fusion enzymes: biotechnological and toxicological prospects, *Expert Opin Drug Metab Toxicol* 3, 847-863.
89. McLean, K. J., Sabri, M., Marshall, K. R., Lawson, R. J., Lewis, D. G., Clift, D., Balding, P. R., Dunford, A. J., Warman, A. J., McVey, J. P., Quinn, A. M., Sutcliffe, M. J., Scrutton, N. S., and Munro, A. W. (2005) Biodiversity of cytochrome P450 redox systems, *Biochem Soc Trans* 33, 796-801.
90. Munro, A. W., Girvan, H. M., and McLean, K. J. (2007) Cytochrome P450--redox partner fusion enzymes, *Biochim Biophys Acta* 1770, 345-359.
91. David, G. L., Romieu, I., Sienra-Monge, J. J., Collins, W. J., Ramirez-Aguilar, M., del Rio-Navarro, B. E., Reyes-Ruiz, N. I., Morris, R. W., Marzec, J. M., and London, S. J. (2003) Nicotinamide adenine dinucleotide (phosphate) reduced:quinone oxidoreductase and glutathione S-transferase M1 polymorphisms and childhood asthma, *Am J Respir Crit Care Med* 168, 1199-1204.
92. Muller, F. (1987) Flavin radicals: chemistry and biochemistry, *Free Radic Biol Med* 3, 215-230.
93. Wang, M., Roberts, D. L., Paschke, R., Shea, T. M., Masters, B. S., and Kim, J. J. (1997) Three-dimensional structure of NADPH-cytochrome P450 reductase: prototype for FMN- and FAD-containing enzymes, *Proc Natl Acad Sci U S A* 94, 8411-8416.
94. Hodgson, A. V., and Strobel, H. W. (1996) Characterization of the FAD binding domain of cytochrome P450 reductase, *Arch Biochem Biophys* 325, 99-106.
95. Sticht, H., and Rosch, P. (1998) The structure of iron-sulfur proteins, *Prog Biophys Mol Biol* 70, 95-136.
96. Beinert, H., Holm, R. H., and Munck, E. (1997) Iron-sulfur clusters: nature's modular, multipurpose structures, *Science* 277, 653-659.
97. Mathews, R., Charlton, S., Sands, R. H., and Palmer, G. (1974) On the nature of the spin coupling between the iron-sulfur clusters in the eight-iron ferredoxins, *J Biol Chem* 249, 4326-4328.
98. Sevrioukova, I. F. (2005) Redox-dependent structural reorganization in putidaredoxin, a vertebrate-type [2Fe-2S] ferredoxin from *Pseudomonas putida*, *J Mol Biol* 347, 607-621.
99. Sevrioukova, I. F., Li, H., Zhang, H., Peterson, J. A., and Poulos, T. L. (1999) Structure of a cytochrome P450-redox partner electron-transfer complex, *Proc Natl Acad Sci U S A* 96, 1863-1868.
100. Hirakawa, H., Kamiya, N., Tanaka, T., and Nagamune, T. (2007) Intramolecular electron transfer in a cytochrome P450cam system with a site-specific branched structure, *Protein Eng Des Sel* 20, 453-459.
101. Moore, J. N., Newsted, J. L., Hecker, M., Zwiernik, M. J., Fitzgerald, S. D., Kay, D. P., Zhang, X., Higley, E. B., Aylward, L. L., Beckett, K. J., Budinsky, R. A., Bursian, S. J., and Giesy, J. P. (2009) Hepatic P450 enzyme activity, tissue morphology and histology of mink (*Mustela vison*) exposed to polychlorinated dibenzofurans, *Arch Environ Contam Toxicol* 57, 416-425.
102. Leoni, C., Buratti, F. M., and Testai, E. (2008) The participation of human hepatic P450 isoforms, flavin-containing monooxygenases and aldehyde oxidase in the biotransformation of the insecticide fenthion, *Toxicol Appl Pharmacol* 233, 343-352.
103. Cheng, P. Y., and Morgan, E. T. (2001) Hepatic cytochrome P450 regulation in disease states, *Curr Drug Metab* 2, 165-183.
104. Dehal, S. S., and Kupfer, D. (1994) Metabolism of the proestrogenic pesticide methoxychlor by hepatic P450 monooxygenases in rats and humans. Dual pathways

- involving novel ortho ring-hydroxylation by CYP2B, *Drug Metab Dispos* 22, 937-946.
105. McLean, K. J., Marshall, K. R., Richmond, A., Hunter, I. S., Fowler, K., Kieser, T., Gurcha, S. S., Besra, G. S., and Munro, A. W. (2002) Azole antifungals are potent inhibitors of cytochrome P450 mono-oxygenases and bacterial growth in mycobacteria and streptomycetes, *Microbiology* 148, 2937-2949.
  106. Ding, C. Z., Batorsky, R., Bhide, R., Chao, H. J., Cho, Y., Chong, S., Gullo-Brown, J., Guo, P., Kim, S. H., Lee, F., Leftheris, K., Miller, A., Mitt, T., Patel, M., Penhallow, B. A., Ricca, C., Rose, W. C., Schmidt, R., Slusarchyk, W. A., Vite, G., Yan, N., Manne, V. V., and Hunt, J. T. (1999) Discovery and structure-activity relationships of imidazole-containing tetrahydrobenzodiazepine inhibitors of farnesyltransferase, *J Med Chem* 42, 5288.
  107. Tong, Y., Lin, N. H., Wang, L., Hasvold, L., Wang, W., Leonard, N., Li, T., Li, Q., Cohen, J., Gu, W. Z., Zhang, H., Stoll, V., Bauch, J., Marsh, K., Rosenberg, S. H., and Sham, H. L. (2003) Discovery of potent imidazole and cyanophenyl containing farnesyltransferase inhibitors with improved oral bioavailability, *Bioorg Med Chem Lett* 13, 1571-1574.
  108. Hajek, K. K., Cook, N. I., and Novak, R. F. (1982) Mechanism of inhibition of microsomal drug metabolism by imidazole, *J Pharmacol Exp Ther* 223, 97-104.
  109. Sanmukhani, J., Shah, V., Baxi, S., and Tripathi, C. Fixed drug eruption with ornidazole having cross-sensitivity to secnidazole but not to other nitro-imidazole compounds: a case report, *Br J Clin Pharmacol* 69, 703-704.
  110. Verras, A., Kuntz, I. D., and Ortiz de Montellano, P. R. (2004) Computer-assisted design of selective imidazole inhibitors for cytochrome p450 enzymes, *J Med Chem* 47, 3572-3579.
  111. Zhang, W., Ramamoorthy, Y., Kilicarlan, T., Nolte, H., Tyndale, R. F., and Sellers, E. M. (2002) Inhibition of cytochromes P450 by antifungal imidazole derivatives, *Drug Metab Dispos* 30, 314-318.
  112. Suzuki, S., Kurata, N., Nishimura, Y., Yasuhara, H., and Satoh, T. (2000) Effects of imidazole antimycotics on the liver microsomal cytochrome P450 isoforms in rats: comparison of in vitro and ex vivo studies, *Eur J Drug Metab Pharmacokinet* 25, 121-126.
  113. Aussel, C., and Breittmayer, J. P. (1993) Imidazole antimycotics inhibitors of cytochrome P450 increase phosphatidylserine synthesis similarly to K(+)-channel blockers in Jurkat T cells, *FEBS Lett* 319, 155-158.
  114. Maurice, M., Pichard, L., Daujat, M., Fabre, I., Joyeux, H., Domergue, J., and Maurel, P. (1992) Effects of imidazole derivatives on cytochromes P450 from human hepatocytes in primary culture, *FASEB J* 6, 752-758.
  115. Owen, C. P., Dhanani, S., Patel, C. H., Shahid, I., and Ahmed, S. (2006) Synthesis and biochemical evaluation of a range of potent benzyl imidazole-based compounds as potential inhibitors of the enzyme complex 17 $\alpha$ -hydroxylase/17,20-lyase (P450(17 $\alpha$ )), *Bioorg Med Chem Lett* 16, 4011-4015.
  116. Nagai, K., Miyamori, I., Ikeda, M., Koshida, H., Takeda, R., Suhara, K., and Katagiri, M. (1986) Effect of ketoconazole (an imidazole antimycotic agent) and other inhibitors of steroidogenesis on cytochrome P450-catalyzed reactions, *J Steroid Biochem* 24, 321-323.
  117. Helmick, R. A., Fletcher, A. E., Gardner, A. M., Gessner, C. R., Hvitved, A. N., Gustin, M. C., and Gardner, P. R. (2005) Imidazole antibiotics inhibit the nitric oxide dioxygenase function of microbial flavohemoglobin, *Antimicrob Agents Chemother* 49, 1837-1843.
  118. Iizuka, T., Kanegasaki, S., Makino, R., Tanaka, T., and Ishimura, Y. (1985) Pyridine and imidazole reversibly inhibit the respiratory burst in porcine and human

- neutrophils: evidence for the involvement of cytochrome b558 in the reaction, *Biochem Biophys Res Commun* 130, 621-626.
119. Podust, L. M., Poulos, T. L., and Waterman, M. R. (2001) Crystal structure of cytochrome P450 14alpha-sterol demethylase (CYP51) from *Mycobacterium tuberculosis* in complex with azole inhibitors, *Proc Natl Acad Sci U S A* 98, 3068-3073.
  120. Belin, P., Le Du, M. H., Fielding, A., Lequin, O., Jacquet, M., Charbonnier, J. B., Lecoq, A., Thai, R., Courcon, M., Masson, C., Dugave, C., Genet, R., Pernodet, J. L., and Gondry, M. (2009) Identification and structural basis of the reaction catalyzed by CYP121, an essential cytochrome P450 in *Mycobacterium tuberculosis*, *Proc Natl Acad Sci U S A* 106, 7426-7431.
  121. McLean, K. J., Lafite, P., Levy, C., Cheesman, M. R., Mast, N., Pikuleva, I. A., Leys, D., and Munro, A. W. (2009) The Structure of *Mycobacterium tuberculosis* CYP125: molecular basis for cholesterol binding in a P450 needed for host infection, *J Biol Chem* 284, 35524-35533.
  122. Capyk, J. K., Kalscheuer, R., Stewart, G. R., Liu, J., Kwon, H., Zhao, R., Okamoto, S., Jacobs, W. R., Jr., Eltis, L. D., and Mohn, W. W. (2009) Mycobacterial cytochrome p450 125 (cyp125) catalyzes the terminal hydroxylation of c27 steroids, *J Biol Chem* 284, 35534-35542.
  123. Rosloniec, K. Z., Wilbrink, M. H., Capyk, J. K., Mohn, W. W., Ostendorf, M., van der Geize, R., Dijkhuizen, L., and Eltis, L. D. (2009) Cytochrome P450 125 (CYP125) catalyses C26-hydroxylation to initiate sterol side-chain degradation in *Rhodococcus jostii* RHA1, *Mol Microbiol* 74, 1031-1043.
  124. Driscoll, M. D., McLean, K. J., Levy, C., Mast, N., Pikuleva, I. A., Lafite, P., Rigby, S. E., Leys, D., and Munro, A. W. Structural and biochemical characterization of *Mycobacterium tuberculosis* CYP142: evidence for multiple cholesterol 27-hydroxylase activities in a human pathogen, *J Biol Chem* 285, 38270-38282.
  125. Li, J., Zheng, M., Tang, W., He, P. L., Zhu, W., Li, T., Zuo, J. P., Liu, H., and Jiang, H. (2006) Syntheses of triazole-modified zanamivir analogues via click chemistry and anti-AIV activities, *Bioorg Med Chem Lett* 16, 5009-5013.
  126. Zhou, J. H., Cheng, R. M., Song, Y., Li, Y. Z., Yu, Z., Chen, X. T., Xue, Z. L., and You, X. Z. (2005) Syntheses, structures, and magnetic properties of unusual nonlinear polynuclear copper(II) complexes containing derivatives of 1,2,4-triazole and pivalate ligands, *Inorg Chem* 44, 8011-8022.
  127. Obata, M., Kitamura, A., Mori, A., Kameyama, C., Czaplewska, J. A., Tanaka, R., Kinoshita, I., Kusumoto, T., Hashimoto, H., Harada, M., Mikata, Y., Funabiki, T., and Yano, S. (2008) Syntheses, structural characterization and photophysical properties of 4-(2-pyridyl)-1,2,3-triazole rhenium(I) complexes, *Dalton Trans*, 3292-3300.
  128. Huigens, R. W., 3rd, Rogers, S. A., Steinhauer, A. T., and Melander, C. (2009) Inhibition of *Acinetobacter baumannii*, *Staphylococcus aureus* and *Pseudomonas aeruginosa* biofilm formation with a class of TAGE-triazole conjugates, *Org Biomol Chem* 7, 794-802.
  129. Siddiqui, N., and Ahsan, W. Triazole incorporated thiazoles as a new class of anticonvulsants: design, synthesis and in vivo screening, *Eur J Med Chem* 45, 1536-1543.
  130. Olesen, P. H., Sorensen, A. R., Urso, B., Kurtzhals, P., Bowler, A. N., Ehrbar, U., and Hansen, B. F. (2003) Synthesis and in vitro characterization of 1-(4-aminofurazan-3-yl)-5-dialkylaminomethyl-1H-[1,2,3]triazole-4-carboxylic acid derivatives. A new class of selective GSK-3 inhibitors, *J Med Chem* 46, 3333-3341.

131. Pirali, T., Pagliai, F., Mercurio, C., Boggio, R., Canonico, P. L., Sorba, G., Tron, G. C., and Genazzani, A. A. (2008) Triazole-modified histone deacetylase inhibitors as a rapid route to drug discovery, *J Comb Chem* 10, 624-627.
132. Odds, F. C. (2006) Drug evaluation: BAL-8557--a novel broad-spectrum triazole antifungal, *Curr Opin Investig Drugs* 7, 766-772.
133. Hwang, Y. K., Joo, N. H., Tee, G. Y., Tan, P., Tan, L., and Girija, R. (2001) Clinical activity of the new triazole drug voriconazole (UK 109, 496) against disseminated hepatosplenic aspergillosis in a patient with relapsed leukemia, *Haematologia (Budap)* 31, 73-80.
134. Molina, J., Martins-Filho, O., Brener, Z., Romanha, A. J., Loebenberg, D., and Urbina, J. A. (2000) Activities of the triazole derivative SCH 56592 (posaconazole) against drug-resistant strains of the protozoan parasite *Trypanosoma* (Schizotrypanum) *cruzi* in immunocompetent and immunosuppressed murine hosts, *Antimicrob Agents Chemother* 44, 150-155.
135. Driscoll, M. D., McLean, K. J., Cheesman, M. R., Jowitt, T. A., Howard, M., Carroll, P., Parish, T., and Munro, A. W. Expression and characterization of *Mycobacterium tuberculosis* CYP144: Common themes and lessons learned in the *M. tuberculosis* P450 enzyme family, *Biochim Biophys Acta* 1814, 76-87.
136. Johnston, J. B., Kells, P. M., Podust, L. M., and Ortiz de Montellano, P. R. (2009) Biochemical and structural characterization of CYP124: a methyl-branched lipid omega-hydroxylase from *Mycobacterium tuberculosis*, *Proc Natl Acad Sci U S A* 106, 20687-20692.
137. Ouellet, H., Podust, L. M., and de Montellano, P. R. (2008) *Mycobacterium tuberculosis* CYP130: crystal structure, biophysical characterization, and interactions with antifungal azole drugs, *J Biol Chem* 283, 5069-5080.
138. McLean, K. J., Cheesman, M. R., Rivers, S. L., Richmond, A., Leys, D., Chapman, S. K., Reid, G. A., Price, N. C., Kelly, S. M., Clarkson, J., Smith, W. E., and Munro, A. W. (2002) Expression, purification and spectroscopic characterization of the cytochrome P450 CYP121 from *Mycobacterium tuberculosis*, *J Inorg Biochem* 91, 527-541.
139. Leys, D., Mowat, C. G., McLean, K. J., Richmond, A., Chapman, S. K., Walkinshaw, M. D., and Munro, A. W. (2003) Atomic structure of *Mycobacterium tuberculosis* CYP121 to 1.06 Å reveals novel features of cytochrome P450, *J Biol Chem* 278, 5141-5147.
140. Podust, L. M., von Kries, J. P., Eddine, A. N., Kim, Y., Yermalitskaya, L. V., Kuehne, R., Ouellet, H., Warriar, T., Altekoster, M., Lee, J. S., Rademann, J., Oschkinat, H., Kaufmann, S. H., and Waterman, M. R. (2007) Small-molecule scaffolds for CYP51 inhibitors identified by high-throughput screening and defined by X-ray crystallography, *Antimicrob Agents Chemother* 51, 3915-3923.
141. Lua, R. C., and Lichtarge, O. PyETV: a PyMOL evolutionary trace viewer to analyze functional site predictions in protein complexes, *Bioinformatics* 26, 2981-2982.
142. Salmon, F., Taton, M., Benveniste, P., and Rahier, A. (1992) Plant sterol biosynthesis: novel potent and selective inhibitors of cytochrome P450-dependent obtusifoliol 14 alpha-methyl demethylase, *Arch Biochem Biophys* 297, 123-131.
143. Maillot-Vernier, P., Schaller, H., Benveniste, P., and Belliard, G. (1989) Biochemical characterization of a sterol mutant plant regenerated from a tobacco callus resistant to a triazole cytochrome-P-450-obtusifoliol-14-demethylase inhibitor, *Biochem Biophys Res Commun* 165, 125-130.
144. Benko, A. L., Vaduva, G., Martin, N. C., and Hopper, A. K. (2000) Competition between a sterol biosynthetic enzyme and tRNA modification in addition to changes

- in the protein synthesis machinery causes altered nonsense suppression, *Proc Natl Acad Sci U S A* 97, 61-66.
145. Urbina, J. A., Vivas, J., Visbal, G., and Contreras, L. M. (1995) Modification of the sterol composition of *Trypanosoma* (Schizotrypanum) *cruzi* epimastigotes by delta 24(25)-sterol methyl transferase inhibitors and their combinations with ketoconazole, *Mol Biochem Parasitol* 73, 199-210.
  146. Izumi, A., Pinkerton, F. D., Nelson, S. O., Pyrek, J. S., Neill, P. J., Smith, J. H., and Schroepfer, G. J., Jr. (1994) Inhibitors of sterol synthesis. Submicromolar 14 alpha-ethyl-5 alpha-cholest-7-ene-3 beta, 15 alpha-diol causes a major modification of the sterol composition of CHO-K1 cells and a marked change in cell morphology, *J Lipid Res* 35, 1251-1266.
  147. Montemiglio, L. C., Gianni, S., Vallone, B., and Savino, C. Azole drugs trap cytochrome P450 EryK in alternative conformational states, *Biochemistry* 49, 9199-9206.
  148. Billaud, E. M., Antoine, C., Berge, M., Abboud, I., Lefeuvre, S., Benammar, M., and Glotz, D. (2009) Management of metabolic cytochrome P450 3A4 drug-drug interaction between everolimus and azole antifungals in a renal transplant patient, *Clin Drug Investig* 29, 481-486.
  149. Seward, H. E., Roujeinikova, A., McLean, K. J., Munro, A. W., and Leys, D. (2006) Crystal structure of the *Mycobacterium tuberculosis* P450 CYP121-fluconazole complex reveals new azole drug-P450 binding mode, *J Biol Chem* 281, 39437-39443.
  150. Guardiola-Diaz, H. M., Foster, L. A., Mushrush, D., and Vaz, A. D. (2001) Azole-antifungal binding to a novel cytochrome P450 from *Mycobacterium tuberculosis*: implications for treatment of tuberculosis, *Biochem Pharmacol* 61, 1463-1470.
  151. Venkateswarlu, K., Denning, D. W., and Kelly, S. L. (1997) Inhibition and interaction of cytochrome P450 of *Candida krusei* with azole antifungal drugs, *J Med Vet Mycol* 35, 19-25.
  152. Joseph-Horne, T., Hollomon, D., Loeffler, R. S., and Kelly, S. L. (1995) Altered P450 activity associated with direct selection for fungal azole resistance, *FEBS Lett* 374, 174-178.
  153. Zanno, A., Kwiatkowski, N., Vaz, A. D., and Guardiola-Diaz, H. M. (2005) MT FdR: a ferredoxin reductase from *M. tuberculosis* that couples to MT CYP51, *Biochim Biophys Acta* 1707, 157-169.
  154. McLean, K. J., Dunford, A. J., Sabri, M., Neeli, R., Girvan, H. M., Balding, P. R., Leys, D., Seward, H. E., Marshall, K. R., and Munro, A. W. (2006) CYP121, CYP51 and associated redox systems in *Mycobacterium tuberculosis*: towards deconvoluting enzymology of P450 systems in a human pathogen, *Biochem Soc Trans* 34, 1178-1182.
  155. Podust, L. M., Ouellet, H., von Kries, J. P., and de Montellano, P. R. (2009) Interaction of *Mycobacterium tuberculosis* CYP130 with heterocyclic arylamines, *J Biol Chem* 284, 25211-25219.
  156. Lack, N. A., Yam, K. C., Lowe, E. D., Horsman, G. P., Owen, R. L., Sim, E., and Eltis, L. D. Characterization of a carbon-carbon hydrolase from *Mycobacterium tuberculosis* involved in cholesterol metabolism, *J Biol Chem* 285, 434-443.
  157. Yang, X., Nesbitt, N. M., Dubnau, E., Smith, I., and Sampson, N. S. (2009) Cholesterol metabolism increases the metabolic pool of propionate in *Mycobacterium tuberculosis*, *Biochemistry* 48, 3819-3821.
  158. Chipley, J. R., Dreyfuss, M. S., and Smucker, R. A. (1975) Cholesterol metabolism by *Mycobacterium*, *Microbios* 12, 199-207.
  159. Migita, C. T., Salerno, J. C., Masters, B. S., Martasek, P., McMillan, K., and Ikeda-Saito, M. (1997) Substrate binding-induced changes in the EPR spectra of the

- ferrous nitric oxide complexes of neuronal nitric oxide synthase, *Biochemistry* 36, 10987-10992.
160. Sanger, F., Nicklen, S., and Coulson, A. R. (1977) DNA sequencing with chain-terminating inhibitors, *Proc Natl Acad Sci U S A* 74, 5463-5467.
  161. McLean, K. J., Scrutton, N. S., and Munro, A. W. (2003) Kinetic, spectroscopic and thermodynamic characterization of the *Mycobacterium tuberculosis* adrenodoxin reductase homologue FprA, *Biochem J* 372, 317-327.
  162. McIver, L., Leadbeater, C., Campopiano, D. J., Baxter, R. L., Daff, S. N., Chapman, S. K., and Munro, A. W. (1998) Characterisation of flavodoxin NADP+ oxidoreductase and flavodoxin; key components of electron transfer in *Escherichia coli*, *Eur J Biochem* 257, 577-585.
  163. Berry, E. A., and Trumpower, B. L. (1987) Simultaneous determination of hemes a, b, and c from pyridine hemochrome spectra, *Anal Biochem* 161, 1-15.
  164. Carrillo-Munoz, A. J., Quindos, G., Ruesga, M., Alonso, R., del Valle, O., Hernandez-Molina, J. M., McNicholas, P., Loebenberg, D., and Santos, P. (2005) Antifungal activity of posaconazole compared with fluconazole and amphotericin B against yeasts from oropharyngeal candidiasis and other infections, *J Antimicrob Chemother* 55, 317-319.
  165. Dutton, P. L. (1978) Redox potentiometry: determination of midpoint potentials of oxidation-reduction components of biological electron-transfer systems, *Methods Enzymol* 54, 411-435.
  166. Munro, A. W., Noble, M. A., Robledo, L., Daff, S. N., and Chapman, S. K. (2001) Determination of the redox properties of human NADPH-cytochrome P450 reductase, *Biochemistry* 40, 1956-1963.
  167. Ost, T. W., Miles, C. S., Munro, A. W., Murdoch, J., Reid, G. A., and Chapman, S. K. (2001) Phenylalanine 393 exerts thermodynamic control over the heme of flavocytochrome P450 BM3, *Biochemistry* 40, 13421-13429.
  168. Sreerama, N., and Woody, R. W. (2000) Estimation of protein secondary structure from circular dichroism spectra: comparison of CONTIN, SELCON, and CDSSTR methods with an expanded reference set, *Anal Biochem* 287, 252-260.
  169. Kabsch, W. Xds, *Acta Crystallogr D Biol Crystallogr* 66, 125-132.
  170. Potterton, E., Briggs, P., Turkenburg, M., and Dodson, E. (2003) A graphical user interface to the CCP4 program suite, *Acta Crystallogr D Biol Crystallogr* 59, 1131-1137.
  171. (1994) The CCP4 suite: programs for protein crystallography, *Acta Crystallogr D Biol Crystallogr* 50, 760-763.
  172. Winn, M. D., Ashton, A. W., Briggs, P. J., Ballard, C. C., and Patel, P. (2002) Ongoing developments in CCP4 for high-throughput structure determination, *Acta Crystallogr D Biol Crystallogr* 58, 1929-1936.
  173. Adams, P. D., Afonine, P. V., Bunkoczi, G., Chen, V. B., Davis, I. W., Echols, N., Headd, J. J., Hung, L. W., Kapral, G. J., Grosse-Kunstleve, R. W., McCoy, A. J., Moriarty, N. W., Oeffner, R., Read, R. J., Richardson, D. C., Richardson, J. S., Terwilliger, T. C., and Zwart, P. H. PHENIX: a comprehensive Python-based system for macromolecular structure solution, *Acta Crystallogr D Biol Crystallogr* 66, 213-221.
  174. Murshudov, G. N., Vagin, A. A., and Dodson, E. J. (1997) Refinement of macromolecular structures by the maximum-likelihood method, *Acta Crystallogr D Biol Crystallogr* 53, 240-255.
  175. Navaza, J. (2001) Implementation of molecular replacement in AMoRe, *Acta Crystallogr D Biol Crystallogr* 57, 1367-1372.

176. Saxild, H. H., and Nygaard, P. (1991) Regulation of levels of purine biosynthetic enzymes in *Bacillus subtilis*: effects of changing purine nucleotide pools, *J Gen Microbiol* 137, 2387-2394.
177. Senecoff, J. F., McKinney, E. C., and Meagher, R. B. (1996) De novo purine synthesis in *Arabidopsis thaliana*. II. The PUR7 gene encoding 5'-phosphoribosyl-4-(N-succinocarboxamide)-5-aminoimidazole synthetase is expressed in rapidly dividing tissues, *Plant Physiol* 112, 905-917.
178. Machowski, E. E., Dawes, S., and Mizrahi, V. (2005) TB tools to tell the tale-molecular genetic methods for mycobacterial research, *Int J Biochem Cell Biol* 37, 54-68.
179. Munro, A. W., McLean, K. J., Marshall, K. R., Warman, A. J., Lewis, G., Roitel, O., Sutcliffe, M. J., Kemp, C. A., Modi, S., Scrutton, N. S., and Leys, D. (2003) Cytochromes P450: novel drug targets in the war against multidrug-resistant *Mycobacterium tuberculosis*, *Biochem Soc Trans* 31, 625-630.
180. Lew, J. M., Kapopoulou, A., Jones, L. M., and Cole, S. T. TubercuList - 10 years after, *Tuberculosis (Edinb)*.
181. Marri, P. R., Bannantine, J. P., and Golding, G. B. (2006) Comparative genomics of metabolic pathways in Mycobacterium species: gene duplication, gene decay and lateral gene transfer, *FEMS Microbiol Rev* 30, 906-925.
182. Fu, L. M., and Fu-Liu, C. S. (2007) The gene expression data of *Mycobacterium tuberculosis* based on Affymetrix gene chips provide insight into regulatory and hypothetical genes, *BMC Microbiol* 7, 37.
183. Yao, Y., Xie, Y., and Kim, K. S. (2006) Genomic comparison of *Escherichia coli* K1 strains isolated from the cerebrospinal fluid of patients with meningitis, *Infect Immun* 74, 2196-2206.
184. Heel, R. C., Brogden, R. N., Speight, T. M., and Avery, G. S. (1978) Econazole: a review of its antifungal activity and therapeutic efficacy, *Drugs* 16, 177-201.
185. Schar, G., Kayser, F. H., and Dupont, M. C. (1976) Antimicrobial activity of econazole and miconazole in vitro and in experimental candidiasis and aspergillosis, *Chemotherapy* 22, 211-220.
186. Strippqli, V., D'Auria, F. D., and Simonetti, N. (1990) In vitro antimicrobial activity of econazole and miconazole sulfosalicylate, *Drugs Exp Clin Res* 16, 237-242.
187. Gabal, M. A. (1986) Antifungal activity of ketoconazole with emphasis on zoophilic fungal pathogens, *Am J Vet Res* 47, 1229-1234.
188. Odds, F. C., Milne, L. J., Gentles, J. C., and Ball, E. H. (1980) The activity in vitro and in vivo of a new imidazole antifungal, ketoconazole, *J Antimicrob Chemother* 6, 97-104.
189. Shadomy, S. (1971) In vitro antifungal activity of clotrimazole (Bay b 5097), *Infect Immun* 4, 143-148.
190. Yamaguchi, H., Uchida, K., Kawasaki, K., and Matsunaga, T. (1989) [In vitro activity of fluconazole, a novel bistriazole antifungal agent], *Jpn J Antibiot* 42, 1-16.
191. Van Cutsem, J. M., and Thienpont, D. (1972) Miconazole, a broad-spectrum antimycotic agent with antibacterial activity, *Chemotherapy* 17, 392-404.
192. Hiratani, T., and Yamaguchi, H. (1991) [In vitro antifungal activity of itraconazole: a comparative study with ketoconazole], *Jpn J Antibiot* 44, 580-587.
193. Wulfig, C., Lombardero, J., and Pluckthun, A. (1994) An *Escherichia coli* protein consisting of a domain homologous to FK506-binding proteins (FKBP) and a new metal binding motif, *J Biol Chem* 269, 2895-2901.
194. McLean, K. J., Warman, A. J., Seward, H. E., Marshall, K. R., Girvan, H. M., Cheesman, M. R., Waterman, M. R., and Munro, A. W. (2006) Biophysical characterization of the sterol demethylase P450 from *Mycobacterium tuberculosis*, its cognate ferredoxin, and their interactions, *Biochemistry* 45, 8427-8443.

195. Commoner, B., and Lipkin, D. (1949) The Application of the Beer-Lambert Law to Optically Anisotropic Systems, *Science* 110, 41-43.
196. Dawson, J. H., Andersson, L. A., and Sono, M. (1982) Spectroscopic investigations of ferric cytochrome P-450-CAM ligand complexes. Identification of the ligand trans to cysteinate in the native enzyme, *J Biol Chem* 257, 3606-3617.
197. Kelly, S. M., Jess, T. J., and Price, N. C. (2005) How to study proteins by circular dichroism, *Biochim Biophys Acta* 1751, 119-139.
198. Sreerama, N., and Woody, R. W. (1993) A self-consistent method for the analysis of protein secondary structure from circular dichroism, *Anal Biochem* 209, 32-44.
199. Andersson, L. A., and Peterson, J. A. (1995) Active-site analysis of ferric P450 enzymes: hydrogen-bonding effects on the circular dichroism spectra, *Biochem Biophys Res Commun* 211, 389-395.
200. Provencher, S. W., and Glockner, J. (1981) Estimation of globular protein secondary structure from circular dichroism, *Biochemistry* 20, 33-37.
201. Sonnichsen, F. D., Van Eyk, J. E., Hodges, R. S., and Sykes, B. D. (1992) Effect of trifluoroethanol on protein secondary structure: an NMR and CD study using a synthetic actin peptide, *Biochemistry* 31, 8790-8798.
202. Almog, R. (1983) A study on the positive ellipticity in the circular dichroism of ribonuclease A, *Biophys Chem* 18, 391-395.
203. Loew, G. H., Herman, Z. S., Rohmer, M. M., Goldblum, A., and Pudzianowski, A. (1981) Structure, spectra, and function of model cytochrome P450, *Ann N Y Acad Sci* 367, 192-218.
204. Poulos, T. L., Finzel, B. C., and Howard, A. J. (1987) High-resolution crystal structure of cytochrome P450cam, *J Mol Biol* 195, 687-700.
205. Ogata, M. (1988) Synthesis of antifungal imidazoles and triazoles, *Ann N Y Acad Sci* 544, 12-31.
206. Perfect, J. R., and Durack, D. T. (1985) Penetration of imidazoles and triazoles into cerebrospinal fluid of rabbits, *J Antimicrob Chemother* 16, 81-86.
207. Lupetti, A., Danesi, R., Campa, M., Del Tacca, M., and Kelly, S. (2002) Molecular basis of resistance to azole antifungals, *Trends Mol Med* 8, 76-81.
208. Ahmad, Z., Sharma, S., and Khuller, G. K. (2006) The potential of azole antifungals against latent/persistent tuberculosis, *FEMS Microbiol Lett* 258, 200-203.
209. Riley, P., and Hanzlik, R. P. (1994) Electron transfer in P450 mechanisms. Microsomal metabolism of cyclopropylbenzene and p-cyclopropylanisole, *Xenobiotica* 24, 1-16.
210. Anzenbacher, P. (1979) Oxidation-reduction potentials of haem proteins, *Nature* 282, 757-758.
211. Ingledew, W. J., Salerno, J. C., and Ohnishi, T. (1976) Thermodynamic resolution of cytochrome P450 and characterization of an iron-sulfur center in rat liver microsomal preparations, *Arch Biochem Biophys* 174, 298-304.
212. Munro, A. W., Daff, S. N., Turner, K. L., and Chapman, S. K. (1997) Redox characterisation of flavocytochrome P-450 BM3 from *Bacillus megaterium*, *Biochem Soc Trans* 25, S628.
213. Das, A., Grinkova, Y. V., and Sligar, S. G. (2007) Redox potential control by drug binding to cytochrome P450 3A4, *J Am Chem Soc* 129, 13778-13779.
214. Finn, R. D., Basran, J., Roitel, O., Wolf, C. R., Munro, A. W., Paine, M. J., and Scrutton, N. S. (2003) Determination of the redox potentials and electron transfer properties of the FAD- and FMN-binding domains of the human oxidoreductase NR1, *Eur J Biochem* 270, 1164-1175.
215. Tsujimura, S., Kuriyama, A., Fujieda, N., Kano, K., and Ikeda, T. (2005) Mediated spectroelectrochemical titration of proteins for redox potential measurements by a

- separator-less one-compartment bulk electrolysis method, *Anal Biochem* 337, 325-331.
216. Sligar, S. G. (1976) Coupling of spin, substrate, and redox equilibria in cytochrome P450, *Biochemistry* 15, 5399-5406.
217. Daff, S. N., Chapman, S. K., Turner, K. L., Holt, R. A., Govindaraj, S., Poulos, T. L., and Munro, A. W. (1997) Redox control of the catalytic cycle of flavocytochrome P-450 BM3, *Biochemistry* 36, 13816-13823.
218. Dunford, A. J., McLean, K. J., Sabri, M., Seward, H. E., Heyes, D. J., Scrutton, N. S., and Munro, A. W. (2007) Rapid P450 heme iron reduction by laser photoexcitation of *Mycobacterium tuberculosis* CYP121 and CYP51B1. Analysis of CO complexation reactions and reversibility of the P450/P420 equilibrium, *J Biol Chem* 282, 24816-24824.
219. Yang, A. S., and Honig, B. (1993) On the pH dependence of protein stability, *J Mol Biol* 231, 459-474.
220. Nagano, S., Li, H., Shimizu, H., Nishida, C., Ogura, H., Ortiz de Montellano, P. R., and Poulos, T. L. (2003) Crystal structures of epothilone D-bound, epothilone B-bound, and substrate-free forms of cytochrome P450epoK, *J Biol Chem* 278, 44886-44893.
221. Liang, Y. (2008) Applications of isothermal titration calorimetry in protein science, *Acta Biochim Biophys Sin (Shanghai)* 40, 565-576.
222. Balme, A., Hervas, M., Campos, L. A., Sancho, J., De la Rosa, M. A., and Navarro, J. A. (2001) A comparative study of the thermal stability of plastocyanin, cytochrome c(6) and Photosystem I in thermophilic and mesophilic cyanobacteria, *Photosynth Res* 70, 281-289.
223. McLean, M. A., Maves, S. A., Weiss, K. E., Krepich, S., and Sligar, S. G. (1998) Characterization of a cytochrome P450 from the acidothermophilic archaea *Sulfolobus solfataricus*, *Biochem Biophys Res Commun* 252, 166-172.
224. Balasubramaniam, A., and Panpalia, G. M. (2001) Drug adjuvant interaction study using DSC supported by isothermal method, *Drug Dev Ind Pharm* 27, 475-480.
225. Archakov, A. I., Uvarov, V. Y., Bachmanova, G. I., Sukhomudrenko, A. G., and Myasoedova, K. N. (1981) The conformation and thermal stability of soluble cytochrome P-450 and cytochrome P-450 incorporated into liposomal membranes, *Arch Biochem Biophys* 212, 378-384.
226. Quilici, L., Praud Tabaries, A., Benaim, J., and Tabaries, F. (2002) [Measurement and differentiation method of carbon in municipal solid waste incineration (MSWI) bottom ash using differential scanning calorimetry (DSC)], *Environ Technol* 23, 757-766.
227. Koch-Schmidt, A. C., and Mosbach, K. (1977) Studies on conformation of soluble and immobilized enzymes using differential scanning calorimetry. 1. Thermal stability of nicotinamide adenine dinucleotide dependent dehydrogenases, *Biochemistry* 16, 2101-2105.
228. LeLean, J. E., Moon, N., Dunham, W. R., and Coon, M. J. (2000) EPR spectrometry of cytochrome P450 2B4: effects of mutations and substrate binding, *Biochem Biophys Res Commun* 276, 762-766.
229. Beinert, H. (2003) EPR on the P450(cam) system in the late 1960s with Gunny and his gang: insights concerning the structure of Fe-S proteins and the spin states of P450, *Biochem Biophys Res Commun* 312, 45-47.
230. Vinck, E., Van Doorslaer, S., Dewilde, S., Mitrikas, G., Schweiger, A., and Moens, L. (2006) Analyzing heme proteins using EPR techniques: the heme-pocket structure of ferric mouse neuroglobin, *J Biol Inorg Chem* 11, 467-475.

231. Chevion, M., Traum, M. M., Blumberg, W. E., and Peisach, J. (1977) High resolution EPR studies of the fine structure of heme proteins. Third harmonic detection approach, *Biochim Biophys Acta* 490, 272-278.
232. Gaffney, B. J. (2009) EPR of Mononuclear Non-Heme Iron Proteins, *Biol Magn Reson* 28, 233-268.
233. Frantz, S., Hartmann, H., Doslik, N., Wanner, M., Kaim, W., Kummerer, H. J., Denninger, G., Barra, A. L., Duboc-Toia, C., Fiedler, J., Ciofini, I., Urban, C., and Kaupp, M. (2002) Multifrequency EPR study and density functional g-tensor calculations of persistent organorhenium radical complexes, *J Am Chem Soc* 124, 10563-10571.
234. Fittipaldi, M., Garcia-Rubio, I., Trandafir, F., Gromov, I., Schweiger, A., Bouwen, A., and Van Doorslaer, S. (2008) A multi-frequency pulse EPR and ENDOR approach to study strongly coupled nuclei in frozen solutions of high-spin ferric heme proteins, *J Phys Chem B* 112, 3859-3870.
235. Zakhariyeva, O., Grodzicki, M., Trautwein, A. X., Veeger, C., and Rietjens, I. M. (1998) Molecular orbital study of porphyrin-substrate interactions in cytochrome P450 catalysed aromatic hydroxylation of substituted anilines, *Biophys Chem* 73, 189-203.
236. Porro, C. S., Kumar, D., and de Visser, S. P. (2009) Electronic properties of pentacoordinated heme complexes in cytochrome P450 enzymes: search for an Fe(I) oxidation state, *Phys Chem Chem Phys* 11, 10219-10226.
237. Tang, J., Sanchez Costa, J., Smulders, S., Molnar, G., Bousseksou, A., Teat, S. J., Li, Y., van Albada, G. A., Gamez, P., and Reedijk, J. (2009) Two-step spin-transition iron(III) compound with a wide [high spin-low spin] plateau, *Inorg Chem* 48, 2128-2135.
238. Decker, A., Rohde, J. U., Klinker, E. J., Wong, S. D., Que, L., Jr., and Solomon, E. I. (2007) Spectroscopic and quantum chemical studies on low-spin FeIV=O complexes: Fe-O bonding and its contributions to reactivity, *J Am Chem Soc* 129, 15983-15996.
239. Rath, S. P., Olmstead, M. M., and Balch, A. L. (2004) The effects of axial ligands on electron distribution and spin states in iron complexes of octaethylxophlorin, intermediates in heme degradation, *J Am Chem Soc* 126, 6379-6386.
240. Shaik, S., Kumar, D., and de Visser, S. P. (2008) A valence bond modeling of trends in hydrogen abstraction barriers and transition states of hydroxylation reactions catalyzed by cytochrome P450 enzymes, *J Am Chem Soc* 130, 10128-10140.
241. Yamashita, T., Hoashi, Y., Watanabe, K., Tomisugi, Y., Ishikawa, Y., and Uno, T. (2004) Roles of heme axial ligands in the regulation of CO binding to CooA, *J Biol Chem* 279, 21394-21400.
242. Franke, A., Stochel, G., Jung, C., and Van Eldik, R. (2004) Substrate binding favors enhanced NO binding to P450cam, *J Am Chem Soc* 126, 4181-4191.
243. de Vries, S., and Albracht, S. P. (1979) Intensity of highly anisotropic low-spin heme EPR signals, *Biochim Biophys Acta* 546, 334-340.
244. Mitchell, D. M., Aasa, R., Adelroth, P., Brzezinski, P., Gennis, R. B., and Malmstrom, B. G. (1995) EPR studies of wild-type and several mutants of cytochrome c oxidase from *Rhodobacter sphaeroides*: Glu286 is not a bridging ligand in the cytochrome a<sub>3</sub>-CuB center, *FEBS Lett* 374, 371-374.
245. Takizawa, T., Yoshikawa, H., Yamada, M., and Morita, H. (2002) Expression of nitric oxide synthase isoforms and detection of nitric oxide in rat placenta, *Am J Physiol Cell Physiol* 282, C762-767.
246. Davydov, R., Kappl, R., Huttermann, J., and Peterson, J. A. (1991) EPR-spectroscopy of reduced oxyferrous-P450cam, *FEBS Lett* 295, 113-115.

247. Girvan, H. M., Seward, H. E., Toogood, H. S., Cheesman, M. R., Leys, D., and Munro, A. W. (2007) Structural and spectroscopic characterization of P450 BM3 mutants with unprecedented P450 heme iron ligand sets. New heme ligation states influence conformational equilibria in P450 BM3, *J Biol Chem* 282, 564-572.
248. Kirk, M. L., and Peariso, K. (2003) Recent applications of MCD spectroscopy to metalloenzymes, *Curr Opin Chem Biol* 7, 220-227.
249. Ookubo, S., Nozawa, T., and Hatano, M. (1989) Solvent effect on MCD of Fe(III) heme complexes: magnetic circular dichroism spectra of five-coordinated high-spin iron(III) protoporphyrin-IX-dimethylester in the visible region and their environmental effect. A characterization of the visible electronic transitions in Fe(III) high-spin porphyrins, *J Inorg Biochem* 35, 305-317.
250. Sharonov Yu, A., Pismensky, V. F., Greschner, S., and Ruckpaul, K. (1987) Low- and ultralow-temperature magnetic circular dichroism studies of reduced cytochromes P-450-LM2 and P-420-LM2 and of photo-products of their co-complexes. The spin-state and axial ligation of heme iron, *Biochem Biophys Res Commun* 146, 165-172.
251. Weber, C., Michel, B., and Bosshard, H. R. (1987) Spectroscopic analysis of the cytochrome c oxidase-cytochrome c complex: circular dichroism and magnetic circular dichroism measurements reveal change of cytochrome c heme geometry imposed by complex formation, *Proc Natl Acad Sci U S A* 84, 6687-6691.
252. Simpkin, D., Palmer, G., Devlin, F. J., McKenna, M. C., Jensen, G. M., and Stephens, P. J. (1989) The axial ligands of heme in cytochromes: a near-infrared magnetic circular dichroism study of yeast cytochromes c, c1, and b and spinach cytochrome f, *Biochemistry* 28, 8033-8039.
253. Marboutin, L., Boussac, A., and Berthomieu, C. (2006) Redox infrared markers of the heme and axial ligands in microperoxidase: Bases for the analysis of c-type cytochromes, *J Biol Inorg Chem* 11, 811-823.
254. Andersson, L. A., Johnson, A. K., and Peterson, J. A. (1997) Active site analysis of P450 enzymes: comparative magnetic circular dichroism spectroscopy, *Arch Biochem Biophys* 345, 79-87.
255. Green, A. J., Rivers, S. L., Cheeseman, M., Reid, G. A., Quaroni, L. G., Macdonald, I. D., Chapman, S. K., and Munro, A. W. (2001) Expression, purification and characterization of cytochrome P450 Biol: a novel P450 involved in biotin synthesis in *Bacillus subtilis*, *J Biol Inorg Chem* 6, 523-533.
256. Winkler, R. ESIprot: a universal tool for charge state determination and molecular weight calculation of proteins from electrospray ionization mass spectrometry data, *Rapid Commun Mass Spectrom* 24, 285-294.
257. Claverol, S., Burlet-Schiltz, O., Gairin, J. E., and Monsarrat, B. (2003) Characterization of protein variants and post-translational modifications: ESI-MSn analyses of intact proteins eluted from polyacrylamide gels, *Mol Cell Proteomics* 2, 483-493.
258. Mendes, M. A., Chies, J. M., de Oliveira Dias, A. C., Filho, S. A., and Palma, M. S. (2003) The shielding effect of glycerol against protein ionization in electrospray mass spectrometry, *Rapid Commun Mass Spectrom* 17, 672-677.
259. Ye, H. (2006) Simultaneous determination of protein aggregation, degradation, and absolute molecular weight by size exclusion chromatography-multiangle laser light scattering, *Anal Biochem* 356, 76-85.
260. Pop, C. V., and Neamtu, S. (2008) Aggregation of red blood cells in suspension: study by light-scattering technique at small angles, *J Biomed Opt* 13, 041308.
261. Tappan, D. V. (1966) A light scattering technique for measuring protein concentration, *Anal Biochem* 14, 171-182.

262. Oliva, A., Llabres, M., and Farina, J. B. (2001) Comparative study of protein molecular weights by size-exclusion chromatography and laser-light scattering, *J Pharm Biomed Anal* 25, 833-841.
263. Ilari, A., and Savino, C. (2008) Protein structure determination by x-ray crystallography, *Methods Mol Biol* 452, 63-87.
264. Arndt, U., and Bloomer, A. (1999) New developments in X-ray optics for macromolecular crystallography using laboratory X-ray sources, *Curr Opin Struct Biol* 9, 609-614.
265. Guengerich, F. P. (2006) Cytochrome P450s and other enzymes in drug metabolism and toxicity, *AAPS J* 8, E101-111.
266. Gay, S. C., Roberts, A. G., and Halpert, J. R. Structural Features of Cytochromes P450 and Ligands that Affect Drug Metabolism as Revealed by X-ray Crystallography and NMR, *Future Med Chem* 2, 1451-1468.
267. Omura, T. Structural diversity of cytochrome P450 enzyme system, *J Biochem* 147, 297-306.
268. Poulos, T. L. (2005) Structural and functional diversity in heme monooxygenases, *Drug Metab Dispos* 33, 10-18.
269. Hannemann, F., Bichet, A., Ewen, K. M., and Bernhardt, R. (2007) Cytochrome P450 systems--biological variations of electron transport chains, *Biochim Biophys Acta* 1770, 330-344.
270. Lewis, D. F., and Hlavica, P. (2000) Interactions between redox partners in various cytochrome P450 systems: functional and structural aspects, *Biochim Biophys Acta* 1460, 353-374.
271. Hlavica, P., Schulze, J., and Lewis, D. F. (2003) Functional interaction of cytochrome P450 with its redox partners: a critical assessment and update of the topology of predicted contact regions, *J Inorg Biochem* 96, 279-297.
272. McCoy, A. J. (2007) Solving structures of protein complexes by molecular replacement with Phaser, *Acta Crystallogr D Biol Crystallogr* 63, 32-41.
273. Zhu, J., Cheng, L., Fang, Q., Zhou, Z. H., and Honig, B. Building and refining protein models within cryo-electron microscopy density maps based on homology modeling and multiscale structure refinement, *J Mol Biol* 397, 835-851.
274. Verras, A., and Ortiz de Montellano, P. R. (2006) Protein dynamics and imidazole binding in cytochrome P450 enzymes, *Biochem Soc Trans* 34, 1170-1172.
275. Lee, Y. T., Wilson, R. F., Rupniewski, I., and Goodin, D. B. P450cam visits an open conformation in the absence of substrate, *Biochemistry* 49, 3412-3419.
276. Oprea, T. I., Hummer, G., and Garcia, A. E. (1997) Identification of a functional water channel in cytochrome P450 enzymes, *Proc Natl Acad Sci U S A* 94, 2133-2138.
277. Lesburg, C. A., and Duca, J. S. (2008) soaPDB: a web application for searching the Protein Data Bank, organizing results, and receiving automatic email alerts, *Nucleic Acids Res* 36, W252-254.
278. Hassell, A. M., An, G., Bledsoe, R. K., Bynum, J. M., Carter, H. L., 3rd, Deng, S. J., Gampe, R. T., Grisard, T. E., Madauss, K. P., Nolte, R. T., Rocque, W. J., Wang, L., Weaver, K. L., Williams, S. P., Wisely, G. B., Xu, R., and Shewchuk, L. M. (2007) Crystallization of protein-ligand complexes, *Acta Crystallogr D Biol Crystallogr* 63, 72-79.
279. Danley, D. E. (2006) Crystallization to obtain protein-ligand complexes for structure-aided drug design, *Acta Crystallogr D Biol Crystallogr* 62, 569-575.
280. Asherie, N. (2004) Protein crystallization and phase diagrams, *Methods* 34, 266-272.
281. Cotes, K., Dhouib, R., Douchet, I., Chahinian, H., de Caro, A., Carriere, F., and Canaan, S. (2007) Characterization of an exported monoglyceride lipase from

- Mycobacterium tuberculosis* possibly involved in the metabolism of host cell membrane lipids, *Biochem J* 408, 417-427.
282. Johnson, R., Streicher, E. M., Louw, G. E., Warren, R. M., van Helden, P. D., and Victor, T. C. (2006) Drug resistance in *Mycobacterium tuberculosis*, *Curr Issues Mol Biol* 8, 97-111.
  283. Pandey, A. K., and Sasseti, C. M. (2008) Mycobacterial persistence requires the utilization of host cholesterol, *Proc Natl Acad Sci U S A* 105, 4376-4380.
  284. Sasseti, C. M., and Rubin, E. J. (2003) Genetic requirements for mycobacterial survival during infection, *Proc Natl Acad Sci U S A* 100, 12989-12994.
  285. Brudey, K., Driscoll, J. R., Rigouts, L., Prodinger, W. M., Gori, A., Al-Hajoj, S. A., Allix, C., Aristimuno, L., Arora, J., Baumanis, V., Binder, L., Cafrune, P., Cataldi, A., Cheong, S., Diel, R., Ellermeier, C., Evans, J. T., Fauville-Dufaux, M., Ferdinand, S., Garcia de Viedma, D., Garzelli, C., Gazzola, L., Gomes, H. M., Gutierrez, M. C., Hawkey, P. M., van Helden, P. D., Kadival, G. V., Kreiswirth, B. N., Kremer, K., Kubin, M., Kulkarni, S. P., Liens, B., Lillebaek, T., Ho, M. L., Martin, C., Mokrousov, I., Narvskaia, O., Ngeow, Y. F., Naumann, L., Niemann, S., Parwati, I., Rahim, Z., Rasolofo-Razanamparany, V., Rasolonavalona, T., Rossetti, M. L., Rusch-Gerdes, S., Sajduda, A., Samper, S., Shemyakin, I. G., Singh, U. B., Somoskovi, A., Skuce, R. A., van Soolingen, D., Streicher, E. M., Suffys, P. N., Tortoli, E., Tracevska, T., Vincent, V., Victor, T. C., Warren, R. M., Yap, S. F., Zaman, K., Portaels, F., Rastogi, N., and Sola, C. (2006) *Mycobacterium tuberculosis* complex genetic diversity: mining the fourth international spoligotyping database (SpolDB4) for classification, population genetics and epidemiology, *BMC Microbiol* 6, 23.
  286. McLean, K. J., and Munro, A. W. (2008) Structural biology and biochemistry of cytochrome P450 systems in *Mycobacterium tuberculosis*, *Drug Metab Rev* 40, 427-446.
  287. Parker, J. E., Merkamm, M., Manning, N. J., Pompon, D., Kelly, S. L., and Kelly, D. E. (2008) Differential azole antifungal efficacies contrasted using a *Saccharomyces cerevisiae* strain humanized for sterol 14 alpha-demethylase at the homologous locus, *Antimicrob Agents Chemother* 52, 3597-3603.
  288. Locuson, C. W., Hutzler, J. M., and Tracy, T. S. (2007) Visible spectra of type II cytochrome P450-drug complexes: evidence that "incomplete" heme coordination is common, *Drug Metab Dispos* 35, 614-622.
  289. Isin, E. M., and Guengerich, F. P. (2008) Substrate binding to cytochromes P450, *Anal Bioanal Chem* 392, 1019-1030.
  290. Ouellet, H., Johnston, J. B., and Ortiz de Montellano, P. R. The *Mycobacterium tuberculosis* cytochrome P450 system, *Arch Biochem Biophys* 493, 82-95.
  291. Parajuli, N., Basnet, D. B., Chan Lee, H., Sohng, J. K., and Liou, K. (2004) Genome analyses of *Streptomyces peuceitius* ATCC 27952 for the identification and comparison of cytochrome P450 complement with other *Streptomyces*, *Arch Biochem Biophys* 425, 233-241.
  292. Podust, L. M., Kim, Y., Arase, M., Neely, B. A., Beck, B. J., Bach, H., Sherman, D. H., Lamb, D. C., Kelly, S. L., and Waterman, M. R. (2003) The 1.92-Å structure of *Streptomyces coelicolor* A3(2) CYP154C1. A new monooxygenase that functionalizes macrolide ring systems, *J Biol Chem* 278, 12214-12221.
  293. Lamb, D. C., Ikeda, H., Nelson, D. R., Ishikawa, J., Skaug, T., Jackson, C., Omura, S., Waterman, M. R., and Kelly, S. L. (2003) Cytochrome p450 complement (CYPome) of the avermectin-producer *Streptomyces avermitilis* and comparison to that of *Streptomyces coelicolor* A3(2), *Biochem Biophys Res Commun* 307, 610-619.

294. Prior, J. E., Shokati, T., Christians, U., and Gill, R. T. Identification and characterization of a bacterial cytochrome P450 for the metabolism of diclofenac, *Appl Microbiol Biotechnol* 85, 625-633.
295. Zhao, B., Lin, X., Lei, L., Lamb, D. C., Kelly, S. L., Waterman, M. R., and Cane, D. E. (2008) Biosynthesis of the sesquiterpene antibiotic albaflavenone in *Streptomyces coelicolor* A3(2), *J Biol Chem* 283, 8183-8189.
296. Correia, M. A., Farrell, G. C., Olson, S., Wong, J. S., Schmid, R., Ortiz de Montellano, P. R., Beilan, H. S., Kunze, K. L., and Mico, B. A. (1981) Cytochrome P-450 heme moiety. The specific target in drug-induced heme alkylation, *J Biol Chem* 256, 5466-5470.
297. Hudecek, J., Hodek, P., Anzenbacherova, E., and Anzenbacher, P. (2007) Structural analysis of cytochromes P450 shows differences in flexibility of heme 2- and 4-vinyls, *Biochim Biophys Acta* 1770, 413-419.
298. Yoshida, Y., Noshiro, M., Aoyama, Y., Kawamoto, T., Horiuchi, T., and Gotoh, O. (1997) Structural and evolutionary studies on sterol 14-demethylase P450 (CYP51), the most conserved P450 monooxygenase: II. Evolutionary analysis of protein and gene structures, *J Biochem* 122, 1122-1128.
299. Lewis, D. F. (2003) P450 structures and oxidative metabolism of xenobiotics, *Pharmacogenomics* 4, 387-395.
300. Gustafsson, M. C., Roitel, O., Marshall, K. R., Noble, M. A., Chapman, S. K., Pessequeiro, A., Fulco, A. J., Cheesman, M. R., von Wachenfeldt, C., and Munro, A. W. (2004) Expression, purification, and characterization of *Bacillus subtilis* cytochromes P450 CYP102A2 and CYP102A3: flavocytochrome homologues of P450 BM3 from *Bacillus megaterium*, *Biochemistry* 43, 5474-5487.
301. Minguez, F., Chiu, M. L., Lima, J. E., Nique, R., and Prieto, J. (1994) Activity of fluconazole: postantifungal effect, effects of low concentrations and of pretreatment on the susceptibility of *Candida albicans* to leucocytes, *J Antimicrob Chemother* 34, 93-100.
302. Warrilow, A. G., Jackson, C. J., Parker, J. E., Marczylo, T. H., Kelly, D. E., Lamb, D. C., and Kelly, S. L. (2009) Identification, characterization, and azole-binding properties of *Mycobacterium smegmatis* CYP164A2, a homolog of ML2088, the sole cytochrome P450 gene of *Mycobacterium leprae*, *Antimicrob Agents Chemother* 53, 1157-1164.
303. Schoneboom, J. C., Neese, F., and Thiel, W. (2005) Toward identification of the compound I reactive intermediate in cytochrome P450 chemistry: a QM/MM study of its EPR and Mossbauer parameters, *J Am Chem Soc* 127, 5840-5853.
304. Rittle, J., and Green, M. T. Cytochrome P450 compound I: capture, characterization, and C-H bond activation kinetics, *Science* 330, 933-937.
305. Peisach, J., and Blumberg, W. E. (1970) Electron paramagnetic resonance study of the high- and low-spin forms of cytochrome P-450 in liver and in liver microsomes from a methylcholanthrene-treated rabbit, *Proc Natl Acad Sci U S A* 67, 172-179.
306. Lehnerer, M., Schulze, J., Achterhold, K., Lewis, D. F., and Hlavica, P. (2000) Identification of key residues in rabbit liver microsomal cytochrome P450 2B4: importance in interactions with NADPH-cytochrome P450 reductase, *J Biochem* 127, 163-169.
307. Ke, N., Baudry, J., Makris, T. M., Schuler, M. A., and Sligar, S. G. (2005) A retinoic acid binding cytochrome P450: CYP120A1 from *Synechocystis* sp. PCC 6803, *Arch Biochem Biophys* 436, 110-120.
308. Rux, J. J., and Dawson, J. H. (1991) Magnetic circular dichroism spectroscopy as a probe of axial heme ligand replacement in semisynthetic mutants of cytochrome c, *FEBS Lett* 290, 49-51.

309. Bracete, A. M., Sono, M., and Dawson, J. H. (1991) Effects of cyanogen bromide modification of the distal histidine on the spectroscopic and ligand binding properties of myoglobin: magnetic circular dichroism spectroscopy as a probe of distal water ligation in ferric high-spin histidine-bound heme proteins, *Biochim Biophys Acta* 1080, 264-270.
310. Schaffer, A. (1991) Absorption, circular dichroism, and magnetic circular dichroism spectroscopy of metallothionein, *Methods Enzymol* 205, 529-540.
311. Sharonov Iu, A. (1992) [Electron-conformational interactions at the active site of reduced bacterial cytochrome P450cam induced by a substrate and analysis of the electron structure of heme], *Mol Biol (Mosk)* 26, 1251-1262.
312. Girvan, H. M., Toogood, H. S., Littleford, R. E., Seward, H. E., Smith, W. E., Ekanem, I. S., Leys, D., Cheesman, M. R., and Munro, A. W. (2009) Novel haem co-ordination variants of flavocytochrome P450BM3, *Biochem J* 417, 65-76.
313. Sono, M., Perera, R., Jin, S., Makris, T. M., Sligar, S. G., Bryson, T. A., and Dawson, J. H. (2005) The influence of substrate on the spectral properties of oxyferrous wild-type and T252A cytochrome P450-CAM, *Arch Biochem Biophys* 436, 40-49.
314. Sharonov Iu, A. (1986) [Electron structure of the heme of reduced cytochrome P450 and P420 from the data of low-temperature magnetic circular dichroism], *Mol Biol (Mosk)* 20, 440-450.
315. Lamb, D. C., Fowler, K., Kieser, T., Manning, N., Podust, L. M., Waterman, M. R., Kelly, D. E., and Kelly, S. L. (2002) Sterol 14alpha-demethylase activity in *Streptomyces coelicolor* A3(2) is associated with an unusual member of the CYP51 gene family, *Biochem J* 364, 555-562.
316. Zhao, B., Lei, L., Vassilyev, D. G., Lin, X., Cane, D. E., Kelly, S. L., Yuan, H., Lamb, D. C., and Waterman, M. R. (2009) Crystal structure of albaflavenone monooxygenase containing a moonlighting terpene synthase active site, *J Biol Chem* 284, 36711-36719.
317. Edwards, R. J., Murray, B. P., Boobis, A. R., and Davies, D. S. (1989) Identification and location of alpha-helices in mammalian cytochromes P450, *Biochemistry* 28, 3762-3770.
318. Todorovic, S., Jung, C., Hildebrandt, P., and Murgida, D. H. (2006) Conformational transitions and redox potential shifts of cytochrome P450 induced by immobilization, *J Biol Inorg Chem* 11, 119-127.
319. Ichinose, H., Michizoe, J., Maruyama, T., Kamiya, N., and Goto, M. (2004) Electron-transfer reactions and functionalization of cytochrome P450cam monooxygenase system in reverse micelles, *Langmuir* 20, 5564-5568.
320. Seward, H. E., Girvan, H. M., and Munro, A. W. (2005) Cytochrome P450s: creating novel ligand sets, *Dalton Trans*, 3419-3426.
321. Makris, T. M., von Koenig, K., Schlichting, I., and Sligar, S. G. (2007) Alteration of P450 distal pocket solvent leads to impaired proton delivery and changes in heme geometry, *Biochemistry* 46, 14129-14140.
322. Guengerich, F. P., Sohl, C. D., and Chowdhury, G. Multi-step oxidations catalyzed by cytochrome P450 enzymes: Processive vs. distributive kinetics and the issue of carbonyl oxidation in chemical mechanisms, *Arch Biochem Biophys*.
323. Meunier, B., de Visser, S. P., and Shaik, S. (2004) Mechanism of oxidation reactions catalyzed by cytochrome p450 enzymes, *Chem Rev* 104, 3947-3980.
324. Hlavica, P. (2007) Control by substrate of the cytochrome p450-dependent redox machinery: mechanistic insights, *Curr Drug Metab* 8, 594-611.
325. Sage, J. T., Morikis, D., and Champion, P. M. (1991) Spectroscopic studies of myoglobin at low pH: heme structure and ligation, *Biochemistry* 30, 1227-1237.

326. Lawson, R. J., Leys, D., Sutcliffe, M. J., Kemp, C. A., Cheesman, M. R., Smith, S. J., Clarkson, J., Smith, W. E., Haq, I., Perkins, J. B., and Munro, A. W. (2004) Thermodynamic and biophysical characterization of cytochrome P450 BioI from *Bacillus subtilis*, *Biochemistry* 43, 12410-12426.
327. Maves, S. A., and Sligar, S. G. (2001) Understanding thermostability in cytochrome P450 by combinatorial mutagenesis, *Protein Sci* 10, 161-168.
328. Chun, Y. J., Shimada, T., Waterman, M. R., and Guengerich, F. P. (2006) Understanding electron transport systems of *Streptomyces* cytochrome P450, *Biochem Soc Trans* 34, 1183-1185.
329. Ortiz de Montellano, P. R. (1995) The 1994 Bernard B. Brodie Award Lecture. Structure, mechanism, and inhibition of cytochrome P450, *Drug Metab Dispos* 23, 1181-1187.
330. Brenner, S., Hay, S., Munro, A. W., and Scrutton, N. S. (2008) Inter-flavin electron transfer in cytochrome P450 reductase - effects of solvent and pH identify hidden complexity in mechanism, *FEBS J* 275, 4540-4557.
331. Urlacher, V. B., Lutz-Wahl, S., and Schmid, R. D. (2004) Microbial P450 enzymes in biotechnology, *Appl Microbiol Biotechnol* 64, 317-325.
332. Ivanov, Y. D., Kanaeva, I. P., Karuzina, II, Usanov, S. A., Hui Bon Hoa, G., Sligar, S. G., and Archakov, A. I. (2001) Revelation of ternary complexes between redox partners in cytochrome P450-containing monooxygenase systems by the optical biosensor method, *J Inorg Biochem* 87, 175-184.
333. Holden, M., Mayhew, M., Bunk, D., Roitberg, A., and Vilker, V. (1997) Probing the interactions of putidaredoxin with redox partners in camphor P450 5-monooxygenase by mutagenesis of surface residues, *J Biol Chem* 272, 21720-21725.
334. Mowat, C. G., Gazur, B., Campbell, L. P., and Chapman, S. K. Flavin-containing heme enzymes, *Arch Biochem Biophys* 493, 37-52.
335. Hazzard, J. T., Govindaraj, S., Poulos, T. L., and Tollin, G. (1997) Electron transfer between the FMN and heme domains of cytochrome P450BM-3. Effects of substrate and CO, *J Biol Chem* 272, 7922-7926.
336. Tuckey, R. C., Woods, S. T., and Tajbakhsh, M. (1997) Electron transfer to cytochrome P-450scc limits cholesterol-side-chain-cleavage activity in the human placenta, *Eur J Biochem* 244, 835-839.
337. Mayoral, T., Martinez-Julvez, M., Perez-Dorado, I., Sanz-Aparicio, J., Gomez-Moreno, C., Medina, M., and Hermoso, J. A. (2005) Structural analysis of interactions for complex formation between Ferredoxin-NADP+ reductase and its protein partners, *Proteins* 59, 592-602.
338. Nazor, J., and Schwaneberg, U. (2006) Laboratory evolution of P450 BM-3 for mediated electron transfer, *Chembiochem* 7, 638-644.
339. Bell, S. G., Dale, A., Rees, N. H., and Wong, L. L. A cytochrome P450 class I electron transfer system from *Novosphingobium aromaticivorans*, *Appl Microbiol Biotechnol* 86, 163-175.
340. Santos, R., Fernandes, J., Fernandes, N., Oliveira, F., and Cadete, M. (2007) *Mycobacterium parascrofulaceum* in acidic hot springs in Yellowstone National Park, *Appl Environ Microbiol* 73, 5071-5073.
341. Stingley, R. L., Brezna, B., Khan, A. A., and Cerniglia, C. E. (2004) Novel organization of genes in a phthalate degradation operon of *Mycobacterium vanbaalenii* PYR-1, *Microbiology* 150, 3749-3761.
342. Willumsen, P. A., Nielsen, J. K., and Karlson, U. (2001) Degradation of phenanthrene-analogue azaarenes by *Mycobacterium gilvum* strain LB307T under aerobic conditions, *Appl Microbiol Biotechnol* 56, 539-544.

343. Sng, L. H., Koh, T. H., Toney, S. R., Floyd, M., Butler, W. R., and Tan, B. H. (2004) Bacteremia caused by *Gordonia bronchialis* in a patient with sequestered lung, *J Clin Microbiol* 42, 2870-2871.
344. (1990) Corrections. Cloning and sequence analysis of adrenodoxin reductase cDNA from bovine adrenal cortex, *J Biochem* 108, 1070.
345. Atsuta, Y., and Okuda, K. (1978) Isolation of rat liver mitochondrial ferredoxin and its reductase active in the 5 $\beta$ -cholestane-3 $\alpha$ , 7 $\alpha$ , 12 $\alpha$ -triol 26-hydroxylase, *J Biol Chem* 253, 4653-4658.
346. Dunford, A. J., Marshall, K. R., Munro, A. W., and Scrutton, N. S. (2004) Thermodynamic and kinetic analysis of the isolated FAD domain of rat neuronal nitric oxide synthase altered in the region of the FAD shielding residue Phe1395, *Eur J Biochem* 271, 2548-2560.
347. Balconi, E., Pennati, A., Crobu, D., Pandini, V., Cerutti, R., Zanetti, G., and Aliverti, A. (2009) The ferredoxin-NADP<sup>+</sup> reductase/ferredoxin electron transfer system of *Plasmodium falciparum*, *FEBS J* 276, 3825-3836.
348. Milani, M., Balconi, E., Aliverti, A., Mastrangelo, E., Seeber, F., Bolognesi, M., and Zanetti, G. (2007) Ferredoxin-NADP<sup>+</sup> reductase from *Plasmodium falciparum* undergoes NADP<sup>+</sup>-dependent dimerization and inactivation: functional and crystallographic analysis, *J Mol Biol* 367, 501-513.
349. Karplus, P. A., Daniels, M. J., and Herriott, J. R. (1991) Atomic structure of ferredoxin-NADP<sup>+</sup> reductase: prototype for a structurally novel flavoenzyme family, *Science* 251, 60-66.
350. Correll, C. C., Ludwig, M. L., Bruns, C. M., and Karplus, P. A. (1993) Structural prototypes for an extended family of flavoprotein reductases: comparison of phthalate dioxygenase reductase with ferredoxin reductase and ferredoxin, *Protein Sci* 2, 2112-2133.
351. Niviere, V., Fieschi, F., Decout, J. L., and Fontecave, M. (1996) Is the NAD(P)H:flavin oxidoreductase from *Escherichia coli* a member of the ferredoxin-NADP<sup>+</sup> reductase family?. Evidence for the catalytic role of serine 49 residue, *J Biol Chem* 271, 16656-16661.
352. Papandreou, P., and Rakitzis, E. T. (1989) Determination of NADH<sub>2</sub>-ferricyanide oxidoreductase (cytochrome b<sub>5</sub> reductase, diaphorase) activity of human erythrocytes by an analysis of the time-dependence of NADH<sub>2</sub> oxidation, *Clin Chim Acta* 181, 189-196.
353. Hasumi, H., Nakamura, S., Koga, K., Yoshizumi, H., Parcels, J. H., and Kimura, T. (1982) Further physicochemical studies on the complex formation between iron-sulfur proteins and flavoproteins from spinach chloroplast and beef adrenal cortex electron-transfer systems, *J Biochem* 91, 135-141.
354. Cryle, M. J., Matovic, N. J., and De Voss, J. J. (2003) Products of cytochrome P450(BioI) (CYP107H1)-catalyzed oxidation of fatty acids, *Org Lett* 5, 3341-3344.
355. Krapp, A. R., Rodriguez, R. E., Poli, H. O., Paladini, D. H., Palatnik, J. F., and Carrillo, N. (2002) The flavoenzyme ferredoxin (flavodoxin)-NADP(H) reductase modulates NADP(H) homeostasis during the soxRS response of *Escherichia coli*, *J Bacteriol* 184, 1474-1480.
356. Jenkins, C. M., and Waterman, M. R. (1994) Flavodoxin and NADPH-flavodoxin reductase from *Escherichia coli* support bovine cytochrome P450c17 hydroxylase activities, *J Biol Chem* 269, 27401-27408.
357. Fischer, F., Raimondi, D., Aliverti, A., and Zanetti, G. (2002) *Mycobacterium tuberculosis* FprA, a novel bacterial NADPH-ferredoxin reductase, *Eur J Biochem* 269, 3005-3013.

358. Arakaki, A. K., Ceccarelli, E. A., and Carrillo, N. (1997) Plant-type ferredoxin-NADP<sup>+</sup> reductases: a basal structural framework and a multiplicity of functions, *FASEB J* 11, 133-140.
359. Gibney, B. R., Mulholland, S. E., Rabanal, F., and Dutton, P. L. (1996) Ferredoxin and ferredoxin-heme maquettes, *Proc Natl Acad Sci U S A* 93, 15041-15046.
360. Chen, K., Bonagura, C. A., Tilley, G. J., McEvoy, J. P., Jung, Y. S., Armstrong, F. A., Stout, C. D., and Burgess, B. K. (2002) Crystal structures of ferredoxin variants exhibiting large changes in [Fe-S] reduction potential, *Nat Struct Biol* 9, 188-192.
361. Baumann, B., Sticht, H., Scharpf, M., Sutter, M., Haehnel, W., and Rosch, P. (1996) Structure of *Synechococcus elongatus* [Fe<sub>2</sub>S<sub>2</sub>] ferredoxin in solution, *Biochemistry* 35, 12831-12841.
362. Moulis, J. M. (1996) Molecular cloning and expression of the gene encoding *Chromatium vinosum* 2[4Fe-4S] ferredoxin, *Biochim Biophys Acta* 1308, 12-14.
363. Fujinaga, J., and Meyer, J. (1993) Cloning and expression in *Escherichia coli* of the gene encoding the [2Fe-2S] ferredoxin from *Clostridium pasteurianum*, *Biochem Biophys Res Commun* 192, 1115-1122.
364. Cammack, R., Neumann, J., Nelson, N., and Hall, D. O. (1971) Circular dichroism studies of the complex between ferredoxin and ferredoxin-NADP reductase, *Biochem Biophys Res Commun* 42, 292-297.
365. Ta, D. T., and Vickery, L. E. (1992) Cloning, sequencing, and overexpression of a [2Fe-2S] ferredoxin gene from *Escherichia coli*, *J Biol Chem* 267, 11120-11125.
366. Jensen, L. H. (1974) X-ray structural studies of ferredoxin and related electron carriers, *Annu Rev Biochem* 43, 461-507.
367. Leal, S. S., and Gomes, C. M. (2007) Studies of the molten globule state of ferredoxin: structural characterization and implications on protein folding and iron-sulfur center assembly, *Proteins* 68, 606-616.
368. Knaff, D. B., Smith, J. M., and Chain, R. K. (1980) Circular dichroism studies of ferredoxin:protein complexes, *Arch Biochem Biophys* 199, 117-122.
369. Przysiecki, C. T., Meyer, T. E., and Cusanovich, M. A. (1985) Circular dichroism and redox properties of high redox potential ferredoxins, *Biochemistry* 24, 2542-2549.
370. Bes, M. T., Parisini, E., Inda, L. A., Saraiva, L. M., Peleato, M. L., and Sheldrick, G. M. (1999) Crystal structure determination at 1.4 Å resolution of ferredoxin from the green alga *Chlorella fusca*, *Structure* 7, 1201-1211.
371. Giastas, P., Pinotsis, N., Efthymiou, G., Wilmanns, M., Kyritsis, P., Moulis, J. M., and Mavridis, I. M. (2006) The structure of the 2[4Fe-4S] ferredoxin from *Pseudomonas aeruginosa* at 1.32-Å resolution: comparison with other high-resolution structures of ferredoxins and contributing structural features to reduction potential values, *J Biol Inorg Chem* 11, 445-458.
372. Moulis, J. M., Sieker, L. C., Wilson, K. S., and Dauter, Z. (1996) Crystal structure of the 2[4Fe-4S] ferredoxin from *Chromatium vinosum*: evolutionary and mechanistic inferences for [3/4Fe-4S] ferredoxins, *Protein Sci* 5, 1765-1775.
373. Sery, A., Housset, D., Serre, L., Bonicel, J., Hatchikian, C., Frey, M., and Roth, M. (1994) Crystal structure of the ferredoxin I from *Desulfovibrio africanus* at 2.3 Å resolution, *Biochemistry* 33, 15408-15417.
374. Kissinger, C. R., Adman, E. T., Sieker, L. C., Jensen, L. H., and LeGall, J. (1989) The crystal structure of the three-iron ferredoxin II from *Desulfovibrio gigas*, *FEBS Lett* 244, 447-450.
375. Stephens, P. J., Jensen, G. M., Devlin, F. J., Morgan, T. V., Stout, C. D., Martin, A. E., and Burgess, B. K. (1991) Circular dichroism and magnetic circular dichroism of *Azotobacter vinelandii* ferredoxin I, *Biochemistry* 30, 3200-3209.

376. Stephens, P. J., McKenna, C. E., McKenna, M. C., Nguyen, H. T., and Devlin, F. (1981) Circular dichroism and magnetic circular dichroism of reduced molybdenum-iron protein of *Azotobacter vinelandii* nitrogenase, *Biochemistry* 20, 2857-2864.
377. Hasumi, H. (1982) Analyses of optical absorption and circular dichroism spectra of spinach ferredoxin at alkaline pH, *J Biochem* 92, 1049-1057.
378. Palmer, G., Brintzinger, H., and Estabrook, R. W. (1967) Spectroscopic studies on spinach ferredoxin and adrenodoxin, *Biochemistry* 6, 1658-1664.
379. Clements, A. P., Kilpatrick, L., Lu, W. P., Ragsdale, S. W., and Ferry, J. G. (1994) Characterization of the iron-sulfur clusters in ferredoxin from acetate-grown *Methanosarcina thermophila*, *J Bacteriol* 176, 2689-2693.
380. Hu, Z., Jollie, D., Burgess, B. K., Stephens, P. J., and Munck, E. (1994) Mossbauer and EPR studies of *Azotobacter vinelandii* ferredoxin I, *Biochemistry* 33, 14475-14485.
381. Stout, G. H., Turley, S., Sieker, L. C., and Jensen, L. H. (1988) Structure of ferredoxin I from *Azotobacter vinelandii*, *Proc Natl Acad Sci U S A* 85, 1020-1022.
382. Ghosh, D., Furey, W., Jr., O'Donnell, S., and Stout, C. D. (1981) Structure of a 7Fe ferredoxin from *Azotobacter vinelandii*, *J Biol Chem* 256, 4185-4192.
383. Howard, J. B., Lorsbach, T. W., Ghosh, D., Melis, K., and Stout, C. D. (1983) Structure of *Azotobacter vinelandii* 7Fe ferredoxin. Amino acid sequence and electron density maps of residues, *J Biol Chem* 258, 508-522.
384. Stout, C. D., Stura, E. A., and McRee, D. E. (1998) Structure of *Azotobacter vinelandii* 7Fe ferredoxin at 1.35 Å resolution and determination of the [Fe-S] bonds with 0.01 Å accuracy, *J Mol Biol* 278, 629-639.
385. Shaw, N. M., Birch, O. M., Tinschert, A., Venetz, V., Dietrich, R., and Savoy, L. A. (1998) Biotin synthase from *Escherichia coli*: isolation of an enzyme-generated intermediate and stoichiometry of S-adenosylmethionine use, *Biochem J* 330 ( Pt 3), 1079-1085.
386. Deeni, Y. Y., Paine, M. J., Ayrton, A. D., Clarke, S. E., Chenery, R., and Wolf, C. R. (2001) Expression, purification, and biochemical characterization of a human cytochrome P450 CYP2D6-NADPH cytochrome P450 reductase fusion protein, *Arch Biochem Biophys* 396, 16-24.
387. Jenkins, C. M., and Waterman, M. R. (1998) NADPH-flavodoxin reductase and flavodoxin from *Escherichia coli*: characteristics as a soluble microsomal P450 reductase, *Biochemistry* 37, 6106-6113.
388. Wang, Z. Q., Lawson, R. J., Buddha, M. R., Wei, C. C., Crane, B. R., Munro, A. W., and Stuehr, D. J. (2007) Bacterial flavodoxins support nitric oxide production by *Bacillus subtilis* nitric-oxide synthase, *J Biol Chem* 282, 2196-2202.
389. Lawson, R. J., von Wachenfeldt, C., Haq, I., Perkins, J., and Munro, A. W. (2004) Expression and characterization of the two flavodoxin proteins of *Bacillus subtilis*, YkuN and YkuP: biophysical properties and interactions with cytochrome P450 BioI, *Biochemistry* 43, 12390-12409.
390. Neeli, R., Sabri, M., McLean, K. J., Dunford, A. J., Scrutton, N. S., Leys, D., and Munro, A. W. (2008) Trp(359) regulates flavin thermodynamics and coenzyme selectivity in *Mycobacterium tuberculosis* FprA, *Biochem J* 411, 563-570.
391. Martinez-Julvez, M., Medina, M., and Velazquez-Campoy, A. (2009) Binding thermodynamics of ferredoxin:NADP<sup>+</sup> reductase: two different protein substrates and one energetics, *Biophys J* 96, 4966-4975.
392. Jelesarov, I., and Bosshard, H. R. (1994) Thermodynamics of ferredoxin binding to ferredoxin:NADP<sup>+</sup> reductase and the role of water at the complex interface, *Biochemistry* 33, 13321-13328.

393. Bruns, C. M., and Karplus, P. A. (1995) Refined crystal structure of spinach ferredoxin reductase at 1.7 Å resolution: oxidized, reduced and 2'-phospho-5'-AMP bound states, *J Mol Biol* 247, 125-145.
394. Pueyo, J. J., Gomez-Moreno, C., and Mayhew, S. G. (1991) Oxidation-reduction potentials of ferredoxin-NADP<sup>+</sup> reductase and flavodoxin from *Anabaena* PCC 7119 and their electrostatic and covalent complexes, *Eur J Biochem* 202, 1065-1071.
395. Yakunin, A. F., Hallenbeck, P. C., Troshina, O., and Gogotov, I. N. (1993) Purification and properties of a bacterial-type ferredoxin from the nitrogen-fixing cyanobacterium *Anabaena variabilis* ATCC29413, *Biochim Biophys Acta* 1163, 124-130.
396. Kuznetsova, S., Knaff, D. B., Hirasawa, M., Lagoutte, B., and Setif, P. (2004) Mechanism of spinach chloroplast ferredoxin-dependent nitrite reductase: spectroscopic evidence for intermediate states, *Biochemistry* 43, 510-517.
397. Isas, J. M., and Burgess, B. K. (1994) Purification and characterization of a NADP<sup>+</sup>/NADPH-specific flavoprotein that is overexpressed in FdI- strains of *Azotobacter vinelandii*, *J Biol Chem* 269, 19404-19409.
398. Seo, D., Kamino, K., Inoue, K., and Sakurai, H. (2004) Purification and characterization of ferredoxin-NADP<sup>+</sup> reductase encoded by *Bacillus subtilis* yumC, *Arch Microbiol* 182, 80-89.
399. Crobu, D., Canevari, G., Milani, M., Pandini, V., Vanoni, M. A., Bolognesi, M., Zanetti, G., and Aliverti, A. (2009) *Plasmodium falciparum* ferredoxin-NADP<sup>+</sup> reductase His286 plays a dual role in NADP(H) binding and catalysis, *Biochemistry* 48, 9525-9533.
400. Xu, F., Bell, S. G., Peng, Y., Johnson, E. O., Bartlam, M., Rao, Z., and Wong, L. L. (2009) Crystal structure of a ferredoxin reductase for the CYP199A2 system from *Rhodospseudomonas palustris*, *Proteins* 77, 867-880.
401. Ogura, H., Nishida, C. R., Hoch, U. R., Perera, R., Dawson, J. H., and Ortiz de Montellano, P. R. (2004) EpoK, a cytochrome P450 involved in biosynthesis of the anticancer agents epothilones A and B. Substrate-mediated rescue of a P450 enzyme, *Biochemistry* 43, 14712-14721.
402. Munro, A. W., Malarkey, K., McKnight, J., Thomson, A. J., Kelly, S. M., Price, N. C., Lindsay, J. G., Coggins, J. R., and Miles, J. S. (1994) The role of tryptophan 97 of cytochrome P450 BM3 from *Bacillus megaterium* in catalytic function. Evidence against the 'covalent switching' hypothesis of P-450 electron transfer, *Biochem J* 303 ( Pt 2), 423-428.